Vol. 65 ▪ No. 1 ▪ January 2024

JNM

The Journal of Nuclear Medicine

JNM Podcasts
jnm.snmjournals.org/podcasts

The debut episode discussing FAP is coming soon!

FEATURED ARTICLE

Imaging of Myocardial $\alpha_v\beta_3$ Integrin Expression for Evaluation of Myocardial Injury After Acute Myocardial Infarction. Wail Nammas et al. See page 132.

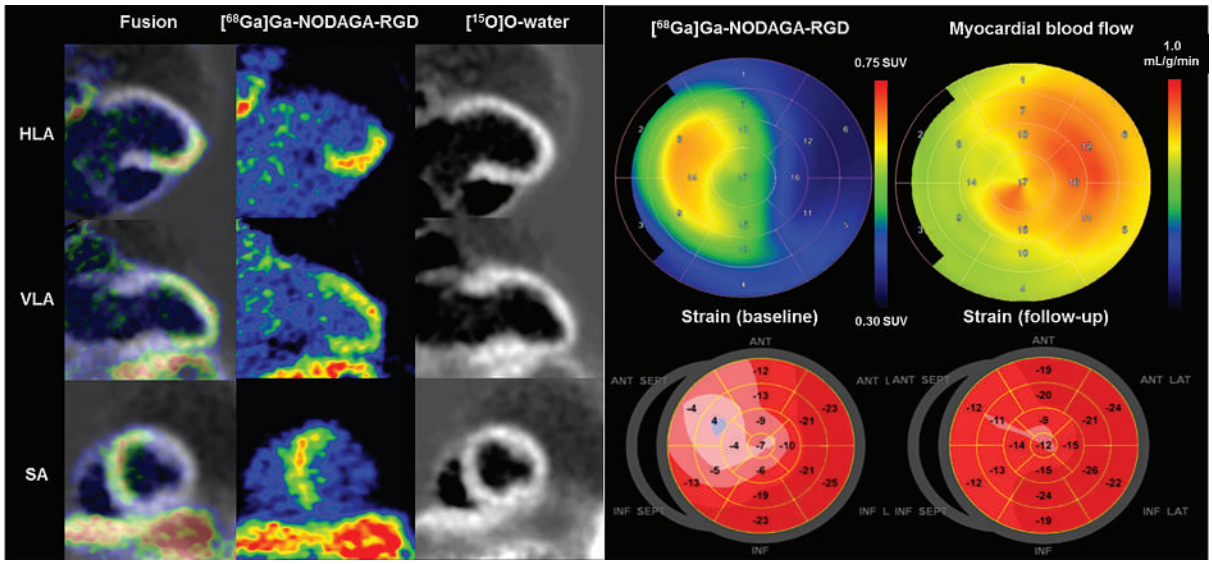

Novel minigastrin analogs: Investigating a promising theranostic agent targeting medullary thyroid cancer. Thomas Günther et al. See page 33.

SNMMI SOCIETY OF NUCLEAR MEDICINE & MOLECULAR IMAGING

2024 ACNM/SNMMI **HOT TOPICS** Webinar Series

SNMMI and ACNM are excited to announce the lineup for the 2024 Hot Topics Webinar Series. **These informative webinars will take place at 12:00 pm ET on the second Tuesday of each month and are complimentary for ACNM and SNMMI members.**

- **History of Nuclear Medicine Technology**
  January 9 | *Fred Fahey*
- **AI in Nuclear Medicine: State of the Union**
  February 13 | *Katherine Zukotynski*
- **Prostate Radioligand Therapy Prior to Chemotherapy**
  March 12 | *Oliver Sartor*
- **PET/MR for Pediatrics**
  April 9 | *Helen Nadel*
- **Evolving Landscape of Prostate Cancer Imaging**
  May 14 | *François Bénard*
- **The Evolution of PRRT for NET–Y90, Lu177, Ac225**
  June-SNMMI AM | *Lisa Bodei*
- **Advancing Precision Therapeutics in Dementia–How Does Imaging Fit In?**
  July 9 | *Sandra Black*
- **Contemporary Approach to PET Myocardial Perfusion Imaging**
  August 13 | *Panithaya Chareonthaitawee*
- **ER/PR/HER2-Targeted Imaging for Breast Cancer**
  September 10 | *Farrokh Dehdashti*
- **PET for Histiocytosis/ Erdheim Chester Disease**
  October 8 | *Sonia Mahajan*
- **What is New in Infection Imaging?**
  November 12 | *Ora Israel*
- **Prostate Cancer Imaging Agents–Is There a Difference?**
  December 10 | *Wolfgang Weber*

SNMMI SOCIETY OF NUCLEAR MEDICINE & MOLECULAR IMAGING

ACNM American College of Nuclear Medicine

Register today!

www.acnmonline.org/webinars

SCAN QR CODE FOR MORE INFORMATION

Innovate. Illuminate.

June 8-11

2024 SNMMI ANNUAL MEETING

CANADA TORONTO

The premier educational, scientific, research, and networking event in nuclear medicine and molecular imaging, the SNMMI Annual Meeting provides physicians, technologists, pharmacists, laboratory professionals, and scientists with an in-depth view of the latest research and development in the field as well as providing insights into practical applications for the clinic.

Mark your calendars to join us in Toronto, June 8-11, 2024, for a front-row seat to explore the most important nuclear medicine and molecular imaging science and research happening throughout the world.

Registration is opening soon!

Registration Opening Soon!

SNMMI SOCIETY OF NUCLEAR MEDICINE & MOLECULAR IMAGING

ANNUAL MEETING

JNM

Volume 65 • Number 1 • January 2024

DISCUSSIONS WITH LEADERS

STATE OF THE ART

HOT TOPICS

ONCOLOGY

Clinical

Basic

THERANOSTICS

Clinical

Basic

JNM The Journal of NUCLEAR MEDICINE

The Official Publication of **SNMMI**

MISSION STATEMENT: *The Journal of Nuclear Medicine* advances the knowledge and practice of molecular imaging and therapy and nuclear medicine to improve patient care through publication of original basic science and clinical research.

JNM (ISSN 0161-5505 [print]; ISSN 2159-662X [online]) is published monthly by SNMMI, 1850 Samuel Morse Drive, Reston, VA 20190-5316. Periodicals postage is paid at Herndon, VA, and additional mailing offices. Postmaster, send address changes to *The Journal of Nuclear Medicine,* 1850 Samuel Morse Drive, Reston, VA 20190-5316. The costs of publication of all nonsolicited articles in *JNM* were defrayed in part by the payment of page charges. Therefore, and solely to indicate this fact, these articles are hereby designated "advertisements" in accordance with 18 USC section 1734.

DISCLOSURE OF COMMERCIAL INTEREST: Johannes Czernin, MD, editor-in-chief of *The Journal of Nuclear Medicine,* has indicated that he is a founder of Sofie Biosciences and holds equity in the company and in intellectual property invented by him, patented by the University of California, and licensed to Sofie Biosciences. He is also a founder and board member of Trethera Therapeutics and holds equity in the company and in intellectual property invented by him, patented by the University of California, and licensed to Triangle. He also serves on the medical advisory board of Actinium Pharmaceuticals and on the scientific advisory boards of POINT Biopharma, RayzeBio, and Jubilant Pharma and is a consultant for Amgen. No other potential conflicts of interest were reported. Manuscripts submitted to *JNM* with potential conflicts are handled by a guest editor.

EDITORIAL COMMUNICATIONS should be sent to: Editor-in-Chief, Johannes Czernin, MD, *JNM* Office, SNMMI, 1850 Samuel Morse Drive, Reston, VA 20190-5316. Phone: (703) 326-1185; Fax: (703) 708-9018. To submit a manuscript, go to https://submit-jnm.snmjournals.org.

BUSINESS COMMUNICATIONS concerning permission requests should be sent to the publisher, SNMMI, 1850 Samuel Morse Drive, Reston, VA 20190-5316; (703) 708-9000; home page address: jnm.snmjournals.org. Subscription requests and address changes should be sent to Membership Department, SNMMI at the address above. Notify the Society of change of address and telephone number at least 30 days before date of issue by sending both the old and new addresses. Claims for copies lost in the mail are allowed within 90 days of the date of issue. Claims are not allowed for issues lost as a result of insufficient notice of change of address. For information on advertising, contact Team SNMMI (Kevin Dunn, Rich Devanna, and Charlie Meitner; (201) 767-4170; fax: (201) 767-8065; TeamSNMMI@cunnasso.com). Advertisements are subject to editorial approval and are restricted to products or services pertinent to nuclear medicine. Closing date is the first of the month preceding the date of issue.

INDIVIDUAL SUBSCRIPTION RATES for the 2024 calendar year are $665 within the United States and Canada; $714 elsewhere. Make checks payable to the SNMMI. CPC IPM Sales Agreement No. 1415158. Sales of individual back copies from 1999 through the current issue are available for $60 at http://www.snmmi.org/subscribe (subscriptions@snmmi.org; fax: (703) 667-5134). Individual articles are available for sale online at http://jnm.snmjournals.org.

DISCOVER SNMMI

ADVANCING NUCLEAR MEDICINE & MOLECULAR IMAGING

The Society of Nuclear Medicine and Molecular Imaging (SNMMI) is a leading organization dedicated to advancing the fields of nuclear medicine and molecular imaging, with a mission to improve healthcare through research, education, advocacy, and professional development opportunities. SNMMI serves as a vital hub for healthcare professionals and researchers to collaborate, access cutting-edge resources, and drive innovations that enhance patient care.

Join us in our mission to revolutionize patient care through nuclear medicine and molecular imaging.

MEMBERSHIP BENEFITS

Become an SNMMI member and gain access to a world of benefits, including:

- ❑ Exclusive educational resources.
- ❑ Networking opportunities with experts.
- ❑ Professional development programs.
- ❑ Member-only events and publications.

CONNECT WITH US

SNMMI | SOCIETY OF NUCLEAR MEDICINE & MOLECULAR IMAGING

WHAT IS AN SNMMI RPT CENTER OF EXCELLENCE?

To learn more and apply, visit
www.snmmi.org/RPTCOE

SNMMI created the Radiopharmaceutical Therapy (RPT) Center of Excellence (COE) Program to allow centers with expertise in RPT to showcase their capabilities and services, including research. A designation means that your site has the personnel, expertise, and equipment to manage the care of patients requiring RPT. The designations levels are Comprehensive, Clinical, or Basic Therapy Center.

Targeted RPTs are changing the way patients with cancer are treated. These advances have allowed providers to treat and manage a multitude of other cancers and diseases. Not all sites have the expertise to use these agents clinically or in clinical trials.

If your site has experience with one or more radiopharmaceutical therapies, we encourage you to apply for the SNMMI RPTCOE designation.

COMPREHENSIVE RPT CENTER

An application fee of $1,500 for members and $2,500 for non-members is required for a 2-year designation.

SCAN QR CODE TO APPLY

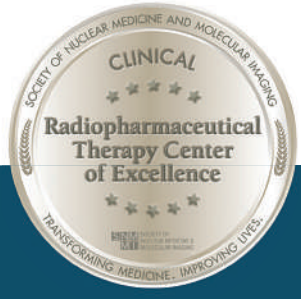

CLINICAL RPT CENTER

An application fee of $900 for members and $1,500 for non-members is required for a 2-year designation.

SCAN QR CODE TO APPLY

BASIC RPT CENTER

The designation does not require any application fee and is valid for a 2-year designation.

SCAN QR CODE TO APPLY

Expanding the influence of SNMMI: Johannes Czernin talks with Virginia Pappas, SNMMI CEO, about her career in professional society leadership. . . . . ***Page 1***

AI for PET and SPECT: Balaji and colleagues present a survey of state-of-the-art artificial intelligence methods for PET and SPECT image enhancement and identify emerging trends, including likelihood of clinical benefit.. . . . . ***Page 4***

Time to retire PIOPED? Zuckier and Boone review the history and current relevance of clinical practice based on the 1990 Prospective Investigation of Pulmonary Embolism Diagnosis study and call for development of innovative artificial intelligence–powered approaches. . . . . ***Page 13***

^{18}F-FET PET and MRSI in glioma: Mauler and colleagues compare the contributions of MR spectroscopic imaging and amino acid PET in improving detection of tumor tissue in untreated patients with suspected glioma. . . . . ***Page 16***

Pediatric PET/MRI and COVID-19 vaccine: Luthria and colleagues explore the ability of ^{18}F-FDG PET/MR imaging to reveal thymus activation in addition to local lymph node reactions after COVID-19 vaccination in children with extrathoracic cancers. . . . . ***Page 22***

LAG-3 PET for monitoring immunotherapy: Quan and colleagues evaluate a PET approach for assessing immunotherapy response in lung cancer by imaging upregulation of lymphocyte activation gene 3–expressing tumor-infiltrating lymphocytes. . . . . ***Page 25***

Preclinical evaluation of CCK-2R ligands: Günther and colleagues describe initial basic and murine stability studies with 2 DOTA-MGS5–derived ligands targeting the cholecystokinin-2 receptor and report on proof-of-concept studies with [^{68}Ga]Ga-DOTA-CCK-66 in patients with medullary thyroid cancer. . . . . ***Page 33***

^{18}F-FAPI-74 versus ^{18}F-FDG: Xu and colleagues investigate the diagnostic accuracy of ^{18}F-fibroblast activation protein inhibitor-74 PET/CT in gastric, liver, and pancreatic cancers and compare the results with those from ^{18}F-FDG PET/CT. . . . . ***Page 40***

^{68}Ga-FAPI PET in pancreatic neoplasms: Spektor and colleagues validate fibroblast activation protein as a target for PET imaging by analyzing immunohistochemical FAP expression in low- and high-grade intraductal papillary mucinous neoplasms and pancreatic ductal adenocarcinomas. . . . . ***Page 52***

FAPI tracer uptake in epididymis: Maliha and colleagues characterize occasional epididymal uptake patterns of [^{68}Ga]Ga-fibroblast activation protein inhibitor-46 on PET in 55 men. . ***Page 59***

Cell-free DNA and [^{68}Ga]Ga-PSMA-11: Kluge and colleagues explore the relationship and prognostic value of cell-free DNA concentrations and PSMA-positive tumor volume in men with prostate cancer undergoing [^{68}Ga]Ga-PSMA-11 PET/CT imaging. . . . . ***Page 63***

Safety in the VISION dosimetry substudy: Herrmann and colleagues analyze ^{177}Lu-PSMA-617 renal and multiorgan safety in patients with metastatic castration-resistant prostate cancer in the VISION dosimetry substudy and look at organ-at-risk cumulative absorbed doses predicted from cycle 1 treatment data. . . . . ***Page 71***

Long-term nephrotoxicity and ^{177}Lu-PSMA RLT: Steinhelfer and colleagues evaluate post–^{177}Lu-PSMA estimated glomerular filtration rate dynamics over ≥12 mo in patients with metastatic castration-resistant prostate cancer. . . . . ***Page 79***

PSMA RLT and renal impairment: Ravi Kumar and Hofman provide perspective on PSMA radioligand therapy in prostate cancer and on challenges associated with researching long-term safety in patient groups with limited survival and multiple comorbidities. . . . . ***Page 85***

PSMA PET segmentation versus histopathology: Wang and colleagues assess the accuracy of intraprostatic tumor volume measurements on PSMA-targeted ^{18}F-DCFPyL PET/CT made with various segmentation methods and compare these with histopathologic results. . . . . ***Page 87***

Real-world validation of PRIMARY score: Emmett and colleagues assess the reproducibility and diagnostic accuracy of the PRIMARY score in a large cohort of patients who underwent multiparametric MRI and ^{68}Ga-PSMA PET before diagnostic prostate biopsy.. . . . . ***Page 94***

Boronic acid–based FAP radioligands: Poplawski and colleagues detail preclinical development of PNT6555, a boronic acid–based, fibroblast activation protein-α–targeted radiotheranostic for imaging and treatment of FAP-positive tumors. . . . . ***Page 100***

^{212}Pb-pretargeted theranostics for pancreatic cancer: Bauer and colleagues demonstrate the feasibility and safety of pretargeted α-particle therapy with ^{212}Pb in pancreatic ductal adenocarcinoma and discuss dose limitations and potential adverse effects. . . . . ***Page 109***

^{68}Ga-pentixafor in primary aldosteronism: Ding and colleagues investigate the clinical value of ^{68}Ga-pentixafor PET/CT in subtype diagnosis of primary aldosteronism patients with adrenal micronodules <1 cm in diameter and compare results with those from routine clinical methods. . . . . ***Page 117***

QA and RPT dosimetry: Kayal and colleagues from an IAEA research group report on disparities in structured analyses of radiopharmaceutical therapy SPECT/CT images acquired at various sites using the same protocol and software, highlighting the need for quality assurance. . . . . ***Page 125***

$\alpha_v\beta_3$ integrin expression after AMI: Nammas and colleagues prospectively evaluate determinants of myocardial uptake of [^{68}Ga]Ga-NODAGA-RGD, a PET tracer targeting $\alpha_v\beta_3$ integrin, and its associations with left ventricular function in patients after acute myocardial infarction. . . . . ***Page 132***

Automated cardiac PET MC: Kuronuma and colleagues develop an automated motion correction algorithm for time–activity curves used in compartmental modeling and compare the predictive value of PET myocardial blood flow with and without this correction in coronary artery disease. . . . . ***Page 139***

^{18}F-FDG PET or MRI for brain age gap: Doering and colleagues compare MRI- and ^{18}F-FDG PET–derived brain age gap assessments with cognitive performance, neuropathologic burden, and disease progression in normal, cognitively declining, and cognitively impaired individuals. . . . . ***Page 147***

Baseline PET radiomics in GAINED study: Carlier and colleagues research the potential added value of baseline predictive PET radiomics features in survival of patients in this randomized phase III trial in diffuse large B-cell lymphoma. . . . . ***Page 156***

Multiple myeloma and [^{99m}Tc]Tc-PentixaTec: Enke and colleagues present a case study of whole-body imaging with this tracer in a patient with relapsed multiple myeloma and discuss its potential as an alternative to C-X-C motif chemokine receptor 4–targeted PET vectors. . . . . ***Page 163***

Expanding the Mission and Influence of SNMMI

A Conversation Between Johannes Czernin and Virginia Pappas About Her Career in SNMMI Leadership

Virginia Pappas[1] and Johannes Czernin[2]

[1]Society of Nuclear Medicine and Molecular Imaging, Reston, Virginia; and [2]David Geffen School of Medicine at UCLA, Los Angeles, California

Johannes Czernin, MD, editor-in-chief of *The Journal of Nuclear Medicine* and a professor at the David Geffen School of Medicine at UCLA, talked with Virginia Pappas, CAE, chief executive officer (CEO) of the Society of Nuclear Medicine and Molecular Imaging (SNMMI), about her career in professional society leadership. For more than 45 years she has worked in various capacities to advance the society's mission and the interests of its diverse membership. Her involvement in multiple efforts to make the wider medical community aware of the evolving roles of nuclear medicine has resulted in authorship of more than 50 peer-reviewed publications. In June 2023 she was recognized as an honorary SNMMI Fellow for her many years of service to the society.

Dr. Czernin: *Virginia, you have been an SNMMI leader for quite some time. How did you enter the field of nuclear medicine?*

Ms. Pappas: In 1978 I was working for a hematologist at Cabrini Health in Manhattan in the blood bank, but I looked for a change. I applied for an open position at the (then) Society of Nuclear Medicine. I knew nothing about association management or nuclear medicine, and the proposed position paid less than another job that I was offered at Cornell. But I liked the opportunity and started out as assistant to the director of administration, working directly with the executive director. What it brought to me was not only work in nuclear medicine and medicine in general but also association management, which turned into a career. A few years later I became first the director of administration and then the deputy executive director, and over the course of time, I have held just about every director position. My time at the society has always been creative, always doing something different. And that's how I ended up in my current position.

Dr. Czernin: *When did you become the CEO?*

Ms. Pappas: March 1, 2002.

Dr. Czernin: *How many members did SNMMI have when you started?*

Ms. Pappas: The society had 17,000–18,000 members. Membership has decreased slightly over time, because not enough nuclear medicine physicians and technologists have entered the field to replace those who have retired.

Dr. Czernin: *With the emergence of theranostics as the major driving force in nuclear medicine, do you already see a change? Are physicians coming back?*

Ms. Pappas: Not yet, but we do anticipate growth. I see a resurgence of interest and enthusiasm, especially among younger nuclear medicine practitioners. We're developing programs for them, such as the SNMMI Future Leaders Academy. We are also actively reaching out to residents and medical students to attract them to the field.

Virginia Pappas, CAE

Dr. Czernin: *Eli Lilly and Company recently acquired POINT Biopharma Global, Inc., and the Novartis acquisition of Advanced Accelerator Applications is a well-known story. The National Institutes of Health offer various funding mechanisms to foster industry–academia collaborations, thus suggesting that these collaborations are no longer considered immoral. The same awareness has emerged in academic institutions that need the support of industry to create startup companies to monetize intellectual property they create. Are you creating a home for smaller biotech as well as major pharmaceutical companies in SNMMI, so that they can become corporate or individual members?*

Ms. Pappas: Yes and no. As a specialty society, we have to follow very strict rules about the involvement of industry in our programs and education. We don't have an industry membership category, but we do have affiliate memberships for individuals who work for industry. Although these members can't serve on committees or influence our strategic plan directly or indirectly, we offer a lot of advantages for companies. Through the Industry Partners Circle of our Center for Molecular Imaging Innovation and Translation, we invite industry and academia to come together to improve scientific collaborations. They meet at least once a year to tackle issues in this area.

Dr. Czernin: *SNMMI now has around 15,000 members. This year's hybrid annual meeting had a high attendance of around 7,000. Do you see the European Association of Nuclear Medicine (EANM) as the major competitor? Is such competition actually good, in that it creates a larger market?*

Ms. Pappas: We have a very friendly competition with the EANM. Both our meetings attract attendees from around the world, and membership is international for both societies. We compete mainly on the format of meetings and types of programming, and as you mention, competition is actually good for both organizations. In the United States, our biggest competition comes from the radiology societies, since many of our physician members are now dual boarded in radiology and nuclear medicine.

DOI: 10.2967/jnumed.123.267086

Dr. Czernin: *You have made significant progress in selecting more attractive meeting sites, which makes the meeting more competitive. Sites such as Washington, DC, Toronto, Vancouver, Chicago, and New Orleans are really attractive. This helps to increase in-person attendance.*

Ms. Pappas: The SNMMI meeting has grown over the years, and we have specific space requirements for our meeting. The scientific program committee decided to rotate through a few large cities, thus making the meeting more attractive and competitive.

Dr. Czernin: *SNMMI has created the Value Initiative. Could you describe its purpose and the targeted outcomes?*

Ms. Pappas: Satoshi Minoshima, MD, PhD, created the idea for the SNMMI Value Initiative, which seeks to educate and promote the value of nuclear medicine to the community at large, including industry and government. This initiative focuses on quality of practice, research and discovery, advocacy, workforce pipeline and lifelong learning, outreach, and organizational strength and stability. We have raised more than $10 million in 6 years, which has enabled SNMMI to increase programming and activities in every single domain. It has increased the enthusiasm of industry participants at our meetings for supporting SNMMI in other areas, including exhibits, advertising, and sponsorship.

The society's core values are innovation, education, and research. Our number 1 goal (as it has been for many years) is to continue the growth of the profession and help our members with resources and education. The SNMMI Mars Shot for Nuclear Medicine, Molecular Imaging, and Molecularly Targeted Radiopharmaceutical Therapy, created by Richard Wahl, MD, is an example of the ways in which we're working to enhance research in the profession.

Dr. Czernin: *One initiative that was talked about was attracting young people to join the field, even involving high school students by offering educational opportunities. Is that something that is still being pursued in terms of making the field better known?*

Ms. Pappas: Yes. We're working with science teacher organizations and with medical student organizations to increase awareness of the field, as well as actively engaging with the American Medical Association in their medical student and resident sections. We also just created a video series, "Jobs of Tomorrow," to educate young people on the career opportunities available for physicians, scientists, and technologists within the profession. The workforce pipeline domain's goals are to develop programs and find ways to encourage physician–scientists and technologists to enter the field.

Dr. Czernin: *Let me get back to the SNMMI annual meeting. Heather Jacene, MD, is doing an excellent job as chair of the scientific program committee. Of course, professional scientific meetings are always works in progress, but what areas of improvement would you like to see for the meeting?*

Ms. Pappas: One of the main goals of the new SNMMI strategic plan is to reimagine the annual meeting. Dr. Jacene and the scientific program committee are doing a wonderful job. Changes will be made over the next several years to make the annual meeting more entertaining and interactive, as well as adding more meeting spaces where people can network. Simplifying the meeting is also a consideration, by streamlining the sessions, avoiding duplication in programming, and improving the poster sessions. This is a heavy lift, since SNMMI has so many constituents.

Dr. Czernin: *That was my next question. The EANM website lists 15 major committees. SNMMI has innumerable committees and subcommittees. The meeting design should be led by a small leadership group that then recruits people who know about specific areas. They can then help with recruiting the best national and international speakers. Do you agree that we have too many committees at SNMMI?*

Ms. Pappas: Another major goal of the SNMMI strategic plan is to redesign the governance structure. Yes, there are too many committees, and we just keep adding more. We find it difficult to eliminate committees once they are created, even when they no longer have significant roles. The redesign task force is looking very critically at duplication and whether some committees are still needed. However, we have 3 distinct constituents in our membership, each with its own foci and needs: the technologist component, the practicing physicians, and the scientists. The redesign task force is currently working on this and has completed a survey looking at every single committee to ask, "What is your goal? What are your objectives? Have these been met? Are you still current? Are you still needed today?"

Dr. Czernin: *Isn't it difficult for a committee to say, "We're no longer needed"?*

Ms. Pappas: Yes.

`SNMMI is a wonderful source of innovation and vision. Nuclear medicine and theranostics are among the most exciting fields in medicine. The patient-centric creativity and innovation keep us all engaged. New therapies have turned around the visibility and image of nuclear medicine and are making extraordinary differences in the lives of our patients.´

Dr. Czernin: *Wouldn't it be more efficient to ask leadership to decide whether a committee is still needed? I asked that once of a previous program chair, and the response was, "But I cannot disenfranchise the committees." I replied, "Oh, you have to. There's no way around it. You have to disenfranchise the committees."*

Ms. Pappas: The redesign task force will spend the next year performing surveys and interviewing other organizations to be able to make recommendations to SNMMI leadership and the board of directors. The goal is to simplify the governance structure. I really believe that with a redesign, we will eliminate a large number of committees and improve our structure and function. We have more than 100 committees right now and more than 700 associated volunteers, not including speakers and editorial board members.

Dr. Czernin: *That's a nightmare!*

Ms. Pappas: Yes, and we have limited staff resources to manage them.

Dr. Czernin: *The structure of governance and leadership of SNMMI is also different from that of other organizations, where presidents may be in office for 2 or 3 years to get work done. SNMMI has 1-year terms.*

Ms. Pappas: There have been some discussions about increasing the SNMMI presidential term to 2 years. But the 1-year term has not been a problem, because SNMMI leadership members work closely together, beginning with the vice-president-elect term. So before assuming office, our presidents have 2 years of

active preparation in understanding the issues, meeting international leaders, etc.

Dr. Czernin: *Fairly recently you initiated a survey of the SNMMI membership. What were the key outcomes? What were the membership's most important and relevant concerns or suggestions?*

Ms. Pappas: We conducted several surveys, including one for the website and another for the SNMMI strategic plan. Regarding the website, a redesign is absolutely necessary to create a more modern site to which members can come to locate essential information for professional needs and to answer questions about SNMMI. Our new website is planned to be up and running in June 2024.

The survey of our members identified several opportunities and challenges, including the need to focus on theranostics and capacity building, improve communication and messaging so that members know what we are doing for them, follow through with organizational redesign and restructuring of the society, and address workforce pipeline and reimbursement issues.

Dr. Czernin: *Based on the strategic initiatives, what are the priorities for the next 3–5 years?*

Ms. Pappas: Radiopharmaceutical therapy (RPT) is obviously at the top of the list, including creating educational programs in RPT, advancing our Therapy Center of Excellence program, and establishing productive relationships with referring physicians. Improving patient access to high-quality treatment centers is another important priority. As mentioned before, target efforts also include redesigning the annual meeting and society governance structure, improving and increasing communication, enhancing educational opportunities, and creating a platform for a new and more user-friendly learning management system. We would also like to become more integrated and established within the National Comprehensive Cancer Network and similar alliances. All these are priorities.

Dr. Czernin: *All these future goals will cost money. Are new finance models under consideration? Is it allowed to ask industry for support?*

Ms. Pappas: If the Value Initiative continues to be strong, we're raising more than $2 million/year. If this continues at the current level, it's more than enough to help us do the work we need to do.

Dr. Czernin: *Who is supporting the Value Initiative?*

Ms. Pappas: Around 35 companies contribute to the Value Initiative. This may grow significantly with the growing industry interest in theranostics. The funds raised are used to further the goals of the Value Initiative domains. We have many meetings with industry, including in one-on-one settings, as part of the Value Initiative and via industry advisory board meetings. Companies can share information, provide feedback, and give us suggestions about areas in which we could improve. Often strategies of the society align with those of these companies.

Dr. Czernin: *Any good enterprise must have a leadership succession plan, whether short- or long-term. What is your succession plan at SNMMI?*

Ms. Pappas: A good association will conduct a search via a search company, and the succession can be from within or from the outside. The good news about SNMMI is that we have a strong leadership team. If needed, our leadership team and the board could step up and assign an interim CEO. I was the interim director 3 times during periods when the society searched for a new executive director. The society will run very competently with or without me. To handpick someone would not be the best way to go about succession.

Dr. Czernin: *We usually end this discussion by asking the interviewee for a special message about our field for young people. What would be your message for the next generation, either the administrative leaders or people joining the field of nuclear medicine?*

Ms. Pappas: SNMMI is a wonderful source of innovation and vision. Nuclear medicine and theranostics are among the most exciting fields in medicine. The patient-centric creativity and innovation keep us all engaged. New therapies have turned around the visibility and image of nuclear medicine and are making extraordinary differences in the lives of our patients.

Dr. Czernin: *With this I thank you for your service and contributions and for sharing your views with our readers.*

Artificial Intelligence for PET and SPECT Image Enhancement

Vibha Balaji[1], Tzu-An Song[1], Masoud Malekzadeh[1], Pedram Heidari[2], and Joyita Dutta[1]

[1]*Department of Biomedical Engineering, University of Massachusetts Amherst, Amherst, Massachusetts; and* [2]*Division of Nuclear Medicine and Molecular Imaging, Department of Radiology, Massachusetts General Hospital, Boston, Massachusetts*

Nuclear medicine imaging modalities such as PET and SPECT are confounded by high noise levels and low spatial resolution, necessitating postreconstruction image enhancement to improve their quality and quantitative accuracy. Artificial intelligence (AI) models such as convolutional neural networks, U-Nets, and generative adversarial networks have shown promising outcomes in enhancing PET and SPECT images. This review article presents a comprehensive survey of state-of-the-art AI methods for PET and SPECT image enhancement and seeks to identify emerging trends in this field. We focus on recent breakthroughs in AI-based PET and SPECT image denoising and deblurring. Supervised deep-learning models have shown great potential in reducing radiotracer dose and scan times without sacrificing image quality and diagnostic accuracy. However, the clinical utility of these methods is often limited by their need for paired clean and corrupt datasets for training. This has motivated research into unsupervised alternatives that can overcome this limitation by relying on only corrupt inputs or unpaired datasets to train models. This review highlights recently published supervised and unsupervised efforts toward AI-based PET and SPECT image enhancement. We discuss cross-scanner and cross-protocol training efforts, which can greatly enhance the clinical translatability of AI-based image enhancement tools. We also aim to address the looming question of whether the improvements in image quality generated by AI models lead to actual clinical benefit. To this end, we discuss works that have focused on task-specific objective clinical evaluation of AI models for image enhancement or incorporated clinical metrics into their loss functions to guide the image generation process. Finally, we discuss emerging research directions, which include the exploration of novel training paradigms, curation of larger task-specific datasets, and objective clinical evaluation that will enable the realization of the full translation potential of these models in the future.

Key Words: artificial intelligence; denoising; superresolution; PET; SPECT

J Nucl Med 2024; 65:4–12
DOI: 10.2967/jnumed.122.265000

PET and SPECT are nuclear medicine–based molecular imaging modalities that generate 3-dimensional (3D) visualizations of the biodistribution of exogenous radiotracers. These modalities provide functional and physiological information and are vital for disease diagnostics, staging, treatment planning, and therapeutic evaluation for a wide range of disorders, including many cancer types, neurodegenerative disorders, cardiovascular disease, and musculoskeletal disorders (*1–6*). Recent advances in hardware and software have greatly enhanced the quantitative capabilities of PET and SPECT imaging, addressing issues related to both high noise and low spatial resolution, while also augmenting their traditionally semiquantitative clinical utility. The emergence of artificial intelligence (AI) has brought forth a multitude of image enhancement techniques for denoising, deblurring, and partial-volume correction of PET and SPECT images. AI-based enhancement methods can be implemented after reconstruction into existing PET/SPECT clinical workflows to achieve purely software-based improvement in image quality without expensive hardware upgrades. These models that learn image representations directly from data benefit from the increasing volume (i.e., more training examples) and variety (i.e., a diverse training population) of training datasets. AI-based image enhancement techniques accomplish a range of tasks, including boosting the signal-to-noise ratio, enhancing spatial resolution, shortening scan times, and reducing radiotracer dose. In this review, we discuss emerging denoising and deblurring techniques that can be potentially transformative for PET and SPECT imaging.

Most AI-based image enhancement techniques rely on a deep-learning model that receives a corrupt image as its input and generates a clean image as its output. For denoising, the corrupt input image is noisy, whereas for deblurring, it is low resolution. Deblurring efforts for PET and SPECT encompass partial volume correction approaches that seek to mitigate the partial volume effect. The latter arises from the blurring of tissue boundaries (the predominant factor for modalities such as PET and SPECT) and discretizing the image space (*7*). Unlike image reconstruction, AI-based image enhancement models do not require raw data and can be readily trained and validated by existing image repositories. These methods are thus rapidly gaining popularity in nuclear medicine, where large image-domain datasets are much more accessible than list-mode or sinogram datasets. AI models for image enhancement have consistently outperformed filtering, deconvolution, and other traditional analytic or model-based iterative approaches for denoising or partial volume correction. AI has led to new approaches for multimodality fusion (*8*) that can provide improved cross-modality anatomic guidance to PET and SPECT using information from high-resolution MRI or CT. The evolution of deep neural network architectures, training strategies, and data requirements over the past several years has contributed to the accuracy, usability, robustness, and versatility of these models.

Figure 1 presents a Preferred Reporting Items for Systematic Reviews and Meta-Analyses (PRISMA) flowchart illustrating this review's systematic article selection process, and Figure 2 offers a breakdown of the selected articles. We exclude articles that involve

Received Apr. 14, 2023; revision accepted Oct. 10, 2023.
For correspondence or reprints, contact Joyita Dutta (jdutta@umass.edu).
Published online Nov. 9, 2023.

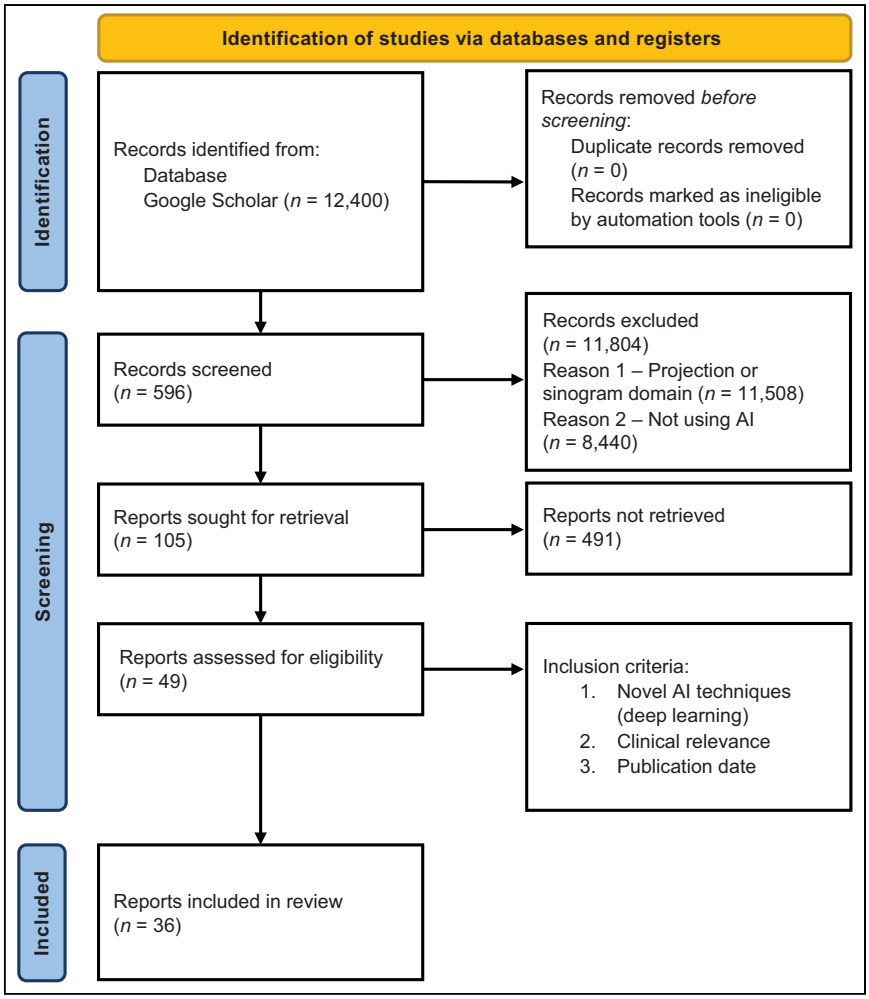

FIGURE 1. PRISMA flow diagram demonstrating selection strategy of research articles included in review.

projection- or sinogram-domain approaches, data correction techniques, and motion compensation methods. In the subsequent sections, we present a survey of recent works on PET and SPECT image enhancement and highlight emerging areas in this field. We provide an overview of predominant deep-learning architectures, loss functions, and training strategies relevant to PET and SPECT image enhancement. We then present and chronologically tabulate a selection of related articles for each modality, emphasizing publications from the last 2 y. A discussion of emerging directions concludes the review.

NOTEWORTHY

- A variety of recent advances in deep neural network architectures, loss functions, and training strategies have facilitated the application of AI models to PET and SPECT image enhancement.
- Unlike supervised learning models, which require paired corrupt and clean images for training, emerging unsupervised approaches obviate paired training data and are better suited for most clinical image enhancement applications.
- Task-based objective clinical evaluation of AI-based approaches for PET and SPECT image enhancement is required to ensure their future clinical and diagnostic use.

TECHNICAL CONSIDERATIONS FOR AI-BASED IMAGE ENHANCEMENT

Deep-learning models are characterized by multilayered network architectures that learn complex feature representations at various levels of abstraction directly from the data. Figure 3 illustrates a typical supervised learning setup for an image-denoising task. In this setup, the neural network's layer weights are iteratively adjusted during the training phase to minimize a loss function that compares the denoised image with a target low-noise or noiseless image. The denoised image is assessed using evaluation metrics in the subsequent validation phase.

Network Architectures

The current state of the art in PET and SPECT image enhancement features a variety of network architectures. Early implementations used convolutional neural networks (CNNs) that reduce computational complexity via parameter sharing. Many CNNs discussed here have an encoder–decoder structure, wherein an encoder estimates a latent representation through downsampling operations and a decoder upsamples it to match the input image's dimensions. Skip connections are often used to recover finer details.

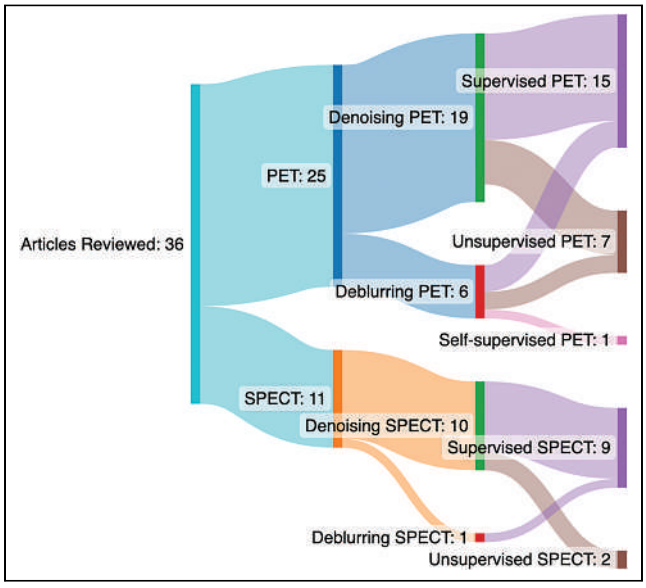

FIGURE 2. Categorywise split of selected articles reviewed here.

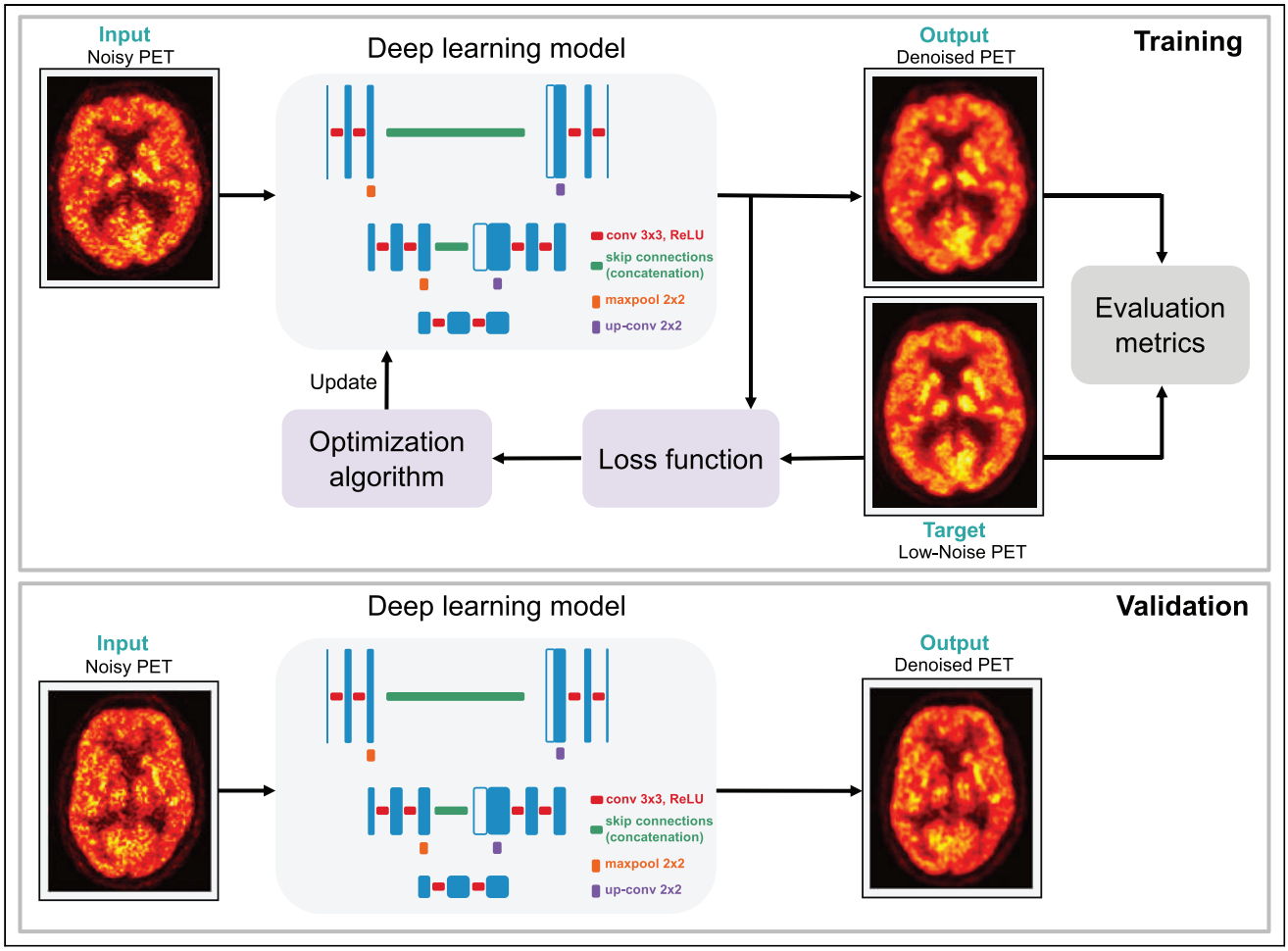

FIGURE 3. Typical supervised framework for PET image denoising using deep learning with training phase that minimizes loss function and validation phase that evaluates deep-learning model's performance. conv = convolution; ReLU = rectified linear unit; maxpool = maximum pooling; up-conv = upsampling convolution.

The U-Net (*9*), which evolved from fully convolutional architectures, has a U-shaped structure with a contracting path followed by a symmetric expanding path. It is widely used in image enhancement models, including those for PET and SPECT, with most being 3D because of the nature of the input images (*10*). Promising variants include conditional U-Nets, capturing mutual conditional dependence across modalities (*11*), and coupled U-Nets, containing modified single U-Nets that are interconnected for reduced learning redundancy (*12*).

The deep image prior (DIP) (*13*) is a widely used convolutional architecture for medical image enhancement that relies on a generator to learn clean image characteristics directly from noisy data without prior training. DIP architectures often use U-Net-like generators. In the case of PET image synthesis, anatomical images can be used for DIP initialization.

Generative adversarial networks (GANs) consist of a generator network that synthesizes an enhanced version of a subject's corrupt input image and a discriminator network that assesses how realistic the synthetic image is by comparing it with a clean image from the same subject or an unpaired clean image from a different subject (*14*). Both networks are jointly trained in competition with each other. Various GAN variants have been applied to PET and SPECT image enhancement, including conditional GANs (cGANs), which use additional prior information to guide image synthesis (*15*), and cycleGANs, which use 2 generator–discriminator pairs and can be trained with unpaired datasets (*16*).

Transformer architectures have shown potential in enhancing PET images by capturing long-range dependencies between different image regions (*17*). Additionally, diffusion models, which progressively contaminate the training data with increasing noise levels and then reverse the process to recover the data, are gaining popularity in medical imaging (*18*).

Loss Functions

Alongside network architecture, the loss function, which compares the target and predicted output, has a profound impact on model performance. Standard loss functions used in training image enhancement models include mean-squared error and mean absolute error. These functions compute the L2 and L1 norms, respectively, of voxelwise differences between the enhanced and target images. Mean-squared error is more sensitive to outliers in the training data. These loss functions lack sensitivity to visual perception, as they ignore voxel interactions and overall image structure. Perceptual loss functions address this limitation by using a pretrained network to assess high-level content and global structure in the enhanced and target images. GANs use adversarial loss

functions, which are a type of loss function used to determine whether images synthesized by a generator network have characteristics comparable to target images. However, joint generator–discriminator training can be unstable. Among GAN variants, Wasserstein GANs implement adversarial losses based on Wasserstein distances and have more training stability and less sensitivity to network architecture and parameter selection than regular GANs. CycleGANs use cycle-consistency loss functions to reduce the number of mappings between corrupt and clean image domains.

Training Strategies

Conventional supervised learning frameworks, such as the one illustrated in Figure 3, require paired clinical datasets for training, which are easy to simulate but challenging to obtain clinically as they require dual scans or access to raw data for synthesizing low-count images from standard-count ones. Furthermore, supervised learning models may not generalize well across datasets. Unsupervised approaches are thus gaining traction as they obviate the need for paired training data. Certain approaches rely solely on corrupt input data. For example, Noise2Noise (*19*) uses noisy inputs exclusively during training. Methods such as DIP benefit from the addition of anatomic information or from population-based unsupervised pretraining, which has a regularizing effect (*20*).

PET IMAGE ENHANCEMENT

Table 1 showcases many recent efforts that use AI for PET image enhancement. Most works on PET image enhancement focus on the image denoising task, the goal of which is to generate standard- or high-count PET images from noisy, low-count inputs. Early attempts using AI for PET denoising involved supervised CNNs. One study used an autocontext CNN with a sequence of convolutional modules to denoise ^{18}F-FDG PET images and examined the impact of additional anatomic T1-weighted MRI inputs on denoising performance (*21*). A dose reduction factor of 200× was reported using an encoder–decoder architecture that outperformed autocontext CNNs, nonlocal means filtering, block matching, and 3D filtering (*22*). A shift toward generative models helped overcome the limitations of traditional CNNs in capturing the underlying statistical distribution of PET images. One paper proposed a progressive refinement scheme based on concatenated 3D cGANs (*23*). Their network relied on a U-Net-like generator. Concatenated 3D cGANs were compared with single 3D cGANs, 2-dimensional cGANs, and U-Nets using ^{18}F-FDG PET brain scans from both healthy subjects and patients with mild cognitive impairment. One of the first applications of AI-based denoising to a non–^{18}F-FDG dataset was a cGAN-based ultralow-count PET imaging technique applied to ^{18}F-florbetaben scans for amyloid plaques in the brain (*24*). Importantly, the loss function in this work included a task-specific perceptual loss term that compares actual and predicted amyloid status determined by 2 expert radiologists. One paper proposed a locality-adaptive GAN model for PET image denoising in which the parametric weights are location-dependent and channel-dependent, providing a more economic way to fuse multimodal information than standard CNNs, where weights are shared across voxel locations and input channels (*25*). One work reported task-specific evaluations conducted by clinicians to determine overall image quality and lesion detectability for a denoising model based on a 3D U-Net architecture (*26*). Dilated convolutional kernels have been proposed in the context of PET image denoising to enable CNNs to capture a larger spatial context and detect features more robustly without the expensive downsampling and upsampling of internal representations (*27*). Several GAN refinements have improved GAN denoising performance in standard supervised learning scenarios. These include self-attention (*28*), cycleGAN implementations (*29*), and alternative loss functions such as the Wasserstein loss (*30*). As with other imaging modalities, there is currently great interest in diffusion models in the PET field. One paper proposed a diffusion model for PET denoising that leveraged an MRI-based prior and reported results based on ^{18}F-FDG and ^{18}F-MK-6240 radiotracers (*31*). A spatially adaptive technique and a transformer fusion network outperformed existing U-Net methods using a spatially adaptive block to extract features from both T1-weighted MRI and PET and a transformer network that established a pixelwise relationship between the 2 modalities (*32*). A Spach transformer was developed for PET denoising, which can capture long-range information efficiently, and outperformed other transformer networks and U-Nets (*33*). Notably, whereas the models were trained using ^{18}F-FDG and ^{18}F-ACBC (fluciclovine) data, the test dataset included 2 additional tracers, ^{18}F-DCFPyL and ^{68}Ga-DOTA-TATE, which were not used for model training.

In recent years, the research emphasis has largely shifted toward unsupervised models that can be trained using a single noisy image (no clean ground-truth images needed for training). The DIP has successfully performed unsupervised denoising using single noisy PET images (*34*). An extension of this idea showed improved results via population-level pretraining followed by individual fine-tuning (*35*). Noise2Void is another unsupervised approach applied for PET image denoising (*36*). It uses a single noisy input and is based on the idea of a blind spot network to estimate the intensity of a central pixel from its neighbors in a noisy image patch. Noise2Void has also been demonstrated to benefit from population-level pretraining and individual fine-tuning.

A key challenge with most supervised denoising approaches is their poor generalizability across different noise levels. A personalized denoising strategy has been proposed that uses different noise levels for training and incorporates a weighting factor that is based on the noise level in a task-dependent manner (*37*). A federated learning framework for PET image denoising was successfully tested with a simulated dataset with different noise settings corresponding to protocols from different institutions (*38*). Generalizability concerns also emphasize methods that can be adapted across scanners and tracers. One study customized a cGAN model for cross-scanner and cross-tracer optimization working with 3 scanner models (GE Healthcare Discovery MI, Siemens Biograph mCT, and Siemens Biograph Vision) and 3 radiotracers (^{18}F-FDG, ^{18}F-fluoroethyl-L-tyrosine (^{18}F-FET), and ^{18}F-florbetapir) (*39*). The results were independently assessed by 3 clinicians to ensure clinical utility.

Another key research theme for PET image enhancement centers around image deblurring and the related tasks superresolution and partial volume correction. A supervised approach for superresolving PET images by mapping from the lower-resolution Siemens HR+ scanner to the higher-resolution Siemens HRRT scanner used a very deep CNN with anatomic and spatial inputs (*40*). Later, a self-supervised solution to the same problem was proposed using a cycleGAN-like architecture and incorporating simulation guidance (*41*). This model was trained using unpaired low- and high-resolution images from the 2 scanners. A supervised cycleGAN framework was used to map PET image inputs not corrected for partial volume to outputs corrected for partial volume (*42*). The method was applied to ^{18}F-FDG, ^{18}F-flortaucipir, ^{18}F-flutemetamol, and ^{18}F-fluorodopa

TABLE 1
Summary of AI Approaches for PET Image Enhancement

Paper	Data details	Architecture	Loss function
Xiang et al. (*21*)	16 brain ^{18}F-FDG PET + T1 MRI	Autocontext CNN	MSE
Xu et al. (*22*)	9 brain ^{18}F-FDG PET + T1 MRI	U-Net	MAE
Wang et al. (*23*)	16 brain ^{18}F-FDG PET	Concatenated 3D cGAN with a 3D U-Netlike generator	MAE; cGAN
Ouyang et al. (*24*)	39 brain ^{18}F-florbetaben PET	cGAN with U-Net-like generator	MAE; cGAN; perceptual; content
Wang et al. (*25*)	20 simulated + 16 clinical brain ^{18}F-FDG PET, T1 MRI, diffusion tensor imaging	Locality adaptive multimodality GAN	MAE; adversarial
Schaefferkoetter et al. (*26*)	31 lung ^{18}F-FDG PET	U-Net	MSE
Spuhler et al. (*27*)	35 brain ^{18}F-FDG PET	Dilated U-Net	MAE
Xue et al. (*28*)	10 whole-body ^{18}F-FDG PET	3D attention residual least-squares GAN	MSE; least-squares adversarial
Zhao et al. (*29*)	109 brain ^{18}F-FDG PET/CT	Supervised cycleGAN	Adversarial; cycle consistency; identity
Gong et al. (*30*)	9 cardiac torso ^{18}F-FDG PET	Parameter-transferred Wasserstein GAN	MSE; Adversarial
Gong et al. (*31*)	120 brain ^{18}F-FDG PET; 140 brain ^{18}F-MK-6240 PET + T1 MRI	Denoising diffusion probabilistic model	MSE
Zhang et al. (*32*)	70 brain ^{18}F-FDG PET + T1 MRI	Spatially adaptive and transformer fusion network	MAE
Cui et al. (*34*)	10 lung ^{68}Ga-PRGD2 PET/CT; 30 lung ^{18}F-FDG PET/T1 MRI	Modified 3D U-Net with DIP	MSE
Cui et al. (*35*)	10 lung ^{68}Ga-PRGD2 PET/CT; 30 lung ^{18}F-FDG PET/T1 MRI	Modified 3D U-Net with DIP	MSE
Song et al. (*36*)	20 simulated brain ^{18}F-FDG PET; 17 brain ^{18}F-FDG PET + T1 MRI	Noise2Void (U-Net with 3 resolution levels)	MSE
Liu et al. (*37*)	195 cardiac torso ^{18}F-FDG PET	3D U-Net	MSE
Zhou et al. (*38*)	Heterogeneous multiinstitutional PET	Deep attention residual U-Net	MSE
Xue et al. (*39*)	310 brain across ^{18}F-FDG, ^{18}F-FET, ^{18}F-florbetapir PET	cGAN	Conventional content; voxelwise
Jang et al. (*33*)	44 whole-body ^{18}F-FDG, 40 whole-body ^{18}F-ACBC, 10 whole-body ^{18}F-DCFPyL, 18 whole-body ^{68}Ga-DOTATATE	Spach transformer	Charbonnier
Song et al. (*40*)	20 simulated brain ^{18}F-FDG PET; 30 clinical brain ^{18}F-FDG PET + T1 MRI	Very deep superresolution CNN	MAE
Song et al. (*41*)	20 simulated brain ^{18}F-FDG PET; 30 clinical brain ^{18}F-FDG PET	Self-supervised superresolution (CycleGAN)	Adversarial; cycle consistency; total variation
Sanaat et al. (*42*)	50 brain ^{18}F-FDG, 50 brain ^{18}F-flortaucipir, 36 brain ^{18}F-flutemetamol, 76 brain ^{18}F-fluoro-DOPA + T1 MRI	CycleGAN	Adversarial
Sanaat et al. (*43*)	100 brain ^{18}F-FDG, 100 ^{18}F-flortaucipir, 100 brain ^{18}F-flutemetamol	CycleGAN	Adversarial
Azimi et al. (*44*)	160 brain ^{18}F-FDG PET/CT	Attention-based network (U-Net)	MSE
Mehranian et al. (*45*)	273 whole-body ^{18}F-FDG PET	3D residual U-Net	MSE

MSE = mean-squared error; MAE = mean absolute error; ^{18}F-ACBC = 1-amino-3-^{18}F-fluorocyclobutane-1-carboxylic acid.

datasets. In a joint denoising and partial volume correction framework, a cycleGAN variant was also trained in supervised mode to generate standard-count partial-volume–corrected PET images from low-count inputs for 3 tracers (^{18}F-FDG, ^{18}F-flortaucipir, and ^{18}F-flutemetamol) (*43*). A similar concept was also presented using a U-Net–based model for joint denoising and partial volume correction (*44*). Time-of-flight PET imaging has been shown to improve the image signal-to-noise ratio significantly. Although most denoising works focus on reducing scan time or tracer dose, one AI-based denoising approach computed time-of-flight–quality images from non–time-of-flight PET image inputs (*45*).

SPECT IMAGE ENHANCEMENT

Several recent efforts that use AI for SPECT image enhancement are highlighted in Table 2. Similar to PET reports, most papers on SPECT image enhancement focus on image denoising models, which generate standard- or high-count SPECT images from noisy, low-count inputs. One of the earliest applications of AI for SPECT myocardial perfusion imaging (MPI) using a ^{99m}Tc-sestamibi rest-and-stress protocol involved a 3D convolutional autoencoder to map low-count SPECT images (1/8 and 1/16 of standard) to standard-count images (*46*). An extension of this work reported comparisons of several convolutional autoencoder architectures and evaluated the denoising model for the clinical task of perfusion-defect detection at several successively reduced dose levels (1/2, 1/4, 1/8, and 1/16 of standard count) (*47*). The paper also showed that dose-specific models outperformed a one-size-fits-all model trained using inputs at different noise levels. Pix2Pix, a cGAN architecture, was applied to ^{99m}Tc-sestamibi stress scans with reduced counts (7/10 to 1/10 of standard) and led to improved denoising performance relative to convolutional autoencoders and conventional gaussian and Butterworth filters (*48*). A dual-gated (cardiac and respiratory) SPECT MPI study suggested that using a patient's own dataset for training a cGAN architecture was superior to conventional training based on cross-patient data (*49*). The cGAN led to the lowest noise level but also exhibited the poorest defect detection performance compared with CNN and U-Net. One recent study provided a theoretical framework for assessing signal detection accuracy for AI-based SPECT denoising and demonstrated the utility of virtual clinical trials in the evaluation of AI-based approaches (*50*). This study highlighted discrepancies between image-based and task-based evaluation outcomes and stressed the significance of task-based objective evaluation for denoising SPECT images.

Although most denoising studies focus on the reduction of the radiotracer dose, several studies specifically focus on the reduction of scan duration. One SPECT MPI study compared the denoising performance of a CNN with residual learning for half-time versus half-projection datasets (i.e., halving the scan duration vs. halving the number of projection views) and reported stronger performance for the former (*51*). Another study focused on scan-time reduction for pediatric patients with kidney disease imaged using ^{99m}Tc-dimercaptosuccinic acid and showed that a 3D residual U-Net for denoising led to good diagnostic performance for the detectability of defects in the renal cortex despite a reduction in the scan time (*52*). By using a U^{2}Net, a novel 2-layer nested U-shaped structure with a residual U-block that effectively captures contextual information on different scales, 1 study demonstrated good lesion detectability performance for ultra-high-speed (1/7 of standard scan time) SPECT bone imaging using ^{99m}Tc-methyl diphosphonate (*53*). Notably, the model incorporated a lesion attenuation loss function to enhance its accuracy at generating SUV measures for lesion regions.

TABLE 2
Summary of Deep-Learning Techniques for SPECT Image Enhancement

Paper	Data details	Architecture	Loss function
Ramon et al. (*46*)	930 cardiac torso ^{99m}Tc-sestamibi	3D convolutional autoencoder	MSE
Ramon et al. (*47*)	1,052 cardiac torso ^{99m}Tc-sestamibi	Convolutional autoencoder, CNN	MSE
Sun et al. (*48*)	100 simulated; 20 cardiac torso clinical ^{99m}Tc-sestamibi	Pix2Pix GAN	MAE; adversarial
Sohlberg et al. (*49*)	93 cardiac torso ^{99m}Tc-tetrososmin	CNN, residual network, U-Net, cGAN	MSE
Yu et al. (*50*)	4,800 simulated	CNN	MSE
Shiri et al. (*51*)	363 cardiac torso ^{99m}Tc-sestamibi	Deep residual neural network	MSE
Lin et al. (*52*)	112 cardiac torso ^{99m}Tc-DMSA	3D residual U-Net	MSE
Pan et al. (*53*)	20 cardiac torso ^{99m}Tc-MDP SPECT/CT	Lesion-attention weighted U^{2}Net	MAE; structural similarity index
Liu et al. (*54*)	895 cardiac torso ^{99m}Tc-sestamibi	Noise2Noise (U-Net)	MSE
Liu et al. (*55*)	1,050 cardiac torso ^{99m}Tc-sestamibi	3D-coupled UNet	MSE
Xie et al. (*56*)	28 cardiac ^{99m}Tc-RBC	Densely connected multidimensional dynamic U-Net	MAE; structural similarity index; Sobel operator; intramyocardial blood volume

MSE = mean-squared error; MAE = mean absolute error; DMSA = pentavalent dimercaptosuccinic acid; MDP = methyl diphosphonate; RBC = red blood cell.

Some SPECT MPI image denoising efforts leverage recent advances in unsupervised learning. One such effort uses Noise2-Noise, a deep-learning framework for denoising that is trained without clean images but requires 2 noisy realizations of a ground-truth image, one used as the input and the other as the training target (*54*). The study used a coupled U-Net architecture that incorporates multiple U-Nets to reuse feature maps within the network. To evaluate the detection performance for perfusion defects at multiple contrast levels, the authors used a bootstrap procedure to generate multiple noise realizations from list-mode clinical acquisitions. Furthermore, the study was extended to quantify perfusion defect detection accuracy using receiver operating characteristics on a large training and validation dataset for SPECT MPI, which included 1,050 human subjects (*55*). Notably, the results revealed significant discrepancies between image-based and task-based evaluation and underscored the importance of task-based objective evaluation in SPECT image denoising. They demonstrated that pretraining with subsequent fine-tuning can meaningfully enhance the detectability of perfusion defects.

Applications of AI for SPECT image enhancement tasks other than denoising are still emerging. One paper proposed a segmentation-free partial volume correction approach for SPECT MPI, which uses a densely connected multidimensional dynamic network that allows adaptive adjustment of convolutional kernels after training (*56*). Importantly, the approach incorporated intramyocardial blood volume into the loss function to add clinical relevance to the generated images.

DISCUSSION

We have presented here a summary of recent progress in AI-based PET and SPECT image enhancement. AI-based techniques have shown great promise in enhancing image quality by reducing levels of noise and blur and have shown clinical promise in many task-based evaluation studies. Importantly, many studies have suggested that AI-based denoising approaches can reduce radiotracer dose and scan times without sacrificing diagnostic accuracy. AI-based models have also been more successful than their predecessors at combining multimodal information (e.g., using CT or MRI for PET or SPECT image enhancement).

AI-based image enhancement is of great clinical significance. Denoising approaches can lead to reductions in radiotracer dose or scan duration. Whereas the former reduces patient radiation exposure and addresses challenges arising from radionuclide shortages, the latter enhances patient comfort, increases scanning throughput, and reduces motion artifacts that could compromise diagnostic accuracy. Several of the cited papers show that denoising could improve both image quantitation and lesion detectability in addition to improving scan logistics. Deblurring approaches can mitigate partial volume effects that can compromise the accuracy of quantitative image-based metrics such as SUV ratios computed from small regions of interest. This is of particular importance in the imaging of neurodegenerative diseases, where image-based quantitative metrics from small anatomic targets could have diagnostic or prognostic value. The growing clinical relevance of AI-based image enhancement is underscored by the availability of U.S. Food and Drug Administration–approved vendor-neutral commercial software such as SubtlePET (Subtle Medical) for AI-based denoising, as exemplified in a study using SubtlePET's CNN to enhance low-count scans to diagnostic quality (*57*).

Despite the field's initial focus on supervised learning techniques that require paired clean and corrupt images for model training, an array of promising unsupervised or weakly supervised alternatives has emerged in the PET and SPECT fields in recent years. Most of these approaches either use only corrupt images for training or use corrupt inputs with unpaired training targets. These methods are attractive because of their easy applicability to most clinical datasets when ground-truth images for training are not available. However, they tend to produce inferior image quality and are often slower than their supervised counterparts. Thus, there is active research interest in further developing unsupervised approaches.

Although AI-based methods have consistently outperformed traditional approaches in terms of image-based figures of merit, whether the improved image quality leads to a tangible clinical benefit remains a topic of continued research and investigation. Accordingly, there is an increased focus in the current literature on task-based objective clinical evaluation of these approaches. Interestingly, several of the noted approaches for both PET and SPECT have incorporated clinical metrics (such as amyloid positivity or lesion detectability) into their loss functions to encourage clinically meaningful solutions. Furthermore, the incorporation of multimodal fusion, which integrates information from different imaging modalities such as CT and MRI, holds promise for improving diagnostic accuracy.

Although a sizable fraction of existing research is focused on ^{18}F-FDG PET and SPECT MPI, applications to other tracers are rapidly expanding. Transfer-learning strategies are facilitating the application of data-hungry AI models to smaller datasets for newer radiotracers, which can enable model fine-tuning with limited data using cross-tracer pretraining (*39*,*58*,*59*). Unsupervised models have also leveraged transfer-learning paradigms using a combination of population-level pretraining and individual fine-tuning (*36*). Transfer learning has also aided cross-scanner image-mapping strategies that are enabling purely software-based generation of higher-resolution images mimicking the image characteristics of state-of-the-art scanner models (*41*).

Although most clinical applications of image enhancement techniques are currently aimed at diagnostics, given the growing significance of radiopharmaceutical therapy, clinical applications of AI-based image enhancement could span beyond diagnostics, as image-quality improvements due to AI could potentially lead to more accurate image-based dosimetry. Given the privacy and security concerns surrounding health care, there is also a growing interest in federated learning approaches for image enhancement, wherein code sharing can circumvent the many challenges associated with data sharing, thus enabling the creation of robust models trained and validated over multiple sites and data sources.

CONCLUSION

AI methods have shown great promise in improving the quality and utility of PET and SPECT images. From traditional CNNs to more advanced GANs and transformer networks, deep-learning architectures have been applied to a range of clinical applications. Although encouraging results based on both image-domain and task-based evaluations have been reported, several roadblocks linger for the clinical translation of AI tools. Accordingly, there is a pressing need for large disease-specific datasets, standardized evaluation metrics, and integration of image enhancement tools with

existing clinical workflows. The future of AI in PET and SPECT imaging holds great potential to improve diagnostic accuracy, enable novel clinical applications, and ultimately benefit patients.

DISCLOSURE

This research was supported by grants R01AG072669 and R03AG070750. No other potential conflict of interest relevant to this article was reported.

REFERENCES

1. Hicks RJ, Hofman MS. Is there still a role for SPECT–CT in oncology in the PET–CT era? *Nat Rev Clin Oncol.* 2012;9:712–720.
2. Hooker JM, Carson RE. Human positron emission tomography neuroimaging. *Annu Rev Biomed Eng.* 2019;21:551–581.
3. Best SRD, Haustrup N, Pavel DG. Brain SPECT as an imaging biomarker for evaluating effects of novel treatments in psychiatry: a case series. *Front Psychiatry.* 2022;12:713141.
4. Palestro CJ. Radionuclide imaging of musculoskeletal infection: a review. *J Nucl Med.* 2016;57:1406–1412.
5. Garcia EV, Slomka P, Moody JB, Germano G, Ficaro EP. Quantitative clinical nuclear cardiology, part 1: established applications. *J Nucl Cardiol.* 2020;27:189–201.
6. Slomka PJ, Moody JB, Miller RJH, Renaud JM, Ficaro EP, Garcia EV. Quantitative clinical nuclear cardiology, part 2: evolving/emerging applications. *J Nucl Cardiol.* 2021;28:115–127.
7. Soret M, Bacharach SL, Buvat I. Partial-volume effect in PET tumor imaging. *J Nucl Med.* 2007;48:932–945.
8. Zhou T, Ruan S, Canu S. A review: deep learning for medical image segmentation using multi-modality fusion. *Array.* 2019;3–4:100004.
9. Ronneberger O, Fischer P, Brox T. U-Net: convolutional networks for biomedical image segmentation. arXiv website. https://arxiv.org/abs/1505.04597. Published May 18, 2015. Accessed October 24, 2023.
10. Çiçek Ö, Abdulkadir A, Lienkamp SS, Brox T, Ronneberger O. 3D U-Net: learning dense volumetric segmentation from sparse annotation. arXiv website. https://arxiv.org/abs/1606.06650. Published June 21, 2016. Accessed October 24, 2023.
11. Zhang L, Zhang W, Japkowicz N. Conditional-UNet: a condition-aware deep model for coherent human activity recognition from wearables. arXiv webstie. https://arxiv.org/abs/2004.09376. Published April 15, 2020. Accessed October 24, 2023.
12. Tang Z, Peng X, Li K, Metaxas DN. Towards efficient U-Nets: a coupled and quantized approach. *IEEE Trans Pattern Anal Mach Intell.* 2020;42:2038–2050.
13. Ulyanov D, Vedaldi A, Lempitsky V. Deep image prior. *Int J Comput Vis.* 2020;128:1867–1888.
14. Goodfellow I, Pouget-Abadie J, Mirza M, et al. Generative adversarial nets. In: Ghahramani Z, Welling M, Cortes C, Lawrence N, Weinberger KQ, eds. *Advances in Neural Information Processing Systems.* Vol 27. Curran Associates, Inc.; 2014:2672–2680.
15. Mirza M, Osindero S. Conditional generative adversarial nets. arXiv website. https://arxiv.org/abs/1411.1784. Published November 6, 2014. Accessed October 24, 2023.
16. Zhu J-Y, Park T, Isola P, Efros AA. Unpaired image-to-image translation using cycle-consistent adversarial networks. Paper presented at: 2017 IEEE International Conference on Computer Vision (ICCV); October 22–29, 2017; Venice, Italy.
17. Vaswani A, Shazeer N, Parmar N, et al. Attention is all you need. arXiv website. https://arxiv.org/abs/1706.03762. Published June 12, 2017. Accessed October 24, 2023.
18. Ho J, Jain A, Abbeel P. Denoising diffusion probabilistic models. arXiv website. https://arxiv.org/abs/2006.11239. Published June 19, 2020. Accessed October 24, 2023.
19. Lehtinen J, Munkberg J, Hasselgren J, et al. Noise2Noise: learning image restoration without clean data. arXiv website. https://arxiv.org/abs/1803.04189. Published March 12, 2018. Accessed October 24, 2023.
20. Erhan D, Manzagol P-A, Bengio Y, Bengio S, Vincent P. The difficulty of training deep architectures and the effect of unsupervised pre-training. Paper presented at: Proceedings of the Twelfth International Conference on Artificial Intelligence and Statistics; April 16-18, 2009; Clearwater Beach, FL.
21. Xiang L, Qiao Y, Nie D, An L, Wang Q, Shen D. Deep auto-context convolutional neural networks for standard-dose PET image estimation from low-dose PET/MRI. *Neurocomputing.* 2017;267:406–416.
22. Xu J, Gong E, Pauly J, Zaharchuk G. 200x low-dose PET reconstruction using deep learning. arXiv website. https://arxiv.org/abs/1712.04119. Published December 12, 2017. Accessed October 24, 2023.
23. Wang Y, Yu B, Wang L, et al. 3D conditional generative adversarial networks for high-quality PET image estimation at low dose. *Neuroimage.* 2018;174:550–562.
24. Ouyang J, Chen KT, Gong E, Pauly J, Zaharchuk G. Ultra-low-dose PET reconstruction using generative adversarial network with feature matching and task-specific perceptual loss. *Med Phys.* 2019;46:3555–3564.
25. Wang Y, Zhou L, Yu B, et al. 3D auto-context-based locality adaptive multi-modality GANs for PET synthesis. *IEEE Trans Med Imaging.* 2019;38:1328–1339.
26. Schaefferkoetter J, Yan J, Ortega C, et al. Convolutional neural networks for improving image quality with noisy PET data. *EJNMMI Res.* 2020;10:105.
27. Spuhler K, Serrano-Sosa M, Cattell R, DeLorenzo C, Huang C. Full-count PET recovery from low-count image using a dilated convolutional neural network. *Med Phys.* 2020;47:4928–4938.
28. Xue H, Teng Y, Tie C, et al. A 3D attention residual encoder–decoder least-square GAN for low-count PET denoising. *Nucl Instrum Methods Phys Res A.* 2020;983:164638.
29. Zhao K, Zhou L, Gao S, et al. Study of low-dose PET image recovery using supervised learning with cycleGAN. *PLoS One.* 2020;15:e0238455.
30. Gong Y, Shan H, Teng Y, et al. Parameter-transferred Wasserstein generative adversarial network (PT-WGAN) for low-dose PET image denoising. *IEEE Trans Radiat Plasma Med Sci.* 2021;5:213–223.
31. Gong K, Johnson KA, El Fakhri G, Li Q, Pan T. PET image denoising based on denoising diffusion probabilistic models. arXiv website. https://arxiv.org/abs/2209.06167. Published September 13, 2022. Accessed October 24, 2023.
32. Zhang L, Xiao Z, Zhou C, et al. Spatial adaptive and transformer fusion network (STFNet) for low-count PET blind denoising with MRI. *Med Phys.* 2022;49:343–356.
33. Jang S-I, Pan T, Li Y, et al. Spach transformer: spatial and channel-wise transformer based on local and global self-attentions for PET image denoising. arXiv website. https://arxiv.org/abs/2209.03300. Published September 7, 2022. Accessed October 24, 2023.
34. Cui J, Gong K, Guo N, et al. PET image denoising using unsupervised deep learning. *Eur J Nucl Med Mol Imaging.* 2019;46:2780–2789.
35. Cui J, Gong K, Guo N, et al. Populational and individual information based PET image denoising using conditional unsupervised learning. *Phys Med Biol.* 2021;66:155001.
36. Song T-A, Yang F, Dutta J. Noise2Void: unsupervised denoising of PET images. *Phys Med Biol.* 2021;66:214002.
37. Liu Q, Liu H, Mirian N, et al. A personalized deep learning denoising strategy for low-count PET images. *Phys Med Biol.* 2022;67:145014.
38. Zhou B, Miao T, Mirian N, et al. Federated transfer learning for low-dose PET denoising: a pilot study with simulated heterogeneous data. *IEEE Trans Radiat Plasma Med Sci.* 2023;7:284–295.
39. Xue S, Guo R, Bohn KP, et al. A cross-scanner and cross-tracer deep learning method for the recovery of standard-dose imaging quality from low-dose PET. *Eur J Nucl Med Mol Imaging.* 2022;49:1843–1856.
40. Song T-A, Chowdhury SR, Yang F, Dutta J. Super-resolution PET imaging using convolutional neural networks. *IEEE Trans Comput Imaging.* 2020;6:518–528.
41. Song T-A, Chowdhury SR, Yang F, Dutta J. PET image super-resolution using generative adversarial networks. *Neural Netw.* 2020;125:83–91.
42. Sanaat A, Shooli H, Böhringer AS, et al. A cycle-consistent adversarial network for brain PET partial volume correction without prior anatomical information. *Eur J Nucl Med Mol Imaging.* 2023;50:1881–1896.
43. Sanaat A, Boehringer A, Ghavabesh A, et al. Deep-PVC: a deep learning model for synthesizing full-dose partial volume corrected PET images from low-dose images. Paper presented at: 2021 Virtual IEEE Nuclear Science Symposium and Medical Imaging Conference (NSS/MIC); October 16–23, 2021; Piscataway, NJ.
44. Azimi M-S, Kamali-Asl A, Ay M-R, Arabi H, Zaidi H. A novel attention-based convolutional neural network for joint denoising and partial volume correction of low-dose PET images. Paper presented at: 2021 Virtual IEEE Nuclear Science Symposium and Medical Imaging Conference (NSS/MIC); October 16–23, 2021; Piscataway, NJ.
45. Mehranian A, Wollenweber SD, Walker MD, et al. Deep learning–based time-of-flight (ToF) image enhancement of non-ToF PET scans. *Eur J Nucl Med Mol Imaging.* 2022;49:3740–3749.
46. Ramon AJ, Yang Y, Pretorius PH, Johnson KL, King MA, Wernick MN. Initial investigation of low-dose SPECT-MPI via deep learning. Paper presented at: 2018 IEEE Nuclear Science Symposium and Medical Imaging Conference Proceedings (NSS/MIC); November 10–17, 2018; Sydney, NSW, Australia.

47. Ramon AJ, Yang Y, Pretorius PH, Johnson KL, King MA, Wernick MN. Improving diagnostic accuracy in low-dose SPECT myocardial perfusion imaging with convolutional denoising networks. *IEEE Trans Med Imaging.* 2020;39:2893–2903.
48. Sun J, Du Y, Li C, Wu T-H, Yang B, Mok GSP. Pix2Pix generative adversarial network for low dose myocardial perfusion SPECT denoising. *Quant Imaging Med Surg.* 2022;12:3539–3555.
49. Sohlberg A, Kangasmaa T, Constable C, Tikkakoski A. Comparison of deep learning-based denoising methods in cardiac SPECT. *EJNMMI Phys.* 2023;10:9.
50. Yu Z, Rahman MA, Laforest R, et al. Need for objective task-based evaluation of deep learning-based denoising methods: a study in the context of myocardial perfusion SPECT. *Med Phys.* 2023;50:4122–4137.
51. Shiri I, Sabet KA, Arabi H, et al. Standard SPECT myocardial perfusion estimation from half-time acquisitions using deep convolutional residual neural networks. *J Nucl Cardiol.* 2021;28:2761–2779.
52. Lin C, Chang Y-C, Chiu H-Y, Cheng C-H, Huang H-M. Reducing scan time of paediatric ^{99m}Tc-DMSA SPECT via deep learning. *Clin Radiol.* 2021;76:315.e13–315.e20.
53. Pan B, Qi N, Meng Q, et al. Ultra high speed SPECT bone imaging enabled by a deep learning enhancement method: a proof of concept. *EJNMMI Phys.* 2022;9:43.
54. Liu J, Yang Y, Wernick MN, Pretorius PH, King MA. Deep learning with noise-to-noise training for denoising in SPECT myocardial perfusion imaging. *Med Phys.* 2021;48:156–168.
55. Liu J, Yang Y, Wernick MN, Pretorius PH, Slomka PJ, King MA. Improving detection accuracy of perfusion defect in standard dose SPECT-myocardial perfusion imaging by deep-learning denoising. *J Nucl Cardiol.* 2022;29:2340–2349.
56. Xie H, Liu Z, Shi L, et al. Segmentation-free PVC for cardiac SPECT using a densely-connected multi-dimensional dynamic network. *IEEE Trans Med Imaging.* 2023;42:1325–1336.
57. Chaudhari AS, Mittra E, Davidzon GA, et al. Low-count whole-body PET with deep learning in a multicenter and externally validated study. *NPJ Digit Med.* 2021;4:127.
58. Chen X, Hendrik Pretorius P, Zhou B, et al. Cross-vender, cross-tracer, and cross-protocol deep transfer learning for attenuation map generation of cardiac SPECT. *J Nucl Cardiol.* 2022;29:3379–3391.
59. Liu H, Wu J, Lu W, Onofrey JA, Liu Y-H, Liu C. Noise reduction with cross-tracer and cross-protocol deep transfer learning for low-dose PET. *Phys Med Biol.* 2020;65:185006.

Is It Time to Retire PIOPED?

Lionel S. Zuckier[1] and Sean Logan Boone[2]

[1]*Division of Nuclear Medicine, Department of Radiology, Montefiore Medical Center and Albert Einstein College of Medicine, Bronx, New York; and* [2]*Department of Radiology, St. Joseph's Hospital and Medical Center, Phoenix, Arizona*

Since its publication in 1990 (*1*), the Prospective Investigation of Pulmonary Embolism Diagnosis (PIOPED) study has played a central role in informing algorithms used to diagnose pulmonary embolism (PE). Indeed, PIOPED-based algorithms maintain a central role in current best practices and procedure standards (*2*). Given that most early-career practitioners and trainees were born after the PIOPED results were released in 1990, its chronology bears retelling.

PIOPED was a National Institutes of Health–financed prospective, multiinstitutional study that analyzed the diagnostic usefulness of ventilation–perfusion lung scintigraphy in acute PE (*1,3–5*). Symptomatic adult subjects were enrolled and imaged by planar scintigraphy after administration of ^{133}Xe gas and ^{99m}Tc-macroaggregated albumin. PIOPED was notable for its prospective interpretation criteria, large cohort of patients, efforts to avoid selection bias, and rigorous gold standard, including pulmonary catheter angiography, which was performed on most subjects. Though not the first to do so, PIOPED used a probabilistic model of reporting, casting the lung scan results as normal/near normal or as low, intermediate (indeterminate), or high probability for PE.

The original PIOPED investigation was flawed from the start. Because it was a prospective trial, the criteria for scintigraphic interpretation were assigned before initiation; unfortunately, these were ultimately determined to be suboptimal. This Achilles' heel led to poor correlation between scintigraphic interpretation and interventional angiography, the standard of truth used in the trial (*1*). A lackluster outcome contributed to impugning of lung scintigraphy's value in the minds of many clinicians, bringing about its near demise (*6*). The PIOPED investigators subsequently moved beyond their initial error by retrospective reanalysis of the study's large data pool, giving rise to revised (*7*) or modified (*8*) PIOPED criteria, which were then prospectively tested in new patient cohorts, though generally with a weaker, composite, clinical gold standard (*9*). These revised criteria have been incorporated into various diagnostic protocols (*2,10*). After the original PIOPED study, PIOPED II and III were conducted, which were National Institutes of Health–funded trials of spiral CT angiography (*11*) and gadolinium-enhanced MR angiography (*12*) for the diagnosis of PE, which bear only tangential relevance to our current discussion.

Incredibly, accrual of patients in the PIOPED study occurred over 37 y ago; at that time the term *evidence-based medicine* had not yet been coined (*13*), Technegas (Cyclomedica) was a new product available in only limited markets (*14*), SPECT cameras were being initially introduced in the clinic, and SPECT/CT did not yet exist (*15*). In essence, the landscape of clinical nuclear medicine bore little resemblance to the current terrain. Is the venerable PIOPED too dated and dissonant to be applicable in the contemporary environment? It is telling that a similar question was raised in this journal some 15 y ago (*6*). We will first reflect on the contributions made by PIOPED to lung scintigraphy and consider which of these features, if any, retain currency in the modern era, over 30 y since their introduction.

Two types of validity are required for a research study to support clinical practice (*16,17*). Internal validity (or study quality) refers to the confidence we have that the study incorporates minimal bias, based on best research practices such as randomization and masking, leading to conclusions that are internally consistent and accurate. External validity (or generalizability) refers to whether the conclusions derived from the sample of subjects studied can be extended to other broader populations of patients. This is often achieved by recruiting subjects from multiple institutions and ensuring that they reflect a wide variety of demographic backgrounds. The PIOPED study excelled in internal validity, based on data that were robust, complete, extensive, and validated, including an exceptional gold standard. These data were harnessed to generate new and optimized revised interpretation criteria, which de facto converted the lackluster prospective trial into a powerful retrospective study. In its day, PIOPED also reflected excellent external validity, based on contemporary best imaging practices that were performed on more than 1,400 study participants across 6 different institutions. As population, equipment, radiopharmaceuticals, and techniques have changed over the ensuing 30 y of practice, the study's external validity has been gradually eroded. Patients undergoing lung scintigraphy today are markedly different from those studied during PIOPED, with a much lower prevalence of PE. From a technical perspective, only a minority of practitioners still use ^{133}Xe gas for ventilation, instead substituting aerosol ventilation methods (*18*), and this fraction may further decrease now that Technegas has been approved by the United States Food and Drug Administration and will be adopted into the market. γ-cameras have progressed from analog acquisition and display to fully digital systems, with superior resolution and larger fields of view than in the time of PIOPED. Numerous practitioners have also moved beyond planar imaging to embrace tomography (especially in Canada and Europe (*18,19*)), whereas many more physicians would be amenable to this change if reflected in updated guidelines. Reinartz has succinctly pointed out that in no other realm of scintigraphy do we limit ourselves to nontomographic imaging (*6*). The concern that tomography will lead to visualization

Received Oct. 3, 2023; revision accepted Oct. 10, 2023.
For correspondence, contact Lionel S. Zuckier (lzuckier@montefiore.org).
Published online Nov. 2, 2023.

DOI: 10.2967/jnumed.123.266186

and overcalling of small, insignificant defects would be best allayed by updated criteria and education, not by throttling imaging data. In toto, it seems clear that changes in practice patterns have led to an insidious decline in external validity that has eclipsed any advantage gained from the original superior internal validity of the PIOPED data.

A further feature of the PIOPED interpretation schemata is their Bayesian or probabilistic reporting nomenclature, although these, in fact, were introduced by other investigators predating PIOPED (*20*). It is a mathematic truism that calculation of posttest probability of disease must take into account the a priori probabilities (*21,22*). Furthermore, clinical diagnostic imaging has been moving toward—not away from—standardized reporting, use of clearly defined criteria, and probabilistic interpretation, as evidenced by the proliferation of "-RADS" systems of reporting throughout radiology (*23–26*). For these idealized reasons, the PIOPED criteria were prescient, incorporating medical decision making into the science of diagnostic imaging. Nonetheless, on a practical level, the Bayesian categorization of test results is judged by many as tedious, misunderstood, and impractical. Categorization of the images into 3 or 4 categories ranging from normal/near normal through high probability differs radically from binary interpretations customarily applied in much of medical imaging, including CT pulmonary angiography, which is currently the dominant radiographic method of evaluating PE. If clinicians do not comprehend the nuances of a probabilistic diagnosis, more harm than benefit may result. Has the complexity of PIOPED been shown to really improve outcomes in the field or is it in fact unhelpful and poorly understood? Previous research has shown that there is significant variability in how referring and even interpreting physicians understand the probability categories, particularly intermediate- and low-probability results (*27–29*).

How can we move beyond PIOPED? Can we develop new criteria, replete with both internal and external validity, that will incorporate a Bayesian framework of diagnosis but will also be manageable and understandable? Can the principles of evidence-based medicine inherent in the PIOPED design be ported to our current practice paradigms? In fact, a universal methodology to replace PIOPED has not emerged in the intervening 33 y since it was developed because of the difficulty of replicating the high-quality data, the extensive clinical experience, and the need to embed scan findings into an integrated diagnostic strategy (*10*). For example, the European Association of Nuclear Medicine criteria (*19*), although widely used in Canada and Europe, have not been universally embraced in the United States, at least in part due to concern that the acquisition technique and diagnostic criteria for reporting tomographic (SPECT) ventilation–perfusion scans are variable and have not been sufficiently validated (*30,31*).

It seems conceivable that artificial intelligence (AI) techniques have the potential to inherit the mantle of PIOPED. Many of the rigorous concepts that were embodied in the PIOPED approach can now be applied within AI interpretation of lung scintigraphy, including harvesting of extensive pretest, test, and validated outcome data, correlated by complex deep learning models (*32–34*). Many features enter into an expert's evaluation of lung scintigraphy, often exceeding the performance of published diagnostic algorithms (*35*). The improved performance of expert evaluation has been attributed to the use of intangible and unique Gestalt factors (*36,37*), versus additional personal, though not codified, rules of interpretation (*38*). This is clearly the province of AI. Lung scintigraphy was in fact one of the earliest medical imaging applications of AI (*39–42*), with a flurry of activity in the 1990s and early 2000s (*43–45*), though as CT pulmonary angiography became the dominant clinical diagnostic modality in PE, it also became the primary focus of AI research (*46*). The senescence of PIOPED should be countered by development of powerful techniques of AI interpretation. In that manner, we can enhance the role of scintigraphy in patients with suspected PE while simultaneously improving diagnostic outcomes.

DISCLOSURE

No potential conflict of interest relevant to this article was reported.

REFERENCES

1. PIOPED Investigators. Value of the ventilation/perfusion scan in acute pulmonary embolism. Results of the prospective investigation of pulmonary embolism diagnosis (PIOPED). *JAMA.* 1990;263:2753–2759.
2. Parker JA, Coleman RE, Grady E, et al. SNM practice guideline for lung scintigraphy 4.0. *J Nucl Med Technol.* 2012;40:57–65.
3. Gottschalk A, Juni JE, Sostman HD, et al. Ventilation-perfusion scintigraphy in the PIOPED study. Part I. Data collection and tabulation. *J Nucl Med.* 1993;34: 1109–1118.
4. Gottschalk A, Sostman HD, Coleman RE, et al. Ventilation-perfusion scintigraphy in the PIOPED study. Part II. Evaluation of the scintigraphic criteria and interpretations. *J Nucl Med.* 1993;34:1119–1126.
5. Worsley DF, Alavi A. Comprehensive analysis of the results of the PIOPED study. *J Nucl Med.* 1995;36:2380–2387.
6. Reinartz P. To PIOPED, or not to PIOPED. *J Nucl Med.* 2008;49:1739–1740.
7. Sostman HD, Coleman RE, DeLong DM, Newman GE, Paine S. Evaluation of revised criteria for ventilation-perfusion scintigraphy in patients with suspected pulmonary embolism. *Radiology.* 1994;193:103–107.
8. Freitas JE, Sarosi MG, Nagle CC, Yeomans ME, Freitas AE, Juni JE. Modified PIOPED criteria used in clinical practice. *J Nucl Med.* 1995;36:1573–1578.
9. Dronkers CEA, van der Hulle T, Le Gal G, et al. Towards a tailored diagnostic standard for future diagnostic studies in pulmonary embolism: communication from the SSC of the ISTH. *J Thromb Haemost.* 2017;15:1040–1043.
10. Le Roux PY, Le Pennec R, Salaun PY, Zuckier LS. Scintigraphic diagnosis of acute pulmonary embolism: from basics to best practices. *Semin Nucl Med.* May 2, 2023 [Epub ahead of print].
11. Sostman HD, Stein PD, Gottschalk A, Matta F, Hull R, Goodman L. Acute pulmonary embolism: sensitivity and specificity of ventilation-perfusion scintigraphy in PIOPED II study. *Radiology.* 2008;246:941–946.
12. Stein PD, Chenevert TL, Fowler SE, et al. Gadolinium-enhanced magnetic resonance angiography for pulmonary embolism: a multicenter prospective study (PIOPED III). *Ann Intern Med.* 2010;152:434–W143.
13. Smith R, Rennie D. Evidence-based medicine: an oral history. *JAMA.* 2014;311: 365–367.
14. Bailey DL, Roach PJ. A brief history of lung ventilation and perfusion imaging over the 50-year tenure of the editors of *Seminars in Nuclear Medicine. Semin Nucl Med.* 2020;50:75–86.
15. Hutton BF. The origins of SPECT and SPECT/CT. *Eur J Nucl Med Mol Imaging.* 2014;41(suppl 1):S3–S16.
16. Degtiar I, Rose S. A review of generalizability and transportability. *Annu Rev Stat Appl.* 2023;10:501–524.
17. Kamper SJ. Generalizability: linking evidence to practice. *J Orthop Sports Phys Ther.* 2020;50:45–46.
18. Le Roux PY, Pelletier-Galarneau M, De Laroche R, et al. Pulmonary scintigraphy for the diagnosis of acute pulmonary embolism: a survey of current practices in Australia, Canada, and France. *J Nucl Med.* 2015;56:1212–1217.
19. Bajc M, Schumichen C, Gruning T, et al. EANM guideline for ventilation/perfusion single-photon emission computed tomography (SPECT) for diagnosis of pulmonary embolism and beyond. *Eur J Nucl Med Mol Imaging.* 2019;46: 2429–2451.
20. McNeil BJ. Ventilation-perfusion studies and the diagnosis of pulmonary embolism: concise communication. *J Nucl Med.* 1980;21:319–323.
21. Vea HW, Sirotta PS, Nelp WB. Ventilation-perfusion scanning for pulmonary embolism: refinement of predictive value through Bayesian analysis. *AJR.* 1985; 145:967–972.

22. Deeks JJ, Altman DG. Diagnostic tests 4: likelihood ratios. *BMJ.* 2004;329: 168–169.
23. Palanisamy PK, Dev B, Sheela MC. BI-RADS: an overview. In: Dev B, Joseph LD, eds. *Holistic Approach to Breast Disease.* Springer; 2023:53–60.
24. Turkbey B, Rosenkrantz AB, Haider MA, et al. Prostate imaging reporting and data system version 2.1: 2019 update of prostate imaging reporting and data system version 2. *Eur Urol.* 2019;76:340–351.
25. Tessler FN, Middleton WD, Grant EG, et al. ACR thyroid imaging, reporting and data system (TI-RADS): white paper of the ACR TI-RADS committee. *J Am Coll Radiol.* 2017;14:587–595.
26. Elsayes KM, Kielar AZ, Chernyak V, et al. LI-RADS: a conceptual and historical review from its beginning to its recent integration into AASLD clinical practice guidance. *J Hepatocell Carcinoma.* 2019;6:49–69.
27. Gray HW, McKillop JH, Bessent RG. Lung scan reporting language: what does it mean? *Nucl Med Commun.* 1993;14:1084–1087.
28. Gray HW, McKillop JH, Bessent RG. Lung scan reports: interpretation by clinicians. *Nucl Med Commun.* 1993;14:989–994.
29. Siegel A, Holtzman SR, Bettmann MA, Black WC. Clinicians' perceptions of the value of ventilation-perfusion scans. *Clin Nucl Med.* 2004;29:419–425.
30. Duffett L, Castellucci LA, Forgie MA. Pulmonary embolism: update on management and controversies. *BMJ.* 2020;370:m2177.
31. Konstantinides SV, Meyer G, Becattini C, et al. ESC guidelines for the diagnosis and management of acute pulmonary embolism developed in collaboration with the European Respiratory Society (ERS): the task force for the diagnosis and management of acute pulmonary embolism of the European Society of Cardiology (ESC). *Eur Respir J.* 2019;54:1901647.
32. Visvikis D, Lambin P, Beuschau Mauridsen K, et al. Application of artificial intelligence in nuclear medicine and molecular imaging: a review of current status and future perspectives for clinical translation. *Eur J Nucl Med Mol Imaging.* 2022;49: 4452–4463.
33. Seifert R, Weber M, Kocakavuk E, Rischpler C, Kersting D. Artificial intelligence and machine learning in nuclear medicine: future perspectives. *Semin Nucl Med.* 2021;51:170–177.
34. Currie G, Rohren E. Intelligent imaging in nuclear medicine: the principles of artificial intelligence, machine learning and deep learning. *Semin Nucl Med.* 2021;51: 102–111.
35. Sullivan DC, Coleman RE, Mills SR, Ravin CE, Hedlund LW. Lung scan interpretation: effect of different observers and different criteria. *Radiology.* 1983;149: 803–807.
36. Sostman HD, Gottschalk A. Evaluation of patients with suspected venous thromboembolism. In: Gottschalk A, Hoffer P, Potchen EJ, eds. *Diagnostic Nuclear Medicine.* Williams and Wilkins; 1988:502–521.
37. Alderson PO. Scintigraphic diagnosis of pulmonary embolism: where do we go from here? *Radiology.* 1994;193:22–23.
38. Freeman LM, Krynyckyi B, Zuckier LS. Enhanced lung scan diagnosis of pulmonary embolism with the use of ancillary scintigraphic findings and clinical correlation. *Semin Nucl Med.* 2001;31:143–157.
39. Tourassi GD, Floyd CE, Sostman HD, Coleman RE. Acute pulmonary embolism: artificial neural network approach for diagnosis. *Radiology.* 1993;189:555–558.
40. Patil S, Henry JW, Rubenfire M, Stein PD. Neural network in the clinical diagnosis of acute pulmonary embolism. *Chest.* 1993;104:1685–1689.
41. Fisher RE, Scott JA, Palmer EL. Neural networks in ventilation-perfusion imaging. *Radiology.* 1996;198:699–706.
42. Scott JA, Fisher RE, Palmer EL. Neural networks in ventilation-perfusion imaging. Part II. Effects of interpretive variability. *Radiology.* 1996;198:707–713.
43. Scott JA. Using artificial neural network analysis of global ventilation-perfusion scan morphometry as a diagnostic tool. *AJR.* 1999;173:943–948.
44. Holst H, Astrom K, Jarund A, et al. Automated interpretation of ventilation-perfusion lung scintigrams for the diagnosis of pulmonary embolism using artificial neural networks. *Eur J Nucl Med.* 2000;27:400–406.
45. Holst H, Mare K, Jarund A, et al. An independent evaluation of a new method for automated interpretation of lung scintigrams using artificial neural networks. *Eur J Nucl Med.* 2001;28:33–38.
46. Jabbarpour A, Ghassel S, Lang J, et al. The past, present, and future role of artificial intelligence in ventilation/perfusion scintigraphy: a systematic review. *Semin Nucl Med.* April 18, 2023 [Epub ahead of print].

Diagnostic Accuracy of MR Spectroscopic Imaging and ^{18}F-FET PET for Identifying Glioma: A Biopsy-Controlled Hybrid PET/MRI Study

Jörg Mauler[1], Philipp Lohmann[1,2], Andrew A. Maudsley[3], Sulaiman Sheriff[3], Moritz Hoevels[2], Anna-Katharina Meissner[4], Christina Hamisch[2], Anna Brunn[5,6], Martina Deckert[5,6], Christian P. Filss[1,7], Gabriele Stoffels[1], Jürgen Dammers[1], Maximillian I. Ruge[2,8], Norbert Galldiks[1,8,9], Felix M. Mottaghy[7,8,10], Karl-Josef Langen[1,7,8], and N. Jon Shah[1,11,12]

[1]Institute of Neuroscience and Medicine (INM-3/INM-4/INM-11), Forschungszentrum Juelich, Juelich, Germany; [2]Department of Stereotactic and Functional Neurosurgery, Faculty of Medicine and University Hospital Cologne, University of Cologne, Cologne, Germany; [3]Department of Radiology, Miller School of Medicine, University of Miami, Miami, Florida; [4]Department of General Neurosurgery, Faculty of Medicine and University Hospital Cologne, University of Cologne, Cologne, Germany; [5]Institute of Neuropathology, Faculty of Medicine and University Hospital Cologne, University of Cologne, Cologne, Germany; [6]Institute of Neuropathology, University Hospital Düsseldorf and Medical Faculty, Heinrich Heine University Düsseldorf, Düsseldorf, Germany; [7]Department of Nuclear Medicine, RWTH Aachen University Hospital, Aachen, Germany; [8]Center for Integrated Oncology, Universities of Aachen, Bonn, Cologne, and Duesseldorf, Germany; [9]Department of Neurology, Faculty of Medicine and University Hospital Cologne, University of Cologne, Cologne, Germany; [10]Department of Radiology and Nuclear Medicine, Maastricht University Medical Center, Maastricht, The Netherlands; [11]Department of Neurology, RWTH Aachen University Hospital, Aachen, Germany; and [12]JARA-BRAIN-Translational Medicine, Aachen, Germany

Contrast-enhanced MRI is the method of choice for brain tumor diagnostics, despite its low specificity for tumor tissue. This study compared the contribution of MR spectroscopic imaging (MRSI) and amino acid PET to improve the detection of tumor tissue. **Methods:** In 30 untreated patients with suspected glioma, *O*-(2-[^{18}F]fluoroethyl)-L-tyrosine (^{18}F-FET) PET; 3-T MRSI with a short echo time; and fluid-attenuated inversion recovery, T2-weighted, and contrast-enhanced T1-weighted MRI were performed for stereotactic biopsy planning. Serial samples were taken along the needle trajectory, and their masks were projected to the preoperative imaging data. Each sample was individually evaluated neuropathologically. ^{18}F-FET uptake and the MRSI signals choline (Cho), *N*-acetyl-aspartate (NAA), creatine, myoinositol, and derived ratios were evaluated for each sample and classified using logistic regression. The diagnostic accuracy was evaluated by receiver operating characteristic analysis. **Results:** On the basis of the neuropathologic evaluation of tissue from 88 stereotactic biopsies, supplemented with ^{18}F-FET PET and MRSI metrics from 20 areas on the healthy-appearing contralateral hemisphere to balance the glioma/nonglioma groups, ^{18}F-FET PET identified glioma with the highest accuracy (area under the receiver operating characteristic curve, 0.89; 95% CI, 0.81–0.93; threshold, 1.4 × background uptake). Among the MR spectroscopic metabolites, Cho/NAA normalized to normal brain tissue showed the highest diagnostic accuracy (area under the receiver operating characteristic curve, 0.81; 95% CI, 0.71–0.88; threshold, 2.2). The combination of ^{18}F-FET PET and normalized Cho/NAA did not improve the diagnostic performance. **Conclusion:** MRI-based delineation of gliomas should preferably be supplemented by ^{18}F-FET PET.

Key Words: MR spectroscopic imaging; ^{18}F-FET PET; brain tumors; multimodal imaging; stereotactic biopsy

Received May 11, 2023; revision accepted Aug. 22, 2023.
For correspondence or reprints, contact Jörg Mauler (j.mauler@fz-juelich.de).
Published online Oct. 26, 2023.

J Nucl Med 2024; 65:16–21
DOI: 10.2967/jnumed.123.265868

Currently, contrast-enhanced MRI is the method of choice for diagnosis and treatment monitoring in patients with brain tumors (*1*), but differentiation between the tumor center, infiltration zone, and peritumoral tissue changes, such as edema, may be challenging, particularly in patients with nonenhancing gliomas (*2*). Consequently, accurate delineation of glioma extent based on conventional MRI alone may be challenging. Accurate imaging-based tumor localization is essential for treatment planning and for identifying the most metabolically active parts for biopsy planning (*3*,*4*), especially when biopsy sampling is difficult, such as in the brain stem (*5*).

Advanced MRI methods and amino acid PET are of value to obtain additional diagnostic information in clinically challenging situations (*6*). In brain tumor diagnostics, amino acid PET has been recommended by the Response Assessment in Neuro-Oncology Working Group as a supplement to structural MRI (*7*). In contrast to ^{18}F-FDG, uptake of radiolabeled amino acids is low in normal brain tissue, and brain tumors can be depicted with high tumor-to-background contrast. A key feature of common amino acid tracers such as *O*-(2-[^{18}F]fluoroethyl)-L-tyrosine (^{18}F-FET) is their ability to pass through the intact blood–brain barrier, which enables depiction of the tumor mass beyond contrast enhancement on MRI and of nonenhancing gliomas (*6*,*8*). Local maxima of ^{18}F-FET uptake in heterogeneous gliomas usually colocalize with the highest ^{18}F-FDG uptake, but ^{18}F-FET PET is considerably more sensitive than ^{18}F-FDG PET for biopsy guidance (*6*).

Another approach for detecting neoplastic tissue with high accuracy is the use of metabolic markers derived from MR spectroscopic imaging (MRSI) (*9*). Most commonly, the MR signal of increased total choline (Cho), which reflects the abnormal Cho

metabolism in cancers (*10*), is used as a marker of malignant transformation. However, the congruency between the tumor borders delineated by the increased Cho–to–*N*-acetyl-aspartate (NAA) ratio measured using MRSI, compared with ^{18}F-FET uptake, has been investigated in only a few studies. The comparison of 2-dimensional spatially resolved MRSI and ^{18}F-FET uptake showed a congruency greater than 75% in 15 patients with gliomas (*11*). In contrast to that finding, a study using 3-dimensional volumetric brain MRSI found a low level of overlap, 40%, and an average distance of 0.9 cm between the centers of mass of both modalities (*12*).

Recently, the combination of conventional and advanced MRI methods, as well as ^{18}F-FET PET, was investigated in a biopsy-controlled study, but the added value of MRSI could not be assessed because of missing spectroscopic data from the tumor area (*13*).

The aim of this study was to investigate the diagnostic accuracy of ^{18}F-FET PET and MRSI and their combined use to identify neoplastic tissue in patients with newly diagnosed lesions indicative of glioma, with histopathology as the gold standard. The imaging findings were validated by tissue obtained from spatially correlated stereotactic biopsies, which were mapped into the preoperative imaging data on the basis of coordinates from the stereotactic surgery.

MATERIALS AND METHODS

Patients

The study was based on a series of 35 consecutive patients with structural MRI findings indicating glioma and in whom a stereotactic biopsy was planned for clinical reasons such as nonenhancing tumors or an unclear differential diagnosis. The patients were scheduled for ^{18}F-FET PET–guided stereotactic biopsy as part of clinical management and underwent hybrid ^{18}F-FET PET/MRSI before biopsy. Patients with incomplete sets of multimodal data or with data of low spectral quality were withdrawn from the study. The study adhered to the standards established in the Declaration of Helsinki and was approved by the ethical committee of the medical faculty of the RWTH Aachen University (EK 096/18). All patients gave written informed consent before the measurement.

MRI

All studies were performed on a Siemens 3-T TIM Trio MRI scanner with a Siemens 8-channel head coil. At the time of the ^{18}F-FET PET measurement, T1-weighted MR images were acquired before and after the administration of a gadolinium-based contrast agent (Dotarem; Guerbet) in addition to T2-weighted and fluid-attenuated inversion recovery images. The supplemental materials (available at http://jnm.snmjournals.org) provide further details.

A second contrast-enhanced T1-weighted MRI scan was acquired just before the stereotactic surgery, and a cranial CT scan was conducted with the attached stereotactic frame for biopsy planning.

MRSI

The high-resolution 3-dimensional volumetric MRSI acquisition covered the cerebrum and used a spin-echo excitation with echo-planar readout (*14*), an echo time of 17.6 ms, an acquisition time of 16 min, and integrated lipid and water suppression. The metabolite signals were scaled with an unsuppressed water reference signal from interleaved measurements. The supplemental materials provide further details.

PET Imaging

The amino acid ^{18}F-FET was produced and applied as described previously (*15*). All patients fasted for at least 12 h before the PET measurement and were injected intravenously with 3 MBq of ^{18}F-FET per kilogram of body weight. The dynamic ^{18}F-FET PET acquisition over 50 min was performed using a Siemens BrainPET insert (*16*). The supplemental materials provide further details. All reconstructed frames (isotropic resolution, 1.25 mm) were smoothed with a 2.5-mm gaussian kernel, and motion was corrected using PMOD (version 3.5; PMOD Technologies LLC). The summed images from 20 to 40 min after injection were used for the analysis.

Stereotactic Biopsies

Before stereotactic biopsy, contrast-enhanced MRI and ^{18}F-FET PET were spatially registered on an intraoperatively obtained cranial CT scan as a basic image for planning the biopsy trajectory. The trajectory targeted the area with the highest ^{18}F-FET uptake while avoiding vessels and eloquent brain areas. The samples were classified or reclassified according to the 2021 World Health Organization (WHO) classification of tumors of the central nervous system taxonomy (supplemental materials) (*17*). The biopsies were taken an average of 11 d after the PET measurements (SD, 11 d; minimum, 3 d; maximum, 56 d).

For ethical reasons, samples could not be taken from healthy brain tissue; thus, the number of control samples was underrepresented. To balance the groups of samples for statistical analysis, virtual negative biopsies (i.e., the noninvasive examination of healthy-appearing contralateral brain regions using ^{18}F-FET PET and MRSI) were performed on the contralateral side. The supplemental materials provide further details.

Data Analysis

The spectroscopic data were reconstructed using the Metabolite Imaging and Data Analysis System software package (*18*). After the interpolation of the raw data to $64 \times 64 \times 32$ voxels ($4.375 \times 4.375 \times 5.625$ mm^3), a final spatial resolution of 108 mm^3 was gained. The data were transformed into volumetric metabolite maps using automatic spectral analysis and after signal normalization to the simultaneously acquired water reference signal (*19*). The maps comprised the metabolite distributions of Cho, creatine (Cr), NAA, and myoinositol (mIno). For the final analysis, ratio maps of Cho/NAA, NAA/Cr, Cho/Cr, and mIno/Cr were calculated.

The ^{18}F-FET PET data, the MRSI data, all other MRI data, and the biopsy track masks were registered to the T1-weighted data. Masks of the tumor and the surrounding edema were manually delineated on the basis of the fluid-attenuated inversion recovery and T2-weighted data (*12*) and used to keep the normalization to the water signal devoid of distortions caused by the edema of the tumor tissue.

The ^{18}F-FET uptake and MRSI metabolite data were normalized to the respective background signals, which were given by the mean signal outside the area delineated by the previously described tumor masks. This procedure is referred to below as normalization to normal-appearing tissue. The normalized ^{18}F-FET images, ^{18}F-FET$_n$ (in this paper, signals normalized to normal-appearing tissue signal levels are denoted by subscript "n"), were resampled to the resolution of the metabolite maps. In addition to the normalized metabolite values, the nonnormalized values were analyzed to enable comparison with literature values.

The biopsy masks were down-sampled to match the spatial resolution of the spectroscopic data. Voxels with a biopsy partial volume of less than 50% or an underlying spectral line width outside the interval from 3 to 12 Hz were excluded from further analysis.

The histologic findings "glial tumor" and "infiltration zone" were labeled as tumor tissue in terms of PET/MRSI. Benign results and findings that were positive only on the microscopic scale, such as "proliferated brain tissue with tumor cells," were considered negative.

The threshold for neoplastic tissue based on different metabolite combinations or ^{18}F-FET uptake was determined by logistic regression as described in the supplemental materials.

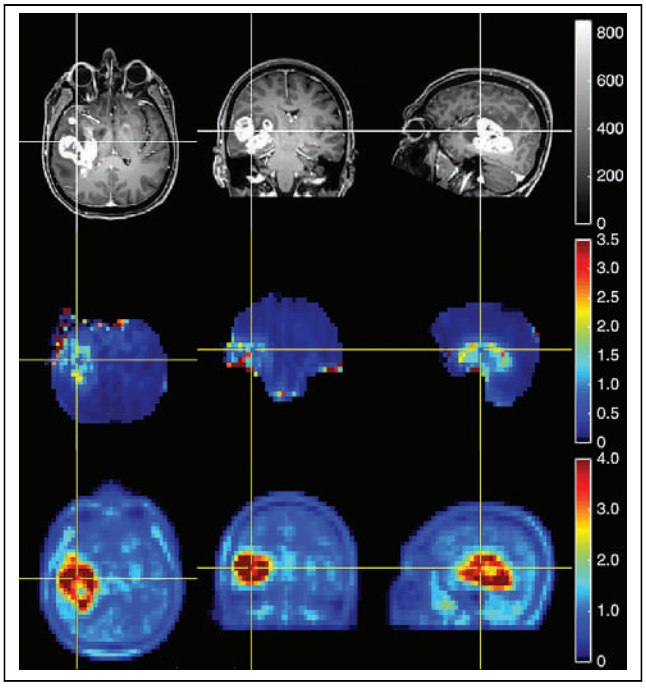

FIGURE 1. Example of registered contrast-enhanced T1-weighted MRI (top; arbitrary units), corresponding Cho/NAA spectroscopic image (middle), and ^{18}F-FET PET (bottom) of patient 18, who was diagnosed with glioblastoma, IDH wild-type, central nervous system WHO grade 4. ^{18}F-FET$_n$ data were resliced and resampled to resolution of MRSI data. Position of crosshairs marks location of biopsy.

RESULTS

From July 2018 to September 2020, a series of 35 patients with suspected brain tumors was recruited for the study. After the exclusion of 4 patients because of low spectral quality and 1 patient because of missing biopsy coordinates, the analyzed group included 30 patients (14 women and 16 men) with an average age (±SD) of 48 ± 13 y (range, 27–82 y).

Supplemental Table 1 shows the individual characteristics and neuropathologic diagnoses according to the 2021 WHO classification of tumors of the central nervous system, and Supplemental Table 2 shows patients excluded because of insufficient spectral quality. In total, 9 patients with enhancing gliomas, 15 patients with nonenhancing gliomas, 2 patients with enhancing lesions other than gliomas, and 4 patients with nonglioma lesions without contrast enhancement were included.

Patient 4 had the contradicting findings of vasculitis, contrast enhancement, and high ^{18}F-FET uptake (2.6). Because the follow-up biopsy 18 mo later showed a glioblastoma (IDH wild-type; central nervous system WHO grade 4), the first biopsy was considered a sampling error, and the later diagnosis was used.

Per patient, 2.9 ± 1.2 (range, 2–7) cylindric specimens with a diameter of 2.8 mm and a length of 5–10 mm were obtained along 1–2 biopsy trajectories. Eighteen biopsies were excluded because of the low spectral quality of the corresponding MR spectrum. The ^{18}F-FET PET and MRSI data were acquired 13 ± 12 d before the biopsies, and the T1-weighted series for biopsy planning was measured 3 ± 5 d before surgery. In total, 108 multimodal datasets, comprising 88 real biopsies supplemented with 20 virtual negative biopsies, were included in the analysis. Fifty-four biopsies were neuropathologically evaluated as glioma tissue. Figure 1 shows an example of a multimodal MRSI and ^{18}F-FET PET dataset at spectroscopic imaging resolution and registered to the anatomic T1-weighted data. Because the planning of the biopsy trajectories was based on the ^{18}F-FET uptake and the MRI results but did not take into account the MRSI results, the biopsy sites did not necessarily coincide with the sites of maximum spectroscopic signal (Fig. 2).

Among the analyses of the single-modality data, uptake of ^{18}F-FET$_n$ resulted in the highest diagnostic accuracy, with an averaged area under the receiver operating characteristic curve (AUC) of 0.89 after cross-validation (SD, 0.003; 95% CI, 0.81–0.93), which is linked to an uptake threshold of 1.4 times the background uptake (Tables 1 and 2).

Generally, the accuracy of the metabolite results generated from MRSI increased by up to 0.06 if the signals were normalized to normal-appearing tissue and additionally to another metabolite signal (such as Cho/NAA). When the diagnostic distinction between glial tumor and normal tissue was based on the spectroscopic marker Cho/NAA$_n$, the accuracy decreased to an average AUC of 0.81 (SD, 0.004; 95% CI, 0.71–0.88), based on a Cho/NAA$_n$ threshold of 2.2. All other analyzed spectroscopic signals, NAA/Cr$_n$ (AUC, 0.78), Cho$_n$ (AUC, 0.77), NAA$_n$ (AUC, 0.74), Cho/Cr$_n$ (AUC, 0.72), mIno$_n$ (AUC, 0.70), and mIno/Cr$_n$ (AUC, 0.70), showed lower accuracies. The result of Cr did not pass the significance threshold. The receiver operating characteristic curves of the 5 highest accuracy values are compared in Figure 3.

The combined analysis of the markers with the highest accuracy, ^{18}F-FET$_n$ uptake and Cho/NAA$_n$, did not pass the significance threshold of a *P* value of 0.05 or less. The results may indicate the tendency toward slightly improved accuracy (AUC, 0.90; Cho/NAA

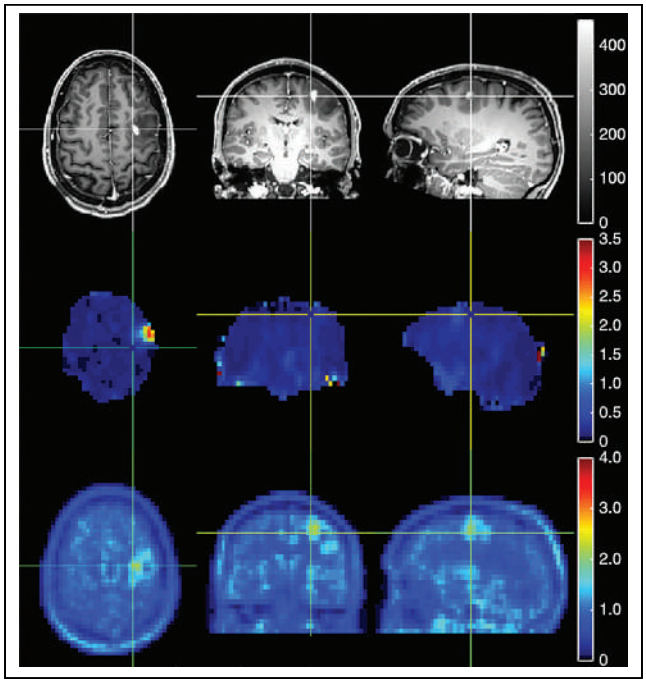

FIGURE 2. Contrast-enhanced T1-weighted MRI (top; arbitrary units), registered Cho/NAA spectroscopic signals (middle), and ^{18}F-FET PET (bottom) from patient 1, diagnosed with astrocytoma, IDH1-mutant, central nervous system WHO grade 3. Biopsy positions were based on ^{18}F-FET enhancement and therefore did not necessarily coincide with sites of maximum Cho/NAA ratios. Position of crosshairs marks location of biopsy.

TABLE 1
Results Depending on Different Model Terms in Logistic Regression Analysis

Marker	AUC	95% CI	Threshold	*P* intercept	*P* slope
FET_n*	0.89	0.81–0.93	1.4	3.7 e−06	3.4 e−06
Cho/NAA_n*	0.81	0.71–0.88	2.16	5 e−04	2 e−04
Cho/NAA*	0.79	0.68–0.86	0.65	0.0014	4.8 e−04
Cho/Cr_n*	0.72	0.61–0.80	1.65	7.5 e−04	6.9 e−04
Cho/Cr*	0.71	0.60–0.80	0.39	8.6 e−04	8 e−04
NAA/Cr_n*	0.78	0.68–0.86	0.76	4.8 e−05	1.8 e−05
NAA/Cr*	0.75	0.65–0.84	0.86	1.1 e−04	2.9 e−05
$mIno/Cr_n$*	0.70	0.59–0.79	0.99	0.006	0.004
Cho_n*	0.77	0.67–0.85	1.37	0.001	0.001
Cho*	0.71	0.60–0.80	10,594	0.037	0.024
NAA_n*	0.74	0.64–0.83	0.66	2.4 e−04	9 e−05
NAA*	0.72	0.61–0.81	22,129	0.003	0.001
$mIno_n$*	0.70	0.59–0.79	0.87	0.01	0.01
FET_n, Cho/NAA_n	0.90	0.82–0.94	NA	2.6 e−06	6.2 e−05; 0.305
FET_n, Cho/NAA	0.89	0.81–0.94	NA	2.4 e−06	3.5 e−05; 0.563

*$P < 0.05$ in all terms of model.
NA = not applicable.
All models contain constant and 1 or 2 linear terms, which represent level of markers ^{18}F-FET, Cho, NAA, Cr, mIno, and ratios thereof. Table is limited to results in which normalized metabolite signal reached AUC of 0.70 or more.

term, $P = 0.3$) compared with the ^{18}F-FET_n uptake (AUC, 0.89) and Cho/NAA_n (AUC, 0.81) alone. The results obtained after introducing an interaction term between ^{18}F-FET_n and Cho/NAA_n are shown in Supplemental Table 3.

The subgroup analysis of gliomas without contrast enhancement showed a slightly decreased AUC of 0.88 (95% CI, 0.75–0.94) when the diagnosis was based on ^{18}F-FET_n uptake and an increased AUC of 0.85 (95% CI, 0.72–0.93) for Cho/NAA_n. Compared with the values from all patients, the threshold values dropped to 1.3 for ^{18}F-FET_n and increased to 2.3 for Cho/NAA_n.

Accordingly, compared with the evaluation of the entire group of patients, the restriction to gliomas with contrast enhancement showed a higher diagnostic accuracy for ^{18}F-FET_n and a lower accuracy for Cho/NAA_n. ^{18}F-FET_n–based diagnosis resulted in an AUC of 0.91 (95% CI, 0.80–0.96; threshold, 1.5). Using Cho/NAA_n for diagnosis resulted in an AUC of 0.77 (95% CI, 0.61–0.88; threshold, 2.0).

TABLE 2
Results of Leave-One-Out Cross-Validation

Parameter	^{18}F-FET	Cho/NAA
Mean AUC ± SD	0.89 ± 0.003	0.81 ± 0.004
Mean threshold ± SD	1.4 ± 0.01	2.16 ± 0.04
Accuracy	0.78	0.71
Sensitivity	0.76	0.59
Specificity	0.80	0.83
Positive predictive value	0.79	0.78
Negative predictive value	0.77	0.67

The ^{18}F-FET_n–based diagnostics showed more accurate results, with 78% correctly classified samples compared with 71% correct classifications in the leave-one-out cross-validation for Cho/NAA_n (Table 2). ^{18}F-FET had superior sensitivity, 76%, whereas Cho/NAA showed better specificity, 83%. The positive predictive value of

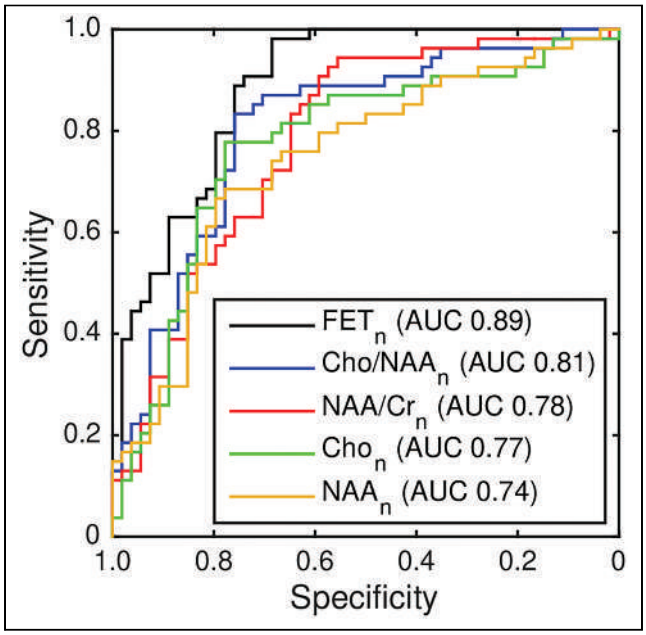

FIGURE 3. Receiver operating characteristic curves of ^{18}F-FET_n PET and MRSI metabolic markers Cho/NAA_n, NAA/Cr_n, Cho_n, and NAA_n based on analysis of 88 biopsies and 20 imaging data points from normal-appearing brain tissue.

^{18}F-FET$_n$ uptake was similar to that of Cho/NAA$_n$ (79% vs. 78%), and its negative predictive value was higher than that of Cho/NAA$_n$ (77% vs. 67%).

DISCUSSION

The major finding of this study is the higher accuracy of ^{18}F-FET$_n$ uptake than of Cho/NAA$_n$ for the imaging-based diagnosis of tumor tissue in enhancing and nonenhancing gliomas. Glioma delineation was optimal with the ^{18}F-FET$_n$–based tumor-to-background ratio of 1.4 and a Cho/NAA$_n$ of at least 2.2.

When ^{18}F-FET uptake was considered, the trend toward the highest diagnostic accuracy was found in enhancing gliomas. Cho/NAA$_n$ showed a trend toward higher accuracy in nonenhancing gliomas but still had a lower value than ^{18}F-FET$_n$. Given the relatively low number of patients, the corresponding overlapping 95% CIs do not allow a clear statement and may be responsible for the observed counterintuitive tendency toward lower accuracy for Cho/NAA$_n$ in enhancing gliomas. However, the trend toward the higher diagnostic accuracy of ^{18}F-FET$_n$ is consistent with previously reported results (*13*).

Regardless of contrast enhancement, ^{18}F-FET PET–based diagnosis generally showed higher diagnostic accuracy than Cho/NAA. Hence, ^{18}F-FET PET is significantly more sensitive for identifying glioma tissue, albeit at the cost of a somewhat decreased specificity compared with Cho/NAA.

The selection of metabolites and derived ratios includes those that can be determined with high accuracy at 3 T (*20*). The individual signals from Cho and NAA showed lower accuracy than their ratio. This finding is consistent with the finding that although Cho is variably elevated in different glioma types, NAA is reduced nonuniformly as a broad marker of neuronal loss (*21*). Compared with Cho/NAA, the other investigated metabolite signals, Cho, NAA, NAA/Cr, Cho/Cr, mIno, and mIno/Cr, generally showed lower accuracy in diagnosing glioma. Frequently, study results are reported as metabolite ratios, such as Cho/NAA, without further normalization. This study showed higher accuracies if signal ratios were additionally normalized to normal-appearing tissue.

Four of 35 patients (11%) were excluded from the analysis because of insufficient spectral quality. In addition, 18 samples had to be excluded from the remaining group of 106 samples (17%) for the same reason, which reduces the clinical utility of MRSI.

Within the limitations given by a different patient group, the observed ^{18}F-FET tumor threshold of 1.4 times the background uptake confirms the previously reported value and the widely used threshold of 1.6 (*22*,*23*). Besides the fact that the threshold values were determined with different PET scanners and influenced by different point spread functions, the current study included fewer subjects and more patients with gliomas showing equivocal findings on MRI. Therefore, the slightly decreased threshold in our study should be considered with caution and requires further biopsy-controlled studies in larger patient groups.

Relatively few studies have calibrated glioma–to–normal-tissue thresholds using coordinate-controlled biopsies. The found threshold of 0.65 for the absolute Cho/NAA ratio corresponds to the previously published integral Cho/NAA ratio (not corrected for proton number) of at least 2, which, however, was determined for a longer echo time (135 ms instead of 17 ms) using spatial 2-dimensional MRSI and approximately the 3-fold measured voxel size from a smaller group of patients (*24*). Data acquired with an even larger voxel size and long echo time resulted in a minimum ratio of 1.3 (*25*). This value was obtained from predominantly high-grade gliomas and fits as a lower limit to our threshold value.

The accuracy of the results depends on the decision as to which neuropathologic findings are considered positive for tumor tissue. In the presented analysis, the presence of single tumor cells in the tissue samples was not rated as tumor tissue because such findings are not accessible with either imaging method in view of the limited spatial resolution.

A limitation of this study was the small number of patients and the large proportion of equivocal MRI findings, often due to lack of contrast enhancement. Nevertheless, because diagnosis is particularly difficult in these patients, the importance and value of amino acid PET for this group of patients is further emphasized. A further limitation was the study design, which favored ^{18}F-FET over MRSI; planning of biopsy tracks to target the most metabolically active part of the tumor was based on ^{18}F-FET PET, because MRSI data were not yet available at the time of biopsy. Therefore, the use of MR spectroscopic data for biopsy planning (*26*,*27*) could not be properly compared with the use of ^{18}F-FET PET data. A further consequence of the study design was a lack of Cho/NAA-positive but ^{18}F-FET–negative samples. Therefore, the relevance of a high Cho/NAA ratio with low ^{18}F-FET uptake—which may indicate gliosis, inflammation, or demyelination (*3*,*28*,*29*) or a later recurrence and reduced progression-free survival (*26*,*30*)—remains to be addressed in future studies. Generally, in this study, histology was considered the gold standard for defining the diagnosis since the biopsies were analyzed by 2 experienced neuropathologists according to the 2021 WHO classification of tumors of the central nervous system.

The multimodal approach using MRSI, ^{18}F-FET PET, and neuropathology necessitates the combination of data from the millimeter scale down to the submillimeter scale. Only the ^{18}F-FET PET data can be down-sampled to a spectroscopic imaging resolution, whereas the neuropathologic results are bound to the dimensions of the biopsy cylinders. Accordingly, possible location errors are on this order of magnitude. Since the ^{18}F-FET concentration in the blood compartment is high in the first hour after administration, special attention during the evaluation was placed on ensuring that the ^{18}F-FET signal was not partially confused with an increased signal contribution from blood vessels (*15*). In rare cases, however, after the resampling of the ^{18}F-FET data to the resolution of the metabolite maps, contamination of the larger voxels cannot be completely ruled out. Moreover, the MRSI data bear the MR spectroscopy inherent chemical shift displacement error. With the given readout gradient of 13.72 mT/m, this error is a fraction of the nominal voxel size in the anterior–posterior direction and, therefore, negligible for the analysis in spectroscopic imaging resolution.

CONCLUSION

Amino acid PET using the tracer ^{18}F-FET allows the diagnosis and identification of viable glioma tissue with a high diagnostic accuracy. For a mixed group of enhancing and nonenhancing gliomas, tumor delineation was most accurate with an ^{18}F-FET uptake threshold of 1.4 times the background signal. MRSI provides the highest diagnostic accuracy, with a Cho/NAA$_n$ threshold of 2.2. Further data are required to assess the possible diagnostic benefit of the combined analysis of ^{18}F-FET uptake and MR spectroscopic metabolites, such as Cho/NAA, and to assess the diagnostic meaning of Cho/NAA-positive but ^{18}F-FET–negative findings.

DISCLOSURE

Norbert Galldiks and Philipp Lohmann received honoraria from Blue Earth Diagnostics for lectures. Norbert Galldiks received honoraria from Telix Pharmaceuticals for advisory board participation. Karl-Josef Langen and Felix Mottaghy received honoraria from Telix Pharmaceuticals for consultancy services. No other potential conflict of interest relevant to this article was reported.

ACKNOWLEDGMENTS

We thank Silke Frensch, Kornelia Frey, Natalie Judov, Trude Plum, Suzanne Schaden, and Lutz Tellmann for assistance with the patient studies, and we thank Johannes Ermert, Silke Grafmüller, Erika Wabbals, and Sascha Rehbein for radiosynthesis of the ^{18}F-FET. We greatly appreciate Claire Rick's English proofreading.

KEY POINTS

QUESTION: What is the diagnostic accuracy of ^{18}F-FET PET and MRSI for the detection of glioma?

PERTINENT FINDINGS: Validated using tissue samples from stereotactic biopsies, ^{18}F-FET PET identified glioma with an accuracy of 0.89. The MRSI marker Cho/NAA showed a diagnostic accuracy of 0.81.

IMPLICATIONS FOR PATIENT CARE: MRI-based delineation of gliomas should preferably be supplemented by ^{18}F-FET PET.

REFERENCES

1. Pope WB, Brandal G. Conventional and advanced magnetic resonance imaging in patients with high-grade glioma. *Q J Nucl Med Mol Imaging.* 2018;62:239–253.
2. Hygino da Cruz LC Jr, Rodriguez I, Domingues RC, Gasparetto EL, Sorensen AG. Pseudoprogression and pseudoresponse: imaging challenges in the assessment of posttreatment glioma. *AJNR.* 2011;32:1978–1985.
3. Floeth FW, Pauleit D, Wittsack H-J, et al. Multimodal metabolic imaging of cerebral gliomas: positron emission tomography with [^{18}F]fluoroethyl-L-tyrosine and magnetic resonance spectroscopy. *J Neurosurg.* 2005;102:318–327.
4. Misch M, Guggemos A, Driever PH, et al. ^{18}F-FET-PET guided surgical biopsy and resection in children and adolescence with brain tumors. *Childs Nerv Syst.* 2015;31:261–267.
5. Purohit B, Kamli AA, Kollias SS. Imaging of adult brainstem gliomas. *Eur J Radiol.* 2015;84:709–720.
6. Langen KJ, Galldiks N, Hattingen E, Shah NJ. Advances in neuro-oncology imaging. *Nat Rev Neurol.* 2017;13:279–289.
7. Albert NL, Weller M, Suchorska B, et al. Response Assessment in Neuro-Oncology Working Group and European Association for Neuro-Oncology recommendations for the clinical use of PET imaging in gliomas. *Neuro Oncol.* 2016;18:1199–1208.
8. Lohmann P, Stavrinou P, Lipke K, et al. FET PET reveals considerable spatial differences in tumour burden compared to conventional MRI in newly diagnosed glioblastoma. *Eur J Nucl Med Mol Imaging.* 2019;46:591–602.
9. Widhalm G, Krssak M, Minchev G, et al. Value of H-1-magnetic resonance spectroscopy chemical shift imaging for detection of anaplastic foci in diffusely infiltrating gliomas with non-significant contrast-enhancement. *J Neurol Neurosurg Psychiatry.* 2011;82:512–520.
10. Glunde K, Penet M-F, Jiang L, Jacobs MA, Bhujwalla ZM. Choline metabolism-based molecular diagnosis of cancer: an update. *Expert Rev Mol Diagn.* 2015;15:735–747.
11. Stadlbauer A, Nimsky C, Buslei R, et al. Proton magnetic resonance spectroscopic imaging in the border zone of gliomas: correlation of metabolic and histological changes at low tumor infiltration: initial results. *Invest Radiol.* 2007;42:218–223.
12. Mauler J, Maudsley AA, Langen K-J, et al. Spatial relationship of glioma volume derived from ^{18}F-FET PET and volumetric MR spectroscopy imaging: a hybrid PET/MRI study. *J Nucl Med.* 2018;59:603–609.
13. Verburg N, Koopman T, Yaqub MM, et al. Improved detection of diffuse glioma infiltration with imaging combinations: a diagnostic accuracy study. *Neuro Oncol.* 2020;22:412–422.
14. Ebel A, Maudsley AA. Detection and correction of frequency instabilities for volumetric ^{1}H echo-planar spectroscopic imaging. *Magn Reson Med.* 2005;53:465–469.
15. Langen KJ, Stoffels G, Filss C, et al. Imaging of amino acid transport in brain tumours: positron emission tomography with O-(2-[^{18}F]fluoroethyl)-L-tyrosine (FET). *Methods.* 2017;130:124–134.
16. Herzog H, Langen K-J, Weirich C, et al. High resolution BrainPET combined with simultaneous MRI. *Nuklearmedizin.* 2011;50:74–82.
17. Louis DN, Perry A, Wesseling P, et al. The 2021 WHO Classification of Tumors of the Central Nervous System: a summary. *Neuro Oncol.* 2021;23:1231–1251.
18. Maudsley AA, Darkazanli A, Alger JR, et al. Comprehensive processing, display and analysis for in vivo MR spectroscopic imaging. *NMR Biomed.* 2006;19:492–503.
19. Soher BJ, Young K, Govindaraju V, Maudsley AA. Automated spectral analysis III: application to in vivo proton MR spectroscopy and spectroscopic imaging. *Magn Reson Med.* 1998;40:822–831.
20. Henning A. Proton and multinuclear magnetic resonance spectroscopy in the human brain at ultra-high field strength: a review. *Neuroimage.* 2018;168:181–198.
21. Dowling C, Bollen AW, Noworolski SM, et al. Preoperative proton MR spectroscopic imaging of brain tumors: correlation with histopathologic analysis of resection specimens. *AJNR.* 2001;22:604–612.
22. Rapp M, Heinzel A, Galldiks N, et al. Diagnostic performance of ^{18}F-FET PET in newly diagnosed cerebral lesions suggestive of glioma. *J Nucl Med.* 2013;54:229–235.
23. Pauleit D, Floeth F, Hamacher K, et al. O-(2-[^{18}F]fluoroethyl)-L-tyrosine PET combined with MRI improves the diagnostic assessment of cerebral gliomas. *Brain.* 2005;128:678–687.
24. Guo J, Yao C, Chen H, et al. The relationship between Cho/NAA and glioma metabolism: implementation for margin delineation of cerebral gliomas. *Acta Neurochir (Wien).* 2012;154:1361–1370.
25. Vigneron D, Bollen A, McDermott M, et al. Three-dimensional magnetic resonance spectroscopic imaging of histologically confirmed brain tumors. *Magn Reson Imaging.* 2001;19:89–101.
26. Zhong J, Huang V, Gurbani SS, et al. 3D whole-brain metabolite imaging to improve characterization of low-to-intermediate grade gliomas. *J Neurooncol.* 2021;153:303–311.
27. Abdelaziz O, Eshra M, Belal A, Elshafei M. Diagnostic value of magnetic resonance spectroscopy compared with stereotactic biopsy of intra-axial brain lesions. *J Neurol Surg A Cent Eur Neurosurg.* 2016;77:283–290.
28. Hayashi T, Kumabe T, Jokura H, et al. Inflammatory demyelinating disease mimicking malignant glioma. *J Nucl Med.* 2003;44:565–569.
29. Majós C, Aguilera C, Alonso J, et al. Proton MR spectroscopy improves discrimination between tumor and pseudotumoral lesion in solid brain masses. *AJNR.* 2009;30:544–551.
30. Cordova JS, Shu H-KG, Liang Z, et al. Whole-brain spectroscopic MRI biomarkers identify infiltrating margins in glioblastoma patients. *Neuro Oncol.* 2016;18:1180–1189.

Increased Metabolic Activity of the Thymus and Lymph Nodes in Pediatric Oncology Patients After Coronavirus Disease 2019 Vaccination

Gaurav Luthria*[1], Lucia Baratto*[1], Lisa Adams[1], Wipawee Morakote[1,2], and Heike E. Daldrup-Link[1,3]

[1]*Division of Pediatric Radiology, Department of Radiology, Lucile Packard Children's Hospital, Stanford University, Stanford, California;* [2]*Department of Radiology, Faculty of Medicine, Chiang Mai University, Chiang Mai, Thailand; and* [3]*Pediatric Hematology/Oncology, Department of Pediatrics, Lucile Packard Children's Hospital, Stanford University, Stanford, California*

We hypothesized that ^{18}F-FDG PET/MRI would reveal thymus activation in children after coronavirus disease 2019 (COVID-19) vaccination. **Methods:** We retrospectively analyzed the ^{18}F-FDG PET/MRI scans of 6 children with extrathoracic cancer before and after COVID-19 vaccination. We compared pre- and postvaccination SUV_{max}, mean apparent diffusion coefficient, and size of the thymus and axillary lymph nodes using a paired *t* test. **Results:** All 6 patients showed increased ^{18}F-FDG uptake in the axillary lymph nodes after vaccination ($P = 0.03$). In addition, these patients demonstrated increased ^{18}F-FDG uptake in the thymus. When compared with baseline, the postvaccination scans of these patients demonstrated an increased mean thymic SUV ($P = 0.02$), increased thymic size ($P = 0.13$), and decreased thymic mean apparent diffusion coefficient ($P = 0.08$). **Conclusion:** ^{18}F-FDG PET/MRI can reveal thymus activation in addition to local lymph node reactions in children after COVID-19 vaccination.

Key Words: COVID-19 vaccine; thymus; lymphadenopathy; ^{18}F-FDG PET/MRI; pediatric oncology

J Nucl Med 2024; 65:22–24
DOI: 10.2967/jnumed.123.266271

The coronavirus disease 2019 (COVID-19) pandemic sparked the rapid development and deployment of messenger RNA (mRNA) vaccines to millions of people, including children (*1*). Recent efforts to understand the immune response to mRNA vaccines revealed germinal center responses in axillary lymph nodes (*2*). In adults, an increased size and metabolic activity of axillary lymph nodes have been described after COVID-19 vaccination (*3*). A retrospective study showed that 54% (75/140) of adult patients had ^{18}F-FDG–avid lymph nodes ipsilateral to the mRNA vaccine injection site on ^{18}F-FDG PET/CT scans (*4*). Similarly, a large nationwide cohort study reported that 46% of vaccinated patients (332/728) had ^{18}F-FDG–avid axillary lymph nodes (*5*).

Received Jul. 3, 2023; revision accepted Sep. 17, 2023.
For correspondence or reprints, contact Heike E. Daldrup-Link (heiked@stanford.edu).
*Contributed equally to this work.
Published online Oct. 26, 2023.

In patients with cancer, an increase in the size and metabolic activity of lymph nodes can indicate tumor recurrence or progression and play an important role in guiding treatment decisions. Several case reports have demonstrated that vaccine-related lymphadenopathy may confound disease assessment in oncology patients such as those with breast cancer (*6*), metastatic melanoma (*7*,*8*), or Hodgkin lymphoma (*9*). Therefore, it is important to understand typical imaging findings that allow differentiation of vaccination from cancer-related lymphadenopathy.

COVID-19 vaccinations were initially Food and Drug Administration–approved for adults only and then were extended to children and teenagers. Unfortunately, our knowledge of postvaccination ^{18}F-FDG PET imaging findings in children and young adults remains limited. Experimental studies have demonstrated strong T-cell activation in response to mRNA vaccines (*10*). Since children have T-cell–rich thymus tissue (*11*), we hypothesized that ^{18}F-FDG PET/MRI would reveal an increased metabolic activity in the thymus in addition to that in the local lymph nodes after COVID-19 vaccination.

MATERIALS AND METHODS

Study Design

This was a secondary analysis of medical imaging data obtained as part of a retrospective study on pediatric cancer staging with whole-body ^{18}F-FDG PET/MRI, which was approved by our institutional review board (approval 48854). The inclusion criteria included children or young adults diagnosed with cancer, receipt of at least 1 dose of the COVID-19 vaccine, and completion of at least 2 ^{18}F-FDG PET/MRI examinations, one before and one after vaccination. The exclusion criteria involved any instances of nonsimultaneous ^{18}F-FDG PET/MRI. We included 6 children and young adults: 5 female and 1 male, with a mean age (±SD) of 13.67 ± 3.67 y (range, 10–19 y). All 6 patients had an extrathoracic malignancy.

^{18}F-FDG PET/MRI Protocol

All patients underwent clinical standard ^{18}F-FDG PET/MRI studies before and after COVID-19 vaccination. The scans were obtained on average 49.83 ± 45.67 d after the most recent vaccination dose (range, 6–121 d). All patients received the Pfizer-BioNTech vaccine. Of the 6 patients, 2 received a total of 3 intramuscular vaccination doses at separate intervals, 2 were administered 2 doses of vaccine, and 2 received a single vaccination dose. All vaccinations were completed before the postvaccination ^{18}F-FDG PET/MRI scan. Before each PET imaging study, the patients fasted for at least 6 h. The serum glucose level at the time of ^{18}F-FDG injection was less than 120 mg/dL. ^{18}F-FDG PET/MR images were acquired 60–70 min after intravenous administration of ^{18}F-FDG (3–5 MBq/kg of body weight), using a 3-T PET/MRI scanner (Signa;

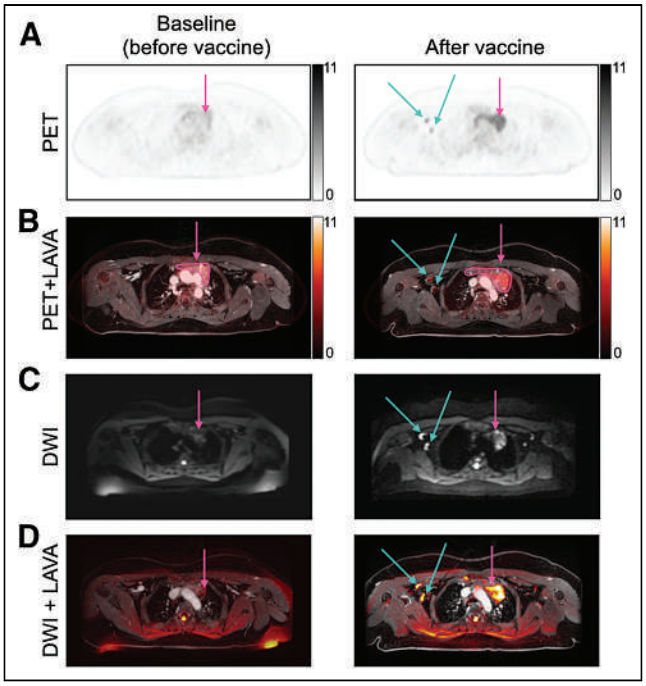

FIGURE 1. Axial ^{18}F-FDG PET (A), ^{18}F-FDG PET/T1-weighted gradient echo (LAVA) MRI (B), axial DW MRI (C), and DW MRI/LAVA MRI (D) in 14-y-old girl with bilateral ovarian Sertoli-Leydig tumors. Scans were obtained 3 mo before first COVID-19 vaccination dose (first column) and 2 mo after third vaccination dose (6 mo after first vaccination; second column). After vaccination, ^{18}F-FDG PET and ^{18}F-FDG PET/LAVA MRI showed increased uptake in thymus (pink arrows in A and B) and axillary lymph nodes (blue arrow in A and B); similarly, DW MRI and DW MRI/LAVA MRI showed restricted diffusion in thymus (pink arrows in C and D) and axillary lymph nodes (blue arrows in C and D). DWI = diffusion-weighted imaging; LAVA = liver acquisition with volume acquisition.

GE Healthcare). The PET data acquisition time was 3 min 30 s per bed position (89 slices per bed position) for 5–9 bed positions.

^{18}F-FDG PET images were reconstructed using ordered-subset expectation maximization with 2 iterations and 28 subsets. A 2-point Dixon sequence was used for attenuation correction of the PET/MR images. The obtained ^{18}F-FDG PET images were then color-encoded and fused with MRI scans using MIM software (version 7.0.5; MIM Software Inc.).

MRI included an axial contrast-enhanced T1-weighted liver acquisition with volume acquisition (repetition time, 4.2 ms; echo time, 1.7 ms; fractional anisotropy, 15; slice thickness, 3.4 mm) for coregistration with ^{18}F-FDG PET data, as well as axial diffusion-weighted images (repetition time, 7,824 ms; echo time, 56 ms; *b* values, 50 and 800 s/mm^2; slice thickness, 6 mm). The apparent diffusion coefficient (ADC) maps were automatically generated by the software.

Image Analysis

One board-certified radiologist and 1 board-certified nuclear medicine physician jointly evaluated the original and fused whole-body ^{18}F-FDG PET/MRI and diffusion-weighted MRI scans and determined the size, metabolic activity, and restricted diffusion of the axillary lymph nodes and thymus in each patient. The readers were not aware of the clinical data or vaccination status of the patient while analyzing images. On ^{18}F-FDG PET images, a fixed SUV scale (threshold, 42%) and color table were used. An increased ^{18}F-FDG uptake was defined as focal tracer uptake higher than that of the mediastinal blood pool. The SUV_{max} was measured by placing a 3-dimensional volume of interest in the thymus and lymph nodes. The longest and shortest transverse diameters of the thymus were calculated as well.

For analysis of diffusion-weighted MRI, mean ADC values were measured through operator-defined regions of interests. All measurements were obtained using MIM software (version 7.0.5) and OsiriX software (version 10.0, 64 bits; Pixmeo).

Statistical Analysis

Statistical analysis was performed with Microsoft Excel. Continuous data are presented as mean ± SD. The 2-tailed paired *t* test was used to compare differences in the SUV_{max} and mean ADC of the axillary lymph nodes and thymus before and after vaccination, as well as changes in thymic size. A *P* value of less than 0.05 was considered significant.

RESULTS

Evaluation of 6 patients revealed uniformly normal axillary lymph nodes and thymus at baseline, with a metabolic activity below that of the mediastinal blood pool. After COVID-19 vaccination, there was a marked increase in the metabolic activity in the ipsilateral axillary lymph nodes across all patients (Fig. 1). The mean SUV_{max} of the axillary lymph nodes increased by a factor of 3.0, from 0.87 ± 0.44 before vaccination to 2.61 ± 1.21 after vaccination ($P = 0.03$).

In addition, all 6 patients who were previously diagnosed with extrathoracic cancers also demonstrated an increased size, increased metabolic activity, and restricted diffusion of the lymph nodes and thymus after COVID-19 vaccination (Fig. 1). The mean SUV_{max} of the thymus increased 2-fold, from 1.77 ± 0.97 before vaccination to 3.46 ± 1.35 after vaccination ($P = 0.017$). The size of the thymus, approximated as the product of the shortest and longest transverse diameters, increased 1.7-fold, from 7.02 ± 5.41 to 11.91 ± 11.85 cm ($P = 0.13$). The mean ADC of the lymph nodes decreased from 1.11 to 0.92 ($P = 0.26$), and the

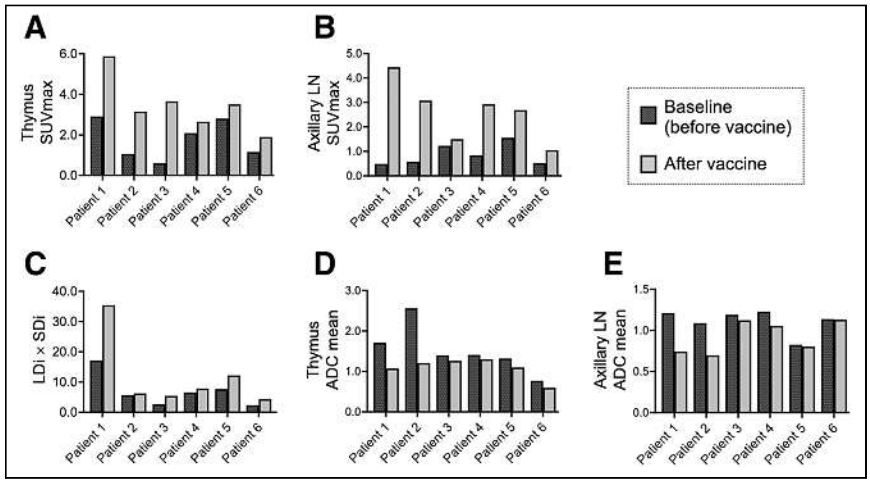

FIGURE 2. ^{18}F-FDG PET/MRI parameters before and after COVID-19 vaccination: SUV_{max} of thymus and axillary lymph nodes (A and B), LDi × SDi of thymus (C), mean ADC of thymus (D), and mean ADC of lymph nodes (E). Follow-up ^{18}F-FDG PET/MRI scans for patients 1, 2, 3, 4, 5, and 6 were obtained 76, 21, 66, 9, 121, and 6 d after their last vaccination, respectively. SUV_{max} of thymus ($P = 0.02$) and axillary lymph nodes ($P = 0.03$) significantly increased after vaccination, thymic size approximated by LDi × SDi increased ($P = 0.13$), and mean ADC of thymus ($P = 0.08$) and axillary lymph nodes ($P = 0.07$) decreased. Significance was computed using 2-tailed paired *t* test. LDi = longest transverse diameter; SDi = shortest transverse diameter.

mean ADC of the thymus decreased from 1.53 to 1.09 ($P = 0.08$). Data are shown in Figure 2.

DISCUSSION

Here we show for the first time, to our knowledge, that ^{18}F-FDG PET/MRI can reveal thymus activation in addition to local lymph node reactions in children after COVID-19 vaccination. Six patients demonstrated increased ^{18}F-FDG uptake and restricted diffusion of the locoregional lymph nodes and thymus after receiving the COVID-19 vaccination. The observed decrease in the mean ADC values of the thymus after vaccination indicates increased cellularity of the thymus tissue, which could be related to immune cell infiltration or proliferation in response to the vaccination. The observed increase in the SUV_{max} of the thymus after vaccination indicates increased metabolic activity of the thymus tissue, which could be related to immune cell activation.

Our results are consistent with a recent case study reporting increased ^{18}F-FDG uptake in the thymus and left axillary lymph nodes in a 35-y-old woman after vaccination (*12*). The history of recent vaccination, the combination of metabolically active axillary lymph nodes and thymus, and the absence of bone marrow activation can all help with the correct diagnosis.

Differential diagnoses include recurrent or metastatic cancer and thymic rebound after chemotherapy (*13*). In survivors of leukemia and lymphoma, thymic hyperplasia after completion of chemotherapy is typically characterized by thymic enlargement and hypermetabolism, without changes in local lymph nodes (*14*). Thymic rebound after chemotherapy is often accompanied by an increased metabolic activity of the bone marrow. By contrast, our patients demonstrated activated lymph nodes and normal bone marrow. Radiologic evaluation of the morphologic and metabolic appearance of the thymus allowed us to exclude tumor lesions. Thymic tumors cause mass effects (i.e., compression of the veins, deviation of the trachea), which were not observed. ^{18}F-FDG uptake of the thymus was homogeneous and bilateral, and no focal ^{18}F-FDG uptake was observed, suggesting that the increased metabolic activity was of an inflammatory nature.

It is important to note limitations in our current analysis. Further studies with larger sample sizes are needed to confirm our findings. The interval between vaccination and imaging, combined with the fact that immunologic responses can vary significantly among individuals (*15*), may contribute to a wide range of immune responses to vaccination. Expanding our analysis to include patients who have autoimmune diseases or are heavily immunosuppressed, as well as conducting a time-series analysis to examine changes in the metabolic activity of the thymus and lymph nodes after vaccination, could provide a more nuanced understanding of how vaccination is represented on ^{18}F-FDG PET/MRI. However, our current study's retrospective nature makes this kind of time-series analysis challenging. Understanding the duration of thymic activity after vaccination and modulatory factors affecting thymic activity can assist in optimizing vaccine administration and imaging schedules to avoid confounding results.

CONCLUSION

The detection of increased ^{18}F-FDG activity in the local lymph nodes and thymus after COVID-19 vaccination on ^{18}F-FDG PET/MRI scans could be helpful to confirm a vaccine-induced immune response in cancer patients. ^{18}F-FDG PET/MRI can reveal thymus activation in addition to local lymph node reactions in children after COVID-19 vaccination. These findings underscore the importance of verifying a patient's vaccination status before an imaging examination, as vaccination-associated changes can lead to false-positive diagnoses.

DISCLOSURE

This work was supported by a grant from the National Cancer Institute (Grant No. R01CA269231). No other potential conflict of interest relevant to this article was reported.

KEY POINTS

QUESTION: Does ^{18}F-FDG PET/MRI reveal thymus and lymph node activity after COVID-19 vaccine administration?

PERTINENT FINDINGS: We evaluated ^{18}F-FDG PET/MRI scans for 6 children and young adults before and after COVID-19 vaccine administration. The scans demonstrated thymus activation in addition to local lymph node reactions in children after COVID-19 vaccination.

IMPLICATIONS FOR PATIENT CARE: Understanding postvaccination imaging findings in patients with cancer is important because these results may be confounded with tumor relapse or metastasis.

REFERENCES

1. Polack FP, Thomas SJ, Kitchin N, et al. Safety and efficacy of the BNT162b2 mRNA Covid-19 vaccine. *N Engl J Med.* 2020;383:2603–2615.
2. Lederer K, Bettini E, Parvathaneni K, et al. Germinal center responses to SARS-CoV-2 mRNA vaccines in healthy and immunocompromised individuals. *Cell.* 2022;185:1008–1024.e15.
3. Yoshikawa T, Miki S, Nakao T, Koshino S, Hayashi N, Abe O. Axillary lymphadenopathy after Pfizer-BioNTech and Moderna COVID-19 vaccination: MRI evaluation. *Radiology.* 2023;306:270–278.
4. Skawran S, Gennari AG, Dittli M, et al. [^{18}F]FDG uptake of axillary lymph nodes after COVID-19 vaccination in oncological PET/CT: frequency, intensity, and potential clinical impact. *Eur Radiol.* 2022;32:508–516.
5. Cohen D, Krauthammer SH, Wolf I, Even-Sapir E. Hypermetabolic lymphadenopathy following administration of BNT162b2 mRNA Covid-19 vaccine: incidence assessed by [^{18}F]FDG PET-CT and relevance to study interpretation. *Eur J Nucl Med Mol Imaging.* 2021;48:1854–1863.
6. Brown AH, Shah S, Groves AM, Wan S, Malhotra A. The challenge of staging breast cancer with PET/CT in the era of COVID vaccination. *Clin Nucl Med.* 2021; 46:1006–1010.
7. Indini A, Costa S, Ierardi AM, Rijavec E, Passoni E, Grossi F. COVID-19 vaccination mimicking lymph-node progression in a patient with melanoma: a case report. *Melanoma Res.* 2021;31:490–493.
8. Czepczyński R, Szczurek J, Mackiewicz J, Ruchała M. Interference of COVID-19 vaccination with PET/CT leads to unnecessary additional imaging in a patient with metastatic cutaneous melanoma: case report. *Front Oncol.* 2021;11:690443.
9. Landete E, Gómez-Fernández I, González-Gascón-y-Marín I, et al. Hypermetabolic abdominal and cervical lymph nodes mimicking Hodgkin lymphoma relapse on FDG PET/CT after adenovirus-vectored COVID-19 vaccine. *Hum Vaccin Immunother.* 2021;17:5129–5132.
10. Painter MM, Mathew D, Goel RR, et al. Rapid induction of antigen-specific CD4+ T cells is associated with coordinated humoral and cellular immunity to SARS-CoV-2 mRNA vaccination. *Immunity.* 2021;54:2133–2142.e3.
11. Jerushalmi J, Frenkel A, Bar-Shalom R, Khoury J, Israel O. Physiologic thymic uptake of ^{18} F-FDG in children and young adults: a PET/CT evaluation of incidence, patterns, and relationship to treatment. *J Nucl Med.* 2009;50:849–853.
12. von Tresckow J, von Tresckow B, Reinhardt HC, Herrmann K, Berliner C. Thymic hyperplasia after mRNA based Covid-19 vaccination. *Radiol Case Rep.* 2021;16: 3744–3745.
13. Nasseri F, Eftekhari F. Clinical and radiologic review of the normal and abnormal thymus: pearls and pitfalls. *Radiographics.* 2010;30:413–428.
14. Siegel RL, Miller KD, Fuchs HE, Jemal A. Cancer statistics, 2021. *CA Cancer J Clin.* 2021;71:7–33.
15. Brodin P, Davis MM. Human immune system variation. *Nat Rev Immunol.* 2017; 17:21–29.

Noninvasive Monitoring of Immunotherapy in Lung Cancer by Lymphocyte Activation Gene 3 PET Imaging of Tumor-Infiltrating Lymphocytes

Zhen Quan*[1,2], Zhaoguo Han*[1–3], Yang Yang*[1,2], Jiannan Wang[1,2], Hui Wang[4], Lili Yang[1,2], Rong A[1,2], Xinxin Hu[1,2], Jing Wang[1,2], Xiaona Li[1,2], Xiaoqian Li[1,2], Hong Yu[1,2], Wei Chen[5], Kai Wang[1,2], and Xilin Sun[1,2]

[1]Department of Nuclear Medicine, Fourth Hospital of Harbin Medical University, Harbin, Heilongjiang, China; [2]NHC Key Laboratory of Molecular Probe and Targeted Diagnosis and Therapy, Molecular Imaging Research Center (MIRC) of Harbin Medical University, Harbin, Heilongjiang, China; [3]Biomedical Research Imaging Center (BRIC), The University of North Carolina at Chapel Hill, Chapel Hill, North Carolina; [4]Department of Hematology, Shandong Cancer Hospital and Institute, Shandong First Medical University and Shandong Academy of Medical Sciences, Jinan, Shandong, China; and [5]Department of Nuclear Medicine and Laboratory of Clinical Nuclear Medicine, West China Hospital, Sichuan University, Chengdu, Sichuan, China

Although immunotherapy has revolutionized the entire cancer treatment landscape, small fractions of patients respond to immunotherapy. Early identification of responders may improve patient management during immunotherapy. In this study, we evaluated a PET approach for monitoring immunotherapy in lung cancer by imaging the upregulation of lymphocyte activation gene 3 (LAG-3)–expressing (LAG-3$^+$) tumor-infiltrating lymphocytes (TILs). **Methods:** We synthesized a LAG-3–targeted molecular imaging probe, [^{68}Ga]Ga-NOTA-C25 and performed a series of in vitro and in vivo assays to test its specificity. Next, [^{68}Ga]Ga-NOTA-C25 PET was used to monitor immunotherapy in murine lung cancer–bearing mice and in humanized mouse models for assessing clinical translational potential, with confirmation by immunostaining and flow cytometry analysis. **Results:** [^{68}Ga]Ga-NOTA-C25 PET could noninvasively detect intertumoral differences in LAG-3$^+$ TIL levels in different tumor models. Importantly, in Lewis lung carcinoma tumor models treated with an agonist of a stimulator of interferon genes, [^{68}Ga]Ga-NOTA-C25 PET also detected an immunophenotyping transition of the tumor from "cold" to "hot" before changes in tumor size. Meanwhile, animals carrying "hot" tumor showed more significant tumor inhibition and longer survival than those carrying "cold" tumor. [^{68}Ga]Ga-NOTA-C25 PET also showed markedly higher tumor uptake in immune system–humanized mice carrying human non–small cell lung cancer than immunodeficient models. **Conclusion:** [^{68}Ga]Ga-NOTA-C25 PET could be used to noninvasively monitor the early response to immunotherapy by imaging LAG-3$^+$ TILs in lung cancer. [^{68}Ga]Ga-NOTA-C25 PET also exhibited excellent translational potential, with great significance for the precise management of lung cancer patients receiving immunotherapy.

Key Words: lung cancer; immunotherapy; LAG-3; TIL; PET

J Nucl Med 2024; 65:25–32
DOI: 10.2967/jnumed.123.266002

Lung cancer is the leading cause of cancer death globally, and approximately 80% of lung cancers are non–small cell lung cancer (NSCLC) (*1*). Although immunotherapy has been approved for NSCLC, with certain survival benefits (*2*), numerous patients have been unresponsive (*3*). Cancer immunotherapy depends on rescuing CD8$^+$ T cells from inhibitory status to activation, for the elimination of tumor cells (*4*). During this process, immunophenotypes of the tumor can be categorized by the abundance of tumor-infiltrating lymphocytes (TILs) in the tumor immune microenvironment. Specifically, immune "hot" tumors have abundant TILs, whereas "cold" tumors lack TILs (*5*). It has been well established that the treatment response to immunotherapy is strongly associated with tumor TIL abundance, particularly CD8$^+$ T cells, which play a central role in improving the response to cancer immunotherapy (*6*).

Lymphocyte activation gene 3 (LAG-3) is a type I transmembrane protein mainly expressed in T cell–based TILs. It has become an important next-generation immune checkpoint after programmed cell death protein 1 (PD-1)/programmed death ligand 1 and cytotoxic T lymphocyte-associated antigen 4 (*7*). Naïve and resting T cells do not express LAG-3, but activated T cells could upregulate LAG-3 expression (*8,9*). Thus, LAG-3 expression upregulation correlates with the early phase of T cell activation, as observed in lung cancer patients (*7,9,10*). The Food and Drug Administration approved the first LAG-3 immune checkpoint inhibitor (ICI; relatlimab) in combination with nivolumab for cancer immunotherapy in 2022 (*11*). Clinical studies showed that relatlimab combined with nivolumab significantly improved progression-free survival compared with nivolumab monotherapy in NSCLC (*8,12*). Moreover, a high level of LAG-3–expressing (LAG-3$^+$) TILs was shown to be an independent positive prognostic factor in stage I–IIIB lung cancer patients (*9*). Hence, LAG-3$^+$ TILs may be a useful biomarker for identifying the immunotherapy response at early times.

PET/CT has been extensively applied in clinical molecular imaging for tumor theranostics (*13*). PD-1/programmed death ligand 1–targeted PET has been used to predict the response to ICIs and has been shown to be superior to immunohistochemistry (*14*). Recent imaging studies focused on early-stage immune biomarkers (OX-40 and inducible costimulator) (*15,16*) and downstream biomarkers (interleukin 2 and granzyme B) of the immune reaction (*17,18*). These studies demonstrated potential in assessing the tumor immunotherapy response, particularly conspicuous for granzyme B PET (*19*). However, a weak correlation was also reported in a clinical trial (*20*). Effort needs to be put toward

Received May 7, 2023; revision accepted Oct. 14, 2023.
For correspondence or reprints, contact Xilin Sun (sunxl@ems.hrbmu.edu.cn).
*Contributed equally to this work.
Published online Nov. 16, 2023.

developing novel molecular imaging biomarkers for evaluating immunotherapy.

C25, a 9-amino-acid cyclic peptide (CVPMTYRAC), was identified recently as having a high affinity for both human and murine LAG-3 (*21*). As is well known, peptide-based molecular imaging has been widely studied due to multiple advantages, including favorable pharmacokinetics and easy modification and radiolabeling (*22*). In this study, we report a LAG-3–targeted molecular imaging probe, [^{68}Ga]Ga-NOTA-C25, and assessed the feasibility of [^{68}Ga]Ga-NOTA-C25 PET in detecting LAG-3$^+$ TILs and monitoring the treatment response to monotherapy in lung cancer tumor models.

MATERIALS AND METHODS

Synthesis and Characterization of [^{68}Ga]Ga-NOTA-C25

The precursor NOTA-C25 was rationally designed and synthesized. NOTA-C25 (50.37 μg; 0.038 μmol) was added to [^{68}Ga]$GaCl_3$ (296 MBq in 0.6 mL of 0.05 M HCl), and the pH was adjusted to 4.6 for radiolabeling. The reaction mixture was purified with a C18 cartridge by radio–thin-layer chromatography to obtain [^{68}Ga]Ga-NOTA-C25 for quality control and stability. The specific activity of [^{68}Ga]Ga-NOTA-C25 was calculated on the basis of radiolabeling records ($n \geq 3$). Under the same protocol, [^{68}Ga]Ga-NOTA-scrambled C25 was also prepared for subsequent in vitro and in vivo assays. More details are provided in the supplemental materials (supplemental materials are available at http://jnm.snmjournals.org).

Immune Stimulation for Flow Cytometry and Cell Uptake

Immune cells from C57BL/6 mice and human peripheral blood mononuclear cells (hPBMCs; catalog no. HPA01091; Hope Biotechnology) were used. Immune stimulation with an activation cocktail (catalog no. 423301; BioLegend) on C57BL/6 mouse–derived immune cells and phytohemagglutinin-M (catalog no. 11082132001; Sigma) on hPBMCs was performed for flow cytometry analysis of LAG-3 and CD8. Cell uptake of [^{68}Ga]Ga-NOTA-C25 or [^{68}Ga]Ga-NOTA-scrambled C25 (0.037 MBq/mL; 6.788×10^{-9} μM) was performed by blocking assays with nonradiolabeled C25 (9.613×10^{-6} μM) and anti–LAG-3 antibody (αLAG-3; 1.333×10^{-7} μM) to test probe specificity. Detailed protocols are provided in the supplemental materials.

Cells and Animal Models

Cells (murine lung cancer: CMT-167, KLN-205, and Lewis lung carcinoma (LLC); human lung cancer: H460) were cultured at 37°C with 5% CO_2 to prepare animal models by subcutaneous transplantation in the right shoulder at different densities. Tumor volume was measured every other day using a caliper, and tumor volume was calculated as (length × width^2)/2. All animal protocols were approved by the Animal Care Committee at the Fourth Hospital of Harbin Medical University. More details are provided in the supplemental materials.

PET/CT Imaging and Biodistribution Study

When the tumor volume reached about 300 mm^3, CMT-167, KLN-205, and LLC tumor–bearing mice were injected with approximately 7.4 MBq of [^{68}Ga]Ga-NOTA-C25 or [^{68}Ga]Ga-NOTA-scrambled C25 (~1.8 μg in 100 μL; 0.0014 μmol; with a specific activity of 5.45 ± 0.25 [mean ± SD] GBq/μmol) via the tail vein. PET/CT scanning and biodistribution were performed at different time points after injection of the probe. In blocking assays, C25 peptide (100 μg in 100 μL; 0.0961 μmol) or 200 μg (in 100 μL; 0.0014 μmol) of antimouse LAG-3 antibody (catalog no. BE0174; Bioxcell) was coinjected with [^{68}Ga]Ga-NOTA-C25 into CMT-167– and KLN-205–bearing mice for blocked PET and biodistribution (*23*). Furthermore, PET/CT imaging and biodistribution based on [^{68}Ga]Ga-NOTA-scrambled C25 were also performed in KLN-205 models with the same protocol as that mentioned earlier. Detailed information is provided in the supplemental materials.

In Vivo PET for Monitoring Immunotherapy

When the tumor volume reached 50–100 mm^3 at 10 d after transplantation, LLC models were randomly divided into 4 groups ($n \geq 6$) for receiving immunotherapy with anti–PD-1 antibody (αPD-1; intraperitoneal administration of 10 mg/kg of body weight), an agonist of a stimulator of interferon genes (STING) (benzothiophene oxobutanoic acid (MSA-2); subcutaneous administration of 25 mg/kg of body weight), combination therapy (αPD-1 + MSA-2), and phosphate-buffered saline (PBS) as a control. Tumor volume and survival time were recorded. [^{68}Ga]Ga-NOTA-C25 PET/CT was performed at days 4 and 13 during treatment, and animals were euthanized to collect tumors, tumor-draining lymph nodes (TDLN), spleen, and thymus for biodistribution or flow cytometry detection of CD8$^+$ LAG-3$^+$ T cells. Detailed protocols are provided in the supplemental materials.

LAG-3 PET in Immune System–Humanized NSCLC Models

Immune system–humanized NSCLC models were established in H460 tumor models by injecting hPBMCs and not injecting hPBMCs as an immunodeficient control, with flow cytometry verification of the proportion of hCD3$^+$ hCD45$^+$ lymphocytes as previously published (*24,25*). [^{68}Ga]Ga-NOTA-C25 PET/CT was performed as described earlier. More details are provided in the supplemental materials.

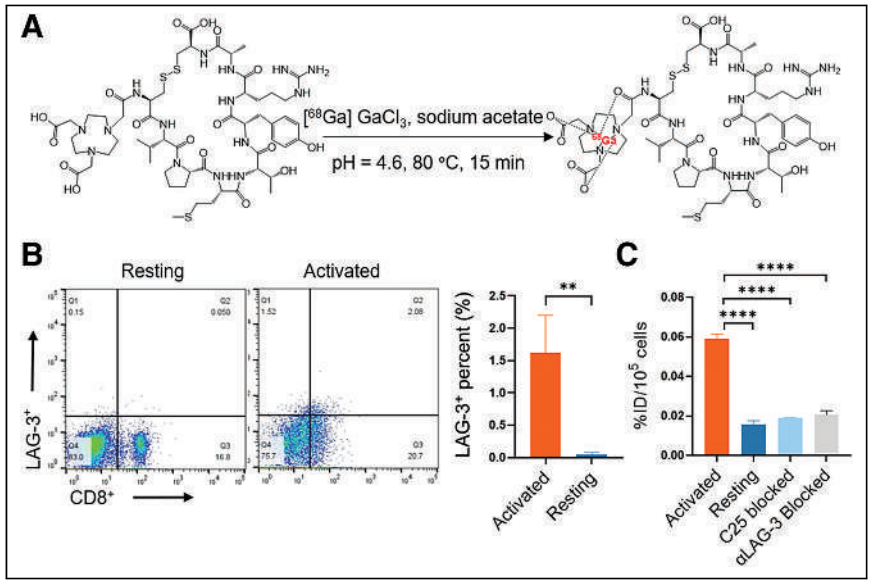

FIGURE 1. (A) Radiochemical synthesis of [^{68}Ga]Ga-NOTA-C25. (B) Flow cytometry and quantitative analysis of CD8$^+$ LAG-3$^+$ in murine immune cells that were activated or resting. (C) Cell uptake of [^{68}Ga]Ga-NOTA-C25 (6.788×10^{-9} μM) in murine immune cells with blocking assays by nonradiolabeled C25 (9.613×10^{-6} μM) and αLAG-3 (1.333×10^{-7} μM). $n = 3$. $^{**}P < 0.01$. $^{****}P < 0.0001$.

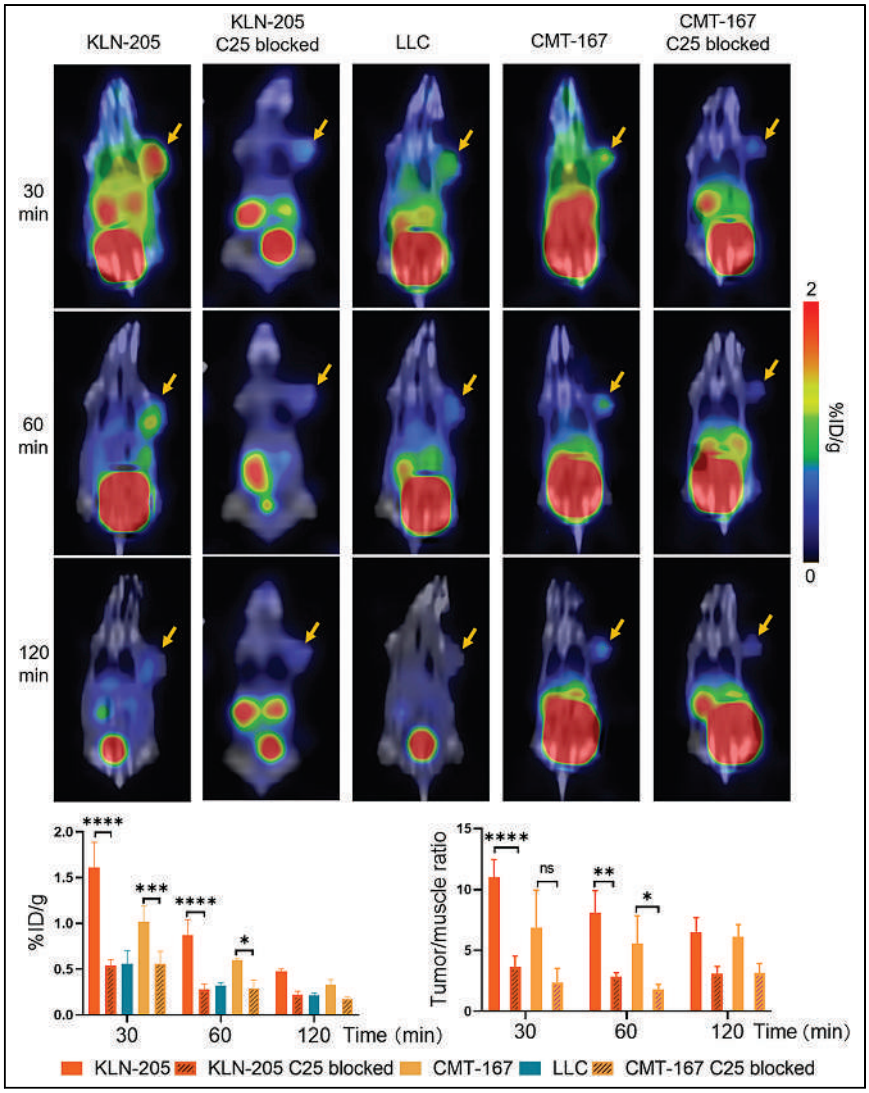

FIGURE 2. Representative PET/CT images and quantitative analysis in KLN-205, CMT-167, and LLC tumor–bearing mice at 30, 60, and 120 min after injection of [^{68}Ga]Ga-NOTA-C25 with blocking assays by nonradiolabeled C25 (100 μg in 100 μL; 0.0961 μmol). Yellow arrows indicate tumor. $n \geq 3$. *$P < 0.05$. **$P < 0.01$. ***$P < 0.001$. ****$P < 0.0001$.

Immunofluorescence Staining

Tumor sections from different murine tumor models, treated animals, or humanized animal models were fixed for immunofluorescence staining of CD3 and LAG-3. Detailed protocols are provided in the supplemental materials.

In Vivo Biologic Activity Experiments

LLC subcutaneous xenograft mouse models were established. When the tumor volume reached 200–300 mm^3, LLC tumor models were divided into 3 groups for injection with [^{68}Ga]Ga-NOTA-C25 (7.4 MBq; 1.8 μg in 100 μL; 0.0014 μmol), a blocking dose of C25 (100 μg in 100 μL; 0.0961 μmol), and PBS as a control. Samples of peripheral blood, spleen, and tumor were harvested from these 3 groups at 1 and 48 h after injection for flow cytometry tests of CD8$^+$ γ-interferon–positive percentages. Detailed information is provided in the supplemental materials.

Statistical Analysis

All data analysis was performed on GraphPad Prism 9.0 (GraphPad Software). A 1- or 2-way ANOVA and an unpaired 2-tailed Student *t* test were used for statistical analysis when appropriate. Results are presented as mean ± SD. A *P* value of less than 0.05 was considered as statistically significant.

RESULTS

Synthesis and In Vitro Characterization of [^{68}Ga]Ga-NOTA-C25

NOTA-C25 was obtained with a purity of 98.54% and confirmed through high-resolution mass spectrometry to have a molecular weight of 1325.5541 (Suppl. Fig. 1). [^{68}Ga]Ga-NOTA-C25 was efficiently radiolabeled, with a radiochemical yield of greater than 85% and a radiochemical purity of greater than 99% (Fig. 1A; Suppl. Fig. 2A). The molar activity of [^{68}Ga]Ga-NOTA-C25 was calculated as 5.45 ± 0.25 GBq/μmol. [^{68}Ga]Ga-NOTA-C25 remained stable in both serum and PBS for at least 240 min of incubation (Suppl. Fig. 2). The oil–water partition coefficient was determined to be −3.550 ± 0.311, indicating the probe's hydrophilicity. In addition, [^{68}Ga]Ga-NOTA-scrambled C25 was prepared using the same protocol as that mentioned earlier and served as a scrambled probe in subsequent experiments.

Immune stimulation and cell uptake experiments were performed on murine CD8$^+$ T cells. Results showed that CD8$^+$ T cells exhibited significantly higher LAG-3 expression after stimulation than resting groups ($P < 0.01$) (Fig. 1B), as detected by flow cytometry. Consistently, stimulation-activated CD8$^+$ T cells exhibited higher [^{68}Ga]Ga-NOTA-C25 uptake than resting groups, and the uptake in activated groups could be specifically blocked by coincubation with nonradiolabeled C25 peptide and αLAG-3 ($P < 0.0001$) (Fig. 1C). However, there was no significant difference in cell uptake of [^{68}Ga]Ga-NOTA-scrambled C25 among activated, resting, and blocked groups of immune cells, corroborating the specificity of [^{68}Ga]Ga-NOTA-C25 for LAG-3 (Suppl. Fig. 3).

Imaging LAG-3$^+$ TILs In Vivo by [^{68}Ga]Ga-NOTA-C25 PET

[^{68}Ga]Ga-NOTA-C25 PET was used to detect LAG-3$^+$ TILs in vivo in CMT-167, KLN-205, and LLC tumor models. Representative PET/CT images and quantitative analysis are showed in Figure 2. [^{68}Ga]Ga-NOTA-C25 could reach whole-body distribution as early as 30 min after injection and showed "fast-in" and "fast out" trends, with gradually reduced uptake over time in all tumors. Tumor uptake of [^{68}Ga]Ga-NOTA-C25 was highest in KLN-205 tumors, moderate in CMT-167 tumors, and at baseline levels in LLC tumors, with similar trends in tumor/muscle ratios. Blocking PET with nonradiolabeled C25 showed that the tumor uptake and tumor/muscle ratio could both be significantly decreased in CMT-167 and KLN-205 tumor models; however, a greater impact of blocking was observed in the latter. Biodistribution (Suppl. Fig. 4; Suppl. Fig. 5; Suppl. Table 1) showed consistent trends and confirmed the PET results. Differences in [^{68}Ga]Ga-NOTA-C25 distribution among CMT-167, KLN-205, and

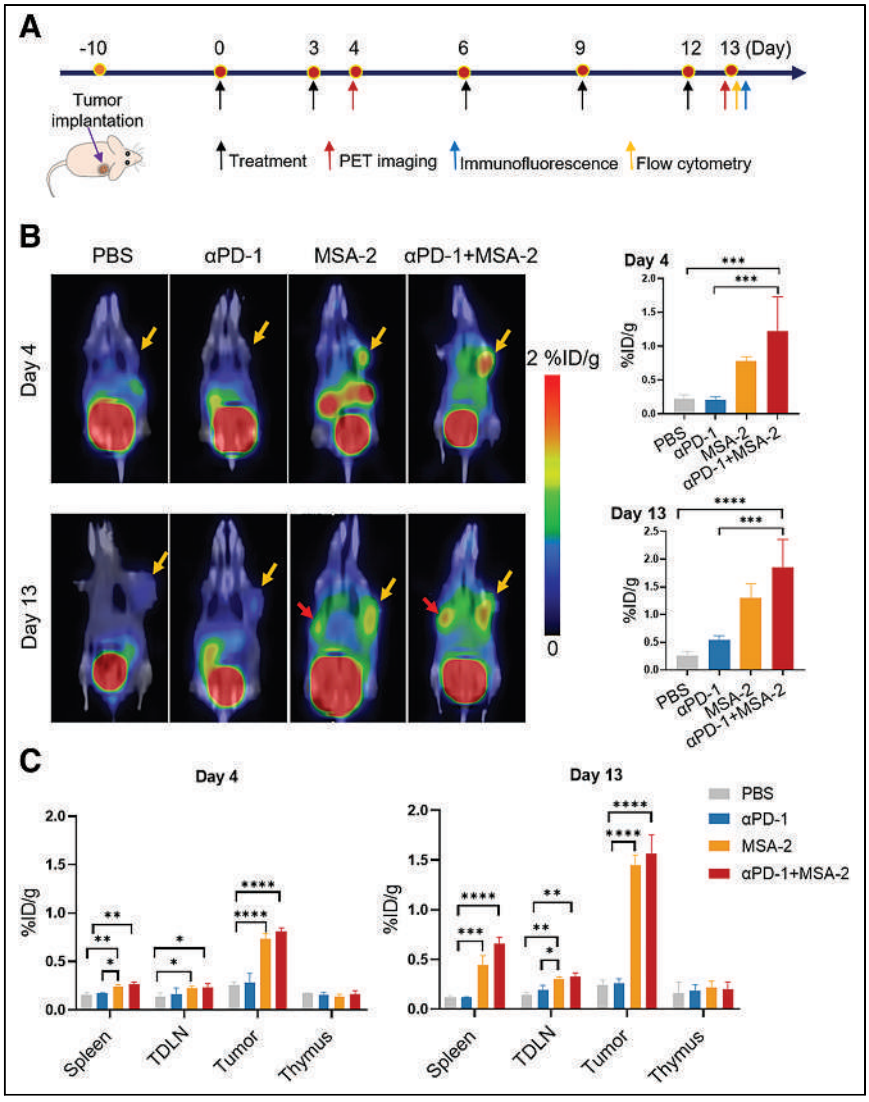

FIGURE 3. (A) Time line of immunotherapy and PET imaging in LLC tumor–bearing mice. (B) Representative [^{68}Ga]Ga-NOTA-C25 PET/CT and quantitative analysis in LLC models treated with PBS, αPD-1, MSA-2, and αPD-1 + MSA-2 at days 4 and 13. Yellow arrows indicate tumor. Red arrows indicate spleen. (C) Biodistribution in tumor and main immune organs excised from LLC models at days 4 and 13. $n \geq 6$. *$P < 0.05$. **$P < 0.01$. ***$P < 0.001$. ****$P < 0.0001$.

LLC tumors demonstrated the potential of LAG-3 PET in detecting tumor immune microenvironment heterogeneity.

αLAG-3–blocked PET at 60 min after injection (Suppl. Figs. 4B and 4C) showed reductions in the tumor uptake and tumor/muscle ratio similar to those seen with C25-blocked PET in both CMT-167 and KLN-205 tumor models. Biodistribution results were consistent with PET results (Suppl. Fig. 5; Suppl. Table 2). However, KLN-205 tumors merely showed a baseline uptake of [^{68}Ga]Ga-NOTA-scrambled C25 at all time points, and the biodistribution of [^{68}Ga]Ga-NOTA-scrambled C25 in KLN-205 tumors at 60 min after injection also confirmed the PET results (Suppl. Fig. 6). These results indicated the specificity of [^{68}Ga]Ga-NOTA-C25 in vivo. Moreover, there was a good correlation of [^{68}Ga]Ga-NOTA-C25 uptake between biodistribution and PET results for KLN-205, CMT-167, and LLC tumors (Suppl. Fig. 7).

Immunostaining results (Suppl. Fig. 8) showed that CD3$^+$ LAG-3$^+$ fluorescence intensity was more abundant in CMT-167 and KLN-205 tumors than in LLC tumors. In summary, these findings demonstrated the feasibility of [^{68}Ga]Ga-NOTA-C25 PET for detecting LAG-3$^+$ TILs in vivo, and LLC tumors could be categorized as immune "cold" by [^{68}Ga]Ga-NOTA-C25 PET.

In Vivo Detection of LAG-3$^+$ TIL Upregulation Induced by STING Agonists in Lung Cancer

The ability of [^{68}Ga]Ga-NOTA-C25 PET to monitor LAG-3$^+$ TIL dynamics was assessed in LLC tumors, which were determined to be immune "cold" as described earlier. [^{68}Ga]Ga-NOTA-C25 PET was performed at days 4 and 13 to monitor LAG-3$^+$ TIL dynamics (Fig. 3A). At day 4, tumor uptake of [^{68}Ga]Ga-NOTA-C25 in the MSA-2 and MSA-2 + αPD-1 groups was significantly increased compared with that in the αPD-1 or PBS group (Fig. 3B). A similar trend was observed at day 13. However, MSA-2 could induce incremental immune stimulation, as revealed by higher tumor uptake in the MSA-2 group (1.30 ± 0.22 percentage injected dose [%ID]/g) and the MSA-2 + αPD-1 group (1.85 ± 0.41 %ID/g) at day 13 than at day 4 ($P < 0.05$). Interestingly, the spleen could be clearly visualized by PET at day 13 in the MSA-2 + αPD-1 and MSA-2 groups, suggesting that the STING agonist or a combination with αPD-1 may increase peripheral immune activation (Fig. 3B).

These results were corroborated by the ex vivo biodistribution (Fig. 3C). Specifically, higher probe uptake was observed in tumors, TNLD, and spleen in the MSA-2 + αPD-1 and MSA-2 groups than in the αPD-1 or PBS group at day 4 and even more obviously at day 13. These results further indicated that MSA-2–based treatment caused incremental immune stimulation over time. Flow cytometry analysis at day 13 also showed that the STING agonist induced significant immune responses in the MSA-2 + αPD-1 and MSA-2 groups, as revealed by a higher abundance of CD8$^+$ LAG-3$^+$ T cells in tumors, TDLN, and spleen in these groups than in the αPD-1 or PBS group (Fig. 4). Moreover, there was a good correlation between [^{68}Ga]Ga-NOTA-C25 PET and CD8$^+$ LAG-3$^+$ T cell levels in tumors at day 13 for the combination therapy and PBS groups (Suppl. Fig. 9). Immunostaining of LAG-3 and CD3 on tumor sections at day 13 showed trends similar to those seen with PET, thereby confirming that MSA-2 + αPD-1 and MSA-2 could induce higher infiltration of LAG-3$^+$ TILs than αPD-1 or PBS (Fig. 5).

LAG-3 PET Imaging for Monitoring Immunotherapy

Having demonstrated that [^{68}Ga]Ga-NOTA-C25 PET can accurately monitor LAG-3$^+$ TIL upregulation during immunotherapy, we subsequently analyzed its value in estimating the immunotherapy response and survival benefit in lung cancer. Tumor volume changes

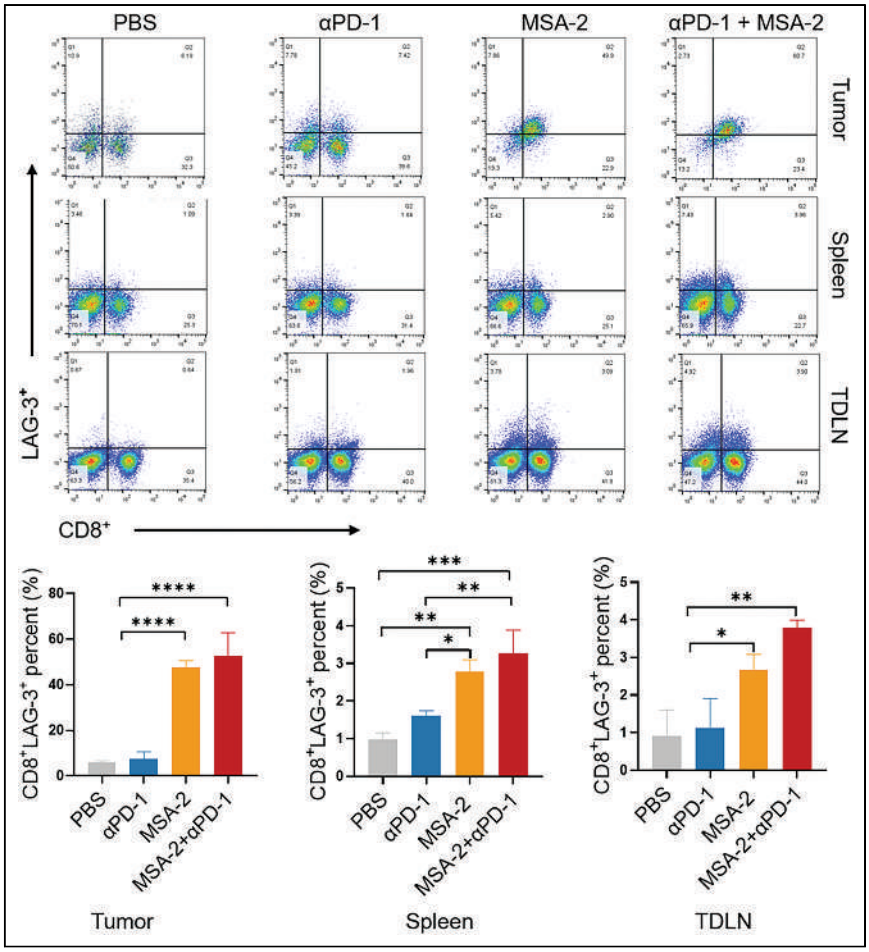

FIGURE 4. Flow cytometry detection of $CD8^+LAG\text{-}3^+$ T cells and quantitative analysis in tumor, spleen, and TDLN excised from LLC tumor models at day 13. $n \geq 6$. $^*P < 0.05$. $^{**}P < 0.01$. $^{***}P < 0.001$. $^{****}P < 0.0001$.

and survival (excluding animal death or animal condition beyond the ethical standard) during treatment were recorded for the aforementioned treatment groups (Fig. 6A; Suppl. Fig. 10A). Tumor volume increased significantly faster in the PBS and αPD-1 groups than in the MSA-2 and MSA-2 + αPD-1 groups. Importantly, these differences in tumor size were detectable from day 6, whereas differences in tumor uptake measured by [^{68}Ga]Ga-NOTA-C25 PET could be discerned as earlier as day 4. These results showed that LAG-3 PET can monitor the early response to immunotherapy before tumor size changes. The MSA-2 + αPD-1 group exhibited the best survival with the longest time, more than 47 d, significantly longer than those of the PBS group ($P < 0.01$) and the αPD-1 group ($P < 0.05$) (Fig. 6B). Similar trends were observed in the MSA-2 group. There was no significant weight loss during treatment (Suppl. Fig. 10B). In addition, we confirmed that the dosages of the probe and blocking C25 could not induce immunostimulatory effects (Suppl. Fig. 11). Overall, these findings suggested that LAG-3 PET was a promising molecular imaging approach for monitoring immunotherapy in lung cancer by visualizing the immunophenotyping transition in tumors from immune "cold" to immune "hot."

LAG-3 PET in Immune System–Humanized NSCLC

Stimulation-activated hPBMCs expressed higher $hCD8^+$ $hLAG\text{-}3^+$ than resting hPBMCs ($P < 0.01$) (Suppl. Fig. 12; Fig. 7A). Consistently, activated hPBMCs exhibited higher [^{68}Ga]Ga-NOTA-C25 uptake than resting hPBMCs ($P < 0.01$) (Fig. 7B) and could be specifically blocked by nonradiolabeled C25 ($P < 0.05$). Next, we assessed the in vivo targeting of [^{68}Ga]Ga-NOTA-C25 to $hLAG\text{-}3^+$ TILs in human NSCLC H460 tumor–bearing mice established with a humanized immune system (H460-HIS), using immunoincompetent H460 models as controls. The establishment of the H460-HIS and H460 models was verified by flow cytometry analysis (Suppl. Fig. 13) as previously reported (*24*). Representative PET/CT images and quantitative analysis (Fig. 7C) showed that H460-HIS tumors exhibited higher tumor uptake than H460 tumors ($P < 0.05$). H460-HIS showed the highest tumor/muscle ratio at 60 min (20.23 ± 2.05), significantly higher than that of H460 (10.98 ± 0.75) ($P < 0.01$). H460 also showed lower background radioactivity than H460-HIS due to the lack of $hLAG\text{-}3^+$ TILs. These results further indicated the accuracy of [^{68}Ga]Ga-NOTA-C25 PET in detecting $hLAG\text{-}3^+$ TILs.

Consistent with the PET results, $hLAG\text{-}3^+$ TIL levels were significantly higher in H460-HIS tumors than in H460 tumors, as detected by flow cytometry and immunostaining (Suppl. Fig. 14). In the biodistribution analysis (Suppl. Table 3), H460-HIS tumors also exhibited higher tumor uptake than H460 tumors ($P < 0.05$). Similar trends were observed in major lymphoid organs. These results indicated the excellent performance of [^{68}Ga]Ga-NOTA-C25 PET in noninvasively detecting $hLAG\text{-}3^+$ TILs and highlighted the clinical translational potential of [^{68}Ga]Ga-NOTA-C25 PET for monitoring immunotherapy in lung cancer patients.

DISCUSSION

Under immunosurveillance and selective pressure of the host immune system, tumor cells experience a transition from elimination to equilibrium and, finally, to immune escape (*26,27*). Immunotherapy strategies have been developed to overcome the escape mechanism and reactivate the host immune system to eliminate tumor cells; these include ICIs, cancer vaccines, and adoptive immune cell therapy. Among these, ICIs have raised the most research interest over the past decade, leading to significant advances in the field (*6,28*). To date, 8 ICIs have been approved by the Food and Drug Administration; these include the first approved LAG-3 ICI in combination with nivolumab (*11,29*). However, a low response rate was reported for all ICIs (*30,31*). Thus, the development of approaches for the early identification of responders in the precise management of immunotherapy is critical. Studies showed that molecular imaging is an excellent tool for noninvasively monitoring the immunotherapy response (*32*). Since LAG-3 is a promising next-generation immune checkpoint, when effective immunotherapies relieve immunosuppression and expose

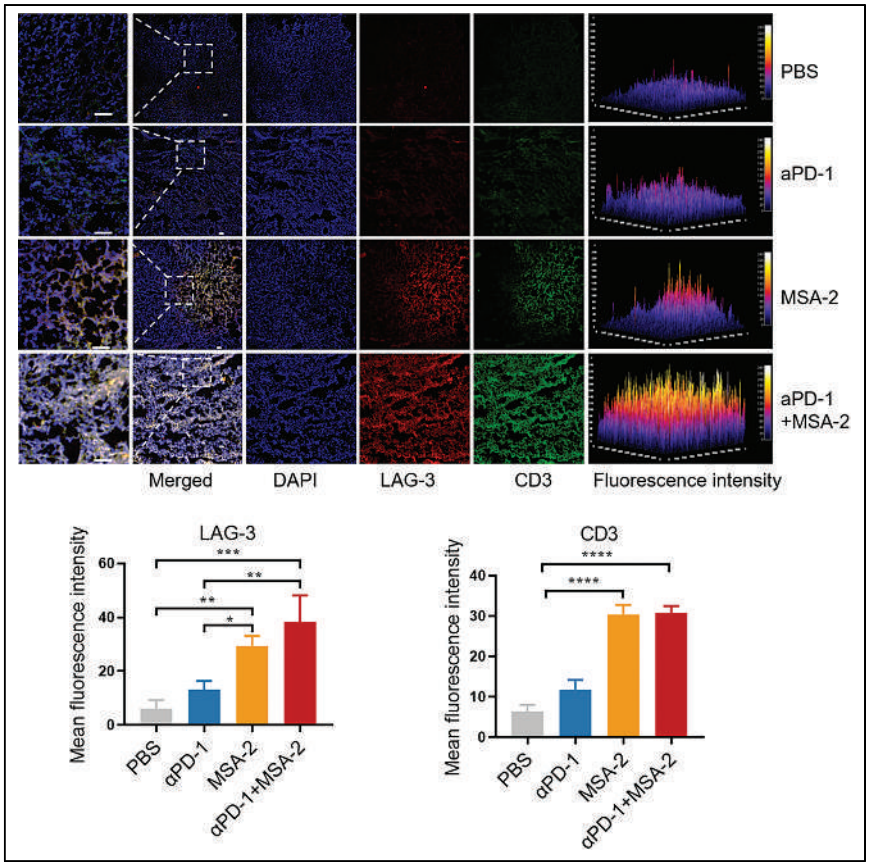

FIGURE 5. Immunofluorescence images and quantitative analysis of LAG-3 and CD3 staining in tissue sections from LLC models at day 13. Blue = DAPI. Green = CD3. Red = LAG-3. Scale bar, 50 μm. $n = 3$. *$P < 0.05$. **$P < 0.01$. ***$P < 0.001$. ****$P < 0.0001$.

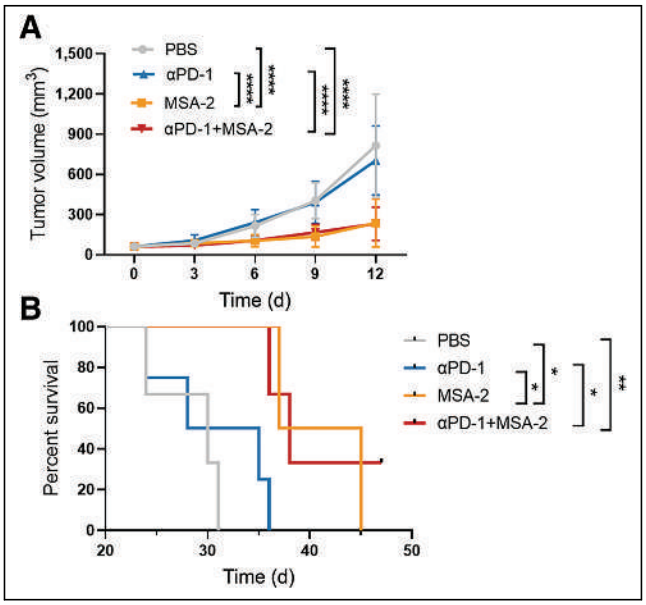

FIGURE 6. (A) Tumor growth curves of LLC tumor–bearing mice treated with PBS, αPD-1, MSA-2, and αPD-1 + MSA-2. (B) Survival analysis of LLC models for different groups. $n \geq 6$. *$P < 0.05$. **$P < 0.01$. ****$P < 0.0001$.

tumor antigens to the immune system, LAG-3 may upregulate specifically in TILs, particularly in $CD8^+$ T cells (*7,10,33*); therefore, it may be an ideal molecular imaging biomarker for monitoring the early immunotherapy response. Compared with previously reported LAG-3 single-domain antibody–based micro-SPECT imaging (*34*), in the present study, we reported a LAG-3–specific peptide-based PET agent and acquired clear images with a clinical scanner in both mice and humanized mouse models. In particular, we verified the feasibility of LAG-3 PET for monitoring the early response to immunotherapy in lung cancer, providing more evidence that LAG-3 served as a molecular imaging marker in cancer immunotherapy. More recently, exciting advancement in the clinical translation of LAG-3 imaging has been made; a LAG-3 antibody–based PET agent, [^{89}Zr]Zr-BI-754111, also showed favorable performance for monitoring immune infiltration in patients after PD-1 treatment (*35*). However, peptide probes are superior to antibodies as diagnostic agents, offering rapid imaging and clearance, favorable pharmacokinetics, and low cost (*22*).

Studies have shown that a STING agonist can increase the immunotherapy response in solid tumors by enhancing immune infiltration, particularly in immune "cold" tumors (*36–38*). Hence, in the present study, LLC tumors infiltrated with low levels of $LAG\text{-}3^+$ TILs were selected for STING agonist–based immunotherapy. Our results showed that MSA-2–based immunotherapy was effective; importantly, [^{68}Ga]Ga-NOTA-C25 PET could detect a tumor immunophenotyping transition from "cold" to "hot"—an early immunotherapy response—before tumor size changes. In addition, animals carrying LAG-3 PET–detected "hot" tumors exhibited significant tumor growth retardation and longer survival. In contradistinction, "cold" tumors progressed rapidly, with shorter survival. Above all, our results demonstrated that LAG-3 PET is reliable for monitoring the early immunotherapy response in lung cancer. However, we noted that lung uptake of [^{68}Ga]Ga-NOTA-C25 could be blocked in both PET and biodistribution analyses; this condition might have been caused by immune cells residing in the lungs, recruited immune cells, and a complex immune microenvironment.

Rapid tumor accumulation and background clearance of [^{68}Ga]Ga-NOTA-C25 promoted optimal PET imaging. However, longitudinal studies may need to focus on improving the specificity of the peptide-based probe. The fact that high-resolution small-animal PET/CT was not used here may have limited the imaging of smaller organs, such as TDLN. However, clear images obtained from clinical PET/CT with wide fields of view were undoubtedly beneficial for clinical translation. In addition, LAG-3 PET may also play a significant role in guiding the application of Food and Drug Administration–approved LAG-3–based combination therapy for cancer treatment.

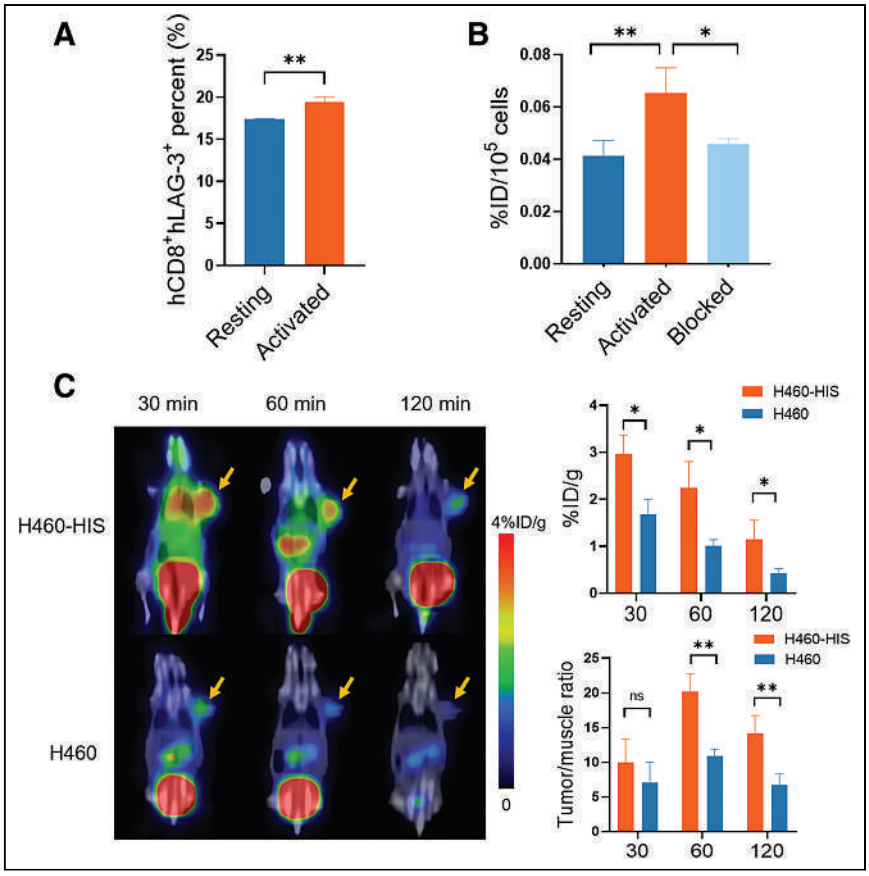

FIGURE 7. (A) Quantitative analysis of flow cytometry for hCD8$^+$hLAG-3$^+$ in hPBMCs. (B) Cell uptake and blocking assays (nonradiolabeled C25, 9.613×10^{-6} μM) of [^{68}Ga]Ga-NOTA-C25 in hPBMCS. (C) Representative PET/CT images and quantitative analysis in H460 and H460-HIS tumor models at 60 min after injection of [^{68}Ga]Ga-NOTA-C25. Yellow arrows indicate tumor. $n = 3$. *$P < 0.05$. **$P < 0.01$.

CONCLUSION

[^{68}Ga]Ga-NOTA-C25 PET is a reliable approach to noninvasively detecting LAG-3$^+$ TILs with excellent clinical translation potential. [^{68}Ga]Ga-NOTA-C25 PET can visualize the tumor immunophenotyping transition from "cold" to "hot" under effective immunotherapy and may be used to stratify lung cancer patients for the early identification of immunotherapy responders.

KEY POINTS

QUESTION: Can LAG-3 PET be used to monitor the early response to immunotherapy in lung cancer?

PERTINENT FINDINGS: [^{68}Ga]Ga-NOTA-C25 PET could detect a tumor immunophenotyping transition during immunotherapy by targeting LAG-3$^+$ TILs and was a reliable approach for monitoring the early treatment response before tumor size changes.

IMPLICATIONS FOR PATIENT CARE: [^{68}Ga]Ga-NOTA-C25 PET showed excellent clinical translation potential and is a promising noninvasive imaging method for monitoring the immunotherapy response to provide precise management of immunotherapy in lung cancer patients.

DISCLOSURE

Financial support was provided by National Natural Science Foundation of China (81627901, 82102101, 82202226), Natural Science Foundation of Heilongjiang Province (JQ2020H002, JJ2022LH0959), HMU Marshal Initiative Funding (HMU-MIF-21003), Tou-Yan Innovation Team Program of Heilongjiang Province (2019-15), and Heilongjiang Provincial Key Laboratory of Molecular Imaging Foundation. No other potential conflict of interest relevant to this article was reported.

ACKNOWLEDGMENT

Some graphic elements were provided by Figdraw with permission (WWSWO8cfbf).

REFERENCES

1. Siegel RL, Miller KD, Fuchs HE, Jemal A. Cancer statistics, 2022. *CA Cancer J Clin.* 2022;72:7–33.
2. Spigel DR, Faivre-Finn C, Gray JE, et al. Five-year survival outcomes from the PACIFIC trial: durvalumab after chemoradiotherapy in stage III non-small-cell lung cancer. *J Clin Oncol.* 2022;40:1301–1311.
3. Puzanov I, Diab A, Abdallah K, et al. Managing toxicities associated with immune checkpoint inhibitors: consensus recommendations from the Society for Immunotherapy of Cancer (SITC) Toxicity Management Working Group. *J Immunother Cancer.* 2017;5:95–122.
4. Tu L, Guan R, Yang H, et al. Assessment of the expression of the immune checkpoint molecules PD-1, CTLA4, TIM-3 and LAG-3 across different cancers in relation to treatment response, tumor-infiltrating immune cells and survival. *Int J Cancer.* 2020;147:423–439.
5. Galon J, Bruni D. Approaches to treat immune hot, altered and cold tumours with combination immunotherapies. *Nat Rev Drug Discov.* 2019;18:197–218.
6. Kraehenbuehl L, Weng CH, Eghbali S, Wolchok JD, Merghoub T. Enhancing immunotherapy in cancer by targeting emerging immunomodulatory pathways. *Nat Rev Clin Oncol.* 2022;19:37–50.
7. Andrews LP, Cillo AR, Karapetyan L, Kirkwood JM, Workman CJ, Vignali DAA. Molecular pathways and mechanisms of LAG3 in cancer therapy. *Clin Cancer Res.* 2022;28:5030–5039.
8. Nguyen LT, Ohashi PS. Clinical blockade of PD1 and LAG3: potential mechanisms of action. *Nat Rev Immunol.* 2015;15:45–56.
9. Datar I, Sanmamed MF, Wang J, et al. Expression analysis and significance of PD-1, LAG-3, and TIM-3 in human non-small cell lung cancer using spatially resolved and multiparametric single-cell analysis. *Clin Cancer Res.* 2019;25:4663–4673.
10. Bae J, Lee SJ, Park CG, Lee YS, Chun T. Trafficking of LAG-3 to the surface on activated T cells via its cytoplasmic domain and protein kinase C signaling. *J Immunol.* 2014;193:3101–3112.
11. FDA approves anti-LAG3 checkpoint. *Nat Biotechnol.* 2022;40:625.
12. Tawbi HA, Schadendorf D, Lipson EJ, et al. Relatlimab and nivolumab versus nivolumab in untreated advanced melanoma. *N Engl J Med.* 2022;386:24–34.
13. Rowe SP, Pomper MG. Molecular imaging in oncology: current impact and future directions. *CA Cancer J Clin.* 2022;72:333–352.
14. Bensch F, van der Veen EL, Lub-de Hooge MN, et al. ^{89}Zr-atezolizumab imaging as a non-invasive approach to assess clinical response to PD-L1 blockade in cancer. *Nat Med.* 2018;24:1852–1858.
15. Alam IS, Mayer AT, Sagiv-Barfi I, et al. Imaging activated T cells predicts response to cancer vaccines. *J Clin Invest.* 2018;128:2569–2580.
16. Simonetta F, Alam IS, Lohmeyer JK, et al. Molecular imaging of chimeric antigen receptor T cells by ICOS-immunoPET. *Clin Cancer Res.* 2021;27:1058–1068.

17. van der Veen EL, Suurs FV, Cleeren F, et al. Development and evaluation of interleukin-2–derived radiotracers for PET imaging of T cells in mice. *J Nucl Med.* 2020;61:1355–1360.
18. Larimer BM, Bloch E, Nesti S, et al. The effectiveness of checkpoint inhibitor combinations and administration timing can be measured by granzyme B PET imaging. *Clin Cancer Res.* 2019;25:1196–1205.
19. Zhou H, Wang Y, Xu H, et al. Noninvasive interrogation of CD8+ T cell effector function for monitoring early tumor responses to immunotherapy. *J Clin Invest.* 2022;132:e161065.
20. van de Donk PP, Wind TT, Hooiveld-Noeken JS, et al. Interleukin-2 PET imaging in patients with metastatic melanoma before and during immune checkpoint inhibitor therapy. *Eur J Nucl Med Mol Imaging.* 2021;48:4369–4376.
21. Zhai W, Zhou X, Wang H, et al. A novel cyclic peptide targeting LAG-3 for cancer immunotherapy by activating antigen-specific $CD8^+$ T cell responses. *Acta Pharm Sin B.* 2020;10:1047–1060.
22. Kumar D, Lisok A, Dahmane E, et al. Peptide-based PET quantifies target engagement of PD-L1 therapeutics. *J Clin Invest.* 2019;129:616–630.
23. Zhou X, Jiang J, Yang X, et al. First-in-humans evaluation of a PD-L1–binding peptide PET radiotracer in non–small cell lung cancer patients. *J Nucl Med.* 2022; 63:536–542.
24. Chuprin J, Buettner H, Seedhom MO, et al. Humanized mouse models for immuno-oncology research. *Nat Rev Clin Oncol.* 2023;20:192–206.
25. De La Rochere P, Guil-Luna S, Decaudin D, Azar G, Sidhu SS, Piaggio E. Humanized mice for the study of immuno-oncology. *Trends Immunol.* 2018;39:748–763.
26. Dunn GP, Bruce AT, Ikeda H, Old LJ, Schreiber RD. Cancer immunoediting: from immunosurveillance to tumor escape. *Nat Immunol.* 2002;3:991–998.
27. Dunn GP, Old LJ, Schreiber RD. The three Es of cancer immunoediting. *Annu Rev Immunol.* 2004;22:329–360.
28. Kennedy LB, Salama AKS. A review of cancer immunotherapy toxicity. *CA Cancer J Clin.* 2020;70:86–104.
29. Wu Q, Qian W, Sun X, Jiang S. Small-molecule inhibitors, immune checkpoint inhibitors, and more: FDA-approved novel therapeutic drugs for solid tumors from 1991 to 2021. *J Hematol Oncol.* 2022;15:143–205.
30. Haslam A, Prasad V. Estimation of the percentage of US patients with cancer who are eligible for and respond to checkpoint inhibitor immunotherapy drugs. *JAMA Netw Open.* 2019;2:e192535.
31. Hegde PS, Chen DS. Top 10 challenges in cancer immunotherapy. *Immunity.* 2020;52:17–35.
32. van de Donk PP, Oosting SF, Knapen DG, et al. Molecular imaging to support cancer immunotherapy. *J Immunother Cancer.* 2022;10:e004949.
33. Chocarro L, Blanco E, Zuazo M, et al. Understanding LAG-3 signaling. *Int J Mol Sci.* 2021;22:5282.
34. Lecocq Q, Awad RM, De Vlaeminck Y, et al. Single-domain antibody nuclear imaging allows noninvasive quantification of LAG-3 expression by tumor-infiltrating leukocytes and predicts response of immune checkpoint blockade. *J Nucl Med.* 2021;62:1638–1644.
35. Miedema IHC, Huisman MC, Zwezerijnen GJC, et al. ^{89}Zr-immuno-PET using the anti-LAG-3 tracer [^{89}Zr]Zr-BI 754111: demonstrating target specific binding in NSCLC and HNSCC. *Eur J Nucl Med Mol Imaging.* 2023;50:2068–2080.
36. Wu J, Dobbs N, Yang K, Yan N. Interferon-independent activities of mammalian STING mediate antiviral response and tumor immune evasion. *Immunity.* 2020;53: 115–126.e5.
37. Zheng J, Mo J, Zhu T, et al. Comprehensive elaboration of the cGAS-STING signaling axis in cancer development and immunotherapy. *Mol Cancer.* 2020;19:133–151.
38. Yi M, Zheng X, Niu M, Zhu S, Ge H, Wu K. Combination strategies with PD-1/PD-L1 blockade: current advances and future directions. *Mol Cancer.* 2022;21:28–54.

Preclinical Evaluation of Minigastrin Analogs and Proof-of-Concept [^{68}Ga]Ga-DOTA-CCK-66 PET/CT in 2 Patients with Medullary Thyroid Cancer

Thomas Günther*[1], Nadine Holzleitner*[1], Oliver Viering[2], Roswitha Beck[1], Georgine Wienand[2], Alexander Dierks[2], Christian H. Pfob[2], Ralph A. Bundschuh[2], Malte Kircher[2], Constantin Lapa[2], and Hans-Jürgen Wester[1]

[1]*Department of Chemistry, Chair of Pharmaceutical Radiochemistry, TUM School of Natural Sciences, Technical University of Munich, Garching, Germany; and* [2]*Nuclear Medicine, Faculty of Medicine, University of Augsburg, Augsburg, Germany*

Because of the need for radiolabeled theranostics for the detection and treatment of medullary thyroid cancer (MTC), and the yet unresolved stability issues of minigastrin analogs targeting the cholecystokinin-2 receptor (CCK-2R), our aim was to address in vivo stability, our motivation being to develop and evaluate DOTA-CCK-66 (DOTA-γ-glu-PEG_3-Trp-(*N*-Me)Nle-Asp-1-Nal-NH_2, PEG: polyethylene glycol) and DOTA-CCK-66.2 (DOTA-glu-PEG_3-Trp-(*N*-Me)Nle-Asp-1-Nal-NH_2), both derived from DOTA-MGS5 (DOTA-glu-Ala-Tyr-Gly-Trp-(*N*-Me)Nle-Asp-1-Nal-NH_2), and clinically translate [^{68}Ga]Ga-DOTA-CCK-66. **Methods:** ^{64}Cu and ^{67}Ga labeling of DOTA-CCK-66, DOTA-CCK-66.2, and DOTA-MGS5 was performed at 90°C within 15 min (1.0 M NaOAc buffer, pH 5.5, and 2.5 M 4-(2-hydroxyethyl)-1-piperazineethanesulfonic acid buffer, respectively). ^{177}Lu labeling of these 3 compounds was performed at 90°C within 15 min (1.0 M NaOAc buffer, pH 5.5, 0.1 M sodium ascorbate). CCK-2R affinity of ^{nat}Ga/^{nat}Cu/^{nat}Lu-labeled DOTA-CCK-66, DOTA-CCK-66.2, and DOTA-MGS5 was examined on AR42J cells. The in vivo stability of ^{177}Lu-labeled DOTA-CCK-66 and DOTA-MGS5 was examined at 30 min after injection in CB17-SCID mice. Biodistribution studies at 1 h ([^{67}Ga]Ga-DOTA-CCK-66) and 24 h ([^{177}Lu]Lu-DOTA-CCK-66/DOTA-MGS5) after injection were performed on AR42J tumor–bearing CB17-SCID mice. In a translation to the human setting, [^{68}Ga]Ga-DOTA-CCK-66 was administered and whole-body PET/CT was acquired at 120 min after injection in 2 MTC patients. **Results:** Irrespective of the metal or radiometal used (copper, gallium, lutetium), high CCK-2R affinity (half-maximal inhibitory concentration, 3.6–6.0 nM) and favorable lipophilicity were determined. In vivo, increased numbers of intact peptide were found for [^{177}Lu]Lu-DOTA-CCK-66 compared with [^{177}Lu]Lu-DOTA-MGS5 in murine urine (23.7% ± 9.2% vs. 77.8% ± 2.3%). Overall tumor-to-background ratios were similar for both ^{177}Lu-labeled analogs. [^{67}Ga]Ga-DOTA-CCK-66 exhibited accumulation (percentage injected dose per gram) that was high in tumor (19.4 ± 3.5) and low in off-target areas (blood, 0.61 ± 0.07; liver, 0.31 ± 0.02; pancreas, 0.23 ± 0.07; stomach, 1.81 ± 0.19; kidney, 2.51 ± 0.49) at 1 h after injection. PET/CT examination in 2 MTC patients applying [^{68}Ga]Ga-DOTA-CCK-66 confirmed multiple metastases. **Conclusion:** Because of the high in vivo stability and favorable overall preclinical performance of [$^{nat/67}$Ga]Ga-/[$^{nat/177}$Lu]Lu-DOTA-CCK-66, a proof-of-concept clinical investigation of [^{68}Ga]Ga-DOTA-CCK-66 was completed. As several lesions could be identified and excellent biodistribution patterns were observed, further patient studies applying [^{68}Ga]Ga- and [^{177}Lu]Lu-DOTA-CCK-66 are warranted.

Received Aug. 11, 2023; revision accepted Oct. 19, 2023.

For correspondence or reprints, contact Thomas Günther (thomas.guenther@tum.de).

*Contributed equally to this work.

Published online Nov. 9, 2023.

Key Words: DOTA-CCK-66; clinical translation; CCK-2R; medullary thyroid cancer

J Nucl Med 2024; 65:33–39
DOI: 10.2967/jnumed.123.266537

Despite progress in cancer treatment, metastasis still accounts for more than 90% and remains the primary cause of cancer death (*1*). For medullary thyroid cancer (MTC), which accounts for less than 3% of all thyroid cancers, the 10-y survival rate for patients who already had distant metastases at initial diagnosis was only 40% (*2,3*). Because of the limited role of conventional therapies in metastatic MTC not amenable to local treatment (*4,5*), and given the fact that tyrosine kinase inhibitors including antiangiogenic as well as selective RET (rearranged during transfection) inhibitors—though effective—can cause significant toxicity or induce resistance (*6,7*), alternative treatment options for early detection of MTC are needed. Elevated basal calcitonin plasma levels are common in MTC patients and can be measured after calcium or pentagastrin stimulation testing (*8,9*). Patients with confirmed elevated calcitonin levels usually undergo PET imaging using, for example, 3,4-dihydroxy-6-[^{18}F]fluoro-L-phenylalanine ([^{18}F]F-DOPA), given the neuroendocrine origin of MTC cells (*10*). Despite good detection rates using [^{18}F]F-DOPA PET/CT for primary and metastatic MTC, an even improved sensitivity at lower calcitonin levels would be desirable (*11–13*). Moreover, even if metastases are accurately identified by [^{18}F]F-DOPA PET/CT, there is no therapeutic analog available for this compound for subsequent radioligand therapy.

The cholecystokinin-2 receptor (CCK-2R) has been shown to be overexpressed on most MTC cells, thus promoting the development of several different compounds addressing this target over the last few years (*14–18*). CCK-2R ligands carrying a DOTA chelator can be used for imaging (^{68}Ga-labeled) or radioligand therapy (^{177}Lu-labeled)—an advantage over [^{18}F]F-3,4-dihydroxyphenylalanine (DOPA). Apart from ^{68}Ga, ^{64}Cu could be an interesting alternative for PET imaging because of its favorable half-life (12.7 h) and positron energy (653 keV), enabling later imaging time points and high spatial resolution (*19*). However, the low metabolic stability of minigastrin derivatives targeting CCK-2R is still a problem that affects therapeutic efficacy. Several cleavage sites were reported for minigastrin analogs (Tyr-Gly, Gly-Trp, and Asp-Phe) (*20*), of which some were chemically addressed in DOTA-MGS5 (DOTA-glu-Ala-Tyr-Gly-Trp-(*N*-Me)Nle-Asp-1-Nal-NH_2, Fig. 1) (*21*). In vivo

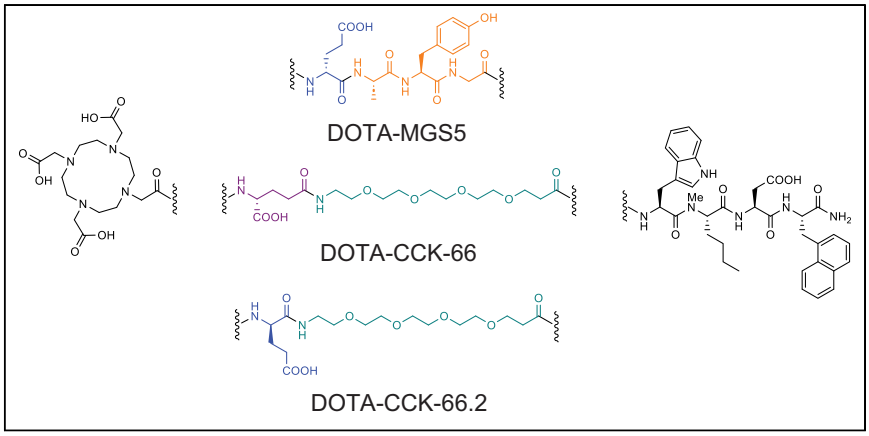

FIGURE 1. Chemical structures of compounds evaluated. All comprise same C-terminal tetrapeptide binding motif and N-terminal DOTA chelator but differ in linker section. Orange = Ala-Tyr-Gly sequence; green = PEG_3 moiety; blue = α-bridged D-glutamic acid moiety; violet = γ-bridged D-glutamic acid moiety.

properties in animals and first patient data thus looked promising for [^{68}Ga]Ga-DOTA-MGS5 (*21,22*).

However, particularly the cleavage sites Tyr-Gly and Gly-Trp are still not addressed in this compound. Therefore, we recently reported on a series of CCK-2R ligands in which we substituted the N-terminal L-amino acids in DOTA-MGS5 (*H*-glu-Ala-Tyr-Gly) by simple polyethylene glycol (PEG) linkers. Interestingly, we observed a lower in vitro stability in human serum (*23*), although the introduction of PEG linkers usually increases stability (*24*). Because negative charges at the N-terminus of minigastrin analogs seem to increase metabolic stability (*25*), we introduced either a γ-D-glutamic acid (γ-glu) or a α-D-glutamic acid (glu) moiety between the DOTA chelator and the PEG_3 linker of DOTA-CCK-64 (DOTA-PEG_3-Trp-(*N*-Me)Nle-Asp-1-Nal-NH_2), which resulted in DOTA-CCK-66 (DOTA-γ-glu-PEG_3-Trp-(N-Me)Nle-Asp-1-Nal-NH_2) and DOTA-CCK-66.2 (DOTA-glu-PEG_3-Trp-(*N*-Me)Nle-Asp-1-Nal-NH_2) (Fig. 1). Furthermore, this study aimed to elucidate whether this simple modification could tackle the stability issues observed in previous studies. Hence, a comparative preclinical evaluation of DOTA-CCK-66, DOTA-CCK-66.2, and DOTA-MGS5, each labeled with [$^{nat/64}$Cu]copper, [$^{nat/67}$Ga]gallium, or [$^{nat/177}$Lu]lutetium, encompassed the determination of CCK-2R affinity (half-maximal inhibitory concentration [IC_{50}]) on AR42J cells, lipophilicity (expressed as n-octanol/phosphate-buffered saline distribution coefficient [log$D_{7.4}$]), human serum albumin binding, in vivo stability, and biodistribution studies on AR42J tumor–bearing mice. Moreover, we selected [^{68}Ga]Ga-DOTA-CCK-66 for proof-of-concept PET/CT examinations in 2 MTC patients.

MATERIALS AND METHODS

Synthesis and Labeling Procedures

Precursor synthesis was conducted via solid-phase peptide synthesis using an *H*-Rink Amide ChemMatrix resin (loading, 0.55 mmol/g; Sigma-Aldrich Chemie GmbH). Characterization of all compounds is provided in Supplemental Figures 1–9 (supplemental materials are available at http://jnm.snmjournals.org). Purification was accomplished via reversed-phase high-performance liquid chromatography (RP-HPLC).

^{64}Cu- and ^{177}Lu-labeling of DOTA-CCK-66, DOTA-CCK-66.2, and DOTA-MGS5 was completed using an established protocol (*26*). ^{67}Ga-labeling of these 3 compounds was performed analogously using 4-(2-hydroxyethyl)-1-piperazineethanesulfonic acid (2.5 M in H_2O) buffer. Detailed descriptions of all labeling procedures ($^{nat/68}$Ga, $^{nat/64}$Cu, $^{nat/177}$Lu) are provided in the supplemental materials. [^{64}Cu]$CuCl_2$ was purchased from DSD-Pharma GmbH. [^{67}Ga]$GaCl_3$ was acquired from Curium. [^{177}Lu]$LuCl_3$ was purchased from ITM Isotope Technologies Munich SE.

The synthesis of [^{68}Ga]Ga-DOTA-CCK-66 for human PET/CT studies was completed in agreement with good manufacturing practices using a good-radiopharmaceutical-practice module (Scintomics GmbH) equipped with an SC-01 gallium peptide labeling kit (ABX). [^{68}Ga]$GaCl_3$ was obtained from a ^{68}Ge/^{68}Ga-generator (GalliAD; IRE Elit Radiopharma). A 900 ± 300 MBq activity of the ^{68}Ga-eluate was combined with a solution of the DOTA-CCK-66 precursor (50 μg) and NaOAc buffer in the reactor and heated. Afterward, the solution was transferred onto a Sep-Pak C18 Light cartridge (Waters) for purification. The cartridge was washed with water and eluted with ethanol, and the solution was diluted with phosphate-buffered saline. Subsequently, sterile filtration was completed using a Millex-GV filter (Merck KGaA). Quality control was conducted using thin-layer chromatography (NH_4OAc/MeOH; Agilent) and HPLC measurement against the corresponding reference compound, [^{nat}Ga]Ga-DOTA-CCK-66. Furthermore, a sterile filter integrity test, a limulus amebocyte lysate, and a postapplication sterility test were performed.

In Vitro Experiments

The CCK-2R affinity (by means of IC_{50}) of ^{nat}Ga/^{nat}Cu/^{nat}Lu-labeled DOTA-CCK-66, DOTA-CCK-66.2, and DOTA-MGS5 and the log$D_{7.4}$ of ^{67}Ga/^{64}Cu/^{177}Lu-labeled DOTA-CCK-66, DOTA-CCK-66.2, and DOTA-MGS5 were determined according to a published procedure (*27*). Human serum albumin binding of ^{nat}Ga/^{nat}Cu/^{nat}Lu-labeled DOTA-CCK-66, DOTA-CCK-66.2, and DOTA-MGS5 was determined by high-performance affinity chromatography (Supplemental Fig. 10), as previously reported (*28,29*). In vitro stability studies of ^{177}Lu-labeled DOTA-CCK-66, DOTA-CCK-66.2, and DOTA-MGS5 in human serum were completed in analogy to a published procedure (*30*). A detailed description of in vitro experiments is provided in the supplemental materials.

In Vivo Experiments

Animal Experiments. All animal experiments were approved by the General Administration of Upper Bavaria (ROB-55.2-1-2532.Vet_02-18-109) and completed using a previously published protocol (*26*). All animal studies were in compliance with the ARRIVE (Animal Research: Reporting of In Vivo Experiments) guidelines (supplemental materials).

In vivo stability studies at 30 min after intravenous injection (n = 3) were completed according to a published procedure using about 30–40 MBq (1 nmol) of [^{177}Lu]Lu-DOTA-CCK-66 and [^{177}Lu]Lu-DOTA-MGS5, respectively, for each animal (*26*).

For biodistribution studies, approximately 2–4 MBq (100 pmol, 150 μL) of [^{67}Ga]Ga-DOTA-CCK-66, [^{177}Lu]Lu-DOTA-CCK-66, or [^{177}Lu]Lu-DOTA-MGS5 were injected into the tail vein of anesthetized (2% isoflurane) 2- to 3-mo-old female AR42J tumor–bearing CB17-SCID mice (n = 4). Organs were removed and weighed, and the accumulated radioactivity was measured in a γ-counter (Perkin Elmer) after euthanasia at 1 h (^{67}Ga-labeled) and 24 h (^{177}Lu-labeled) after injection.

Imaging studies using [^{67}Ga]Ga-DOTA-CCK-66, [^{177}Lu]Lu-DOTA-CCK-66, or [^{177}Lu]Lu-DOTA-MGS5 were performed according to a

published protocol (*26*). Static images were recorded at $t = 1$ and 24 h after injection (anesthesia by 2% isoflurane, $n = 1$) with an acquisition time of $t +$ (45–60 min) using a high-energy general-purpose rat and mouse collimator via MILabs acquisition software versions 11.00 and 12.26 from MILabs.

For competition studies ($n = 2$), a 3.03 mg/kg concentration (40 nmol) of [^{nat}Ga]Ga-DOTA-MGS5 (10^{-3} M in phosphate-buffered saline) was coinjected with [^{67}Ga]Ga-DOTA-CCK-66 (100 pmol), or a 3.25 mg/kg concentration (40 nmol) of [^{nat}Lu]Lu-DOTA-MGS5 (10^{-3} M in phosphate-buffered saline) was coadministered with [^{177}Lu]Lu-DOTA-CCK-66 (100 pmol).

Acquired data were statistically analyzed using the Student *t*-test via Excel (Microsoft Corp.) and OriginPro software (version 9.7; OriginLab Corp.). Acquired *P* values of less than 0.05 were considered statistically significant.

Clinical PET/CT. [^{68}Ga]Ga-DOTA-CCK-66 was applied for restaging purposes in 2 MTC patients (male, aged 64 y, and female, aged 46 y). Both patients presented with rising calcitonin levels and calcitonin doubling times shorter than 24 mo at the time of PET/CT imaging, indicating tumor progression. Before CCK-2R–directed imaging, [^{18}F]F-DOPA PET/CT had been negative in both subjects, prompting further diagnostic work-up. The application is allowed by the German Medical Act (§13 2b Arzneimittelgesetz), which waives the need for institutional review board approval. Both patients gave written informed consent after receiving comprehensive medical information from a board-certified nuclear medicine physician. All procedures were completed in accordance with the Declaration of Helsinki and its later amendments and the legal considerations of clinical guidelines. The ethical compliance of this approach was confirmed by the local Ethics Committee of Ludwig-Maximilians-Universität München (approval 23-0627).

A detailed description of the patients' histories is provided in the supplemental materials. Both patients underwent [^{68}Ga]Ga-DOTA-CCK-66 whole-body imaging using a PET/CT scanner (Biograph mCT 40; Siemens Healthineers) at 120 min after injection of 151 and 193 MBq of [^{68}Ga]Ga-DOTA-CCK-66 (~18 μg each), respectively. Whole-body CT imaging was performed as auxiliary CT (120 kVp, 40 mAs). PET datasets were reconstructed using a standard protocol provided by the manufacturer (2 iterations, 21 subsets), corrected for randoms, scatter, decay, and attenuation (using whole-body auxiliary CT).

RESULTS

Synthesis and Radiolabeling

The synthesized precursors were obtained in yields of 3%–7% (chemical purity > 95%) after RP-HPLC purification. Labeling using a 2.5-fold excess of [^{nat}Ga]Ga$(NO_3)_3$, [^{nat}Lu]LuCl_3, or [^{nat}Cu]Cu$(OAc)_2$ resulted in quantitative yields. No purification step was conducted before in vitro experiments, as no effects of free metal ions on overall affinity data was observed in previous experiments (*26*). ^{177}Lu, ^{67}Ga, and ^{64}Cu labeling of DOTA-CCK-66, DOTA-CCK-66.2, and DOTA-MGS5 was performed manually, each resulting in radiochemical yields and purities of more than 95% and molar activities of 10–50 GBq/μmol (non–decay-corrected). All compounds were used without further purification.

The synthesized batches of [^{68}Ga]Ga-DOTA-CCK-66 used for proof-of-concept studies in 2 MTC patients yielded 150 ± 50 MBq (~56% non–decay-corrected). All specifications were fulfilled. The pH of the 16-mL solution was 7.5. Both the ^{nat}Ga-labeled reference compound and the ^{68}Ga-labeled product showed the same retention times using RP-HPLC. The radiochemical purity determined by

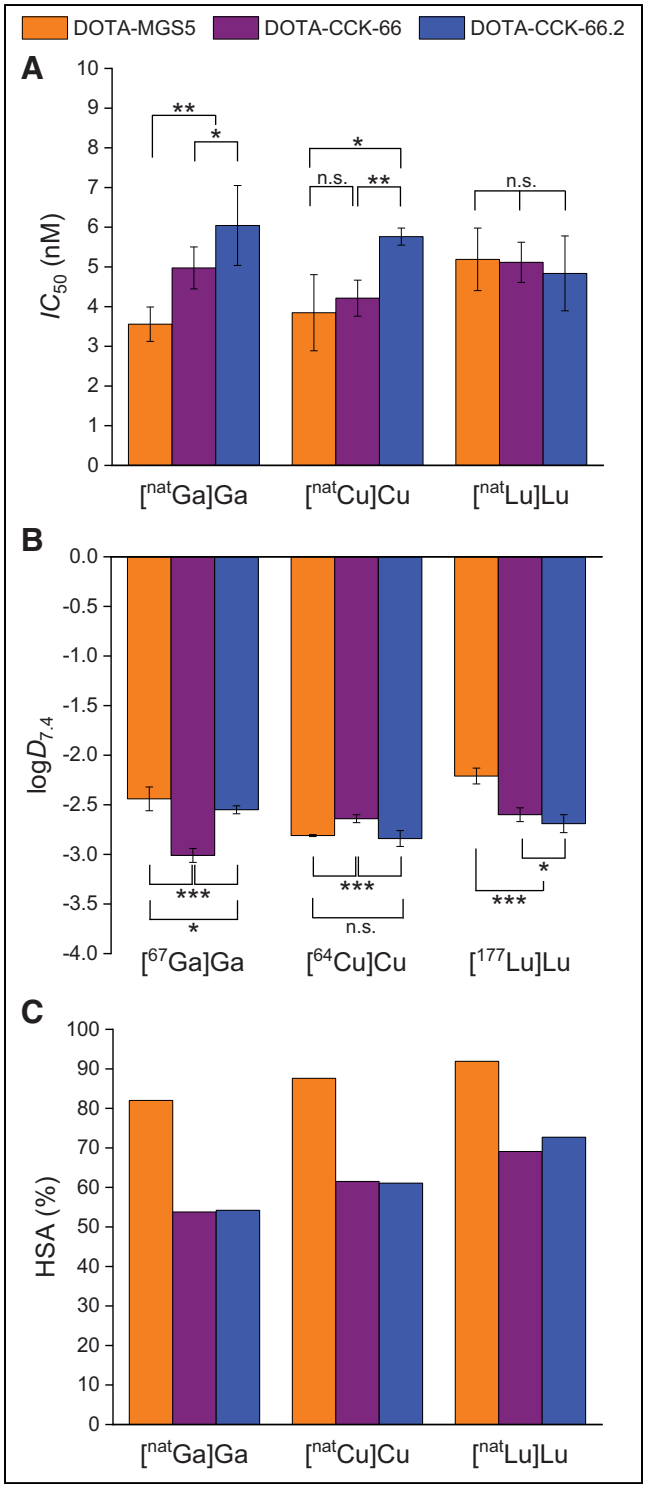

FIGURE 2. In vitro data of $^{nat/64}$Cu-, $^{nat/67}$Ga-, and $^{nat/177}$Lu-labeled CCK-2R ligands. Data are expressed as mean ± SD. (A) Affinity data ($n = 3$) on AR42J cells (2.0×10^5 cells per well) using [^{177}Lu]Lu-DOTA-PP-F11N (0.3 pmol/well) as radiolabeled reference (3 h, 37°C, RPMI 1640, 5 mM L-Gln, 5 mL nonessential amino acids [×100], 10% fetal calf serum + 5% bovine serum albumin [*v/v*]). (B) log$D_{7.4}$ ($n = 6$). (C) Human serum albumin binding as determined by high-performance affinity chromatography. n.s. = not significant. *$P < 0.05$. **$P < 0.01$. ***$P < 0.0001$.

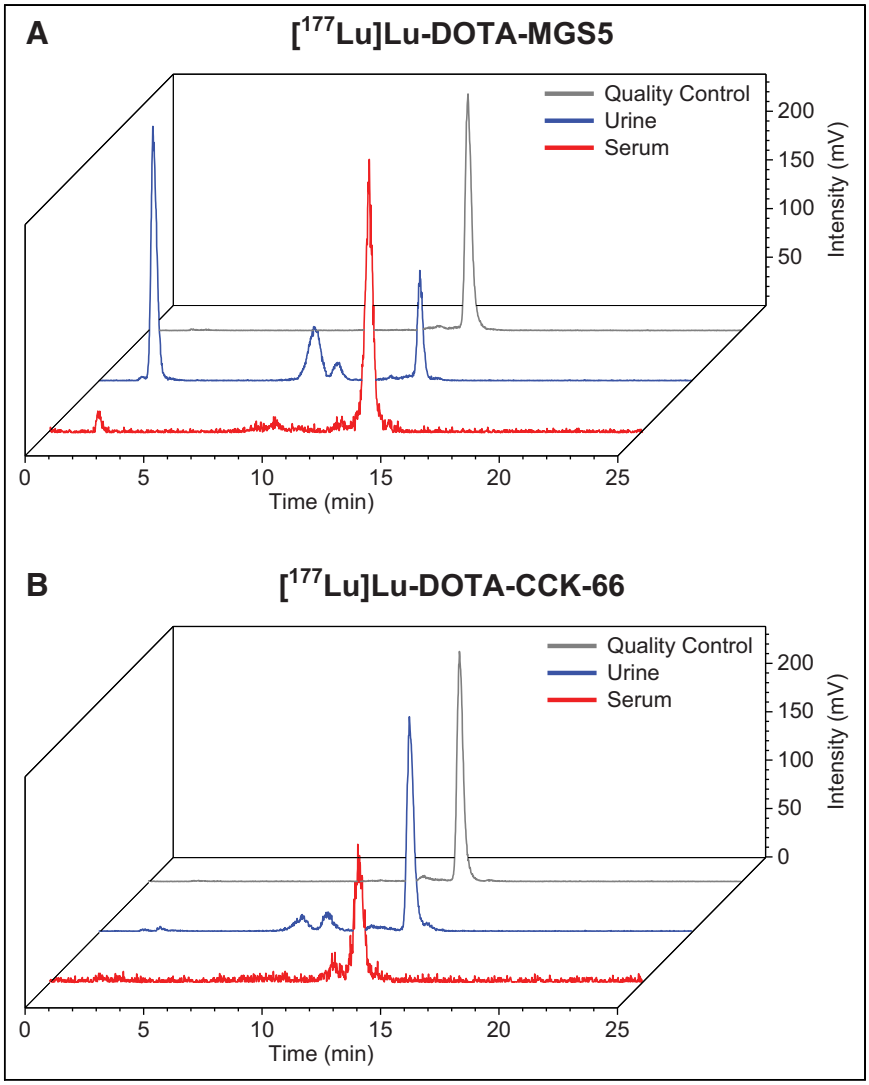

FIGURE 3. In vivo stability of CCK-2R ligands: amount of intact compound at 30 min after injection (3 each) in murine serum (red) and urine (blue) for [^{177}Lu]Lu-DOTA-MGS5 (A) and [^{177}Lu]Lu-DOTA-CCK-66 (B) (quality control in gray).

RP-HPLC was higher than 95%, and the content of unbound [^{68}Ga]Ga species was less than 0.8%. Thin-layer chromatography measurement also revealed less than 0.8% of unbound [^{68}Ga]Ga^{3+}.

In Vitro Characterization

All 3 compounds exhibited high CCK-2R affinity on AR42J cells (IC_{50}, 3.6–6.0 nM, irrespective of whether ^{nat}Ga-, ^{nat}Cu-, or ^{nat}Lu-labeled; Fig. 2A; Supplemental Table 1). [^{nat}Ga]Ga-DOTA-MGS5 revealed significantly lower IC_{50} values than [^{nat}Ga]Ga-DOTA-CCK-66 and -66.2 ($P < 0.004$), and [^{nat}Cu]Cu-DOTA-CCK-66.2 displayed significantly higher IC_{50} values than [^{nat}Cu]Cu-DOTA-MGS5 and [^{nat}Cu]Cu-DOTA-CCK-66 ($P < 0.03$). Distribution coefficients ($\log D_{7.4}$) were in the range of −3.0 to −2.2 for all 3 ligands, independent of whether ^{67}Ga-, ^{64}Cu-, or ^{177}Lu-labeled (Fig. 2B, Supplemental Table 1). [^{67}Ga]Ga-DOTA-CCK-66 revealed significantly lower $\log D_{7.4}$ values than [^{67}Ga]Ga-DOTA-MGS5 and [^{67}Ga]Ga-DOTA-CCK-66.2 ($P < 0.0001$), [^{64}Cu]Cu-DOTA-CCK-66 exhibited significantly higher $\log D_{7.4}$ values than [^{64}Cu]Cu-DOTA-MGS5 and [^{64}Cu]Cu-DOTA-CCK-66.2 ($P < 0.0001$), and [^{177}Lu]Lu-DOTA-MGS5 displayed significantly higher $\log D_{7.4}$ values than [^{177}Lu]Lu-DOTA-CCK-66 and -66.2 ($P < 0.0001$). Both DOTA-CCK-66 and DOTA-CCK-66.2 exhibited distinctly lower human serum albumin binding than DOTA-MGS5, irrespective of the radiometal used (Fig. 2C; Supplemental Table 2). In vitro stability studies in human serum (37°C, 72 h) showed comparable numbers of intact tracer for all 3 ^{177}Lu-labeled CCK-2R ligands (Supplemental Fig. 11, Supplemental Table 3). Because of the overall similar, but slightly more favorable, in vitro properties of DOTA-CCK-66 (independent of the metals used), DOTA-CCK-66.2 was excluded from further experiments.

In Vivo Characterization

In total, 25 animals were used for in vivo stability (2 × 3), biodistribution (3 × 4), imaging (3 × 1), and competition (2 × 2) studies. Intact compound was similar between [^{177}Lu]Lu-DOTA-CCK-66 and [^{177}Lu]Lu-DOTA-MGS5 in murine serum (78.5% ± 3.1% vs. 82.0% ± 0.1%) at 30 min after injection but was higher for [^{177}Lu]Lu-DOTA-CCK-66 than for [^{177}Lu]Lu-DOTA-MGS5 in the urine (77.8% ± 2.3% vs. 23.7% ± 9.2%, $P < 0.001$) (Fig. 3). Biodistribution studies on AR42J tumor–bearing mice revealed high initial tumor uptake (19.4 ± 3.5 percentage injected dose per gram [%ID/g]) for [^{67}Ga]Ga-DOTA-CCK-66, whereas off-target accumulation in all organs was less than 2.6 %ID/g at 1 h after injection (Fig. 4A; Supplemental Table 4). At 24 h after injection, [^{177}Lu]Lu-DOTA-CCK-66 displayed slightly lower activity levels in the tumor than did [^{177}Lu]Lu-DOTA-MGS5 (8.6 ± 1.1 %ID/g vs. 11.0 ± 1.2 %ID/g, $P < 0.02$) but also slightly lower off-target activity retention in most organs (stomach, $P < 0.01$), which resulted in comparable tumor-to-background ratios overall (Supplemental Tables 4 and 5).

Imaging studies (Fig. 4B) corroborated the biodistribution profiles well, revealing high activity levels in the tumor and low levels in all organs for [^{67}Ga]Ga-DOTA-CCK-66 (1 h after injection), as well as for [^{177}Lu]Lu-DOTA-CCK-66 and [^{177}Lu]Lu-DOTA-MGS5 (24 h after injection). Competition studies of both [^{67}Ga]Ga-DOTA-CCK-66 (1 h after injection) and [^{177}Lu]Lu-DOTA-CCK-66 (24 h after injection) using an excess of [^{nat}Ga]Ga-/[^{nat}Lu]Lu-DOTA-MGS5 confirmed specificity of tumor uptake (Supplemental Fig. 12; Supplemental Table 4).

Because of its overall in vitro and in vivo properties [^{68}Ga]Ga-DOTA-CCK-66 was selected for proof-of-concept PET/CT application in 2 MTC patients.

Proof-of-Concept Study in Humans

[^{68}Ga]Ga-DOTA-CCK-66-PET showed a favorable biodistribution, with the highest uptake in tumor lesions and the CCK-2R–expressing stomach. Besides the kidneys, ureters, and bladder

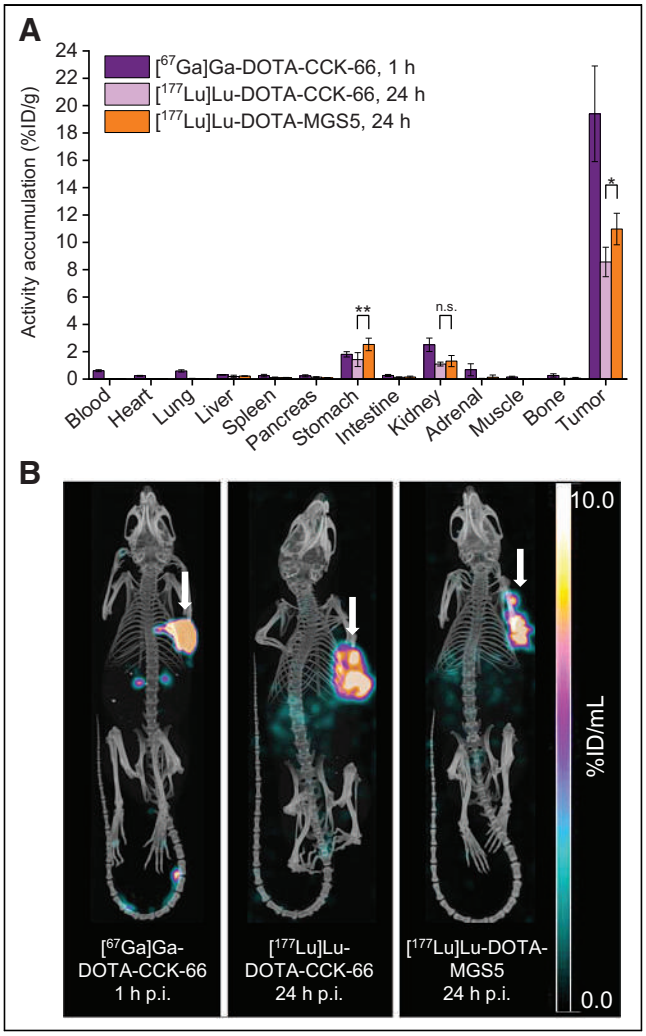

FIGURE 4. (A) Biodistribution of [^{67}Ga]Ga-DOTA-CCK-66 (1 h after injection), as well as [^{177}Lu]Lu-DOTA-CCK-66 and [^{177}Lu]Lu-DOTA-MGS5 (24 h after injection), in selected organs in AR42J tumor–bearing CB17-SCID mice (100 pmol each). Data are %ID/g (mean ± SD, 4 each). (B) Maximum-intensity projection of AR42J tumor (arrows)–bearing CB17-SCID mice (1 each) injected with [^{67}Ga]Ga-DOTA-CCK-66, as well as [^{177}Lu]Lu-DOTA-CCK-66 and [^{177}Lu]Lu-DOTA-MGS5 (100 pmol each). Images were acquired at either 1 or 24 h after injection. n.s. = not significant; p.i. = after injection. *$P < 0.05$. **$P < 0.01$.

(due to excretion), no significant activity levels were found in other organs. [^{68}Ga]Ga-DOTA-CCK-66 was well tolerated, and no side effects or changes in vital signs were observed during the tracer's slow intravenous injection (~2 min) or thereafter (with a follow-up period of 4 h).

A 64-y-old male patient who had initially undergone thyroidectomy and cervical lymph node dissection had a long history of disease, with several local and lymph node recurrences, and presented at the time of PET/CT imaging with a rising calcitonin level of 110 pg/mL and a calcitonin doubling time of 16 mo. On [^{68}Ga]Ga-DOTA-CCK-66 PET/CT, suggestive CCK-2R–expressing lymph nodes were detected in the left retroclavicular region and in the upper mediastinum (Fig. 5). Subsequently, the lymph nodes were surgically resected and histologically confirmed as lymph node metastases of MTC.

A 46-y-old female patient who had undergone thyroidectomy and cervical lymph node dissection, as well as external-beam radiation of the thyroid bed due to local tumor remnants, showed a rising calcitonin level of 380 pg/mL and a calcitonin doubling time of 5 mo at the time of PET/CT imaging. [^{68}Ga]Ga-DOTA-CCK-66 detected several lymph node metastases (bilaterally hilar, right retroclavicular), liver metastases (in both liver lobes), and bone metastases (atlas, right eighth rib, right femur, right os ischii) (Fig. 6). In comparison to the [^{18}F]FDG PET/CT available for this patient, [^{68}Ga]Ga-DOTA-CCK-66 detected additional lymph node, liver, and bone metastases.

DISCUSSION

Because of the ongoing need for novel and improved treatment options for MTC patients, several CCK-2R ligands have been reported over the last few years, particularly compounds addressing the stability issues of minigastrin derivatives by chemical design (*15–18*). In our group, we developed a series of radiohybrid-based minigastrin analogs that revealed a high activity accumulation in the tumor but also suffered from elevated kidney retention due to the presence of a silicon-fluoride acceptor moiety and several negative charges within the linker section (*27,30*). Therefore, we recently focused on shorter CCK-2R ligands and aimed to address metabolic stability by the introduction of PEG linkers, which, however, resulted in a lower stability (*23*). To address this matter in this study, we made some minor modifications within the linker sequence of our minigastrin derivatives and completed in vitro and in vivo evaluations, as well as initiating clinical translation of our most favorable compound.

Synthesis of the precursors was easily accessible via solid-phase peptide synthesis, and complexation proceeded quantitatively, irrespective of the metal or radiometal used. Because of their structural similarity, both novel compounds and the reference peptide, DOTA-MGS5, revealed a comparable CCK-2R affinity and favorable log$D_{7.4}$. On the basis of the similar but slightly more favorable in vitro properties of the DOTA-CCK-66 peptide over the DOTA-CCK-66.2 peptide, we excluded the latter from further evaluation.

In vivo stability at 30 min after injection was comparable for both [^{177}Lu]Lu-DOTA-CCK-66 and [^{177}Lu]Lu-DOTA-MGS5 in murine serum but distinctly different in murine urine, as the former revealed a 3-fold higher amount of intact compound than the reference. This finding suggests that [^{177}Lu]Lu-DOTA-CCK-66 is cleared from the blood mostly intact whereas [^{177}Lu]Lu-DOTA-MGS5 is cleared predominantly metabolized. Because of their structural similarity, this beneficial property can be attributed to the introduction of a γ-glu moiety between the DOTA and the PEG_3 linker, because a previous compound that differed from DOTA-CCK-66 only by the absence of this γ-glu unit exhibited a noticeably lower stability (*23*). The amount of intact peptide in the urine even surpassed that of a recently reported CCK-2R ligand, [^{177}Lu]Lu-DOTA-$(GABOB)_2$-β-Ala-Trp-(*N*-Me)Nle-Asp-1-Nal-NH_2, which also substituted N-terminal amino acids by unnatural moieties and revealed high in vivo stability (77.8% ± 2.3% vs. ~60%) (*16*).

Because of its high metabolic stability, [^{67}Ga]Ga-DOTA-CCK-66 demonstrated a high accumulation of activity in the tumor at 1 h after injection, whereas off-target accumulation was either low or cleared rapidly, resulting in low activity levels in all organs, even in the CCK-2R–expressing stomach. Hence, favorable tumor-to-background ratios were determined and were approximately 2-fold higher in all organs than reported for [^{68}Ga]Ga-DOTA-MGS5 (*21*). The more rapid clearance rates corroborate the distinctly lower human

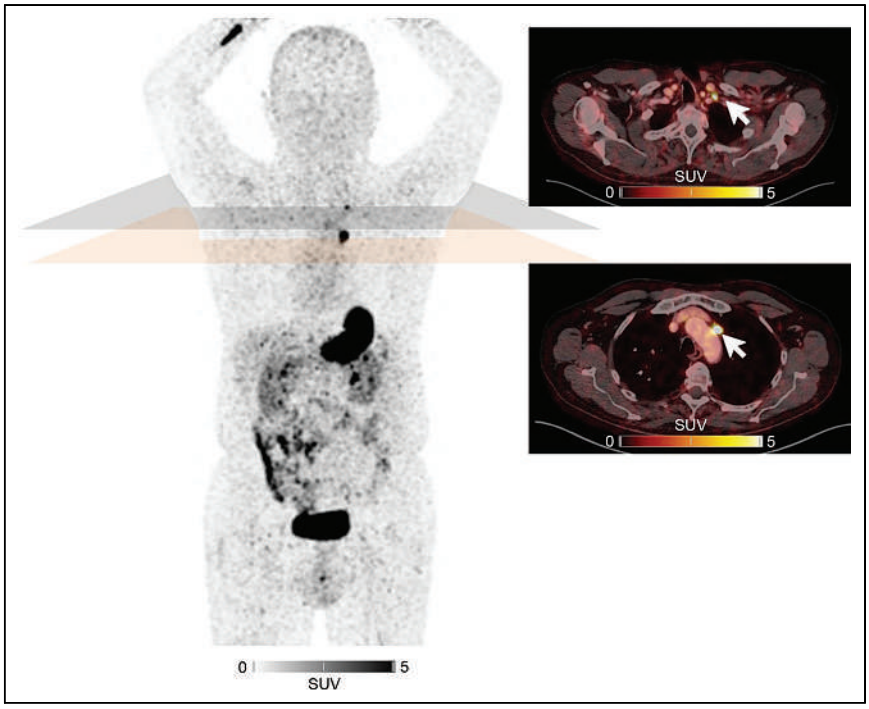

FIGURE 5. Maximum-intensity projection (left) and fused transaxial slices (right) of 64-y-old male MTC patient undergoing PET/CT at 2 h after intravenous injection of 151 MBq of [^{68}Ga]Ga-DOTA-CCK-66. CCK-2R–expressing lymph node metastases could be detected in left retroclavicular region and in upper mediastinum (arrows).

serum albumin binding observed by high-performance affinity chromatography, a finding that might be responsible for the favorably low activity uptake overall (apart from the tumor). The comparison of [^{68}Ga]Ga-DOTA-MGS5 and [^{68}Ga]Ga-DOTA-CCK-66 is a limitation of this study, as biodistribution studies of these compounds have been performed by different groups using different mouse models (BALB/c vs. CB17-SCID) and tumor models (A431-CCK2R vs. AR42J), as well as precursor amounts (20 vs. 100 pmol) (*21*). Comparison of the ^{177}Lu-labeled analogs at 24 h after injection using the same modalities revealed similar tumor-to-background ratios overall, indicating that [^{177}Lu]Lu-DOTA-MGS5 and [^{177}Lu]Lu-DOTA-CCK-66 might be equivalent in the application for radioligand therapy. However, further clinical investigation is needed.

On the basis of the favorable preclinical data of [^{67}Ga]Ga-DOTA-CCK-66, its ^{68}Ga-analog was selected for a clinical proof-of-concept investigation. [^{68}Ga]Ga-DOTA-CCK-66 PET/CT on 2 MTC patients at 120 min after injection revealed high uptake in tumor lesions and the physiologically CCK-2R–expressing stomach. Furthermore, off-target accumulation was low, corroborating the biodistribution profiles in mice well. Hence, several lymph node, bone, and liver metastases could be identified in these 2 MTC patients. Interestingly, we could observe a higher tumor-to-organ contrast at 120 min than at 60 min after injection. A similar trend was also reported for [^{68}Ga]Ga-DOTA-MGS5 (*22*), indicating a slightly decelerated tumor accumulation and a fast off-target clearance of these minigastrin analogs. On the basis of these observations and the similar in vitro properties of [^{nat}Cu]Cu-DOTA-CCK-66, PET/CT examinations using [^{64}Cu]Cu-DOTA-CCK-66 could be a viable alternative in the future, since it would enable later imaging time points.

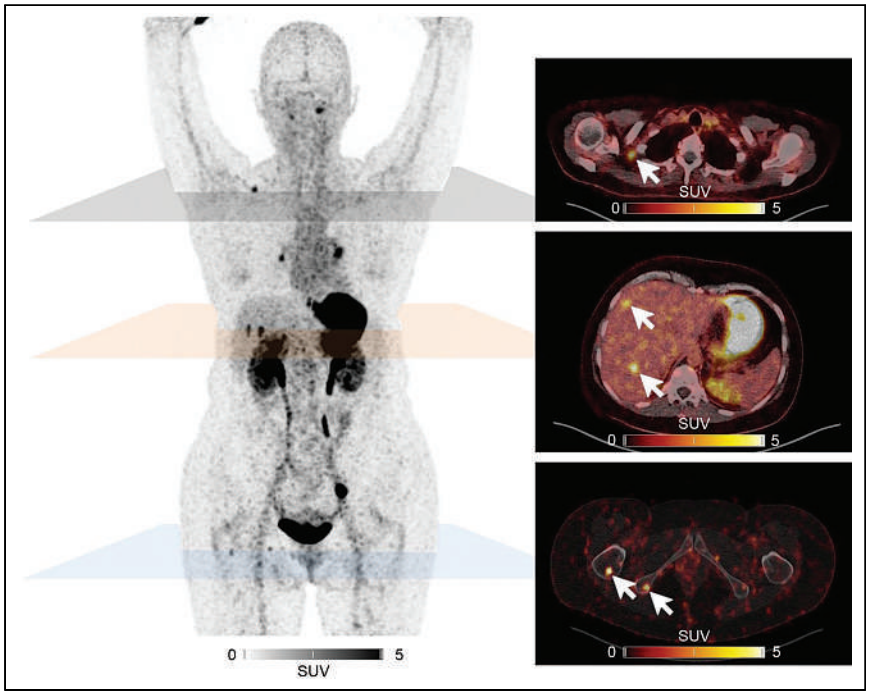

FIGURE 6. Maximum-intensity projections (left) and fused transaxial sections (right) of 46-y-old female MTC patient undergoing PET/CT at 2 h after intravenous injection of 193 MBq of [^{68}Ga]Ga-DOTA-CCK-66. Several lymph node (e.g., right retroclavicular), liver, and bone metastases (e.g., right femur and right ischium) could be detected (arrows).

[^{68}Ga]Ga-DOTA-CCK-66 PET/CT did not show any biosafety issues and allows for radioligand therapy using [^{177}Lu]Lu-DOTA-CCK-66, which might represent an advantage of radiolabeled CCK-2R ligands over [^{18}F]FDG or [^{18}F]F-DOPA. On the basis of the fast renal activity clearance and low activity accumulation observed in the kidneys, we do not expect any issues regarding kidney toxicity using [^{177}Lu]Lu- or even [^{225}Ac]Ac-DOTA-CCK-66 for radioligand therapy. However, activity retention in the human stomach was higher than observed in the murine stomach and has to be monitored carefully during the first treatment cycles to prevent toxicity. Furthermore, the fact that the feasibility of [^{68}Ga]Ga-DOTA-CCK-66 has been shown only for single patients to date is a limitation of this study, thus demanding further clinical evaluation of this compound to verify its clinical value.

CONCLUSION

[^{67}Ga]Ga-DOTA-CCK-66 revealed excellent preclinical characteristics, particularly high in vivo stability and rapid activity clearance, thus providing good tumor-to-background ratios. A proof-of-concept investigation on 2 MTC patients using [^{68}Ga]Ga-DOTA-CCK-66 PET/CT showed favorable biodistribution patterns and identified several lesions, which could be histopathologically confirmed as metastases of MTC. One advantage of this compound over the MTC imaging gold standard, [^{18}F]F-DOPA, is the possibility for ^{177}Lu labeling for subsequent radioligand therapy. Therefore, additional patient studies using [^{68}Ga]Ga- or [^{64}Cu]Cu-DOTA-CCK-66, as well as [^{177}Lu]Lu- or even [^{225}Ac]Ac-DOTA-CCK-66, are warranted to elucidate the clinical value of this theranostic tool.

DISCLOSURE

This study was funded by Deutsche Forschungsgemeinschaft (DFG, German Research Foundation—461577150). Thomas Günther received the 2023 Sanjiv Sam Gambhir–Philips and the 2023 Translational Research and Applied Medicine fellowship for support at Stanford University. A patent application on CCK-2R–targeted compounds including DOTA-CCK-66 with Thomas Günther, Nadine Holzleitner, Constantin Lapa, and Hans-Jürgen Wester as inventors has been filed. Hans-Jürgen Wester is founder and shareholder of Scintomics GmbH, Munich, Germany. No other potential conflict of interest relevant to this article was reported.

KEY POINTS

QUESTION: Can a simplistic design modification of the clinically applied CCK-2R ligand [^{68}Ga]Ga-DOTA-MGS5 improve preclinical and clinical characteristics?

PERTINENT FINDINGS: [^{64}Cu]Cu-/[^{67}Ga]Ga-/[^{177}Lu]Lu-DOTA-CCK-66 displayed similar in vitro and in vivo properties to the reference compound but a noticeably improved in vivo stability, which resulted in favorable activity clearance and, thus, tumor-to-organ contrast in animals and proof-of-concept [^{68}Ga]Ga-DOTA-CCK-66 PET/CT applications.

IMPLICATIONS FOR PATIENT CARE: Although further [^{68}Ga]Ga-DOTA-CCK-66 PET/CT (and [^{177}Lu]Lu-/[^{225}Ac]Ac-DOTA-CCK-66 for treatment) applications in MTC patients have to be completed, these preliminary results suggest a promising theranostic candidate for clinical use.

REFERENCES

1. Ganesh K, Massagué J. Targeting metastatic cancer. *Nat Med.* 2021;27:34–44.
2. Thyroid cancer: statistics. Cancer.net website. https://www.cancer.net/cancer-types/thyroid-cancer/statistics#:~:text=In%202023%2C%20an%20estimated%2043%2C720,with%20thyroid%20cancer%20in%202020. Published August 2023. Accessed October 30, 2023.
3. Roman S, Lin R, Sosa JA. Prognosis of medullary thyroid carcinoma: demographic, clinical, and pathologic predictors of survival in 1252 cases. *Cancer.* 2006;107:2134–2142.
4. Stamatakos M, Paraskeva P, Stefanaki C, et al. Medullary thyroid carcinoma: the third most common thyroid cancer reviewed. *Oncol Lett.* 2011;2:49–53.
5. Wells SA Jr, Asa SL, Dralle H, et al. Revised American Thyroid Association guidelines for the management of medullary thyroid carcinoma. *Thyroid.* 2015;25:567–610.
6. Vodopivec DM, Hu MI. RET kinase inhibitors for RET-altered thyroid cancers. *Ther Adv Med Oncol.* 2022;14:17588359221101691.
7. Hadoux J, Schlumberger M. Chemotherapy and tyrosine-kinase inhibitors for medullary thyroid cancer. *Best Pract Res Clin Endocrinol Metab.* 2017;31:335–347.
8. Karges W, Dralle H, Raue F, et al. Calcitonin measurement to detect medullary thyroid carcinoma in nodular goiter: German evidence-based consensus recommendation. *Exp Clin Endocrinol Diabetes.* 2004;112:52–58.
9. Hennessy JF, Wells SAJ, Ontjes DA, Cooper CW. A comparison of pentagastrin injection and calcium infusion as provocative agents for the detection of medullary carcinoma of the thyroid. *J Clin Endocrinol Metab.* 1974;39:487–495.
10. Giovanella L, Treglia G, Iakovou I, Mihailovic J, Verburg FA, Luster M. EANM practice guideline for PET/CT imaging in medullary thyroid carcinoma. *Eur J Nucl Med Mol Imaging.* 2020;47:61–77.
11. Treglia G, Castaldi P, Villani MF, et al. Comparison of ^{18}F-DOPA, ^{18}F-FDG and ^{68}Ga-somatostatin analogue PET/CT in patients with recurrent medullary thyroid carcinoma. *Eur J Nucl Med Mol Imaging.* 2012;39:569–580.
12. Brammen L, Niederle MB, Riss P, et al. Medullary thyroid carcinoma: do ultrasonography and F-DOPA-PET-CT influence the initial surgical strategy? *Ann Surg Oncol.* 2018;25:3919–3927.
13. Terroir M, Caramella C, Borget I, et al. F-18-dopa positron emission tomography/computed tomography is more sensitive than whole-body magnetic resonance imaging for the localization of persistent/recurrent disease of medullary thyroid cancer patients. *Thyroid.* 2019;29:1457–1464.
14. von Guggenberg E, Kolenc P, Rottenburger C, Mikolajczak R, Hubalewska-Dydejczyk A. Update on preclinical development and clinical translation of cholecystokinin-2 receptor targeting radiopharmaceuticals. *Cancers (Basel).* 2021;13:5776.
15. Zavvar TS, Hörmann AA, Klingler M, et al. Effects of side chain and peptide bond modifications on the targeting properties of stabilized minigastrin analogs. *Pharmaceuticals (Basel).* 2023;16:278.
16. Hörmann AA, Klingler M, Rangger C, et al. Effect of N-terminal peptide modifications on in vitro and in vivo properties of ^{177}Lu-labeled peptide analogs targeting CCK2R. *Pharmaceutics.* 2023;15:796.
17. Grob NM, Schibli R, Behe M, Valverde IE, Mindt TL. 1,5-disubstituted 1,2,3-triazoles as amide bond isosteres yield novel tumor-targeting minigastrin analogs. *ACS Med Chem Lett.* 2021;12:585–592.
18. Sauter AW, Mansi R, Hassiepen U, et al. Targeting of the cholecystokinin-2 receptor with the minigastrin analog ^{177}Lu-DOTA-PP-F11N: does the use of protease inhibitors further improve in vivo distribution? *J Nucl Med.* 2019;60:393–399.
19. Braune A, Oehme L, Freudenberg R, et al. Comparison of image quality and spatial resolution between ^{18}F, ^{68}Ga, and ^{64}Cu phantom measurements using a digital Biograph Vision PET/CT. *EJNMMI Phys.* 2022;9:58.
20. Ocak M, Helbok A, Rangger C, et al. Comparison of biological stability and metabolism of CCK2 receptor targeting peptides, a collaborative project under COST BM0607. *Eur J Nucl Med Mol Imaging.* 2011;38:1426–1435.
21. Klingler M, Summer D, Rangger C, et al. DOTA-MGS5, a new cholecystokinin-2 receptor-targeting peptide analog with an optimized targeting profile for theranostic use. *J Nucl Med.* 2019;60:1010–1016.
22. Von Guggenberg E, Uprimny C, Klinger M, et al. Preliminary clinical experience with cholecystokinin-2 receptor PET/CT using the ^{68}Ga-labeled minigastrin analog DOTA-MGS5 in patients with medullary thyroid cancer. *J Nucl Med.* 2023;64:859–862.
23. Holzleitner N, Gunther T, Daoud-Gadieh A, Lapa C, Wester HJ. Investigation of the structure-activity relationship at the N-terminal part of minigastrin analogs. *EJNMMI Res.* 2023;13:65.
24. Khandare J, Minko T. Polymer–drug conjugates: progress in polymeric prodrugs. *Prog Polym Sci.* 2006;31:359–397.
25. Good S, Walter MA, Waser B, et al. Macrocyclic chelator-coupled gastrin-based radiopharmaceuticals for targeting of gastrin receptor-expressing tumours. *Eur J Nucl Med Mol Imaging.* 2008;35:1868–1877.
26. Günther T, Deiser S, Felber V, Beck R, Wester HJ. Substitution of L-tryptophan by a-methyl-L-tryptophan in ^{177}Lu-RM2 results in ^{177}Lu-AMTG, a high-affinity gastrin-releasing peptide receptor ligand with improved in vivo stability. *J Nucl Med.* 2022;63:1364–1370.
27. Holzleitner N, Günther T, Beck R, Lapa C, Wester H-J. Introduction of a SiFA moiety into the D-glutamate chain of DOTA-PP-F11N results in radiohybrid-based CCK-2R-targeted compounds with improved pharmacokinetics in vivo. *Pharmaceuticals (Basel).* 2022;15:1467.
28. Valko K, Nunhuck S, Bevan C, Abraham MH, Reynolds DP. Fast gradient HPLC method to determine compounds binding to human serum albumin. Relationships with octanol/water and immobilized artificial membrane lipophilicity. *J Pharm Sci.* 2003;92:2236–2248.
29. Yamazaki K, Kanaoka M. Computational prediction of the plasma protein-binding percent of diverse pharmaceutical compounds. *J Pharm Sci.* 2004;93:1480–1494.
30. Günther T, Holzleitner N, Di Carlo D, Urtz-Urban N, Lapa C, Wester H-J. Development of the first ^{18}F-labeled radiohybrid-based minigastrin derivative with high target affinity and tumor accumulation by substitution of the chelating moiety. *Pharmaceutics.* 2023;15:826.

Fibroblast Activation Protein–Targeted PET/CT with ^{18}F-Fibroblast Activation Protein Inhibitor-74 for Evaluation of Gastrointestinal Cancer: Comparison with ^{18}F-FDG PET/CT

Weizhi Xu*[1–3], Jiayu Cai*[1–3], Tianxing Peng*[1–3], Tinghua Meng[1–3], Yizhen Pang[1–3], Long Sun[1–3], Hua Wu[1–3], Jingjing Zhang[4–7], Xiaoyuan Chen[4–8], and Haojun Chen[1–3]

[1]*Department of Nuclear Medicine, First Affiliated Hospital of Xiamen University, Xiamen, China;* [2]*Minnan PET Center, First Affiliated Hospital of Xiamen University, Xiamen, China;* [3]*Xiamen Key Laboratory of Radiopharmaceuticals, School of Medicine, Xiamen University, Xiamen, China;* [4]*Department of Diagnostic Radiology, Yong Loo Lin School of Medicine, National University of Singapore, Singapore;* [5]*Department of Surgery, Yong Loo Lin School of Medicine, National University of Singapore, Singapore;* [6]*Department of Chemical and Biomolecular Engineering, College of Design and Engineering, National University of Singapore, Singapore;* [7]*Department of Biomedical Engineering, College of Design and Engineering, National University of Singapore, Singapore; and* [8]*Institute of Molecular and Cell Biology, Agency for Science, Technology, and Research (A*STAR), Singapore*

Fibroblast activation protein is overexpressed in the stroma of several cancer types. ^{18}F-fibroblast activation protein inhibitor (FAPI)–74 is a PET tracer with high selectivity for fibroblast activation protein and has shown high accumulation in human tumors in clinical studies. However, the use of ^{18}F-FAPI-74 for PET imaging of gastrointestinal cancer has not been systematically investigated. Herein, we investigated the diagnostic accuracy of ^{18}F-FAPI-74 (^{18}F-LNC1005) PET/CT in gastric, liver, and pancreatic cancers and compared the results with those of ^{18}F-FDG PET/CT. **Methods:** This prospective study analyzed patients with confirmed gastric, liver, or pancreatic malignancies who underwent concurrent ^{18}F-FDG and ^{18}F-FAPI-74 PET/CT between June 2022 and December 2022. PET/CT findings were confirmed by histopathology or radiographic follow-up. ^{18}F-FDG and ^{18}F-FAPI-74 uptake and tumor-to-background ratios were compared using the Wilcoxon signed-rank test. The McNemar test was used to compare the diagnostic accuracy of the 2 scans. **Results:** Our cohort consisted of 112 patients: 49 with gastric cancer, 39 with liver cancer, and 24 with pancreatic cancer. Among them, 69 patients underwent PET/CT for initial staging and 43 for recurrence detection. Regarding lesion-based diagnostic accuracy, ^{18}F-FAPI-74 PET/CT showed higher sensitivity than did ^{18}F-FDG in the detection of primary tumors (gastric cancer, 88% [22/25] vs. 60% [15/25], $P = 0.016$; liver cancer, 100% [22/22] vs. 82% [18/22], $P = 0.125$; pancreatic cancer, 100% [22/22] vs. 86% [19/22], $P = 0.250$), local recurrence (92% [23/25] vs. 56% [14/25]; $P = 0.021$), involved lymph nodes (71% [41/58] vs. 40% [23/58]; $P < 0.001$), and bone and visceral metastases (98% [350/358] vs. 47% [168/358]; $P < 0.001$). Compared with ^{18}F-FDG, ^{18}F-FAPI-74 PET/CT upstaged 17 patients' TNM staging among all treatment-naïve patients (17/69, 25%) and changed the clinical management of 4 patients (4/43, 9%) in whom recurrence or metastases were detected. **Conclusion:** ^{18}F-FAPI-74 PET/CT is superior to ^{18}F-FDG PET/CT in detecting primary tumors, local recurrence, lymph node involvement, and bone and visceral metastases in gastric, pancreatic, and liver cancers, with higher uptake in most primary and metastatic lesions.

Key Words: PET; CT; ^{18}F-FAPI-74; ^{18}F-FDG; gastrointestinal tumors

Received Jul. 12, 2023; revision accepted Sep. 27, 2023.

For correspondence or reprints, contact Haojun Chen (leochen0821@foxmail.com) or Xiaoyuan Chen (chen.shawn@nus.edu.sg).

*Contributed equally to this work.

Published online Oct. 26, 2023.

J Nucl Med 2024; 65:40–51
DOI: 10.2967/jnumed.123.266329

According to the latest global cancer statistics, the incidence and mortality rates of gastrointestinal tumors, including gastric, hepatic, and pancreatic cancers, are increasing annually and account for a considerable proportion of other cancers, especially in eastern Asia (*1*). Therefore, early and accurate diagnosis is essential for their prognosis.

^{18}F-FDG PET/CT has been introduced as a supplement to endoscopic ultrasonography, CT, and MRI for the diagnosis and staging of gastrointestinal tumors. Although ^{18}F-FDG PET/CT is a valuable imaging technique for tumor staging and recurrence detection (*2*), some limitations exist for gastrointestinal malignancies. First, the relatively low sensitivity of ^{18}F-FDG PET/CT for lymph node (LN), liver, and peritoneal metastases from gastrointestinal cancer affects the accuracy of tumor staging (*3–5*). Second, physiologic uptake in the gastrointestinal tract interferes with the detection of metastatic lesions, particularly for peritoneal metastases. Third, low ^{18}F-FDG uptake is commonly observed in specific cancer types, including gastric signet ring cell carcinomas, mucinous adenocarcinomas, and hepatocellular carcinomas (HCCs) (*6*). Therefore, the development of a valid PET tracer is expected to improve the diagnosis of gastrointestinal cancer and contribute to individualized patient care.

Fibroblast activation protein (FAP), overexpressed by cancer-associated fibroblasts (CAFs) in more than 90% of epithelial tumors, is a membrane-anchored serine protease with dipeptidyl peptidase and endopeptidase activities (*7*). FAP inhibitor (FAPI), a quinoline-based ligand targeting FAP, can be used as a PET imaging tracer to visualize the tumor stroma (*8,9*). In previous studies, ^{68}Ga-FAPIs have been shown to be superior to ^{18}F-FDG in various cancers (*8,10,11*). ^{18}F (half-life, 110 min) is an ideal radionuclide for PET imaging featuring a high positron yield of 97%, a low mean positron range of 0.5 mm, a longer half-life than ^{68}Ga (110 vs. 68 min), and no simultaneous γ-ray emission (*12*). In addition, with the popularization of medical cyclotrons, ^{18}F may be more

suitable for promoting this imaging modality to benefit patients. A new PET imaging tracer, ^{18}F-FAPI-74, has been successfully used to image patients with various cancers (*13,14*). However, the use of ^{18}F-FAPI-74 in gastrointestinal tumors remains limited. In this single-center prospective study, we aimed to investigate the diagnostic accuracy of ^{18}F-FAPI-74 (^{18}F-LNC1005) PET/CT for gastric, liver, and pancreatic cancers and compare the results with those of ^{18}F-FDG PET/CT.

MATERIALS AND METHODS

Patients

This study was approved by the institutional review board and was registered at ClinicalTrials.gov (NCT05430841). All participants provided written informed consent. With agreement from the oncologists and upon the determination of eligibility, patients were consecutively recruited for enrollment in the study from June 2022 and December 2022 at the First Affiliated Hospital of Xiamen University. Inclusion criteria were patients who had been diagnosed with or who were suspected of having gastric, liver, and pancreatic cancers before treatment; patients with suspected recurrence or metastases as a result of clinical findings or other diagnostic imaging, such as CT, MRI, or ultrasound, after treatment; agreement to perform both ^{18}F-FDG and ^{18}F-FAPI-74 PET/CT; and performance of the 2 scans with an interval of less than 1 wk. Exclusion criteria were patients with nonmalignant disease and pathologically proven nongastrointestinal tumors, patients who received any other treatment 4 wk before PET imaging, and inability or unwillingness of the research participant, parent, or legal representative to provide written informed consent.

Synthesis of ^{18}F-FDG and ^{18}F-FAPI-74

^{18}F-FDG was manufactured using the coincidence ^{18}F-FDG synthesizer (Tracer Lab FxFN; GE Healthcare) according to methods described by our laboratory (*15*). The precursor for ^{18}F-FAPI-74 (^{18}F-LNC1005) was obtained from Yantai Lannacheng Biotechnology Co. Ltd. for research and development purposes. Radiolabeling with aluminum-^{18}F-fluoride was realized according to a previously reported protocol (*14*). Radiochemical purity and sterility tests were conducted in-house at an institutional radiochemistry facility. Radiochemical purities of ^{18}F-FDG and ^{18}F-FAPI-74 exceeded 95%, both meeting sterility standards and injection criteria for human administration.

Acquisition of PET/CT Images

For ^{18}F-FDG PET/CT, patients fasted for more than 6 h, and blood glucose levels were monitored before they received an injection of ^{18}F-FDG (5.55 MBq/kg). PET/CT images (1.5 min per bed position) were acquired with an uptake time of 63.0 ± 4.9 min (range, 50–75 min). For ^{18}F-FAPI-74 PET/CT, imaging was performed (1.5 min per bed position) with an uptake time of 63.3 ± 4.0 min (range, 50–80 min) after receiving an injection of 210.9 ± 48.1 MBq (range, 129.5–333 MBq). Patients were scanned using a hybrid PET/CT scanner (Discovery MI; GE Healthcare) with the following CT parameters: tube voltage with a 110-kV current, 80 mA, and slice thickness of 3.75 mm. All obtained data were transferred to Advantage Workstation (version AW 4.7; GE Healthcare). Data reconstruction was performed using the Bayesian penalized likelihood reconstruction algorithm (Q.clear; GE Healthcare) with a penalization factor of 500. Reconstructed images were coregistered and displayed.

Imaging Review and Analysis

Advantage Workstation was used to analyze ^{18}F-FDG and ^{18}F-FAPI-74 PET/CT images. To prevent bias, images were separated into 2 sets according to the radiotracer and interpreted independently by 2 teams of 4 nuclear medicine physicians. ^{18}F-FAPI-74 PET/CT images were analyzed by experts with more than 10 y of experience in nuclear oncology, whereas ^{18}F-FDG PET/CT images were analyzed by experts with 5 y of experience in nuclear oncology. The reviews were conducted without considering other imaging modalities, such as CT, MRI, and pathologic results, as well as the information from the other PET/CT scan, and reviewers were provided with the patient's medical history and indication for PET/CT. Differences in opinion were resolved by consensus.

Semiquantitative analysis was performed by manually drawing regions of interest around tumor lesions on transaxial images. For ^{18}F-FAPI-74 and ^{18}F-FDG, lesions were considered positive in cases with nonphysiologic foci of increased radiotracer uptake on PET images. Lesions were considered negative in cases with no pathologic uptake on PET images. SUV_{max} was automatically calculated to quantify tracer uptake in primary tumors, involved LNs, and bone and visceral metastases. The tumor-to-background ratio (TBR) was computed using the following formula: TBR = SUV_{max}-t / SUV_{mean}-b, where SUV_{max}-t refers to the SUV_{max} of the primary or metastatic tumors and SUV_{mean}-b refers to the SUV_{mean} of the healthy background tissue surrounding each lesion.

Reference Standards

Surgery or biopsy results were used as reference standards for the final diagnosis. Radical excision and LN dissection were performed in 14 patients, and biopsies for suggestive lesions were performed in 84 patients (1 biopsy per patient). To evaluate the diagnostic accuracy of PET/CT for LN staging, images were reviewed by the surgeon to identify corresponding resected LNs in the PET images. Serial tumor marker follow-up (minimum of 6 mo), clinical examination results, and standard-of-care imaging (including ultrasound, contrast-enhanced CT, bone scan, or MRI) were used as reference standards to validate PET/CT findings when tissue biopsy was not applicable. Lesions were considered malignant if they met any of the following follow-up criteria: typical malignant features confirmed by multimodal medical imaging, significant progression on follow-up imaging, and significant posttreatment tumor size decrease. The minimum follow-up time was 6 mo.

Statistical Analysis

Statistical analyses were performed using SPSS software (version 26.0; IBM Inc.). The number of positive lesions shown using ^{18}F-FAPI-74 and ^{18}F-FDG PET/CT was compared using the McNemar test, and the Wilcoxon signed-rank test was used to assess differences in SUV_{max} and TBR between the 2 scans. The McNemar test was used to evaluate the diagnostic accuracy of ^{18}F-FAPI-74 and ^{18}F-FDG PET/CT. The mean and SD were calculated for normally distributed measurements, and the median and range were calculated for nonnormal measurements. The 95% CIs for the diagnostic accuracy data were calculated using the Wilson score method. A statistically significant difference between the comparison groups was indicated when a 2-tailed P value of less than 0.05 was considered. To evaluate the correlation between continuous variables with nonnormal distribution, the Spearman rank correlation coefficient was calculated. A P value of less than 0.05 (2-tailed) was used as the significance level for all statistical analyses.

RESULTS

Patient Characteristics

The study cohort consisted of 112 patients (76 men, 36 women): 49 with gastric cancer (31/49 men; median age, 62 y), 39 with liver cancer (31/39 men; median age, 62 y), and 24 with pancreatic cancer (14/24 men; median age, 60.5 y). Sixty-nine patients (62%) underwent PET/CT for initial tumor staging, and 43 patients (38%)

TABLE 1
Patient Characteristics

Cancer type	Patients (*n*)	Age (y)	M/F ratio (*n*)	Indication for PET/CT	Examination before PET/CT	Patient status	Histopathology
Gastric	49	62 (38–80)	31:18	Primary staging (*n* = 25)	Endoscopy (*n* = 25)	Treatment-naïve (*n* = 25)	Adenocarcinoma (*n* = 44)
				Recurrence detection or PD (*n* = 24)		Previous chemotherapy (*n* = 2)	GSRCC (*n* = 5)
						Previous surgery (*n* = 5)	
						Comprehensive treatment after surgery (*n* = 17)	
Liver	39	62 (33–84)	31:8	Primary staging (*n* = 22)	Biopsy (*n* = 8)	Treatment-naïve (*n* = 22)	HCC (*n* = 31)
				Recurrence detection or PD (*n* = 17)	Enhanced CT or MRI (*n* = 14)	Previous TACE or HAIC (*n* = 2)	ICC (*n* = 8)
						Previous surgery (*n* = 3)	
						Comprehensive treatment after surgery (*n* = 12)	
Pancreatic	24	60.5 (35–86)	14:10	Primary staging (*n* = 22)	Biopsy (*n* = 11)	Treatment-naïve (*n* = 22)	PDAC (*n* = 21)
				Recurrence detection or PD (*n* = 2)	Enhanced CT or MRI (*n* = 11)	Previous surgery (*n* = 2)	Squamous cancer (*n* = 1)
							Undifferentiated carcinoma (*n* = 1)
							Mucinous adenocarcinoma (*n* = 1)

PD = progressive disease; GSRCC = gastric signet ring cell carcinoma; TACE = transcatheter arterial chemoembolization; HAIC = hepatic artery infusion chemotherapy; ICC = intrahepatic cholangiocellular carcinoma; PDAC = pancreatic ductal adenocarcinoma.

Continuous data are median and range.

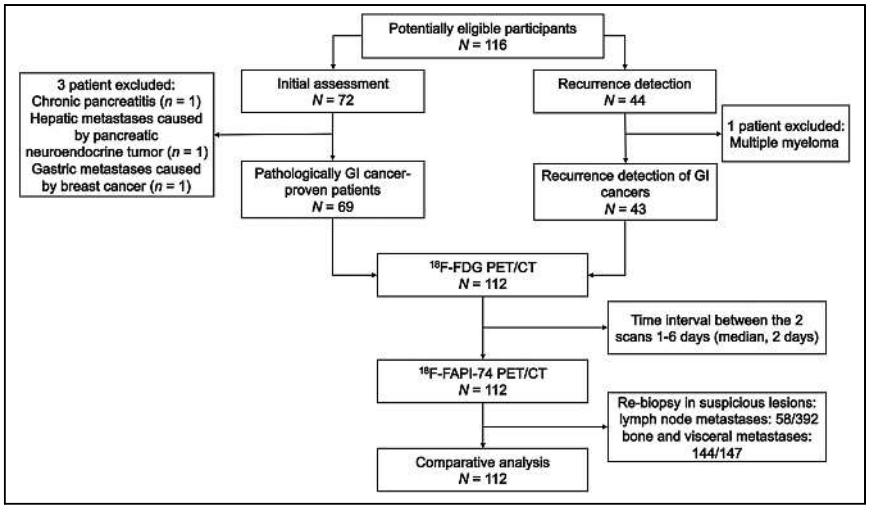

FIGURE 1. Flow diagram shows patient selection details. GI = gastrointestinal.

underwent PET/CT to detect tumor recurrence or metastasis. ^{18}F-FDG and ^{18}F-FAPI-74 PET/CT scans were performed with a median interval of 2 d between examinations (range, 1–6 d). The patients' clinical characteristics are listed in Table 1, and the research flowchart is shown in Figure 1.

All patients tolerated the examination well. No drug-related pharmacologic effects or physiologic responses occurred. All observed parameters (e.g., blood pressure, heart rate, and body temperature) remained normal and unchanged during and after the examination. No patients reported subjective symptoms. Compared with ^{18}F-FDG, ^{18}F-FAPI-74 PET/CT showed excellent image contrast with low background activity throughout the body. Representative images from patients with gastric, liver, and pancreatic cancers are shown in Figure 2.

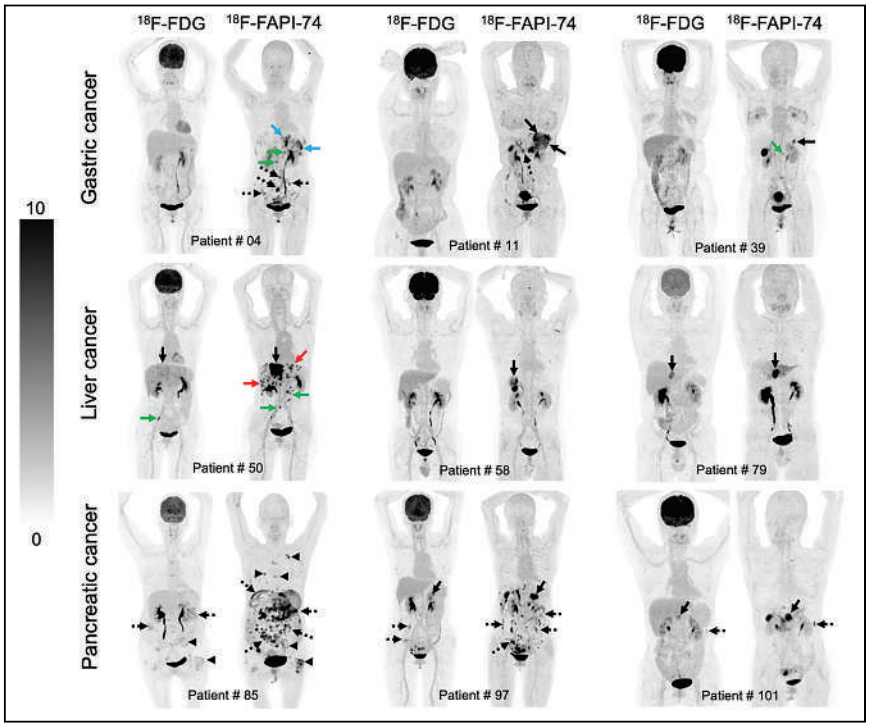

FIGURE 2. Nine representative patients who underwent ^{18}F-FDG and ^{18}F-FAPI-74 PET imaging. ^{18}F-FAPI-74 PET outperforms ^{18}F-FDG PET in detecting primary tumors (patients 11, 39, 50, 58, 79, and 101; solid black arrows), local recurrences (patient 4; blue arrows), abdomen LN metastases (patients 4 and 50; green arrows), intrahepatic metastases (patient 50; red arrows), bone metastases (patient 85; arrowheads), and peritoneal metastases (patients 4, 11, 85, 97, and 101; dotted arrows).

Comparison of ^{18}F-FAPI-74 and ^{18}F-FDG Uptake in Gastric Cancer

Patients with gastric cancer (n = 49) were diagnosed with adenocarcinoma (n = 44) and signet ring cell carcinoma (n = 5). Among 25 patients for primary staging, ^{18}F-FAPI-74 PET/CT visualized most primary tumors (22/25, 88%), whereas ^{18}F-FDG PET/CT missed 9 primary tumors (16/25, 64%; Supplemental Table 1 [supplemental materials are available at http://jnm.snmjournals.org]). A greater number of suggestive LNs were visualized using ^{18}F-FAPI-74 PET/CT than using ^{18}F-FDG PET/CT (88% [104/118] vs. 55% [65/118]; $P < 0.001$), with higher radiotracer uptake (median SUV_{max}, 6.2 vs. 2.9; $P < 0.001$) and TBR in abdominal regions (median, 4.5 vs. 1.7; $P < 0.001$) and supradiaphragmatic regions (median, 4.4 vs. 2.6; $P = 0.010$). Regarding bone and visceral metastases, ^{18}F-FAPI-74 PET/CT demonstrated a greater number of peritoneal metastases than did ^{18}F-FDG (100% [145/145] vs. 64% [38/145]; $P < 0.001$), with higher radiotracer uptake (median SUV_{max}, 6.9 vs. 2.5; $P < 0.001$) and TBR (median, 5.8. vs. 1.4; $P < 0.001$). Compared with ^{18}F-FDG, ^{18}F-FAPI-74 PET/CT showed similar lesion detectability and tracer uptake in local recurrence and bone metastases (Supplemental Table 1). Representative cases demonstrating the superiority of ^{18}F-FAPI-74 over ^{18}F-FDG in gastric cancer are shown in Figure 3.

Comparison of ^{18}F-FAPI-74 and ^{18}F-FDG Uptake in Liver Cancer

Patients with liver cancer (n = 39) were diagnosed with HCC (n = 31) and intrahepatic cholangiocarcinoma (n = 8). ^{18}F-FAPI-74 PET/CT visualized all primary tumors (22/22, 100%), whereas ^{18}F-FDG PET/CT missed 4 primary tumors (18/22, 82%). ^{18}F-FAPI-74 PET/CT showed superiority over ^{18}F-FDG in detecting intrahepatic metastases (90% [46/51] vs. 53% [27/51]; $P < 0.001$), peritoneal metastases (100% [8/8] vs. 25% [2/8]; $P = 0.031$), local recurrence (92% [12/13] vs. 38% [5/13]; $P = 0.016$), and suggestive LNs (97% [36/37] vs. 43% [16/37]; $P < 0.001$), with significantly higher tracer uptake and TBR in most lesions (Supplemental Table 1). Representative cases of liver cancer are presented in Figure 4. ^{18}F-FDG showed more metastatic lesions than did ^{18}F-FAPI-74 in 2 patients with HCC. Regarding the 2 patients, 13 lesions (4 LN metastases and 9 intrahepatic metastases) showed low to mild uptake on ^{18}F-FAPI-74 PET/CT.

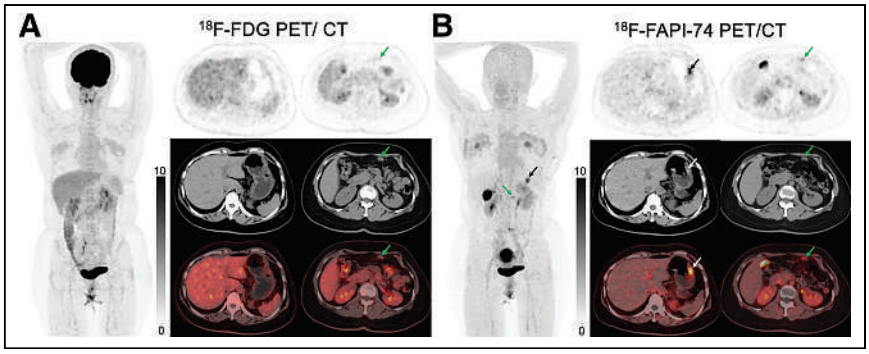

FIGURE 3. Representative case of gastric cancer detected using ^{18}F-FAPI-74 PET/CT but missed using ^{18}F-FDG PET/CT. (A) 38-y-old woman with pathologically confirmed gastric signet ring cell carcinoma underwent initial staging using ^{18}F-FDG PET/CT, which shows involved periintestinal LNs (arrows) only in CT image. (B) ^{18}F-FAPI-74 PET/CT shows intense radiotracer uptake in primary lesion (both black and white arrows) and periintestinal LN (green arrows). Subsequent percutaneous biopsy in this LN confirmed metastatic disease (focal activity above right kidney indicates physiologic gallbladder uptake).

The patient with more lesions seen on ^{18}F-FDG PET/CT is presented in Figure 5.

Comparison of ^{18}F-FAPI-74 and ^{18}F-FDG Uptake in Pancreatic Cancer

Patients with pancreatic cancer (n = 24) were diagnosed with pancreatic duct adenocarcinoma (n = 21), squamous cell carcinoma (n = 1), mucinous adenocarcinoma (n = 1), and undifferentiated carcinoma (n = 1). Positive ^{18}F-FAPI-74 and ^{18}F-FDG uptake (median SUV_{max}, 16.5 vs. 7.3) in primary tumors was observed in 22 and 19 patients, respectively. ^{18}F-FAPI-74 PET/CT showed more metastatic lesions than did ^{18}F-FDG, especially in liver metastases (100% [51/51] vs. 55% [28/51]; $P < 0.001$) and peritoneal metastases (100% [41/41] vs. 44% [18/41]; $P < 0.001$). In addition, greater numbers of suggestive LNs (97% [36/37] vs. 41% [15/37]; $P < 0.001$) were visualized using ^{18}F-FAPI-74 PET/CT, with higher radiotracer uptake in abdominal regions (median SUV_{max}, 9.6 vs. 2.5; $P < 0.001$) and supradiaphragmatic regions (median SUV_{max}, 11.6 vs. 3.8; $P = 0.028$). In the semiquantitative analysis, SUV_{max} with ^{18}F-FAPI-74 was higher than with ^{18}F-FDG in primary tumors (median SUV_{max}, 16.5 vs. 7.3; $P < 0.001$), liver metastases (median SUV_{max}, 7.5 vs. 4.0; $P < 0.001$), peritoneal metastases (median SUV_{max}, 8.2 vs. 2.8; $P < 0.001$), and bone metastases (median SUV_{max}, 5.3 vs. 3.1; $P = 0.009$). Representative cases of pancreatic cancer are shown in Figure 6.

Diagnostic Accuracy of ^{18}F-FAPI-74 and ^{18}F-FDG PET/CT

Primary tumors from 69 patients were confirmed by biopsy (n = 57) and surgery (n = 12). ^{18}F-FAPI-74 PET/CT had significantly higher sensitivity than did ^{18}F-FDG PET/CT for primary tumor detection (96% [66/69] vs. 75% [52/69]; $P < 0.001$), especially for diagnosis of gastric cancer (88% [22/25] vs. 60% [15/25]; $P = 0.016$). We were unable to obtain false-positive PET data for primary tumors because of restrictions on the study's inclusion criteria. Therefore, the specificity and accuracy of ^{18}F-FAPI-74 and ^{18}F-FDG PET/CT for primary tumor assessment could not be established.

To assess the diagnostic accuracy of local recurrence, 43 patients were evaluated by radiographic follow-up (n = 14), biopsy (n = 27), and surgery (n = 2). Local recurrence was confirmed in 25 patients. Lesion-based sensitivity, specificity, and accuracy for ^{18}F-FAPI-74 PET/CT were 92% (23/25), 94% (17/18), and 93% (40/43) and for ^{18}F-FDG PET/CT were 56% (14/25), 89% (16/18), and 70% (30/43), respectively. Thus, ^{18}F-FAPI-74 PET/CT had significantly greater sensitivity (92% [23/25] vs. 56% [14/25]; $P = 0.021$) and accuracy (93% [40/43] vs. 70% [30/43]; $P = 0.039$) than did ^{18}F-FDG for the diagnosis of local recurrence (Table 2).

To evaluate diagnostic performance for LN metastases, 392 LNs in 14 patients were evaluated by histology (extended LN dissection was performed, along with radical excision). Among these, 58 metastatic LNs were confirmed in 8 patients. Nodular-based sensitivity, specificity, and accuracy were 71% (41/58), 95% (318/334), and 92% (359/392) for ^{18}F-FAPI-74 PET/CT and 40% (23/58), 96% (321/334), and 88% (344/392) for ^{18}F-FDG PET/CT, respectively. Thus, ^{18}F-FAPI-74 PET/CT had significantly greater sensitivity (71% [41/58] vs. 40% [23/58]; $P < 0.001$) and accuracy (92% [359/392] vs. 88% [344/392]; $P = 0.001$) than did ^{18}F-FDG PET/CT for the diagnosis of LN metastases (Table 2).

In all pathologically proven LNs, ^{18}F-FDG–derived SUV_{max} in metastatic lesions demonstrated a significant correlation with LN size (ratio SUV_{max} [correlation coefficient], 0.440; $P = 0.036$). However, SUV_{max} derived from ^{18}F-FAPI-74 PET/CT did not exhibit a significant association with LN size ($P = 0.219$). In the subgroup analysis specifically focused on gastric cancer, both SUV_{max} (ratio SUV_{max} [correlation coefficient], 0.729; $P < 0.001$) and TBR (ratio TBR [correlation coefficient], 0.588; $P = 0.001$) derived from ^{18}F-FAPI-74 PET/CT were found to be significantly correlated with LN size. ^{18}F-FDG PET/CT missed 35 LNs with an average size of 7.3 mm (range, 3–14 mm), whereas ^{18}F-FAPI-74 PET/CT missed 17 LNs with

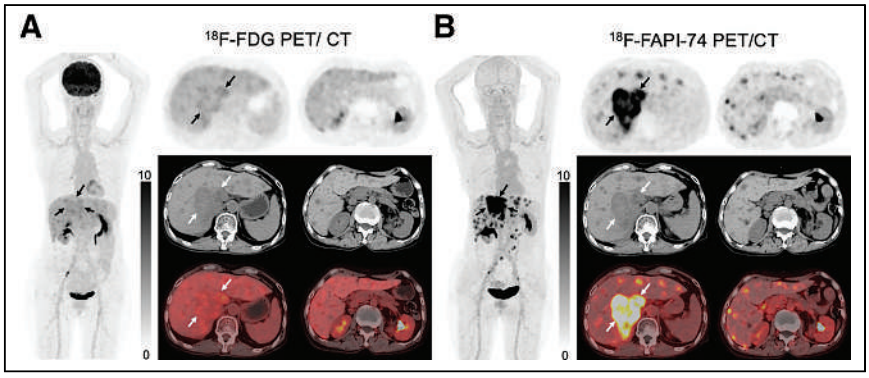

FIGURE 4. Representative case of metastatic liver cancer (intrahepatic cholangiocarcinoma). (A) 69-y-old woman with pathologically confirmed intrahepatic cholangiocarcinoma underwent initial staging using ^{18}F-FDG PET/CT, which shows low to moderate radiouptake in primary tumor (arrows). (B) ^{18}F-FAPI-74 PET/CT shows intense radiotracer uptake in primary lesion (arrows) and more intrahepatic metastases with intense uptake.

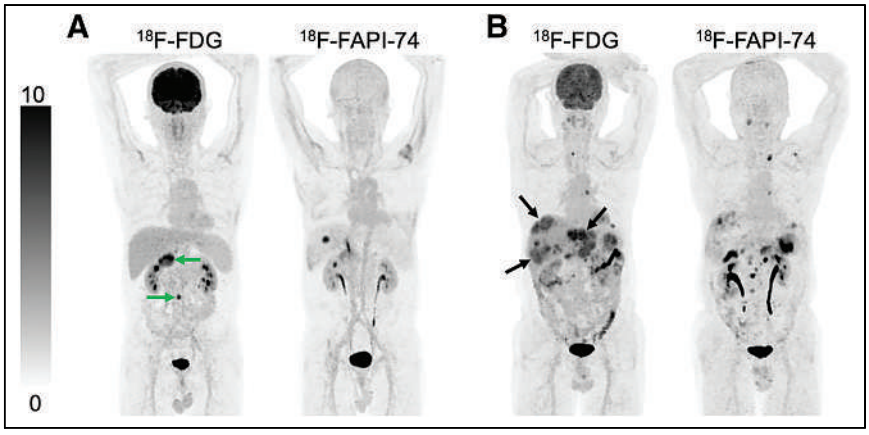

FIGURE 5. (A) 46-y-old man underwent ^{18}F-FDG PET/CT for recurrence detection with subsequent biopsy-confirmed abdominal LN metastases. It shows high radiotracer uptake in abdominal LN metastases (arrows). ^{18}F-FAPI-74 PET/CT shows lower radiotracer uptake and fewer abdominal LN metastases. Focal activity in liver indicates physiologic uptake in gallbladder. (B) 62-y-old man with pathologically confirmed liver cancer underwent initial staging with ^{18}F-FDG PET/CT, which shows more intrahepatic metastases with higher tracer uptake (arrows) than did ^{18}F-FAPI-74 PET/CT.

an average size of 6.5 mm (range, 3–13 mm). Therefore, ^{18}F-FAPI-74 PET/CT may have lower sensitivity in the detection of LNs that are less than 7 mm.

To assess the diagnostic accuracy of bone and visceral metastases, 432 suspected metastatic lesions from 89 patients were demonstrated using various imaging modalities. The lesions' evaluation entailed multimodal imaging findings (n = 21), radiographic follow-up (n = 264), and biopsy (n = 147). Among these, 358 lesions were confirmed as metastatic in 62 patients, with 144 lesions identified by percutaneous biopsy, 21 confirmed using multimodal imaging, and 193 validated through radiographic follow-up. ^{18}F-FAPI-74 PET/CT had significantly greater sensitivity (98% [350/358] vs. 47% [168/358]; $P < 0.001$) than did ^{18}F-FDG PET/CT for diagnosis of bone and visceral metastases, especially for detection of peritoneal metastases (100% [194/194] vs. 30% [58/194]; $P < 0.001$) and liver metastases (95% [97/102] vs. 54% [55/102]; $P < 0.001$).

Changes in Initial Assessment and Recurrence Detection After ^{18}F-FAPI-74 PET/CT

Among all treatment-naïve patients, ^{18}F-FAPI-74 PET/CT led to upstaging of the clinical TNM stage in 17 patients (25%, 17/69) compared with the stage resulting from ^{18}F-FDG PET/CT (TNM stage upstaged in 7/25 gastric cancer, 6/22 liver cancer, and 4/22 pancreatic cancer patients). Of 69 treatment-naïve patients, ^{18}F-FAPI-74 PET/CT showed superior primary tumor detection in 10 patients (visualized using ^{18}F-FAPI-74 but missed using ^{18}F-FDG), demonstrated larger disease extent of peritoneal metastases in 9 patients, and visualized more LN, visceral, and bone metastases in 28 patients (Table 3). Regarding 43 patients with detected recurrence or metastases, true-positive rates (patient-based) for ^{18}F-FDG and ^{18}F-FAPI-74 PET/CT were 56% (14/25) and 92% (23/25), respectively, per patient. Of the 43 restaging patients, ^{18}F-FAPI-74 PET/CT showed superior local recurrence detection in 4 patients (visualized using ^{18}F-FAPI but missed using ^{18}F-FDG), demonstrated larger disease extent of peritoneal metastases in 18 patients, and visualized a greater number of LN, visceral, and bone metastases in 14 patients. Finally, ^{18}F-FAPI-74 PET/CT changed the clinical management of 4 patients with detected recurrence or metastases (9%, 4/43; Table 4).

DISCUSSION

This study investigated the clinical utility of ^{18}F-FAPI-74 PET/CT for primary staging and recurrence or metastasis detection in patients with gastrointestinal cancer. We found that ^{18}F-FAPI-74 is a promising PET tracer that can be used for imaging gastric, liver, and pancreatic cancers, with intense radiotracer uptake and clear tumor delineation in most primary and metastatic lesions. ^{18}F-FAPI-74 PET/CT was better at detecting primary tumors and revealed more metastatic lesions than did ^{18}F-FDG, leading to TNM stage upgrading.

Previous studies have shown the limitations of ^{18}F-FDG PET/CT in detecting gastrointestinal malignancies, especially in mucinous adenocarcinoma, signet ring cell carcinoma (*16*), and HCC (*10*). Recent studies using ^{68}Ga-FAPI (^{68}Ga-FAPI-04/46) have demonstrated its superiority over ^{18}F-FDG for the diagnosis of gastrointestinal cancer (*17*). However, the use of ^{18}F-FAPI for diagnosing gastrointestinal cancer has not yet been systematically established. Consistent with a previous ^{68}Ga-FAPI study (*18*), ^{18}F-FAPI-74 PET/CT outperformed ^{18}F-FDG PET/CT in detecting primary and metastatic lesions in gastrointestinal cancer, particularly for gastric cancer. In this study, ^{18}F-FAPI-74 PET/CT detected primary tumors that were missed by ^{18}F-FDG PET/CT in 28% of the patients, including 3 patients with gastric signet ring cell carcinomas. This emphasizes the advantage of using ^{18}F-FAPI-74 PET/CT in this specific histologic type, especially for tumor diagnosis in early stages. However, unlike previous studies, we found no evidence of differences between ^{18}F-FDG and ^{18}F-FAPI-74 PET/CT for the detection of primary

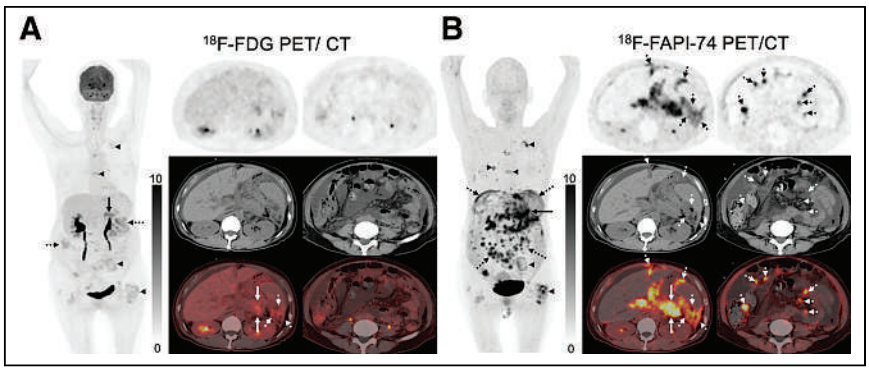

FIGURE 6. Representative case of widespread peritoneal metastatic pancreatic cancer (pancreatic ductal adenocarcinoma). (A) 55-y-old woman with biopsy-confirmed bone metastases underwent ^{18}F-FDG PET/CT for detection of primary tumor; low uptake is shown in primary lesion (solid arrows), peritoneal metastases (dotted arrows), and bone metastases (arrowheads). ^{18}F-FAPI-74 PET/CT shows intense uptake in these lesions. (B) In addition, ^{18}F-FAPI-74 PET/CT shows larger extent of peritoneal metastases than does ^{18}F-FDG.

TABLE 2
Diagnostic Accuracy of ^{18}F-FAPI-74 and ^{18}F-FDG PET/CT for Detection of Primary and Metastatic Tumors Using Lesion-Based Analysis

	^{18}F-FDG			^{18}F-FAPI-74			*P* (^{18}F-FDG vs. ^{18}F-FAPI)		
Cancer type	Sensitivity	Specificity	Accuracy	Sensitivity	Specificity	Accuracy	Sensitivity	Specificity	Accuracy
Primary tumor									
Gastric	60% [39–81] (15/25)	NA	NA	88% [69–97] (22/25)	NA	NA	0.016	NA	NA
Liver	82% [62–96] (18/22)	NA	NA	100% [87–100] (22/22)	NA	NA	0.125	NA	NA
Pancreatic	86% [67–98] (19/22)	NA	NA	100% [87–100] (22/22)	NA	NA	0.250	NA	NA
Total	75% [63–85] (52/69)	NA	NA	96% [87–99] (66/69)	NA	NA	<0.001	NA	NA
Local recurrence									
Gastric	73% [44–90] (8/11)	85% [54–100] (11/13)	79% [59–94] (19/24)	91% [64–100] (10/11)	92% [68–100] (12/13)	92% [76–99] (22/24)	0.625	>0.999	0.453
Liver	38% [13–65] (5/13)	100% [69–100] (4/4)	53% [31–73] (9/17)	92% [68–99] (12/13)	100% [69–100] (4/4)	94% [73–100] (16/117)	0.016	NA	0.016
Total*	56% [36–77] (14/25)	89% [68–97] (16/18)	70% [56–81] (30/43)	92% [78–99] (23/25)	94% [76–99] (17/18)	93% [82–98] (40/43)	0.021	>0.999	0.039
LN metastases	40% [28–53] (23/58)	96% [94–98] (321/334)	88% [85–91] (344/392)	71% [57–81] (41/58)	95% [93–97] (318/334)	92% [90–94] (359/392)	<0.001	0.250	0.001
Bone and visceral metastases									
Liver	54% [45–63] (55/102)	NA	NA	95% [89–98] (97/102)	NA	NA	<0.001	NA	NA
Peritoneal	30% [24–36] (58/194)	NA	NA	100% [98–100] (194/194)	NA	NA	<0.001	NA	NA
Bone	89% [79–95] (50/56)	NA	NA	96% [86–99] (54/56)	NA	NA	0.125	NA	NA
Lung	83% [50–97] (5/6)	NA	NA	83% [50–97] (5/6)	NA	NA	NA	NA	NA
Total	47% [42–52] (168/358)	NA	NA	98% [95–99] (350/358)2	NA	NA	<0.001	NA	NA

*Diagnostic accuracy for recurrent pancreatic cancer was unavailable because of limited number of patients ($n = 2$).
NA = not applicable.
Data in brackets are 95% CIs. Data in parentheses are numbers of lesions used to calculate percentage.

TABLE 3
Comparative Results for Initial Staging in Gastrointestinal Tumors Using Patient-Based Analysis

Primary staging	Stage with ^{18}F-FDG PET/CT					Stage with ^{18}F-FAPI-74 PET/CT								
Cancer type	Undetected	I	II	III	IV	Undetected	I	II	III	IV	Equal	^{18}F-FAPI superior	^{18}F-FDG superior	Stage upgraded
Gastric (n = 25)	10	0	4	8	3	3	0	8	9	5	18	n = 10 (40%)	NA	n = 7 (28%)
												Primary tumors visualized by ^{18}F-FAPI but missed by ^{18}F-FDG (n = 7)		
												More LN, visceral, or bone mets (n = 4)		
												Larger disease extent of peritoneal mets (n = 4)		
Liver (n = 22)	3	6	2	6	5	0	7	3	4	8	16	n = 13 (59%)	n = 1 (5%)	n = 6 (27%)
												Intrahepatic tumors visualized by ^{18}F-FAPI but missed by ^{18}F-FDG (n = 4)*	More intrahepatic tumors	
												More intrahepatic tumors (n = 7)		
												More LN, visceral, or bone mets (n = 8)		
Pancreatic (n = 22)	2	5	6	0	9	0	5	5	0	12	18	n = 14 (64%)	NA	n = 4 (18%)
												Primary tumors visualized by ^{18}F-FAPI but missed by ^{18}F-FDG (n = 3)*		
												More LN, visceral, or bone mets (n = 9)		
												Larger disease extent of peritoneal mets (n = 5)		
Total (n = 69)	15	11	12	14	17	3	12	16	13	25	52	n = 37 (54%)	n = 1 (1%)	n = 17 (25%)

*Including 1 patient whose primary tumor is not shown on ^{18}F-FDG PET/CT but for whom distant metastases were revealed.
NA = not applicable; Mets = metastases.

TABLE 4
Comparative Results for Recurrence Detection in Gastrointestinal Tumors Using Patient-Based Analysis

Recurrence or PD	^{18}F-FDG PET/CT		^{18}F-FAPI-74 PET/CT				
Cancer type	Negative (*n*)	Positive (*n*)	Negative (*n*)	Positive (*n*)	Equal	^{18}F-FAPI superior	^{18}F-FDG superior
Gastric	4	20	0	24	4	*n* = 20 (83%)	*n* = 1 (4%)
						Local recurrence visualized by ^{18}F-FAPI but missed by ^{18}F-FDG (*n* = 2)	Local recurrence visualized by ^{18}F-FDG but missed by ^{18}F-FAPI (*n* = 1)
						More LN, visceral, or bone mets (*n* = 9)	
						Larger disease extent of peritoneal mets (*n* = 17)	
Liver	3	14	1	16	12	*n* = 4 (24%)	*n* = 1 (6%)
						Intrahepatic mets visualized by ^{18}F-FAPI but missed by ^{18}F-FDG (*n* = 2)	More LN, visceral, or bone mets (*n* = 1)
						2More intrahepatic tumors (*n* = 3)	
						More LN, visceral, or bone mets (*n* = 1)	
Pancreatic	0	2	0	2	0	*n* = 2 (100%)	NA
						More LN, visceral, or bone mets (*n* = 1)	
						Larger disease extent of peritoneal mets (*n* = 1)	
Total	7	36	1	42	16	26 (60%)	2 (5%)

PD = progressive disease; *n* = number of patients; mets = metastases; NA = not applicable.

tumors in liver and pancreatic cancers. This may result from the advanced tumor stage of enrolled patients and the limited number of participants. Thus, TNM stages were upgraded after ^{18}F-FAPI-74 PET/CT in 25% of patients with initial staging, and clinical management was modified in 9% of those with recurrence or progressive disease.

Nodal staging of patients with gastrointestinal cancer is crucial for its treatment and prognosis (*19*). However, ^{18}F-FDG PET/CT has low to moderate sensitivity for LN staging in patients with gastrointestinal cancer, which may underestimate tumor stage and affect subsequent treatment regimens (*20,21*). Consistent with previous studies, the detection sensitivity of LNs shown using ^{18}F-FAPI was higher than that of ^{18}F-FDG in gastrointestinal cancer (79%–82% vs. 54%–59%, lesion-based sensitivity) (*16,22*). Thus, ^{18}F-FAPI-74 PET/CT demonstrated nodal staging superior to that of ^{18}F-FDG. This may overcome existing problems in accurately assessing LNs and aid in guiding surgical resection.

There is a significant correlation between both SUV_{max} and TBR derived from ^{18}F-FAPI-74 and size of LNs (especially in gastric cancer), in agreement with previous research (*23*). Previous studies have demonstrated a close association between the expression of FAP and the depth of tumor invasion, TNM staging, LN metastasis, and distant metastasis (*24*). In addition, it has been reported that the degree of hypoxia is positively correlated with tumor size and is a strong inducer of FAP expression in CAFs (*25,26*). As a result, small LNs may exhibit mild hypoxia, resulting in lower uptake of ^{18}F-FAPI-74 in these lesions. This hypothesis has the potential to elucidate the connection between both SUV_{max} and TBR derived from ^{18}F-FAPI-74 and LN size.

Accurate diagnosis of peritoneal metastasis involvement is crucial in determining the resectability of a tumor and plays a significant role in the prognosis of patients with gastrointestinal disorders (*27*). However, ^{18}F-FDG has a low detection rate of peritoneal metastasis, limiting its utility in staging and surgical planning (*6,28*). In our study, ^{18}F-FAPI-74 PET/CT showed a higher detection rate and larger disease extent of peritoneal metastases than did ^{18}F-FDG PET/CT. This may be explained by the strong tumor-induced fibrotic response that occurs when the tumor invades peritoneal tissue and by low tracer uptake within the digestive tract (*14,29*). Accurate evaluation of intrahepatic metastasis will affect the choice of treatment methods and median overall survival, especially in patients with hepatic oligometastasis (*30*). Although ^{18}F-FAPI-74 PET/CT shows physiologic uptake in the biliary system (*31*), it does not affect observation of intrahepatic lesions because of low tracer uptake in normal liver parenchyma. Consistent with previous ^{18}F-FAPI-based studies (85%–97% vs. 52%–80%, lesion-based sensitivity) (*10,32*), ^{18}F-FAPI-74 PET/CT showed a higher detection rate of intrahepatic metastases than did ^{18}F-FDG PET/CT.

We observed that ^{18}F-FAPI-74 PET/CT resulted in changes in TNM staging in 28% and 18% of patients with gastric and pancreatic cancers, respectively. The impact on TNM staging was particularly pronounced in cases of progressive disease and tumor recurrence, which is in line with our previous findings (*16,22*). Moreover, changes of 22% and 17% in patient management were observed after the introduction of ^{18}F-FAPI-74 PET/CT in gastric and pancreatic cancers, respectively, demonstrating the power of this imaging modality to alter patient care. ^{18}F-FAPI PET/CT appears to be superior to other modalities in the detection of peritoneal metastases, which is a challenging indication with conventional imaging and ^{18}F-FDG PET/CT because of their relatively low sensitivity. The data from this study suggest that PET/CT is a promising diagnostic approach for peritoneal metastases and that it is more sensitive than conventional imaging and ^{18}F-FDG PET/CT. In summary, in patients with gastric and pancreatic cancers in which ^{18}F-FDG PET/CT shows low performance, ^{18}F-FAPI-74 PET/CT demonstrates great potential in terms of higher uptake and superior lesion detectability, which becomes particularly noticeable with bigger tumors, higher stages, and the signet ring cell carcinoma histologic type. Moreover, there are some encouraging preliminary results regarding therapy response evaluation by ^{18}F-FAPI PET (*33*) to be further investigated.

MRI has high sensitivity in the detection of liver cancer, whereas a previous study demonstrated that ^{68}Ga-FAPI PET/CT and MRI have similar sensitivity in the identification of primary liver tumors and intrahepatic metastatic lesions (*10*). In our study, ^{18}F-FAPI-74 PET/CT was able to detect extrahepatic metastases in 36% of patients with liver cancer, emphasizing the potential added value of ^{18}F-FAPI-74 PET/CT in the evaluation of extrahepatic lesions. Therefore, ^{18}F-FAPI-74 PET/CT may play a complementary role to MRI in liver cancer, making it a promising candidate as the future modality of choice in tumor staging, molecular image–guided radiotherapy, and perhaps even molecular imaging–guided discrimination among liver tumors.

However, our result was inconsistent with a previous study (*11*), in which ^{18}F-FDG detected more liver metastases (181 vs. 104; $P < 0.001$) and yielded higher tracer uptake (mean, 8.6 vs. 6.0; $P = 0.001$) than did ^{18}F-FAPI in pancreatic cancer. This difference may be caused by the difference in the origin of CAFs, which leads to different phenotypes and functions of CAFs (*34*). This may cause uneven distribution of CAF markers such as FAP-α (*35,36*). A similar finding was observed in patients with HCC. In this study, a patient with recurrent HCC showed increased ^{18}F-FDG but low ^{18}F-FAPI-74 uptake in LN metastases, and histopathologic examination confirmed a well-differentiated HCC in the metastatic LNs. A similar observation was made in another patient with multiple intrahepatic metastases, and histopathology confirmed the presence of a moderately differentiated HCC. Previous research has indicated that most well- to moderately differentiated HCCs presented relatively low FAP expression, along with low ^{18}F-FAPI uptake, particularly in comparison to poorly differentiated HCCs (*37*). In addition to the degree of tumor differentiation, the relatively low ^{18}F-FAPI uptake in the HCC lesions may be related to the considerable intratumor spatial heterogeneity of the histomorphologic profile, along with the complexity of tumor biology.

In our study, there was an overlap in uptake intensity in the pancreatic primary tumor and in the tumor-induced obstructive pancreatitis of the pancreatic parenchyma (50% of patients showed intense uptake in the entire pancreas). Studies using ^{68}Ga-FAPI PET/CT have observed a similar phenomenon, confirming increased pancreatic uptake in cases of inflammation-induced fibrosis (*38*). Delayed imaging has been previously investigated as a solution to distinguish between fibrosis and tumors, with positive results observed in some patients (*22*). However, larger sample sizes are needed to verify the feasibility of using the delayed PET scans.

Although ^{18}F-FAPI-74 PET/CT showed higher tracer uptake and sensitivity than did ^{18}F-FDG PET/CT for most bone and visceral metastases, it was found to yield more false-positive lesions caused by nonspecific fibrosis. In our study, false-positive uptake of ^{18}F-FAPI was observed in bone (periarthritis, fibroosseous lesions, degenerative osteophyte, ischemic necrosis, and fracture), lung (pulmonary tuberculosis), thyroid (adenoma), uterus (uterine fibroids),

and breast (mammary hyperplasia; Supplemental Table 2). It is inappropriate to characterize a lesion as benign or malignant referencing solely the ^{18}F-FAPI uptake. The comprehensive combination of other imaging findings and clinical information is needed.

In contrast to previous clinical investigations on ^{18}F-FAPI, our study brings forth some important nuances and enhancements. We presented the comparative results and a subgroup analysis of the diagnostic accuracy of ^{18}F-FAPI-74 versus ^{18}F-FDG PET/CT in gastric, pancreatic, and liver cancers, which were not extensively covered in previous work. In addition, we calculated and compared the SUV_{max} and TBRs derived from these 2 PET scans, providing more depth to our results. Our study on ^{18}F-FAPI-74 PET/CT in gastrointestinal cancer involves a larger patient population than that of a recent study conducted by Watabe et al. (*39*), encompassing 112 as opposed to 31 patients. Moreover, pathologic evaluation via surgery or biopsy was performed in 88% (98/112) of the patients in this study, adding robustness to the ^{18}F-FAPI-74 PET/CT findings. We also provide observations on the diagnostic accuracy for LN metastases.

Our study has several limitations. First, this was a single-center study, which may have caused selection bias. Second, histopathologic results were unavailable for a subset of lesions, because not all PET-positive findings were biopsied. Third, more than half of the enrolled patients (55%) in this study were at an advanced TNM stage (III and IV). The role of ^{18}F-FAPI-74 PET/CT in detecting early disease requires further investigation.

CONCLUSION

Our results suggest that the diagnostic accuracy of ^{18}F-FAPI-74 in gastric, pancreatic, and liver cancers was higher than that of ^{18}F-FDG. However, in terms of specificity, ^{18}F-FAPI-74 did not exhibit a significant advantage over ^{18}F-FDG. This nuanced understanding of the results positions our work as a contribution to ongoing research in this field.

Compared with ^{18}F-FDG, ^{18}F-FAPI-74 PET/CT requires no fasting or blood glucose level monitoring, resulting in a shorter preparation time and improved patient flow. In addition, the physiologic uptake of ^{18}F-FAPI-74 PET/CT was lower than that of ^{18}F-FDG PET/CT in the gastrointestinal tract, enhancing image contrast. Therefore, in addition to higher lesion detectability, ^{18}F-FAPI-74 PET/CT offers greater potential value during the examination process and during image acquisition, ultimately benefiting patients.

KEY POINTS

QUESTION: Is ^{18}F-FAPI-74 PET/CT imaging useful for the evaluation of gastrointestinal cancer?

PERTINENT FINDINGS: This prospective study analyzed patients with confirmed gastric, liver, or pancreatic malignancies who underwent concurrent ^{18}F-FDG and ^{18}F-FAPI-74 PET/CT. The findings of the study showed that ^{18}F-FAPI-74 PET/CT is superior to ^{18}F-FDG in detecting primary tumors and metastatic lesions in gastric, pancreatic, and liver cancers, with higher radiotracer uptake in most primary and metastatic lesions.

IMPLICATIONS FOR PATIENT CARE: The use of ^{18}F-FAPI-74 PET/CT is expected to improve the diagnosis of gastrointestinal cancer and contribute to individualized patient care.

DISCLOSURE

This work was funded by the National Natural Science Foundation of China (82071961 and 82272037), Key Scientific Research Program for Young Scholars in Fujian (2021ZQNZD016), Fujian Natural Science Foundation for Distinguished Young Scholars (2022D005), Fujian Research and Training Grants for Young and Middle-aged Leaders in Healthcare, The National University of Singapore (NUHSRO/2020/133/Startup/08, NUHSRO/2023/008/NUSMed/TCE/LOA, NUHSRO/2021/034/TRP/09/Nanomedicine), National Medical Research Council (MOH-001388-00, CG21A PR1005), Singapore Ministry of Education (MOE-000387-00), and National Research Foundation (NRF-000352-00). Xiaoyuan Chen is co-founder of the Yantai LNC Biotechnology. No other potential conflicts of interest relevant to this article was reported.

REFERENCES

1. Sung H, Ferlay J, Siegel RL, et al. Global cancer statistics 2020: GLOBOCAN estimates of incidence and mortality worldwide for 36 cancers in 185 countries. *CA Cancer J Clin.* 2021;71:209–249.
2. Scott AM. Current status of positron emission tomography in oncology. *Intern Med J.* 2001;31:27–36.
3. Herrmann K, Ott K, Buck AK, et al. Imaging gastric cancer with PET and the radiotracers ^{18}F-FLT and ^{18}F-FDG: a comparative analysis. *J Nucl Med.* 2007;48:1945–1950.
4. Iwata Y, Shiomi S, Sasaki N, et al. Clinical usefulness of positron emission tomography with fluorine-18-fluorodeoxyglucose in the diagnosis of liver tumors. *Ann Nucl Med.* 2000;14:121–126.
5. Yoshioka T, Yamaguchi K, Kubota K, et al. Evaluation of ^{18}F-FDG PET in patients with advanced, metastatic, or recurrent gastric cancer. *J Nucl Med.* 2003;44:690–699.
6. Shimada H, Okazumi S, Koyama M, Murakami K. Japanese Gastric Cancer Association Task Force for Research Promotion: clinical utility of ^{18}F-fluoro-2-deoxyglucose positron emission tomography in gastric cancer. A systematic review of the literature. *Gastric Cancer.* 2011;14:13–21.
7. Christiansen VJ, Jackson KW, Lee KN, Downs TD, McKee PA. Targeting inhibition of fibroblast activation protein-alpha and prolyl oligopeptidase activities on cells common to metastatic tumor microenvironments. *Neoplasia.* 2013;15:348–358.
8. Chen H, Pang Y, Wu J, et al. Comparison of [^{68}Ga]Ga-DOTA-FAPI-04 and [^{18}F]FDG PET/CT for the diagnosis of primary and metastatic lesions in patients with various types of cancer. *Eur J Nucl Med Mol Imaging.* 2020;47:1820–1832.
9. Giesel FL, Kratochwil C, Lindner T, et al. ^{68}Ga-FAPI PET/CT: biodistribution and preliminary dosimetry estimate of 2 DOTA-containing FAP-targeting agents in patients with various cancers. *J Nucl Med.* 2019;60:386–392.
10. Guo W, Pang Y, Yao L, et al. Imaging fibroblast activation protein in liver cancer: a single-center post hoc retrospective analysis to compare [^{68}Ga]Ga-FAPI-04 PET/CT versus MRI and [^{18}F]-FDG PET/CT. *Eur J Nucl Med Mol Imaging.* 2021;48:1604–1617.
11. Zhang Z, Jia G, Pan G, et al. Comparison of the diagnostic efficacy of ^{68}Ga-FAPI-04 PET/MR and ^{18}F-FDG PET/CT in patients with pancreatic cancer. *Eur J Nucl Med Mol Imaging.* 2022;49:2877–2888.
12. Fowler JS, Ido T. Initial and subsequent approach for the synthesis of ^{18}FDG. *Semin Nucl Med.* 2002;32:6–12.
13. Lindner T, Altmann A, Giesel F, et al. ^{18}F-labeled tracers targeting fibroblast activation protein. *EJNMMI Radiopharm Chem.* 2021;6:26.
14. Giesel FL, Adeberg S, Syed M, et al. FAPI-74 PET/CT using either ^{18}F-AlF or cold-kit ^{68}Ga labeling: biodistribution, radiation dosimetry, and tumor delineation in lung cancer patients. *J Nucl Med.* 2021;62:201–207.
15. Yu S. Review of F-FDG synthesis and quality control. *Biomed Imaging Interv J.* 2006;2:e57.
16. Pang Y, Zhao L, Luo Z, et al. Comparison of ^{68}Ga-FAPI and ^{18}F-FDG uptake in gastric, duodenal, and colorectal cancers. *Radiology.* 2021;298:393–402.
17. Li C, Tian Y, Chen J, et al. Usefulness of [^{68}Ga]FAPI-04 and [^{18}F]FDG PET/CT for the detection of primary tumour and metastatic lesions in gastrointestinal carcinoma: a comparative study. *Eur Radiol.* 2023;33:2779–2791.
18. Kosmala A, Serfling SE, Schlotelburg W, et al. Impact of ^{68}Ga-FAPI-04 PET/CT on staging and therapeutic management in patients with digestive system tumors. *Clin Nucl Med.* 2023;48:35–42.
19. Hackert T, Buchler MW. Pancreatic cancer: advances in treatment, results and limitations. *Dig Dis.* 2013;31:51–56.

20. Seevaratnam R, Cardoso R, McGregor C, et al. How useful is preoperative imaging for tumor, node, metastasis (TNM) staging of gastric cancer? A meta-analysis. *Gastric Cancer.* 2012;15(suppl 1):S3–S18.
21. Findlay JM, Antonowicz S, Segaran A, et al. Routinely staging gastric cancer with ^{18}F-FDG PET-CT detects additional metastases and predicts early recurrence and death after surgery. *Eur Radiol.* 2019;29:2490–2498.
22. Pang Y, Zhao L, Shang Q, et al. Positron emission tomography and computed tomography with [^{68}Ga]Ga-fibroblast activation protein inhibitors improves tumor detection and staging in patients with pancreatic cancer. *Eur J Nucl Med Mol Imaging.* 2022;49:1322–1337.
23. Wang H, Zhu W, Ren S, et al. ^{68}Ga-FAPI-04 versus ^{18}F-FDG PET/CT in the detection of hepatocellular carcinoma. *Front Oncol.* 2021;11:693640.
24. Gao LM, Wang F, Zheng Y, Fu ZZ, Zheng L, Chen LL. Roles of fibroblast activation protein and hepatocyte growth factor expressions in angiogenesis and metastasis of gastric cancer. *Pathol Oncol Res.* 2019;25:369–376.
25. Ammirante M, Shalapour S, Kang Y, Jamieson CA, Karin M. Tissue injury and hypoxia promote malignant progression of prostate cancer by inducing CXCL13 expression in tumor myofibroblasts. *Proc Natl Acad Sci USA.* 2014;111:14776–14781.
26. Carmona-Bozo JC, Manavaki R, Woitek R, et al. Hypoxia and perfusion in breast cancer: simultaneous assessment using PET/MR imaging. *Eur Radiol.* 2021;31:333–344.
27. Sato H, Maeda K, Kotake K, Sugihara K, Takahashi H. Factors affecting recurrence and prognosis after R0 resection for colorectal cancer with peritoneal metastasis. *J Gastroenterol.* 2016;51:465–472.
28. Soussan M, Des Guetz G, Barrau V, et al. Comparison of FDG-PET/CT and MR with diffusion-weighted imaging for assessing peritoneal carcinomatosis from gastrointestinal malignancy. *Eur Radiol.* 2012;22:1479–1487.
29. Kwon KJ, Shim KN, Song EM, et al. Clinicopathological characteristics and prognosis of signet ring cell carcinoma of the stomach. *Gastric Cancer.* 2014;17:43–53.
30. Yang J, Zhang J, Lui W, et al. Patients with hepatic oligometastatic pancreatic body/tail ductal adenocarcinoma may benefit from synchronous resection. *HPB (Oxford).* 2020;22:91–101.
31. Kou Y, Jiang X, Yao Y, et al. Physiological tracer distribution and benign lesion incidental uptake of Al^{18}F-NOTA-FAPI-04 on PET/CT imaging. *Nucl Med Commun.* 2022;43:847–854.
32. Şahin E, Elboğa U, Çelen YZ, Sever ÖN, Çayırlı YB, Çimen U. Comparison of ^{68}Ga-DOTA-FAPI and ^{18}FDG PET/CT imaging modalities in the detection of liver metastases in patients with gastrointestinal system cancer. *Eur J Radiol.* 2021;142:109867.
33. Kuten J, Levine C, Shamni O, et al. Head-to-head comparison of [^{68}Ga]Ga-FAPI-04 and [^{18}F]-FDG PET/CT in evaluating the extent of disease in gastric adenocarcinoma. *Eur J Nucl Med Mol Imaging.* 2022;49:743–750.
34. Neesse A, Bauer CA, Öhlund D, et al. Stromal biology and therapy in pancreatic cancer: ready for clinical translation? *Gut.* 2019;68:159–171.
35. Öhlund D, Handly-Santana A, Biffi G, et al. Distinct populations of inflammatory fibroblasts and myofibroblasts in pancreatic cancer. *J Exp Med.* 2017;214:579–596.
36. Sugimoto H, Mundel TM, Kieran MW, Kalluri R. Identification of fibroblast heterogeneity in the tumor microenvironment. *Cancer Biol Ther.* 2006;5:1640–1646.
37. Shi X, Xing H, Yang X, et al. Fibroblast imaging of hepatic carcinoma with ^{68}Ga-FAPI-04 PET/CT: a pilot study in patients with suspected hepatic nodules. *Eur J Nucl Med Mol Imaging.* 2021;48:196–203.
38. Kleeff J, Whitcomb DC, Shimosegawa T, et al. Chronic pancreatitis. *Nat Rev Dis Primers.* 2017;3:17060.
39. Watabe T, Naka S, Tatsumi M, et al. Initial evaluation of [^{18}F]FAPI-74 PET for various histopathologically confirmed cancers and benign lesions. *J Nucl Med.* 2023;64:1225–1231.

Immunohistochemical FAP Expression Reflects ^{68}Ga-FAPI PET Imaging Properties of Low- and High-Grade Intraductal Papillary Mucinous Neoplasms and Pancreatic Ductal Adenocarcinoma

Anna-Maria Spektor*[1], Ewgenija Gutjahr*[2], Matthias Lang[3], Frederik M. Glatting[1,4], Thilo Hackert[5], Thomas Pausch[3], Christine Tjaden[3], Mathias Schreckenberger[6], Uwe Haberkorn[1,7], and Manuel Röhrich[1,6]

[1]Department of Nuclear Medicine, University Hospital Heidelberg, Heidelberg, Germany; [2]Institute of Pathology, University Hospital Heidelberg, Heidelberg, Germany; [3]Department of General, Visceral, and Transplantation Surgery, University Hospital Heidelberg, Heidelberg, Germany; [4]Clinical Cooperation Unit Molecular and Radiation Oncology, German Cancer Research Center, Heidelberg, Germany; [5]Department of General, Visceral, and Thoracic Surgery, University Hospital Hamburg, Hamburg, Germany; [6]Department of Nuclear Medicine, University Hospital Mainz, Mainz, Germany; and [7]Clinical Cooperation Unit Nuclear Medicine, German Cancer Research Center, Heidelberg, Germany

Pancreatic intraductal papillary mucinous neoplasms (IPMNs) are grossly visible (typically > 5 mm) intraductal epithelial neoplasms of mucin-producing cells, arising in the main pancreatic duct or its branches. According to the current 2-tiered grading scheme, these lesions are categorized as having either low-grade (LG) dysplasia, which has a benign prognosis, or high-grade (HG) dysplasia, which formally represents a carcinoma in situ and thus can transform to pancreatic ductal adenocarcinoma (PDAC). Because both entities require different treatments according to their risk of becoming malignant, a precise pretherapeutic diagnostic differentiation is inevitable for adequate patient management. Recently, our group has demonstrated that ^{68}Ga-fibroblast activation protein (FAP) inhibitor (FAPI) PET/CT shows great potential for the differentiation of LG IPMNs, HG IPMNs, and PDAC according to marked differences in signal intensity and tracer dynamics. The purpose of this study was to biologically validate FAP as a target for PET imaging by analyzing immunohistochemical FAP expression in LG IPMNs, HG IPMNs, and PDAC and comparing with SUV and time to peak (TTP) measured in our prior study. **Methods:** To evaluate the correlation of the expression level of FAP and α-smooth muscle actin (αSMA) in neoplasm-associated stroma depending on the degree of dysplasia in IPMNs, 98 patients with a diagnosis of LG IPMN, HG IPMN, PDAC with associated HG IPMN, or PDAC who underwent pancreatic surgery at the University Hospital Heidelberg between 2017 and 2023 were identified using the database of the Institute of Pathology, University Hospital Heidelberg. In a reevaluation of hematoxylin- and eosin-stained tissue sections of formalin-fixed and paraffin-embedded resection material from the archive, which was originally generated for histopathologic routine diagnostics, a regrading of IPMNs was performed by a pathologist according to the current 2-tiered grading scheme, consequently eliminating the former diagnosis of "IPMN with intermediate-grade dysplasia." For each case, semithin tissue sections of 3 paraffin blocks containing neoplasm were immunohistologically stained with antibodies directed against FAP and αSMA. In a masked approach, a semiquantitative analysis of the immunohistochemically stained slides was finally performed by a pathologist by adapting the immunoreactive score (IRS) and human epidermal growth factor receptor 2 (Her2)/neu score to determine the intensity and percentage of FAP- and αSMA-positive cells. Afterward, the IRS of 14 patients who underwent ^{68}Ga-FAPI-74 PET/CT in our previous study was compared with their SUV_{max}, SUV_{mean}, and TTP for result validation. **Results:** From 98 patients, 294 specimens (3 replicates per patient) were immunohistochemically stained for FAP and αSMA. Twenty-three patients had LG IPMNs, 11 had HG IPMNs, 10 had HG IPMNs plus PDAC, and 54 had PDAC. The tumor stroma was in all cases variably positive for FAP. The staining intensity, percentage of FAP-positive stroma, IRS, and Her2/neu score increased with higher malignancy. αSMA expression could be shown in normal pancreatic stroma as well as within peri- and intraneoplastic desmoplastic reaction. No homogeneous increase in intensity, percentage, IRS, and Her2/neu score with higher malignancy was observed for αSMA. The comparison of the mean IRS of FAP with the mean SUV_{max}, SUV_{mean}, and TTP of ^{68}Ga-GAPI-74 PET/CT showed a matching value increasing with higher malignancy in ^{68}Ga-FAPI-74 PET imaging and immunohistochemical FAP expression. **Conclusion:** The immunohistochemical staining of IPMNs and PDAC validates FAP as a biology-based stromal target for in vivo imaging. Increasing expression of FAP in lesions with a higher degree of malignancy matches the expectation of a stronger FAP expression in PDAC and HG IPMNs than in LG IPMNs and corroborates our previous findings of higher SUVs and a longer TTP in PDAC and HG IPMNs than in LG IPMNs.

Key Words: fibroblast activation protein; FAPI; PDAC; IPMN; IHC; α-SMA

J Nucl Med 2024; 65:52–58
DOI: 10.2967/jnumed.123.266393

Pancreatic intraductal papillary mucinous neoplasms (IPMNs) are a precursor lesion of the highly lethal pancreatic ductal adenocarcinoma (PDAC), which has a 5-y survival rate of less than 10% (*1,2*). Pathologically, IPMNs can be subdivided into lesions with either low-grade (LG) or high-grade (HG) epithelial dysplasia (*3*). In clinical routine, IPMNs are usually evaluated via MRI or endoscopic ultrasound using the European guidelines for pancreatic

Received Jul. 18, 2023; revision accepted Oct. 17, 2023.
For correspondence or reprints, contact Manuel Röhrich (manuel.roehrich@med.uni-heidelberg.de).
*Contributed equally to this work.

cystic neoplasms or the Fukuoka consensus criteria (2017), which define worrisome features to differentiate between LG and HG IPMNs. Whereas LG IPMNs that lack worrisome features need only be followed up, HG IPMNs have a high risk of transforming into PDAC and thus should undergo surgery (*4,5*). Although MRI and endoscopic ultrasound have a high sensitivity, they lack high specificity, making them good for detecting IPMNs but not for determining their entity (*6*). In our prior study, we showed that PET using ^{68}Ga-labeled fibroblast activation protein (FAP) inhibitors (FAPIs) combined with CT has the potential to differentiate between LG IPMNs and HG IPMNs. In particular, PET imaging–derived parameters (such as time to peak [TTP]) showed high ensitivity and specificity for differentiation between IPMN subtypes (*7*).

PDAC and other epithelial tumors are surrounded by a vast tumor stroma expressing fibroblast activation protein (FAP) and α-smooth muscle actin (αSMA), which act as markers for activated, cancer-associated fibroblasts (CAFs) (*8,9*). CAFs play an important role in tumor progression by promoting tumor growth, invasion, metastasis and therapy resistance (*10*). FAP belongs to the serine protease family and is involved in the control of fibroblast growth, tissue repair, and epithelial carcinogenesis (*11,12*). Thus, a neoplastic transformation process is usually associated with an increase in stromal FAP expression whereas FAP is nearly undetectable in healthy tissue and benign lesions (*8*). αSMA, being involved in cell motility, is usually expressed in pericytes, myoepithelial cells, smooth muscle cells, and myofibroblasts and is consequently found in normal, reactive, and neoplastic tissue (*13*). Especially, αSMA is an established marker for CAFs in various cancers, among them PDAC (*14*).

In previous evaluations of ^{68}Ga-FAPI PET/CT, we observed lower ^{68}Ga-FAPI uptake in precursor lesions (e.g., lung fibrosis and pancreatitis) than in carcinoma (*15,16*). These results were in line with our IPMN findings showing markedly lower FAPI-74 uptake in LG than HG IPMNs, as well as a shorter TTP in dynamic PET imaging (*7*). This led to the hypothesis that FAP expression and thus the FAPI avidity of pancreatic lesions increase with higher malignancy. To elucidate differences in FAP expression between LG and HG IPMNs that may underlie their differential appearance on ^{68}Ga-FAPI74 PET/CT and to validate FAP as a biology-based target for PET imaging, we performed immunohistochemistry on a larger series of LG IPMN, HG IPMN, and PDAC specimens.

MATERIALS AND METHODS

All procedures performed in studies involving human participants conformed with the ethical standards of the institutional or national research committee and with the Helsinki declaration (1964) and its later amendments or comparable ethical standards. This retrospective study was approved by the local advisory ethic committee (study S-115/2020).

Histomorphology-Based Classification of Specimens

Hematoxylin- and eosin-stained tissue sections of the surgical material of patients with a diagnosis of LG IPMN, HG IPMN, or PDAC who underwent surgery at the University Hospital Heidelberg between 2017 and 2021 were provided by the EPZ biobank archive (Department of Surgery of the University Hospital Heidelberg) in accordance with the regulations of the tissue bank and the approval of the ethics committee of the University Hospital Heidelberg. All tissue slides were histologically evaluated by an experienced pathologist, who chose representative areas containing IPMN or PDAC tissue and reference tissue. Three representative specimens reflecting the neoplastic growth pattern, especially regarding the ratio of neoplastic epithelial cells to stroma and the grading of neoplasm, were selected for each patient. All specimens were classified as LG IPMN, HG IPMN, HG IPMN plus PDAC, or PDAC. IPMN was defined as a proliferation of intraductal columnar cells producing mucin and was classified as LG or HG dysplasia by the highest degree of cytoarchitectural and nuclear atypia of the epithelium. LG IPMN showed monomorphic columnar cells, which might show mitosis and papillary projections as well as slight to moderate nuclear atypia. In contrast, HG IPMN showed nuclear stratification with loss of polarity, pleomorphism, severe atypia, and papillae with irregular branching and budding (*3*). PDAC showed ductlike glandular structures arbitrarily infiltrating the pancreatic parenchyma. PDAC was divided into 4 groups from well differentiated to poorly differentiated: grade 1 (G1), grade 2 (G2), grade 3 (G3), and grade 4 (G4). Neoplastic irregular glands surrounded by strong to loosely arranged desmoplastic stroma containing fibroblasts and myofibroblasts, as well as scattered macrophages and lymphocytes, were interpreted as characteristics common to all (*17*).

FAP and αSMA Immunohistochemistry

For the lesion areas chosen as described above, semithin tissue sections 4 μm thick were prepared from corresponding paraffin blocks generated from resected tissue after fixation in 4% buffered formalin for 24 h at room temperature. Tissue sections were treated with Ultra Cell Conditioning Solution (Roche) buffer (pH 8.0) for antigen retrieval. Immunohistochemical staining was performed using the following antibodies: anti-FAPa (1:100; Abcam [reference number ab207178]) and anti-αSMA (ready to use; Cell Signaling Technology [reference number 760-2833]). Automated immunostaining was done using the BenchMark Ultra automated staining platform (Roche) with the OptiView DAB immunohistochemistry detection kit (Roche), Autostainer Link 48 (Agilent), and the EnVision Flex kit (Agilent). Stained tissue sections were mounted with Consul-Mount (Thermo Fisher Scientific) and scanned by Aperio AT2 (Leica; magnification, 1:400) for analysis.

Semiquantitative Analysis

FAP and αSMA expression was assessed both in adjacent nonmalignant tissue and in IPMN or PDAC regions marked by premalignant or malignant cell clusters with surrounding stroma. A semiquantitative analysis adapted from Remmele and Stegner (*18*) was used to interpret the immunohistochemistry. Scores were assigned according to the percentage stain distribution, with a score of 0 indicating 0%; 1 indicating less than 10%, 2 indicating 10%–50%, 3 indicating 51%–80%, and 4 indicating more than 80%. Additionally, stain intensity was scored, with a score of 0 indicating no stain, 1 indicating a low stain intensity, 2 indicating a medium stain intensity, and 3 indicating a high stain intensity. By multiplying the percentage score (0–4 points) with the intensity score (0–3 points), the immunoreactive score (IRS) consisting of 0–12 points was obtained. These points were further classified into 3 groups, with IRS scores 0–1 becoming group 0 (negative), 2–3 becoming group 1 (positive with weak expression), 4–8 becoming group 2 (positive with mild expression), and 9–12 becoming group 3 (positive with strong expression), to match the human epidermal growth factor receptor 2 (Her2)/neu score of the American Society of Clinical Oncology/College of American Pathologists guideline for the evaluation of estrogen and progesterone receptor status in breast cancer. In this Her2/neu score, 0 means that less than 10% of cells are stained, 1+ means that more than 10% cells are minimally stained, 2+ means that more than 10% cells are moderately stained, and 3+ means that more than 10% cells are strongly stained, with a score of 0 or 1+ being classified as negative, 2+ as mildly positive, and 3+ as strongly positive (*19*).

^{68}Ga-FAPI-74 PET/CT

The synthesis and radioactive labeling of FAPI-74 and the PET imaging procedures are described in a report about our recent PET-imaging project on IPMNs (*7*) and were previously described by others (*20–22*); 14 of the 98 patients included in this work had undergone ^{68}Ga-FAPI-74 PET/CT in that project. For PET imaging, a Siemens Biograph mCT Flow scanner was used, according to previously published protocols (*16*). Static PET scans were acquired 60 min after injection. Dynamic PET scans were additionally performed as previously described (*16*). PET data were analyzed retrospectively, and static (SUV_{max} and SUV_{mean}) and dynamic (TTP) PET parameters were extracted as previously described (*7*).

Statistical Analysis

When there were 3 or more different subgroups, significant differences between staining results or imaging parameters were determined using 1-way ANOVA with Bonferroni multiple-comparison tests, and 4 levels of significance were discriminated ($P < 0.05$, $P < 0.01$, $P < 0.001$, and $P < 0.0001$). For the subgroup analysis of 2 groups for Supplemental Figure 3 (supplemental materials are available at http://jnm.snmjournals.org), an unpaired t test was used and P values of less than 0.05 were defined as statistically significant. All statistical analyses were performed using GraphPad Prism, version 10.

RESULTS

Immunohistochemical staining against FAP and αSMA was performed on 294 specimens (3 specimens per patient) of 98 treatment-naïve patients (47 female and 51 male; average age at diagnosis, 66.47 y [range, 43–83 y] for women and 65.53 y [range, 47–84 y] for men). Twenty-three patients were diagnosed with LG IPMN, 11 with HG IPMN, and 10 with HG IPMN plus PDAC, of whom 8 had G2 PDAC and 2 had G3 PDAC. Fifty-four patients were diagnosed with PDAC, of whom 2 had G1 PDAC, 33 had G2 PDAC, and 19 had G3 PDAC. The most frequent localization of the lesions was the pancreas head (61 patients), followed by the cauda (15 patients) and corpus (13 patients). In 4 patients, the lesion was at the junction of the head and corpus, and in 2 patients, the lesion was at the junction of the corpus and cauda. In 2 patients, the lesion was in the whole pancreas, and in 1 patient, the lesion extended from the processus uncinatus to the cauda (Supplemental Table 1).

Results of Immunohistochemical Staining

FAP. Although a weak immunohistochemical reactivity against FAP could be observed in the tumor-free pancreatic stroma, significantly higher expression was detected in neoplasia-associated peri- and intratumoral desmoplastic stroma, with the tendency increasing with malignancy grade. However, a strong, unspecific immunopositivity for FAP could also be shown for epithelial tumor cells in several specimens.

LG IPMNs showed a less FAP-positive stromal reaction and a lower FAP intensity than HG IPMNs. The mean IRS was 2.09 (±2.13; median, 2.0) for LG IPMNs, 3.0 (±3.77; median, 2.0) for HG IPMNs, 7.4 (±4.6; median, 7.5) for HG IPMNs plus PDAC, and 9.67 (±3.21; median, 12) for PDAC (Fig. 1A). Mean Her2/neu scores were 0.61 (±0.72; median, 1.0) for LG IPMNs, 0.91 (±1.04; median, 1.0) for HG IPMNs, 2.10 (±1.1; median, 2.5) for HG IPMNs plus PDAC, and 2.67 (±0.7; median, 3.0) for PDAC (Fig. 1B). Similarly, both criteria—the intensity of the immunohistochemical reaction (reflected by intensity score) and the percentage of FAP-positive stroma (reflected by percentage score)—increased with a higher risk of malignant transformation (Figs. 1C and 1D).

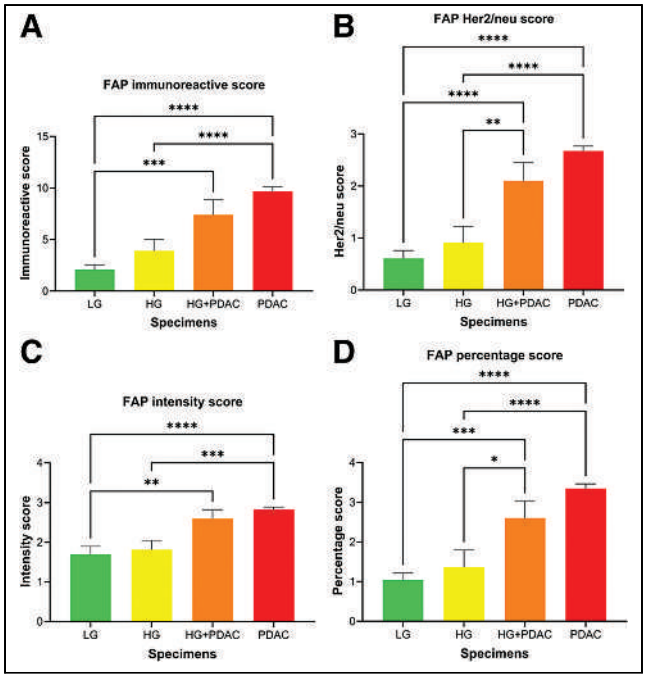

FIGURE 1. Mean values (±SEM) of FAP IRS (A), Her2/neu score (B), intensity score (C), and percentage score (D) of LG IPMNs, HG IPMNs, HG IPMNs with PDAC, and PDAC. P values are for 1-way ANOVA with Bonferroni multiple-comparison tests. *$P < 0.05$. **$P < 0.01$. ***$P < 0.001$. ****$P < 0.0001$.

Regarding grading, the mean IRS, Her2/neu score, intensity score, and percentage score were lower for HG IPMNs plus G2 PDAC than for HG IPMNs plus G3 PDAC, with a mean IRS of 6.75 (±3.96; median, 6.0) versus 12.0 (±0.0; median, 12) and a mean Her2/neu score of 2.13 (±0.99; median, 2.0) versus 3.0 (±0.0; median, 3.0). In G1 PDAC, the mean IRS and the mean Her2/neu score were lower than for HG plus G2 PDAC and G3 PDAC, with a mean IRS of 3.5 (±3.54; median, 3.5) for G1 versus 9.82 (±3.23; median, 12.0) for G2 versus 10.05 (±2.63; median, 12.0) for G3, as well as a mean Her2/neu score of 1.0 (±1.41; median, 1.0) for G1, 2.76 (±0.56; median, 3.0) for G2, and 3.0 (±0.0; median, 3.0) for G3 (Supplemental Figs. 1A and 1B). Only slight differences were observed between the intensity score and the percentage of moderately and poorly differentiated PDAC (Supplemental Figs. 1C and 1D). Of note, in all specimens, tumor-free islets of FAP-positive Langerhans were observed.

αSMA. In this study, αSMA expression could be shown in normal pancreatic stroma and within peri- and intraneoplastic desmoplastic reaction.

The mean IRS of LG IPMNs, at 6.04 (±3.25; median, 6.0), was higher than that of HG IPMNs, at 3.91(±3.70; median, 2.0), whereas the mean IRS of HG IPMNs plus PDAC, at 8.1 (±3; median, 7.0), was slightly lower than that of PDAC, at 8.73 (±2.86; median, 8.0) (Fig. 2A). Similarly, the Her2/neu score showed means of 2.26 (±0.62; median, 2.0) for LG IPMNs, 1.64 (±0.92; median, 2.0) for HG IPMNs, 2.4 (±0.52; median, 2.0) for HG IPMNs plus PDAC, and 2.36 (±0.7; median, 2.0) for PDAC (Fig. 2B). LG IPMNs had a higher mean intensity and percentage score than HG IPMNs. Both LG and HG IPMNs had lower mean

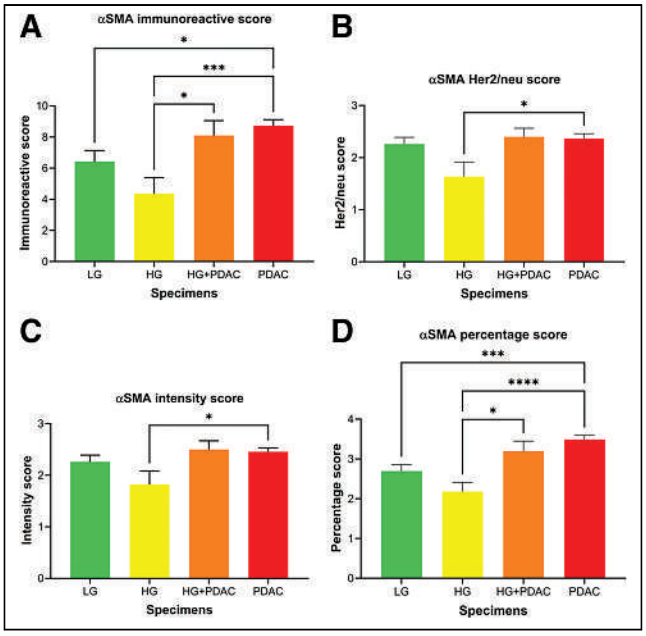

FIGURE 2. Mean values (±SEM) of αSMA IRS (A), Her2/neu score (B), intensity score (C), and percentage score (D) of LG IPMNs, HG IPMNs, HG IPMNs with PDAC, and PDAC. *P* values are for 1-way ANOVA with Bonferroni multiple-comparison tests. *$P < 0.05$. ***$P < 0.001$. ****$P < 0.0001$.

intensity and percentage scores than HG IPMNs plus PDAC and PDAC, whereas the differences between HG IPMNs plus PDAC and PDAC were minimal (Figs. 2C and 2D).

Regarding grading, HG IPMNs plus G2 PDAC, HG IPMNs plus G3 PDAC, and PDAC (G1–G3) showed the mean IRS, Her2/neu score, intensity score, and percentage score to be at a similar level, without marked differences (Supplemental Fig. 2).

Immunohistochemical results concerning FAP and αSMA expression in IPMNs plus PDAC and PDAC subdivided by grading are pictured in Supplemental Figures 3 and 4.

Comparison of FAP Expression and ^{68}Ga-FAPI-74b Uptake

For 14 patients who underwent ^{68}Ga-FAPI-74 PET/CT, the mean IRS, SUV_{max}, SUV_{mean}, and TTP were compared. Of these, 4 had LG IPMNs, 4 had HG IPMNs, 4 had HG IPMNs plus G2 PDAC, and 2 had HG IPMNs plus G3 PDAC.

LG IPMNs had a mean IRS of 1.8 (±1.7; median, 1.5), a mean SUV_{max} of 3.7 (±2.1; median, 3.5), a mean SUV_{mean} of 2.1 (±1.3; median, 1.8), and a mean TTP of 45.0 s (±0.0 s; median, 45 s). HG IPMNs had a mean IRS of 3.8 (±5.6; median, 1.5), a mean SUV_{max} of 5.1 (±1.6; median, 4.9), a mean SUV_{mean} of 2.5 (±0.6; median, 2.3), and a mean TTP of 247.5 s (±173.4 s; median, 232.5 s). HG IPMNs plus PDAC had a mean IRS of 6.8 (±5.7; median, 7.0), a mean SUV_{max} of 9.1 (±6.0; median, 7.7), a mean SUV_{mean} of 4.8 (±3.4; median, 3.7), and a mean TTP of 408.0 s (±147.5 s; median, 450 s) (Fig. 3). The concordant increase in FAP expression and ^{68}Ga-FAPI-74 uptake on PET/CT is visualized in Figure 4.

Regarding grading, HG IPMNs plus G2 PDAC showed a mean IRS of 4.3 (±5.2; median, 2.0), a mean SUV_{max} of 6.1 (±2.3; median, 5.9), a mean SUV_{mean} of 3.0 (±1.0; median, 2.8), and a mean TTP of 360.0 s (±184.3 s; median, 285.0 s). The highest values were observed for HG IPMNs plus G3 PDAC, with a mean IRS of 12.0 (±0; median, 12.0), a mean SUV_{max} of 15.0 (±7.5; median, 15.0), a mean SUV_{mean} of 8.3 (±4.4; median, 8.3), and a mean TTP of 480.0 s (±42.4 s; median, 480.0 s) (Supplemental Fig. 5). In summary, the IRS reflecting FAP expression increases with higher malignancy in accordance with the increasing mean SUV_{max}, SUV_{mean}, and TTP, with higher malignancy observed in our previous study.

DISCUSSION

Summary of Results

In this study we performed immunohistochemistry with antibodies directed against FAP and α-SMA on FFPE material of LG IPMNs, HG IPMNs, HG IPMNs plus PDAC, and PDAC. The semiquantitative analysis of FAP staining showed a rising IRS with increasing malignancy, confirming our previous finding and showing concordance between the mean IRS and the mean SUV_{max}, SUV_{mean}, and TTP. A higher IRS for α-SMA was observed in PDAC than in LG IPMNs, but a clear ascending order of IRS with increasing malignancy was missing.

Validation and Comparison of FAPI PET/CT-Acquired Data and FAP Expression

We observed a higher percentage of FAP-positive stroma and a stronger staining intensity in HG IPMNs than in LG IPMNs. The IRS underlines this outcome in that the mean HG IPMNs were twice as high as the IRS of LG IPMNs, thus demonstrating stronger FAP expression in HG IPMNs than in LG IPMNs. These results are similar to those of other studies, validating their FAPI PET/CT–acquired data by immunohistochemistry (*15,23*). Consequently, these findings are in line with our previous results showing a higher SUV_{max} and SUV_{mean} and a longer TTP in HG IPMNs than in LG IPMNs (*7*). Besides, our results are in accord with the outcome of a further prospective study revealing a strong correlation between SUVs and the IRS of FAP in patients with various solid tumors (*24*). By adding specimens of HG IPMNs plus PDAC and PDAC to our study, we could demonstrate a constant increase in the IRS of FAP (and thus its stronger expression) with higher malignancy. Because FAP is a marker of CAFs, which are associated with tumor progression and poor prognosis (*25*), our findings suggest that ^{68}Ga-FAPI PET/CT–acquired data project the histopathologic diagnosis by SUV and TTP and may harbor the potential to predict malignant progression.

FAP Expression in Tumor-Free Pancreatic Stroma and in Epithelial Tumor Cells

FAP, forming a homodimeric integral membrane gelatinase as a member of the serine protease family, promotes extracellular matrix degradation. Consequently, it participates not only in tumor growth but also in nonmalignant processes such as inflammation with a fibrotic component and tissue remodeling. Therefore, a weak immunohistochemical positivity against this protein was observed in tumor-free pancreatic stroma, an observation that is usually characterized by a minimal inflammatory reaction to the production of aggressive, autodigestive enzymes by exocrine ductal cells and of a periductal microleakage of this enzyme-containing secretion, resulting in necrosis of single exocrine cells. Additionally, FAP is involved in pericellular proteolysis of the extracellular matrix and hence promotes cell adhesion and migration. Thus, FAP is nonspecifically expressed in α-cells of Langerhans insulae (*26*). However, FAP expression has also been shown for β-cells, endothelial cells, macrophages, and ductal cells in

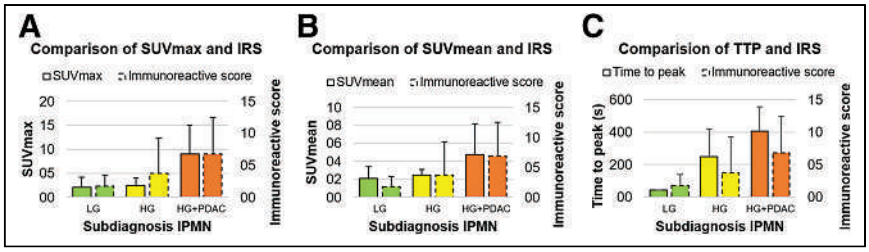

FIGURE 3. Comparison of mean values (with SD) of IRS with SUV_{max} (A), SUV_{mean} (B), and TTP (C) of LG IPMNs, HG IPMNs, and HG IPMNs plus PDAC as parameters of static and dynamic ^{68}Ga-FAPI-74 PET imaging observed in our previous study.

normal pancreatic parenchyma (as indicated by a search of the Human Protein Atlas in September 2023). This observation could also explain the strong unspecific immunoreactivity of several epithelial tumor cells in pancreatic carcinomas. Especially in the context of possible protein function in the control of epithelial–mesenchymal interactions during epithelial carcinogenesis (as indicated by a search of the RefSeq database in September 2023), further investigations are required to better understand the role of FAP expression in epithelial tumor cells.

Tumor Microenvironment and PDAC Progression

A possible mechanistic explanation for the differential FAP expression of LG IPMNs, HG IPMNs, and PDAC could be the role of the tumor microenvironment and CAFs during the carcinogenesis of PDAC. At the earlier stages of PDAC development, a proinflammatory tumor microenvironment may support tumor initiation (*27,28*). During cancer progression, the fibrotic and immune suppressive effects of the tumor microenvironment promote invasion and induce chemoresistance (*29*). CAFs act as major mediators of these differential, protumorigenic tumor microenvironment functions (*30*). CAFs are a heterogeneous population because they can develop from different cell types, such as pancreatic stellate cells, resident fibroblasts, epithelial cells, or even fat cells (*14,31*). Even more importantly, CAFs are a dynamic population that changes its biologic activity and antigen signature during cancer development (*27*). Our findings suggest that the portion of FAP-positive CAFs or the expression level of FAP in CAFs increases during PDAC cancer genesis, possibly due to changes in the tumor microenvironment composition and its increasing profibrotic function over time. Although we observed an ascending IRS with increasing malignancy for FAP, the IRS of αSMA was higher in HG IPMNs with PDAC and PDAC than in LG and HG IPMNs but showed no clear ascending score with higher malignancy. Although αSMA is a common marker for CAFs besides FAP, it is not expressed consistently in each tissue containing CAFs. Öhlund et al. observed 2 subtypes of CAFs with distinct functions in PDAC and with different expression of αSMA. Although the inflammatory CAFs are characterized by low αSMA expression, the myofibroblastic CAFs show an elevated expression of αSMA (*14*). In a comparison of PDAC versus IPMNs, Bernard et al. identified inflammatory CAFs only in PDAC whereas myofibroblastic CAFs were present in PDAC as well as in both LG and HG IPMNs, with higher representation in the latter samples (*32*). On the one hand, our findings of a stronger αSMA positivity in PDAC than in IPMNs suit this observation of different αSMA expression in both lesions depending on the subpopulation of CAFs present. On the other hand, the inverse αSMA positivity in HG versus LG IPMNs and the equal αSMA expression of PDAC (G1–G3) lead us to the hypothesis that αSMA is not as suitable as FAP as a marker for malignant progression of IPMNs and aggressiveness of PDAC.

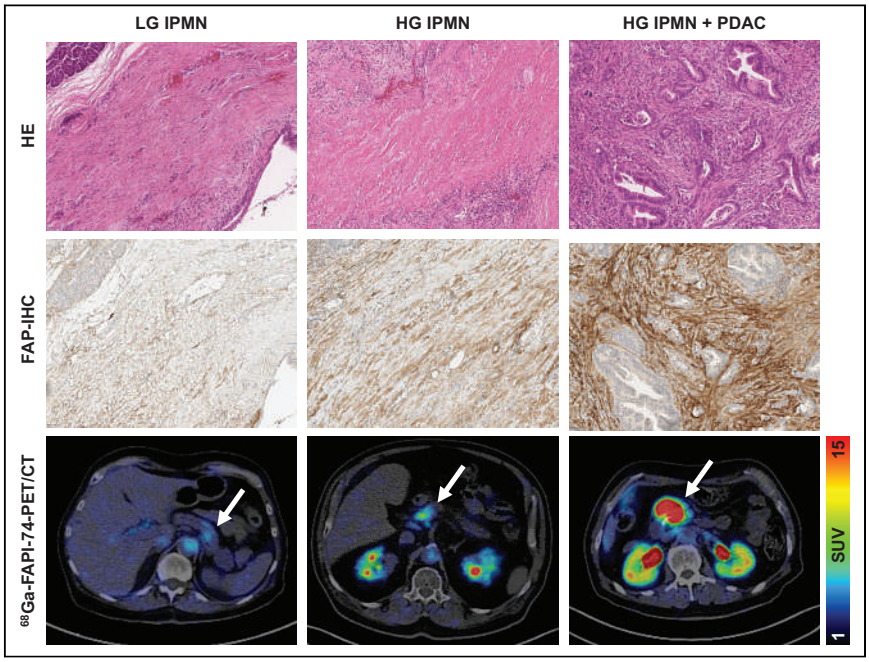

FIGURE 4. Representative hematoxylin and eosin staining (×20), immunohistochemical staining against FAP (×20), and corresponding axial PET/CT with ^{68}Ga-FAPI-74 images of 3 patients with LG IPMNs in pancreatic tail, HG IPMNs in pancreatic head, and HG IPMNs plus PDAC in pancreatic head (scale bars = 50 μm; arrows indicate pancreatic lesions). HE = hematoxylin and eosin; IHC = immunohistochemistry.

Clinical Implications

The increasing expression of FAP with higher malignancy was measurable concordantly as well by immunohistochemistry as by ^{68}Ga-FAPI PET. This suggests that FAP expression has the potential to become a malignancy marker for pancreatic lesions. In a primary setting, ^{68}Ga-FAPI PET–based or biopsy-based immunohistochemical evaluation of FAP positivity could be helpful to estimate the risk of malignancy of pancreatic lesions and support decision making regarding a possible resection or watch-and-wait strategy. For PDAC patients, immunohistochemical FAP expression of resected tumors or FAP avidity of tumor manifestations measured by ^{68}Ga-FAPI PET may have prognostic value and support treatment decisions—in particular with respect to the role of FAP-positive CAF in chemo- and radioresistance (*33–35*). Finally, ^{68}Ga-FAPI PET holds potential as a monitoring tool for systemic PDAC therapies, especially if

CAF-targeted therapies are applied in the future (*36*). The evaluation of FAP immunohistochemistry and ^{68}Ga-FAPI PET in these clinical settings is a promising subject for future prospective clinical trials.

Limitations

Although the results of our histopathologic target validation study are promising, several limitations must be considered. The major limitation is that the method of semiquantitative analysis does not allow exclusion of a certain interobserver deviation. A computer-automated evaluation of the staining results might be a more precise method for further studies. The second limitation is the relatively small number of specimens per diagnosis. Despite staining 3 slides per diagnosis to increase the validity of our findings, the SDs are somewhat high and could be reduced by larger patient cohorts. The unproportioned specimens' distribution must be considered when interpreting the results. With regard to our comparison of immunohistochemistry results and PET imaging, only a small group (14/98) of patients underwent ^{68}Ga-FAPI PET imaging. Summarizing, our results must be interpreted with caution and should be confirmed by prospective studies with larger patient cohorts.

CONCLUSION

This analysis of FAP immunohistochemistry in synopsis with the static and dynamic parameters of ^{68}Ga-FAPI-74 PET/CT shows an ascending order of FAP positivity from LG IPMNs to PDAC, confirming increasing FAPI avidity with higher malignancy in pancreatic lesions. To allow possible predictions on the progression of the disease through ^{68}Ga-FAPI PET/CT, further analysis of immunohistochemistry and PET parameters in larger prospective studies are needed.

DISCLOSURE

This work was funded by grant 13N 13341 from the Federal Ministry of Education and Research. Uwe Haberkorn has filed a patent application for quinoline-based FAP-targeting agents for imaging and therapy in nuclear medicine and has shares of a consultancy group for iTheranostics. No other potential conflict of interest relevant to this article was reported.

ACKNOWLEDGMENTS

We thank the EPZ biobank archive in Heidelberg for providing the slides and Tim Rau (NCT tissue bank in Heidelberg) for excellent technical assistance with staining and immunohistochemistry.

KEY POINTS

QUESTION: Do FAP expression and thus FAPI avidity in pancreatic lesions increase with higher malignancy?

PERTINENT FINDINGS: FAP positivity in LG IPMNs, HG IPMNs, PDAC deriving from HG IPMNs, and PDAC increases with rising malignancy and is in concordance with ^{68}Ga-FAPI PET/CT parameters.

IMPLICATIONS FOR PATIENT CARE: ^{68}Ga-FAPI PET–acquired data reflect the FAP expression of pathologic subclasses of IPMNs and might predict further malign transformation into PDAC. Further analyses of IRS and SUV or TTP in prospective studies with larger cohorts are needed.

REFERENCES

1. Mizrahi JD, Surana R, Valle JW, Shroff RT. Pancreatic cancer. *Lancet.* 2020;395:2008–2020.
2. Buerke B, Domagk D, Heindel W, Wessling J. Diagnostic and radiological management of cystic pancreatic lesions: important features for radiologists. *Clin Radiol.* 2012;67:727–737.
3. Basturk O, Esposito I, Fukushima N, et al. Pancreatic intraductal papillary mucinous neoplasm. In: *Digestive System Tumors.* 5th ed. International Agency for Research on Cancer; 2019:310–314.
4. European Study Group on Cystic Tumors of the Pancreas. European evidence-based guidelines on pancreatic cystic neoplasms. *Gut.* 2018;67:789–804.
5. Tanaka M, Fernández-del Castillo C, Kamisawa T, et al. Revisions of international consensus Fukuoka guidelines for the management of IPMN of the pancreas. *Pancreatology.* 2017;17:738–753.
6. Liu H, Cui Y, Shao J, Shao Z, Su F, Li Y. The diagnostic role of CT, MRI/MRCP, PET/CT, EUS and DWI in the differentiation of benign and malignant IPMN: a meta-analysis. *Clin Imaging.* 2021;72:183–193.
7. Lang M, Spektor AM, Hielscher T, et al. Static and dynamic ^{68}Ga-FAPI PET/CT for the detection of malignant transformation of intraductal papillary mucinous neoplasia of the pancreas. *J Nucl Med.* 2023;64:244–251.
8. Altmann A, Haberkorn U, Siveke J. The latest developments in imaging of fibroblast activation protein. *J Nucl Med.* 2021;62:160–167.
9. Bu L, Baba H, Yoshida N, et al. Biological heterogeneity and versatility of cancer-associated fibroblasts in the tumor microenvironment. *Oncogene.* 2019;38:4887–4901.
10. Gascard P, Tlsty TD. Carcinoma-associated fibroblasts: orchestrating the composition of malignancy. *Genes Dev.* 2016;30:1002–1019.
11. Hamson EJ, Keane FM, Tholen S, Schilling O, Gorrell MD. Understanding fibroblast activation protein (FAP): substrates, activities, expression and targeting for cancer therapy. *Proteomics Clin Appl.* 2014;8:454–463.
12. Kelly T. Fibroblast activation protein-alpha and dipeptidyl peptidase IV (CD26): cell-surface proteases that activate cell signaling and are potential targets for cancer therapy. *Drug Resist Updat.* 2005;8:51–58.
13. Ravi M, Boaz K, Natarajan S, Lewis A, Prasad M, Yellapurkar S. Expression of α-smooth muscle actin in benign and malignant salivary gland tumors: an immunohistochemical study. *Indian J Pathol Microbiol.* 2018;61:479–484.
14. Öhlund D, Handly-Santana A, Biffi G, et al. Distinct populations of inflammatory fibroblasts and myofibroblasts in pancreatic cancer. *J Exp Med.* 2017;214:579–596.
15. Röhrich M, Naumann P, Giesel FL, et al. Impact of ^{68}Ga-FAPI PET/CT imaging on the therapeutic management of primary and recurrent pancreatic ductal adenocarcinomas. *J Nucl Med.* 2021;62:779–786.
16. Röhrich M, Leitz D, Glatting FM, et al. Fibroblast activation protein–specific PET/CT imaging in fibrotic interstitial lung diseases and lung cancer: a translational exploratory study. *J Nucl Med.* 2022;63:127–133.
17. Hruban RH, Adsay NV, Esposito INF, et al. Pancreatic ductal adenocarcinoma In: *Digestive System Tumors.* 5th ed. International Agency for Research on Cancer; 2019:322–332.
18. Remmele W, Stegner HE. Recommendation for uniform definition of an immunoreactive score (IRS) for immunohistochemical estrogen receptor detection (ER-ICA) in breast cancer tissue. *Pathologe.* 1987;8:138–140.
19. Kaemmerer D, Peter L, Lupp A, et al. Comparing of IRS and Her2 as immunohistochemical scoring schemes in gastroenteropancreatic neuroendocrine tumors. *Int J Clin Exp Pathol.* 2012;5:187–194.
20. Lindner T, Loktev A, Altmann A, et al. Development of quinoline-based theranostic ligands for the targeting of fibroblast activation protein. *J Nucl Med.* 2018;59:1415–1422.
21. Loktev A, Lindner T, Mier W, Debus J, Altmann A, Jäger D, et al. A tumor-imaging method targeting cancer-associated fibroblasts. *J Nucl Med.* 2018;59:1423–1429.
22. Lindner T, Altmann A, Giesel F, et al. ^{18}F-labeled tracers targeting fibroblast activation protein. *EJNMMI Radiopharm Chem.* 2021;6:26.
23. Röhrich M, Syed M, Liew DP, et al. ^{68}Ga-FAPI-PET/CT improves diagnostic staging and radiotherapy planning of adenoid cystic carcinomas: imaging analysis and histological validation. *Radiother Oncol.* 2021;160:192–201.
24. Mona CE, Benz MR, Hikmat F, et al. Correlation of ^{68}Ga-FAPi-46 PET biodistribution with FAP expression by immunohistochemistry in patients with solid cancers: interim analysis of a prospective translational exploratory study. *J Nucl Med.* 2022;63:1021–1026.
25. Fitzgerald AA, Weiner LM. The role of fibroblast activation protein in health and malignancy. *Cancer Metastasis Rev.* 2020;39:783–803.
26. Busek P, Hrabal P, Fric P, Sedo A. Co-expression of the homologous proteases fibroblast activation protein and dipeptidyl peptidase-IV in the adult human Langerhans islets. *Histochem Cell Biol.* 2015;143:497–504.

27. Clark CE, Hingorani SR, Mick R, Combs C, Tuveson DA, Vonderheide RH. Dynamics of the immune reaction to pancreatic cancer from inception to invasion. *Cancer Res.* 2007;67:9518–9527.
28. Wörmann SM, Diakopoulos KN, Lesina M, Algul H. The immune network in pancreatic cancer development and progression. *Oncogene.* 2014;33:2956–2967.
29. Storz P, Crawford HC. Carcinogenesis of pancreatic ductal adenocarcinoma. *Gastroenterology.* 2020;158:2072–2081.
30. Richards KE, Zeleniak AE, Fishel ML, Wu J, Littlepage LE, Hill R. Cancer-associated fibroblast exosomes regulate survival and proliferation of pancreatic cancer cells. *Oncogene.* 2017;36:1770–1778.
31. Öhlund D, Elyada E, Tuveson D. Fibroblast heterogeneity in the cancer wound. *J Exp Med.* 2014;211:1503–1523.
32. Bernard V, Semaan A, Huang J, et al. Single-cell transcriptomics of pancreatic cancer precursors demonstrates epithelial and microenvironmental heterogeneity as an early event in neoplastic progression. *Clin Cancer Res.* 2019;25:2194–2205.
33. Huang W, Zhang L, Yang M, et al. Cancer-associated fibroblasts promote the survival of irradiated nasopharyngeal carcinoma cells via the NF-kappaB pathway. *J Exp Clin Cancer Res.* 2021;40:87.
34. Ji X, Ji J, Shan F, Zhang Y, Chen Y, Lu X. Cancer-associated fibroblasts from NSCLC promote the radioresistance in lung cancer cell lines. *Int J Clin Exp Med.* 2015;8:7002–7008.
35. Nariai Y, Mishima K, Yoshimura Y, Sekine J. FAP-1 and NF-kappaB expressions in oral squamous cell carcinoma as potential markers for chemo-radio sensitivity and prognosis. *Int J Oral Maxillofac Surg.* 2011;40:419–426.
36. Zhou X, Zhang P, Liu N, et al. Enhancing chemotherapy for pancreatic cancer through efficient and sustained tumor microenvironment remodeling with a fibroblast-targeted nanosystem. *J Control Release.* 2023;361:161–177.

Erratum

In the article "^{61}Cu-Labeled Radiotracers: Alternative or Choice?," by Fani and Nicolas (*J Nucl Med.* 2023;64:1855–1857), the fourth row in Table 1 mistakenly states β^+ 39.0 for ^{64}Cu; however, β^- 39.0 is the correct decay, yield (%). The authors regret the error.

Characterizing Normal Variant [^{68}Ga]Ga-FAPI-46 Uptake in the Epididymis

Peter George Maliha*, Masatoshi Hotta*, Johannes Czernin, and Jeremie Calais

Ahmanson Translational Theranostics Division, Department of Molecular and Medical Pharmacology, UCLA, Los Angeles, California

The biodistribution of fibroblast activation protein inhibitor (FAPI) PET tracers includes the kidneys, bladder, uterus, breast, muscles, and bone marrow. We describe its occasional uptake patterns in the epididymis. **Methods:** Epididymal [^{68}Ga]Ga-FAPI-46 uptake was retrospectively analyzed in 55 PET/CT studies of 55 men. Uptake intensity (SUV), pattern (diffuse, focal, or multifocal), laterality, and location (epididymal head with or without body/tail) were analyzed. Electronic medical records were reviewed to determine the presence of epididymis-related disease. **Results:** Epididymal [^{68}Ga]Ga-FAPI-46 uptake was observed in 8 of 55 (15%) subjects, with bilateral epididymal head uptake in all cases and epididymal body/tail uptake in 6 of 8 (75%) cases, 5 of 6 (83%) bilaterally and 1 of 6 (17%) unilaterally. The average SUV_{max} was greater in the epididymal heads than in the epididymal bodies/tails, with an SUV_{max} of 4.1 versus 3.0 ($P < 0.001$). No subject had epididymal disease related to the uptake. **Conclusion:** [^{68}Ga]Ga-FAPI-46 uptake in the epididymis occurs occasionally and does not appear related to epididymal disease.

Key Words: FAPI; normal variant; epididymal head; epididymis; incidental

J Nucl Med 2024; 65:59–62
DOI: 10.2967/jnumed.123.266013

Fibroblast activation protein (FAP) is a type II integral membrane glycoprotein enzyme, with functions relating to extracellular matrix remodeling and fibrogenesis. This protein is expressed by cancer-associated fibroblast subpopulations (CAF-S1 and CAF-S4) that may be present in more than 90% of epithelial cancers with a desmoplastic reaction (*1–3*). It is also expressed by the normal activated fibroblasts in inflammation and fibrosis but is not significantly expressed in healthy tissues (*1,4,5*).

FAP inhibitor (FAPI) radiopharmaceuticals have been developed to target FAP to investigate their potential in the diagnosis and treatment of multiple oncologic or nononcologic processes (*4*).

The normal biodistribution of FAPI PET tracers includes mainly the uterus, kidneys, bladder, and to a lower level the breast, muscles, and bone marrow (*6,7*). While analyzing [^{68}Ga]Ga-FAPI-46 PET/CT studies as part of multiple clinical trials, we identified occasional epididymal uptake. The goal of this study was to further characterize [^{68}Ga]Ga-FAPI-46 PET/CT uptake in the epididymis.

Received May 8, 2023; revision accepted Sep. 27, 2023.
For correspondence or reprints, contact Peter George Maliha (peter.maliha@mail.mcgill.ca).
*Contributed equally to this work.
Guest editor: Rodney Hicks, Peter MacCallum Cancer Institute
Published online Nov. 9, 2023.

MATERIALS AND METHODS

We screened our database of 92 patients (56 men, 36 women) who underwent [^{68}Ga]Ga-FAPI-46 PET/CT in the clinical trials NCT04147494, NCT04457232, NCT04457258, NCT04459273, or NCT05365802 from December 18, 2019, to April 18 2023. The PET scans of all 56 male patients were retrospectively analyzed. The scans were acquired with a Siemens Biograph mCT scanner and a Siemens Biograph 64 TruePoint scanner. The CT scans were low-dose (120 keV, 30 mAs, slice thickness of 5 mm) and acquired without intravenous contrast medium. Uptake in the epididymides was evaluated in consensus by 2 nuclear medicine physicians. The epididymal structures were located on PET/CT by reviewing axial, coronal, and sagittal planes. Tracer uptake pattern (diffuse, focal, or multifocal), laterality, and location (epididymal head with or without body/tail) were noted. Uptake in the body or tail was recorded as being in the same structure (i.e., body/tail) as the body and tail could not be distinguished on PET/CT because of their small size. The SUV_{max} of the epididymal structures was collected by drawing 1-cm spheric volume of interests in the superior pole of the testes and in the region of most intense uptake in the epididymal bodies/tails. Blood pool SUV_{mean} was measured with a 1-cm spheric volume of interest in the descending thoracic aorta at the level of the carina. Epididymal SUV_{max}/blood pool SUV_{mean} ratios were calculated. We defined mild, moderate, and intense uptake as being ratios of 3 or less, 3–4, and more than 4, respectively. We reviewed the electronic medical records of all patients with any epididymal uptake to determine the presence of epididymis-related disease (e.g., epididymitis, epididymal tumor lesions, and epididymal cysts) by checking the past medical history and by searching the electronic medical record for the keyword *epididymis*. Paired *t* tests were performed using R software to assess the mean differences in uptake between the analyzed structures. The Shapiro–Wilk test was used to confirm no significant departure from normal distributions in the analyzed data. A Welch *t* test was performed using R to compare the age of the subjects with and without uptake in the epididymis.

The study was approved by the UCLA institutional review board (approval 22-001287), and the need for written informed consent was waived because of the retrospective design.

RESULTS

In total, the [^{68}Ga]Ga-FAPI-46 uptake in the epididymides of 55 of 56 men was analyzed. One PET/CT study was excluded because of poor image quality (excessive noise). The mean age of the population was 63 y (range, 24–85 y). The mean injected activity and time from injection to imaging were 181 MBq (range, 129–204 MBq) and 61 min (range, 47–100 min), respectively.

Of all subjects, 8 of 55 (15%) had uptake in their epididymides (Fig. 1). Of the 8 subjects with epididymal uptake, 8 of 8 (100%) had focal uptake in both epididymal heads (total, 16 epididymal heads), 6 of 8 (75%) had linear uptake in the epididymal bodies/tails, 5 of 6 (83%) had uptake bilaterally, and 1 of 6 (17%) had uptake unilaterally on the right (total, 11 epididymal bodies/tails).

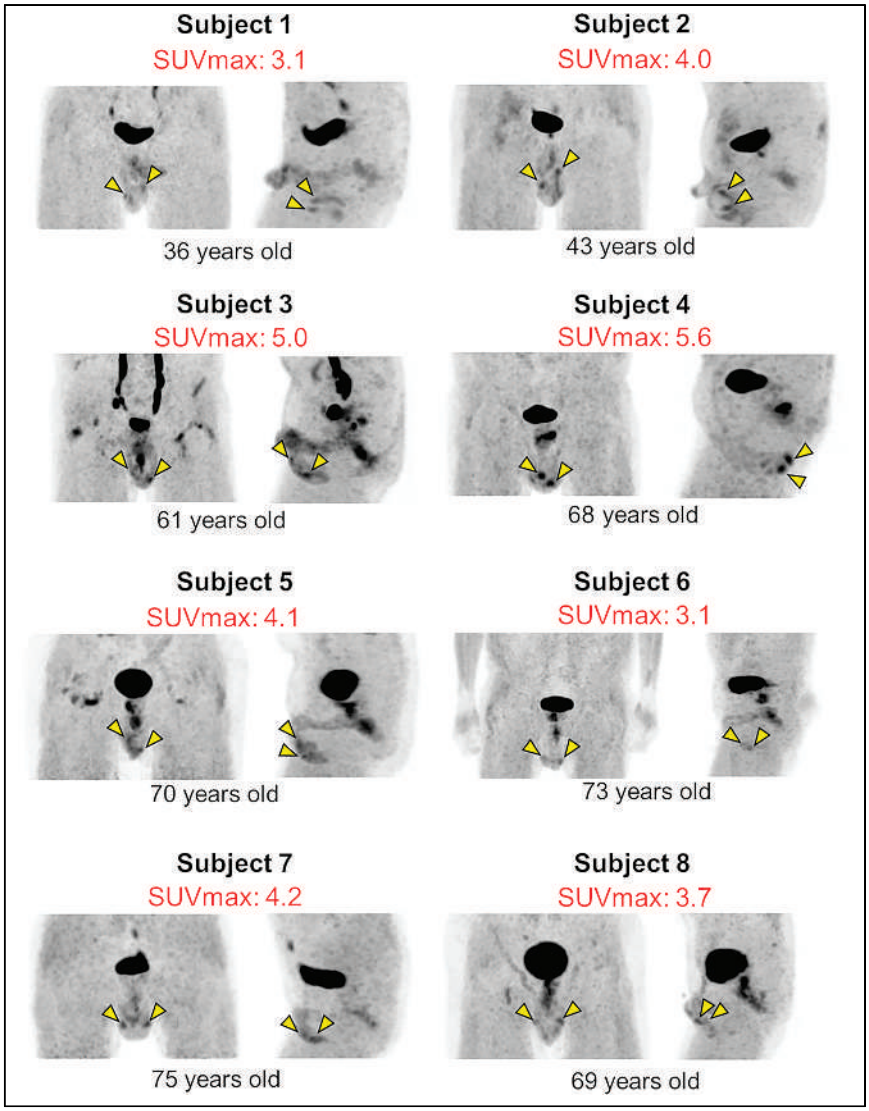

FIGURE 1. Maximum-intensity projection anterior (left) and lateral (right) images of all 8 subjects with epididymal [^{68}Ga]Ga-FAPI-46 uptake (arrowheads).

Table 1 describes the SUVs and signal-to-background ratios in all 8 subjects. Figures 2 and 3 and Supplemental Figures 1–3 illustrate examples of mild, moderate, and intense uptake in the epididymis (supplemental materials are available at http://jnm.snmjournals.org).

The uptake intensity in the epididymal heads ranged from mild to intense (7/16 [44%] mild, 4/16 [25%] moderate, and 5/16 [31%] intense), with a mean SUV_{max} of 3.9 (range, 2.6–5.6) and a mean SUV_{max}/SUV_{mean} blood pool ratio of 3.4 (range, 2.1–5.3).

The uptake intensity in the epididymal bodies/tails ranged from mild to moderate (9/11 [82%] mild and 2/11 [18%] moderate), with a mean SUV_{max} of 3.0 (range, 2.6–3.5) and a mean epididymal SUV_{max}/SUV_{mean} blood pool ratio of 2.7 (range, 2.0–3.3).

In subjects with uptake in both the epididymal heads and the epididymal bodies/tails, the mean SUV_{max} was greater in the heads (SUV_{max}, 4.1 vs. 3.0, $P < 0.001$, $n = 11$).

There was a small difference in the mean SUV_{max} between the right and left epididymal heads (3.7 vs. 4.1, respectively, $P = 0.040$, $n = 8$). There was no difference in the SUV_{max} between the right and left epididymal bodies/tails that had bilateral uptake (3.0 vs. 3.0, $P = 0.87$, $n = 5$).

There was no significant difference in the average age of the subjects between those with epididymal uptake (average, 62 y; range, 36–75 y) and those without (average, 63 y; range, 24–85 y) ($P = 0.82$). In these 8 patients with epididymal uptake, the median follow-up time after PET/CT was 4.8 mo (range, 1–28 mo). Two subjects

TABLE 1
Epididymal [^{68}Ga]Ga-FAPI-46 SUVs and Signal-to-Background Ratios

	Epididymal head (R)		Epididymal head (L)		Epididymal body/tail (R)		Epididymal body/tail (L)	
Subject no.	SUV_{max}	SUV_{max}/BP SUV_{mean}	SUV_{max}	SUV_{max}/BP SUV_{mean}	SUV_{max}	SUV_{max}/BP SUV_{mean}	SUV_{max}	SUV_{max}/BP SUV_{mean}
1	3.1	3.1	3.0	3.0	2.7	2.7	2.8	2.8
2	4.0	3.6	4.0	3.6	2.8	2.5	3.2	2.9
3	4.1	3.4	5.0	4.2	3.4	2.8	3.3	2.8
4	5.6	5.3	5.6	5.3	3.5	3.3	3.2	3.0
5	3.9	2.1	4.1	2.2	None	None	None	None
6	2.6	2.2	3.1	2.6	None	None	None	None
7	3.7	4.1	4.2	4.7	2.7	3.0	None	None
8	2.8	2.2	3.7	2.8	2.6	2.0	2.6	2.0

BP = blood pool; none = no uptake above background.

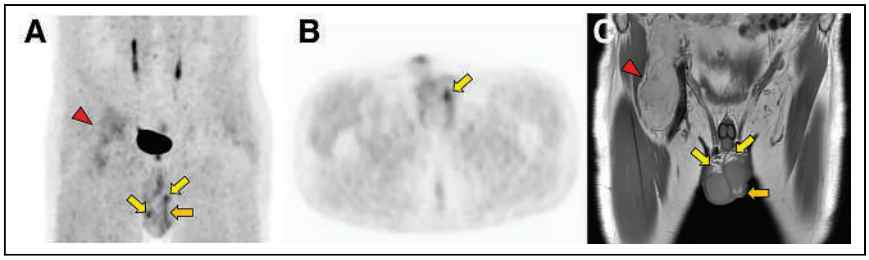

FIGURE 2. Subject 2 (43-y-old man) from Table 1. Shown are [^{68}Ga]Ga-FAPI-46 maximum-intensity projection coronal PET (A), axial PET (B), and coronal T1-weighted MR images (C). Moderate uptake is demonstrated bilaterally in epididymal heads (yellow arrows). Mild uptake is demonstrated in left epididymal body/tail (orange arrows). There was mild uptake in right epididymal body/tail (not shown). Epididymal tissue was demonstrated on MRI, with no epididymal disease reported. Biopsy-proven hibernoma with mild uptake was noted (arrowheads).

had less than 3 mo of follow-up (31 and 55 d), and 6 of 8 had more than 3 mo of follow-up.

On follow-up, no subject had known clinical epididymal disease related to [^{68}Ga]Ga-FAPI-46 uptake. One subject (subject 8, Fig. 1 and Table 1) had a documented left epididymal cyst diagnosed on ultrasound 5 mo before undergoing [^{68}Ga]Ga-FAPI-46 PET/CT. However, this subject had uptake in both epididymal heads and bodies/tails, making this pathology unlikely the cause of the uptake.

DISCUSSION

The epididymis, a tightly coiled structure divided into a head, body, and tail, spans from the upper testicular pole to the lower testicular pole and can reach 6 m in length when uncoiled (*8*). The largest part of the epididymis is its head, with its thickness typically measuring 10–12 mm in the anteroposterior dimension. The body and tail are smaller, with the body having an average thickness of 1–2 mm (*9*). The epididymis has multiple functions regarding sperm maturation, storage, and transport (*10*).

During our [^{68}Ga]Ga-FAPI-46 PET trials, we noticed occasional epididymal uptake in our [^{68}Ga]Ga-FAPI-46 cohort, and the goal of this analysis was to formally assess this uptake. We were able to retrospectively identify uptake in the epididymis in a minority of our study population (8/55, 15%).

None of these 8 patients had known epididymal disease. Epididymal uptake was always present bilaterally in the head, most often mild and slightly more prominent on the left, with associated less intense unilateral or bilateral uptake in the body/tail.

FAP and FAP RNA expression in the epididymis has been observed on histopathology (*11*). In the Human Protein Atlas, FAP expression in the epididymis and testes has been quantified as moderate by immunohistochemical staining patterns. FAP RNA expression in the epididymis has been quantified as greater than in the testes (by normalized transcripts per million) (*12*).

The exact cause of occasional [^{68}Ga]Ga-FAPI-46 uptake in the epididymis is unclear but suggests the presence of occasional fibrosis and inflammation, which is supported by the known presence of inflammatory cells and fibroblast growth factor receptors in the epididymis (*13*). This uptake may also reflect epididymal hyperemia.

Uptake patterns in the epididymal head have also been described with [^{18}F]piflufolastat, [^{68}Ga]Ga-DOTANOC, and [^{177}Lu]Lu-DOTATATE, potentially explained by prostate-specific membrane antigen and somatostatin receptor expression in inflammatory cells such as macrophages (*14–17*). No association between age and [^{68}Ga]Ga-FAPI-46 uptake in the epididymis was found in our study. Because our study population was small, other potential clinical factors potentially influencing epididymal [^{68}Ga]Ga-FAPI-46 uptake were not evaluated. Further larger prospective studies are warranted.

As a main limitation of the study, there was no histopathologic validation of the observed PET signal. The focal uptake in the upper pole of the testes was presumed located in the epididymal head because it is the only focal structure in that region and because adjacent blood pool uptake is unlikely since [^{68}Ga]Ga-FAPI-46 signal in the blood pool is minimal. Linear uptake inferior to the epididymal head was presumed located in the epididymal body/tail as it is the only structure that could have this uptake pattern: it would be unusual for only a portion of the tunica vaginalis to express FAP. The systematically observed greater uptake in the epididymal head than in the body/tail can be in part explained by the size difference in the structures, leading to a greater partial-volume effect in the smaller epididymal body/tail. The study population was small, and other potential clinical factors potentially influencing epididymal [^{68}Ga]Ga-FAPI-46 uptake were therefore not evaluated. Further larger prospective studies are warranted.

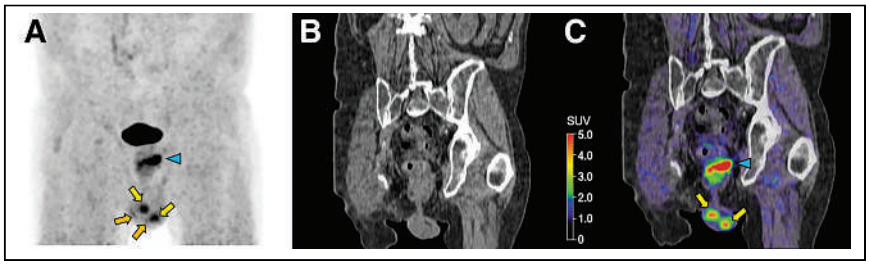

FIGURE 3. Subject 4 (68-y-old man) from Table 1. Shown are [^{68}Ga]Ga-FAPI-46 PET maximum-intensity projection coronal PET (A), CT (B), and PET/CT (C) images. Intense uptake is demonstrated bilaterally in epididymal heads (yellow arrows). Moderate uptake is demonstrated in epididymal bodies/tails (orange arrows). Intense uptake is demonstrated in site of treated anal abscess (arrowheads).

CONCLUSION

To our knowledge, this is the first reported study describing epididymal [^{68}Ga]Ga-FAPI-46 uptake patterns. Although the exact cause of this uptake remains unknown, it is important to avoid unnecessary additional investigations by being aware that occasionally there is [^{68}Ga]Ga-FAPI-46 uptake in the epididymis unrelated to known clinically manifested epididymal disease. To define the true incidence of FAP expression in the epididymis, larger study populations are needed.

DISCLOSURE

No potential conflict of interest relevant to this article was reported.

KEY POINTS

QUESTION: What are the [^{68}Ga]Ga-FAPI-46 epididymal uptake characteristics on PET/CT?

PERTINENT FINDINGS: Fifteen percent of our study population had epididymal uptake unrelated to epididymal disease.

IMPLICATIONS FOR PATIENT CARE: While interpreting [^{68}Ga]Ga-FAPI-46 PET/CT studies, readers should be aware that occasional epididymal uptake unrelated to known epididymal disease can be seen.

REFERENCES

1. Zhao L, Chen J, Pang Y, et al. Fibroblast activation protein-based theranostics in cancer research: a state-of-the-art review. *Theranostics.* 2022;12:1557–1569.
2. Loktev A, Lindner T, Burger EM, et al. Development of fibroblast activation protein-targeted radiotracers with improved tumor retention. *J Nucl Med.* 2019;60:1421–1429.
3. Peltier A, Seban RD, Buvat I, Bidard FC, Mechta-Grigoriou F. Fibroblast heterogeneity in solid tumors: from single cell analysis to whole-body imaging. *Semin Cancer Biol.* 2022;86:262–272.
4. Mori Y, Dendl K, Cardinale J, Kratochwil C, Giesel FL, Haberkorn U. FAPI PET: fibroblast activation protein inhibitor use in oncologic and nononcologic disease. *Radiology.* 2023;306:e220749.
5. Kalluri R. The biology and function of fibroblasts in cancer. *Nat Rev Cancer.* 2016;16:582–598.
6. Meyer C, Dahlbom M, Lindner T, et al. Radiation dosimetry and biodistribution of ^{68}Ga-FAPI-46 PET imaging in cancer patients. *J Nucl Med.* 2020;61:1171–1177.
7. Hotta M, Rieger AC, Jafarvand MG, et al. Non-oncologic incidental uptake on FAPI PET/CT imaging. *Br J Radiol.* 2023;96:20220463.
8. Wijesekera NT, Gonsalves MA, Patel U. The male pelvis. In: Mitchell A, Healy JC, Butler P, eds. *Applied Radiological Anatomy.* 2nd ed. Cambridge University Press; 2012:230–246.
9. Deurdulian C, Mittelstaedt CA, Chong WK, Fielding JR. US of acute scrotal trauma: optimal technique, imaging findings, and management. *Radiographics.* 2007;27:357–369.
10. James ER, Carrell DT, Aston KI, Jenkins TG, Yeste M, Salas-Huetos A. The role of the epididymis and the contribution of epididymosomes to mammalian reproduction. *Int J Mol Sci.* 2020;21:5377.
11. Tissue expression of FAP: staining in epididymis. The Human Protein Atlas website. https://www.proteinatlas.org/ENSG00000078098-FAP/tissue/epididymis. Accessed October 18, 2023.
12. Tissue expression of FAP: summary. The Human Protein Atlas website. https://www.proteinatlas.org/ENSG00000078098-FAP/tissue. Accessed October 18, 2023.
13. Robaire B, Hinton BT. The epididymis. In: Plant TM, Zeleznik AJ, eds. *Knobil and Neill's Physiology of Reproduction.* 4th ed. Academic Press; 2015:691–771.
14. Maliha PG, Singerman J, Abikhzer G, Probst S. Physiologic prostate-specific membrane antigen-targeted ^{18}F-DCFPyL uptake in the epididymis head newly appreciated on digital PET/CT. *Nucl Med Commun.* 2021;42:490–494.
15. Parihar AS, Sood A, Sood A, Gulati A, Mittal BR. Demonstration of focal physiologic in-vivo somatostatin receptor expression in the caput epididymis of the testes on ^{68}Ga-DOTANOC PET/CT and ^{177}Lu-DOTATATE post-therapy whole body scintigraphy. *Asia Ocean J Nucl Med Biol.* 2020;8:132–135.
16. Li X, Bauer W, Kreissl MC, et al. Specific somatostatin receptor II expression in arterial plaque: ^{68}Ga-DOTATATE autoradiographic, immunohistochemical and flow cytometric studies in apoE-deficient mice. *Atherosclerosis.* 2013;230:33–39.
17. Wang M, Yang Y, Cansever D, et al. Two populations of self-maintaining monocyte-independent macrophages exist in adult epididymis and testis. *Proc Natl Acad Sci USA.* 2021;118:e2013686117.

Examining the Relationship and Prognostic Significance of Cell-Free DNA Levels and the PSMA-Positive Tumor Volume in Men with Prostate Cancer: A Retrospective–Prospective [^{68}Ga]Ga-PSMA-11 PET/CT Study

Kilian Kluge[1,2], Holger Einspieler[1], David Haberl[1], Clemens Spielvogel[1,2], Stefan Stoiber[2,3], Chrysoula Vraka[1], Laszlo Papp[4], Sabine Wunsch[1], Gerda Egger[3], Gero Kramer[5], Bernhard Grubmüller[5–7], Shahrokh Shariat[5,6,8–12], Marcus Hacker[1], Lukas Kenner[2,3], and Alexander Haug[1,2]

[1]Division of Nuclear Medicine, Department of Biomedical Imaging and Image-Guided Therapy, Medical University of Vienna, Vienna, Austria; [2]Christian Doppler Laboratory for Applied Metabolomics, Medical University of Vienna, Vienna, Austria; [3]Department of Pathology, Medical University of Vienna, Vienna, Austria; [4]Center for Medical Physics and Biomedical Engineering, Medical University of Vienna, Vienna, Austria; [5]Department of Urology, Medical University of Vienna, Vienna, Austria; [6]Department of Urology and Andrology, University Hospital Krems, Krems, Austria; [7]Karl Landsteiner University of Health Sciences, Krems, Austria; [8]Karl Landsteiner Institute of Urology and Andrology, Vienna, Austria; [9]Department of Urology, University of Texas Southwestern Medical Center, Dallas, Texas; [10]Division of Urology, Department of Special Surgery, University of Jordan, Amman, Jordan; [11]Department of Urology, Second Faculty of Medicine, Charles University, Prague, Czech Republic; and [12]Department of Urology, Weill Cornell Medical College, New York, New York

Functional imaging with prostate-specific membrane antigen (PSMA) ligands has emerged as the standard imaging method for prostate cancer (PCA). In parallel, the analysis of blood-derived, cell-free DNA (cfDNA) has been shown to be a promising quantitative biomarker of PCA aggressiveness and patient outcome. This study aimed to evaluate the relationship and prognostic value of cfDNA concentrations and the PSMA-positive tumor volume (PSMA-TV) in men with PCA undergoing [^{68}Ga]Ga-PSMA-11 PET/CT imaging. **Methods:** We recruited 148 men with histologically proven PCA (mean age, 70.7 ± 7.7 y) who underwent [^{68}Ga]Ga-PSMA-11 PET/CT (184.9 ± 18.9 MBq) and blood sampling between March 2019 and August 2021. Among these, 74 (50.0%) had hormone-sensitive PCA and 74 (50.0%) had castration-resistant PCA (CRPC). All patients provided written informed consent before blood sample collection and imaging. The cfDNA was extracted and quantified, and PSMA-expressing tumor lesions were delineated to extract the PSMA-TVs. The Spearman coefficient assessed correlations between PSMA-TV and cfDNA concentrations and cfDNA's relation with clinical parameters. The Kruskal–Wallis test examined the mean cfDNA concentration differences based on PSMA-TV quartiles for significantly correlated patient groups. Log-rank and multivariate Cox regression analyses evaluated the prognostic significance of high and low cfDNA and PSMA-TV levels for overall survival. **Results:** Weak positive correlations were found between cfDNA concentration and PSMA-TV in the overall group ($r = 0.16$, $P = 0.049$) and the CRPC group ($r = 0.31$, $P = 0.007$) but not in hormone-sensitive PCA patients ($r = -0.024$, $P = 0.837$). In the CRPC cohort, cfDNA concentrations significantly differed between PSMA-TV quartiles 4 and 1 ($P = 0.002$) and between quartiles 4 and 2 ($P = 0.016$). Survival outcomes were associated with PSMA-TV ($P < 0.0001$, $P = 0.004$) but not cfDNA ($P = 0.174$, $P = 0.12$), as per the log-rank and Cox regression analysis. **Conclusion:** These findings suggest that cfDNA might serve as a biomarker of advanced, aggressive CRPC but does not reliably reflect total tumor burden or prognosis. In comparison, [^{68}Ga]Ga-PSMA-11 PET/CT provides a highly granular and prognostic assessment of tumor burden across the spectrum of PCA disease progression.

Key Words: liquid biopsy; cell-free DNA; prostate cancer; PSMA; PET/CT

J Nucl Med 2024; 65:63–70
DOI: 10.2967/jnumed.123.266158

Despite substantial diagnostic and therapeutic innovations in recent years, prostate cancer (PCA) remains a leading cause of cancer-related mortality in men (*1*).

As PCA progresses from initially localized and hormone-sensitive PCA (hsPC) to progressively metastatic and castration-resistant PCA (CRPC)—a transition predominantly characterized by a loss of reliance on gonadal androgen signaling (*2,3*)—periodic reassessment of tumor progression is critical to enable appropriate therapy adjustments (*4*).

Hybrid imaging with PET/CT using prostate-specific membrane antigen (PSMA) ligands (*5*) has emerged as the diagnostic imaging gold standard using highly sensitive and specific radiotracers not reliant on the Warburg effect (*6*), as they enable highly accurate PCA staging (*7,8*), frequently leading to changes in disease management (*9*).

In parallel, the analysis of blood-derived, cell-free DNA (cfDNA) has recently gained scientific traction (*10*) in oncology because of its minimally invasive nature and the wealth of predictive and prognostic information it is able to provide. In healthy individuals, cfDNA is

Received Jun. 13, 2023; revision accepted Sep. 27, 2023.
For correspondence or reprints, contact Alexander Haug (alexander.haug@meduniwien.ac.at).
Published online Nov. 30, 2023.

believed to originate primarily from apoptosis or necrosis of hematopoietic cells (*11,12*). In cancer patients, tumor and tumor-microenvironment–constituting cells also have been shown (*13,14*) to shed DNA (circulating-tumor DNA) into the bloodstream by apoptosis, necrosis (*15*), and even active secretion (*16*). As a result, supraphysiologic cfDNA concentrations are frequently observed in cancer patients (*17–19*).

Genomic and epigenomic interrogations of circulating-tumor DNA using approaches based on polymerase chain reaction or next-generation sequencing enable in-depth profiling of PCA biology, evolution, and prognostic trajectory (*20–23*). However, simple quantification of cfDNA levels was shown to be a cost-effective, prognostic, and predictive biomarker in several studies (*24,25*), including 2 multicenter, taxane-evaluating phase III chemotherapy trials (*24*). Likewise, qualitative and semiquantitative analysis of PSMA-ligand PET/CT imaging has repeatedly been demonstrated to yield valuable biomarkers of disease outcome and therapy responses (*26*).

To date, the relationship between functional imaging assessments of tumor burden and cfDNA levels has been investigated only using [^{18}F]fluorocholine PET/CT imaging (*27*). However, in the setting of [^{68}Ga]Ga-PSMA-HBED-CC ([^{68}Ga]Ga-PSMA-11) PET/CT, the association between cfDNA levels and PSMA-positive tumor volume (PSMA-TV), as well as their comparative prognostic value, remains unexplored.

We hypothesized that cfDNA levels correlate with functionally imaged tumor volumes and that both methods yield survival outcome–associated information.

This study aimed to assess the relationship between cfDNA levels and PSMA-TV, as well as their prognostic value, in men with PCA undergoing [^{68}Ga]Ga-PSMA-11 PET/CT imaging.

MATERIALS AND METHODS

Study Design

In this single-center study, PCA patients referred for [^{68}Ga]Ga-PSMA-11 PET/CT imaging at the Medical University of Vienna between March 2019 and August 2021 were prospectively recruited. Only patients with histologically proven PCA were included, excluding those with other active or previous malignancies (Fig. 1). Blood samples were collected for cfDNA analysis after obtaining written informed consent. This study was approved by the ethics committee of the Medical University of Vienna (approval 1649/2016).

Clinical data were gleaned retrospectively from the medical records. Follow-up and overall survival (OS) data were sourced from Statistics Austria (censoring date, May 12, 2023). The primary endpoints of this study were, first, the relationship between cfDNA concentrations and PSMA-TV and, second, the prognostic value of cfDNA and PSMA-TV levels stratified according to high- and low-level groups. The secondary endpoint was the association of cfDNA concentration with PSMA-TV quartiles, in case the first primary endpoint was met (supplemental methods; supplemental materials are available at http://jnm.snmjournals.org).

Plasma Sample Collection and Storage, DNA Extraction, and Quantification

Blood samples were collected in cfDNA BCT tubes (Streck Inc.) before tracer injection and centrifuged to remove any cellular debris. The resulting plasma was stored at −80°C (supplemental methods). The QIAamp Circulating Nucleic Acid Kit (Qiagen) was used to extract cfDNA from plasma according to the manufacturer's instructions, and the resultant cfDNA was stored at −20°C for further analysis. cfDNA was quantified on a Fragment Analyzer (Agilent) using an HS Next-Generation Sequencing Fragment Kit (Agilent). PROSize software (version 2.0; Agilent) analyzed the electropherograms and quantified cfDNA concentration, expressed as ng/μL of elution volume (example electrophoresis reports are shown in the supplemental materials).

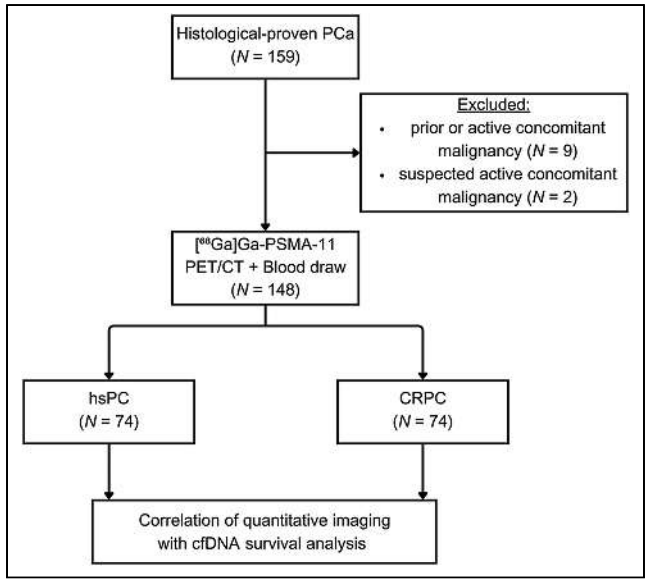

FIGURE 1. CONSORT (Consolidated Standards of Reporting Trials) diagram.

Imaging Protocol and Image Analysis

All scans were performed using a Biograph TruePoint PET/CT scanner (Siemens Healthineers), with patients receiving an intravenous injection of a mean of 184.9 MBq (±18.9 SD) of [^{68}Ga]Ga-PSMA-11. One-hour after injection, static whole-body scans were obtained from the skull base to the upper femur.

First, CT scans were acquired, followed by PET scans, which were reconstructed using a point-spread-function–based algorithm.

Two nuclear medicine physicians analyzed the images using Hybrid 3-dimensional software (version 4.0.0; Hermes Medical Solutions), manually delineating all PSMA-expressing primary and secondary tumor lesions. The PSMA-TV was extracted from all delineated lesions analogously to the calculation of the metabolic tumor volume, and the dominant tumor fraction, contributing most to overall PSMA-TV, was defined (supplemental methods).

Statistical Analysis

Continuous variables are expressed as mean (±SD), and discrete outcomes are expressed as absolute and relative (%) frequencies.

The Shapiro–Wilk test assessed the normality of variables; correlations of variables were assessed using the Spearman coefficient; heteroskedasticity was checked with the Levene test. The difference in mean cfDNA levels according to PSMA-TV quartiles was assessed using the Kruskal–Wallis test, facultatively followed by the Dunn-Bonferroni post hoc test. χ^2 testing assessed associations between dominant tumor lesion fraction and PSMA-TV quartiles. The Kaplan–Meier test estimated OS probabilities; the log-rank test compared survival distributions between groups with high and low cfDNA and PSMA-TV (cutoff, respective median levels). Multivariate Cox regression analysis evaluated the relationship between OS and the binary variables cfDNA concentration and PSMA-TV, which were checked for multicollinearity and proportional hazards with the Belsley–Kuh–Welsch technique and Schoenfeld residuals, respectively. The α-risk

was set at 5% for all analyses, conducted with EasyMedStat software (version 3.24) (supplemental methods).

RESULTS

Clinical Cohort

In total, 148 patients (age, 70.7 ± 7.7 y; prostate-specific antigen [PSA], 107.67 ± 454.10) with histologically proven PCA were recruited. The median follow-up duration was 19 mo (range, 0–49 mo). OS was 90.5% (95% CI, 84.4%–94.2%) at 12 mo and 87.1% (CI, 80.5%–91.6%) at 24 mo. The clinical and demographic characteristics are presented in Table 1.

Associations of cfDNA Levels with Imaging Findings, Demographic Data, and Clinical Data

A weak positive correlation between cfDNA concentration and PSMA-TV was observed in the overall cohort ($r = 0.16$, $P = 0.049$) and the CRPC group ($r = 0.31$, $P = 0.007$) but not in the hsPC group ($r = -0.024$, $P = 0.837$) (Fig. 2).

In the overall cohort, a moderate positive correlation was found between PSA level and PSMA-TV ($r = 0.64$, $P < 0.001$), and weak positive correlations were identified between cfDNA concentration and PSA ($r = 0.23$, $P = 0.01$), lactate dehydrogenase ($r = 0.29$, $P = 0.039$), and age ($r = 0.19$, $P = 0.02$). cfDNA and hemoglobin concentrations ($r = -0.26$, $P = 0.058$) showed a

TABLE 1
Demographic and Clinical Patient Data

Variable	hsPC ($n = 74$)	CRPC ($n = 74$)
Age at inclusion (y)	69.9 ± 7.8 (50.0–85.0)	71.5 ± 7.5 (49.0–85.0)
Tracer dose (MBq)	185.6 ± 20.7 (134.0–300.0)	184.3 ± 17.1 (149.0–263.0)
cfDNA (ng/μL)	0.745 ± 0.654 (0.0009–4.25)	1.04 ± 1.42 (0.0818–9.49)
PSMA-TV (cm^3)	14.2 ± 76.7 (0.0–659.1)	175.5 ± 369.2 (0.0–1,597.7)
PSMA-positive lesion		
Any lesion	51 (68.9%)	64 (86.5%)
Prostate lesion	25 (33.8%)	19 (25.7%)
Lymph node lesion	26 (35.1%)	37 (50.0%)
Bone lesion	14 (18.9%)	48 (64.9%)
Organ lesion	4 (5.4%)	13 (17.6%)
Dominant fraction		
Prostate	19 (25.7%)	5 (6.8%)
Lymph node	22 (29.7%)	19 (25.7%)
Bone	8 (10.8%)	39 (52.7%)
Organ	2 (2.7%)	1 (1.4%)
PSA (ng/dL)*	24.98 ± 105.34 (0.09–761.0)	186.42 ± 618.29 (0.01–3,689.0)
Hemoglobin (g/dL)†	14.06 ± 1.64 (12.1–17.8)	11.96 ± 1.84 (7.8–15.4)
Lactate dehydrogenase (U/L)‡	201.21 ± 47.37 (149.0–312.0)	250.05 ± 229.26 (130.0–1,573.0)
Systemic therapies while PET		
Antihormonal therapies	4 (5.41%)	55 (78.57%)
Cytotoxic therapies	1 (1.35%)	3 (16.67%)
Systemic therapies after PET		
Local	24 (55.8%)	10 (23.3%)
Local + ADT	6 (14.0%)	—
ADT	9 (20.9%)	14 (32.6%)
CHT	1 (2.3%)	2 (4.7%)
CHT + ADT	1 (2.3%)	—
^{177}Lu-PSMA	1 (2.3%)	16 (37.2%)
Study	1 (2.3%)	1 (2.3%)
Mean follow-up (mo)	19.8 ± 13.5 (0.0–47.9)	16.0 ± 14.0 (0.0–49.0)

*n = 14 and 11 data missing in hsPC and CRPC groups, respectively.
†n = 59 and 35 data missing in hsPC and CRPC groups, respectively.
‡n = 60 and 36 data missing in hsPC and CRPC groups, respectively.
ADT = androgen deprivation therapy; CHT = concurrent hormone therapy.
Qualitative data are number and percentage; continuous data are mean ± SD and range. Local disease comprised prostate and seminal vesicle lesions.

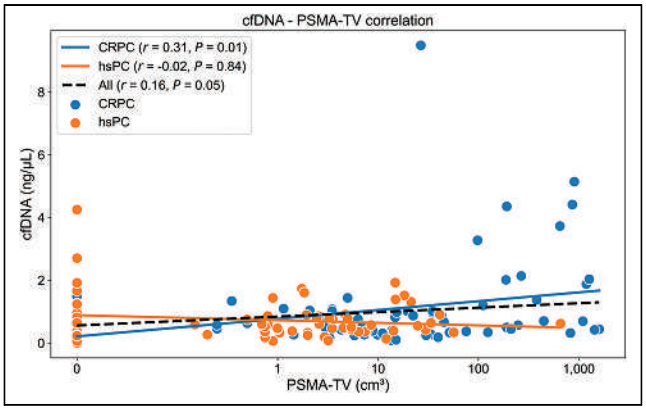

FIGURE 2. Scatterplot illustrating correlations between cfDNA concentrations and PSMA-TV in all, hsPC, and CRPC patients. PSMA-TV levels have been logarithmically transformed ($\log^2 n$) for scale comparability.

weak negative trend, whereas there was a moderate, significant negative correlation between bone PSMA-TV and hemoglobin ($r = -0.56$, $P < 0.001$) (Fig. 3).

Comparison of cfDNA Levels According to PSMA-TV Quartiles

Median cfDNA concentrations across PSMA-TV quartiles did not differ significantly ($P = 0.095$) in the overall cohort, whereas there were significant differences in the CRPC group ($P = 0.012$).

Pairwise post hoc analyses revealed significant cfDNA concentration differences for PSMA-TV quartile 4 (Q4) versus quartile 1 (Q1) ($P = 0.016$) and Q4 versus quartile 2 (Q2) ($P = 0.002$) (Fig. 4; Tables 2 and 3).

Associations of Dominant Tumor Lesion Fraction with PSMA-TV Quartiles

In the overall cohort, the PSMA-TV distribution based on dominant tumor lesion fractions differed significantly ($P < 0.001$). For prostate, Q1 was 2.6%, Q2 was 32.4%, quartile 3 (Q3) was 27.8%, and Q4 was 2.7%. For lymph node, Q1 was 7.9%, Q2 was 48.7%, Q3 was 41.7%, and Q4 was 13.5%. For bone, Q1 was 2.6%, Q2 was 18.9%, Q3 was 27.8%, and Q4 was 78.4%. For organ, Q1 was 0.0%, Q2 was 0.0%, Q3 was 2.8%, and Q4 was 5.4%.

In the CRPC group, the PSMA-TV distribution according to the dominant tumor lesion fractions differed significantly ($P < 0.001$). For prostate, Q1 was 5.3%, Q2 was 21.1%, and Q3–Q4 was 0.0%. For lymph node, Q1 was 21.1%, Q2 was 47.4%, Q3 was 29.4%, and Q4 was 5.3%. For bone, Q1 was 21.1%, Q2 was 31.6%, Q3 was 64.7%, and Q4 was 94.7%. For organ, Q1 was 0.0%, Q2 was 0.0%, Q3 was 5.9%, and Q4 was 0.0% (Fig. 4).

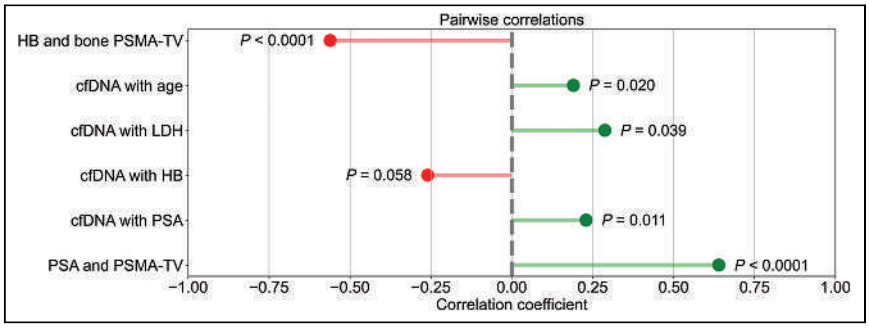

FIGURE 3. Lollipop plots illustrating correlations between cfDNA and PSMA-TV with several variables. HB = hemoglobin.

OS Analysis

Survival distributions of the cfDNA high (12 mo, 86.1%; CI, 75.7–92.3) and low (12 mo, 94.7%; CI, 86.4–98.0) groups did not significantly differ ($P = 0.174$). However, there was a significant difference in survival distributions between PSMA-TV high (12 mo, 82.1%; CI, 71.6–89.0) and low (12 mo, 100.0%; CI, 100.0–100.0) groups ($P < 0.0001$). Likewise, there was a significant difference in survival distributions between the cfDNA high–PSMA-TV high (12 mo, 73.0%; CI, 55.6–84.4), cfDNA high–PSMA-TV low (12 mo, 100.0%; CI, 100.0–100.0), cfDNA low–PSMA-TV high (12 mo, 90.2%; CI, 76.1–96.2), and cfDNA low–PSMA-TV low (12 mo, 100.0%; CI, 100.0–100.0) groups ($P = 0.0003$). In the multivariate Cox regression analysis, there were significant hazard differences between the PSMA-TV high (hazard ratio, 18.89; CI, 2.52–141.68) and low (hazard ratio, 0.0529; CI, 0.00706–0.397) groups ($P = 0.004$) but not between the cfDNA high (hazard ratio, 2.12; CI, 0.833–5.38) and low (hazard ratio, 0.472; CI, 0.186–1.2) groups ($P = 0.12$) (Table 4; Fig. 5).

DISCUSSION

Over the last decade, the arsenal of minimally invasive methods to assess PCA and its trajectory has vastly expanded. Functional imaging using PSMA-ligand PET/CT has been shown to stage PCA with unprecedented, disease management–changing detection rates (*7,8,28,29*) and to yield prognostic and predictive information on therapy responses to local and systemic approaches alike (*26*). In parallel, the quantification of blood-derived cfDNA has been shown repeatedly to be a valuable biomarker of PCA aggressiveness and response to taxane-based chemotherapies (*24,25*).

In this study, we investigated the relationship between cfDNA concentration and PSMA-TV as assessed by [^{68}Ga]Ga-PSMA-11 PET/CT imaging in patients with PCA according to their castration status to evaluate to what extent these methods yield associated measures of tumor burden. Furthermore, we aimed to compare the prognostic value of cfDNA and PSMA-TV measures in terms of OS.

Our findings revealed a weak positive correlation between cfDNA concentrations and PSMA-TV in the overall cohort and the CRPC group. In contrast, neither a significant nor a trending correlation was observed in hsPC patients.

Interestingly, the overall correlation between cfDNA levels and PSMA-TV appeared to be driven primarily by high-volume disease in the CRPC subgroup (Fig. 2), which was composed mainly of osseous metastases (Fig. 4D). This hypothesis is corroborated by the observed significant differences in the CRPC group between high-volume Q4 disease and low-volume Q1 ($P = 0.016$) and Q2 ($P = 0.002$) disease in conjunction with the nonsignificant cfDNA differences in the overall cohort between any PSMA-TV quartiles. Several authors (*17,30*) have described the same dependency of cfDNA levels and high-volume, advanced disease. Chen et al. (*17*) investigated whether cfDNA concentrations and DNA fragment lengths could differentiate between localized and advanced PCA and reported that cfDNA concentrations were elevated in metastatic CRPC patients in comparison to localized disease but did not significantly differ between localized disease and healthy controls. In line with these findings, we did not observe a significant or

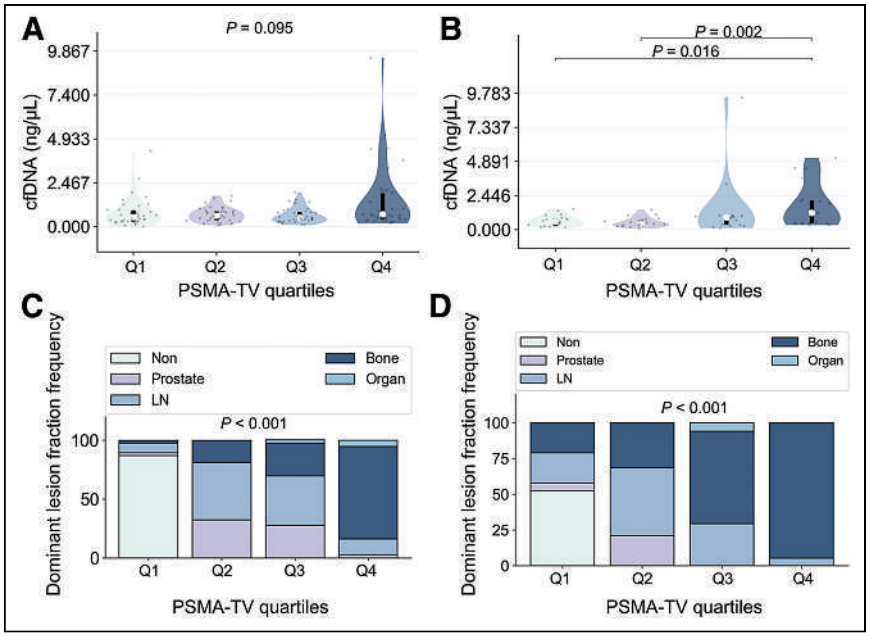

FIGURE 4. Violin plots showing relationship between cfDNA concentrations and PSMA-TV quartiles for all (A) and CRPC (B) patients. Bar plots illustrate frequency of dominant tumor lesion fraction according to PSMA-TV quartiles in all (C) and CRPC (D) patients. LN = lymph node.

tangibly trending association in the hsPC subgroup.

We assume that this observation is caused by the combination of 2 factors. First, the hsPC subgroup had a substantially lower tumor burden than the CRPC subgroup (mean PSMA-TV: hsPC, 14.16 ± 76.68; CRPC, 175.54 ± 369.15), missing the high-volume proportion that appeared to drive the association in the CRPC subgroup. Second, the transition from hsPC to CRPC, which is mediated through various changes in the genetic and posttranscriptional profiles of PCAs and alternative modes of androgen biosynthesis (*2,3*), is clinically associated with more aggressive behavior and higher rates of proliferation. As cfDNA is believed to be shed into the bloodstream by hematopoietic (*11,12*) and tumor cells (*14,15*) through apoptosis and necrosis, this might explain why cfDNA concentrations and PSMA-TV correlate weakly only in our CRPC cohort, as they might more readily outgrow their blood supply.

In conclusion, we reason that cfDNA levels did not correlate with PSMA-TV in

TABLE 2
Unpaired Kruskal–Wallis Distribution of PSMA-TV Quartiles and Corresponding cfDNA Concentrations for Overall and CRPC Patient Groups

			cfDNA								
Group	Quartile	PSMA-TV range (cm^3)	*n*	Mean	Mean 95% CI	SD	Minimum	Q1	Median	Q3	Maximum
All	Q1	0–0.2	38	0.769	0.503–1.03	0.809	0.0009	0.282	0.528	0.919	4.25
	Q2	0.2–3.5	37	0.679	0.54–0.818	0.417	0.0674	0.355	0.61	0.86	1.73
	Q3	3.5–23.6	36	0.632	0.483–0.781	0.44	0.0818	0.352	0.488	0.83	1.92
	Q4	23.6–1,597.7	37	1.48	0.856–2.11	1.88	0.183	0.421	0.694	1.88	9.49
CRPC	Q1	−1.0–3.0	19	0.625	0.431–0.818	0.402	0.126	0.284	0.581	0.822	1.49
	Q2	3.0–14.0	19	0.516	0.345–0.687	0.354	0.0818	0.265	0.403	0.665	1.44
	Q3	14.0–108.0	17	1.32	0.178–2.46	2.22	0.102	0.337	0.871	0.981	9.49
	Q4	108.0–1,598.0	19	1.72	0.965–2.48	1.57	0.32	0.472	1.2	2.09	5.14

TABLE 3
Post Hoc Adjusted Pairwise Table Displaying cfDNA Differences Between PSMA-TV Quartiles in CRPC Group

Quartile	Median difference	Mean difference	Mean difference in 95% CI	*P*
Q1 vs. Q2	0.18	0.11	−0.23 to 0.44	0.451
Q1 vs. Q3	−0.29	−0.7	−2.11 to 0.71	0.38
Q1 vs. Q4	−0.62	−1.1	−2.11 to −0.086	0.016
Q3 vs. Q2	0.47	0.8	−0.6 to 2.21	0.107
Q4 vs. Q2	0.8	1.21	0.2 to 2.21	0.002
Q4 vs. Q3	0.33	0.4	−1.33 to 2.13	0.146

TABLE 4
Multivariate Cox Regression of Relationship Between OS and Binary Explanatory Variables cfDNA and PSMA-TV

Variable	Hazard ratio	95% CI	*P*
cfDNA group			0.12
Low	0.472	0.186–1.2	
High	2.12	0.833–5.38	
PSMA-TV group			0.004
High	18.89	2.52–141.68	
Low	0.0529	0.00706–0.397	

the hsPC group because of their less proliferative nature and lower disease volumes, whereas the weak correlation in the CRPC was driven mainly by the increasingly proliferative and aggressive high-volume, bone-metastasis disease fraction.

To contextualize cfDNA levels with known prognostic demographic and clinical markers of PCA, we explored the association between cfDNA concentrations and age, PSA level, hemoglobin level, and lactate dehydrogenase level. Age and cfDNA level were weakly yet significantly associated, which has been reported by several authors (*31*), suggesting various mechanisms of cfDNA accumulation such as cellular senescence and decreased bloodstream clearance (*32,33*). PSA and cfDNA levels were also weakly associated, as reported by others (*34,35*), probably because of PSA's positive relationship with PSMA-TV (Fig. 3).

Furthermore, lactate dehydrogenase levels, a common signifier of cellular destruction and a long-established negative prognostic biomarker in advanced PCA (*36*), correlated positively with cfDNA levels. Although we did not observe a significant correlation between hemoglobin and cfDNA levels, a negative trend was tangible. We hypothesize that this potential relationship might be caused by increased depression of hematopoietic tissue in advanced, metastatic PCA, because the dominant tumor lesion fraction was contributed mainly by osseous lesions in the higher-tumor quartiles, and there was a moderate negative correlation between bone PSMA-TV and hemoglobin levels (Fig. 3). Next, we conducted a survival analysis to assess the prognostic value of cfDNA and PSMA-TV levels by stratifying the overall cohort into high- and low-level groups using the respective median value as the cutoff. We observed significantly different survival distributions when binarily stratified into high- and low-volume PSMA-TV groups (Fig. 5B), which is in line with Has Simsek et al.'s report of a significant association of total PSMA-derived tumor volume with OS (*37*). However, no significant survival differences were seen in the high- and low-level cfDNA groups (Fig. 5A), which runs contrary to several studies (*17,24*) that reported significant associations between cfDNA levels and OS in men with CRPC undergoing taxane-based chemotherapy. To determine whether there might be a synergistic prognostic biomarker potential, we defined a compound-stratified approach combining the high- and low-cfDNA groups, which yielded no additional prognostic value (Fig. 5C) over a binary PSMA-TV stratifier. A multivariate Cox regression analysis corroborated these findings.

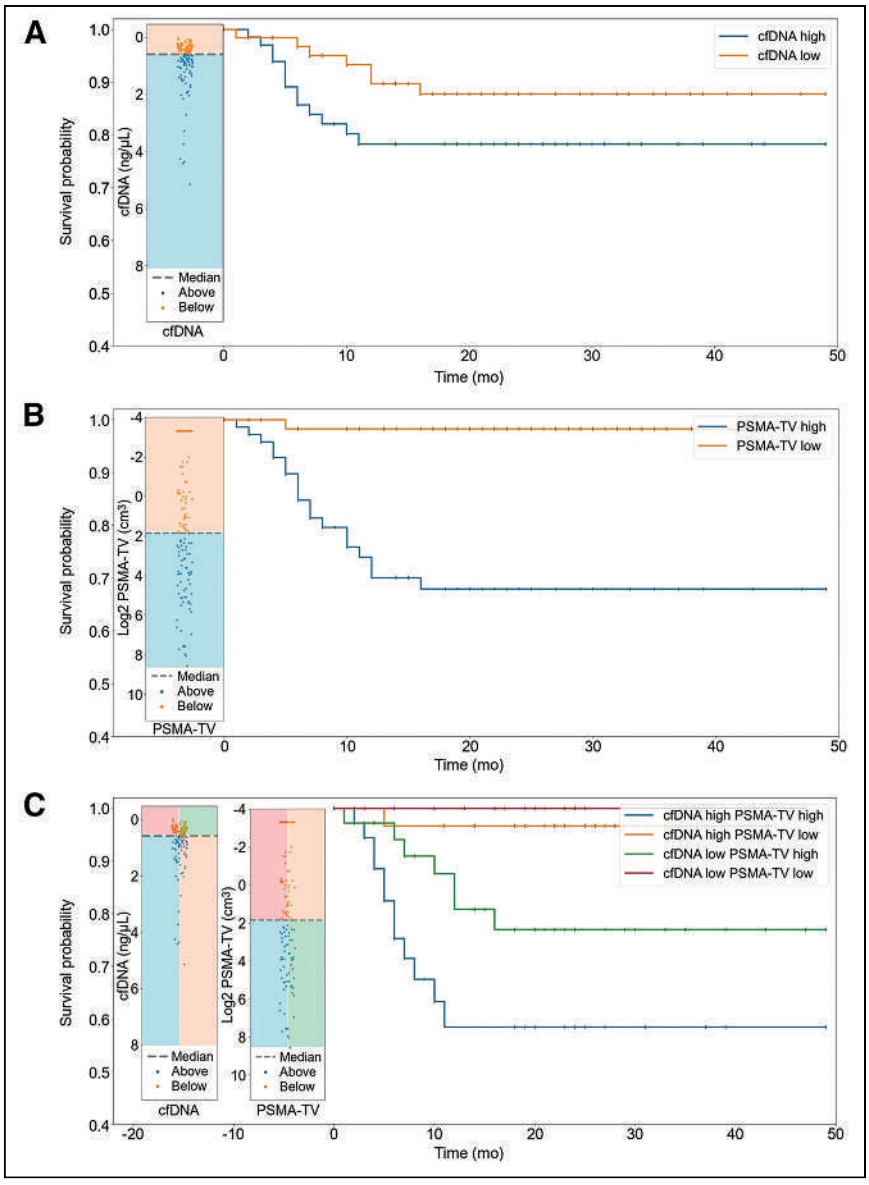

FIGURE 5. Kaplan–Meier curves illustrating survival probabilities between high- and low-cfDNA groups (A), high- and low–PSMA-TV groups (B), and compound-stratified groups (C).

However, as there was a slight trend (Fig. 5B) toward lower survival probabilities in the high-cfDNA group, we hypothesize that our study might be underpowered to detect survival differences based on cfDNA concentrations, as only 19 patients had passed until the date of censoring (May 2023).

Our study had several limitations, and the results should therefore be interpreted with caution. First, since it was a single-center study, we were relying on retrospective and partly incomplete clinical data, which can negatively influence

generalizability. Second, the survival analysis might have been underpowered, as only a fraction of patients had passed until censoring, which also made a castration-status-resolved survival analysis unfeasible. Third, the used metabolic tumor volume analogue PSMA-TV might not prove to be the most robust PSMA-PET parameter for survival analysis in the future, as artificial intelligence–derived measures could potentially yield more applicable metrics going forward.

However, although our study had several limitations, it is important to acknowledge its strengths. Blood sampling immediately before tracer injection ensured optimal biologic synchronicity and thereby the comparability of cfDNA and PET/CT findings. Furthermore, the nonintentional but proportional inclusion of hsPC and CRPC patients enabled a balanced, comparative analysis according to castration status. Last, we mitigated potential biases of record keeping by relying strictly on the central death registry of the national statistics service for the outcome analysis.

Future research will focus on investigating specifically the cfDNA's tumor fraction in relationship to [^{68}Ga]Ga-PSMA-11 PET/CT imaging to explore the degree of mutual information on tumor burden and prognosis, thereby potentially informing future liquid biopsy studies regarding quantitative lower limits of detection and exploring potential synergies of combined diagnostic and prognostic use.

CONCLUSION

Our findings suggest that cfDNA might be a biomarker of advanced, aggressive CRPC but does not reliably reflect total tumor burden. In comparison, [^{68}Ga]Ga-PSMA-11 PET/CT provides a highly granular and prognostic assessment of tumor burden across the spectrum of PCA disease progression.

DISCLOSURE

Financial support was received from the Austrian Federal Ministry for Digital and Economic Affairs; the National Foundation for Research, Technology and Development; and the Christian Doppler Research Association. Siemens Healthineers provided financial and scientific support. No other potential conflict of interest relevant to this article was reported.

KEY POINTS

QUESTION: Are cfDNA concentrations related to [^{68}Ga]Ga-PSMA-11 PET/CT PSMA-TV, and do they provide comparable prognostic information in men with PCA?

PERTINENT FINDINGS: In this single-center [^{68}Ga]Ga-PSMA-11 PET/CT imaging study comparing cfDNA levels with PSMA-TV in 148 men with histologically proven PCA (hsPC, $n = 74$; CRPC, $n = 74$), cfDNA levels were only weakly associated with high-volume CRPC and, contrary to the PSMA-TV, not associated with OS.

IMPLICATIONS FOR PATIENT CARE: These findings suggest that cfDNA might be a biomarker of advanced, aggressive CRPC but does not reliably reflect total tumor burden or prognosis. In comparison, [^{68}Ga]Ga-PSMA-11 PET/CT provides a highly granular and prognostic assessment of tumor burden across the whole spectrum of PCA disease progression.

ACKNOWLEDGMENTS

The Core Facility Genomics and the Core Facility Bioinformatics of CEITEC Masaryk University are gratefully acknowledged for cfDNA extraction and associated analysis.

REFERENCES

1. Sung H, Ferlay J, Siegel RL, et al. Global cancer statistics 2020: GLOBOCAN estimates of incidence and mortality worldwide for 36 cancers in 185 countries. *CA Cancer J Clin.* 2021;71:209–249.
2. Feng Q, He B. Androgen receptor signaling in the development of castration-resistant prostate cancer. *Front Oncol.* 2019;9:858.
3. Watson PA, Arora VK, Sawyers CL. Emerging mechanisms of resistance to androgen receptor inhibitors in prostate cancer. *Nat Rev Cancer.* 2015;15:701–711.
4. Parker C, Castro E, Fizazi K, et al. Prostate cancer: ESMO clinical practice guidelines for diagnosis, treatment and follow-up. *Ann Oncol.* 2020;31:1119–1134.
5. Ghosh A, Heston WDW. Tumor target prostate specific membrane antigen (PSMA) and its regulation in prostate cancer. *J Cell Biochem.* 2004;91:528–539.
6. Jadvar H. Molecular imaging of prostate cancer with PET. *J Nucl Med.* 2013;54:1685–1688.
7. Hope TA, Eiber M, Armstrong WR, et al. Diagnostic accuracy of ^{68}Ga-PSMA-11 PET for pelvic nodal metastasis detection prior to radical prostatectomy and pelvic lymph node dissection: a multicenter prospective phase 3 imaging trial. *JAMA Oncol.* 2021;7:1635–1642.
8. Eissa A, Elsherbiny A, Coelho RF, et al. The role of ^{68}Ga-PSMA PET/CT scan in biochemical recurrence after primary treatment for prostate cancer: a systematic review of the literature. *Minerva Urol Nefrol.* 2018;70:462–478.
9. Pozdnyakov A, Kulanthaivelu R, Bauman G, Ortega C, Veit-Haibach P, Metser U. The impact of PSMA PET on the treatment and outcomes of men with biochemical recurrence of prostate cancer: a systematic review and meta-analysis. *Prostate Cancer Prostatic Dis.* 2023;26:240–248.
10. Casanova-Salas I, Athie A, Boutros PC, et al. Quantitative and qualitative analysis of blood-based liquid biopsies to inform clinical decision-making in prostate cancer. *Eur Urol.* 2021;79:762–771.
11. Stroun M, Lyautey J, Lederrey C, Olson-Sand A, Anker P. About the possible origin and mechanism of circulating DNA apoptosis and active DNA release. *Clin Chim Acta.* 2001;313:139–142.
12. Lui YYN, Chik K-W, Chiu RWK, Ho C-Y, Lam CWK, Lo YMD. Predominant hematopoietic origin of cell-free DNA in plasma and serum after sex-mismatched bone marrow transplantation. *Clin Chem.* 2002;48:421–427.
13. Mouliere F, Thierry AR. The importance of examining the proportion of circulating DNA originating from tumor, microenvironment and normal cells in colorectal cancer patients. *Expert Opin Biol Ther.* 2012;12(suppl 1):S209–S215.
14. Thierry AR, El Messaoudi S, Gahan PB, Anker P, Stroun M. Origins, structures, and functions of circulating DNA in oncology. *Cancer Metastasis Rev.* 2016;35:347–376.
15. Jahr S, Hentze H, Englisch S, et al. DNA fragments in the blood plasma of cancer patients: quantitations and evidence for their origin from apoptotic and necrotic cells. *Cancer Res.* 2001;61:1659–1665.
16. Schwarzenbach H, Hoon DSB, Pantel K. Cell-free nucleic acids as biomarkers in cancer patients. *Nat Rev Cancer.* 2011;11:426–437.
17. Chen E, Cario CL, Leong L, et al. Cell-free DNA concentration and fragment size as a biomarker for prostate cancer. *Sci Rep.* 2021;11:5040.
18. Jung K, Stephan C, Lewandowski M, et al. Increased cell-free DNA in plasma of patients with metastatic spread in prostate cancer. *Cancer Lett.* 2004;205:173–180.
19. Salvi S, Gurioli G, De Giorgi U, et al. Cell-free DNA as a diagnostic marker for cancer: current insights. *Onco Targets Ther.* 2016;9:6549–6559.
20. Ulz P, Belic J, Graf R, et al. Whole-genome plasma sequencing reveals focal amplifications as a driving force in metastatic prostate cancer. *Nat Commun.* 2016;7:12008.
21. Belic J, Graf R, Bauernhofer T, et al. Genomic alterations in plasma DNA from patients with metastasized prostate cancer receiving abiraterone or enzalutamide. *Int J Cancer.* 2018;143:1236–1248.
22. Dillinger T, Sheibani-Tezerji R, Pulverer W, et al. Identification of tumor tissue-derived DNA methylation biomarkers for the detection and therapy response evaluation of metastatic castration resistant prostate cancer in liquid biopsies. *Mol Cancer.* 2022;21:7.
23. Fettke H, Ng N, Hauser C, et al. Circulating tumor DNA and outcomes with lutetium-PSMA in advanced prostate cancer: preliminary results from an Australian study [abstract]. *Cancer Res.* 2022;82(suppl):532.

24. Mehra N, Dolling D, Sumanasuriya S, et al. Plasma cell-free DNA concentration and outcomes from taxane therapy in metastatic castration-resistant prostate cancer from two phase III trials (FIRSTANA and PROSELICA). *Eur Urol.* 2018; 74:283–291.
25. Kienel A, Porres D, Heidenreich A, Pfister D. cfDNA as a prognostic marker of response to taxane based chemotherapy in patients with prostate cancer. *J Urol.* 2015;194:966–971.
26. Alongi P, Laudicella R, Lanzafame H, et al. PSMA and choline PET for the assessment of response to therapy and survival outcomes in prostate cancer patients: a systematic review from the literature. *Cancers (Basel).* 2022;14:1770.
27. Kwee S, Song MA, Cheng I, Loo L, Tiirikainen M. Measurement of circulating cell-free DNA in relation to ^{18}F-fluorocholine PET/CT imaging in chemotherapy-treated advanced prostate cancer. *Clin Transl Sci.* 2012;5:65–70.
28. Combes AD, Palma CA, Calopedos R, et al. PSMA PET-CT in the diagnosis and staging of prostate cancer. *Diagnostics (Basel).* 2022;12:2594.
29. Pozdnyakov A, Kulanthaivelu R, Bauman G, Ortega C, Veit-Haibach P, Metser U. The impact of PSMA PET on the treatment and outcomes of men with biochemical recurrence of prostate cancer: a systematic review and meta-analysis. *Prostate Cancer Prostatic Dis.* 2023;26:240–248.
30. Schweizer MT, Gulati R, Beightol M, et al. Clinical determinants for successful circulating tumor DNA analysis in prostate cancer. *Prostate.* 2019;79:701–708.
31. Aucamp J, Bronkhorst AJ, Badenhorst CPS, Pretorius PJ. The diverse origins of circulating cell-free DNA in the human body: a critical re-evaluation of the literature. *Biol Rev Camb Philos Soc.* 2018;93:1649–1683.
32. Jylhävä J, Kotipelto T, Raitala A, Jylhä M, Hervonen A, Hurme M. Aging is associated with quantitative and qualitative changes in circulating cell-free DNA: the Vitality 90+ study. *Mech Ageing Dev.* 2011;132:20–26.
33. Jylhävä J, Nevalainen T, Marttila S, Jylhä M, Hervonen A, Hurme M. Characterization of the role of distinct plasma cell-free DNA species in age-associated inflammation and frailty. *Aging Cell.* 2013;12:388–397.
34. Feng J, Gang F, Li X, et al. Plasma cell-free DNA and its DNA integrity as biomarker to distinguish prostate cancer from benign prostatic hyperplasia in patients with increased serum prostate-specific antigen. *Int Urol Nephrol.* 2013;45:1023–1028.
35. Hegemann M, Stenzl A, Bedke J, Chi KN, Black PC, Todenhöfer T. Liquid biopsy: ready to guide therapy in advanced prostate cancer? *BJU Int.* 2016;118: 855–863.
36. Halabi S, Small EJ, Kantoff PW, et al. Prognostic model for predicting survival in men with hormone-refractory metastatic prostate cancer. *J Clin Oncol.* 2003;21: 1232–1237.
37. Has Simsek D, Kuyumcu S, Karadogan S, et al. Can PSMA-based tumor burden predict response to docetaxel treatment in metastatic castration-resistant prostate cancer? *Ann Nucl Med.* 2021;35:680–690.

Renal and Multiorgan Safety of ^{177}Lu-PSMA-617 in Patients with Metastatic Castration-Resistant Prostate Cancer in the VISION Dosimetry Substudy

Ken Herrmann[1], Kambiz Rahbar[2], Matthias Eiber[3], Richard Sparks[4], Nicholas Baca[4], Bernd J. Krause[5], Michael Lassmann[6], Walter Jentzen[1], Jun Tang[7], Daniela Chicco[8], Patrick Klein[9], Lars Blumenstein[10], Jean-René Basque[11], and Jens Kurth[5]

[1]*Department of Nuclear Medicine, University of Duisburg-Essen and German Cancer Consortium, University Hospital Essen, Essen, Germany;* [2]*Department of Nuclear Medicine, University Hospital Münster, Münster, Germany;* [3]*Technical University of Munich, Munich, Germany;* [4]*CDE Dosimetry Services, Knoxville, Tennessee;* [5]*Department of Nuclear Medicine, Rostock University Medical Center, Rostock, Germany;* [6]*Department of Nuclear Medicine, University Hospital Würzburg, Würzburg, Germany;* [7]*Novartis Pharmaceuticals Corporation, East Hanover, New Jersey;* [8]*Advanced Accelerator Applications, a Novartis Company, Turin, Italy;* [9]*Novartis Institutes for BioMedical Research, East Hanover, New Jersey;* [10]*Novartis Institutes for BioMedical Research, Basel, Switzerland; and* [11]*Novartis Pharma AG, Basel, Switzerland*

In the VISION trial, [^{177}Lu]Lu-PSMA-617 (^{177}Lu-PSMA-617) plus protocol-permitted standard of care significantly improved overall survival and radiographic progression-free survival compared with standard of care alone in patients with prostate-specific membrane antigen–positive metastatic castration-resistant prostate cancer. This VISION dosimetry substudy quantified absorbed doses of ^{177}Lu-PSMA-617 in the kidneys and other organs. **Methods:** Participants were a separate cohort of 30 nonrandomized patients receiving standard of care plus ^{177}Lu-PSMA-617 at 7.4 GBq per cycle for up to 6 cycles. Blood samples, whole-body conjugate planar image scintigraphy, and abdominal SPECT/CT images were collected. SPECT/CT images were collected at 2, 24, 48, and 168 h after administration in cycle 1 and at a single time point 48 h after administration in cycles 2–6. Outcomes were absorbed dose per unit activity per cycle and cumulative absorbed dose over all cycles. Cumulative absorbed doses were predicted by extrapolation from cycle 1, and calculation of observed values was based on measurements of cycle 1 and cycles 2–6. Safety was also assessed. **Results:** Mean (±SD) absorbed doses per cycle in the kidneys were 0.43 ± 0.16 Gy/GBq in cycle 1 and 0.44 ± 0.21 Gy/GBq in cycles 2–6. The observed and predicted 6-cycle cumulative absorbed doses in the kidneys were 15 ± 6 and 19 ± 7 Gy, respectively. Observed and predicted cumulative absorbed doses were similar in other at-risk organs. Safety findings were consistent with those in the VISION study; no patients experienced renal treatment-emergent adverse events of a grade higher than 3. **Conclusion:** The renal cumulative absorbed ^{177}Lu-PSMA-617 dose was below the established limit. ^{177}Lu-PSMA-617 had a good overall safety profile, and low renal radiotoxicity was not a safety concern. Cumulative absorbed doses in at-risk organs over multiple cycles can be predicted by extrapolation from cycle 1 data in patients with metastatic castration-resistant prostate cancer receiving ^{177}Lu-PSMA-617.

Key Words: ^{177}Lu; prostate-specific membrane antigen; metastatic castration-resistant prostate cancer; radioligand therapy

J Nucl Med 2024; 65:71–78
DOI: 10.2967/jnumed.123.265448

Radioligand therapy selectively targets cell-surface proteins expressed on cancer cells and spares most normal tissues (*1*). Prostate-specific membrane antigen (PSMA) is highly expressed in prostate cancer cells, with limited expression in nonprostate cancer cells (*2–4*). Radioligand therapies targeting PSMA are promising new treatments for patients with metastatic castration-resistant prostate cancer (mCRPC) (*5–7*).

[^{177}Lu]Lu-PSMA-617 (^{177}Lu-PSMA-617) is a high-affinity PSMA-targeted small-molecule radioligand therapy that delivers β-particle radiation specifically to prostate cancer lesions (*8–10*). The randomized, open-label, pivotal, phase 3 VISION study showed that ^{177}Lu-PSMA-617 prolonged radiographic progression-free survival (hazard ratio, 0.40; 99.2% CI, 0.29–0.57; $P < 0.001$) and overall survival (hazard ratio, 0.62; 95% CI, 0.52–0.74; $P < 0.001$) when added to protocol-permitted standard of care in patients with advanced PSMA-positive mCRPC (*11*). The incidence of adverse events of grade 3 or above was higher with ^{177}Lu-PSMA-617 than without, but health-related quality of life and pain were not adversely affected (*11*).

The kidneys have long been recognized as dose-limiting organs for therapeutic radiopharmaceuticals, with a historical cumulative absorbed dose limit of 23 Gy (*12*,*13*). This limit is based on external beam radiation therapy (EBRT) and has not been revised on the basis of experience with systemic radiopharmaceuticals. In patients receiving ^{177}Lu-PSMA-617, the kidneys are exposed to radiation because urinary excretion is the principal route of elimination and because PSMA is expressed in proximal tubular cells (*14*). Other organs at risk of radiotoxicity with ^{177}Lu-PSMA-617 include the lacrimal glands, salivary glands, and red marrow (*15–17*). The lacrimal and salivary glands are at risk because of physiologic uptake due to a combination of PSMA-specific and nonspecific mechanisms (*18*,*19*). Red marrow is at risk because reserve is often depleted by previous

Received Jan. 31, 2023; revision accepted Oct. 10, 2023.
For correspondence or reprints, contact Ken Herrmann (ken.herrmann@uk-essen.de).
Published online Nov. 30, 2023.

cytotoxic therapies (*20*) and radiation-induced myelosuppression can occur. Characterizing the biodistribution of ^{177}Lu-PSMA-617 in a dosimetry study is therefore crucial for informed assessment of the risk of radiation-induced adverse events (*13*,*21*). Similar to EBRT, dosimetry studies of radiopharmaceutical therapies should be performed to improve the understanding of the effects of radiation exposure. Some countries have therefore made dosimetry studies a legal requirement (*22*,*23*).

The VISION study included a dosimetry substudy that aimed to enhance the assessment of the safety profile of ^{177}Lu-PSMA-617 and to contextualize exposure levels against historical EBRT limits in patients with mCRPC. We used a simplified dosimetry approach based on conventional multiple-time-point imaging in cycle 1 and single-time-point imaging in cycles 2–6 (*24*). We report absorbed radiation doses in kidneys and other organs, as well as safety and tolerability findings and pharmacokinetic data. We also investigated whether cumulative absorbed radiation doses over multiple cycles of ^{177}Lu-PSMA-617 treatment can be predicted by extrapolation from cycle 1 dosimetry data.

MATERIALS AND METHODS

Patients

A separate nonrandomized cohort of 30 eligible patients was enrolled into the dosimetry substudy at 4 sites in Germany. The patient selection criteria were the same as for the pivotal VISION study (*11*). Full details are provided in the supplemental materials (available at http://jnm.snmjournals.org).

Treatment

In addition to protocol-permitted standard of care, all patients in the substudy received ^{177}Lu-PSMA-617 (7.4 GBq, 200 mCi) per cycle every 6 wk for up to 6 cycles. The treatment regimen and patient management were identical to those in the pivotal VISION study (*11*).

Objectives

The primary objectives were to conduct whole-body and organ dosimetry of ^{177}Lu-PSMA-617 and to characterize its biodistribution. We investigated whether cumulative absorbed doses extrapolated from cycle 1 dosimetry data could predict observed cumulative absorbed doses for multiple cycles of ^{177}Lu-PSMA-617 treatment. Analyses focused on organs at risk of radiotoxicity from ^{177}Lu-PSMA-617 (kidneys, lacrimal glands, salivary glands, and red marrow).

The secondary objectives were to evaluate the safety and tolerability of ^{177}Lu-PSMA-617, to evaluate cardiac function during treatment, to define the pharmacokinetic profile of ^{177}Lu-PSMA-617, and to characterize the radiometabolites of ^{177}Lu-PSMA-617 in urine.

Results were analyzed descriptively and separately from those of the pivotal VISION study.

Image Acquisition and Dosimetry

Whole-body conjugate planar image scintigraphy and abdominal SPECT/CT images were collected at 2, 24, 48, and 168 h after administration in cycle 1 and at a single time point 48 h after administration in cycles 2–6 (Fig. 1). This was selected as the most convenient single time point lying in the center of the complete curve collected in cycle 1. Technical details of the used imaging systems and applied acquisition and reconstruction protocols are shown in Supplemental Table 1 (*25*). Whole-body and specific organ-absorbed doses (*26*–*28*) for cycles 2–6 were derived using single-time-point data and individual time–activity curves generated for cycle 1. Blood samples were collected in cycle 1 only, at time points immediately before administration, immediately after administration (assigned as 1 min), and at approximately 20 min and 1, 2, 4, 24, 48, 72, and 144 h after administration (Fig. 1). Red marrow–absorbed doses were based on an assay of blood samples and the remainder-of-body activity from cycle 1 using the standard blood-based methodology (*29*). Absorbed doses were estimated using OLINDA/EXM software version 2.2.2 (Hermes Medical Solutions). Lacrimal gland dosimetry used the MIRD/Radiation Dose Assessment Resource method (*17*,*30*–*37*).

Dosimetry outcomes were absorbed dose per unit activity (Gy/GBq) during cycle 1 and cycles 2–6 and predicted and observed cumulative absorbed dose (Gy) over all 6 cycles (44.4 GBq). Cumulative absorbed doses were predicted by extrapolation from multiple-time-point cycle 1 data in all patients, and calculation of observed values was based on multiple-time-point cycle 1 data and measurements of additional single-time-point cycles 2–6. Predicted and observed cumulative absorbed doses were compared statistically using Hotelling T-squared tests with Bonferroni adjustment for multiple comparisons. Full details are provided in the supplemental materials.

Safety and Tolerability

Treatment-emergent adverse events (TEAEs) were monitored throughout the substudy and were defined as those occurring from the first administration of treatment up to and including 30 d after the last administration or before receipt of subsequent anticancer treatment, whichever occurred first. TEAEs in the renal toxicity safety topic of interest were increased blood creatinine level, acute kidney injury, increased blood urea level, proteinuria, kidney failure, and decreased urine output. TEAEs in the nausea and vomiting safety topic of interest were nausea, vomiting, and retching. TEAEs in the bone marrow suppression safety topic of interest were anemia, thrombocytopenia, lymphopenia, leukopenia, neutropenia, pancytopenia, febrile neutropenia, bicytopenia, bone marrow failure, and normocytic anemia. TEAEs in the dry mouth safety topic of interest were dry mouth, aptyalism, dry lips, and dry throat. TEAEs in the hepatotoxicity safety topic of interest were increased aspartate aminotransferase, increased blood alkaline phosphatase, hypoalbuminemia, increased alanine aminotransferase, hyperbilirubinemia, ascites, increased γ-glutamyltransferase, acute hepatic failure, cholestasis, hepatic encephalopathy, hepatic failure, hepatic lesion, hepatitis, hepatocellular injury, increased international normalized ratio, jaundice, and increased transaminases. TEAEs were assessed using the Common Terminology Criteria for Adverse Events (CTCAE) version 5.0.

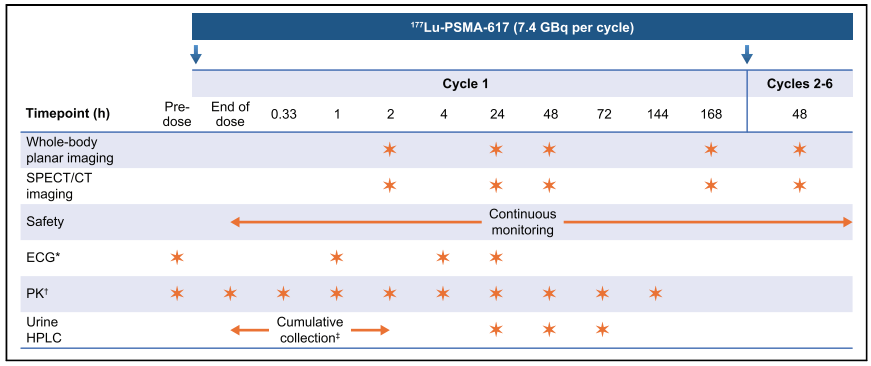

FIGURE 1. Study design and assessments. Asterisk shows that blood pressure was measured before each electrocardiogram (ECG). Dagger symbol is blood pharmacokinetic (PK) samples that were collected after ECGs when time points overlapped. Double dagger shows whole urine collection that was required between end of dose and 2 h after dose before first image. HPLC = high-performance liquid chromatography.

Study Conduct

The VISION study was registered on ClinicalTrials.gov (NCT03511664) and was conducted in accordance with the principles of the Declaration of Helsinki, the International Conference on Harmonization Good Clinical Practice, and applicable local regulations. Independent ethics review boards approved the trial protocol at each trial site. All patients in the pivotal study and the present dosimetry substudy signed written informed consent forms before enrollment.

RESULTS

Patients

All 30 enrolled patients received at least 1 cycle of ^{177}Lu-PSMA-617 plus standard of care. In cycle 1, multiple-time-point dosimetry was performed in 29 patients—1 patient received ^{177}Lu-PSMA-617 but was unable to tolerate the imaging procedures required for dosimetry because of intense bone pain. One patient underwent imaging at 24 h in cycle 2 for clinical reasons and then at 48 h in all subsequent cycles. In addition, single-time-point dosimetry was performed in 21 patients who completed cycles 2 and 3, in 19 patients who completed cycle 4, in 13 patients who completed cycle 5, and in 10 patients who completed all 6 cycles.

A total of 18 patients (60.0%) discontinued all study treatments. Reasons for discontinuation of ^{177}Lu-PSMA-617 were disease progression ($n = 7$), investigator decision ($n = 4$), adverse events ($n = 3$), withdrawal of consent to treatment ($n = 2$), death ($n = 2$), lack of clinical benefit ($n = 1$), and other ($n = 1$).

Dosimetry

Absorbed Doses per Cycle. In cycle 1, absorbed doses per unit activity among at-risk organs were highest in the lacrimal and salivary glands, with mean values ± SD of 2.10 ± 0.47 and 0.63 ± 0.36 Gy/GBq, respectively, followed by the kidneys at 0.43 ± 0.16 Gy/GBq and red marrow at 0.035 ± 0.020 Gy/GBq (Table 1). Figure 2 shows representative SPECT/CT images of the kidneys

TABLE 1
Absorbed Doses per Unit Activity per Cycle

	Cycle 1*		Cycles 2–6*	
Organ or tissue	Mean	SD	Mean	SD
Lacrimal glands	**2.1 (1.2–3.2)**	**0.47**	**1.8 (0.70–3.9)**	**0.61**
Salivary glands	**0.63 (0.22–1.5)**	**0.36**	**0.63 (0.23–1.4)**	**0.30**
Left colon	0.58 (0.33–1.0)	0.14	0.58 (0.32–0.73)	0.11
Rectum	0.56 (0.32–1.1)	0.14	0.55 (0.31–0.70)	0.10
Kidneys	**0.43 (0.22–0.83)**	**0.16**	**0.44 (0.17–1.0)**	**0.21**
Right colon	0.32 (0.18–0.60)	0.08	0.31 (0.18–0.40)	0.06
Urinary bladder wall	0.32 (0.29–0.43)	0.03	0.33 (0.29–0.43)	0.03
Thyroid	0.26 (0.09–1.69)	0.37	0.21 (0.06–1.6)	0.25
Heart wall	0.17 (0.03–0.52)	0.12	0.15 (0.05–0.37)	0.08
Lungs	0.11 (0.03–0.57)	0.11	0.06 (0.02–0.17)	0.03
Liver	0.090 (0.043–0.220)	0.044	0.11 (0.037–0.26)	0.054
Small intestine	0.071 (0.043–0.220)	0.031	0.065 (0.043–0.083)	0.010
Spleen	0.067 (0.031–0.140)	0.027	0.095 (0.028–0.32)	0.056
Osteogenic cells	0.036 (0.02–0.170)	0.028	0.030 (0.016–0.062)	0.009
Red marrow	**0.035 (0.020–0.13)**	**0.020**	**0.031 (0.021–0.051)**	**0.007**
Adrenal glands	0.033 (0.016–0.15)	0.025	0.028 (0.014–0.060)	0.009
Gallbladder wall	0.028 (0.013–0.15)	0.026	0.023 (0.012–0.055)	0.008
Pancreas	0.027 (0.012–0.15)	0.026	0.021 (0.008–0.051)	0.008
Prostate	0.027 (0.013–0.15)	0.026	0.021 (0.007–0.050)	0.008
Esophagus	0.025 (0.010–0.15)	0.026	0.019 (0.006–0.050)	0.008
Stomach wall	0.025 (0.011–0.15)	0.026	0.019 (0.006–0.050)	0.008
Thymus	0.025 (0.010–0.15)	0.026	0.018 (0.004–0.049)	0.008
Testes	0.023 (0.010–0.14)	0.025	0.017 (0.003–0.046)	0.008
Eyes	0.022 (0.009–0.14)	0.024	0.016 (0.003–0.045)	0.008
Brain	0.007 (0.002–0.025)	0.005	0.006 (0.003–0.028)	0.003
Whole body	0.037 (0.019–0.170)	0.027	0.031 (0.018–0.065)	0.009

*Dosimetry data were available for 29 patients at cycle 1, 21 patients at cycles 2 and 3, 19 patients at cycle 4, 13 patients at cycle 5, and 10 patients at cycle 6.

Bold font indicates organs considered to be at particular risk of radiotoxicity. Data are Gy/GBq.

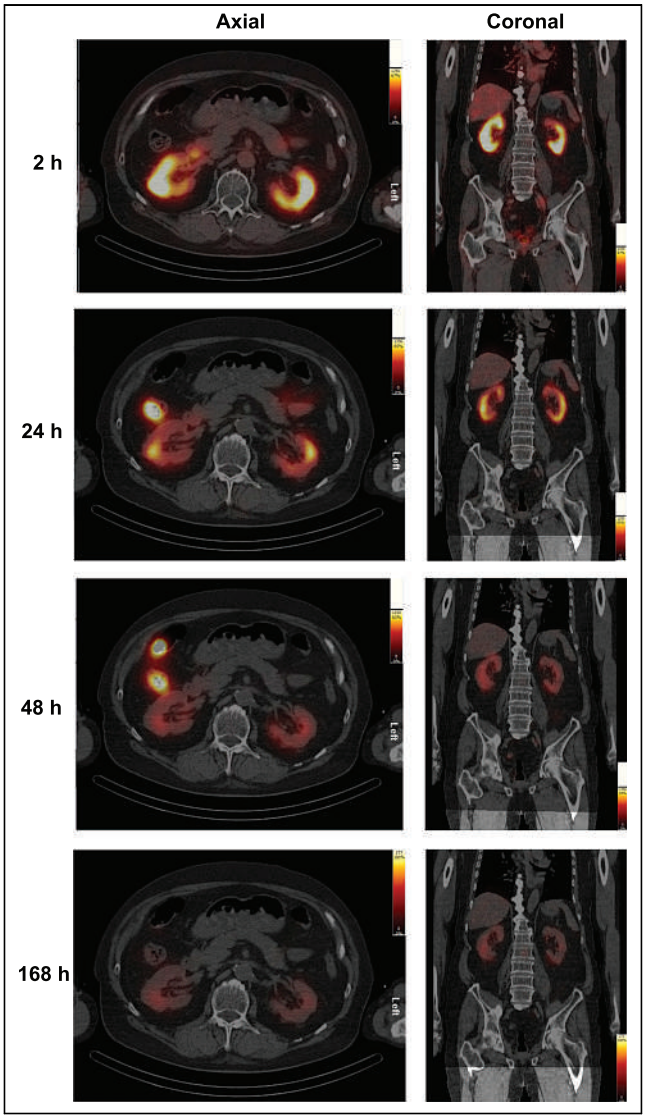

FIGURE 2. Representative SPECT/CT images show kidneys of a patient at various times during cycle 1 of ^{177}Lu-PSMA-617 treatment. SPECT images (black/red/yellow scale) show uptake of ^{177}Lu-PSMA-617 in kidneys (axial and coronal orientations) at 2, 24, 48, and 168 h during cycle 1. Underlaid CT images (gray) are scaled equally. Both image types are maximum-intensity projections.

of a patient taken at 4 time points during cycle 1. Supplemental Figure 1 shows representative contouring of the kidneys on SPECT/CT images taken during cycle 1.

In cycles 2–6, absorbed doses per unit activity per cycle among at-risk organs were similar to those in cycle 1, with the highest mean values in the lacrimal and salivary glands at 1.80 ± 0.61 and 0.63 ± 0.30 Gy/GBq, respectively, followed by the kidneys at 0.44 ± 0.21 Gy/GBq and red marrow at 0.031 ± 0.007 Gy/GBq (Table 1).

Table 1 shows absorbed doses in all organs and tissues assessed. Average percent injected activity is shown in Supplemental Figure 2 and Supplemental Table 2. The normalized number of disintegrations in specific organs is shown in Supplemental Table 3.

Cumulative Absorbed Doses. Predicted 6-cycle cumulative absorbed doses based on extrapolation of cycle 1 data in 29 patients were 92.0 ± 21.0 Gy in the lacrimal glands, 28.0 ± 16.0 Gy in the salivary glands, 19.0 ± 7.3 Gy in the kidneys, and 1.5 ± 0.9 Gy in the red marrow (Table 2). Observed 6-cycle cumulative absorbed doses in the 10 patients who completed all 6 cycles were 77 ± 23 Gy in the lacrimal glands, 30 ± 15 Gy in the salivary glands, 15 ± 6 Gy in the kidneys, and 1.30 ± 0.33 Gy in the red marrow (Table 2). Table 2 shows cumulative doses in all organs and tissues assessed. Supplemental Table 4 shows predicted and observed cumulative absorbed doses in the 10 patients who completed all 6 cycles of treatment.

Predicted versus observed cumulative absorbed doses per cycle in at-risk organs were similar to each other at both the group level and the individual patient level (Fig. 3; Supplemental Fig. 3). For each cycle in cycles 2–6, the predicted values were similar to observed values, independent of the number of patients with data for subsequent cycles. Statistical comparisons of predicted versus observed cumulative doses across all 4 at-risk organs revealed no significant differences (P = 0.19–0.54 in cycles 2–6). Predicted values were generally higher in later treatment cycles compared with the observed values (Fig. 3; Table 2).

Safety and Tolerability

The median duration of ^{177}Lu-PSMA-617 exposure was 5.52 mo (range, 1.4–9.0 mo), with patients receiving a median of 4 cycles and a mean total administered activity of 28.7 ± 10.5 GBq. Across all treatment cycles, similar proportions of patients in this substudy experienced TEAEs as in the pivotal VISION study, including severe, serious, and drug-related adverse events (Supplemental Table 5). TEAEs grouped as safety topics of interest are shown in Table 3. Renal toxicity was reported in 5 of 30 patients (16.7%), of whom 3 of 30 (10%) had increased creatinine levels. The mean cumulative absorbed dose in the kidneys over 6 cycles for patients with reported renal toxicity was 24.42 ± 7.41 Gy versus 17.55 ± 7.80 Gy in those without (based on observed dose when available and on predicted dose when observed dose was not available). No patients experienced renal TEAEs of grade 3 or higher. TEAEs were most frequent in the bone marrow suppression grouping, occurring in 11 of 30 patients (36.7%), of whom 2 of 30 patients (6.7%) had grade 4 events (lymphopenia and thrombocytopenia), 1 of 30 patients (3.3%) had grade 3 events (leukopenia and thrombocytopenia), and 2 of 30 patients (6.7%) had grade 3 events (anemia). TEAEs were also frequent in the nausea and vomiting grouping, occurring in 11 of 30 patients (36.7%) each, followed by fatigue in 6 of 30 patients (20%) and dry mouth in 5 of 30 patients (16.7%) (Table 3).

Toxicity Adverse Events in Cycle 1. During cycle 1, 6 of 30 patients (20%) had 1 or more hematologic adverse events of CTCAE grade 2 or higher, based on worsening from baseline (Supplemental Table 6). The most common of these was anemia in 5 of 30 patients (16.7%). No patients had thrombocytopenia of CTCAE grade 2 or higher.

During cycle 1, 2 patients (6.7%) had salivary gland adverse events, limited to CTCAE grade 1. No patients had lacrimal gland adverse events or renal toxicity during cycle 1 (Supplemental Table 6).

Cardiac Safety. Low uptake of ^{177}Lu-PSMA-617 in the heart wall was observed, with an absorbed dose per unit activity of 0.17 ± 0.12 Gy/GBq in cycle 1 (Table 1).

Least-square mean changes in the corrected Fridericia QT interval from baseline were minimal, ranging from +2.1 to −5.2 ms during the first 24 h of treatment (Supplemental Fig. 4A). Least-square

TABLE 2
Cumulative Absorbed Doses Over 6 Cycles

Organ or tissue	Predicted from cycle 1 data (n = 29)		Observed (n = 10)		
	Mean	SD	Mean	SD	Relative difference
Lacrimal glands	**92 (54–140)**	**21**	**77 (53–115)**	**23**	**+19.5%**
Salivary glands	**28 (10–68)**	**16**	**30 (11–58)**	**15**	**−6.7%**
Left colon	26 (15–45)	6.0	24 (14–29)	4.8	+8.3%
Rectum	25 (14–47)	6.2	23 (13–28)	4.6	+8.7%
Kidneys	**19 (10–37)**	**7.3**	**15 (9.1–29)**	**5.8**	**+26.7%**
Right colon	14 (8.1–27)	3.4	13 (8.0–16)	2.5	+7.7%
Urinary bladder wall	14 (13–19)	1.1	14 (13–15)	0.58	0.0%
Thyroid	11 (3.8–75)	16	9.8 (3.3–48)	14	+12.2%
Heart wall	7.8 (1.4–23)	5.2	5.7 (2.8–11)	3.0	+36.8%
Lungs	4.7 (1.3–25)	4.9	2.5 (1.2–5.4)	1.3	+88.0%
Liver	4.0 (1.9–9.6)	2.0	4.0 (2.1–9.3)	2.1	0.0%
Small intestine	3.1 (1.9–9.9)	1.4	2.7 (2.2–3.1)	0.36	+14.8%
Spleen	3.0 (1.4–6.0)	1.2	3.4 (1.4–8.0)	2.3	−11.8%
Osteogenic cells	1.6 (0.88–7.6)	1.3	1.3 (0.85–2.2)	0.44	+23.1%
Adrenal glands	1.5 (0.70–6.8)	1.1	1.1 (0.62–2.0)	0.41	+36.4%
Red marrow*	**1.5 (0.87–5.9)**	**0.9**	**1.3 (0.93–1.8)**	**0.33**	**+15.4%**
Gallbladder wall	1.2 (0.56–6.7)	1.1	0.96 (0.52–1.8)	0.40	+25.0%
Pancreas	1.2 (0.55–6.7)	1.1	0.90 (0.50–1.8)	0.38	+33.3%
Prostate	1.2 (0.59–6.7)	1.1	0.91 (0.54–1.8)	0.36	+31.9%
Esophagus	1.1 (0.46–6.5)	1.1	0.81 (0.42–1.7)	0.39	+35.8%
Stomach wall	1.1 (0.48–6.6)	1.1	0.83 (0.44–1.7)	0.38	+32.5%
Thymus	1.1 (0.45–6.5)	1.1	0.78 (0.41–1.7)	0.39	+41.0%
Testes	1.0 (0.43–6.3)	1.1	0.74 (0.39–1.6)	0.36	+35.1%
Eyes	1.0 (0.40–6.1)	1.1	0.72 (0.36–1.6)	0.36	+38.9%
Brain	0.3 (0.08–1.1)	0.2	0.27 (0.17–0.41)	0.08	+11.1%
Whole body	1.6 (0.86–7.3)	1.2	1.3 (0.79–2.2)	0.42	+23.1%

*Cycles 2–6 observed data were based on blood samples and remainder-of-body activity from cycle 1 scaled according to respective imaging data. For cycle 6, total injected activity was 44.4 GBq.

Data are Gy. Bold font indicates organs considered to be at particular risk of radiotoxicity.

mean changes in the heart rate from baseline were also minimal, ranging from −0.8 to +3.8 bpm during the first 24 h of treatment (Supplemental Fig. 4B).

Pharmacokinetics

Plasma Profile. After infusion, the peak ^{177}Lu-PSMA-617 plasma concentration was generally reached approximately 20 min after administration (median maximum time, 0.38 h) and was followed by a biexponential decline (Supplemental Fig. 5).

The geometric mean half-life of ^{177}Lu-PSMA-617 from the circulation was approximately 41.6 h (geometric mean coefficient of variation, 68.8%) (Supplemental Table 7).

Urinary Metabolites. Radioactivity in urine at 72 h was decreased by approximately 93% compared with the 0- to 2-h time point. The proportion of intact ^{177}Lu-PSMA-617 in the urine decreased from approximately 95% of total urine radioactivity at 0–2 h to 92% at 24 h, 83% at 48 h, and 68% at 72 h, with radiometabolites accounting for the remaining total radioactivity. The most common radiometabolites in urine were M1, M3, and M4, with a total of 9 peaks (Supplemental Fig. 6).

DISCUSSION

The cumulative dose limit of 23 Gy for the kidneys has been historically derived for EBRT and subsequently applied to radiopharmaceutical use (*12*,*13*). In this dosimetry substudy of the pivotal phase 3 VISION study of ^{177}Lu-PSMA-617 in patients with mCRPC, absorbed doses in all cycles were within accepted limits in the kidneys and other organs at the highest risk of radiotoxicity. Absorbed doses per cycle were highest in the lacrimal and salivary glands, followed by the kidneys and the red marrow. The observed renal cumulative absorbed dose was 15 Gy at cycle 6, which was below the historical limit of 23 Gy (*12*,*13*). TEAEs affecting the kidneys and other organs at risk of radiotoxicity were infrequent and generally of low to moderate severity.

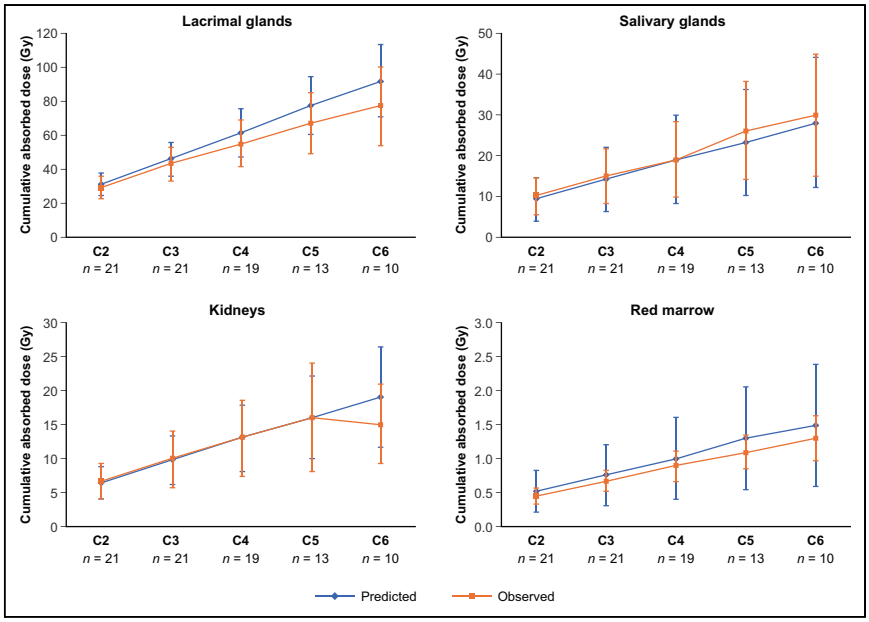

FIGURE 3. Predicted versus observed cumulative absorbed doses per cycle in at-risk organs. Injected activity: cycle 2, 14.8 GBq; cycle 3, 22.2 GBq; cycle 4, 29.6 GBq; cycle 5, 37.0 GBq; cycle 6, 44.4 GBq.

For each of cycles 2–6, the cumulative absorbed doses predicted by extrapolation from cycle 1 data were comparable with the observed cumulative absorbed doses at both the group level and the individual patient level. This observation supports the premise that prediction by extrapolation from cycle 1 dosimetry data allows acceptable estimation of cumulative doses over multiple cycles. Similarly, a recently published study showed that it is feasible to simplify the quantitative imaging protocol by performing dosimetry at the first cycle only (*38*). Predicted cumulative absorbed doses were generally higher than observed cumulative absorbed doses, which is compatible with erring on the side of safety during clinical implementation.

TABLE 3
TEAEs Grouped as Safety Topics of Interest in the Substudy

Safety topic	^{177}Lu-PSMA-617 plus SoC (n = 30)	
	All grades	Grade ≥ 3 (%)
Bone marrow suppression	11 (36.7)	6 (20.0)
Nausea and vomiting	11 (36.7)	0 (0.0)
Fatigue	6 (20.0)	2 (6.7)
Dry mouth	5 (16.7)	0 (0.0)
Renal toxicity	5 (16.7)	0 (0.0)
Hepatotoxicity	2 (6.7)	0 (0.0)
Intracranial hemorrhage	0 (0.0)	0 (0.0)
QT prolongation	0 (0.0)	0 (0.0)
Reproductive toxicity	0 (0.0)	0 (0.0)
Second primary malignancies	0 (0.0)	0 (0.0)

Toxicity was assessed using CTCAE version 5.0. Safety topics occurred on or after start of treatment with ^{177}Lu-PSMA-617 plus standard of care (SoC) up to 30 d after last administration or before initiation of subsequent anticancer treatment. Patient with multiple grades for safety topic is counted only under maximum grade. Data in parentheses are percentages.

The findings of the present study are not directly comparable with previous dosimetry studies of ^{177}Lu-PSMA-617 because of differences in study design, patient selection criteria, and drug manufacturer. Nevertheless, absorbed doses in at-risk organs in the present substudy were consistent with results from previous studies of ^{177}Lu-PSMA-617 in patients with mCRPC for the kidneys (*10*,*39*), salivary glands (*40*,*41*), and red marrow (*40*,*42*–*44*). Data for lacrimal glands have previously been reported with a wide range of values and high variability (*10*,*17*,*42*,*43*,*45*). This variability may be due to small volumes of the lacrimal glands and the planar-only analysis. Interference from activity in the nasal mucosa and interpatient variation of actual lacrimal gland mass can further exacerbate this uncertainty. Contouring the lacrimal glands on a CT scan is an extremely challenging task and requires a high-resolution CT image of the orbital area. On the other hand, ranges of normal volumes of lacrimal glands calculated by CT (e.g., for radiotherapy purposes) have been published (*26*). The findings were also similar but not directly comparable in a prospective dosimetry study of ^{177}Lu-PSMA-617 using fewer cycles and lower administered doses in a small number of patients with low-volume metastatic hormone-sensitive prostate cancer (*46*).

The median duration of ^{177}Lu-PSMA-617 exposure in the 30 patients in the present dosimetry substudy was 5.52 mo, similar to the median exposure of 6.9 mo in 529 patients of the pivotal VISION study. The safety profile of ^{177}Lu-PSMA-617 was also similar between studies (*11*). The incidence of bone marrow suppression was similar between the present substudy (36.7%) and the pivotal VISION study (47.4%). In the renal toxicity safety topic of interest, no patients in the dosimetry substudy and 3.4% in the pivotal study experienced TEAEs of CTCAE grade 3 or higher across all treatment cycles. Recently, the results from a prospective registry study showed that ^{177}Lu-PSMA-617 did not lead to deterioration in kidney function in patients with mCRPC and kidney impairment (*47*).

^{177}Lu-PSMA-617 is internalized by PSMA-expressing tumor cells and some normal cells that express PSMA. This delivers β-particle radiation with high specificity to prostate cancer cells and PSMA-expressing normal cells and their surrounding microenvironment within an approximate 2-mm range. The duration of exposure depends on the radioactive half-life of ^{177}Lu (~1 wk) and its excretion. The present findings demonstrate that ^{177}Lu-PSMA-617 is excreted rapidly into the urine, mainly as the parent compound, with radioactivity in urine at 72 h decreased by approximately 93% from the 0- to 2-h time point. Speculatively, this transient exposure of the kidneys to radioactivity during rapid excretion of unbound ^{177}Lu-PSMA-617 may underlie the low

incidence of renal toxicity in the present substudy and in the pivotal VISION study (*11*).

The gold standard for dosimetry comprises a full multiple-time-point curve for every treatment cycle. However, this approach could be logistically, financially, and clinically challenging because of poor health conditions in most patients with mCRPC. Therefore, a simplified dosimetry method was used in cycles 2–6, with imaging at only a single time point (48 h). From a purely dosimetric point of view, this represents a limitation of the study. It can also, however, be regarded as a strength because it minimizes stress for the patient and mitigates the risks of limited clinical capacity by freeing up scanners and staff. The simplified approach has previously been demonstrated to be valid (*24*). Although it may lead to a slight underestimation of the expected cumulative absorbed doses in the kidneys of patients with mCRPC treated with ^{177}Lu-PSMA-617, the simplified approach is recommended as a reliable and appropriate alternative in patients with poor health status (*24*). An alternative approach to simplify dosimetry would be to use a single-time-point method in all cycles (*48*). Ultimately, using a single time point in cycle 1 and omitting dosimetry from cycle 2 onward might be the next step toward minimizing complexity, costs, and burden for patients. This will require optimization in patient cohorts larger than that in the present VISION substudy.

The number of patients in this substudy was sufficient for good dosimetric characterization. Given the technical and logistic challenges of dosimetry data acquisition over multiple study sites, the collection of SPECT images that included critical organs at all imaging time points represents a strength of the substudy. Another strength is the multicentric approach: the quantitative imaging calibration procedures were standardized across all 4 participating centers and centralized by the same single operator across all study sites to ensure high-quality data. Other studies have shown that standardization and calibration of quantitative imaging across various sites is feasible and can provide data that are comparable between participating sites (*49*). The observed renal cumulative absorbed dose was below the historical limit of 23 Gy (*12*,*13*). This may present an opportunity to improve the ^{177}Lu-PSMA-617 treatment protocol by increasing the dose per cycle or administering extra cycles. Nevertheless, the recommended dose remains 7.4 GBq per cycle for 6 cycles.

CONCLUSION

This VISION substudy expanded the evidence base for the safety profile of ^{177}Lu-PSMA-617, which was shown to extend overall survival and improve radiographic progression-free survival in patients with advanced mCRPC in the pivotal VISION study (*11*). The use of a simplified single-time-point dosimetry method in cycles 2–6 minimized the burden on patients and scanners and is expected to have little meaningful impact on the reliability of the results. ^{177}Lu-PSMA-617 was rapidly eliminated from the body and had a good safety profile, with no patients experiencing renal TEAEs of CTCAE grade 3 or higher. The observed cumulative absorbed doses over 6 cycles of treatment in the kidneys were below the historical EBRT limit of 23 Gy. These data indicate that 44.4 GBq of ^{177}Lu-PSMA-617 can safely be administered cumulatively over 6 cycles without inducing renal toxicity. Cumulative absorbed doses were predictable by extrapolation from cycle 1 dosimetry data. Omitting dosimetry from cycle 2 onward may allow adequate assessment of cumulative organ-absorbed doses and thus reduce imaging burden for patients without unacceptably compromising safety. These prospective safety and dosimetry data provide further support for adoption of ^{177}Lu-PSMA-617 as a treatment option in clinical practice for patients with mCRPC.

DISCLOSURE

Ken Herrmann reports consulting or advisory fees from ABX, Aktis Oncology, Amgen, Bayer, BTG, Curium, Endocyte, GE Healthcare, Ipsen, Novartis, Pharma15, Siemens Healthineers, SIRTEX, Sofie Biosciences, Theragnostics, and Y-mAbs. Kambiz Rahbar reports consulting or advisory fees from ABC CRO, ABX, Bayer, Novartis, and SIRTEX. Matthias Eiber reports consulting or advisory fees from Amgen, Bayer, Blue Earth Diagnostics, Lantheus, rhPSMA, and Telix. Richard Sparks and Nicholas Baca are employees of CDE Dosimetry Services, who were contracted by Novartis to perform this analysis. Bernd Krause reports consultant or advisory fees from Bayer, ITM, and Novartis and research funding from Novartis. Michael Lassmann reports research funding from Ipsen and Nordic Nanovector. Jun Tang, Daniela Chicco, Patrick Klein, Lars Blumenstein, and Jean-René Basque are employees of Novartis or own Novartis stocks/shares. This work was supported by Novartis. No other potential conflict of interest relevant to this article was reported.

ACKNOWLEDGMENTS

We thank the patients and their families, all site investigators, and personnel who participated in the study. We also thank Johny Wehbe, Jonathan Marra, and Laura Phelan of Novartis for their outstanding contributions during the conduct of the study. Under the direction of the authors, Karim Bensaad, PhD, of Oxford PharmaGenesis, Oxford, U.K., provided medical writing support, which was funded by Novartis, in accordance with Good Publication Practice 3 guidelines (https://www.ismpp.org/gpp3).

KEY POINTS

QUESTION: What is the whole-body and organ dosimetry of ^{177}Lu-PSMA-617, and can we predict cumulative absorbed radiation doses over multiple cycles of ^{177}Lu-PSMA-617 in patients with mCRPC by extrapolation from cycle 1 dosimetry data?

PERTINENT FINDINGS: ^{177}Lu-PSMA-617 has a good overall safety profile and low renal radiotoxicity. Furthermore, data from cycle 1 of patients with mCRPC receiving ^{177}Lu-PSMA-617 can be extrapolated to predict cumulative absorbed doses in at-risk organs in additional cycles.

IMPLICATIONS FOR PATIENT CARE: The omission of dosimetry measurements from cycle 2 onward could reduce patient burden and free scanner and staff capacities, without unacceptably compromising safety.

REFERENCES

1. Rowe SP, Gorin MA, Pomper MG. Imaging of prostate-specific membrane antigen with small-molecule PET radiotracers: from the bench to advanced clinical applications. *Annu Rev Med.* 2019;70:461–477.
2. Liu H, Rajasekaran AK, Moy P, et al. Constitutive and antibody-induced internalization of prostate-specific membrane antigen. *Cancer Res.* 1998;58:4055–4060.
3. Minner S, Wittmer C, Graefen M, et al. High level PSMA expression is associated with early PSA recurrence in surgically treated prostate cancer. *Prostate.* 2011;71:281–288.

4. Schutz FA, Buzaid AC, Sartor O. Taxanes in the management of metastatic castration-resistant prostate cancer: efficacy and management of toxicity. *Crit Rev Oncol Hematol.* 2014;91:248–256.
5. Rahbar K, Ahmadzadehfar H, Kratochwil C, et al. German multicenter study investigating ^{177}Lu-PSMA-617 radioligand therapy in advanced prostate cancer patients. *J Nucl Med.* 2017;58:85–90.
6. Ahmadzadehfar H, Rahbar K, Baum RP, et al. Prior therapies as prognostic factors of overall survival in metastatic castration-resistant prostate cancer patients treated with [^{177}Lu]Lu-PSMA-617. A WARMTH multicenter study (the 617 trial). *Eur J Nucl Med Mol Imaging.* 2021;48:113–122.
7. Kratochwil C, Fendler WP, Eiber M, et al. EANM procedure guidelines for radionuclide therapy with ^{177}Lu-labelled PSMA-ligands (^{177}Lu-PSMA-RLT). *Eur J Nucl Med Mol Imaging.* 2019;46:2536–2544.
8. Afshar-Oromieh A, Hetzheim H, Kratochwil C, et al. The theranostic PSMA ligand PSMA-617 in the diagnosis of prostate cancer by PET/CT: biodistribution in humans, radiation dosimetry, and first evaluation of tumor lesions. *J Nucl Med.* 2015;56:1697–1705.
9. Banerjee S, Pillai MR, Knapp FF. Lutetium-177 therapeutic radiopharmaceuticals: linking chemistry, radiochemistry, and practical applications. *Chem Rev.* 2015;115:2934–2974.
10. Violet J, Jackson P, Ferdinandus J, et al. Dosimetry of ^{177}Lu-PSMA-617 in metastatic castration-resistant prostate cancer: correlations between pretherapeutic imaging and whole-body tumor dosimetry with treatment outcomes. *J Nucl Med.* 2019;60:517–523.
11. Sartor O, de Bono J, Chi KN, et al. Lutetium-177-PSMA-617 for metastatic castration-resistant prostate cancer. *N Engl J Med.* 2021;385:1091–1103.
12. Emami B, Lyman J, Brown A, et al. Tolerance of normal tissue to therapeutic irradiation. *Int J Radiat Oncol Biol Phys.* 1991;21:109–122.
13. Sjögreen Gleisner K, Chouin N, Gabina PM, et al. EANM dosimetry committee recommendations for dosimetry of ^{177}Lu-labelled somatostatin-receptor- and PSMA-targeting ligands. *Eur J Nucl Med Mol Imaging.* 2022;49:1778–1809.
14. Morgantetti G, Ng KL, Samaratunga H, Rhee H, Gobe GC, Wood ST. Prostate specific membrane antigen (PSMA) expression in vena cava tumour thrombi of clear cell renal cell carcinoma suggests a role for PSMA-driven tumour neoangiogenesis. *Transl Androl Urol.* 2019;8(suppl 2):S147–S155.
15. Taieb D, Foletti JM, Bardies M, Rocchi P, Hicks RJ, Haberkorn U. PSMA-targeted radionuclide therapy and salivary gland toxicity: why does it matter? *J Nucl Med.* 2018;59:747–748.
16. Heynickx N, Herrmann K, Vermeulen K, Baatout S, Aerts A. The salivary glands as a dose limiting organ of PSMA-targeted radionuclide therapy: a review of the lessons learnt so far. *Nucl Med Biol.* 2021;98-99:30–39.
17. Hohberg M, Eschner W, Schmidt M, et al. Lacrimal glands may represent organs at risk for radionuclide therapy of prostate cancer with [^{177}Lu]DKFZ-PSMA-617. *Mol Imaging Biol.* 2016;18:437–445.
18. Klein Nulent TJW, Valstar MH, de Keizer B, et al. Physiologic distribution of PSMA-ligand in salivary glands and seromucous glands of the head and neck on PET/CT. *Oral Surg Oral Med Oral Pathol Oral Radiol.* 2018;125:478–486.
19. Tönnesmann R, Meyer PT, Eder M, Baranski AC. [^{177}Lu]Lu-PSMA-617 salivary gland uptake characterized by quantitative in vitro autoradiography. *Pharmaceuticals (Basel).* 2019;12:18.
20. Kulkarni HR, Singh A, Schuchardt C, et al. PSMA-based radioligand therapy for metastatic castration-resistant prostate cancer: the Bad Berka experience since 2013. *J Nucl Med.* 2016;57(suppl 3):97S–104S.
21. Delker A, Fendler WP, Kratochwil C, et al. Dosimetry for ^{177}Lu-DKFZ-PSMA-617: a new radiopharmaceutical for the treatment of metastatic prostate cancer. *Eur J Nucl Med Mol Imaging.* 2016;43:42–51.
22. Yonekura Y, Mattsson S, Flux G, et al. ICRP publication 140: radiological protection in therapy with radiopharmaceuticals. *Ann ICRP.* 2019;48:5–95.
23. Konijnenberg M, Herrmann K, Kobe C, et al. EANM position paper on article 56 of the Council Directive 2013/59/Euratom (basic safety standards) for nuclear medicine therapy. *Eur J Nucl Med Mol Imaging.* 2021;48:67–72.
24. Kurth J, Heuschkel M, Tonn A, et al. Streamlined schemes for dosimetry of ^{177}Lu-labeled PSMA targeting radioligands in therapy of prostate cancer. *Cancers (Basel).* 2021;13:3884.
25. Tran-Gia J, Denis-Bacelar AM, Ferreira KM, et al. A multicentre and multinational evaluation of the accuracy of quantitative Lu-177 SPECT/CT imaging performed within the MRTDosimetry project. *EJNMMI Phys.* 2021;8:55.
26. Ljungberg M, Celler A, Konijnenberg MW, et al. MIRD pamphlet no. 26: joint EANM/MIRD guidelines for quantitative ^{177}Lu SPECT applied for dosimetry of radiopharmaceutical therapy. *J Nucl Med.* 2016;57:151–162.
27. Basic anatomical and physiological data for use in radiological protection: reference values. A report of age- and gender-related differences in the anatomical and physiological characteristics of reference individuals. ICRP publication 89. *Ann ICRP.* 2002;32:5–265.
28. Siegel JA, Thomas SR, Stubbs JB, et al. MIRD pamphlet no. 16: techniques for quantitative radiopharmaceutical biodistribution data acquisition and analysis for use in human radiation dose estimates. *J Nucl Med.* 1999;40:37S–61S.
29. Hindorf C, Glatting G, Chiesa C, Linden O, Flux G; EANM Dosimetry Committee. EANM dosimetry committee guidelines for bone marrow and whole-body dosimetry. *Eur J Nucl Med Mol Imaging.* 2010;37:1238–1250.
30. Bingham CM, Castro A, Realini T, Nguyen J, Hogg JP, Sivak-Callcott JA. Calculated CT volumes of lacrimal glands in normal Caucasian orbits. *Ophthal Plast Reconstr Surg.* 2013;29:157–159.
31. Bingham CM, Harris MA, Realini T, Nguyen J, Hogg JP, Sivak-Callcott JA. Calculated computed tomography volumes of lacrimal glands and comparison to clinical findings in patients with thyroid eye disease. *Ophthal Plast Reconstr Surg.* 2014;30:116–118.
32. Bulbul E, Yazici A, Yanik B, Yazici H, Demirpolat G. Evaluation of lacrimal gland dimensions and volume in Turkish population with computed tomography. *J Clin Diagn Res.* 2016;10:TC06–TC08.
33. Gao Y, Moonis G, Cunnane ME, Eisenberg RL. Lacrimal gland masses. *AJR.* 2013;201:W371–W381.
34. Okamoto S, Thieme A, Allmann J, et al. Radiation dosimetry for ^{177}Lu-PSMA I&T in metastatic castration-resistant prostate cancer: absorbed dose in normal organs and tumor lesions. *J Nucl Med.* 2017;58:445–450.
35. Soundy RG, Tyrrell DA, Pickett RD, Stabin M. The radiation dosimetry of ^{99}Tc^{m}-exametazime. *Nucl Med Commun.* 1990;11:791–799.
36. Tamboli DA, Harris MA, Hogg JP, Realini T, Sivak-Callcott JA. Computed tomography dimensions of the lacrimal gland in normal Caucasian orbits. *Ophthal Plast Reconstr Surg.* 2011;27:453–456.
37. Yazici A, Bulbul E, Yazici H, et al. Lacrimal gland volume changes in unilateral primary acquired nasolacrimal obstruction. *Invest Ophthalmol Vis Sci.* 2015;56:4425–4429.
38. Mix M, Renaud T, Kind F, et al. Kidney doses in ^{177}Lu-based radioligand therapy in prostate cancer: is dose estimation based on reduced dosimetry measurements feasible? *J Nucl Med.* 2022;63:253–258.
39. Yadav MP, Ballal S, Tripathi M, et al. Post-therapeutic dosimetry of ^{177}Lu-DKFZ-PSMA-617 in the treatment of patients with metastatic castration-resistant prostate cancer. *Nucl Med Commun.* 2017;38:91–98.
40. Kabasakal L, Toklu T, Yeyin N, et al. Lu-177-PSMA-617 prostate-specific membrane antigen inhibitor therapy in patients with castration-resistant prostate cancer: stability, bio-distribution and dosimetry. *Mol Imaging Radionucl Ther.* 2017;26:62–68.
41. Privé BM, Peters SMB, Muselaers CHJ, et al. Lutetium-177-PSMA-617 in low-volume hormone-sensitive metastatic prostate cancer: a prospective pilot study. *Clin Cancer Res.* 2021;27:3595–3601.
42. Scarpa L, Buxbaum S, Kendler D, et al. The ^{68}Ga/^{177}Lu theragnostic concept in PSMA targeting of castration-resistant prostate cancer: correlation of SUV_{max} values and absorbed dose estimates. *Eur J Nucl Med Mol Imaging.* 2017;44:788–800.
43. Maffey-Steffan J, Scarpa L, Svirydenka A, et al. The ^{68}Ga/^{177}Lu-theragnostic concept in PSMA-targeting of metastatic castration-resistant prostate cancer: impact of post-therapeutic whole-body scintigraphy in the follow-up. *Eur J Nucl Med Mol Imaging.* 2020;47:695–712.
44. Kratochwil C, Giesel FL, Stefanova M, et al. PSMA-targeted radionuclide therapy of metastatic castration-resistant prostate cancer with ^{177}Lu-labeled PSMA-617. *J Nucl Med.* 2016;57:1170–1176.
45. Paganelli G, Sarnelli A, Severi S, et al. Dosimetry and safety of ^{177}Lu PSMA-617 along with polyglutamate parotid gland protector: preliminary results in metastatic castration-resistant prostate cancer patients. *Eur J Nucl Med Mol Imaging.* 2020;47:3008–3017.
46. Peters SMB, Prive BM, de Bakker M, et al. Intra-therapeutic dosimetry of [^{177}Lu]Lu-PSMA-617 in low-volume hormone-sensitive metastatic prostate cancer patients and correlation with treatment outcome. *Eur J Nucl Med Mol Imaging.* 2022;49:460–469.
47. Rosar F, Kochems N, Bartholoma M, et al. Renal safety of [^{177}Lu]Lu-PSMA-617 radioligand therapy in patients with compromised baseline kidney function. *Cancers (Basel).* 2021;13:3095.
48. Brosch-Lenz J, Delker A, Volter F, et al. Toward single-time-point image-based dosimetry of ^{177}Lu-PSMA-617 therapy. *J Nucl Med.* 2023;64:767–774.
49. Lassmann M, Eberlein U, Tran-Gia J. Multicentre trials on standardised quantitative imaging and dosimetry for radionuclide therapies. *Clin Oncol (R Coll Radiol).* 2021;33:125–130.

Long-Term Nephrotoxicity of ^{177}Lu-PSMA Radioligand Therapy

Lisa Steinhelfer*[1,2], Lukas Lunger*[3], Lisena Cala[1], Christian H. Pfob[4], Constantin Lapa[4], Philipp E. Hartrampf[5], Andreas K. Buck[5], Hannah Schäfer[6], Christoph Schmaderer[6], Robert Tauber[3], Julia Brosch-Lenz[1], Bernhard Haller[7], Valentin H. Meissner[3], Karina Knorr[1], Wolfgang A. Weber[1], and Matthias Eiber[1]

[1]*Department of Nuclear Medicine, School of Medicine, and Klinikum Rechts der Isar, Technical University of Munich, Munich, Germany;* [2]*Department of Radiology, School of Medicine, and Klinikum Rechts der Isar, Technical University of Munich, Munich, Germany;* [3]*Department of Urology, School of Medicine, and Klinikum Rechts der Isar, Technical University of Munich, Munich, Germany;* [4]*Nuclear Medicine, Faculty of Medicine, University of Augsburg, Augsburg, Germany;* [5]*Department of Nuclear Medicine, University Hospital Wurzburg, Wurzburg, Germany;* [6]*Department of Nephrology, School of Medicine, and Klinikum Rechts der Isar, Technical University of Munich, Munich, Germany; and* [7]*Institute of AI and Informatics in Medicine, School of Medicine, and Klinikum Rechts der Isar, Technical University of Munich, Munich, Germany*

β-emitting ^{177}Lu targeting prostate-specific membrane antigen (PSMA) is an approved treatment option for metastatic castration-resistant prostate cancer. Data on its long-term nephrotoxicity are sparse. This study aimed to retrospectively evaluate post–^{177}Lu-PSMA estimated glomerular filtration rate (eGFR) dynamics for at least 12 mo in a cohort of metastatic castration-resistant prostate cancer patients. **Methods:** The institutional databases of 3 German tertiary referral centers identified 106 patients who underwent at least 4 cycles of ^{177}Lu-PSMA and had at least 12 mo of eGFR follow-up data. eGFR (by the Chronic Kidney Disease Epidemiology Collaboration formula) at 3, 6, and 12 mo after ^{177}Lu-PSMA radioligand therapy was estimated using monoexponentially fitted curves through available eGFR data. eGFR changes were grouped (≥15%–<30%, moderate; ≥30%–<40%, severe; and ≥40%, very severe). Associations between eGFR changes (%) and nephrotoxic risk factors, prior treatment lines, and number of ^{177}Lu-PSMA cycles were analyzed using multivariable linear regression. **Results:** At least moderate eGFR decreases were present in 45% (48/106) of patients; of those, nearly half (23/48) had a severe or very severe eGFR decrease. A higher number of risk factors at baseline (−4.51, $P = 0.03$) was associated with a greater eGFR decrease. Limitations of the study were the retrospective design, lack of a control group, and limited number of patients with a follow-up longer than 1 y. **Conclusion:** A considerable proportion of patients may experience moderate or severe decreases in eGFR 1 y from initiation of ^{177}Lu-PSMA. A higher number of risk factors at baseline seems to aggravate loss of renal function. Further prospective trials are warranted to estimate the nephrotoxic potential of ^{177}Lu-PSMA.

Key Words: nephrotoxicity; PSMA; radioligand therapy; lutetium; mCRPC

J Nucl Med 2024; 65:79–84
DOI: 10.2967/jnumed.123.265986

Received May 4, 2023; revision accepted Sep. 16, 2023.
For correspondence or reprints, contact Lukas Lunger (lukas.lunger@tum.de).
*Contributed equally to this work.
Published online Oct. 19, 2023.

Prostate-specific membrane antigen (PSMA)–targeted radioligand therapy (RLT) with ^{177}Lu-PSMA-617 was recently approved for the treatment of metastatic castration-resistant prostate cancer (mCRPC) after taxane-based chemotherapy (*1*,*2*). Despite its overall favorable side effect profile, primary safety concerns during ^{177}Lu-PSMA RLT are critical radiation doses to cancer-unaffected sites due to physiologic expression of PSMA (e.g., in the salivary glands and kidneys).

A recent systematic review and metaanalysis reported nephrotoxicity of any stage in 9.5% of 744 patients treated with ^{177}Lu-PSMA (*3*). Consistently, the phase III VISION trial on ^{177}Lu-PSMA (^{177}Lu-PSMA-RLT plus the standard of care versus the standard of care alone) reported renal toxicity of any stage in 8.7% of patients in the intervention arm versus 5.9% in the control arm. Of note, severe renal toxicity (stages 3–5) was observed in 3.4% of patients in the ^{177}Lu-PSMA group and in 2.9% in the group receiving the standard of care alone (*2*).

However, these data may underestimate the long-term incidence of renal toxicity, as it is known from external-beam radiotherapy (EBRT) and other radionuclide therapies that toxicity may develop over a longer period (>1 y) and median survival in the VISION study was only 15.3 mo. We recently reported 3 patients who developed severe radiation nephropathy with a histologically proven renal thrombotic microangiopathylike picture after extensive treatment with ^{177}Lu-PSMA RLT (*4*).

Nephropathy after ^{177}Lu-PSMA RLT is attributed mainly to the renal tubular PSMA expression and the renal excretion of ^{177}Lu-PSMA, resulting in a prolonged retention of the β^- emitter in the kidneys (*5*). Definitive dose limits for RLT are not established, and current thresholds are based on observations with EBRT. Here, homogeneous irradiation of the whole kidneys with 23 and 28 Gy was associated with a 5% and 50% risk of severe radiation nephritis, respectively, within 5 y after treatment (*6*). However, compared with EBRT, the radiation to the kidneys by ^{177}Lu-PSMA is of lower energy, is delivered over a longer period, and is not homogeneously distributed within the kidney tissue (*7*).

Several, mainly retrospective, studies investigated the renal absorbed dose from ^{177}Lu-labeled PSMA ligands. For ^{177}Lu-PSMA 617 and ^{177}Lu-PSMA I&T, mean renal absorbed doses of 0.5 Gy/GBq (SD, 0.2) and 0.7 Gy/GBq (SD, 0.2) have been reported (*8*).

Extrapolating these population-based dose estimates to clinical practice, 4 and 6 cycles with a standard activity of 7.4 GBq of ^{177}Lu-PSMA I&T would result in mean absorbed doses of 20 and 31 Gy, respectively, to the kidneys. Because of the large interindividual variability of renal doses (coefficient of variation, 40%), a significant fraction of patients will receive even substantially higher renal doses exceeding the dose limits established for EBRT (*6*).

The aim of our retrospective analysis was to evaluate long-term changes in the estimated glomerular filtration rate (eGFR) in mCRPC patients who underwent at least 4 cycles of ^{177}Lu-PSMA at 3 German tertiary referral centers. We investigated the association of the number of risk factors associated with impaired renal function at baseline, the number of prior treatment lines, and the number of ^{177}Lu-PSMA cycles with the percentage eGFR decrease 12 mo from initiation of ^{177}Lu-PSMA RLT.

MATERIALS AND METHODS

Patients

For this retrospective analysis, the institutional databases of 3 tertiary referral centers in Germany (Technical University of Munich, University of Wurzburg, and University of Augsburg) were screened for patients who initiated and completed ^{177}Lu-PSMA I&T RLT between December 2015 and May 2021.

Patients were included if they underwent at least 4 cycles of ^{177}Lu-PSMA I&T RLT, had at least 1 y of follow-up eGFR data after treatment initiation, and had no evidence of urinary tract obstruction on pretreatment ^{99m}Tc-mercaptoacetyltriglycine scintigraphy. The retrospective analysis was approved by the local responsible institutional review boards (approvals 115/18S, 2020-40, and 20200609 01).

Institutional eligibility criteria for using ^{177}Lu-PSMA I&T RLT as an individual treatment decision were previously published (*9*). The production and administration of ^{177}Lu-PSMA I&T complied with the German pharmaceutical law (Arzneimittelgesetz, §13.2b) and the responsible regulatory bodies. All patients gave written informed consent and were treated under the conditions of the Declaration of Helsinki, article 37, "Unproven Interventions in Clinical Practice." Each patient received intravenous hydration (500 mL of 0.9% NaCl) starting 30 min before treatment infusion. The ^{177}Lu-PSMA I&T solution was intravenously administered.

Measures

All serum creatinine (Scr) values recorded at baseline and throughout a minimum of 12 mo from the initiation of therapy were collected and used to calculate the eGFR using the Chronic Kidney Disease Epidemiology Collaboration formula. This formula considers factors such as Scr, age, sex, and ethnicity. The Chronic Kidney Disease Epidemiology Collaboration equation is $eGFR = 141 \times \min(Scr/\kappa, 1)^{\alpha} \times \max(Scr/\kappa, 1)^{1.209} \times 0.993^{age}$, where κ is 0.9, α is -0.411, min is the minimum of Scr/κ or 1, and max is the maximum of Scr/κ or 1 (*10*). Renal failure stages were subsequently defined according to Chronic Kidney Disease Epidemiology Collaboration criteria at baseline and at the 12-mo follow-up.

A monoexponential curve was fitted through all available eGFR data (from initiation of treatment to at least 12 mo) for every patient to obtain a standardized eGFR estimate at the predefined time points (3, 6, and 12 mo) (*11*). Supplemental Figure 1 (supplemental materials are available at http://jnm.snmjournals.org) depicts the monoexponential estimates for 2 patients. If patients had follow-up data beyond 12 mo, these were recorded up to a maximum of 36 mo from initiation of therapy.

For every patient, the percentage changes from baseline at the predefined time points (3, 6, and 12 mo) were subsequently calculated. Clinically relevant percentage eGFR decrease cutoffs from baseline were set (≥15%–<30%, moderate; ≥30%–<40%, severe; and ≥40%, very severe) as described elsewhere (*12*,*13*).

Risk factors associated with impaired renal function at baseline (arterial hypertension, diabetes mellitus, age ≥ 65 y (*11*), prior platinum-based chemotherapy) were recorded. Hypertension was defined as the use of antihypertensive drugs (thiazide drugs, β-blockers, angiotensin-converting enzyme inhibitors, angiotensin II receptor antagonists, or calcium channel blockers). Diabetes mellitus was defined as a hemoglobin A1c of at least 6% or the use of antidiabetic medication (insulin or insulin sensitizers).

Statistical Analyses

Data analyses were conducted using SPSS 26 (IBM). Descriptive statistics were used to illustrate patient characteristics. Mean values and SD or median and interquartile range (IQR) were reported, unless indicated otherwise.

A multiple linear regression analysis was computed to determine the association of number of risk factors at baseline, number of prior treatment lines, and number of cycles of ^{177}Lu-PSMA I&T with the percentage eGFR change 12 mo from initiation of ^{177}Lu-PSMA I&T RLT. *P* values of less than 0.05 were considered statistically significant (2-sided test).

RESULTS

Patient Characteristics

Supplemental Figure 2 illustrates the recruitment flowchart. A total of 106 mCRPC patients fulfilled the inclusion criteria and underwent a total of 670 cycles of ^{177}Lu-PSMA RLT. The median number of cycles was 6 (IQR, 5–8), and the median interval between 2 cycles was approximately 6 wk. The median administered activity per cycle and total administered activity of ^{177}Lu-PSMA were 7.4 GBq (IQR, 6.0–7.8 GBq) and 44 GBq (IQR, 35–58 GBq), respectively. Patient characteristics are reported in Table 1.

EGFR May Progressively Deteriorate After Initiation of ^{177}Lu-PSMA

Mean baseline eGFR was 79 mL/min (SD, 17 mL/min). The median overall percentage eGFR decrease after 3, 6, and 12 mo from baseline was 3.5% (IQR, 0.9%–7.9%), 6.9% (IQR, 1.8%–15%), and 13.6% (IQR, 3.6%–28.5%), respectively. Of note, the exploratory analysis of the 20 and 5 patients with follow-up at 24 and 36 mo, respectively, after treatment initiation showed a further decline in eGFR from baseline: the median overall percentage eGFR decrease was 19.6% (IQR, 7.6%–30.6%) and 38.9% (IQR, 28.0%–54.4%) at 24 and 36 mo, respectively. Sequential percentage changes in eGFR from baseline within 12 mo and beyond are shown in Figure 1.

Individual percentage changes in eGFR from baseline for all patients with at least a 3% and less than a 3% eGFR decline at 3 mo are shown in Figure 2. In all patients with an early (≥3%) eGFR decline at 3 mo, eGFR decreased progressively without any trend toward stabilization or recovery throughout the observation period. The age-associated yearly eGFR decline of 1 mL/min for a 70-y-old man without comorbidities serves as a comparator (*14*).

By predefined cutoffs, 1 y after initiation of ^{177}Lu-PSMA I&T, 45% (48/106) of patients experienced an eGFR decrease of at least 15% from baseline (Table 2). More than half of those (52%, 25/48) had at least a severe eGFR decrease (≥30%), corresponding to nearly one quarter of the entire patient cohort (24%, 25/106). In all patients with an eGFR decrease of at least 15% after 12 mo and with an additional follow-up visit, eGFR further decreased at 24 mo (eGFR decline of 28%–77% compared with baseline in 7

TABLE 1
Patient Characteristics (n = 106)

Characteristic	Data
Mean age (y)	73 (SD, 7)
Mean baseline eGFR (mL/min)	84 (SD, 27)
Prior treatment lines	
Abiraterone	87 patients (82%)
Enzalutamide	67 patients (63%)
Docetaxel	60 patients (57%)
Cabazitaxel	16 patients (15%)
^{223}Ra-dichloride	8 patients (8%)
Platinum-based chemotherapy	3 patients (3%)
^{177}Lu-PSMA cycles	
Median	6 cycles (IQR, 5–8)
<6 cycles	33 patients (31%)
≥6 cycles	73 patients (69%)
Risk factors before ^{177}Lu-PSMA treatment*	
0	6 patients (6%)
1	18 patients (16%)
2	43 patients (41%)
3	34 patients (32%)
4	5 patients (5%)

*Arterial hypertension, diabetes mellitus, age ≥ 65 y, prior platinum-based chemotherapy.

patients). In 46% (6/13) of the patients with no or only a mild eGFR decrease (<15%) at 12 mo and an additional follow-up visit, eGFR decreased beyond the 15% cutoff at 24 mo. Quantitatively, the mild eGFR decrease observed at 12 mo nearly doubled at the 24-mo follow-up in those patients. Of 5 patients with a 3-y follow-up, 2 had a moderate eGFR decrease, 1 a severe decrease (30%–40%), and 2 a very severe eGFR decrease by at least 40% from baseline. By chronic kidney disease criteria, the proportion of patients with stage 3 renal failure nearly doubled 12 mo after initiation of ^{177}Lu-PSMA compared with baseline (20% vs. 37%, Table 3).

On the basis of the calculated multivariable linear regression model (enter method, which is commonly set as the default in many statistical programs and involves entering all input variables simultaneously), including number of risk factors at baseline, number of pretreatment lines, and number of cycles of ^{177}Lu-PSMA, only a higher number of risk factors at baseline (−4.51, P = 0.03) was associated with higher percentage eGFR decreases from baseline 12 mo after initiation of treatment (Table 4).

DISCUSSION

In our retrospective analysis, an at least moderate eGFR decline (>15%) 12 mo after treatment initiation was observed in 45% (48/106) of patients undergoing 4 or more cycles of ^{177}Lu-PSMA RLT. A severe eGFR decline (≥30%) was present in 24% (25/106) of all patients. An exploratory analysis in a subset of patients with longer follow-up indicated a further eGFR decline over time. A higher number of risk factors at baseline was associated with a higher percentage eGFR decrease at 12 mo.

Previous dosimetry analyses indicate dose-dependent and substantial irradiation of the kidneys during ^{177}Lu-PSMA RLT, potentially leading to radiation nephropathy when referring to dose limits that were established for EBRT (*6*). Data on the nephrotoxicity of ^{177}Lu-PSMA are sparse, and most studies suggest negligible nephrotoxicity but are limited by a short follow-up and no available dosimetry (*2*,*15*). We have recently reported 3 cases of severe radiation nephropathy after extensive treatment with ^{177}Lu-PSMA RLT (*4*). Long-term data on the effects of ^{177}Lu-PSMA on renal function are urgently needed, especially given its evaluation in early mCRPC (e.g., PSMAfore, SPLASH) and even high-risk localized prostate cancer (e.g., LuTectomy) as well as hormone-sensitive prostate cancer (e.g., PSMAddition, UpFrontPSMA). With a longer life expectancy, those patients could potentially experience renal failure, which is often delayed in radionuclide treatment.

In our retrospective analysis, only a mild and clinically insignificant decrease in eGFR (median, −6.9% from baseline) was observed up to 6 mo after treatment initiation. A previous study reported a mean absolute decrease of 11 mL/min in creatinine clearance based on ^{51}Cr-ethylenediaminetetraacetic acid measurement at 3 mo after ^{177}Lu-PSMA RLT (*16*). In contrast, our study revealed a comparatively smaller eGFR decline of 3 mL/min based on calculation from creatinine levels after the same treatment duration. However, median eGFR further deteriorated and almost doubled within the next 6 mo, suggesting that renal injury may occur both early and late. At the 12-mo follow-up, 45% (48/106) of patients had an at least moderate (≥15%) decrease in eGFR from baseline: of those, 25% (12/48) showed a severe (≥30%) and 27% (13/48) a very severe (≥40%) eGFR decrease. According to chronic kidney disease criteria, there was a nearly 2-fold increase in the percentage of patients experiencing stage 3 renal failure 12 mo after commencing ^{177}Lu-PSMA therapy as compared with the baseline assessment. Although the analysis at later time points is limited by the small number of patients, there was no indication that the annual eGFR decline slowed after 2 and 3 y. We observed that all patients with at least a 3% eGFR decline at 3 mo after treatment initiation further declined at a relatively constant rate of 3% every 3 mo. This rate is substantially higher than the expected age-associated yearly eGFR decline of 1 mL/min for a 70-y-old

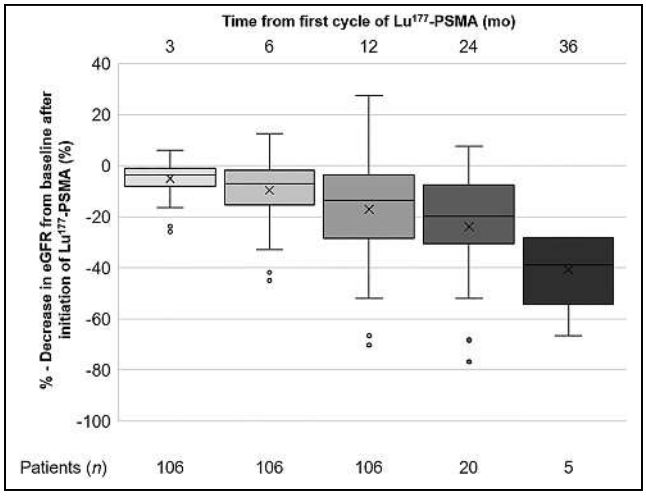

FIGURE 1. Box plots illustrating percentage eGFR decrease from baseline after initiation of ^{177}Lu-PSMA. × within box plots = mean.

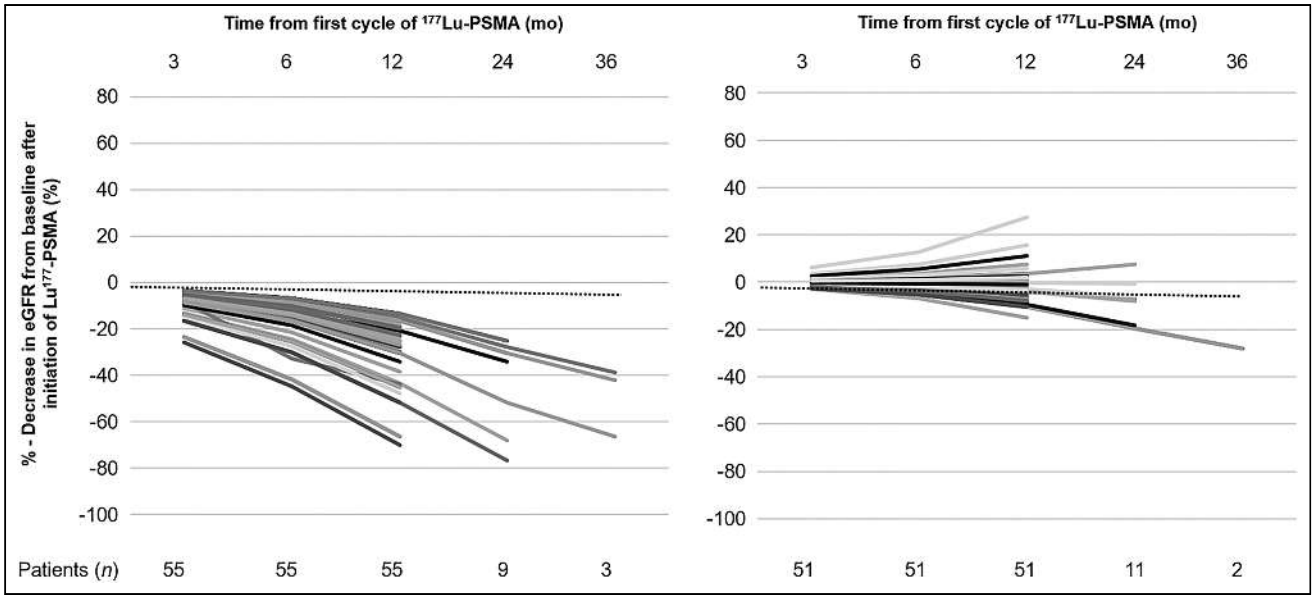

FIGURE 2. Individual percentage changes in eGFR from baseline in 58 patients with ≥3% eGFR decline at 3 mo (left) and 48 patients with <3% or no eGFR decline at 3 mo (right) after ^{177}Lu-PSMA RLT. Dashed line indicates expected age-associated yearly eGFR decline of 1 mL/min for 70-y-old-man without comorbidities, assuming baseline GFR of 85 mL/min. Thus, after 3 y, eGFR would have declined by 3% from baseline in this healthy man.

man without comorbidities (Fig. 2) (*14*). Substantial limitations of this observation are variable baseline eGFR and variable comorbidities in our patient cohort.

Hypothetically extrapolating these estimated eGFR declines of 3% every 3 mo would lead to a 50% reduction in baseline clearance and result in a substantial kidney function loss approximately 5 y after treatment initiation. This loss could be of particular importance with the potential adoption of ^{177}Lu-PSMA in earlier-treatment algorithms: although patients with short overall survival in later stages of the disease may not experience long-term negative effects of radiation nephropathy, the use of ^{177}Lu-PSMA in early mCRPC or even metastatic hormone-sensitive PC could potentially result in significant morbidity for these patients. Ongoing trials on metastatic hormone-sensitive or localized prostate cancer are assessing the safety and efficacy of up to 2 cycles of ^{177}Lu-PSMA (*17*,*18*). These findings are eagerly awaited; however, existing literature focuses primarily on nephrotoxicity in advanced mCRPC, involving significantly more treatment cycles on average. This disparity in regimens and patient groups suggests a potential underestimation of dose-related nephrotoxicity in these earlier-stage trials and further emphasizes the importance of enhancing our understanding of kidney-related effects associated with ^{177}Lu-PSMA.

In the small subgroup of patients with longer follow-up, a moderate eGFR decrease occurred in half the patients (6/13) at 24 mo who had shown no or only mild eGFR decreases (<15%) at the 12-mo follow-up. This result highlights that radiation-mediated loss of renal function can occur at a delayed time even if no clinically significant eGFR changes are present at 12 mo. Similar to peptide receptor radionuclide therapy using somatostatin analogs for treatment of neuroendocrine tumors (*19*), our experience emphasizes that a long-term follow-up is pivotal when aiming to investigate radiation damage due to low-dose β^- radiation. One study examining the clinical course of radiation nephropathy after EBRT found that clinical signs of glomerular pathology may not appear until after an initial 6-mo latency period (*20*,*21*). Often, it may manifest as chronic radiation nephropathy occurring more than 18 mo after exposure to critical radiation doses (*20*,*21*).

The nephrotoxicity seen in our cohort might partly also be attributed to the higher number of cycles per patient (and therefore the applied dose) than in other reports. We specifically focused on patients with at least 4 cycles, resulting in a ^{177}Lu-PSMA median number of 6 cycles in our analysis. When data from the literature are used, this translates to an estimated median renal absorbed dose of 31 Gy, but individually a broad variation in renal doses has been observed (*6*). Yordanova et al. observed no relevant

TABLE 2
Proportion of Patients with eGFR Decreases by ≥15% 1 Year After Initiation of ^{177}Lu-PSMA

eGFR decrease/y	Patients (*n*)
Total ≥ 15%	48 (45%)
≥15%–<30%	23 (48%)
≥30%–<40%	12 (25%)
≥40%	13 (27%)

TABLE 3
Distribution of Renal Failure Stages at Baseline and 1 Year After Initiation of ^{177}Lu-PSMA (*n* = 106)

Chronic kidney disease stage	Baseline (*n*)	12 mo (*n*)
1 (>90 mL/min)	43 (40%)	22 (21%)
2 (60–89 mL/min)	42 (40%)	43 (41%)
3 (30–59 mL/min)	21 (20%)	40 (37%)
4 (15–29 mL/min)	0	1 (1%)

TABLE 4
Multivariable Linear Regression Model for Association of Risk Factors, Pretreatment Lines, and ^{177}Lu-PSMA Cycles Received by 12 Months with Percentage Decrease in eGFR 12 Months from Initiation of ^{177}Lu-PSMA

Variable (*n*)	B	95% CI	β	t	p
Risk factors at baseline	−4.51	−8.52 to −0.50	−0.24	−2.23	0.03
Treatment lines before ^{177}Lu-PSMA	2.53	−0.68 to 5.74	0.15	1.56	0.12
Cycles of ^{177}Lu-PSMA	−1.30	−3.71 to 1.12	−0.11	−1.06	0.29

R^2 adjusted = 0.057 (n = 106). P = 0.029. B = estimated coefficient for predictor variable; β = standardized coefficient (β weight); t = t-statistical for testing significance of coefficient; p = p-value.

nephrotoxicity at a median renal absorbed dose of 16.4 Gy (*15*). In contrast, most of our patients substantially exceeded critical estimated renal radiation doses based on EBRT-based dose limits (23 and 28 Gy (*6*)). On multivariable linear regression, however, the number of treatment cycles was not associated with a greater percentage eGFR decrease from baseline at 12 mo after treatment. In an exploratory analysis, we stratified our cohort by patients undergoing fewer than 6 cycles versus 6 or more cycles, as the latter would result in a median absorbed dose of 31 Gy to the kidneys, exceeding both limits. We observed a higher percentage eGFR decrease from baseline in this group, although not statistically significant. Future studies could benefit from incorporating comprehensive dosimetry data: dosimetry assessment could help elucidate the potentially crucial relationship between absorbed radiation doses to the kidneys and renal function decline and could investigate a potential dose–response relationship that might not have been apparent in our current retrospective analysis due to sample size limitations.

Of interest, the number of risk factors at baseline (diabetes, hypertension, age ≥ 65, or previous platinum chemotherapy) was significantly associated with a greater percentage eGFR decrease from baseline at the 12-mo follow-up. Withholding a potentially effective therapy with a clear survival benefit over preservation of renal function is clearly not an option, especially since it is rather unlikely that any of the treated patients will reach end-stage renal failure with their limited life expectancy. However, accompanying the treatment with best supportive care involving all disciplines and especially nephrologists is key for managing any significant GFR loss and kidney disease–associated comorbidities (e.g., renal anemia and secondary hyperparathyroidism).

Our study had several limitations. First, we selected only patients who received at least 4 cycles of PSMA-directed RLT. This may have led to an overestimation of the general incidence of renal impairment. Second, potentially more advanced parameters of renal function were not available in our retrospective analysis (e.g., cystatin C). Third, although we selected only patients with a least 12 mo of follow-up, data on longer follow-up are available in only a few cases mainly because of the short life expectancy of those patients. Our report currently constitutes the largest (to our knowledge) mCRPC cohort (including both patients with normal and impaired renal function at baseline) undergoing ^{177}Lu-PSMA with a minimum follow-up of 12 mo. The short life expectancy in patients with late-stage mCRPC itself is an important risk factor, given that dehydration and lower oral food and liquid intake are reduced in patients with end-stage progressive disease and aggravate renal impairment. By a strict definition of end-stage progressive disease (overall survival < 6 mo after the 12-mo follow-up and only the best supportive care after ^{177}Lu-PSMA), only 6 of 106 patients fell into this category. Larger studies on earlier-stage patients are warranted to further determine the role and impact of different risk factors regarding ^{177}Lu-PSMA RLT. Finally, we cannot assess to what extent the decrease in renal function over time was caused by use of ^{177}Lu-PSMA or by comorbidities, further complications of prostate cancer (e.g., postrenal obstruction and infections), or late effects of other therapies. Nevertheless, the association between established baseline risk factors and a more significant decline in renal function highlights the need for interdisciplinary consensus, which should consider current risk factors when recommending ^{177}Lu-PSMA treatment. A further limitation is the lack of a control group with ^{177}Lu-PSMA exposure, as potentially confounding factors could have contributed to the loss of kidney function (e.g., advanced disease stage). Nevertheless, the observed eGFR decreases at 12 mo in a cohort with non–end-stage progressive disease suggest at least some contribution of ^{177}Lu-PSMA RLT and warrants further evaluation. Another limitation is the use of a monoexponential function to determine the kidney function at a defined time. The method is generally reliable with multiple time points and is accepted for approximations in the literature but is not as accurate as true measurements at a given time.

CONCLUSION

Our data indicate that in most mCRPC patients undergoing at least 4 cycles of ^{177}Lu-PSMA, renal toxicity is moderate, with mild eGFR decreases up to 12 mo after treatment initiation. However, an at least severe decline in eGFR from baseline occurred in nearly a quarter of the entire cohort, and a further eGFR deterioration was observed in a substantial proportion of patients with longer follow-up. Thus, the results of further prospective trials with follow-up of more than 12 mo are urgently awaited to determine the risk of delayed nephrotoxicity after ^{177}Lu-PSMA RLT in relation to other available treatments. Until such data are available, off-label use of ^{177}Lu-PSMA RLT in patients with an expected life expectancy of more than 2 y should occur only after a careful evaluation of the benefits relative to the risks of progressive and potentially severe renal failure.

DISCLOSURE

Matthias Eiber reports fees from Blue Earth Diagnostics Ltd. (consultant, research funding), Novartis/AAA (consultant, speaker), Telix (consultant), Bayer (consultant, research funding), RayzeBio (consultant), Point Biopharma (consultant), Eckert-Ziegler (speaker), Janssen Pharmaceuticals (consultant, speakers' bureau), Parexel (image review), and Bioclinica (image review) outside the submitted

work and a patent application for radiohybrid PSMA. No other potential conflict of interest relevant to this article was reported.

KEY POINTS

QUESTION: What effect does ^{177}Lu-PSMA RLT have on renal function in mCRPC patients up to 1 y after the start of treatment?

PERTINENT FINDINGS: In this retrospective multicenter cohort study on 106 mCRPC patients undergoing ^{177}Lu-PSMA RLT, most patients experienced no or mild decreases in renal function within 1 y after treatment initiation. However, about 25% had severe eGFR decreases within 12 mo from treatment initiation. Radiation nephropathy appeared delayed: the 12-mo eGFR further deteriorated in patients with longer follow-up.

IMPLICATIONS FOR PATIENT CARE: ^{177}Lu-PSMA can lead to moderate and even severe decreases in renal function within 1 y from initiation of treatment. Prospective data on renal toxicity and with a longer follow-up are unavailable; the off-label use of ^{177}Lu-PSMA RLT in patients with potentially longer survival should therefore occur only after careful evaluation of the benefits relative to the risks of progressive and potentially severe renal failure.

REFERENCES

1. Hofman MS, Emmett L, Sandhu S, et al. [^{177}Lu]Lu-PSMA-617 versus cabazitaxel in patients with metastatic castration-resistant prostate cancer (TheraP): a randomised, open-label, phase 2 trial. *Lancet.* 2021;397:797–804.
2. Sartor O, de Bono J, Chi KN, et al. Lutetium-177-PSMA-617 for metastatic castration-resistant prostate cancer. *N Engl J Med.* 2021;385:1091–1103.
3. Yadav MP, Ballal S, Sahoo RK, Dwivedi SN, Bal C. Radioligand therapy with ^{177}Lu-PSMA for metastatic castration-resistant prostate cancer: a systematic review and meta-analysis. *AJR.* 2019;213:275–285.
4. Schäfer H, Mayr S, Buttner-Herold M, et al. Extensive ^{177}Lu-PSMA radioligand therapy can lead to radiation nephropathy with a renal thrombotic microangiopathy-like picture. *Eur Urol.* 2023;83:385–390.
5. Parihar AS, Chopra S, Prasad V. Nephrotoxicity after radionuclide therapies. *Transl Oncol.* 2022;15:101295.
6. Emami B, Lyman J, Brown A, et al. Tolerance of normal tissue to therapeutic irradiation. *Int J Radiat Oncol Biol Phys.* 1991;21:109–122.
7. Lambert B, Cybulla M, Weiner SM, et al. Renal toxicity after radionuclide therapy. *Radiat Res.* 2004;161:607–611.
8. Kratochwil C, Fendler WP, Eiber M, et al. EANM procedure guidelines for radionuclide therapy with ^{177}Lu-labelled PSMA-ligands (^{177}Lu-PSMA-RLT). *Eur J Nucl Med Mol Imaging.* 2019;46:2536–2544.
9. Heck MM, Tauber R, Schwaiger S, et al. Treatment outcome, toxicity, and predictive factors for radioligand therapy with ^{177}Lu-PSMA-I&T in metastatic castration-resistant prostate cancer. *Eur Urol.* 2019;75:920–926.
10. Levey AS, Stevens LA, Schmid CH, et al. A new equation to estimate glomerular filtration rate. *Ann Intern Med.* 2009;150:604–612.
11. Valkema R, Pauwels SA, Kvols LK, et al. Long-term follow-up of renal function after peptide receptor radiation therapy with ^{90}Y-DOTA^0,Tyr^3-octreotide and ^{177}Lu-DOTA^0, Tyr^3-octreotate. *J Nucl Med.* 2005;46(suppl 1):83S–91S.
12. Levey AS, Gansevoort RT, Coresh J, et al. Change in albuminuria and GFR as end points for clinical trials in early stages of CKD: a scientific workshop sponsored by the National Kidney Foundation in collaboration with the US Food and Drug Administration and European Medicines Agency. *Am J Kidney Dis.* 2020;75:84–104.
13. Levey AS, Inker LA, Matsushita K, et al. GFR decline as an end point for clinical trials in CKD: a scientific workshop sponsored by the National Kidney Foundation and the US Food and Drug Administration. *Am J Kidney Dis.* 2014;64:821–835.
14. Waas T, Schulz A, Lotz J, et al. Distribution of estimated glomerular filtration rate and determinants of its age dependent loss in a German population-based study. *Sci Rep.* 2021;11:10165.
15. Yordanova A, Becker A, Eppard E, et al. The impact of repeated cycles of radioligand therapy using [^{177}Lu]Lu-PSMA-617 on renal function in patients with hormone refractory metastatic prostate cancer. *Eur J Nucl Med Mol Imaging.* 2017;44:1473–1479.
16. Violet J, Sandhu S, Iravani A, et al. Long-term follow-up and outcomes of retreatment in an expanded 50-patient single-center phase II prospective trial of ^{177}Lu-PSMA-617 theranostics in metastatic castration-resistant prostate cancer. *J Nucl Med.* 2020;61:857–865.
17. Dhiantravan N, Emmett L, Joshua AM, et al. UpFrontPSMA: a randomized phase 2 study of sequential ^{177}Lu-PSMA-617 and docetaxel vs docetaxel in metastatic hormone-naïve prostate cancer (clinical trial protocol). *BJU Int.* 2021;128:331–342.
18. Dhiantravan N, Violet J, Eapen R, et al. Clinical trial protocol for LuTectomy: a single-arm study of the dosimetry, safety, and potential benefit of ^{177}Lu-PSMA-617 prior to prostatectomy. *Eur Urol Focus.* 2021;7:234–237.
19. Sundlöv A, Sjogreen-Gleisner K, Svensson J, et al. Individualised ^{177}Lu-DOTATATE treatment of neuroendocrine tumours based on kidney dosimetry. *Eur J Nucl Med Mol Imaging.* 2017;44:1480–1489.
20. Luxton RW, Kunkler PB. Radiation nephritis. *Acta Radiol Ther Phys Biol.* 1964;2:169–178.
21. Klaus R, Niyazi M, Lange-Sperandio B. Radiation-induced kidney toxicity: molecular and cellular pathogenesis. *Radiat Oncol.* 2021;16:43.

Unraveling the Impact of ^{177}Lu-PSMA Radioligand Therapy on Renal Impairment: Distinguishing Causation from Correlation

Aravind S. Ravi Kumar and Michael S. Hofman

Prostate Cancer Theranostics and Imaging Centre of Excellence, Molecular Imaging and Therapeutic Nuclear Medicine, Cancer Imaging, Peter MacCallum Centre Melbourne, and Sir Peter MacCallum Department of Oncology, University of Melbourne, Melbourne, Victoria, Australia

Prostate-specific membrane antigen (PSMA) radioligand therapy (RLT) is transforming prostate cancer management and nuclear medicine practice around the world. Within the last decade, prospective clinical trials have led to widespread adoption of PSMA RLT (*1–3*). Currently, PSMA RLT is generally used in the castration-resistant phase after disease progression on an androgen-receptor–pathway inhibitor and taxane chemotherapy.

Despite [^{177}Lu]Lu-PSMA's being is a life-prolonging therapy, the typical patient undergoing it today has a limited median survival of 15–18 mo. Although safety is well described in this context, radionuclide therapies may have toxicities that may not manifest for years or decades. As theranostics matures and clinical applications emerge in patients with longer life expectancies, questions around longer-term toxicities become relevant. In this context, we congratulate Steinhelfer et al. (*4*) for their attempt to characterize the longer-term nephrotoxicity of [^{177}Lu]Lu-PSMA therapy.

The first [^{177}Lu]Lu-PSMA therapies were administered a decade ago in Germany (*5,6*); it is therefore fitting that long-term nephrotoxicity has been reported from a collaboration of 3 German tertiary referral centers. The VISION trial (*3*) reported renal toxicity in only the 30 d after treatment. Calais et al. reported acute renal toxicity in 1.5% patients in their prospective phase II trial (*7*). Violet et al.'s prospective study (*1*) included 28 of 50 patients with [^{51}Cr]Cr-ethylenediaminetetraacetic acid glomerular filtration rate measured at baseline and 12 wk after therapy, demonstrating a mean decline of 11.7 mL/min.

At first glance, the headline results of the German study of a moderate decrease (namely, a 15%–30% reduction from baseline) in creatinine clearance in 45% of patients in their study group, of whom nearly half had a severe (30%–40%) to very severe (>40%) reduction in creatinine clearance, appears alarming. Declines in renal function were not acute and were observed at time points subsequent to 6 mo after treatment. Renal function declined more in patients who received a higher number of cycles of therapy and declined more quickly than the normally expected rate with longer follow-up.

Received Sep. 25, 2023; revision accepted Nov. 1, 2023.

For correspondence or reprints, contact Aravind S. Ravi Kumar (aravind.ravikumar@petermac.org).

Published online Nov. 16, 2023.

DOI: 10.2967/jnumed.123.266638

However, as with most retrospective research, caveats do emerge as acknowledged in the paper. Chief among these is that causality cannot be attributed to [^{177}Lu]Lu-PSMA in a patient cohort with other comorbidities and risk factors for renal disease and advanced progressive metastatic malignancy, with multiple prior lines of therapies and their own potential long-term impacts on renal function. This is a clinical situation in which there may be confounding complications and general functional decline ultimately leading to renal impairment. If renal function was near normal or normal at baseline, even very severe reductions in measured creatinine clearance as defined in this study may not immediately lead to clinically apparent consequences.

The number of patients with follow-up beyond 12 mo was rather small (20/474 screened patients with 2 y of follow-up and only 5 patients with 3 y of follow-up), limiting the usefulness of these data when considering the potential long-term consequences of the application of [^{177}Lu]Lu-PSMA in earlier phases of disease. Although the cause of patient drop-out is not explicit, it most likely is due to a combination of disease progression and treatment-refractory disease. It is possible some patients responded exceptionally, with longer survival, but stopped therapy before 4 cycles and thus were not eligible for study inclusion.

There are numerous reports of renal dosimetry with PSMA RLT, including early reports of application of amino acid infusions for renal protection (*8*). It is now clear that [^{177}Lu]Lu-PSMA-I&T delivers a slightly higher renal radiation dose than [^{177}Lu]Lu-PSMA-617 (*9*) and that amino acid infusions do not meaningfully reduce renal dose. From a dosimetry perspective, the lacrimal and salivary glands remain the organs most at risk from PSMA RLT.

There is emerging use of other isotopes, such as ^{161}Tb, ^{225}Ac, or ^{212}Pb-labeled PSMA therapies, which may add to the current prostate cancer theranostics landscape (*10*). Microdosimetry tools are also required to better characterize the absorbed doses from the short-range particulate emissions of these isotopes (*11*).

New therapies are typically tested in a phase 1 clinical trial in which the focus is on establishing a tolerable dose based on immediate side effects. This approach is used in oncologic drug trials but is not as well suited to radiopharmaceutical therapies. These are usually well tolerated initially, but longer-term toxicities may then emerge. Our radiation oncology colleagues deal with this issue by defining accepted maximal organ doses (*12*). These limits are extrapolated to radiopharmaceutical therapies, including by regulatory authorities.

However, experience from theranostics in neuroendocrine tumors and long-term follow-up suggests that safe dose limits from low–dose-rate radionuclide therapies are likely to be considerably higher (*13*). Administered activities or number of cycles of therapy could also be individualized with dosimetry.

Long-term follow-up is mandatory, preferably in a rigorous prospective clinical trial setting, or with postmarketing surveillance for approved or established therapies. Importantly, in the context of prostate cancer theranostics, for which clinical trials are being conducted with combination therapies and in earlier-stage disease, standard clinical trial endpoints of response rates, metastasis-free survival, or progression-free survival are not wholly adequate, and longer-term follow-up is strongly recommended for emergent toxicities or for codependence and interactions with other therapies.

Leaving aside nephrotoxicity, a significant longer-term concern with systemically administered radionuclide therapies is hematologic toxicity, including myelodysplasia, acute leukemia, and chronic cytopenias, which may additionally limit delivery of other therapies. With longer experience, this has emerged as a previously underrecognized issue with peptide receptor radionuclide therapy (used singly or as a combination therapy) in neuroendocrine tumors (*14,15*). However, long-term follow-up of the NETTER-1 trial more reassuringly demonstrated myelodysplasia of 2% and no increase in nephrotoxicity compared with controls (*16*). Myelodysplasia has not yet been a reported issue with PSMA RLT, but as the treatment is applied to more patients and in earlier stages of prostate cancer, longer-term follow-up not only becomes feasible but also is mandatory to properly understand the benefits and risks.

The broader prostate cancer therapeutic landscape is complex and ever changing, with many new, effective therapeutic agents and combinations (*17*). Ongoing high-quality studies of PSMA-based theranostics are essential for nuclear medicine to remain an integral part of this medical success story (*18*).

DISCLOSURE

Michael Hofman acknowledges philanthropic/government grant support from the Prostate Cancer Foundation (PCF) funded by CANICA Oslo Norway, the Peter MacCallum Foundation, the Medical Research Future Fund (MRFF), an NHMRC investigator grant, Movember, and the Prostate Cancer Foundation of Australia (PCFA). Michael Hofman also acknowledges research grant support (to the Peter MacCallum Cancer Centre) from Novartis (including AAA and Endocyte), ANSTO, Bayer, Isotopia, and MIM, as well as consulting fees for lectures or advisory boards from Astellas and AstraZeneca in the last 2 y and from Janssen, Merck/MSD, and Mundipharma in the last 5 y. No other potential conflict of interest relevant to this article was reported.

REFERENCES

1. Violet J, Sandhu S, Iravani A, et al. Long-term follow-up and outcomes of retreatment in an expanded 50-patient single-center phase II prospective trial of ^{177}Lu-PSMA-617 theranostics in metastatic castration-resistant prostate cancer. *J Nucl Med.* 2020;61:857–865.
2. Hofman MS, Emmett L, Sandhu S, et al. [^{177}Lu]Lu-PSMA-617 versus cabazitaxel in patients with metastatic castration-resistant prostate cancer (TheraP): a randomised, open-label, phase 2 trial. *Lancet.* 2021;397:797–804.
3. Sartor O, de Bono J, Chi KN, et al. Lutetium-177-PSMA-617 for metastatic castration-resistant prostate cancer. *N Engl J Med.* 2021;385:1091–1103.
4. Steinhelfer L, Lunger L, Cala L, et al. Long-term nephrotoxicity of ^{177}Lu-PSMA radioligand therapy. *J Nucl Med.* 2024;65:79–84.
5. Kratochwil C, Giesel FL, Eder M, et al. [^{177}Lu]lutetium-labelled PSMA ligand-induced remission in a patient with metastatic prostate cancer. *Eur J Nucl Med Mol Imaging.* 2015;42:987–988.
6. Ahmadzadehfar H, Rahbar K, Kurpig S, et al. Early side effects and first results of radioligand therapy with ^{177}Lu-DKFZ-617 PSMA of castrate-resistant metastatic prostate cancer: a two-centre study. *EJNMMI Res.* 2015;5:114.
7. Calais J, Czernin J, Thin P, et al. Safety of PSMA-targeted molecular radioligand therapy with ^{177}Lu-PSMA-617: results from the prospective multicenter phase 2 trial RESIST-PC (NCT03042312). *J Nucl Med.* 2021;62:1447–1456.
8. Baum RP, Kulkarni HR, Schuchardt C, et al. ^{177}Lu-labeled prostate-specific membrane antigen radioligand therapy of metastatic castration-resistant prostate cancer: safety and efficacy. *J Nucl Med.* 2016;57:1006–1013.
9. Schuchardt C, Zhang J, Kulkarni HR, Chen X, Muller D, Baum RP. Prostate-specific membrane antigen radioligand therapy using ^{177}Lu-PSMA I&T and ^{177}Lu-PSMA-617 in patients with metastatic castration-resistant prostate cancer: comparison of safety, biodistribution, and dosimetry. *J Nucl Med.* 2022;63:1199–1207.
10. Kratochwil C, Fendler WP, Eiber M, et al. Joint EANM/SNMMI procedure guideline for the use of ^{177}Lu-labeled PSMA-targeted radioligand-therapy (^{177}Lu-PSMA-RLT). *Eur J Nucl Med Mol Imaging.* 2023;50:2830–2845.
11. Hofmann W, Li WB, Friedland W, et al. Internal microdosimetry of alpha-emitting radionuclides. *Radiat Environ Biophys.* 2020;59:29–62.
12. Dawson LA, Kavanagh BD, Paulino AC, et al. Radiation-associated kidney injury. *Int J Radiat Oncol Biol Phys.* 2010;76(suppl)S108–S115.
13. Geenen L, Nonnekens J, Konijnenberg M, Baatout S, De Jong M, Aerts A. Overcoming nephrotoxicity in peptide receptor radionuclide therapy using [^{177}Lu]Lu-DOTA-TATE for the treatment of neuroendocrine tumours. *Nucl Med Biol.* 2021;102–103:1–11.
14. Goncalves I, Burbury K, Michael M, et al. Characteristics and outcomes of therapy-related myeloid neoplasms after peptide receptor radionuclide/chemoradionuclide therapy (PRRT/PRCRT) for metastatic neuroendocrine neoplasia: a single-institution series. *Eur J Nucl Med Mol Imaging.* 2019;46:1902–1910.
15. Kennedy KR, Turner JH, MacDonald WBG, Claringbold PG, Boardman G, Ransom DT. Long-term survival and toxicity in patients with neuroendocrine tumors treated with ^{177}Lu-octreotate peptide radionuclide therapy. *Cancer.* 2022;128:2182–2192.
16. Strosberg JR, Caplin ME, Kunz PL, et al. ^{177}Lu-Dotatate plus long-acting octreotide versus high-dose long-acting octreotide in patients with midgut neuroendocrine tumours (NETTER-1): final overall survival and long-term safety results from an open-label, randomised, controlled, phase 3 trial. *Lancet Oncol.* 2021;22:1752–1763.
17. Gillessen S, Bossi A, Davis ID, et al. Management of patients with advanced prostate cancer-metastatic and/or castration-resistant prostate cancer: report of the Advanced Prostate Cancer Consensus Conference (APCCC) 2022. *Eur J Cancer.* 2023;185:178–215.
18. Jang A, Kendi AT, Sartor O. Status of PSMA-targeted radioligand therapy in prostate cancer: current data and future trials. *Ther Adv Med Oncol.* 2023;15:17588359231157632.

Comparison of Multiple Segmentation Methods for Volumetric Delineation of Primary Prostate Cancer with Prostate-Specific Membrane Antigen–Targeted ^{18}F-DCFPyL PET/CT

Felicia Wang*[1], Chen Liu*[2,3], Igor Vidal[4], Margarita Mana-Ay[5], Andrew F. Voter[6], Lilja B. Solnes[6–8], Ashley E. Ross[9], Andrei Gafita[6], Edward M. Schaeffer[9], Trinity J. Bivalacqua[10], Kenneth J. Pienta[7,8], Martin G. Pomper[6–8], Martin A. Lodge[6], Daniel Y. Song[7,8,11], Jorge D. Oldan[12], Mohamad E. Allaf[7,8], Angelo M. De Marzo[4,7,8], Sara Sheikhbahaei*[6], Michael A. Gorin*[13], and Steven P. Rowe*[12]

*[1]School of Medicine, Johns Hopkins University, Baltimore, Maryland; [2]Key Laboratory of Carcinogenesis and Translational Research, Ministry of Education, Beijing, China; [3]Department of Nuclear Medicine, Peking University Cancer Hospital and Institute, Beijing, China; [4]Department of Pathology, School of Medicine, Johns Hopkins University, Baltimore, Maryland; [5]Northwestern Medicine, Chicago, Illinois; [6]Russell H. Morgan Department of Radiology and Radiological Science, School of Medicine, Johns Hopkins University, Baltimore, Maryland; [7]Brady Urological Institute, School of Medicine, Johns Hopkins University, Baltimore, Maryland; [8]Department of Urology, School of Medicine, Johns Hopkins University, Baltimore, Maryland; [9]Department of Urology, Feinberg School of Medicine, Northwestern Medicine, Chicago, Illinois; [10]Division of Urology, Perelman Center for Advanced Medicine, University of Pennsylvania, Philadelphia, Pennsylvania; [11]Department of Radiation Oncology and Molecular Radiation Science, Sidney Kimmel Comprehensive Center, School of Medicine, Johns Hopkins University, Baltimore, Maryland; [12]Molecular Imaging and Therapeutics, University of North Carolina, Chapel Hill, North Carolina; and [13]Milton and Carroll Petrie Department of Urology, Icahn School of Medicine at Mount Sinai, New York, New York

This study aimed to assess the accuracy of intraprostatic tumor volume measurements on prostate-specific membrane antigen–targeted ^{18}F-DCFPyL PET/CT made with various segmentation methods. An accurate understanding of tumor volumes versus segmentation techniques is critical for therapy planning, such as radiation dose volume determination and response assessment. **Methods:** Twenty-five men with clinically localized, high-risk prostate cancer were imaged with ^{18}F-DCFPyL PET/CT before radical prostatectomy. The tumor volumes and tumor-to-prostate ratios (TPRs) of dominant intraprostatic foci of uptake were determined using semiautomatic segmentation (applying SUV_{max} percentage [SUV%] thresholds of SUV30%–SUV70%), adaptive segmentation (using adaptive segmentation percentage [A%] thresholds of A30%–A70%), and manual contouring. The histopathologic tumor volume (TV-Histo) served as the reference standard. The significance of differences between TV-Histo and PET-based tumor volume were assessed using the paired-sample Wilcoxon signed-rank test. The Spearman correlation coefficient was used to establish the strength of the association between TV-Histo and PET-derived tumor volume. **Results:** Median TV-Histo was 2.03 cm^3 (interquartile ratio [IQR], 1.16–3.36 cm^3), and median TPR was 10.16%. The adaptive method with an A40% threshold most closely determined the tumor volume, with a median difference of +0.19 (IQR, −0.71 to +2.01) and a median relative difference of +7.6%. The paired-sample Wilcoxon test showed no significant difference in PET-derived tumor volume and TV-Histo using A40%, A50%, SUV40%, and SUV50% threshold segmentation algorithms ($P > 0.05$). For both threshold-based segmentation methods, use of higher thresholds (e.g., SUV60% or SUV70% and A50%–A70%) resulted in underestimation of tumor volumes, and use of lower thresholds (e.g., SUV30% or SUV40% and A30%) resulted in overestimation of tumor volumes relative to TV-Histo and TPR. Manual segmentation overestimated the tumor volume, with a median difference of +2.49 (IQR, 0.42–4.11) and a median relative difference of +130%. **Conclusion:** Segmentation of intraprostatic tumor volume and TPR with an adaptive segmentation approach most closely approximates TV-Histo. This information might be used to guide the primary treatment of men with clinically localized, high-risk prostate cancer.

Key Words: PSMA; Pylarify; PET/CT

J Nucl Med 2024; 65:87–93
DOI: 10.2967/jnumed.123.266005

The ability to accurately localize a tumor and delineate its volume is critical for guiding intended therapies for primary prostate cancer (PCa). Multiparametric MRI is most commonly used for this purpose (*1*). However, substantial evidence exists that multiparametric MRI underestimates tumor volume and has low sensitivity for small intraprostatic lesions (*2*,*3*).

Current treatment options for men with PCa range from active surveillance to radical therapy. Adverse effects of PCa treatment can have profound impacts on a patient's health and quality of life, including impotence, incontinence, and rectal toxicity (*4*). These effects exist because of the complex anatomy surrounding the prostate and the proximity to vital structures, such as the neurovascular bundles, as well as the bladder and rectum (*5*). The risk of damage to these structures is increased with whole-gland treatment options, such as radical prostatectomy and radiation therapy.

Received May 10, 2023; revision accepted Oct. 17, 2023.
For correspondence or reprints, contact Steven P. Rowe (steven_rowe@med.unc.edu).
*Contributed equally to this work.
Published online Nov. 30, 2023.

Focal therapies have the benefit of improving functional outcomes and reducing these off-target effects, but they have been limited historically by the multifocal nature of PCa and the risk of undertreatment (*6*). Optimizing focal therapies requires finding the balance between ensuring maximal treatment and minimizing damage to surrounding tissue. This requires precise and accurate contouring of the tumor volume and subsequent treatment area. Therefore, if we can better recapitulate histologic volume with pretreatment imaging, we can improve the efficacy of various focal or hemigland therapies (*6*). Specifically, with regard to planning for radiotherapy, precise identification of tumor volume is critical for strategic mapping of radiation delivery and dosimetry to minimize these off-target effects (*7*). Precision prostatectomy (*8*) is another more focal surgical treatment option that has shown outcomes for intermediate-risk PCa superior to those of other focal therapies while minimizing the adverse functional effects of radical prostatectomy.

Consequently, there is still a need for additional techniques to accurately identify tumor burden within the prostate. PET with radiotracers targeting prostate-specific membrane antigen (PSMA) have been studied in this context and have shown a high degree of sensitivity and specificity for primary PCa detection (*9*–*11*). Despite this, questions remain about the correlation of the radiotracer signal to the actual volume of the tumor—information that is critical when using PSMA PET for treatment guidance. The high contrast resolution of PSMA PET, with which very high radioactivity concentrations are achievable with PSMA-targeted agents, has the potential to overcome the intrinsic spatial-resolution limitations of other modalities. The use of PSMA PET to boost sites of disease to visibility is already under way, emphasizing the need for accurate PET-based tumor volume determination (*12*) as a means to both personalize treated volume and objectively determine response to therapy.

In this study, we assessed the accuracy of intraprostatic tumor volume measurements made with various segmentation methods on PSMA-targeted ^{18}F-DCFPyL PET/CT and used a gold standard of histopathology for comparison. We focused on SUV-based threshold methods in the interest of developing metrics that would be most easily translated into clinical practice, although we acknowledge the array of more advanced methods that have been investigated (*13*).

MATERIALS AND METHODS

General

This study is a secondary analysis of the intraprostatic findings from a previously published phase II trial studying ^{18}F-DCFPyL PET/CT in men with high-risk PCa undergoing radical prostatectomy (*14*). The original trial was indexed at ClinicalTrials.gov (NCT02151760) and was approved by the local institutional review board (NA_0092956/J1418).

Patients

The study enrolled men with clinically localized, high- or very high–risk PCa, as defined by the National Comprehensive Cancer Network (*15*). Preoperative staging was performed with the aid of conventional imaging, with a combination of ^{99m}Tc-methylene diphosphonate bone scan and either contrast-enhanced CT of the abdomen and pelvis or MRI of the pelvis. Evidence of distant metastatic disease or lymph node involvement on conventional imaging—that is, any lymph node longer than 15 mm on the short axis (*16*)—excluded the patient from participation in the study.

^{18}F-DCFPyL PET/CT Imaging

^{18}F-DCFPyL PET/CT was performed for all patients using an imaging protocol that has been previously described (*17*). Patients received up to 333 MBq (9 mCi) of ^{18}F-DCFPyL administered via slow push through a peripheral intravenous catheter. Patients were instructed to void immediately before the image acquisition process began.

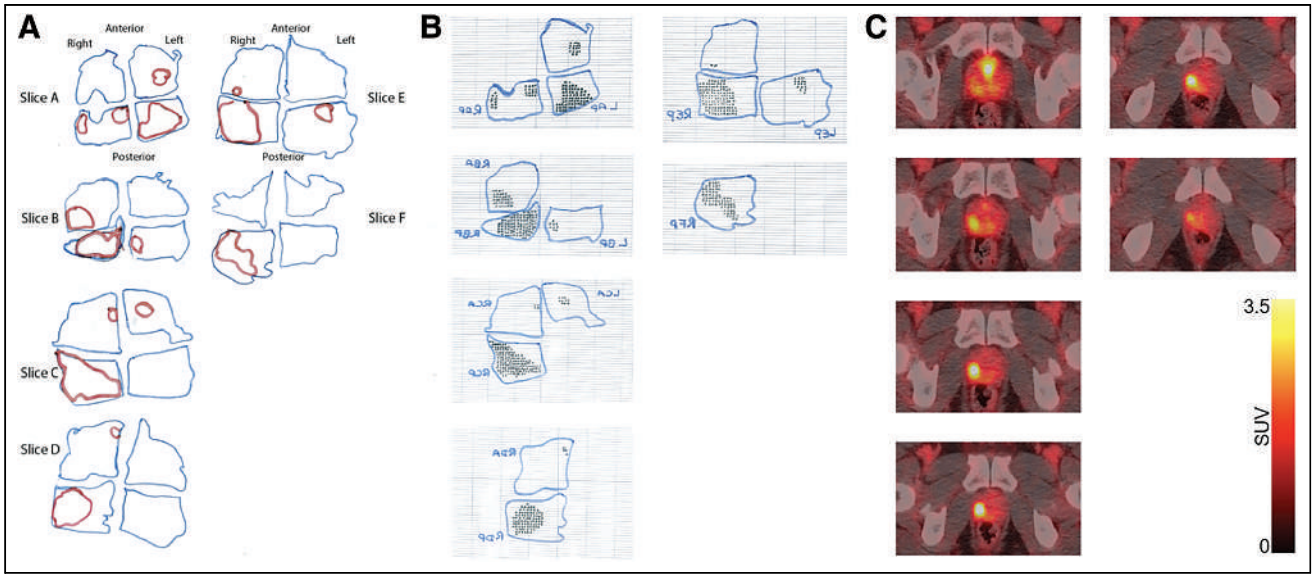

FIGURE 1. (A) Series of transparency tracings of histologic sections of prostate gland (blue outline) and tumor (red outline) from 1 patient in this study. Contours were drawn by hand from original histologic slides stained with hematoxylin and eosin. (B) Corresponding transparency tracings that have been transferred to 1-mm graph paper, with tumor demarcated by small black marks in each 1-mm square that corresponded to presence of tumor. Text is mirrored, because images were flipped to correspond to standard imaging display. Individual squares were determined by interpreting pathologist and confirmed by another pathologist. (C) Axial ^{18}F-DCFPyL PET/CT representative images from same patient. High uptake in right-sided dominant tumor nodule in prostate, extending from base to apex, is similar to pathologic results. PET images were selected to show overall extent of abnormal uptake but do not specifically correspond in slice-dependent manner with histopathologic slides.

Approximately 60 min after administration, a low-dose CT scan without intravenous contrast was obtained for attenuation correction and anatomic localization, followed by PET on either a Biograph mCT (Siemens Healthineers) or a Discovery VCT (GE Healthcare) using protocols that had been optimized to produce closely harmonized performance. The Biograph mCT data were reconstructed using 3-dimensional ordered-subsets expectation maximization with time of flight, 2 iterations, 21 subsets, 4-mm voxels, and a 5-mm, 3-dimensional gaussian filter. Corrections were applied for attenuation (CT-based), scatter (single-scatter simulation), randoms (delayed event subtraction), and dead time. The Discovery VCT data were reconstructed using 3-dimensional ordered-subsets expectation maximization without time of flight, 2 iterations, 21 subsets, 4.7-mm voxels, and a 3-mm, 2-dimensional gaussian filter. Corrections were applied for attenuation (CT-based), scatter (single-scatter simulation), randoms (singles-based), and dead time. These reconstruction parameters resulted in closely matched imaging performance, with recovery coefficients well within the range recommended by the European Association of Nuclear Medicine. For example, replicate experiments (n = 8) involving the National Electrical Manufacturers Association image quality phantom showed mean recovery for the 10-mm sphere of 53.2% (SD, 2.2%) for the Biograph mCT and 50.2% (SD, 3.1%) for the Discovery VCT.

Surgical Pathology

All patients underwent imaging, followed by radical retropubic prostatectomy with bilateral extended pelvic lymph node dissection within 1 wk of the ^{18}F-DCFPyL PET/CT. For routine pathology analysis, the entirety of each prostatectomy specimen was submitted for formalin fixation and paraffin embedding. This entailed sectioning the prostate from apex to base in approximately 3-mm slices and handling the prostate in a manner that allowed the pathologist to determine tissue orientation at all times. After standard-of-care determination of tumor stage, margin status, Gleason score, and grade group, each section of the prostate and seminal vesicles that had been stained with hematoxylin and eosin was reviewed microscopically, and regions of tumor were demarcated using a marking pen. Then, the outline of each slide and the regions of tumor were traced onto transparency paper, keeping the orientation of all 3 axes present such that we obtained 3-dimensional maps of the prostate and tumor lesions (Fig. 1). Subsequently, each section of prostate and seminal vesicles was placed over graph paper with 1-mm squares. The total number of squares subsumed by the prostate and seminal vesicles, as well as by the tumor, was recorded for each patient. Using 3-mm slice thicknesses, it was possible to calculate the volumes of the total glands and the tumor foci. Volumetric analyses were performed by a subspecialty-trained genitourinary pathologist and verified by another genitourinary pathologist with more than 20 y of experience. The nodule harboring the highest Gleason grade was selected for each patient.

Image Analysis

All images were exported to a Mirada workstation running XD3 software (Mirada Medical). The dominant intraprostatic focus of uptake was identified in all patients, and segmentations were performed. These segmentations included the best manual approximation of tumor extent, SUV-based tumor segmentation using the SUV_{max} percentage (SUV%) with varying thresholds of SUV30%–SUV70%, and adaptive segmentation using the adaptive segmentation percentage (A%) with varying thresholds of A30%–A70%. For adaptive segmentations (*18*), the volume-of-interest isocontours were delineated by multiplying the selected SUV_{max} threshold (SUV30%–SUV70%) by the sum of SUV_{max} and an average background value determined by a 3-cm spheric volume of interest in the pelvis that did not include abnormal uptake. The manual segmentations were not done at any preset windowing level; the performing radiologist was allowed to adjust the windowing to account for adjacent activity and was actively changing the window levels during tumor delineation. Imaging-based volumes of the prostate were also obtained.

TABLE 1
Summary Patient Demographics

Characteristic	Data
Age (y)	61 (54.5–67)
PSA (ng/mL)	9.3 (5.7–19.7)
Gleason score	
7	7 (28%)
8	2 (8%)
9	16 (64%)
Staging	
pT2N0	3
pT3aN0	10
pT3aN1	5
pT3bN0	5
pT3bN1	2
Race	
White	18 (72%)
African American	5 (20%)
Other	2 (8%)
Surgical margin	
Positive	8 (32%)
Negative	17 (68%)
Extraprostatic invasion	
Positive	20 (80%)
Negative	5 (20%)
Seminal vesicle invasion	
Positive	7 (28%)
Negative	18 (72%)
TV-Histo (cm^3)	2.03 (1.16–3.36)
Prostate weight (g)	40 (33.84–51.3)
Prostate	
SUV_{max}	2.07 (1.77–2.72)
SUV_{mean}	1.65 (1.33–2.09)
SUV_{peak}	1.90 (1.64–2.38)
Tumor	
SUV_{max}	9.84 (6.62–22.61)
SUV_{peak}	7.10 (4.61–14.97)

PSA = prostate-specific antigen.
Continuous data are median and IQR, and categoric data are frequency (as number of patients) and percentage.

Statistical Analysis

Quantitative variables were tested for normal distribution by the Shapiro–Wilk test. Continuous variables were presented as median and interquartile ratio (IQR), and categoric variables were presented as frequency and percentage.

TABLE 2
Absolute and Relative Percentage Difference of PET-Derived Tumor Volume with Pathology Across Segmentation Methods

Segmentation method	Threshold	Absolute difference	Relative difference (%)	*P*
SUV_{max}	SUV30%	4.14 (0.92 to 13.50)	142 (48 to 735)	<0.001
	SUV40%	0.3 (−0.48 to +3.46)	40 (−24 to +257)	0.09
	SUV50%	−0.3 (−1.04 to +0.92)	−25 (−60 to +78)	0.53
	SUV60%	−0.9 (−1.71 to −0.16)	−57 (−73 to −4)	<0.001
	SUV70%	−1.43 (−2.55 to +0.55)	−78 (−85 to −60)	<0.001
Adaptive	A30%	2.14 (0.46 to 5.2)	61.8 (0.41 to 419.7)	0.001
	A40%	0.19 (−0.71 to +2.01)	7.6 (−30.4 to +164.5)	0.23
	A50%	−0.49 (−1.23 to +0.61)	−28.3 (−61.2 to −35.6)	0.056
	A60%	−1.18 (−2.17 to −0.49)	−61.1 (−76.5 to −32.1)	<0.001
	A70%	−1.64 (−2.69 to −1.64)	−78 (−89.3 to −72.6)	<0.001
Manual		2.49 (0.42 to 4.11)	130 (25 to 216)	

Data are median followed by IQR in parentheses.

For each patient, the absolute and relative differences between PET-derived tumor volume measured by different segmentation methods and histopathologic tumor volume (TV-Histo) were calculated as follows:

$$\text{Absolute difference} = \text{PET volume} - \text{TV-Histo}, \quad \text{Eq. 1}$$

$$\text{Percentage relative difference} = \frac{\text{Absolute difference}}{\text{TV-Histo}} \times 100. \quad \text{Eq. 2}$$

The histopathologic and PET-derived tumor-to-prostate ratios (TPRs) were calculated.

Box plots were used to graphically illustrate the distribution of differences in tumor volumes and TPRs for each segmentation method, showing the median, first and third quartile, and mean and maximum values. The significance of differences between the TV-Histo and PET-based tumor volume and the TPRs were assessed using the paired-sample Wilcoxon signed-rank test. The Spearman correlation coefficient was used to establish the strength of association between TV-Histo and PET-derived tumor volume (*19*). Scatterplots were used to display the relationship between TV-Histo and PET-derived tumor volume across segmentation methods (Supplemental Figs. 1–11 [supplemental materials are available at http://jnm.snmjournals.org]). Statistical significance was defined as a *P* value of less than 0.05. Data were analyzed using SPSS version 26 (IBM).

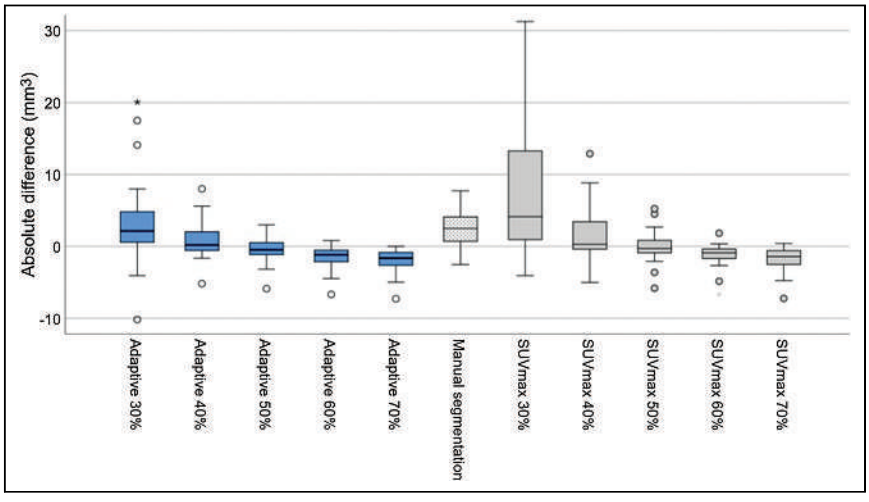

FIGURE 2. Box plot of absolute differences between PET-derived tumor volume and TV-Histo across segmentation methods. Asterisk represents extreme values; circles are outlier values.

RESULTS

Patient Demographics and Surgical Pathology Findings

Twenty-five patients with clinically localized, high-risk PCa were included in this study. Supplemental Table 1 lists individual patient clinical data. A summary of patient demographics and clinicopathologic tumor characteristics is provided in Table 1. Patients had a median prostate-specific antigen level at the time of the scan of 9.3 ng/mL (IQR, 5.7–19.7 ng/mL), and 16 (64%) men had Gleason score 9, 2 (8%) men had Gleason score 8, and 7 (28%) men had Gleason score 7. After prostatectomy, 20 of 25 (80%) patients were found to have extraprostatic involvement. Seminal vesicle invasion was present in 7 of 25 (28%) patients, as was lymph node involvement. The median TV-Histo was 2.03 cm^3 (IQR, 1.16–3.36 cm^3). The median SUV_{max} of the tumor and background prostate was 9.84 (IQR, 6.62–22.61) and 2.07 (IQR, 1.77–2.72), respectively.

Comparison of PET Segmentation Methods to Pathology

Segmentation of the tumor volume using the SUV threshold algorithm (SUV30%–SUV70%), adaptive threshold algorithm (A30%–A70%) (*18*), and the manual method were compared with the ground truth of TV-Histo. The absolute and relative differences in PET-derived tumor volume and TV-Histo across segmentation methods are reported in Table 2. Our results showed that adaptive method with an A40% threshold most closely determined the tumor volume, with a median difference of 0.19 cm^3 (IQR, −0.71 to +2.01 cm^3) and a median relative difference of +7.6%. Among the

TABLE 3
Comparison of Histopathologic and PET-Derived TPRs Across Segmentation Methods

Derivation method	Segmentation method	Threshold	TPR	*P*
Histopathologic			0.04 (0.02–0.09)	
PET	SUV_{max}	SUV30%	0.21 (0.25–0.09)	<0.001
		SUV40%	0.07 (0.04–0.17)	0.08
		SUV50%	0.03 (0.02–0.08)	0.40
		SUV60%	0.02 (0.01–0.04)	<0.001
		SUV70%	0.01 (0.01–0.02)	<0.001
	Adaptive	A30%	0.11 (0.06–0.19)	0.002
		A40%	0.06 (0.03–0.11)	0.29
		A50%	0.03 (0.02–0.05)	0.045
		A60%	0.02 (0.01–0.03)	<0.001
		A70%	0.01 (0.00–0.01)	<0.001
	Manual		0.08 (0.04–0.20)	<0.001

TPR data are median followed by IQR in parentheses.

SUV-based threshold segmentation methods, an SUV50% threshold had the least difference; TV-Histo had a median difference of −0.3 cm^3 (IQR, −1.04 to +0.92 cm^3) and a median relative difference of −25%.

The paired-sample Wilcoxon test showed no significant difference in PET-derived tumor volume and TV-Histo using A40%, A50%, SUV40%, and SUV50% threshold segmentation algorithms ($P > 0.05$). The tumor volumes derived from other segmentation algorithms were significantly different from those of TV-Histo ($P < 0.05$).

Figure 2 displays the distribution of absolute differences in tumor volume for different segmentation methods using a box plot. The box plot illustrates that the A40% segmentation algorithm most closely determined the tumor volume and had the least difference from TV-Histo.

For both threshold-based segmentation methods, use of higher thresholds (e.g., SUV60% or SUV70% and A50%–A70%) resulted in underestimation of tumor volumes, and use of lower thresholds (e.g., SUV30% or SUV40% and A30%) resulted in overestimation of tumor volumes relative to TV-Histo. The manual segmentation method tended to overestimate the tumor volume, with a median difference of +2.49 (IQR, 0.42–4.11) and a median relative difference of +130%.

Spearman correlation coefficient analysis revealed statistically significant low positive correlation between TV-Histo and PET-derived tumor volume in SUV50%–SUV70%, as well as A30%–A50% and A70% ($r = 0.44$, 0.42, and 0.44 for SUV50%, SUV60%, and SUV70%, respectively, and $r = 0.43$, 0.47, 0.48, and 0.49 for A30%, A40%, A50%, and A70%, respectively). It showed moderate positive correlation in A60% ($r = 0.55$) and the manual method ($r = 0.56$) and no significant correlation in the SUV30% and SUV40% thresholds.

This analysis was extended to TPR, with statistically significant low positive correlation between histopathologic and PET-derived TPRs using the SUV70% threshold ($r = 0.47$) and the A40% and A50% thresholds ($r = 0.45$ and 0.49, respectively). Moderate positive correlations were observed for the manual method, as well as the A60% and A70% thresholds ($r = 0.68$ for manual, 0.53 for A60%, and 0.52 for A70%). No significant correlation was seen for the SUV30%–SUV60% thresholds or the A30% threshold.

Scatterplots of TV-Histo, PET-derived tumor volume, and TPRs across segmentation methods are presented in Supplemental Figures 1–11. The reference line ($y = x$) was drawn to show systematic skew in the data.

TPR

Prostate devitalization leads to prostate shrinkage after resection, which may lead to spuriously decreased histopathologic prostate volume and TV-Histo relative to preresection imaging. However, because prostate tumors typically do not have hypervascularity, the prostate parenchyma and tumors are likely to undergo shrinkage to comparable extents, leaving the ratio of the tumor volume to the prostate volume unchanged. Therefore, we evaluated the comparison of histopathologic and PET-derived TPRs across segmentation methods (Table 3). TPR analysis showed that the A40% segmentation and SUV50% threshold methods most closely determined histopathologic TPR ($P = 0.29$ and 0.4, respectively). Figure 3 displays the difference between histopathologic and PET-derived TPRs across segmentation methods.

DISCUSSION

In recent years, there has been a rise in the use of PET imaging with PSMA-targeted agents, such as ^{18}F-DCFPyL, ^{18}F-DCFBC, and ^{68}Ga-PSMA-11, in the detection of PCa (*2*,*19*–*21*). Implementing the best radiotracer in combination with the most accurate segmentation method may significantly improve staging, prognostication, and treatment planning of PCa. However, no segmentation method is considered definitive for delineating tumor volume from ^{18}F-DCFPyL PET/CT. In this article, we demonstrate that an adaptive segmentation methodology most accurately recapitulates TV-Histo, regardless of whether tumor volume or TPR is used.

Various methods exist for determining tumor volume from PET data, including the SUV absolute value cutoff, SUV% threshold, adaptive thresholding, and manual segmentation. In studies

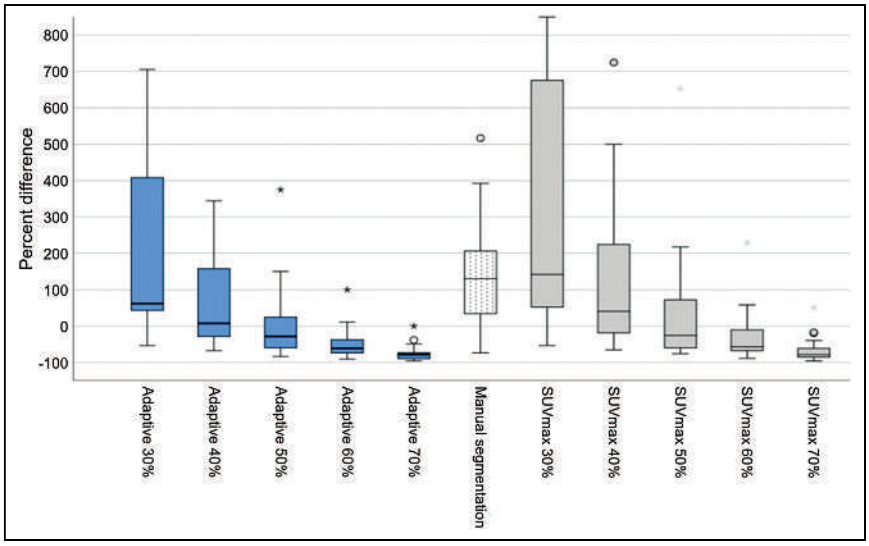

FIGURE 3. Box plot of relative differences between PET-derived tumor volume and TV-Histo across segmentation methods. Asterisks represent extreme values; circles are outlier values.

imaging other cancers using different PET radiotracers, proposed thresholds ranged between 30% and 50% for both the SUV_{max} and the adaptive methods (*22*–*25*). In a study of ^{68}Ga-PSMA-11 PET/CT comparing manual and semiautomatic segmentation methods with SUV_{max} thresholds, the highest sensitivity was achieved with a threshold of SUV20% and the highest specificity was achieved with a threshold of SUV40% or SUV50% (*24*). In our study, the A40% threshold demonstrated the greatest similarity to the ground truth of pathology, minimizing the difference in PET-derived tumor volume versus TV-Histo. Lower thresholds tended to overestimate tumor volume, whereas higher thresholds tended to underestimate tumor volume. Clinically, it may be more advantageous to overestimate, because of the comparative risk of treating benign prostate, than to leave malignant high-grade cells behind. Our findings are in line with studies that have shown that adaptive method performance is superior to that of standard fixed or relative thresholds in the segmentation of tumors (*26*,*27*).

Any study of in vivo imaging versus ex vivo pathology will have limitations. Specifically, both tumors and normal tissues undergo reductions in volume after devitalization, and accounting for such changes is difficult. We calculated ratiometric comparisons of tumor-to-prostate volume because the changes in volume in both types of tissue are likely similar. Furthermore, the patient cohort was limited to patients with high-risk disease. Studies of patients with lower-grade tumors would need to be performed to address segmentation in that population. In addition, the sample size was relatively small, although our study examined a greater number of lesions than other similar studies (*22*–*24*,*28*). Furthermore, the reliance of many of our segmentation methods on SUV-based thresholds suggests that very high–uptake tumors may lead to the exclusion of significant volumes of relevant disease in some patients. However, the use of SUV-based thresholds is easily translatable to the clinic. It is likely that more advanced methods of segmentation, including those derived from machine learning or neural networks (*13*,*29*), may be superior to the methods presented in this article, but those techniques are also more difficult to bring into clinical routine and may require refinement through additional rigorous, task-oriented studies (*29*,*30*). Even with painstakingly annotated data, there will always be comparative limitations. In this study, our inherently analog pathology specimens are being compared with digital imaging. Lastly, our scans were obtained from 2 different scanners, which adds an element of heterogeneity but could indicate broader generalizability to our findings. Detailed evaluations of other datasets of primary tumors relative to volumetric histologic gold standards are necessary. As advanced methods for segmentation become more commonly available in the clinic, we would expect that such methods would have the potential to supplant threshold-based techniques. We would also suggest that artificial intelligence or machine learning methods will be of significant importance in future work (*31*).

CONCLUSION

Accurate understanding of tumor volumes is critical when planning treatment for men with localized PCa. We show that segmentation at an A40% threshold on ^{18}F-DCFPyL PET imaging most closely recapitulates pathologic volume in men with high-risk PCa (using either tumor volume or TPR) relative to other SUV threshold-based techniques. Future work is required to validate this method of tumor segmentation in men with lower-grade disease. In addition, it is unknown whether this method of tumor segmentation applies to other PSMA-targeted PET radiotracers.

DISCLOSURE

This study was funded by NIH/NCI grants P50CA58236, U01CA196390, U54CA274370, P30CA006973, and P41EB024495; U.S. DoD grant W81XWH-18-2-0015; and the Patrick C. Walsh Prostate Cancer Research Fund at Johns Hopkins University. Martin Pomper is a coinventor on a U.S. patent covering ^{18}F-DCFPyL and as such is entitled to a portion of licensing fees and royalties generated by this technology. This arrangement has been reviewed and approved by Johns Hopkins University in accordance with its conflict-of-interest policies. Michael Gorin and Steven Rowe are consultants for Progenics Pharmaceuticals Inc., a wholly owned subsidiary of Lantheus, Inc., and the licensee of ^{18}F-DCFPyL. Kenneth Pienta, Martin Pomper, Michael Gorin, and Steven Rowe have received research funding from Progenics. Angelo De Marzo is a paid consultant or advisor to Merck and Cepheid and has received research funding from Janssen and Myriad for unrelated work. No other potential conflict of interest relevant to this article was reported.

KEY POINTS

QUESTION: What is the best easily translatable method for segmenting primary, high-risk PCa on PSMA PET?

PERTINENT FINDINGS: Segmentation at a threshold of A40% most closely recapitulates primary tumor volume from pathology, whether compared with absolute tumor volume or TPR.

IMPLICATIONS FOR PATIENT CARE: Using the noted segmentation technique may allow more accurate guidance of therapy for primary, high-risk PCa.

REFERENCES

1. Kasivisvanathan V, Rannikko AS, Borghi M, et al. MRI-targeted or standard biopsy for prostate-cancer diagnosis. *N Engl J Med.* 2018;378:1767–1777.
2. Bettermann AS, Zamboglou C, Kiefer S, et al. [^{68}Ga-]PSMA-11 PET/CT and multiparametric MRI for gross tumor volume delineation in a slice by slice analysis with whole mount histopathology as a reference standard: implications for focal radiotherapy planning in primary prostate cancer. *Radiother Oncol.* 2019;141:214–219.
3. Pooli A, Johnson DC, Shirk J, et al. Predicting pathological tumor size in prostate cancer based on multiparametric prostate magnetic resonance imaging and preoperative findings. *J Urol.* 2021;205:444–451.
4. Donovan JL, Hamdy FC, Lane JA, et al. Patient-reported outcomes after monitoring, surgery, or radiotherapy for prostate cancer. *N Engl J Med.* 2016;375:1425–1437.
5. Walz J, Epstein JI, Ganzer R, et al. A critical analysis of the current knowledge of surgical anatomy of the prostate related to optimisation of cancer control and preservation of continence and erection in candidates for radical prostatectomy: an update. *Eur Urol.* 2016;70:301–311.
6. Eldred-Evans D, Tam H, Smith APT, Winkler M, Ahmed HU. Use of imaging to optimise prostate cancer tumour volume assessment for focal therapy planning. *Curr Urol Rep.* 2020;21:38.
7. Weiss E, Hess CF. The impact of gross tumor volume (GTV) and clinical target volume (CTV) definition on the total accuracy in radiotherapy theoretical aspects and practical experiences. *Strahlenther Onkol.* 2003;179:21–30.
8. Sood A, Jeong W, Palma-Zamora I, et al. Description of surgical technique and oncologic and functional outcomes of the precision prostatectomy procedure (IDEAL stage 1-2b study). *Eur Urol.* 2022;81:396–406.
9. Rowe SP, Macura KJ, Mena E, et al. PSMA-based [^{18}F]DCFPyL PET/CT is superior to conventional imaging for lesion detection in patients with metastatic prostate cancer. *Mol Imaging Biol.* 2016;18:411–419.
10. Szabo Z, Mena E, Rowe SP, et al. Initial evaluation of [^{18}F]DCFPyL for prostate-specific membrane antigen (PSMA)-targeted PET imaging of prostate cancer. *Mol Imaging Biol.* 2015;17:565–574.
11. Sanchez-Crespo A. Comparison of gallium-68 and fluorine-18 imaging characteristics in positron emission tomography. *Appl Radiat Isot.* 2013;76:55–62.
12. Zamboglou C, Spohn SKB, Ruf J, et al. PSMA-PET- and MRI-based focal dose escalated radiation therapy of primary prostate cancer: planned safety analysis of a nonrandomized 2-armed phase 2 trial (ARO2020-01). *Int J Radiat Oncol Biol Phys.* 2022;113:1025–1035.
13. Hatt M, Lee JA, Schmidtlein CR, et al. Classification and evaluation strategies of auto-segmentation approaches for PET: report of AAPM task group no. 211. *Med Phys.* 2017;44:e1–e42.
14. Gorin MA, Rowe SP, Patel HD, et al. Prostate specific membrane antigen targeted ^{18}F-DCFPyL positron emission tomography/computerized tomography for the preoperative staging of high risk prostate cancer: results of a prospective, phase II, single center study. *J Urol.* 2018;199:126–132.
15. Moses KA, Sprenkle PC, Bahler C, et al. NCCN Guidelines® insights: prostate cancer early detection, version 1.2023. *J Natl Compr Canc Netw.* 2023;21:236–246.
16. Scher HI, Morris MJ, Stadler WM, et al. Trial design and objectives for castration-resistant prostate cancer: updated recommendations from the Prostate Cancer Clinical Trials Working Group 3. *J Clin Oncol.* 2016;34:1402–1418.
17. Rowe SP, Gorin MA, Hammers HJ, et al. Imaging of metastatic clear cell renal cell carcinoma with PSMA-targeted ^{18}F-DCFPyL PET/CT. *Ann Nucl Med.* 2015;29:877–882.
18. Frings V, van Velden FH, Velasquez LM, et al. Repeatability of metabolically active tumor volume measurements with FDG PET/CT in advanced gastrointestinal malignancies: a multicenter study. *Radiology.* 2014;273:539–548.
19. Das CJ, Razik A, Sharma S. Positron emission tomography in prostate cancer: an update on state of the art. *Indian J Urol.* 2018;34:172–179.
20. Rowe SP, Gage KL, Faraj SF, et al. ^{18}F-DCFBC PET/CT for PSMA-based detection and characterization of primary prostate cancer. *J Nucl Med.* 2015;56:1003–1010.
21. Bodar YJL, Zwezerijnen B, van der Voorn PJ, et al. Prospective analysis of clinically significant prostate cancer detection with [^{18}F]DCFPyL PET/MRI compared to multiparametric MRI: a comparison with the histopathology in the radical prostatectomy specimen, the ProStaPET study. *Eur J Nucl Med Mol Imaging.* 2022;49:1731–1742.
22. Frings V, de Langen AJ, Smit EF, et al. Repeatability of metabolically active volume measurements with ^{18}F-FDG and ^{18}F-FLT PET in non-small cell lung cancer. *J Nucl Med.* 2010;51:1870–1877.
23. Erdi YE, Mawlawi O, Larson SM, et al. Segmentation of lung lesion volume by adaptive positron emission tomography image thresholding. *Cancer.* 1997;80(suppl 12):S2505–S2509.
24. Zamboglou C, Fassbender TF, Steffan L, et al. Validation of different PSMA-PET/CT-based contouring techniques for intraprostatic tumor definition using histopathology as standard of reference. *Radiother Oncol.* 2019;141:208–213.
25. Giesel FL, Sterzing F, Schlemmer HP, et al. Intra-individual comparison of ^{68}Ga-PSMA-11-PET/CT and multi-parametric MR for imaging of primary prostate cancer. *Eur J Nucl Med Mol Imaging.* 2016;43:1400–1406.
26. Im HJ, Bradshaw T, Solaiyappan M, Cho SY. Current methods to define metabolic tumor volume in positron emission tomography: which one is better? *Nucl Med Mol Imaging.* 2018;52:5–15.
27. Tamal M. Intensity threshold based solid tumour segmentation method for positron emission tomography (PET) images: a review. *Heliyon.* 2020;6:e05267.
28. Zamboglou C, Schiller F, Fechter T, et al. ^{68}Ga-HBED-CC-PSMA PET/CT versus histopathology in primary localized prostate cancer: a voxel-wise comparison. *Theranostics.* 2016;6:1619–1628.
29. Liu Z, Mhlanga JC, Siegel BA, Jha AK. Need for objective task-based evaluation of AI-based segmentation methods for quantitative PET. ArXiv website. https://arxiv.org/abs/2303.00640. Published March 1, 2023. Accessed November 6, 2023.
30. Yousefirizi F, Jha AK, Brosch-Lenz J, Saboury B, Rahmim A. Toward high-throughput artificial intelligence-based segmentation in oncological PET imaging. *PET Clin.* 2021;16:577–596.
31. Holzschuh JC, Mix M, Ruf J, et al. Deep learning based automated delineation of the intraprostatic gross tumour volume in PSMA-PET for patients with primary prostate cancer. *Radiother Oncol.* 2023;188:109774.

Reproducibility and Accuracy of the PRIMARY Score on PSMA PET and of PI-RADS on Multiparametric MRI for Prostate Cancer Diagnosis Within a Real-World Database

Louise Emmett[1–3], Nathan Papa[2], William Counter[1], Jeremie Calais[4], Francesco Barbato[5], Irene Burger[6], Matthias Eiber[7], Matthew J. Roberts[8], Shikha Agrawal[1,2], Anthony Franklin[8], Alan Xue[9], Krishan Rasiah[10], Nikeith John[1,3], Daniel Moon[11], Mark Frydenberg[9], John Yaxley[12], Phillip Stricker[13], Keith Wong[1], Geoff Coughlin[12], Troy Gianduzzo[12], Boon Kua[12], Bao Ho[1], Andrew Nguyen[1,3], Victor Liu[1], Jonathan Lee[1], Edward Hsiao[9], Tom Sutherland[15], Elisa Perry[15], Wolfgang P. Fendler[5], and Thomas A. Hope[16]

[1]Department of Theranostics and Nuclear Medicine, St. Vincent's Hospital Sydney, Sydney, New South Wales, Australia; [2]Garvan Institute of Medical Research, Sydney, New South Wales, Australia; [3]St. Vincent's Clinical School, University of New South Wales, Sydney, New South Wales, Australia; [4]Ahmanson Translational Theranostics, Department of Molecular and Medical Pharmacology, David Geffen School of Medicine at UCLA, UCLA, Los Angeles, California; [5]Department of Nuclear Medicine, University of Duisburg–Essen and German Cancer Consortium–University Hospital Essen, Essen, Germany; [6]Department of Nuclear Medicine, Kantonsspital Baden, Baden, Switzerland; [7]Department of Nuclear Medicine, School of Medicine, Technical University Munich, Munich, Germany; [8]Department of Urology, Royal Brisbane and Women's Hospital, Brisbane, Queensland, Australia; [9]Department of Surgery, Faculty of Medicine, Monash University, Melbourne, Victoria, Australia; [10]Department of Urology, Royal North Shore Hospital, Sydney, New South Wales, Australia; [11]Division of Cancer Surgery, Peter MacCallum Cancer Centre, Melbourne, Victoria, Australia; [12]Wesley Hospital, Brisbane, Queensland, Australia; [13]St. Vincent's Prostate Cancer Centre, Darlinghurst, New South Wales, Australia; [14]Department of Nuclear Medicine, Royal North Shore Hospital, Sydney, New South Wales, Australia; [15]Department of Radiology, St. Vincent's Hospital Melbourne, Melbourne, Victoria, Australia; and [16]Department of Radiology and Biomedical Imaging, University of California, San Francisco, San Francisco, California

The PRIMARY score is a 5-category scale developed to identify clinically significant intraprostate malignancy (csPCa) on ^{68}Ga-prostate-specific membrane antigen (PSMA)–11 PET/CT (^{68}Ga-PSMA PET) using a combination of anatomic site, pattern, and intensity. Developed within the PRIMARY trial, the score requires evaluation in external datasets. This study aimed to assess the reproducibility and diagnostic accuracy of the PRIMARY score in a cohort of patients who underwent multiparametric MRI (mpMRI) and ^{68}Ga-PSMA PET before prostate biopsy for the diagnosis of prostate cancer. **Methods:** In total, data from 242 men who had undergone ^{68}Ga-PSMA PET and mpMRI before transperineal prostate biopsy were available for this ethics-approved retrospective study. ^{68}Ga-PSMA PET and mpMRI data were centrally collated in a cloud-based deidentified image database. Six experienced prostate-focused nuclear medicine specialists were trained (1 h) in applying the PRIMARY score with 30 sample images. Six radiologists experienced in prostate mpMRI read images as per the Prostate Imaging–Reporting and Data System (PI-RADS), version 2.1. All images were read (with masking of clinical information) at least twice, with discordant findings sent to a masked third (or fourth) reader as necessary. Cohen κ was determined for both imaging scales as 5 categories and then collapsed to binary (negative and positive) categories (score 1 or 2 vs. 3, 4, or 5). Diagnostic performance parameters were calculated, with an International Society of Urological Pathology grade group of at least 2 (csPCa) on biopsy defined as the gold standard. Combined-imaging–positive results were defined as any PI-RADS score of 4 or 5 or as a PI-RADS score of 1–3 with a PRIMARY score of 3–5. **Results:** In total, 227 patients with histopathology, ^{68}Ga-PSMA PET, and mpMRI imaging before prostate biopsy were included; 33% had no csPCa, and 67% had csPCa. Overall interrater reliability was higher for the PRIMARY scale (κ = 0.70) than for PI-RADS (κ = 0.58) when assessed as a binary category (benign vs. malignant). This was similar for all 5 categories (κ = 0.65 vs. 0.48). Diagnostic performance to detect csPCa was comparable between PSMA PET and mpMRI (sensitivity, 86% vs. 89%; specificity, 76% vs. 74%; positive predictive value, 88% vs. 88%; negative predictive value, 72% vs. 76%). Using combined imaging, sensitivity was 94%, specificity was 68%, positive predictive value was 86%, and negative predictive value was 85%. **Conclusion:** The PRIMARY score applied by first-user nuclear medicine specialists showed substantial interrater reproducibility, exceeding that of PI-RADS applied by mpMRI-experienced radiologists. Diagnostic performance was similar between the 2 modalities. The PRIMARY score should be considered when interpreting intraprostatic PSMA PET images.

Key Words: multiparametric MRI; PSMA; prostate-specific membrane antigen; PET; prostate cancer; diagnosis

J Nucl Med 2024; 65:94–99
DOI: 10.2967/jnumed.123.266164

The diagnosis of clinically significant prostate cancer (csPCa) has improved with the introduction of imaging-targeted biopsy with multiparametric MRI (mpMRI), allowing a proportion of men with normal MRI results to avoid biopsy and allowing MRI-targeted biopsy, improving the diagnosis of high-grade malignancy (*1,2*). The addition of ^{68}Ga-prostate-specific membrane antigen (PSMA)–11 PET/CT (^{68}Ga-PSMA PET) to mpMRI further improved the negative predictive

Received Jun. 14, 2023; revision accepted Oct. 4, 2023.
For correspondence or reprints, contact Louise Emmett (louise.emmett@svha.org.au).
Published online Nov. 30, 2023.

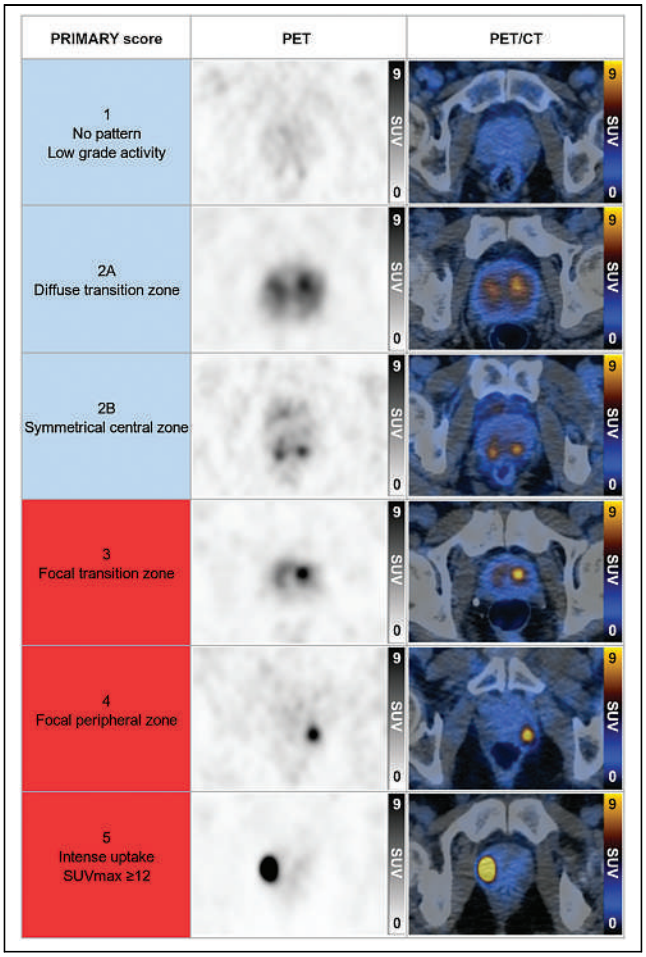

FIGURE 1. Five-point PRIMARY score (*4*).

value for prostate cancer diagnosis in the PRIMARY trial (*3,4*). The primary objective of this study was to validate the PRIMARY score developed in the prospective PRIMARY trial using a dataset of retrospectively collected real-world patients undergoing ^{68}Ga-PSMA PET and mpMRI before prostate biopsy.

MATERIALS AND METHODS

This retrospective project was approved by the Human Research Ethics Board at St. Vincent's Hospital Sydney (approval 2022/ETH00051). Patients from investigating urologists in Australia who had undergone both ^{68}Ga-PSMA PET and mpMRI before initial prostate biopsy were identified. PSMA PET undertaken after biopsy for staging was an exclusion criterion. All patients had clinical data collected, including age, PSA level at the time of imaging, and the dates of imaging and biopsy procedures. The urologists' reasons for biopsy or imaging were not available. ^{68}Ga-PSMA PET and mpMRI were undertaken as per institutional protocols.

Imaging Data Collection

Both ^{68}Ga-PSMA PET and mpMRI data were centrally collated and deidentified on a secure web-based server (MIMcloud; MIM Software) for independent review, with imaging modalities collated into separated imaging datasets to ensure masked reads by imagers. All imaging and clinical data were collated on an institutional REDCap database (St. Vincent's Hospital Sydney) specifically designed for the trial. Case report forms were developed to record both PRIMARY and Prostate Imaging–Reporting and Data System (PI-RADS) scores. The PRIMARY score was documented as previously defined, with 5 categories: score 1, no significant pattern within the prostate; score 2, a diffuse transition or central zone pattern; score 3, focal transition zone activity above twice the background transition zone counts; score 4, focal peripheral zone activity of any intensity; and score 5, an SUV of more than 12 (Fig. 1) (*4*).

Image Reads and Analysis

Deidentified ^{68}Ga-PSMA PET images were independently read by 6 ^{68}Ga-PSMA PET–experienced nuclear medicine physicians according to the PRIMARY score. Each scan was read by 2 readers, with a maximum of 40 scans read by the same 2 readers. To get a single ^{68}Ga-PSMA PET imaging decision per patient, any reader disagreement requiring a masked read by a third reader occurred when the first score was 1 or 2 and the second score was 3, 4, or 5. Before commencing, all nuclear medicine imaging investigators participated in a 1-h training session involving an explanation of the PRIMARY score and a consensus read of 30 ^{68}Ga-PSMA PET scans external to the study dataset. All readers were instructed to use the fused PET/CT images to allow differentiation between transition-zone and peripheral-zone activity. Images were read using the readers' preferred PET image viewer platform.

Six experienced prostate MRI radiologists read mpMRI images as per PI-RADS version 2.1 independently of the PSMA PET or clinical results (*5*). To get a single PI-RADS score per patient, in the event of disagreement on PI-RADS scores between 2 readers, a third masked

TABLE 1
Patient Characteristics (n = 227)

Characteristic	Data
Age (y)	68 (61–74)
PSA (ng/mL)	6.8 (4.8–10.3)
Days from MRI to biopsy	33 (14–79)
Days from PET to biopsy	15 (6–35)
Grade group	
No cancer	58 (26)
1	16 (7.0)
2	49 (22)
3	35 (15)
4	13 (5.7)
5	56 (25)
PI-RADS*	
1	2 (0.9)
2	70 (31)
3	26 (11)
4	56 (25)
5	73 (32)
PRIMARY†	
Negative (1,2)	78 (34)
Positive (3–5)	149 (66)

*Taken as majority score from at least 2 readers.
†Taken as majority read from 2 of 3 readers if discordant.
Qualitative data are number and percentage; continuous data are median and interquartile range.

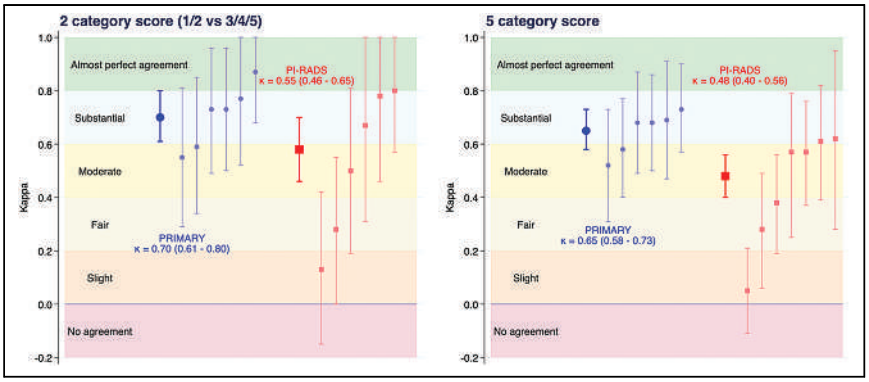

FIGURE 2. Cohen κ-coefficient for PRIMARY and PI-RADS divided into 2 categories or left as 5 categories. Overall coefficient and 95% CI are presented as thicker symbols and lines, with pairwise interrater values presented next to these as thinner, fainter symbols and lines.

tie-breaking read was performed by another expert reader. If this was discordant with the other reads, a fourth read was undertaken.

Histopathology

Histopathology from biopsy was derived from the clinical histopathology report. Transperineal rather than transrectal ultrasound biopsy was undertaken in all cases. The median number of cores was 22. Systematic biopsy was standard, with MRI-guided additional cores also obtained in some cases. The International Society of Urological Pathology (ISUP) grade group reported for the trial was for the index lesion.

Statistical Analysis

The primary outcome of interest was an estimate of the interrater reliability of the PRIMARY score, in its original 5 categories and as a binary evaluation (score 1 or 2 vs. 3, 4, or 5), for nuclear medicine specialists new to using the score. This was measured using the Cohen κ-coefficient, with the interpretations of the value by Landis and Koch adopted in the figures and text (0–0.2 indicating slight agreement; 0.21–0.40, fair agreement; 0.41–0.60, moderate agreement; 0.61–0.80, substantial agreement; and 0.81–1.0, almost perfect or perfect agreement). Additionally, the analogous analysis was performed for the mpMRI read with PI-RADS with the further evaluation for 3 categories of PI-RADS (1 or 2 vs. 3 vs. 4 or 5). The sample size per reader pair aimed to exceed the heuristic of 30 previously proposed in the literature (*6*). Further, we expected heterogeneity between PET reader pairs given the novelty of the scale. Combined with a convenience sample of about 240 patients, it was thus decided to invite 6 readers for each imaging modality. Secondary aims were, first, to calculate diagnostic accuracy for ^{68}Ga-PSMA PET using the PRIMARY score and for mpMRI using PI-RADS, with an ISUP grade group of 2 or more on biopsy being the gold standard; second, to calculate the diagnostic accuracy of a rational combination of imaging modalities based on the original PRIMARY paper (defining combined imaging positivity as PI-RADS 4/5 or PI-RADS 1–3 with a PRIMARY score of 3–5); third, to assess the distribution of ISUP grade group across categories of PI-RADS and binary PRIMARY score; and fourth, to evaluate the association between ISUP grade group and SUV_{max}, defined as the mean SUV_{max} reported by the 2 readers, with the Kruskal–Wallis test and significance set at a P value of less than 0.05. Stata version 17.0MP (StataCorp LLC) was used to generate the figures and analysis.

RESULTS

In total, 242 patients were available for analysis, having undergone ^{68}Ga-PSMA PET and mpMRI, no prior prostate biopsy or treatment for prostate cancer, and subsequent transperineal prostate biopsy. Five had no pathology data available, a further 8 had no MR images available, and 2 more had no PET images available, leaving 227 patients for analysis (Table 1; Supplemental Fig. 1 [supplemental materials are available at http://jnm.snmjournals.org]). Seventy-four men (33%) did not have csPCa, 49 (22%) had ISUP grade group 2 disease, and 104 (46%) had ISUP grade group 3–5 disease.

Reproducibility

The overall κ for binary PRIMARY score categories (1 or 2 vs. 3, 4, or 5) was 0.70 (95% CI, 0.61–0.80), with a percentage agreement of 86% (Fig. 2). Pairwise κ-values ranged from 0.55 to 0.87. Interrater reliability for the full 5-category scale was substantial at 0.65 (95% CI, 0.58–0.73), percentage agreement was 74%, and pairwise κ-values ranged from 0.52 to 0.73. The overall κ for binary PI-RADS (1 or 2 vs. 3, 4, or 5) was moderate at 0.58 (95% CI, 0.46–0.70), with a percentage agreement of 82%. For a 3-group categorization of PI-RADS (1 or 2 vs. 3 vs. 4 or 5), the κ was 0.55 (95% CI, 0.46–0.65), with percentage agreement of 75%, and for the full 5-category scale, the κ was 0.48 (95% CI, 0.40–0.56), with percentage agreement of 61%. Twelve patients had discordant PI-RADS scores among 3 readers and required a fourth read. There were 7 pairs of MRI readers, instead of 6, as the allotment of 1 reader could not be completed (paired reader κ-values are shown in Supplemental Tables 1–5).

Diagnostic Accuracy

In total, 149 (66%) of patients had a positive ^{68}Ga-PSMA PET result (PRIMARY score of 3, 4, or 5), and 155 (68%) had a positive MRI result (PI-RADS score of 3, 4, or 5). The sensitivity of ^{68}Ga-PSMA PET was 86% (95% CI, 79%–91%), and the specificity was 76% (95% CI, 64%–85%), whereas the sensitivity of MRI was 89% (95% CI, 83%–93%), with a specificity of 74% (95% CI, 63%–84%). Individual PET and mpMRI reader sensitivities are represented in Figure 3. The positive predictive value for ^{68}Ga-PSMA PET was 88% (95% CI, 82%–93%), with a negative predictive value of 72% (95% CI, 61%–81%), and the respective

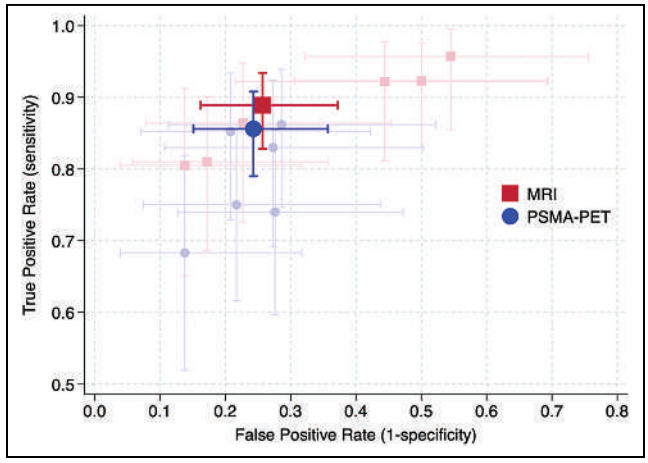

FIGURE 3. Sensitivity vs. (1 − specificity) overall for ^{68}Ga-PSMA PET and MRI derived from PRIMARY and PI-RADS scores, respectively. Faint markers and lines denote individual readers.

TABLE 2
Diagnostic Accuracy for PI-RADS, PRIMARY, and Combination

Parameter	Sensitivity	Specificity	Positive predictive value	Negative predictive value
PRIMARY	86% (79%–91%)	76% (64%–85%)	88% (82%–93%)	72% (61%–81%),
PI-RADS	89% (83%–93%)	74% (63%–84%)	88% (82%–93%	76% (65%–86%)
Combination	94% (89%–97%)	68% (56%–78%).	86% (80%–91%)	85% (73%–93%)

values for MRI were 88% (95% CI, 82%–93%) and 76% (95% CI, 65%–86%). Using the combined ^{68}Ga-PSMA PET/MRI definition of positive findings, the sensitivity was 94% (95% CI, 89%–97%), with a specificity of 68% (95% CI, 56%–78%). The positive predictive value was 86% (95% CI, 80%–91%), and the negative predictive value was 85% (95% CI, 73%–93%) (Table 2; Supplemental Table 6).

Histopathology and Imaging

The distribution of histology grade according to positive or negative ^{68}Ga-PSMA PET finding and category of PI-RADS is demonstrated in Figure 4. In each PI-RADS category, positive ^{68}Ga-PSMA PET results, versus negative, resulted in a higher percentage of csPCa and ISUP grade group 3–5 cancer. Five of 45 patients (11%) with a PI-RADS score of 1 or 2 and ^{68}Ga-PSMA PET–negative results had csPCa, all ISUP grade group 2. One patient of 59 (1.7%) had negative results on combined imaging (PI-RADS score of 3, ^{68}Ga-PSMA PET–negative) and ISUP grade group 5 disease (Fig. 5). This patient's MR images were read 3 times (PI-RADS scores of 2, 3, and 3), and the PET images were read twice (PRIMARY scores of 1 and 2).

SUV_{max} and Grade Group

There was a statistically significant association between PSMA PET SUV_{max}, taken as the mean of 2 readers, and ISUP grade group ($P < 0.001$) (Fig. 6). All patients with an SUV_{max} of more than 12 (PRIMARY score, 5) had csPCa, with 51 of 55 (93%) of those patients being ISUP grade group 3 or higher.

DISCUSSION

The PRIMARY score was developed to optimize the diagnostic accuracy of ^{68}Ga-PSMA PET for csPCa intraprostatically and particularly to improve specificity over an SUV_{max}-based reporting method (*3,4*). The PRIMARY score has been incorporated into PROMISE version 2 for reporting of ^{68}Ga-PSMA PET (*7*). This validation study undertaken on a real-world dataset confirmed the high diagnostic accuracy of the PRIMARY score, with significant reproducibility among readers. Accuracy was equivalent to the MRI PI-RADS score, with better reproducibility, despite the limited experience of the readers with the PRIMARY score.

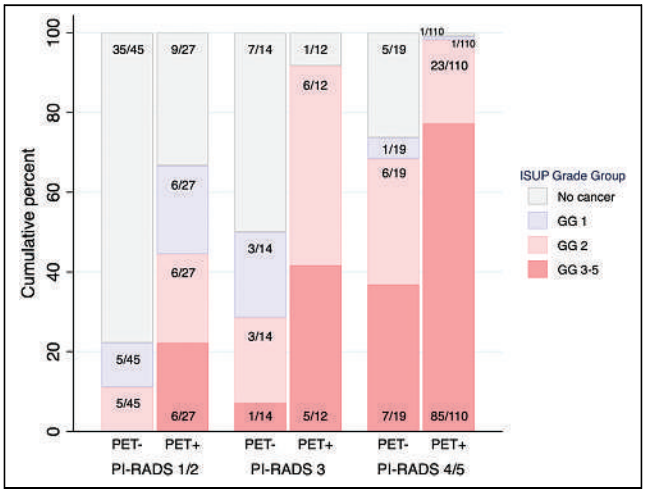

FIGURE 4. Cumulative percentage distribution of ISUP grade group by positive or negative ^{68}Ga-PSMA PET result and 3 categories of PI-RADS. GG = grade group.

Benign intraprostatic patterns of PSMA activity with increased uptake in the transition and central zones are common as a result of benign prostatic hypertrophy and physiologic activity surrounding the ejaculatory ducts in the central zones (*8,9*). However, most malignancy (70%) arises within the peripheral zone of the prostate, with the incidence of transition and central zone malignancy significantly lower (*10*). The PRIMARY score uses this information to weight focal activity in the peripheral and transition zones while classifying diffuse transition zone activity as a benign finding. The initial PRIMARY score publication found that separating patterns of intraprostatic PSMA activity into focal or diffuse improved identification of significant malignancy (*4*). This validation cohort confirmed improved specificity using a pattern-based reporting system rather than an intensity (SUV_{max})-based analysis as was used in the initial PRIMARY paper (*3*).

mpMRI is now the standard of care for the diagnosis of csPCa, with key randomized trials demonstrating improved accuracy and a reduced requirement for biopsy compared with a non–imaging-based transrectal ultrasound biopsy diagnostic paradigm (*2,11*). However, despite better targeting with MRI, a significant number of malignancies are missed using an MRI-targeted approach, with a high proportion of negative biopsies that could potentially have been avoided (*1*). ^{68}Ga-PSMA PET using the PRIMARY score in conjunction with mpMRI may further optimize the diagnosis of prostate cancer, reducing the biopsy requirement and detection of insignificant malignancy while improving sensitivity for csPCa. This is being evaluated further in the prospective randomized PRIMARY2 trial (NCT05154162).

There is a strong association between ISUP grade group on histopathology and ^{68}Ga-PSMA PET intensity, an association that is likely due to the pro-proliferative role of the PSMA receptor in prostate cancer (*12–16*). As with the PRIMARY study, the analysis found that an SUV_{max} of more than 12 was associated with csPCa in 100%, with an ISUP grade group of at least 3 in 93% of those cases. This finding validates the use of PSMA intensity ($SUV_{max} > 12$) as the maximal PRIMARY score, although further work will be required to identify an optimum intensity for a PRIMARY score of 5 if PSMA-targeting peptides other than ^{68}Ga-PSMA are to be utilized.

The Cohen κ demonstrated substantial agreement between the 6 PRIMARY score readers in the study, despite the fact that training was limited to a single 1-h session and despite the lack of harmonization between PET cameras, acquisition protocols, and doses

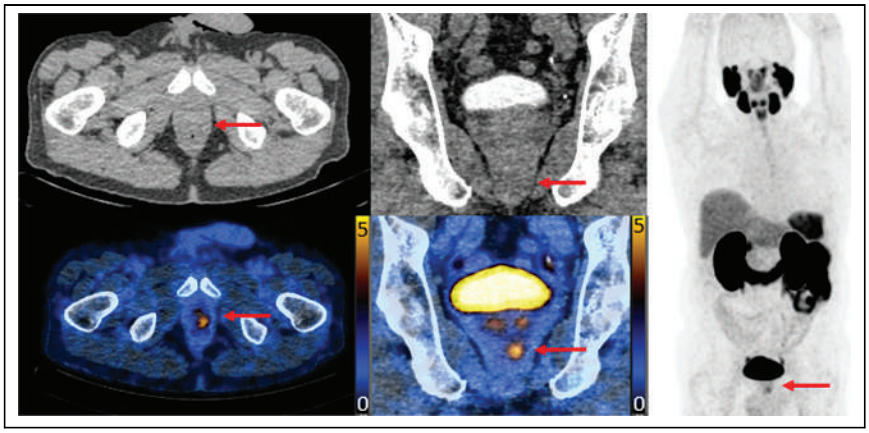

FIGURE 5. PSMA PET imaging for patient with ISUP grade group 5 on histopathology, negative result on ^{68}Ga-PSMA PET central read, and PI-RADS 3 on MRI. Central readers had 1-h training session on PRIMARY score with little prior exposure, and this lesion was missed by both readers. This image is technically PRIMARY score 4 (arrows) with focal lesion apically (SUV_{max}, 3.5).

due to the retrospective nature of the study. There was a single ISUP grade group 5 classified as PSMA-negative by both central readers and with equivocal mpMRI results (PI-RADS score, 3). This scan had focal PSMA avidity apically, fulfilling the criteria for a PRIMARY score of 4. It is expected that the reported diagnostic accuracy of the PRIMARY score will improve with further training of readers. There was a lower κ-score for PI-RADS despite the readers' being high-volume prostate MRI specialists, pointing to reproducibility and simplicity as strengths of the PRIMARY score.

There are important limitations to the study. The study was designed as a real-world dataset to externally evaluate the findings of the PRIMARY trial. As such, it was retrospectively collected, and the reasons for which the urologists requested ^{68}Ga-PSMA PET before biopsy were not documented and will have introduced a selection bias, particularly for the PI-RADS 1 and 2 patients included. Also because of the retrospective design, no camera or dose harmonization was possible. Nevertheless, the results show diagnostic accuracy similar to that of the prospective PRIMARY trial, demonstrating the reproducibility of the score, both for accuracy and among readers. A higher proportion of patients had more aggressive disease on histopathology than in the PRIMARY trial, with a lower proportion of benign or low-grade findings. This factor may have impacted the negative predictive value of the PRIMARY, PI-RADS, and combination scores. In the evaluation of reader agreement for both MRI and PSMA, the study utilized 2 readers—with a third reader for discordance—rather than the 3 readers considered optimal in a registration study (*17*).

Both the PRIMARY trial and this validation study utilized ^{68}Ga-PSMA PET. Although it is likely that the PRIMARY score is translatable to other PSMA PET agents given the focus on pattern and anatomic site, this possibility requires further evaluation.

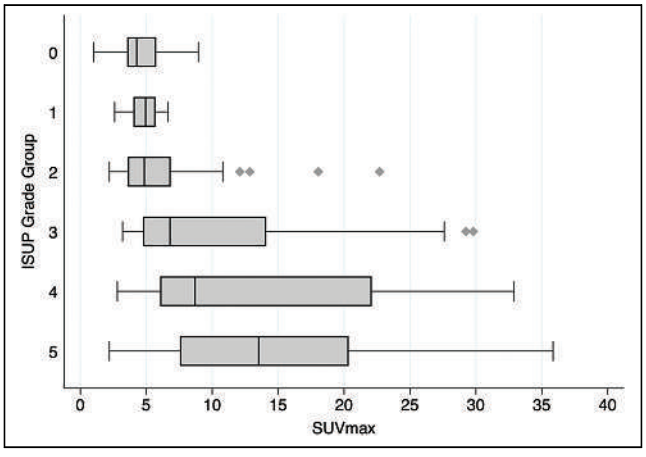

FIGURE 6. Horizontal box plot of SUV_{max} by ISUP grade group, taken as mean of 2 readers' reports. Not shown are 1 ISUP grade group 3 lesion (SUV_{max}, 62) and 2 ISUP grade group 5 lesions (SUV_{max}, 44 and 46).

CONCLUSION

The PRIMARY score showed substantial interrater reproducibility by first-user nuclear medicine specialists, exceeding that of PI-RADS. Diagnostic performance was similar between the 2 modalities. The PRIMARY score should be considered when interpreting intraprostatic PSMA PET images.

DISCLOSURE

Wolfgang Fendler reports fees from SOFIE Biosciences (research funding), Janssen (consultant, speaker), Calyx (consultant, image review), Bayer (consultant, speaker, research funding), Novartis (speaker, consultant), Telix (speaker), GE Healthcare (speaker), and Eczacıbaşı Monrol (speaker) outside the submitted work. Louise Emmett reports funds from Movember (research), Clarity (research, consultant), Novartis (speaker, consultant), Astellas (speaker), Astrazeneca (speaker), and Telix (speaker). Matthias Eiber reports fees from Blue Earth Diagnostics Ltd. (consultant, research funding), Novartis/AAA (consultant, speaker), Telix (consultant), Bayer (consultant, research funding), RayzeBio (consultant), Point Biopharma (consultant), Eckert-Ziegler (speaker), Janssen Pharmaceuticals (consultant, speakers' bureau), Parexel (image review), and Bioclinica (image review) outside the submitted work and a patent application for rhPSMA. No other potential conflict of interest relevant to this article was reported.

KEY POINTS

QUESTION: Is the PRIMARY score an accurate reproducible method for reporting intraprostatic PSMA PET findings in men prior to prostate biopsy, and how does it compare to mpMRI?

PERTINENT FINDINGS: The PRIMARY score is equivalent in diagnostic accuracy to mpMRI when undertaken prior to prostate biopsy in a high-risk population. Further, it is more reproducible than mpMRI despite the readers having limited clinical experience with the score.

IMPLICATIONS FOR PATIENT CARE: A 5-level PRIMARY score incorporating intraprostatic patterns and intensity on ^{68}Ga-PSMA PET/CT shows potential as an accurate method for diagnosing csPCa and should be considered when PSMA PET is undertaken for this purpose.

REFERENCES

1. Ahmed HU, El-Shater Bosaily A, Brown LC, et al. Diagnostic accuracy of multiparametric MRI and TRUS biopsy in prostate cancer (PROMIS): a paired validating confirmatory study. *Lancet.* 2017;389:815–822.
2. Kasivisvanathan V, Emberton M, Moore CM. MRI-targeted biopsy for prostate-cancer diagnosis. *N Engl J Med.* 2018;379:589–590.
3. Emmett L, Buteau J, Papa N, et al. The additive diagnostic value of prostate-specific membrane antigen positron emission tomography computed tomography to multiparametric magnetic resonance imaging triage in the diagnosis of prostate cancer (PRIMARY): a prospective multicentre study. *Eur Urol.* 2021;80:682–689.
4. Emmett L, Papa N, Buteau J, et al. The PRIMARY score: using intraprostatic ^{68}Ga-PSMA PET/CT patterns to optimize prostate cancer diagnosis. *J Nucl Med.* 2022;63:1644–1650.
5. Padhani AR, Weinreb J, Rosenkrantz AB, Villeirs G, Turkbey B, Barentsz J; Prostate Imaging–Reporting and Data System Steering Committee. PI-RADS v2 status update and future directions. *Eur Urol.* 2019;75:385–396.
6. McHugh ML. Interrater reliability: the kappa statistic. *Biochem Med (Zagreb).* 2012;22:276–282.
7. Seifert R, Emmett L, Rowe SP, et al. Second version of the prostate cancer molecular imaging standardized evaluation framework including response evaluation for clinical trials (PROMISE V2). *Eur Urol.* 2023;83:405–412.
8. Ganeshalingam R, Hsiao E. Compressed central zone uptake on PSMA PET/CT: a potential pitfall in interpretation. *Clin Nucl Med.* 2019;44:570–571.
9. Pizzuto DA, Müller J, Mühlematter U, et al. The central zone has increased ^{68}Ga-PSMA-11 uptake: "Mickey Mouse ears" can be hot on ^{68}Ga-PSMA-11 PET. *Eur J Nucl Med Mol Imaging.* 2018;45:1335–1343.
10. McNeal JE, Redwine EA, Freiha FS, Stamey TA. Zonal distribution of prostatic adenocarcinoma. Correlation with histologic pattern and direction of spread. *Am J Surg Pathol.* 1988;12:897–906.
11. Sathianathen NJ, Omer A, Harriss E, et al. Negative predictive value of multiparametric magnetic resonance imaging in the detection of clinically significant prostate cancer in the Prostate Imaging Reporting and Data System era: a systematic review and meta-analysis. *Eur Urol.* 2020;78:402–414.
12. Caromile LA, Shapiro LH. PSMA redirects MAPK to PI3K-AKT signaling to promote prostate cancer progression. *Mol Cell Oncol.* 2017;4:e1321168.
13. Eiber M, Nekolla SG, Maurer T, et al. ^{68}Ga-PSMA PET/MR with multimodality image analysis for primary prostate cancer. *Abdom Imaging.* 2015;40:1769–1771.
14. Kaittanis C, Andreou C, Hieronymus H, et al. Prostate-specific membrane antigen cleavage of vitamin B9 stimulates oncogenic signaling through metabotropic glutamate receptors. *J Exp Med.* 2018;215:159–175.
15. Roberts MJ, Morton A, Papa N, et al. Primary tumour PSMA intensity is an independent prognostic biomarker for biochemical recurrence-free survival following radical prostatectomy. *Eur J Nucl Med Mol Imaging.* 2022;49:3289–3294.
16. Scheltema MJ, Chang JI, Stricker PD, et al. Diagnostic accuracy of ^{68}Ga-prostate-specific membrane antigen (PSMA) positron-emission tomography (PET) and multiparametric (mp)MRI to detect intermediate-grade intra-prostatic prostate cancer using whole-mount pathology: impact of the addition of ^{68}Ga-PSMA PET to mpMRI. *BJU Int.* 2019;124(suppl 1):42–49.
17. Fendler WP, Calais J, Eiber M, et al. Assessment of ^{68}Ga-PSMA-11 PET accuracy in localizing recurrent prostate cancer: a prospective single-arm clinical trial. *JAMA Oncol.* 2019;5:856–863.

Preclinical Development of PNT6555, a Boronic Acid–Based, Fibroblast Activation Protein-α (FAP)–Targeted Radiotheranostic for Imaging and Treatment of FAP-Positive Tumors

Sarah E. Poplawski[1], Robin M. Hallett[2], Mark H. Dornan[2], Kyle E. Novakowski[2], Shuang Pan[1], Anthony P. Belanger[3,4], Quang-De Nguyen[3,5], Wengen Wu[1], Albert E. Felten[2], Yuxin Liu[1], Shin Hye Ahn[3,4], Valerie S. Hergott[2], Barry Jones[1], Jack H. Lai[1], Joe A.B. McCann[2], and William W. Bachovchin[1]

[1]*Department of Developmental, Molecular and Chemical Biology, Tufts University Graduate School of Biomedical Sciences, Boston, Massachusetts;* [2]*POINT Biopharma Global Inc., Indianapolis, Indiana;* [3]*Harvard Medical School, Boston, Massachusetts;* [4]*Molecular Cancer Imaging Facility, Dana-Farber Cancer Institute, Boston, Massachusetts; and* [5]*Lurie Family Imaging Center, Dana-Farber Cancer Institute, Boston, Massachusetts*

The overexpression of fibroblast activation protein-α (FAP) in solid cancers relative to levels in normal tissues has led to its recognition as a target for delivering agents directly to tumors. Radiolabeled quinoline-based FAP ligands have established clinical feasibility for tumor imaging, but their therapeutic potential is limited due to suboptimal tumor retention, which has prompted the search for alternative pharmacophores. One such pharmacophore is the boronic acid derivative *N*-(pyridine-4-carbonyl)-D-Ala-boroPro, a potent and selective FAP inhibitor (FAPI). In this study, the diagnostic and therapeutic (theranostic) potential of *N*-(pyridine-4-carbonyl)-D-Ala-boroPro–based metal-chelating DOTA-FAPIs was evaluated. **Methods:** Three DOTA-FAPIs, PNT6555, PNT6952, and PNT6522, were synthesized and characterized with respect to potency and selectivity toward soluble and cell membrane FAP; cellular uptake of the Lu-chelated analogs; biodistribution and pharmacokinetics in mice xenografted with human embryonic kidney cell–derived tumors expressing mouse FAP; the diagnostic potential of ^{68}Ga-chelated DOTA-FAPIs by direct organ assay and small-animal PET; the antitumor activity of ^{177}Lu-, ^{225}Ac-, or ^{161}Tb-chelated analogs using human embryonic kidney cell–derived tumors expressing mouse FAP; and the tumor-selective delivery of ^{177}Lu-chelated DOTA-FAPIs via direct organ assay and SPECT. **Results:** DOTA-FAPIs and their ^{nat}Ga and ^{nat}Lu chelates exhibited potent inhibition of human and mouse sources of FAP and greatly reduced activity toward closely related prolyl endopeptidase and dipeptidyl peptidase 4. ^{68}Ga-PNT6555 and ^{68}Ga-PNT6952 showed rapid renal clearance and continuous accumulation in tumors, resulting in tumor-selective exposure at 60 min after administration. ^{177}Lu-PNT6555 was distinguished from ^{177}Lu-PNT6952 and ^{177}Lu-PNT6522 by significantly higher tumor accumulation over 168 h. In therapeutic studies, all 3 ^{177}Lu-DOTA-FAPIs exhibited significant antitumor activity at well-tolerated doses, with ^{177}Lu-PNT6555 producing the greatest tumor growth delay and animal survival. ^{225}Ac-PNT6555 and ^{161}Tb-PNT6555 were similarly efficacious, producing 80% and 100% survival at optimal doses, respectively. **Conclusion:** PNT6555 has potential for clinical translation as a theranostic agent in FAP-positive cancer.

Key Words: oncology; FAP; radioligand; theranostic; PET

Received Jul. 13, 2023; revision accepted Oct. 17, 2023.

For correspondence or reprints, contact William W. Bachovchin (william.bachovchin@tufts.edu).

Published online Nov. 30, 2023.

J Nucl Med 2024; 65:100–108
DOI: 10.2967/jnumed.123.266345

Fibroblast activation protein-α (FAP, also called seprase) is a member of the dipeptidyl peptidase 4 (DPP4)–like subfamily of serine proteases (*1–3*). FAP is expressed as either a type II integral membrane glycoprotein (*4*) or a soluble plasma protein containing only the extracellular carboxy-terminal catalytic domain (*5*). Relative to normal tissues, FAP is often highly overexpressed in epithelial tumors on the surface of cancer-associated fibroblasts (CAFs) (*6–8*). Less frequently, FAP is overexpressed on neoplastic cells themselves, in certain sarcomas, for example (*8*).

Although FAP is also upregulated in healing wounds and atherosclerotic, arthritic, and fibrotic lesions (*9–13*), it is recognized as a target for the design of anticancer drugs (*14*). There is particular interest in high-affinity, small-molecule catalytic-site ligands that can be linked to a metal chelator such as DOTA for use as theranostic agents: for example, positron-emitting ^{68}Ga for PET or β-emitting ^{177}Lu, ^{161}Tb (which emits Auger electrons and undergoes β-decay (*15*)), or α-emitting ^{225}Ac for radiotherapy (*16*). Unlike FAP, the related postproline cleaving proteases DPP4 and prolyl endopeptidase (PREP) are widely expressed in normal tissues. DPP4 plays a role in glucose metabolism (*17*), whereas the phenotype of PREP-deficient mice suggests that PREP functions in the central nervous system (*18*). High FAP selectivity is, therefore, essential in FAP-targeted radioligands for application in oncology.

A potent and selective inhibitor of FAP (UAMC1110) that is based on the *N*-4-quinolinoyl-Gly-(2*S*)-cyanoPro scaffold, has provided a lead for the development of quinoline FAP inhibitors (FAPIs) (*19–21*). These FAPIs demonstrated the feasibility of FAP radioligands as PET imaging agents in preclinical models and human cancer patients, but therapeutic potential appeared limited by suboptimal tumor retention (*22*), prompting the exploration of alternative FAP ligands. A more recent clinical candidate, FAP-2286, incorporates a cyclic peptide as the FAP-binding moiety, with the aim of harnessing the entropic advantage available from

conformationally restricted cyclic ligands, so as to achieve greater potency and thereby greater tumor retention (*23*). In a mouse model of FAP-positive cancer (FAP-expressing human embryonic kidney [HEK] cells), ^{177}Lu-FAP-2286 did achieve greater tumor retention and treatment responses than ^{177}Lu-FAPI-46, the leading quinoline derivative (*24*).

A different approach can be based on the boronic acid derivative *N*-(pyridine-4-carbonyl)-D-Ala-boroPro (3099), first discovered and characterized by Poplawski et al. (*25*). The nanomolar potency of 3099 and the high selectivity for FAP over other DPP4-like subfamily enzymes provides the rationale for its investigation as a FAP-targeting moiety. In this study, the feasibility of amino-terminally blocked D-Ala-boroPro as a FAP-targeting element in theranostic radioligands was investigated, with a focus on PNT6555, PNT6952, and PNT6522 (Fig. 1)—in which the DOTA chelator was N-terminally linked to D-alanine by either an aminobenzoic acid residue (PNT6555), a tranexamic acid residue (PNT6952), or a Gly-Gly-Val tripeptide (PNT6522).

MATERIALS AND METHODS

A complete version of Materials and Methods, including details of instrumentation, radiochemistry, in vivo imaging protocols, reagents, reaction buffers, and vendors, is provided in the supplemental materials (supplemental materials are available at http://jnm.snmjournals.org).

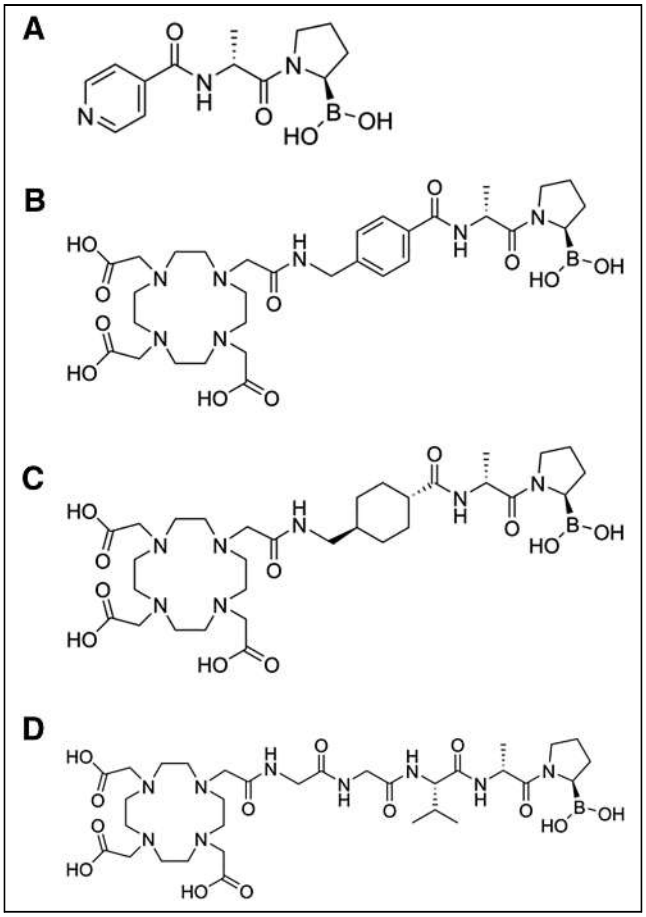

FIGURE 1. Structures of FAP ligands. (A) *N*-(pyridine-4-carbonyl)-D-Ala-boroPro (3099). (B) DOTA-AmBz-D-Ala-boroPro (AmBz: aminomethylbenzoyl) (PNT6555). (C) DOTA-TXA-D-Ala-boroPro (TXA: transexamic acid) (PNT6952). (D) DOTA-Gly-Gly-Val-D-Ala-boroPro (PNT6522).

In Vivo Procedures

The protocol for the tumor model involving HEK cell–derived tumors expressing mouse FAP (HEK-mFAP) was approved by the Dana-Farber Cancer Institute (Boston, Massachusetts) Institutional Animal Care and Use Committee. Mouse serum was collected by cardiac puncture using a protocol approved by the Tufts University Institutional Animal Care and Use Committee.

Synthesis of FAP Ligand Precursors

PNT6555, PNT6522, and PNT6952 were synthesized as previously described by Bachovchin et al. (*26*).

Radiochemistry of ^{68}Ga-, ^{177}Lu-, ^{225}Ac-, and ^{161}Tb-Chelated Compounds

Radioligands were prepared by heating precursors with $^{177}LuCl_3$, $^{68}GaCl_3$, $^{225}Ac(NO_3)_3$, or $^{161}TbCl_3$. Radiochemical identities were confirmed by chromatography.

HEK-mFAP and HEK-Mock Cell Lines

HEK-mFAP and HEK cells transfected with empty vector (HEK-Mock) (*27*) were propagated in standard culture medium with the addition of G418 (Geneticin; Thermo Fisher Scientific) to sustain stable transgene expression.

In Vitro Fluorometric IC_{50} Measurements

Half-maximal inhibitory concentration (IC_{50}) values of FAP ligands for recombinant human FAP, DPP4, and PREP were determined. FAP (pH 7.5), PREP (pH 7.5), and DPP4 (pH 8.0) were incubated at room temperature for 10 min with 1:10 serial dilutions of FAP ligands (PNT6555, PNT6952, and PNT6522) in 96-well plates. 7-Amino-4-methylcoumarin (AMC) fluorogenic substrates (carboxybenzyl (*Z*)-Gly-Pro-AMC for FAP and PREP and Gly-Pro-AMC for DPP4) were added to the reactions at a final concentration of 25 μM. After further incubation for 15 min at room temperature, enzyme activity was measured by fluorimetry ($Ex_{380\ nm}$:$Em_{460\ nm}$). A modified method with *N*-(4-quinolinoyl)-D-Ala-Pro (3144)–AMC as the FAP substrate was also used for IC_{50} assays with recombinant human and mouse FAP. The enzymes were incubated at 37°C for 10 min with 1:10 serial dilutions of FAP ligands. 3144-AMC was added at a final concentration of 25 μM, and incubation was continued for a further 30 min at 37°C before fluorimetry.

For IC_{50} assays with serum samples, 1:10 dilutions of human serum and Sprague–Dawley rat serum and a 1:100 dilution of mouse serum were incubated at 37°C for 10 min with 1:10 serial dilutions of FAP ligands. 3144-AMC was added at a final concentration of 25 μM (rat serum) or 50 μM (human serum and mouse serum), and incubation was continued for a further 30 min at 37°C before fluorimetry.

For IC_{50} assays with cell membrane FAP, HEK-mFAP cells were harvested from bulk cultures grown to approximately 80% confluency and plated in 96-well plates. After incubation overnight, 1:10 serial dilutions of FAP ligands were incubated with the cells for 1 h. 3144-AMC was added at a final concentration of 20 μM, and 37°C incubation was continued for a further 30 min before fluorimetry.

ICP-MS Assay for In Vitro Uptake and Internalization of ^{nat}Lu-Chelated FAP Ligands

In vitro cellular uptake of ^{nat}Lu-FAP ligands was investigated by inductively coupled plasma mass spectrometry (ICP-MS) analysis of total ^{nat}Lu associated with HEK-mFAP or HEK-Mock cells. The internalized fraction represented the ^{nat}Lu remaining after an acid wash to remove any cell membrane–bound inhibitor. HEK-mFAP or HEK-Mock cells were seeded in 6-well plates (Costar) at 4×10^6 cells/2 mL/well in serum-free RPMI 1640 assay medium and incubated (37°C, 5% CO_2) for 18–24 h. Medium was aspirated and replaced with 1, 5, 10, or 100 nM ^{nat}Lu-PNT6555 for the measurement of FAP ligand uptake or with 10 nM ^{nat}Lu-PNT6555, ^{nat}Lu-PNT6952, or

^{nat}Lu-PNT6522 for the measurement of FAP ligand uptake and internalization. After incubation for 1 h at 37°C, the cells were washed twice with 1 mL of ice-cold phosphate-buffered saline (PBS). For the measurement of total cellular FAP ligand uptake ($^{nat}Lu_{total}$), the cells were lysed by incubation at room temperature in 0.3 M NaOH for 5 min, after which the samples were passed through a 23-gauge needle to shear DNA. For the measurement of cellular internalization, 1 mL of ice-cold 50 mM glycine–100 mM NaCl (pH 2.8) buffer was added to the cells after the PBS wash step described before. After incubation at 4°C for 10 min, the cells were washed twice with 1 mL of ice-cold PBS and then lysed as described before to provide samples for the measurement of internalized FAP ligand ($^{nat}Lu_{internal}$). The protein concentrations of the total uptake and internalization samples were measured by the Bradford assay (Bio-Rad). Postlysis samples (300 μL) were microwave digested with 0.5 mL of ultrapure water and 2.0 mL of ultra–high-purity nitric acid. The samples were further diluted with ultrapure water to achieve 2.8% nitric acid. An internal standard (final concentration of indium of 5 ppb) was added to the samples, and indium at 0.1 ppt was added to 500-ppt Lu standards for the creation of a standard curve. ICP-MS was conducted in low-resolution mode. Calibrant intensities were normalized to the intensities of the internal controls, and the intensities in blank samples were subtracted to create linear calibration curves. The total cellular uptake of ^{nat}Lu after incubation of HEK-mFAP cells with 1, 5, 10, or 100 nM ^{nat}Lu-PNT6555 was expressed as the absolute amount (nanograms). The percentage internalization of ^{nat}Lu was calculated as ($^{nat}Lu_{internal}$/$^{nat}Lu_{total}$) × 100.

HEK-mFAP Mouse Tumor Xenograft Model

Six-week-old male Fox Chase mice with severe combined immunodeficiency were injected subcutaneously with HEK-mFAP cells. Tumor growth was determined by measurement of tumor width (W) and length (L) with calipers, and tumor volume (V) expressed in mm^3 was calculated by the formula $V = (W_2 \times 0.5L)$.

Formulation and In Vivo Administration of Radioligands

Radioligands diluted in PBS were administered to anesthetized mice by a single injection into the lateral tail vein.

Biodistribution of ^{68}Ga- and ^{177}Lu-Radioligands In Vivo

HEK-mFAP tumor–bearing mice were injected intravenously with defined doses of ^{68}Ga-PNT6555 or ^{177}Lu-radioligands. At designated time points, blood and tissues were collected from 3 mice per treatment and counted for radioactivity. Tissue weights were measured for determination of the percentage injected dose per gram (%ID/g).

PET and SPECT

After intravenous injection of radioligands, ^{68}Ga imaging by small-animal PET/CT and ^{177}Lu SPECT imaging were performed.

Antitumor Activity of ^{177}Lu-, ^{225}Ac-, and ^{161}Tb-Radioligands In Vivo

Mice bearing HEK-mFAP tumors of the volumes specified in the Results section were administered ^{177}Lu-, ^{225}Ac-, or ^{161}Tb-radioligands, vehicle, or precursor ligands (6 mice per group) on day 1. Health checks were performed, and body weights and tumor dimensions were measured weekly. Mortality or euthanasia was used interchangeably for plotting mouse survival curves. Tumor growth curves were plotted up to the time of the earliest incidence of a mortality/euthanasia endpoint in each of the control and test groups.

Statistical Analysis

In vitro and in vivo data were analyzed using Prism 6 (GraphPad Software), and results are presented as mean ± SEM.

RESULTS

Potency and Selectivity of FAP Inhibitors for Human Recombinant FAP

PNT6555, PNT6952, and PNT6522 when not chelated with metals exhibited low nanomolar IC_{50} values for FAP that were ~200- to ~1000-fold and ~10,000- to ~30,000-fold less, respectively, than the values for PREP and DPP4 (Table 1). The introduction of the metals reduced potency toward FAP by 2- to 48-fold, depending on the compound (Table 1). Metal chelation also reduced affinity for PREP by ≤4-fold. No inhibition of DPP4 was detectable.

Potency of FAP Inhibitors for Biologically Relevant Forms of FAP

The potencies of nonchelated and metal-chelated compound were evaluated toward human and rodent serum FAP, and mouse cell surface FAP in HEK-mFAP cells. The 3144-AMC substrate

TABLE 1
Selective Inhibition of FAP by Precursor and Nonradioactive Lu/Ga-Chelated PNT6555, PNT6952, and PNT6522 In Vitro

	Recombinant human enzyme IC_{50} (nM)*			Selectivity index†	
Compound	FAP	PREP	DPP4	PREP	DPP4
PNT6555	3.9 ± 0.3	900 ± 97	>100,000	230	>26,000
^{177}Lu-PNT6555	16 ± 3.0	4,100 ± 740	>100,000	260	>6,300
^{68}Ga-PNT6555	55 ± 3.0	3,600 ± 510	>100,000	65	>1,800
PNT6952	4.7 ± 0.2	4,700 ± 780	>100,000	1,000	>21,000
^{177}Lu-PNT6952	13 ± 1.2	34,000 ± 10,000	>100,000	2,500	>7,400
^{68}Ga-PNT6952	84 ± 5.3	>10,000	>10,000	>120	>120
PNT6522	12 ± 0.6	9,200 ± 2,000	>100,000	760	>8,300
^{177}Lu-PNT6522	25 ± 2.0	10,000 ± 3,700	>100,000	390	>3,900
^{68}Ga-PNT6522	570 ± 95	37,000 ± 12,000	>100,000	65	>160

*IC_{50} values obtained in fluorometric assays with *Z*-Gly-Pro-AMC (FAP and PREP) and Gly-Pro-AMC (DPP4) substrates are expressed as mean (n = 3) ± SEM.

†Calculated as IC_{50} (PREP)/IC_{50} (FAP) and IC_{50} (DPP4)/IC_{50} (FAP).

TABLE 2
Potency of Inhibition of Soluble Recombinant, Cell Membrane, and Serum Forms of Human and Rodent FAP by Precursor and Nonradioactive Lu/Ga-Chelated PNT6555, PNT6952, and PNT6522 In Vitro

Compound	Recombinant soluble FAP IC_{50} (nM)		HEK-mFAP IC_{50} (nM): mouse	Serum IC_{50} (nM)		
	Human	Mouse		Human	Mouse	Rat
PNT6555	1.8 ± 0.4	0.2 ± 0.01	0.8 ± 0.03	2.5 ± 0.4	0.2 ± 0.01	0.3 ± 0.01
^{177}Lu-PNT6555	6.6 ± 0.5	0.4 ± 0.01	1.2 ± 0.1	10 ± 1.7	0.2 ± 0.02	0.4 ± 0.1
^{68}Ga-PNT6555	98 ± 5.4	17 ± 0.9	47 ± 5.9	100 ± 9.3	16 ± 1.6	24 ± 6.4
PNT6952	0.5 ± 0.1	0.3 ± 0.003	1.2 ± 0.1	1.3 ± 0.3	0.3 ± 0.03	0.3 ± 0.01
^{177}Lu-PNT6952	4.7 ± 0.5	1.6 ± 0.1	6.8 ± 0.6	8.0 ± 2.0	1.9 ± 0.1	1.8 ± 0.1
^{68}Ga-PNT6952	47 ± 6.0	11 ± 1.0	22 ± 1.3	42 ± 5.5	13 ± 0.6	14 ± 2.0
PNT6522	1.9 ± 0.4	0.5 ± 0.1	1.7 ± 0.4	1.4 ± 0.2	0.5 ± 0.04	0.5 ± 0.01
^{177}Lu-PNT6522	4.7 ± 0.3	2.3 ± 0.2	12 ± 0.5	11 ± 2.0	2.5 ± 0.1	3.3 ± 0.1
^{68}Ga-PNT6522	140 ± 30	87 ± 18	82 ± 3.1	190 ± 32	83 ± 7.4	64 ± 5

IC_{50} values obtained in 3144-AMC fluorometric assays are expressed as mean (n = 3) ± SEM.

(Supplemental Fig. 1) (*28*) was used to specifically measure FAP activity in the unfractionated biologic matrices, and as a benchmark for the inhibition of FAP in biologic samples; FAP inhibitor potency toward soluble recombinant FAP was also evaluated with this substrate. When not chelated to metals, the compounds exhibited subnanomolar to low-nanomolar IC_{50} values in assays with all sources of FAP (Table 2). Lu-chelation reduced the potency to a smaller extent than Ga-chelation in both the Z-Gly-Pro-AMC and 3144-AMC assays, and with both soluble and cell membrane forms of FAP (Tables 1 and 2).

Cellular Uptake and Internalization of FAP Inhibitors

The FAP dependence of the cellular uptake of ^{nat}Lu-PNT6555 was investigated by comparing the total uptake in HEK-mFAP versus HEK-Mock cells. Measurement of total cell-associated ^{nat}Lu-PNT6555 by ICP-MS demonstrated that uptake required the expression of FAP (Fig. 2A). ICP-MS measurements of the total cell bound and internalized amounts of ^{nat}Lu in HEK-mFAP cells after 1 h incubation with ^{nat}Lu-PNT6555, ^{nat}Lu-PNT6952 or ^{nat}Lu-PNT6522 indicated that ^{nat}Lu-PNT6555 exhibited the greatest degree of internalization (Fig. 2B).

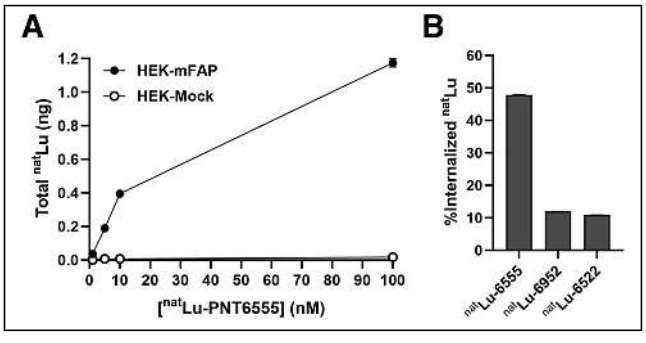

FIGURE 2. Cellular uptake and internalization of ^{nat}Lu-chelated FAP ligands. (A) Total ^{nat}Lu uptake by HEK-mFAP and HEK-Mock cells after 1 h of incubation at 37°C with increasing concentrations of ^{nat}Lu-PNT6555 in vitro. (B) Comparison of internalized fractions of ^{nat}Lu after 1 h of incubation of HEK-mFAP cells with 10 nM ^{nat}Lu-PNT6555, ^{nat}Lu-PNT6952, or ^{nat}Lu-PNT6522 in vitro.

Biodistribution of Radiolabeled FAP Inhibitors in Tumor-Bearing Mice

^{68}Ga-PNT6555 and ^{68}Ga-PNT6952 exhibited selective uptake into HEK-mFAP tumors (Fig. 3A). Small-animal PET indicated that the radioligands rapidly entered the tumors, and while they were progressively cleared from the blood and normal tissues via the kidneys and the bladder, tumor activity increased rapidly over the first 5 min after injection, and more slowly but continuously thereafter (Fig. 3C; Supplemental Fig. 2). Elimination from blood, liver, and muscle resulted in radioligand levels that were distinctly lower in normal tissues than in tumors by ~25 min after administration (Fig. 3C), and high-contrast PET images of tumors were obtained at 60 min (Fig. 3C). All 3 ^{177}Lu-FAP radioligands exhibited selective uptake in tumors 4 h after a single dose in HEK-mFAP tumor–bearing mice (Fig. 4A; Supplemental Fig. 3). Intratumoral levels of all 3 radioligands decreased between 4 and 48 h, but high tumor-to-normal tissue ratios were maintained from 48 to 168 h. Analysis of the area under the curve (AUC) ((%ID/g)·h) for the period from 4 to 168 h indicated that the accumulation of ^{177}Lu-PNT6555 in the tumor was significantly greater than that for ^{177}Lu-PNT6952 or ^{177}Lu-PNT6522 ($P < 0.0001$) (Table 3; Supplemental Table 1), but the increase in ^{177}Lu-PNT6555 between 48 and 168 h was not statistically significant. Although the limited uptake in normal tissues exhibited some variation between the 3 radioligands (Table 3), these differences were not statistically significant (Supplemental Table 1). The highest levels of uptake into normal tissues occurred in kidney, liver, bone and skin for ^{177}Lu-PNT6555, kidney for ^{177}Lu-PNT6952, and kidney and bone for ^{177}Lu-PNT6522 (Table 3; Supplemental Fig. 3). However, the high initial tumor uptake and kinetics of tumor retention resulted in tumor-to-normal tissue AUC ratios of 15 to 19 in these tissues (Table 3). This is illustrated by the pharmacokinetic profiles in tumor and kidney (Fig. 4A), and the retention of ^{177}Lu-PNT6555 in the tumors was apparent in SPECT images collected from 3 to 120 h (Fig. 4B).

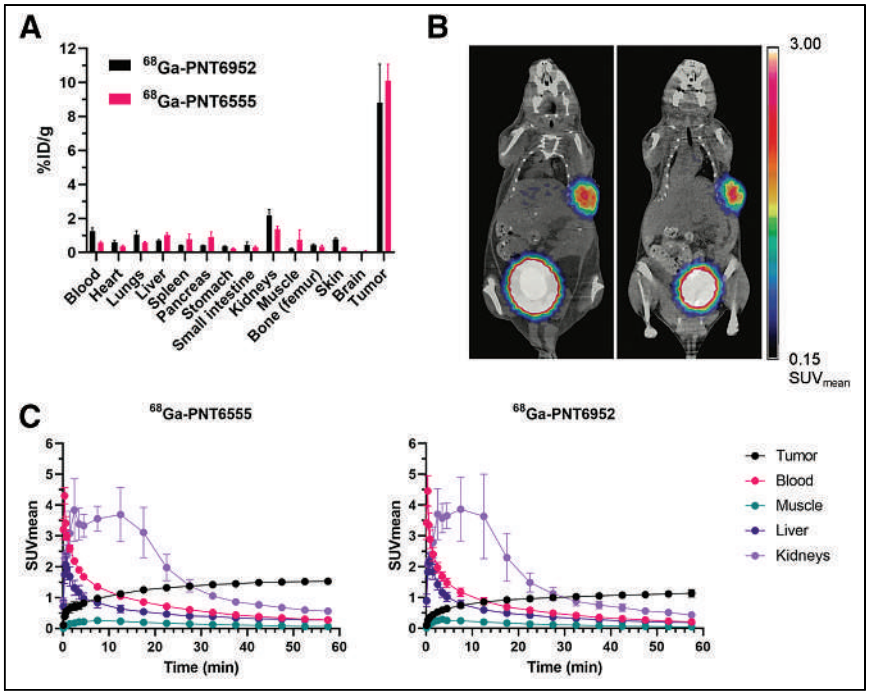

FIGURE 3. Biodistribution, pharmacokinetics, and PET imaging for ^{68}Ga-PNT6555 and ^{68}Ga-PNT6952 in mice bearing ~300-mm^3 HEK-mFAP tumors administered doses of 8–10 MBq. (A) Biodistribution of radioligands 60 min after injection. Mean ± SEM %ID/g values are shown for 3 animals per tissue. (B) Biodistribution of radioligands determined by PET imaging 60 min after administration in representative animals from groups of 3. (C) Time–activity curves for tissue uptake of radioligands determined by PET imaging. SUV_{mean} ± SEM are shown for 3 animals per tissue.

Antitumor Activity of PNT6555, PNT6952, and PNT6522 ^{177}Lu-Radioligands

^{177}Lu-PNT6555, ^{177}Lu-PNT6952, and ^{177}Lu-PNT6522 were administered to HEK-mFAP tumor–bearing mice as a single dose of 15, 30, or 60 MBq. These doses were selected to enable efficacy to be directly compared with ^{177}Lu-FAPI-46 and ^{177}Lu-FAP-2286, previously evaluated in a HEK-FAP tumor model (*24*). ^{177}Lu-radioligands produced dose-dependent delays in tumor growth, whereas no discernable effect was produced by unlabeled precursors (Fig. 5A). On the last day of tumor measurement before mortality in control groups, tumor growth was significantly inhibited at all doses investigated (Supplemental Fig. 4A). ^{177}Lu-PNT6555 produced the longest tumor growth delay (Fig. 5A), with the rank order of efficacy being ^{177}Lu-PNT6555 > ^{177}Lu-PNT6952 > ^{177}Lu-PNT6522. The same rank order was also reflected in animal survival (Fig. 5B). The radioligands appeared to be well tolerated, and weight loss was ≤10% and transient (Supplemental Fig. 5).

Antitumor Activity of ^{225}Ac-PNT6555 and ^{161}Tb-PNT6555

To HEK-mFAP tumor–bearing mice, ^{225}Ac-PNT6555 was administered as a single dose of 5, 25, or 50 kBq, and ^{161}Tb-PNT6555, as a single dose of 15, 30, or 60 MBq. ^{225}Ac-PNT6555 doses were based on single doses of ^{225}Ac-FAPI-46 that were safe and effective in the PANC-1 xenograft model (*29*), and ^{161}Tb-PNT6555 doses, on safe and effective single doses of radiometal targeted to L1 cell adhesion protein or folate receptor (*30*,*31*). Both ^{225}Ac-PNT6555 and ^{161}Tb-PNT6555 produced dose-dependent delays in tumor growth at all dose levels (Fig. 6A), and before mortality of control animals, tumor volumes were significantly reduced (Supplemental Fig. 4B). Mean tumor volume in mice that received nonradiolabeled PNT6555 appeared to be increased above that in vehicle-treated mice in the ^{225}Ac-PNT6555 experiment. Although this effect was statistically significant, it was not pharmacologically meaningful because it was small and not seen in the ^{177}Lu-PNT6555 (Fig. 5A) and ^{161}Tb-PNT6555 experiments (Fig. 6A). ^{225}Ac-PNT6555 and ^{161}Tb-PNT6555 increased animal survival in a dose-dependent manner (Fig. 6B). Both radioligands were well tolerated, as indicated by minimal effect on body weight (Supplemental Fig. 6).

DISCUSSION

The selective inhibition of FAP over the dipeptidyl peptidases and PREP by 3099, which was achieved by the pyridin-4-carbonyl blocking group at the N terminus, and D-alanine at P_2, respectively (*25*), was maintained in PNT6555, PNT6952, and PNT6522. When expressed as a cell membrane protein in HEK-mFAP cells, the catalytic site of FAP was found to be pharmacologically accessible to the D-AlaboroPro–based ligands and to be essential for the cellular uptake of ^{nat}Lu-PNT6555 by HEK-mFAP cells. In vivo, ^{68}Ga-PNT6555 and ^{68}Ga-PNT6952 were selectively retained in HEK-mFAP tumors, resulting in PET images with high tumor-to-background contrast. The biodistribution of ^{177}Lu-PNT6555, ^{177}Lu-PNT6952, and ^{177}Lu-PNT6522 in HEK-mFAP tumor–bearing mice confirmed the selective targeting of the HEK-mFAP tumors and revealed that ^{177}Lu-PNT6555 exhibited the greatest tumor accumulation, consistent with its greater cellular internalization compared with ^{nat}Lu-PNT6952 and ^{nat}Lu-PNT6522 in vitro.

The premise for development of FAP-targeted radioligands is that the tumor-to-normal tissue ratios of FAP activity in human cancer will be sufficient to ensure pharmacologic effects on the tumor while avoiding damage to normal cells and tissues. However, most mouse tumor models fail to mimic the tumor to normal tissue FAP ratios found in humans, with mouse models having both lower levels of FAP in the tumor and higher levels in the blood than humans (*28*) (S.E. Poplawski, PhD, unpublished data, 2011). Nonetheless, an albumin binding FAP-radioligand, ^{177}Lu-FAP6-IP-DOTA, produced significant tumor responses in mice implanted with multiple tumor cell lines that were not engineered to overexpress FAP, and tumor targeting therefore relied on the FAP expressed in the tumor stroma (*32*). However, the levels of responsiveness to ^{177}Lu-FAP6-IP-DOTA across the KB, HT29, U87MG, and 4T1 tumor models investigated did not correlate with ex vivo staining intensity of stromal FAP for reasons that are not well understood (*32*). In comparison to these models, the HEK-mFAP tumor model is artificial and potentially somewhat problematic because the FAP-levels in the tumor are substantially greater than found in most human cancers, and the FAP is expressed on the neoplastic cells rather than on the stromal CAFs, as in human epithelial cancers. Because of the latter, the FAP targeting is directed at the cancer cells rather than the CAFs, as it would be in humans, and it is unclear how this might affect the

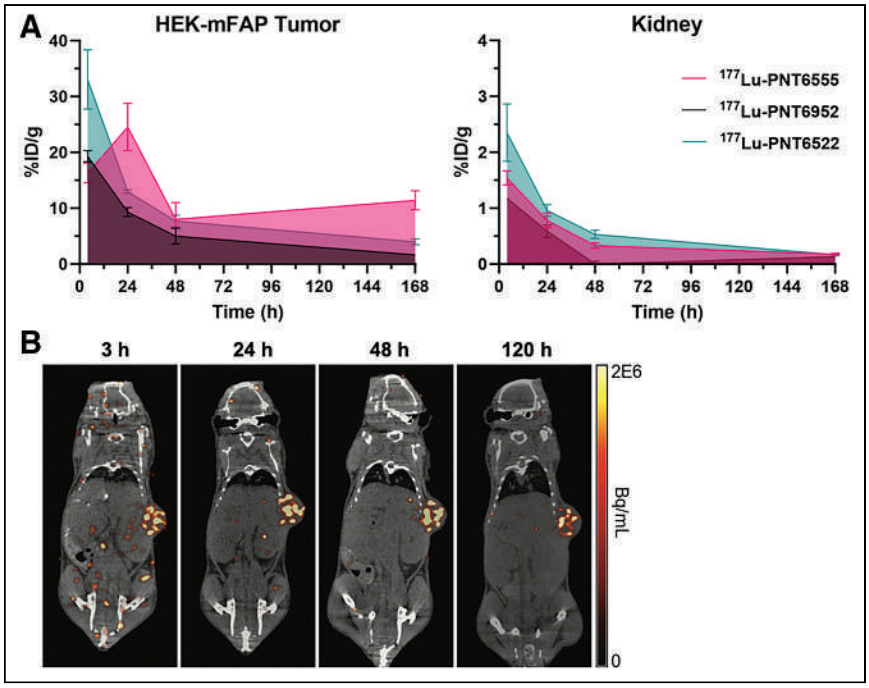

FIGURE 4. Biodistribution and SPECT imaging for ^{177}Lu-radioligands in mice bearing HEK-mFAP tumors administered doses of 6.8–7.8 MBq. (A) ^{177}Lu-PNT6555, ^{177}Lu-PNT6952, and ^{177}Lu-PNT6522 uptake in tumors and kidneys at 4 to 168 h after administration in animals bearing ~171-mm^3 tumors. Mean ± SEM %ID/g values are shown for 3 animals per tissue. Statistical analysis of AUC values indicated significantly greater accumulation in tumors of ^{177}Lu-PNT6555 than of ^{177}Lu-PNT6952 or ^{177}Lu-PNT6522 ($P < 0.0001$), and in kidneys there were no significant differences among AUC values for these radioligands. (B) Biodistribution of ^{177}Lu-PNT6555 determined by SPECT imaging 3, 24, 48, and 120 h after administration in representative animals (from groups of 3) bearing ~355-mm^3 tumors.

translatability of the results to humans. Although the FAP levels are artificially high, the HEK-mFAP model may, nevertheless, have utility because it brings the tumor/blood ratio of FAP closer to that of human cancer patients. Mice have greater circulating FAP levels than humans (*28*), and the tumor/blood ratio is a key determinant of tumor-selective targeting. Thus, the HEK-mFAP model could facilitate comparison of the FAP-targeting potential of various agents and might yield results that are predictive of human efficacy. A previous comparative study of the leading clinical candidates, FAP-2286 and FAPI-46, demonstrated the utility of HEK cells engineered to express human FAP in selection of clinical candidates (*24*), and the results provide feasible benchmarks for the new boronic acid derivatives. In humans, ^{68}Ga-FAPI-46-PET exhibited strong correlation with FAP tissue expression determined by immunohistochemistry (*33*), and ^{68}Ga-FAPI-46 PET/CT appeared to be equivalent to ^{18}F-FDG PET/CT for detection of malignant lesions in head and neck cancer (*34*). Moreover, first-in-human results for ^{177}Lu-FAP-2286 in advanced metastatic disease have demonstrated significant tumor uptake and longer tumor retention times compared with the earlier clinical candidates, FAPI-02 and FAPI-04 (*22*,*35*).

TABLE 3
Tissue Distribution After Intravenous Injection of ^{177}Lu-PNT6555, ^{177}Lu-PNT6952, and ^{177}Lu-PNT6522 in HEK-mFAP Xenograft Model

	AUC ((%ID/g)·h)			Tumor-to-normal tissue ratio		
Tissue	^{177}Lu-PNT6555	^{177}Lu-PNT6952	^{177}Lu-PNT6522	^{177}Lu-PNT6555	^{177}Lu-PNT6952	^{177}Lu-PNT6522
Blood	7.2	1.3	3.5	274.2	639.9	396.7
Heart	13.6	3.7	6.0	144.4	229.3	233.3
Lung	13.5	2.5	7.8	146.3	348.5	180.7
Liver	78.3	9.0	20.5	25.2	95.7	68.6
Spleen	46.7	12.1	24.0	42.2	71.1	58.7
Pancreas	16.0	3.1	6.1	122.9	280.2	231.1
Stomach	16.1	2.3	6.5	122.0	366.4	216.2
Small intestine	15.8	3.4	8.6	124.8	255.2	163.3
Kidney	67.1	32.6	92.9	29.3	26.3	15.2
Muscle	30.5	3.1	12.7	64.5	280.2	110.9
Bone (femur)	94.2	9.2	77.2	20.9	93.4	18.2
Skin	53.4	5.0	23.9	36.9	172.9	59.0
Brain	3.5	1.2	0.7	565.8	702.8	1,961.5
Tumor	1,969.0	857.4	1,408.4			

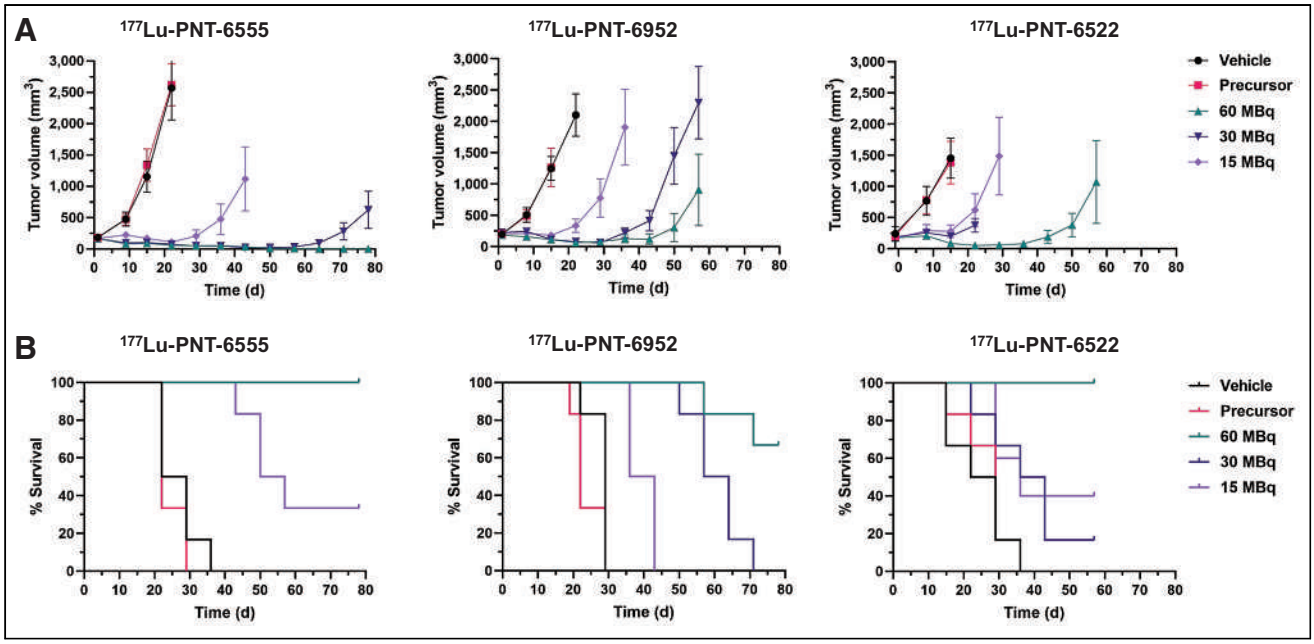

FIGURE 5. Antitumor activity of ^{177}Lu-PNT6555, ^{177}Lu-PNT6952, and ^{177}Lu-PNT6522 in mice bearing HEK-mFAP tumors. Animals bearing tumors that had grown to ~170–260 mm^3 were administered single intravenous injection of vehicle or test agent (6 animals/treatment) on day 1. (A) Tumor growth curves (mean ± SEM). (B) Animal survival curves. First day of tumor measurement was day 1, except in study of ^{177}Lu-PNT6522, for which first day of measurement was 1 day before treatment started. Compared with survival seen with vehicle treatment, survival was significantly increased by ^{177}Lu-PNT6555 and ^{177}Lu-PNT6952 at all 3 doses ($P \leq 0.001$) and by ^{177}Lu-PNT6522 at dose of 60 MBq ($P \leq 0.01$) but not at lower doses.

The biodistribution and PET imaging studies of ^{68}Ga-PNT6555 and ^{68}Ga-PNT6952 reported here demonstrated higher tumor specificity than ^{68}Ga-FAP-2286 or ^{68}Ga-FAPI-46. In addition, the tumor growth delay produced by ^{177}Lu-PNT6555 in the HEK-mFAP tumor model was greater than reported for ^{177}Lu-FAP-2286 and ^{177}Lu-FAPI-46 when the same single doses of 30 MBq were administered (*24*).

In the PANC-1 tumor model, FAP is expressed by stromal CAFs, and 30 MBq ^{177}Lu-FAPI-46 produced only an insignificant trend in tumor growth inhibition (*29*), whereas equivalent doses of ^{177}Lu-PNT6555, ^{177}Lu-PNT6952, and ^{177}Lu-PNT6522 produced much greater, statistically significant responses in the HEK-mFAP model. Similarly, 25 kBq ^{225}Ac-PNT6555 produced a significant HEK-mFAP tumor response, greatly exceeding the effect of ^{225}Ac-FAPI-46 in the PANC-1 model. These results raise an important question with respect to clinical translation. Are the efficacy results in the HEK-mFAP model artefactually exaggerated because of the unnaturally high and homogeneous overexpression of FAP in the HEK cells, or are the results in the PANC-1 model artificially suppressed by a low level of FAP expression in the tumor stroma and a circulating FAP level approximately 15-fold greater than in humans (*28*)? Compared with the tumor/blood FAP ratio in human cancer patients, the ratio in the PANC-1 mouse model might be lower, whereas the ratio in HEK-mFAP model is higher (S.E. Poplawski, PhD, unpublished data, 2010). As this ratio will be a key determinant of selective tumor targeting, it is unclear which model might more reliably predict

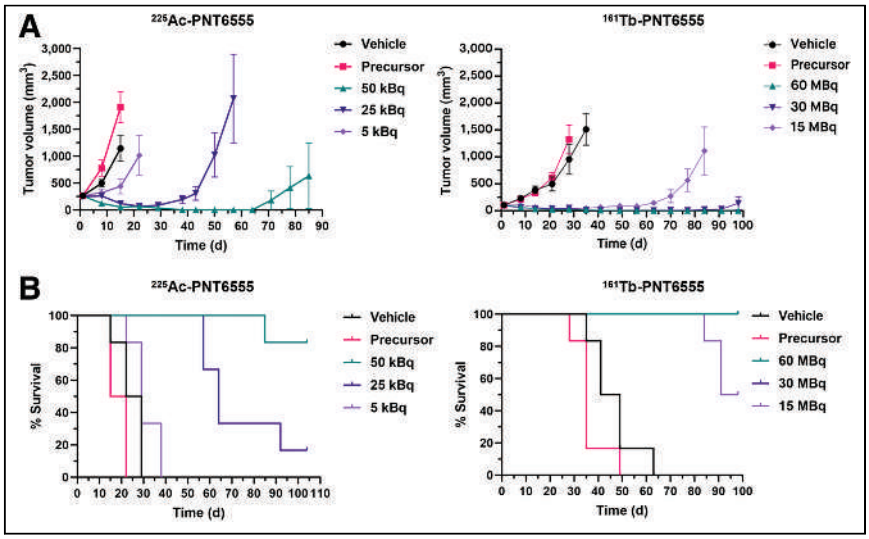

FIGURE 6. Antitumor activity of ^{225}Ac-PNT6555 and ^{161}Tb-PNT6555 in mice bearing HEK-mFAP tumors. Animals bearing tumors that had grown to ~250 mm^3 (^{225}Ac study) or ~100 mm^3 (^{161}Tb study) were administered single intravenous injection of vehicle or test agent (6 animals/treatment) on day 1. (A) Tumor growth curves (mean ± SEM tumor volume). (B) Animal survival curves. First day of tumor measurement was day 1. Compared with survival in precursor-treated animals, survival was significantly increased by ^{225}Ac-PNT6555 (50 and 25 kBq, $P \leq 0.001$; and 5 kBq, $P \leq 0.01$) and by ^{161}Tb-PNT6555 (60, 30, and 15 MBq; $P \leq 0.001$). At 60 and 30 MBq doses of ^{161}Tb-PNT6555, survival was 100%—curves fall on top of each other.

human efficacy. Better mouse models that naturally express greater levels of FAP in the tumor stroma while having less circulating FAP are definitely needed, but comparative results in humans and mice for clinical candidates may ultimately resolve this question.

Clinical translation of the PNT FAP ligands will require preclinical evaluation of possible longer-term adverse effects. In this regard, it is encouraging that tissues associated with known risks of renal and hematologic toxicity (*36*) did not show meaningful accumulation of ^{177}Lu-PNT6555. Any possible sink effect of the serum pool of FAP leading to off-target biodistribution, which would likely be exaggerated in mice, was not observed. In human cancer, FAP-positive CAFs provide critical support for tumor growth and metastasis by production and remodeling of extracellular matrix, release of growth factors and cytokines that directly stimulate tumor growth or promote angiogenesis, and suppression of tumor immunity (*37*). Targeting of FAP-positive stromal CAFs in human cancer, therefore, has potential for antitumor effects in addition to DNA damage in neoplastic cells, as would be expected in FAP-transfected tumor models (*38*). In FAP-positive human cancer there is the opportunity for antitumor effects by direct damage to FAP-expressing CAFs, and bystander effects on adjacent neoplastic cells by cross-fire irradiation and cytotoxic factors released by radiation damaged cells (*39*). Although cross-fire may be greater in larger tumors with β-particles, which have a range beyond a single cell layer, α-particles can afford greater cytotoxicity by producing more double-strand breaks in DNA and chromosomal aberrations (*40*). It appears desirable to optimize the type of radionuclide emission for the clinical stage of the cancer (*40*,*41*). If successfully translated to the clinic, the strong preclinical efficacy of PNT6555 chelated with ^{177}Lu, ^{161}Tb, or ^{225}Ac suggests that 3099-based FAP ligands might offer the flexibility required to deliver α- or β-emitting radiometals to the tumor bed, either concomitantly or sequentially.

CONCLUSION

The preclinical results support the advancement of PNT6555 to the "FAPi Radioligand Open-Label, Phase 1 Study to Evaluate Safety, Tolerability and Dosimetry of [Lu-177]-PNT6555: A Dose Escalation Study for Treatment of Patients with Select Solid Tumors (FRONTIER)" (ClinicalTrials.gov identifier NCT05432193).

DISCLOSURE

This work was funded by POINT Biopharma Global Inc. Sarah Poplawski, Shuang Pan, Wengen Wu, Yuxin Liu, Barry Jones, Jack Lai, and William Bachovchin are employees of Tufts University and collaborate with POINT Biopharma Global Inc. under a sponsored research agreement. William Bachovchin consults for POINT Biopharma Global Inc. and holds stock or stock options in POINT Biopharma Global Inc. Robin Hallett, Mark Dornan, Kyle Novakowski, Valerie Hergott, Albert Felten, and Joe McCann are employees and stockholders of POINT Biopharma Global Inc. Quang-De Nguyen previously consulted for POINT Biopharma Global Inc. and collaborates with POINT Biopharma Global Inc. under a fee-for-service agreement. Anthony Belanger and Shin Hye Ahn collaborate with POINT Biopharma Global Inc. under a fee-for-service agreement.

ACKNOWLEDGMENT

The ^{225}Ac used in this research was supplied by the U.S. Department of Energy Isotope Program managed by the Office of Isotope R&D and Production.

KEY POINTS

QUESTION: Are boronic acid–based DOTA-FAPIs effective as PET tracers and anticancer agents when chelated with diagnostic and therapeutic radiometals?

PERTINENT FINDINGS: Boronic acid–based DOTA-FAPIs are potent, selective inhibitors of soluble and membrane-associated forms of FAP. In a FAP-positive tumor model, the ^{68}Ga-chelates of PNT6555 and PNT6952 exhibited appropriate properties for PET imaging, and the ^{177}Lu-chelates of PNT6555, PNT6952, and PNT6522 produced strong anticancer effects, with PNT6555 exhibiting the most potent antitumor activity when chelated with ^{177}Lu and similar activity when chelated with ^{225}Ac or ^{161}Tb, suggesting versatility in therapeutic applications.

IMPLICATIONS FOR PATIENT CARE: PNT6555- and 3099-based analogs provide feasible alternatives to quinoline-based DOTA-FAPIs, and the preclinical results support their translation to the clinic for theranostic applications in oncology.

REFERENCES

1. Waumans Y, Baerts L, Kehoe K, Lambeir AM, De Meester I. The dipeptidyl peptidase family, prolyl oligopeptidase, and prolyl carboxypeptidase in the immune system and inflammatory disease, including atherosclerosis. *Front Immunol.* 2015;6:387.
2. Busek P, Malik R, Sedo A. Dipeptidyl peptidase IV activity and/or structure homologues (DASH) and their substrates in cancer. *Int J Biochem Cell Biol.* 2004;36:408–421.
3. Rosenblum JS, Kozarich JW. Prolyl peptidases: a serine protease subfamily with high potential for drug discovery. *Curr Opin Chem Biol.* 2003;7:496–504.
4. Scanlan MJ, Raj BK, Calvo B, et al. Molecular cloning of fibroblast activation protein alpha, a member of the serine protease family selectively expressed in stromal fibroblasts of epithelial cancers. *Proc Natl Acad Sci USA.* 1994;91:5657–5661.
5. Lee KN, Jackson KW, Christiansen VJ, Lee CS, Chun JG, McKee PA. Antiplasmin-cleaving enzyme is a soluble form of fibroblast activation protein. *Blood.* 2006;107:1397–1404.
6. Park JE, Lenter MC, Zimmermann RN, Garin-Chesa P, Old LJ, Rettig WJ. Fibroblast activation protein, a dual specificity serine protease expressed in reactive human tumor stromal fibroblasts. *J Biol Chem.* 1999;274:36505–36512.
7. Nurmik M, Ullmann P, Rodriguez F, Haan S, Letellier E. In search of definitions: cancer-associated fibroblasts and their markers. *Int J Cancer.* 2020;146:895–905.
8. Dolznig H, Schweifer N, Puri C, et al. Characterization of cancer stroma markers: in silico analysis of an mRNA expression database for fibroblast activation protein and endosialin. *Cancer Immun.* 2005;5:10.
9. Hamson EJ, Keane FM, Tholen S, Schilling O, Gorrell MD. Understanding fibroblast activation protein (FAP): substrates, activities, expression and targeting for cancer therapy. *Proteomics Clin Appl.* 2014;8:454–463.
10. Liu R, Li H, Liu L, Yu J, Ren X. Fibroblast activation protein: a potential therapeutic target in cancer. *Cancer Biol Ther.* 2012;13:123–129.
11. Acharya PS, Zukas A, Chandan V, Katzenstein AL, Pure E. Fibroblast activation protein: a serine protease expressed at the remodeling interface in idiopathic pulmonary fibrosis. *Hum Pathol.* 2006;37:352–360.
12. Bauer S, Jendro MC, Wadle A, et al. Fibroblast activation protein is expressed by rheumatoid myofibroblast-like synoviocytes. *Arthritis Res Ther.* 2006;8:R171.
13. Garin-Chesa P, Old LJ, Rettig WJ. Cell surface glycoprotein of reactive stromal fibroblasts as a potential antibody target in human epithelial cancers. *Proc Natl Acad Sci USA.* 1990;87:7235–7239.
14. Busek P, Mateu R, Zubal M, Kotackova L, Sedo A. Targeting fibroblast activation protein in cancer: prospects and caveats. *Front Biosci (Landmark Ed).* 2018;23:1933–1968.
15. Alcocer-Ávila ME, Ferreira A, Quinto MA, Morgat C, Hindie E, Champion C. Radiation doses from ^{161}Tb and ^{177}Lu in single tumour cells and micrometastases. *EJNMMI Phys.* 2020;7:33.
16. Calais J. FAP: the next billion dollar nuclear theranostics target? *J Nucl Med.* 2020;61:163–165.
17. Moller DE. New drug targets for type 2 diabetes and the metabolic syndrome. *Nature.* 2001;414:821–827.
18. D'Agostino G, Kim JD, Liu ZW, et al. Prolyl endopeptidase-deficient mice have reduced synaptic spine density in the CA1 region of the hippocampus, impaired LTP, and spatial learning and memory. *Cereb Cortex.* 2013;23:2007–2014.

19. Ryabtsova O, Jansen K, Van Goethem S, et al. Acylated Gly-(2-cyano)pyrrolidines as inhibitors of fibroblast activation protein (FAP) and the issue of FAP/prolyl oligopeptidase (PREP)-selectivity. *Bioorg Med Chem Lett.* 2012;22:3412–3417.
20. Jansen K, Heirbaut L, Cheng JD, et al. Selective inhibitors of fibroblast activation protein (FAP) with a (4-Quinolinoyl)-glycyl-2-cyanopyrrolidine scaffold. *ACS Med Chem Lett.* 2013;4:491–496.
21. Jansen K, Heirbaut L, Verkerk R, et al. Extended structure-activity relationship and pharmacokinetic investigation of (4-quinolinoyl)glycyl-2-cyanopyrrolidine inhibitors of fibroblast activation protein (FAP). *J Med Chem.* 2014;57:3053–3074.
22. Lindner T, Loktev A, Altmann A, et al. Development of quinoline-based theranostic ligands for the targeting of fibroblast activation protein. *J Nucl Med.* 2018;59: 1415–1422.
23. Zboralski D, Hoehne A, Bredenbeck A, et al. Comparative biodistribution and radiotherapeutic efficacy of the fibroblast activation protein (FAP)–targeting agents FAP-2286 and FAPI-46. In: *Proceedings of the Annual Meeting of the American Association of Cancer Research.* Philadelphia, PA: AACR; 2022. Abstract 3317/15.
24. Zboralski D, Hoehne A, Bredenbeck A, et al. Preclinical evaluation of FAP-2286 for fibroblast activation protein targeted radionuclide imaging and therapy. *Eur J Nucl Med Mol Imaging.* 2022;49:3651–3667.
25. Poplawski SE, Lai JH, Li Y, et al. Identification of selective and potent inhibitors of fibroblast activation protein and prolyl oligopeptidase. *J Med Chem.* 2013;56: 3467–3477.
26. Bachovchin WW, Lai H-S, Wu W. FAP-targeted pharmaceuticals and imaging agents, and uses related thereto. WO patent 11707539. July 25, 2023.
27. Cheng JD, Dunbrack RL Jr, Valianou M, Rogatko A, Alpaugh RK, Weiner LM. Promotion of tumor growth by murine fibroblast activation protein, a serine protease, in an animal model. *Cancer Res.* 2002;62:4767–4772.
28. Keane FM, Yao TW, Seelk S, et al. Quantitation of fibroblast activation protein (FAP)-specific protease activity in mouse, baboon and human fluids and organs. *FEBS Open Bio.* 2013;4:43–54.
29. Liu Y, Watabe T, Kaneda-Nakashima K, et al. Fibroblast activation protein targeted therapy using [^{177}Lu]FAPI-46 compared with [^{225}Ac]FAPI-46 in a pancreatic cancer model. *Eur J Nucl Med Mol Imaging.* 2022;49:871–880.
30. Müller C, Reber J, Haller S, et al. Direct in vitro and in vivo comparison of ^{161}Tb and ^{177}Lu using a tumour-targeting folate conjugate. *Eur J Nucl Med Mol Imaging.* 2014;41:476–485.
31. Grünberg J, Lindenblatt D, Dorrer H, et al. Anti-L1CAM radioimmunotherapy is more effective with the radiolanthanide terbium-161 compared to lutetium-177 in an ovarian cancer model. *Eur J Nucl Med Mol Imaging.* 2014;41:1907–1915.
32. Lindeman SD, Mukkamala R, Horner A, et al. Fibroblast activation protein–targeted radioligand therapy for treatment of solid tumors. *J Nucl Med.* 2023; 64:759–766.
33. Mona CE, Benz MR, Hikmat F, et al. Correlation of ^{68}Ga-FAPi-46 PET biodistribution with FAP expression by immunohistochemistry in patients with solid cancers: interim analysis of a prospective translational exploratory study. *J Nucl Med.* 2022;63:1021–1026.
34. Wegen S, van Heek L, Linde P, et al. Head-to-head comparison of [^{68}Ga]Ga-FAPI-46-PET/CT and [^{18}F]F-FDG-PET/CT for radiotherapy planning in head and neck cancer. *Mol Imaging Biol.* 2022;24:986–994.
35. Baum RP, Schuchardt C, Singh A, et al. Feasibility, biodistribution, and preliminary dosimetry in peptide-targeted radionuclide therapy of diverse adenocarcinomas using ^{177}Lu-FAP-2286: first-in-humans results. *J Nucl Med.* 2022;63:415–423.
36. Camus B, Cottereau AS, Palmieri LJ, et al. Indications of peptide receptor radionuclide therapy (PRRT) in gastroenteropancreatic and pulmonary neuroendocrine tumors: an updated review. *J Clin Med.* 2021;10:1267.
37. Sahai E, Astsaturov I, Cukierman E, et al. A framework for advancing our understanding of cancer-associated fibroblasts. *Nat Rev Cancer.* 2020;20:174–186.
38. O'Neill E, Kersemans V, Allen PD, et al. Imaging DNA damage repair in vivo after ^{177}Lu-DOTATATE therapy. *J Nucl Med.* 2020;61:743–750.
39. Xue LY, Butler NJ, Makrigiorgos GM, Adelstein SJ, Kassis AI. Bystander effect produced by radiolabeled tumor cells in vivo. *Proc Natl Acad Sci USA.* 2002;99: 13765–13770.
40. Haberkorn U, Giesel F, Morgenstern A, Kratochwil C. The future of radioligand therapy: alpha, beta, or both? *J Nucl Med.* 2017;58:1017–1018.
41. Feuerecker B, Tauber R, Knorr K, et al. Activity and adverse events of actinium-225-PSMA-617 in advanced metastatic castration-resistant prostate cancer after failure of lutetium-177-PSMA. *Eur Urol.* 2021;79:343–350.

^{212}Pb-Pretargeted Theranostics for Pancreatic Cancer

David Bauer[1], Lukas M. Carter[2], Mohamed I. Atmane[3], Roberto De Gregorio[1], Alexa Michel[1], Spencer Kaminsky[1], Sebastien Monette[3], Mengshi Li[4], Michael K. Schultz[4], and Jason S. Lewis[1,5]

[1]Department of Radiology and Molecular Pharmacology Program, Memorial Sloan Kettering Cancer Center, New York, New York; [2]Department of Medical Physics, Memorial Sloan Kettering Cancer Center, New York, New York; [3]Laboratory of Comparative Pathology, Memorial Sloan Kettering Cancer Center, Weill Cornell Medicine, and Rockefeller University, New York, New York; [4]Perspective Therapeutics, Inc., Coralville, Iowa; and [5]Department of Radiology and Pharmacology Program, Weill Cornell Medical College, New York, New York

Although pancreatic ductal adenocarcinoma (PDAC) is associated with limited treatment options and poor patient outcomes, targeted α-particle therapy (TAT) represents a promising development in the field. TAT shows potential in treating metastatic cancers, including those that have become resistant to conventional treatments. Among the most auspicious radionuclides stands the in vivo α-generator ^{212}Pb. Combined with the imaging-compatible radionuclide ^{203}Pb, this theranostic match is a promising modality rapidly translating into the clinic. **Methods:** Using the pretargeting approach between a radiolabeled 1,2,4,5-tetrazine (Tz) tracer and a *trans*-cyclooctene (TCO) modified antibody, imaging and therapy with radiolead were performed on a PDAC tumor xenograft mouse model. For therapy, 3 cohorts received a single administration of 1.1, 2.2, or 3.7 MBq of the pretargeting agent, [^{212}Pb]Pb-DO3A-PEG$_7$-Tz, whereby administered activity levels were guided by dosimetric analysis. **Results:** The treated mice were holistically evaluated; minimal-to-mild renal tubular necrosis was observed. At the same time, median survival doubled for the highest-dose cohort (10.7 wk) compared with the control cohort (5.1 wk). **Conclusion:** This foundational study demonstrated the feasibility and safety of pretargeted TAT with ^{212}Pb in PDAC while considering dose limitations and potential adverse effects.

Key Words: targeted α-therapy; pretargeting; lead-212; progeny release; lead-203

J Nucl Med 2024; 65:109–116
DOI: 10.2967/jnumed.123.266388

Recent advances in oncology have led to marked improvements in the standard of care for cancer patients. Nevertheless, metastatic relapse remains the principal cause of cancer mortality (*1*).

Targeted α-particle therapy (TAT) is thought to provide optimal properties for treating disseminated micrometastatic diseases and exhibits significant potential, especially for tackling rapidly progressing cancers (*2–4*). TAT aims to selectively deliver α radiation to cancer cells while minimizing treatment-related toxicities. The direct cell-killing effect of α-particles is related to the induction of double-stranded DNA ruptures caused by the impact of the massive particles combined with their high linear energy transfer (50–230 keV/μm). Because of their relatively short effective range (<100 μm), α-emitters minimally cross-irradiate surrounding healthy tissue (*5*).

One increasingly popular radionuclide is the in vivo α-particle generator ^{212}Pb, which emits 1 (net) α-particle and 2 β^--particles within its decay chain (Fig. 1; Supplemental Fig. 1; supplemental materials are available at http://jnm.snmjournals.org). An isotopic theranostic match can be found in ^{203}Pb, which has a half-life of 2.1 d and is suitable for SPECT imaging. Because of the pair's suitable chemical and physical properties, ^{203}Pb and ^{212}Pb are ideal for clinical translation (*6*). However, with a relatively short physical half-life (10.6 h), ^{212}Pb-bearing radiopharmaceuticals require fast pharmacokinetics. Thus, pretargeted radionuclide therapy (PRT) is an especially promising strategy for using ^{212}Pb (*7*).

Our laboratories previously reported the inverse electron-demand Diels-Alder ligation's potential for PRT (*8–11*). In this work, we investigated the pretargeting strategy between the trans-cyclooctene (TCO)–conjugated monoclonal antibody (mAb) 5B1 and ^{212}Pb-radiolabeled Tz conjugates. 5B1 targets the carbohydrate cell surface antigen 19-9, which is overexpressed in pancreatic ductal adenocarcinoma (PDAC)—a uniformly lethal cancer form with limited treatment options (*12*). The pretargeting approach decouples the relatively short physical half-life of the radionuclide from the long biologic half-life of antibodies, promising both high specific binding to the tumor marker and fast clearance of the radiotracer. In a preclinical model, we aimed to prove that this strategy rapidly and safely delivers ^{212}Pb to the tumor. A further advantage of pretargeting is that multiple Tz radiotracers can be subsequently administered with almost identical tumor uptake, as previously reported (*9*). This allows for delivering a diagnostic Tz tracer first and calculating dosimetry estimates, followed by administering the therapeutic one without reinjecting the mAb (Fig. 1). This approach will enable clinicians to better anticipate the outcome of therapy preceded by predictive imaging.

MATERIALS AND METHODS

Information about laboratory equipment, biology, dosimetry, and additional studies can be found in the supplemental materials, as well as the synthesis of the Tz precursors modified with a polyethylene glycol 7 (PEG$_7$) linker and attached to one of the 4 chelators: TCMC (2-[4,7,10-tris(2-amino-2-oxoethyl)-1,4,7,10-tetrazacyclododec-1-yl]acetamide), PSC (2-[4,10-bis(carboxymethyl)-1,4,7,10-tetrazacyclododec-1-yl]-acetamide), DO3A (1,4,7,10-tetraazacyclododecane-1,4,7-triacetic acid), or DOTA (2,2′,2′′,2′′′-(1,4,7,10-tetraazacyclododecane-1,4,7,10-tetrayl)-tetraacetic acid).

All animal procedures were approved by the Institutional Animal Care and Use Committee.

Received Jul. 24, 2023; revision accepted Sep. 28, 2023.
For correspondence or reprints, contact Jason S. Lewis (lewisj2@mskcc.org).
Published online Nov. 9, 2023.

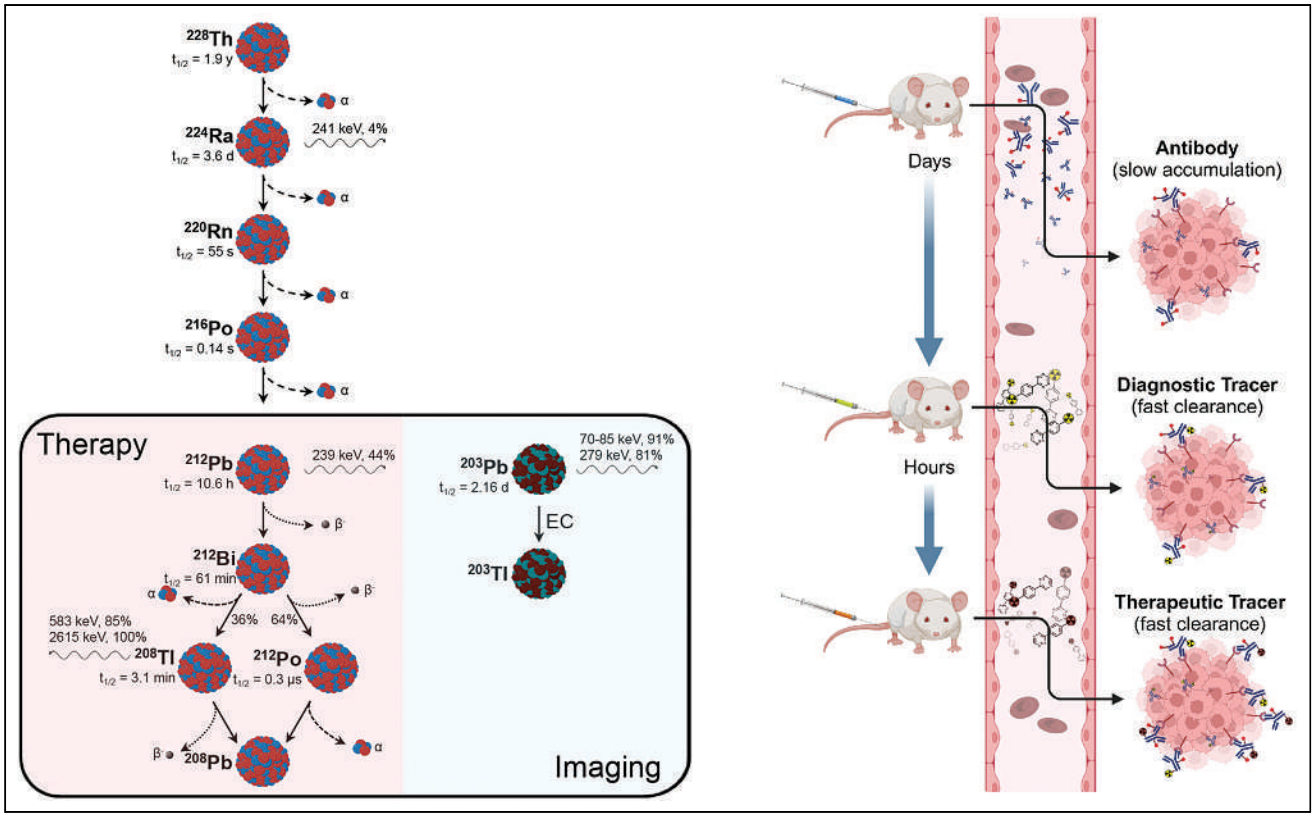

FIGURE 1. Pretargeting with theranostic pair ^{203}Pb and ^{212}Pb. (Left) Decay scheme of in vivo α-generator ^{212}Pb and SPECT-compatible nuclide ^{203}Pb. (Right) Illustration of theranostic pretargeting approach, following concept of reference *9*. This figure was created with BioRender. EC = electron capture; $t_{1/2}$ = half-life.

General Information for In Vivo Studies

For pharmacokinetic assessments, the ^{203}Pb- or ^{64}Cu-labeled Tz was intravenously injected (tail vain) into 8 healthy female athymic nude mice, and the radiotracer distribution was determined in selected organs at 1 and 4 h after injection (n = 4 per time point). The mice were intravenously injected with the 5B1-TCO conjugate (100 μg in sterile filtered phosphate-buffered saline) for pretargeting. Three to 4 d later, the mice received the radiolabeled tracer (2 nmol in phosphate-buffered saline).

Imaging

The mice were anesthetized using 2% isoflurane for imaging. SPECT/CT images with ^{203}Pb (11–37 MBq per mouse) were obtained on a Mediso nanoScan SPECT/CT device equipped with a high-resolution, low-energy, multipinhole collimator detecting the ^{203}Pb characteristic x-rays between 70 and 90 keV. All SPECT images were analyzed using VivoQuant (Invicro) reconstruction software (2020patch1hf2). PET/CT images with ^{64}Cu (~7.4 MBq per mouse) were obtained on an Inveon PET/CT (Siemens) rodent scanner. All PET/CT images were analyzed using the Inveon software suite. The counting rates in the reconstructed images were converted to the mean percentage injected dose per gram of tissue (%ID/g) by applying a system-specific calibration factor. Cerenkov luminescence imaging with ^{212}Pb (recording time, 5 min) was performed with an IVIS Spectrum (PerkinElmer).

For biodistribution studies, the mice were euthanized (CO_2 asphyxiation followed by cervical dislocation), and the tissues of interest were harvested for γ-counting or histologic analyses.

Therapy

A ^{212}Pb PRT dose escalation study was performed to evaluate therapeutic potential and identify potential adverse effects. Sixty mice were implanted with subcutaneous tumor xenografts 5 wk before the study commenced. The width and length of the tumors were determined using a caliper, and the tumor volume was calculated via Equation 1 as described in the literature (*13*).

$$\text{Tumor volume} = \frac{4}{3} \times \left(\frac{\text{length}}{2}\right)^2 \times \frac{\text{width}}{2}. \qquad \text{Eq. 1}$$

Mice with tumor volumes of 100–300 mm^3 were selected and randomized into 5 cohorts (n = 8 per cohort). Two cohorts served as controls and 3 received administered activities of 1.1, 2.2, and 3.7 MBq; the choice of these administered activities was guided by dosimetry estimates and accepted dosimetry thresholds for tumor response and toxicity (*14,15*). The mice received the 5B1-TCO conjugate 1 d after randomization and the ^{212}Pb-labeled Tz 3 d later. Wellness was monitored daily, and tumor volume and body weight were monitored biweekly until the endpoint. The endpoint was defined as a tumor volume of more than 2,000 mm^3, weight loss of more than 20% (compared with initial measurement), or a concerning health condition (e.g., necrotic or ulcerating tumor). After reaching their endpoints, the mice were euthanized, and selected tissues, including tumors, livers, and kidneys, were collected. Selected mice (n = 14 in total) from each cohort were submitted alive to a board-certified veterinary pathologist at the Memorial Sloan Kettering Cancer Center, Weill Cornell Medicine, and the Rockefeller University Laboratory of Comparative Pathology for a holistic evaluation. Blood samples (3 per cohort) were collected weekly via retroorbital blood draws and analyzed with a Hemavet 950 (Drew Scientific).

All data are represented as mean value ± standard error of the mean. The sample sizes were selected regarding statistical considerations,

ethical guidelines, and exigencies of funding. The significance analyses were performed using GraphPad Prism software 9.0, using unpaired 2-tailed *t*, multiple *t,* and log-rank tests.

RESULTS

Chemical Evaluation of Tz-Based Radiotracers

The pharmacokinetic properties of Tz-based radiopharmaceutical systems are essential factors for the success of PRT. Ideally, Tz-based radiopharmaceuticals exhibit short blood retention times and demonstrate low off-target uptake; usually, renal elimination is preferable. For this study, we investigated the previously developed precursor DOTA-PEG_7-Tz (*8*) and 3 additional precursors differing in the attached chelator (Fig. 2A). The 4 precursors are distinct in their theoretic charge (from +2 to −2, when lead-labeled), which might have a substantial influence on their pharmacokinetics (*16,17*). To visualize their relative ionic behavior under physiologic conditions, we performed paper electrophoresis with the ^{212}Pb-labeled radiotracers using phosphate-buffered saline at a pH of 7.4 (*18*), followed by phosphor imaging (Fig. 2B). Worthy of mentioning, the charges are not sharply defined but are a function of the pH and concentration of other coordinating anions and cations. Free Pb^{2+} hydrolyzes under physiologic conditions and predominately forms the $Pb(OH)^+$ species, thus explaining the minimal migration (*19*). The 4 radiotracers showed a clear charge tendency, with DO3A-PEG_7-Tz and PSC-PEG_7-Tz being close to their isoelectric point. It has been previously reported that a slight negative charge facilitates a beneficial pharmacokinetic behavior (*17,20*). These results suggest that DO3A-PEG_7-Tz might show superior performance in vivo, with a relatively short plasma retention time, fast renal clearance, and minimal hepatic clearance.

The radiotracers' lipophilicity was investigated by analytic high-performance liquid chromatography and confirmed by the 1-octanol/phosphate-buffered saline distribution coefficient at pH 7.4 (log $D_{7.4}$) (*21*). The data (Fig. 2C; Supplemental Table 1) affirm that all compounds are susceptible to high aqueous solubility and poor membrane permeability—desirable properties for a pretargeting tracer. The reason for the relatively similar behavior is that the lipophilicity is predominately regulated by the Tz-PEG_7 unit, which all compounds have in common.

All precursors (at a concentration of 10^{-6} M) demonstrated lead incorporation greater than 90% within 15 min at 37°C (Fig. 2D). Further experiments (Supplemental Fig. 2) revealed that a chelator concentration greater than 10^{-6} M and a chelator:metal ratio greater than 50:1 is required to approach quantitative labeling yield. The tracer stability of all ^{203}Pb-labeled tracers was investigated in human serum at 37°C via radio–instant thin-layer chromatography and revealed a release of less than 5% ^{203}Pb over 5 d, indicating that all lead chelates possess excellent stability.

Pharmacokinetics of Radiotracers

The ^{203}Pb-labeled and purified radiotracers (Supplemental Fig. 3) were administered to healthy mice, and their pharmacokinetic behavior was investigated (Fig. 3A). All tracers showed a predominantly renal clearance (>90 %ID/g, Supplemental Fig. 4). The TCMC-based tracer, with the highest positive relative charge in the paper electrophoresis, revealed slightly higher blood retention (0.71 ± 0.05 %ID/g at 1 h), possibly because of increased binding to the negatively charged albumin. Additionally, an

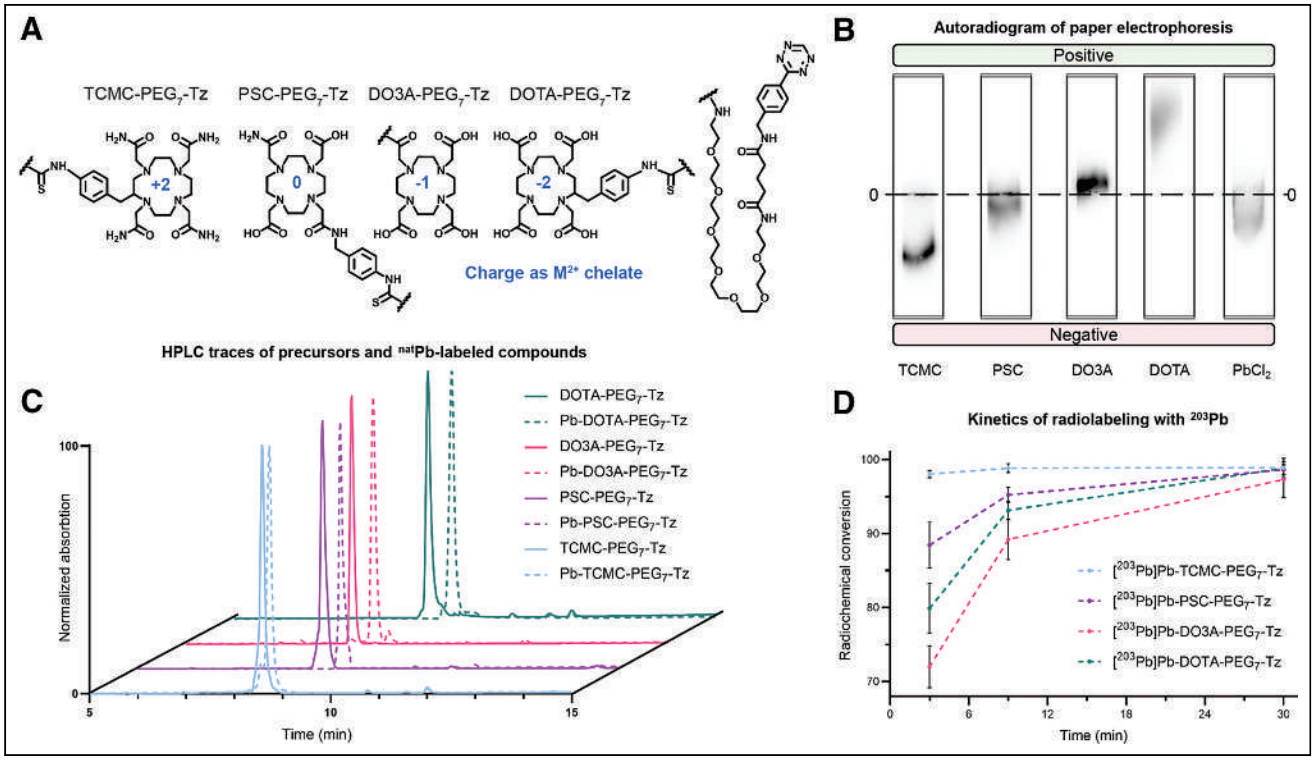

FIGURE 2. Chemical evaluation of Tz compounds. (A) Chemical structures of 4 Tz precursors. (B) Autoradiogram of paper electrophoresis performed with ^{212}Pb-labeled Tz precursors and [^{212}Pb]$PbCl_2$ at pH 7.4. (C) Normalized high-performance liquid chromatography diagrams of free and ^{nat}Pb-labeled Tz compounds (ultraviolet/visible light signal recorded at 254 nm). (D) Radiochemical conversion of Tz precursors (concentration of Tz = 10^{-6} mol/L, at 37°C) with ^{203}Pb measured via radio–instant thin-layer chromatography.

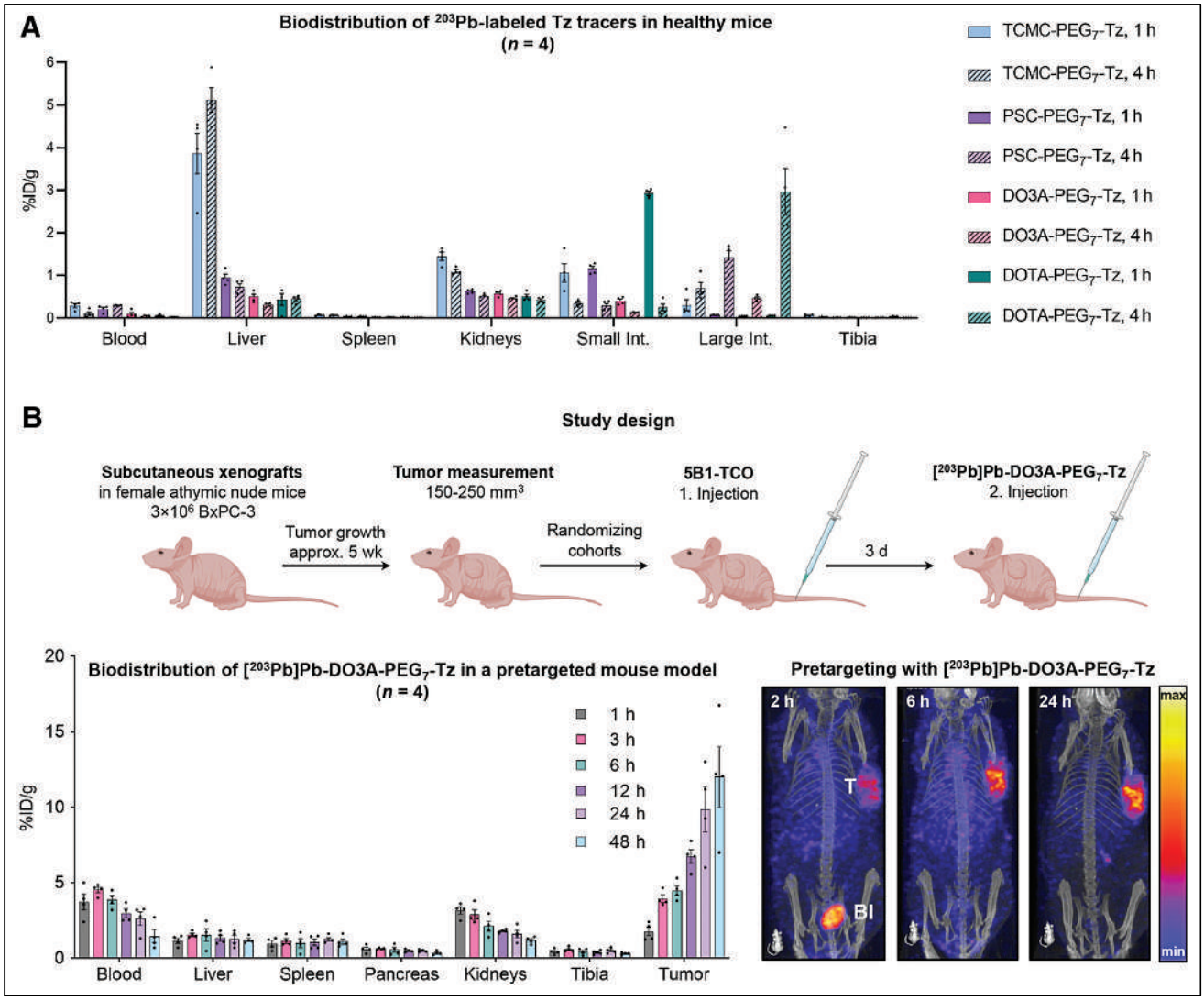

FIGURE 3. Pretargeting study with [^{203}Pb]Pb-DO3A-PEG$_7$-Tz. (A) Biodistribution data of 4 ^{203}Pb-labeled Tz tracers (2 nmol, 0.7 MBq) in healthy female nude mice. (B) Results of initial pretargeting study, with study design shown at top and, at bottom, biodistribution data of [^{203}Pb]Pb-DO3A-PEG$_7$-Tz (2 nmol, 0.7 MBq) in mice pretargeted with 5B1-TCO (100 μg, 0.7 nmol), accompanied by SPECT maximum-intensity projections (2 nmol, 18.5 MBq). Bl = bladder uptake; T = tumor uptake.

increased uptake in kidneys (3.0 ± 0.1 %ID/g at 4 h) and liver (3.5 ± 0.1 %ID/g at 4 h) was observed. The radiotracer with the highest relative negative charge, DOTA, showed partial hepatic clearance, as indicated by intestinal uptake (3.9 ± 0.3 %ID/g at 4 h). This clearance path is unfavorable because of the high radiosensitivity of the intestinal tract. The DO3A derivative showed the best pharmacokinetics, with fast clearance and low uptake in healthy tissue. Interestingly, this outcome could not have been predicted by relying solely on log$D_{7.4}$ values or in vitro stability tests. However, investigating the overall charge (visualized via paper electrophoresis) indicated which radiotracer could provide desirable pharmacokinetics; a slight negative charge (at pH 7.4) was confirmed to be beneficial for fast renal clearance.

Moving forward, the lead candidate, DO3A-PEG$_7$-Tz, radiolabeled with ^{203}Pb was investigated in a murine xenografted PDAC model pretargeted with 5B1-TCO (Fig. 3B). SPECT imaging and a multiple-time-point biodistribution study revealed a tumor uptake of 9.9 ± 1.4 %ID/g at 24 h after Tz injection. The tumor-to-blood ratio was 3.8 ± 1.0, and the tumor-to-muscle ratio at the same time was 27.2 ± 8.4. The increased blood retention (2.6 ± 0.4 %ID/g) can be attributed to still-circulating 5B1-TCO, which reacted with the Tz tracer and slowly accumulated at the tumor site. Within the 48-h interval, no release of ^{203}Pb was observed. These results reflect previously published pretargeting data (*9,22*).

^{212}Bi Release and Dosimetry Estimations

It is essential to underline that ^{212}Pb itself is not the α-emitter but its progeny. Since ^{212}Po has a short half-life of 0.3 μs, its redistribution can be neglected. However, the first daughter—^{212}Bi (half-life, 61 min)—has the potential to redistribute in the body. The conversion from ^{212}Pb to ^{212}Bi happens via low-energy β-decay, and the average recoil energy is approximately 0.52 eV. Hence, the ^{212}Bi release is unlikely to be driven by the recoil, assuming a bond energy of around 3 eV (*23*). However, the yield of conversion electrons from ^{212}Pb is relatively high (38%) and is followed by a cascade of Auger electrons resulting in highly

ionized states for the daughter nuclides (Bi^{4+} to Bi^{7+}), which are postulated to destroy the chelate (*24,25*). If ^{212}Bi is released from the tumor environment, it will localize predominantly in the kidneys (Supplemental Fig. 5) (*8,26*).

Using radiochemical separation methods (Supplemental Fig. 6), we determined via γ-spectroscopy (Supplemental Fig. 7) that on average 40% ± 5% of ^{212}Bi is eliminated from the chelators (Supplemental Table 2). This reflects values previously reported in the literature (*24,27–29*). However, when we were investigating the ^{212}Bi release in a cell assay using the BxPC-3 cell line (Supplemental Fig. 6B), instead of 40% ± 5% only 26% ± 5% unbound ^{212}Bi was detected in the cell medium. When we repeated this experiment but incubated the cells at 4°C, an increased fraction of 34% ± 5% ^{212}Bi was released. We hypothesize that biologic processes such as mitosis, membrane turnover, and endocytosis of the radiotracer facilitate the retention of unbound ^{212}Bi. The possibility of an active bismuth transport mechanism was ruled out by incubating the cells with [^{212}Bi]$BiCl_3$; no ^{212}Bi uptake was detected.

Finally, we investigated the release of ^{212}Bi in vivo using the pretargeting strategy with [^{212}Pb]Pb-DO3A-PEG_7-Tz in our PDAC xenograft mouse model. The mice were euthanized individually 24 h after injection of the radiotracer, and the tissues of interest were measured via γ-counting. We determined that merely 14.6% ± 0.7% of the intratumorally generated ^{212}Bi activity was redistributed. As expected, an additional relative uptake of 58.3% ± 6.4% ^{212}Bi activity (compared with ^{212}Pb) was measured in the kidneys (Fig. 4), reflecting the ^{212}Bi elimination from the tumor.

Summarizing, even though we determined an elimination of 40% ± 5% ^{212}Bi from the chelator, the release of intratumorally generated ^{212}Bi was reduced to 14.6% ± 0.7% in vivo, because of the retention of the progeny within the tumor environment.

Pretargeting dosimetry estimates for murine administration of [^{212}Pb]Pb-DO3A-PEG_7-Tz were determined according to the literature (Fig. 4) (*30–33*). When no daughter redistribution was assumed, the critical organs were the kidneys (6.9 Gy-equivalent/MBq of [^{212}Pb]Pb-DO3A-PEG_7-Tz administered), red marrow (9.5 Gy-equivalent/MBq), and urinary bladder (7.5 Gy-equivalent/MBq) (Supplemental Table 3). When using a conservative organ-level release estimate of 40% ^{212}Bi (highly overestimated as confirmed by the in vivo ^{212}Bi release study showing only 14.6% ± 0.7% release), which is followed by rapid redistribution and kidney accumulation, we calculated that the kidney dose coefficient could increase by nearly an order of magnitude (62 Gy-equivalent/MBq) (Supplemental Table 4). In contrast, dose coefficients for the tumor and other organs consequently decrease by 40%. In either case, myelotoxicity and renal toxicity are determining dose limitations.

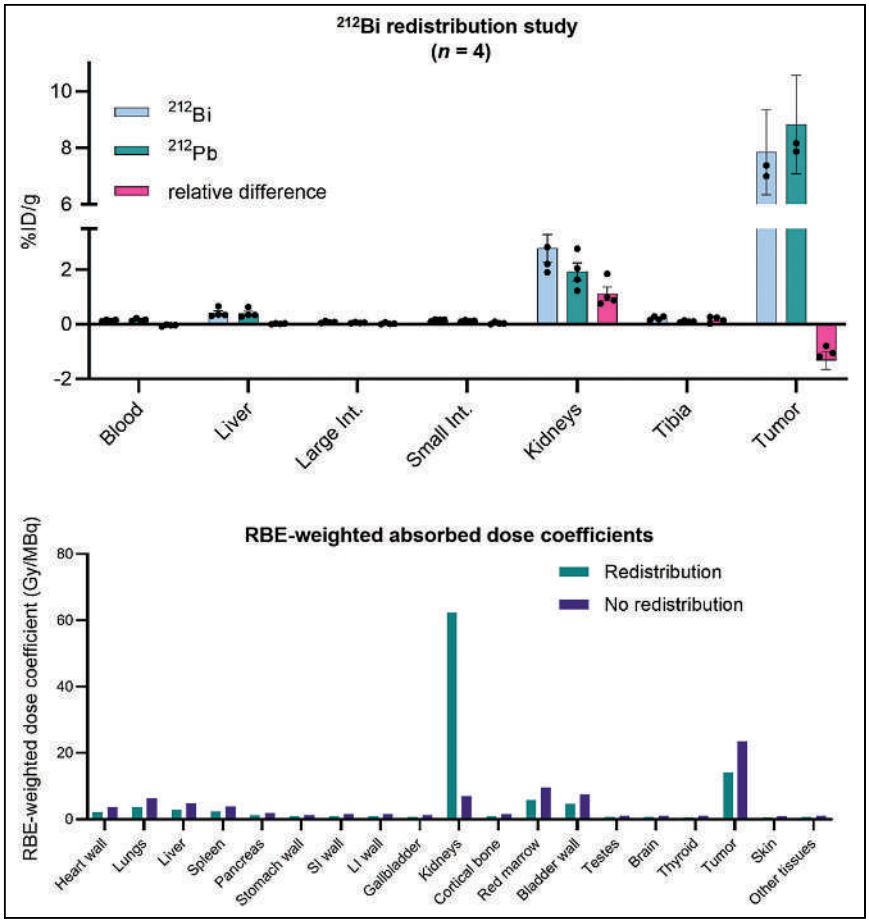

FIGURE 4. ^{212}Bi release and dosimetry estimations. (Top) Biodistribution data of ^{212}Bi, measured 15 min after death, and of ^{212}Pb. (Bottom) Estimated relative biological effectiveness–weighted absorbed dose coefficients for [^{212}Pb]Pb-DO3A-PEG7-Tz (in Gy-equivalent per MBq administered) estimated for different assumptions regarding redistribution of ^{212}Pb's progeny.

Therapy Study with [^{212}Pb]Pb-DO3A-PEG_7-Tz

A therapy study was conducted with [^{212}Pb]Pb-DO3A-PEG_7-Tz (single administration) comprising 5 arms (n = 8 per cohort) with 2 control and 3 therapeutic groups. The 2 control arms consisted of one group that received only 5B1-TCO and one that received an unspecific IgG-TCO mAb followed by administration of 1.1 MBq of [^{212}Pb]Pb-DO3A-PEG_7-Tz 3 d later. For PRT, the pretargeted mice received 1.1, 2.2, or 3.7 MBq of [^{212}Pb]Pb-DO3A-PEG_7-Tz. For these activities, the estimated relative biological effectiveness–weighted dose to the tumor tissue would be expected to induce a response (~20–100 Gy-equivalent) without producing excessive toxicity (Supplemental Fig. 8). The 4 groups that received a radioactive payload (3 d after mAb administration) were imaged 1 d after injection via Cerenkov luminescence imaging (Fig. 5A). The 4 therapeutic arms revealed that the Cerenkov luminescence imaging signal increased between the 3 dose levels. The IgG control arm showed unspecific accumulation in the liver, spleen, and kidneys.

The therapy study was accompanied by complementary imaging via PET using [^{64}Cu]Cu-DO3A-PEG_7-Tz (Fig. 5A) instead of relying on SPECT imaging with [^{203}Pb]Pb-DO3A-PEG_7-Tz. This was a practical consideration since PET imaging allows for easily quantifiable images, higher output, and shorter imaging times. We confirmed that the radiolabeling (Supplemental Fig. 2C)

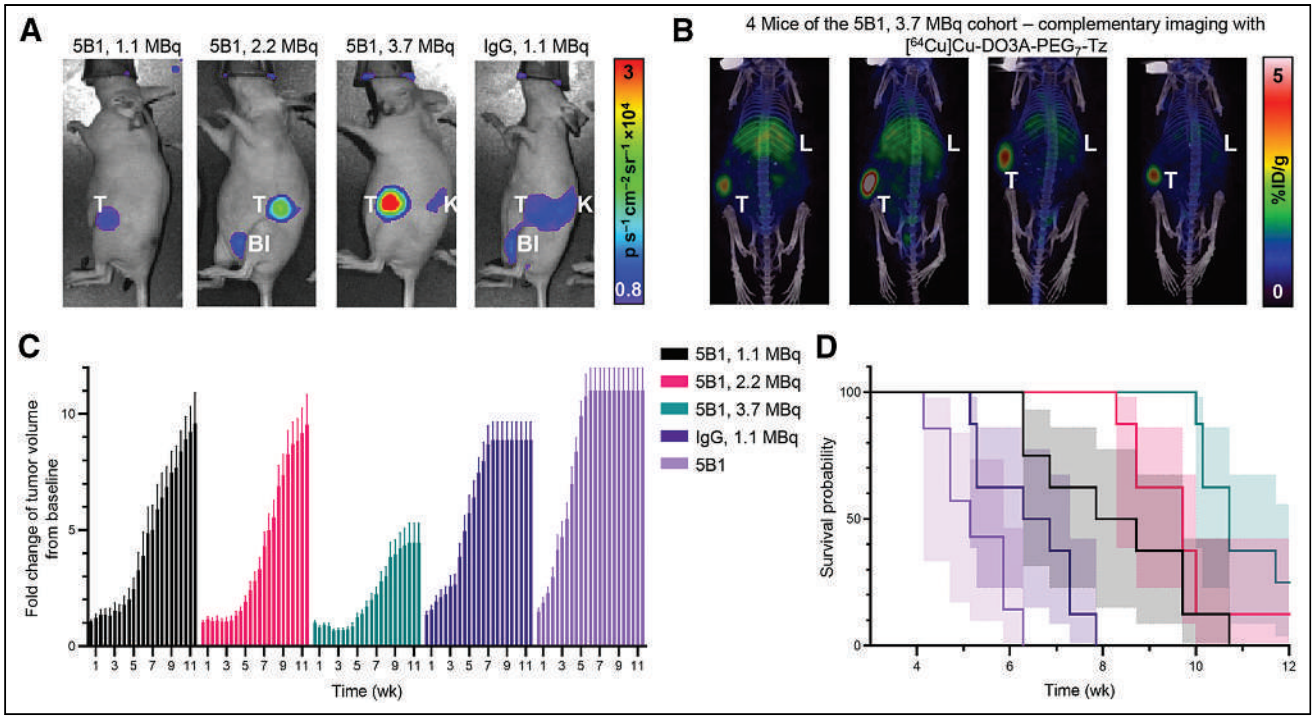

FIGURE 5. Therapy study: pretargeting with [^{212}Pb]Pb-DO3A-PEG$_7$-Tz. (A) Cerenkov luminescence imaging of 4 arms that received [^{212}Pb]Pb-DO3A-PEG$_7$-Tz (2 nmol) via pretargeting 24 h after injection. (B) Maximum-intensity projections (24 h after injection) of 4 mice (3.7-MBq cohort) injected with [^{64}Cu]Cu-DO3A-PEG$_7$-Tz 1 d after therapy to demonstrate complementary PET imaging. (C) Waterfall plot of fold change of tumor volume for each cohort. (D) Survival probability as function of time after Tz injection (n = 8 per cohort). Bl = bladder uptake; K = kidney uptake; T = tumor uptake.

and pharmacokinetics (Supplemental Fig. 9) are similar between the ^{64}Cu- and ^{203}Pb-labeled precursors. Consequently, dosimetry estimates and therapy monitoring can be pursued via either SPECT or PET imaging using ^{203}Pb or ^{64}Cu, respectively, greatly expanding the toolbox. Here, the mice were injected with the PET agent 1 d after receiving the therapeutic dose (4 d after 5B1-TCO administration) to circumvent interference with the Cerenkov luminescence imaging.

Three criteria were established requiring euthanasia of the mice: a tumor burden of more than 2,000 mm^3, weight loss of more than 20%, or a severe health condition (e.g., lethargy, petechiae, or infections). In the first week, the white blood cell count decreased for the 4 cohorts that received activity. The 3.7-MBq cohort was most affected, revealing a count of roughly 0.2×10^3 white blood cells per microliter. The population of platelets and red blood cells decreased minimally within the first 2 wk. By the third week, all cohorts had recovered from the initial impairment, as indicated by the normalized blood panel (Supplemental Fig. 10).

Compared with the 5B1-TCO control group, the PRT cohorts revealed a particular duration of tumor growth retardation, and the effect depended on the received activity. The delayed onset for tumor progression was roughly 5 wk for the 3.7-MBq cohort, 3.5 wk for the 2.2-MBq cohort, and 2.5 wk for the 1.1-MBq cohort (Fig. 5B; Supplemental Fig. 11). A growth suppression of almost 2 wk was observed for the IgG (+1.1 MBq of ^{212}Pb) control cohort; this finding can be attributed to the enhanced permeability and retention effect and stimulated immune response, as previously reported (*34*). After the onset of tumor progression, each cohort reached the endpoint in approximately 5 wk. On average, the median survival was 5.1 wk for the 5B1-TCO cohort and 6.5 wk for the IgG-TCO control cohort. The 1.1-, 2.2-, and 3.7-MBq [^{212}Pb]Pb-DO3A-PEG$_7$-Tz cohorts showed a median survival of 8.3, 9.7, and 10.7 wk, respectively. These data include mice euthanized before reaching the maximum tumor volume. Three mice of the 1.1-MBq cohort, 2 of the 2.2-MBq cohort, and 2 of the 3.7-MBq cohort developed ulcerating tumors. One mouse of the 3.7-MBq cohort and 2 of the IgG-TCO 1.1-MBq cohort showed lethargic behavior. One mouse of the 2.2-MBq cohort died on day 58 due to unidentified causes.

To investigate possible adverse effects of PRT, randomly selected mice from each cohort—after they reached their endpoint—were submitted alive for a comprehensive assessment by board-certified veterinary pathologists. This included a gross examination, a histopathologic examination of selected tissues of interest, and blood work (hematology and serum chemistry) analysis. The only significant changes that could be attributed to the treatment (i.e., radiation injury) in these mice were seen in the kidneys and ovaries (Fig. 6). The other macroscopic, microscopic, hematology, and serum chemistry changes observed in the evaluated mice were not considered treatment-related.

All the microscopically examined treated mice (n = 8) exhibited a bilateral minimal-to-mild tubulonephropathy with tubular epithelial degeneration and necrosis (cellular sloughing, cytoplasmic swelling, pallor, condensation or hypereosinophilia, karyorrhexis, karyolysis or karyomegaly, or attenuation). These changes affected a minimal to mild portion (≈1%–≤10%) of the renal tubules—mainly those found at the corticomedullary junction. These lesions were not observed in the microscopically examined 5B1-TCO control mice (n = 3). These findings resemble renal injuries previously associated with α-emitter treatments in mice, including mice administered ^{212}Pb and ^{225}Ac (*35,36*). Although some mice were slightly more affected than others, the treatment

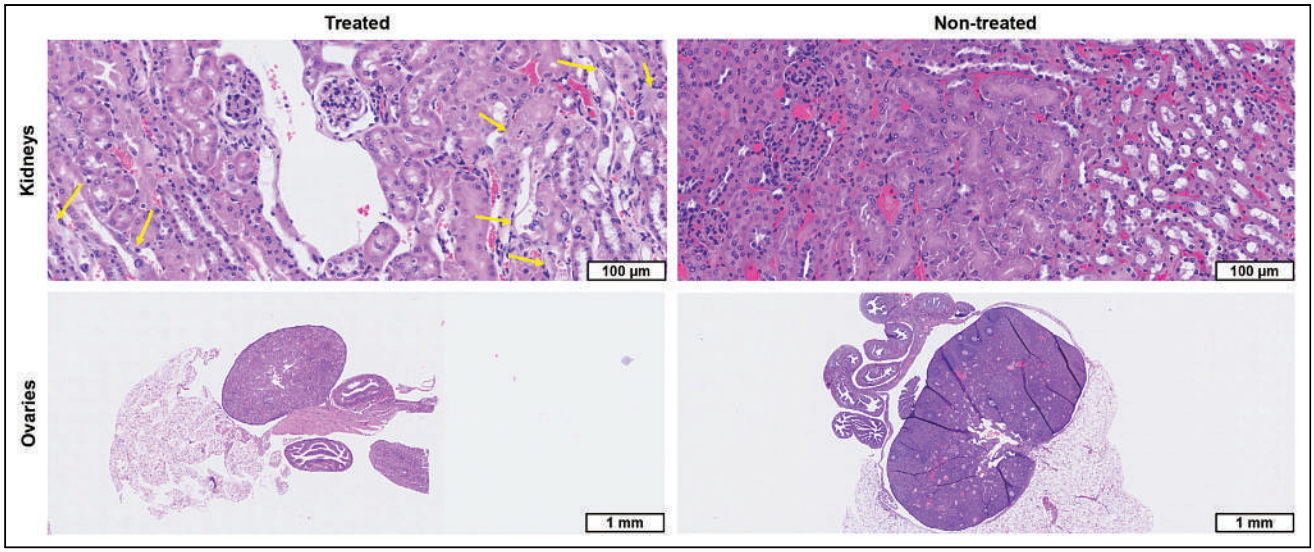

FIGURE 6. Representative histology results. Representative histology of hematoxylin- and eosin-stained kidney (top) and ovarian (bottom) sections of BxPC-3 tumor–bearing female athymic nude mice. (Left) Mice treated with ^{212}Pb. (Right) Control group. Histopathology of kidneys revealed multifocal, minimal-to-mild tubular injury (arrows) affecting approximately 1%–10% of tubules. Control animals showed histologically normal kidneys. Histopathology of treated ovaries revealed diffuse marked ovarian atrophy with complete loss of follicles and corpora lutea.

dosage did not seem to have significantly affected the severity of the kidney lesions. These lesions also did not seem to substantially affect the renal function of these animals, as there were no apparent signs of renal toxicity in the serum chemistry results.

All microscopically examined ovaries from the treated mice ($n = 9$) exhibited marked atrophy. These ovarian changes were not observed in the microscopically examined 5B1-TCO control mice ($n = 6$). Ovarian atrophy can be caused by radiation because of nonreversible injury to germ cells (*37*). Ovaries are radiosensitive organs, and their atrophy has been described as an effect of some radioimmunotherapies in mice (*38*). As all examined ovaries were markedly affected, the treatment dose did not seem to have substantially affected the severity of the ovarian lesions.

The pathology report further highlights that fractionated dosing of [^{212}Pb]Pb-DO3A-PEG$_7$-Tz at 1- to 2-wk intervals could decrease toxicity while possibly increasing the therapeutic response. Reimaging of selected mice 10 wk after receiving the therapeutic dose confirmed that their tumors still highly express the carbohydrate cell surface antigen 19-9 (Supplemental Fig. 12), indicating the feasibility of fractionated dosing.

CONCLUSION

The elementary match pair ^{212}Pb and ^{203}Pb has demonstrated great potential to advance theranostics and promote the translation of TAT. For the relatively short-lived therapeutic nuclide ^{212}Pb, PRT appears to be a promising strategy because of its rapid delivery of the radioactive payload and minimal off-targeting.

Here, we used a xenografted PDAC mouse model and the TCO-modified mAb 5B1 to enable pretargeting with the Tz-based radiotracer [^{203}Pb]Pb-DO3A-PEG$_7$-Tz.

In a single administration study, the efficiency and safety of PRT with ^{212}Pb were evaluated. With the highest administered dose of 3.7 MBq, the average survival time could be doubled compared with the control cohort while maintaining radiotoxicity within acceptable limits. Furthermore, we demonstrated that even when using a noninternalizing vector, the limited redistribution of the daughter nuclide ^{212}Bi does not lead to marked reduction in antitumor potency and does not lead to marked increases in normal-organ toxicity.

The short half-life of ^{212}Pb (10.6 h) would allow for a controlled dose fractionation and weekly-to-biweekly injections. On this regimen, side effects can be minimized, therapy progress can be monitored exactly, and the tumor burden can be further reduced until eventually eliminated. Recently, Keinänen et al. reported on a pretargeting strategy harnessing $^{64/67}$Cu in a colorectal cancer mouse model. They revealed that fractionated dosing with the therapeutic nuclide resulted in prolonged tumor suppression (*9*). Studies with ^{212}Pb administration in biweekly cycles (fractionated dosing) are under way.

This foundational study demonstrated the feasibility and safety of pretargeted TAT with ^{212}Pb in PDAC while considering dose limitations and potential adverse effects.

DISCLOSURE

This work was supported by the donation of Diane and James Rowen (David Bauer and Jason Lewis), the Tow Foundation Fellowship Program (David Bauer), and NCI R35 CA232130 (Jason Lewis). The MSK Small-Animal Imaging Core Facility's technical services were partly funded through NIH Cancer Center support grant P30 CA008748 and NIH Shared Instrumentation grants S10 RR02892-01 and S10 OD016207-01. Technical services provided by the MSK Analytic NMR Core Facility were funded in part through NIH/NCI Cancer Center support grant P30 CA008748. Jason Lewis holds intellectual property related to the application of click and radiopharmaceutical chemistry (patent US11135320B2). This work was supported by Perspective Therapeutics Inc. (Mengshi Li and Michael Schultz are employees). No other potential conflict of interest relevant to this article was reported.

ACKNOWLEDGMENTS

We thank the U.S. Department of Energy Isotope Program (Isotope R&D Production) and Perspective Therapeutics, Inc. for providing the ^{224}Ra/^{212}Pb lead generators as well as Suzanne E. Lapi and Shefali Saini (both at the University of Alabama at Birmingham, Department of Radiology) and John S. Wilson (University of Alberta, Department of Oncology) for providing ^{203}Pb. Furthermore, we thank George Sukenick and Rong Wang (MSK Analytical NMR Core Facility) for supporting NMR and mass spectrometry; the Laboratory of Comparative Pathology (MSK Core Facility) for evaluating the therapy data; and Kishore Pillarsetty, Edwin C. Pratt, Garon Scott (MSK Radiology), and Lawson Spare (ANSTO) for providing advice and support.

KEY POINTS

QUESTION: Is pretargeting a feasible strategy for the theranostic matched pair $^{203/212}$Pb to enable combined imaging and therapy in an adenocarcinoma mouse model?

PERTINENT FINDINGS: Pretargeting is a suitable delivery approach for the short-lived radionuclide ^{212}Pb. This foundational study demonstrates the feasibility and safety of pretargeting TAT with ^{212}Pb—accompanied by complementary imaging with ^{203}Pb (and ^{64}Cu)—in PDAC while considering dose limitations and potential adverse effects.

IMPLICATIONS FOR PATIENT CARE: Pretargeting with radiolead is a promising strategy to improve patient care, especially for cancer entities with currently limited treatment options, such as PDAC. Upcoming studies will elucidate the benefit of dose fractionation, which will minimize side effects while the tumor burden is further reduced until eventually eliminated.

REFERENCES

1. Ganesh K, Massague J. Targeting metastatic cancer. *Nat Med.* 2021;27:34–44.
2. Juzeniene A, Stenberg VY, Bruland OS, Larsen RH. Preclinical and clinical status of PSMA-targeted alpha therapy for metastatic castration-resistant prostate cancer. *Cancers (Basel).* 2021;13:779.
3. Raja C, Graham P, Abbas Rizvi SM, et al. Interim analysis of toxicity and response in phase 1 trial of systemic targeted alpha therapy for metastatic melanoma. *Cancer Biol Ther.* 2007;6:846–852.
4. Jurcic JG, Rosenblat TL. Targeted alpha-particle immunotherapy for acute myeloid leukemia. *Am Soc Clin Oncol Educ Book.* 2014:e126–e131.
5. Kim YS, Brechbiel MW. An overview of targeted alpha therapy. *Tumour Biol.* 2012;33:573–590.
6. McNeil BL, Robertson AKH, Fu W, et al. Production, purification, and radiolabeling of the ^{203}Pb/^{212}Pb theranostic pair. *EJNMMI Radiopharm Chem.* 2021;6:6.
7. Kokov KV, Egorova BV, German MN, et al. ^{212}Pb: production approaches and targeted therapy applications. *Pharmaceutics.* 2022;14:189.
8. Poty S, Carter LM, Mandleywala K, et al. Leveraging bioorthogonal click chemistry to improve ^{225}Ac-radioimmunotherapy of pancreatic ductal adenocarcinoma. *Clin Cancer Res.* 2019;25:868–880.
9. Keinänen O, Fung K, Brennan JM, et al. Harnessing ^{64}Cu/^{67}Cu for a theranostic approach to pretargeted radioimmunotherapy. *Proc Natl Acad Sci USA.* 2020;117:28316–28327.
10. Sarrett SM, Keinanen O, Dayts EJ, et al. Inverse electron demand Diels-Alder click chemistry for pretargeted PET imaging and radioimmunotherapy. *Nat Protoc.* 2021;16:3348–3381.
11. Houghton JL, Zeglis BM, Abdel-Atti D, Sawada R, Scholz WW, Lewis JS. Pretargeted immuno-PET of pancreatic cancer: overcoming circulating antigen and internalized antibody to reduce radiation doses. *J Nucl Med.* 2016;57:453–459.
12. Sarantis P, Koustas E, Papadimitropoulou A, Papavassiliou AG, Karamouzis MV. Pancreatic ductal adenocarcinoma: treatment hurdles, tumor microenvironment and immunotherapy. *World J Gastrointest Oncol.* 2020;12:173–181.
13. Faustino-Rocha A, Oliveira PA, Pinho-Oliveira J, et al. Estimation of rat mammary tumor volume using caliper and ultrasonography measurements. *Lab Anim (NY).* 2013;42:217–224.
14. Larson SM, Carrasquillo JA, Cheung NK, Press OW. Radioimmunotherapy of human tumours. *Nat Rev Cancer.* 2015;15:347–360.
15. Emami B, Lyman J, Brown A, et al. Tolerance of normal tissue to therapeutic irradiation. *Int J Radiat Oncol Biol Phys.* 1991;21:109–122.
16. Yoo J, Reichert DE, Welch MJ. Comparative in vivo behavior studies of cyclen-based copper-64 complexes: regioselective synthesis, x-ray structure, radiochemistry, log P, and biodistribution. *J Med Chem.* 2004;47:6625–6637.
17. Jones-Wilson TM, Deal KA, Anderson CJ, et al. The in vivo behavior of copper-64-labeled azamacrocyclic complexes. *Nucl Med Biol.* 1998;25:523–530.
18. Koźmiński P, Gaweda W, Rzewuska M, et al. Physicochemical and biological study of ^{99m}Tc and ^{68}Ga radiolabelled ciprofloxacin and evaluation of [^{99m}Tc]Tc-CIP as potential diagnostic radiopharmaceutical for diabetic foot syndrome imaging. *Tomography.* 2021;7:829–842.
19. Nikolaychuk PA. The revised potential-pH diagram for Pb-H_2O system. *Ovidius University Annals of Chemistry.* 2018;29:55–67.
20. Lipowska M, Klenc J, Marzilli LG, Taylor AT. Preclinical evaluation of ^{99m}Tc(CO)$_3$-aspartic-*N*-monoacetic acid, a renal radiotracer with pharmacokinetic properties comparable to ^{131}I-*o*-iodohippurate. *J Nucl Med.* 2012;53:1277–1283.
21. Imberti C, Chen YL, Foley CA, et al. Tuning the properties of tris(hydroxypyridinone) ligands: efficient ^{68}Ga chelators for PET imaging. *Dalton Trans.* 2019;48:4299–4313.
22. Membreno R, Cook BE, Zeglis BM. Pretargeted radioimmunotherapy based on the inverse electron demand Diels-Alder reaction. *J Vis Exp.* 2019;143:10.3791/59041.
23. Szucs Z, van Rooyen J, Zeevaart JR. Recoil effect on beta-decaying in vivo generators, interpreted for ^{103}Pd/^{103m}Rh. *Appl Radiat Isot.* 2009;67:1401–1404.
24. Bartoś B, Lyczko K, Kasperek A, Krajewski S, Bilewicz A. Search of ligands suitable for ^{212}Pb/^{212}Bi in vivo generators. *J Radioanal Nucl Chem.* 2013;295:205–209.
25. Auranen K, McCutchan EA. Nuclear data sheets for A=212. *Nucl Data Sheets (NY NY).* 2020;168:117–267.
26. Schwartz J, Jaggi JS, O'Donoghue JA, et al. Renal uptake of bismuth-213 and its contribution to kidney radiation dose following administration of actinium-225-labeled antibody. *Phys Med Biol.* 2011;56:721–733.
27. Su FM, Beaumier P, Axworthy D, Atcher R, Fritzberg A. Pretargeted radioimmunotherapy in tumored mice using an in vivo ^{212}Pb/^{212}Bi generator. *Nucl Med Biol.* 2005;32:741–747.
28. Ruble G, Wu C, Squire RA, Ganswo OA, Strand M. The use of ^{212}Pb-labeled monoclonal antibody in the treatment of murine erythroleukemia. *Int J Radiat Oncol Biol Phys.* 1996;34:609–616.
29. Mirzadeh S, Kumar K, Gansow OA. The chemical fate of ^{212}Bi-DOTA formed by β-decay of ^{212}Pb(DOTA)$^{2-}$. *Radiochim Acta.* 1993;60:1–10.
30. Keenan MA, Stabin MG, Segars WP, Fernald MJ. RADAR realistic animal model series for dose assessment. *J Nucl Med.* 2010;51:471–476.
31. Carter LM, Crawford TM, Sato T, et al. PARaDIM: a PHITS-based Monte Carlo tool for internal dosimetry with tetrahedral mesh computational phantoms. *J Nucl Med.* 2019;60:1802–1811.
32. Bartlett RM, Bolch WE, Brill AB, et al. *MIRD Primer 2022: A Complete Guide to Radiopharmaceutical Dosimetry.* Society of Nuclear Medicine and Molecular Imaging; 2022.
33. Cloutier RJ, Smith SA, Watson EE, Snyder WS, Warner GG. Dose to the fetus from radionuclides in the bladder. *Health Phys.* 1973;25:147–161.
34. Heneweer C, Holland JP, Divilov V, Carlin S, Lewis JS. Magnitude of enhanced permeability and retention effect in tumors with different phenotypes: ^{89}Zr-albumin as a model system. *J Nucl Med.* 2011;52:625–633.
35. Milenic DE, Molinolo AA, Solivella MS, et al. Toxicological studies of ^{212}Pb intravenously or intraperitoneally injected into mice for a phase 1 trial. *Pharmaceuticals (Basel).* 2015;8:416–434.
36. Cheal SM, McDevitt MR, Santich BH, et al. Alpha radioimmunotherapy using ^{225}Ac-proteus-DOTA for solid tumors: safety at curative doses. *Theranostics.* 2020;10:11359–11375.
37. Dixon D, Alison R, Bach U, et al. Nonproliferative and proliferative lesions of the rat and mouse female reproductive system. *J Toxicol Pathol.* 2014;27(suppl):1S–107S.
38. Santich BH, Cheal SM, Ahmed M, et al. A self-assembling and disassembling (SADA) bispecific antibody (BsAb) platform for curative two-step pretargeted radioimmunotherapy. *Clin Cancer Res.* 2021;27:532–541.

Clinical Value of ^{68}Ga-Pentixafor PET/CT in Subtype Diagnosis of Primary Aldosteronism Patients with Adrenal Micronodules

Jie Ding*[1], Xiang Li*[2], Shengyan Liu[3], Yinjie Gao[4], Guoyang Zheng[5], Marcus Hacker[2], Yushi Zhang[5], Anli Tong[4], and Li Huo[1]

[1]Department of Nuclear Medicine, Beijing Key Laboratory of Molecular Targeted Diagnosis and Therapy in Nuclear Medicine and State Key Laboratory of Complex Severe and Rare Diseases, Peking Union Medical College Hospital, Chinese Academy of Medical Science and Peking Union Medical College, Beijing, China; [2]Division of Nuclear Medicine, Department of Biomedical Imaging and Image-Guided Therapy, Medical University of Vienna, Vienna, Austria; [3]Peking Union Medical College Hospital, Chinese Academy of Medical Science and Peking Union Medical College, Beijing, China; [4]Department of Endocrinology and Key Laboratory of Endocrinology, Ministry of Health, Peking Union Medical College Hospital, Chinese Academy of Medical Science and Peking Union Medical College, Beijing, China; and [5]Department of Urological Surgery, Peking Union Medical College Hospital, Chinese Academy of Medical Science and Peking Union Medical College, Beijing, China

Our objective was to investigate the clinical value of ^{68}Ga-pentixafor PET/CT in subtype diagnosis of primary aldosteronism (PA) patients with adrenal micronodules less than 1 cm in diameter and compare it with the routine clinical methods. **Methods:** We used prospective enrollment of PA patients with adrenal micronodules identified by adrenal CT scans to undergo ^{68}Ga-pentixafor PET/CT. Patients were divided into surgically eligible and ineligible groups based on surgical pathology and postoperative follow-up or adrenal venous sampling (AVS) results. Patient management was discussed by a multidisciplinary team. The semiquantitative parameters of PET/CT included SUV_{max} for adrenal lesion and SUV ratios for lesion to liver and lesion to normal adrenal gland. **Results:** In total, 123 PA patients with adrenal micronodules were examined using ^{68}Ga-pentixafor PET/CT, and 104 patients who underwent surgery or successful AVS were included in the analysis (48 ± 10 y old). The sensitivity, specificity, and accuracy of visual analysis using ^{68}Ga-pentixafor PET/CT to identify surgically eligible patients were 90.2%, 72.7%, and 86.5%, respectively, which were significantly higher than those of adrenal CT (73.1%, 53.8%, and 68.3%, respectively) and yielded consistent results in different CT morphologic or age subgroups. In 36 patients who had both AVS and ^{68}Ga-pentixafor PET/CT, the tests showed a 66.7% concordance rate. However, PET/CT was significantly more concordant with surgical outcomes than was AVS in 17 patients who underwent adrenalectomy (82.4% vs. 68.86%). Among the 183 adrenal micronodules included in the study, the semiquantitative diagnostic thresholds for 92 lesions eligible for surgical treatment were an SUV_{max} of at least 4.55, an SUV ratio of at least 2.17 for lesion to liver, and an SUV ratio of at least 1.90 for lesion to normal adrenal gland. All patients benefited from surgical removal of ^{68}Ga-pentixafor–avid microlesions. **Conclusion:** In PA patients with adrenal micronodules, ^{68}Ga-pentixafor PET/CT demonstrated promising diagnostic accuracy in classification and appeared to perform better than adrenal CT. Furthermore, there was also a suggestion of some potential in predicting postoperative efficacy compared with AVS, although these observations require further investigation and verification in larger cohorts.

Received May 24, 2023; revision accepted Oct. 17, 2023.

For correspondence or reprints, contact Li Huo (huoli@pumch.cn) or Anli Tong (tonganli@hotmail.com).

*Contributed equally to this work.

Published online Nov. 30, 2023.

Key Words: C-X-C motif chemokine receptor 4; gallium radioisotopes; PET; primary aldosteronism

J Nucl Med 2024; 65:117–124
DOI: 10.2967/jnumed.123.266061

Primary aldosteronism (PA) is the most prevalent curable form of endocrine hypertension, characterized by low renin and high aldosterone levels (*1*). PA patients are at an increased risk of cardiovascular and cerebrovascular complications (*2*), highlighting the importance of early diagnosis and effective treatment for better outcomes.

The most important clinical classification of PA is differentiating between surgically eligible forms (e.g., unilateral/bilateral aldosterone-producing adenoma [APA] and unilateral adrenocortical hyperplasia [UAH]) and ineligible forms (e.g., bilateral adrenocortical hyperplasia [BAH]) (*3*). Adrenal CT and adrenal venous sampling (AVS) are recommended for PA subtyping by the Endocrine Society practice guidelines (*4*). However, adrenal CT can provide only morphologic, not functional, information. Around 40% of PA patients had nonconcordant adrenal CT and AVS results (*5*). Notably, the evaluation of adrenal microadenomas (≤10 mm) in PA patients is the primary limitation of adrenal imaging (*3*). Besides, AVS is invasive and technically challenging, with only a 50%–80% success rate for right adrenal vein cannulation, and carries the risk of significant complications (*6*).

Previous studies have explored noninvasive alternatives for PA subtyping, particularly in the field of nuclear functional imaging. However, existing methods such as ^{131}I-NP-59 and ^{11}C-metomidate have significant shortcomings, including time-consuming acquisition protocols, low specificity, and the need for pretreatment dexamethasone (*7*). Besides, the short half-life of ^{11}C also limits its clinical use. Identifying and classifying adrenal microlesions remain a major limitation of adrenal imaging in PA patients.

C-X-C motif chemokine receptor 4 (CXCR4) is expressed on the surface of cell membranes, and previous studies have shown that it is highly expressed in most APAs (*8*). ^{68}Ga-pentixafor,

a CXCR4-specific ligand, has shown strong diagnostic efficacy in detecting APAs larger than 1 cm in diameter (*9,10*). However, the performance of ^{68}Ga-pentixafor in characterizing adrenal micronodules remains unclear, and the uptake threshold for identifying the surgically eligible group in PA patients needs to be determined.

Therefore, the present study aimed to evaluate the performance of ^{68}Ga-pentixafor PET/CT in characterizing adrenal micronodules and to compare it with adrenal CT and AVS. The study also aimed to determine the uptake threshold for identifying the surgically eligible group in PA patients. This research will provide valuable insights into the use of ^{68}Ga-pentixafor PET/CT for noninvasive diagnosis of PA and could potentially improve clinical decision-making and patient outcomes.

MATERIALS AND METHODS

Patients

We conducted a prospective study between December 2018 and June 2022 using the following criteria for inclusion: a confirmed diagnosis of PA determined by an endocrinologist with 30 y of experience (the detailed diagnostic criteria are described in our previously published article (*10*)) and an adrenal CT scan showing unilateral or bilateral adrenal micronodules (≤1.0 cm in length) or small nodular hyperplasia (≤1.0 cm in thickness). Exclusion criteria included pregnancy, breastfeeding, or hypertension resulting from other causes. All included patients underwent ^{68}Ga-pentixafor PET/CT (within 30 d after adrenal CT). The decision whether to perform AVS and the method of patient management were made by a multidisciplinary team comprising members from the departments of endocrinology, urology, and nuclear medicine at our hospital. The study protocol is further outlined in the supplemental materials (available at http://jnm.snmjournals.org). Written informed consent to undergo ^{68}Ga-pentixafor PET/CT imaging was obtained from all patients, and the consent form and study protocol were approved by the Ethical Committee of Peking Union Medical College Hospital (institutional review board protocol ZS-1435). We registered the study at ClinicalTrials.gov (NCT04859959). Only patients who underwent adrenalectomy and had a follow-up time of 6–12 mo or who underwent successful AVS were included in the final analysis.

The following data were collected and calculated at baseline: general clinical information, antihypertensive drug dose (defined daily dose based on World Health Organization collaborating center, https://www.whocc.no/atc_%20ddd_index/%202010), aldosterone-to-renin ratio (plasma renin activity < 0.1 ng/mL/h was considered 0.1 ng/mL/h), and adrenal CT results. Six to 12 mo after adrenalectomy, the change in values was recorded.

Adrenal CT

Two experienced radiologists classified the adrenal CT imaging features of PA patients into the following 5 categories based on the morphologic changes in adrenal glands: unilateral single micronodule, unilateral micronodular hyperplasia, bilateral single micronodule, bilateral micronodular hyperplasia, and unilateral single micronodule with contralateral micronodular hyperplasia. Examples of CT performance are shown in Supplemental Figure 1. The diagnostic rules of CT are listed in the supplemental materials. The adrenal CT scans were plain CT scans.

^{68}Ga-Pentixafor PET/CT

The preparation of ^{68}Ga-pentixafor was previously published (*10*). The examination and reconstruction methods for ^{68}Ga-pentixafor PET/CT can be found in the supplemental materials.

Two experienced nuclear medicine physicians who were unaware of the clinical information evaluated the ^{68}Ga-pentixafor PET/CT data using MIM Encore (MIM Software). The first step involved categorizing the lesions as positive or negative for uptake through visual assessment. Then, the SUV_{max} of the adrenal microlesions, the ratio of lesion SUV_{max} to normal-liver SUV_{mean} (LLR), the ratio of lesion SUV_{max} to normal-adrenal-tissue SUV_{mean} (LAR), and the ratio of bilateral adrenal SUV_{max} (SUV_{max} lateralization index) were calculated. The criteria for visual and semiquantitative analysis are detailed in the supplemental materials.

Postoperative Outcome Assessment

Choice of surgical method can be found in the supplemental materials. The interval between adrenalectomy and ^{68}Ga-pentixafor PET/CT ranged from 15 to 45 d. The median duration of follow-up was 8 mo (range, 6–12 mo). Postoperative clinical and biochemical outcomes were assessed according to the international multicenter PA surgical outcome criteria (*11*), which include complete success (cured), partial success (improvement), and absence of success (persistence).

AVS Examination for Subtype Diagnosis

AVS was performed without adrenocorticotropic hormone stimulation in our hospital. The supplemental materials describe the examination and calculation methods.

Diagnostic Criteria

Adrenal micronodules were classified as surgically eligible (including unilateral micro-APA, bilateral micro-APA, and micro-UAH) or

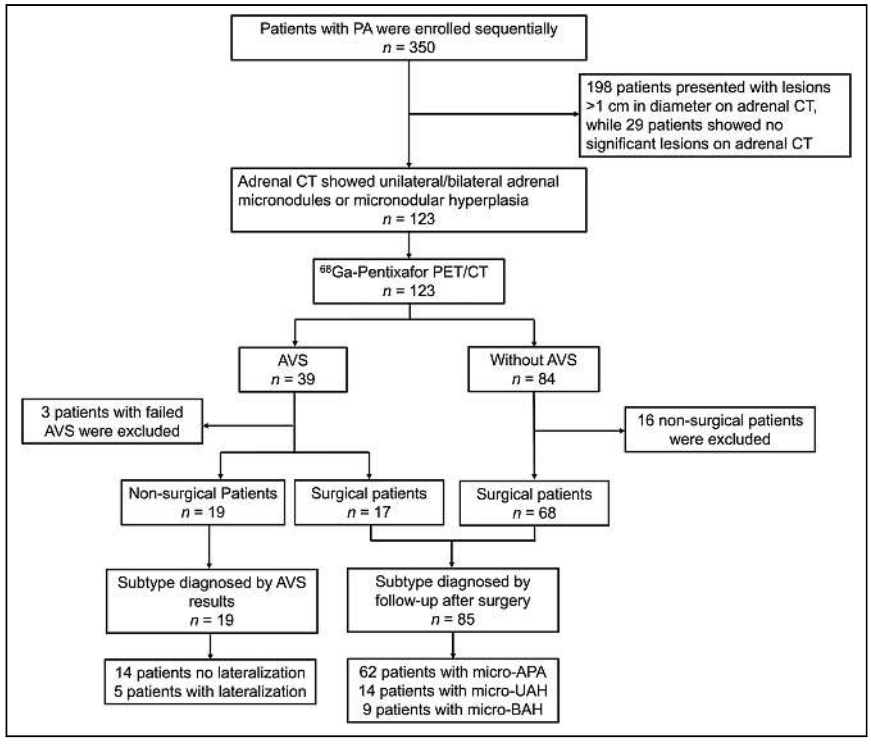

FIGURE 1. Flowchart of PA patients included in study. Because of impact of coronavirus disease 2019 pandemic, surgical treatment of 5 patients with lateralization in AVS had been postponed.

surgically ineligible (including nonfunctioning micronodule and micro-BAH) on the basis of surgical pathology and postoperative follow-up or AVS results. When a patient underwent both surgical treatment and AVS examination, especially when there was a discrepancy between the 2 results, the follow-up results were considered the gold standard for diagnosis. According to whether there were adrenal micronodules requiring surgical resection, the patients were divided into surgically eligible and surgically ineligible groups.

Statistical Analysis

All data were processed by SPSS Statistics 22.0 (IBM) and GraphPad Prism 9 statistical software. Quantitative values are expressed as mean ± SD. Categoric variables are presented as numbers and percentages. Differences between 2 different groups were compared using the independent *t* test or the Mann–Whitney *U* test. The *P* value among 3 different groups was calculated via 1-way ANOVA and χ^2 tests. Receiver-operating characteristic curves were constructed to determine the threshold of semiquantitative parameters of ^{68}Ga-pentixafor PET/CT for the diagnosis of surgically eligible microlesions. The 95% CIs for diagnostic performance measures were calculated using the Wilson score. A *P* value of less than 0.05 was considered statistically significant.

RESULTS

Clinical Characteristics of Included Patients

A total of 123 PA patients with adrenal micronodules underwent ^{68}Ga-pentixafor PET/CT. Nineteen patients were excluded for lacking a diagnostic basis (Fig. 1). Ultimately, 104 PA patients were included in the final analysis, of whom 82 were deemed surgically eligible and 22 surgically ineligible. Their clinical characteristics are in Table 1.

Inconsistent results between AVS and ^{68}Ga-pentixafor PET/CT led to treatment decisions grounded in providing the greatest likelihood of surgical cure for the patient (details can be found in the supplemental materials). Eighty-five patients finally underwent laparoscopic adrenalectomy, including 76 in the surgically eligible group (56 with unilateral micro-APA, 6 with bilateral micro-APA, and 14 with micro-UAH) and 9 in the surgically ineligible group (9 with micro-BAH). The preoperative and postoperative characteristics of these patients are in Supplemental Table 1.

Efficacy of ^{68}Ga-Pentixafor PET/CT Visual Analysis in Diagnosing Surgically Eligible PA Patients

The sensitivity, specificity, and accuracy of ^{68}Ga-pentixafor PET/CT in diagnosing surgically eligible patients (subtype diagnosis) were 90.2%, 86.3%, and 89.4%, respectively, for all 104 enrolled PA patients. The performance of PET/CT is shown in Figure 2. As for the 85 surgical patients, the diagnostic efficacy of PET/CT in subtyping was significantly higher than that of adrenal CT (Table 2, $P < 0.05$). Among the 17 surgical patients who underwent both AVS and PET/CT, the accuracy of AVS examination was lower than that of PET/CT, using postoperative efficacy as the standard (Table 2).

TABLE 1
Clinical Characteristics of Included 104 PA Patients with Adrenal Micronodules

Clinical characteristics	Total (n = 104)	Surgically eligible group (n = 82)	Surgically ineligible group (n = 22)	*P*
Age (y)	48.4 ± 9.9	48.5 ± 10.0	48.0 ± 9.7	0.84
Sex				<0.05
Male	57	38	19	
Female	47	44	3	
Body mass index (kg/m^2)	27.2 ± 5.4	26.2 ± 4.0	31.3 ± 7.6	<0.05
Hypertension	104 (100%)	82 (100%)	22 (100%)	1
Refractory hypertension	26 (25.0%)	17 (20.7%)	4 (44.4%)	0.54
Stage 1 hypertension	2 (1.9%)	1 (1.2%)	1 (4.5%)	0.24
Stage 2 hypertension	28 (26.9%)	25 (30.5%)	3 (13.6%)	
Stage 3 hypertension	74 (71.2%)	56 (68.3%)	18 (81.8%)	
Duration of hypertension (y)	8.1 ± 7.9	8.8 ± 7.1	11.9 ± 7.5	0.09
Systolic pressure (mm Hg)	179.8 ± 22.3	180.2 ± 22.7	178.5 ± 21.1	0.75
Diastolic pressure (mm Hg)	110.9 ± 14.3	110.5 ± 14.1	112.8 ± 15.3	0.50
Preoperative defined daily dose	2.7 ± 1.2	2.6 ± 1.1	3.2 ± 1.4	<0.05
Hypokalemia	69 (66.3%)	55 (67.1%)	14 (63.6%)	0.28
Duration of hypokalemia (y)	3.1 ± 3.0	2.9 ± 2.8	3.8 ± 3.1	0.22
Serum potassium (mmol/L)	3.0 ± 0.5	3.0 ± 0.6	3.0 ± 0.5	0.62
Aldosterone-to-renin ratio ([ng/dL]/[ng/mL/h])	131.0 ± 83.7	131.1 ± 83.0	130.6 ± 88.1	0.98
Serum aldosterone (ng/dL)	20.4 ± 5.7	20.4 ± 5.9	20.7 ± 5.2	0.82
Lesion located on right	36 (34.6%)	31 (37.8%)	5 (22.7%)	0.56
Lesion located on left	29 (27.9%)	25 (30.5%)	4 (18.2%)	
Lesion bilateral	39 (37.5%)	26 (31.7%)	13 (59.1%)	

Qualitative data are number; continuous data are mean and SD.

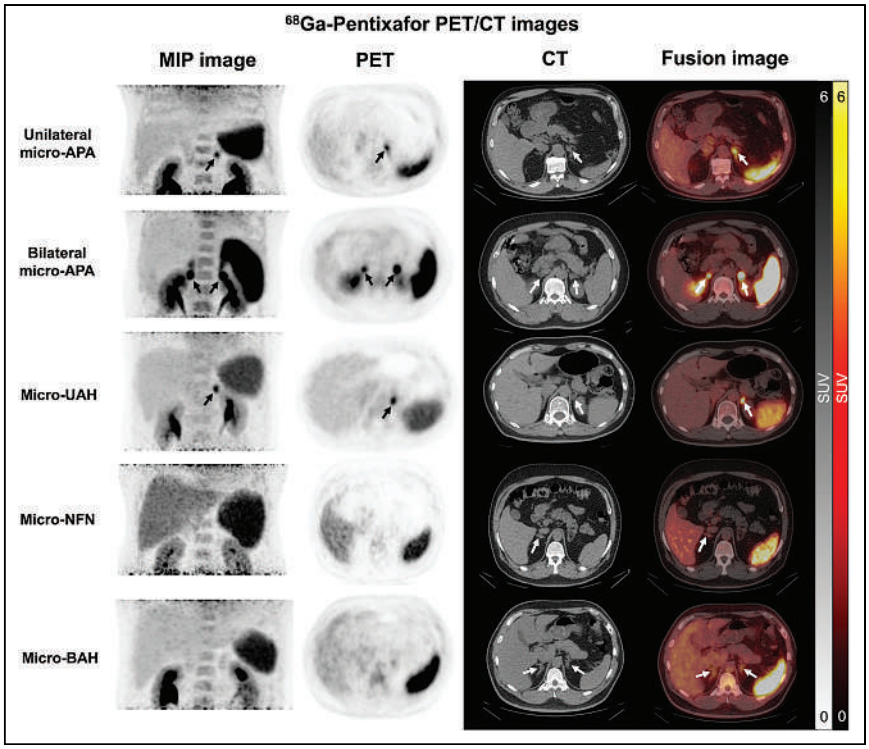

FIGURE 2. Performance of ^{68}Ga-pentixafor PET/CT in PA patients with different adrenal micronodules. MIP = maximum-intensity projection; NFN = nonfunctioning nodule.

Furthermore, ^{68}Ga-pentixafor PET/CT demonstrated better diagnostic performance than adrenal CT in both younger and older patients. In younger patients with unilateral single micronodules on adrenal CT, PET/CT also exhibited significantly higher diagnostic accuracy than adrenal CT (Supplemental Table 2). Additionally, adrenal CT displayed inferior diagnostic performance across various adrenal lesion morphologic groups, as shown in Supplemental Table 3. Examples of ^{68}Ga-pentixafor PET/CT in PA patients with bilateral adrenal micronodules are shown in Figure 3.

Patients with Adrenal Micronodules Who Underwent Both AVS and ^{68}Ga-Penxitafor PET/CT

A total of 36 patients successfully underwent both AVS and ^{68}Ga-pentixafor PET/CT, as shown in Table 3. The consistency rate was 66.7%, which was significantly higher ($P < 0.05$) than the concordance rate between AVS and adrenal CT (47.2%, Supplemental Table 4).

Subsequently, in these 36 patients, the ^{68}Ga-pentixafor SUV_{max} lateralization index values were 1.8 ± 0.7 for patients with unilateral AVS lateralization and 1.4 ± 0.5 for patients without AVS lateralization ($P = 0.06$). When the SUV_{max} lateralization index ratio was given a threshold of at least 1.35, using AVS as the gold standard, the sensitivity and specificity of PET/CT for lateralization were 70.6% and 68.4%, respectively (area under the curve, 0.74; $P < 0.05$).

Lesional Characteristics and Imaging Manifestations

There were 76 micro-APA lesions, 16 micro-UAH lesions, 51 micro-BAH lesions, and 40 nonfunctioning micronodule lesions among the 104 patients in this study. Micro-APA lesions had the highest ^{68}Ga-pentixafor SUV_{max}, LLR, and LAR, followed by micro-UAH, whereas micro-BAH and nonfunctioning micronodule had relatively lower uptake values (Table 4). In this study, pathologic results were obtained for 86 adrenal lesions; the uptake of ^{68}Ga-pentixafor in adenomas was significantly higher than

TABLE 2
Efficacy of ^{68}Ga-Pentixafor PET/CT Visual Analysis in Diagnosing Surgically Eligible PA Patients and Comparison with Adrenal CT and AVS in Patients with Pathology and Postoperative Follow-up

Modality	TP	TN	FP	FN	Sensitivity	Specificity	Accuracy	PPV	NPV
Both CT and PET/CT*									
Adrenal CT	55	6	7	17	76.4% (65.4%–84.7%)	46.2% (23.3%–70.9%)	71.8% (62.2%–81.3%)	88.7% (78.5%–94.4%)	26.1% (12.5%–46.5%)
PET/CT	70	8	1	6	92.1% (86.0%–98.2%)	88.9% (68.3%–100%)	91.8% (85.9%–97.6%)	98.6% (95.9%–100%)	57.1% (31.2%–83.1%)
Both AVS and PET/CT†									
AVS	10	2	2	3	76.9% (49.7%–91.8%)	50.0% (15.0%–85.0%)	70.6% (48.9%–92.2%)	83.3% (55.2%–95.3%)	40.0% (11.8%–77.0%)
PET/CT	11	3	1	2	84.6% (57.8%–95.7%)	75.0% (30.0%–95.4%)	82.4% (64.2%–100%)	91.7% (76.0%–100%)	60.0% (23.1%–88.2%)

*$n = 85$.
†$n = 17$.
TP = true-positive; TN = true-negative; FP = false-positive; FN = false-negative; PPV = positive prediction value; NPV = negative prediction value.
Data in parentheses are 95% CIs.

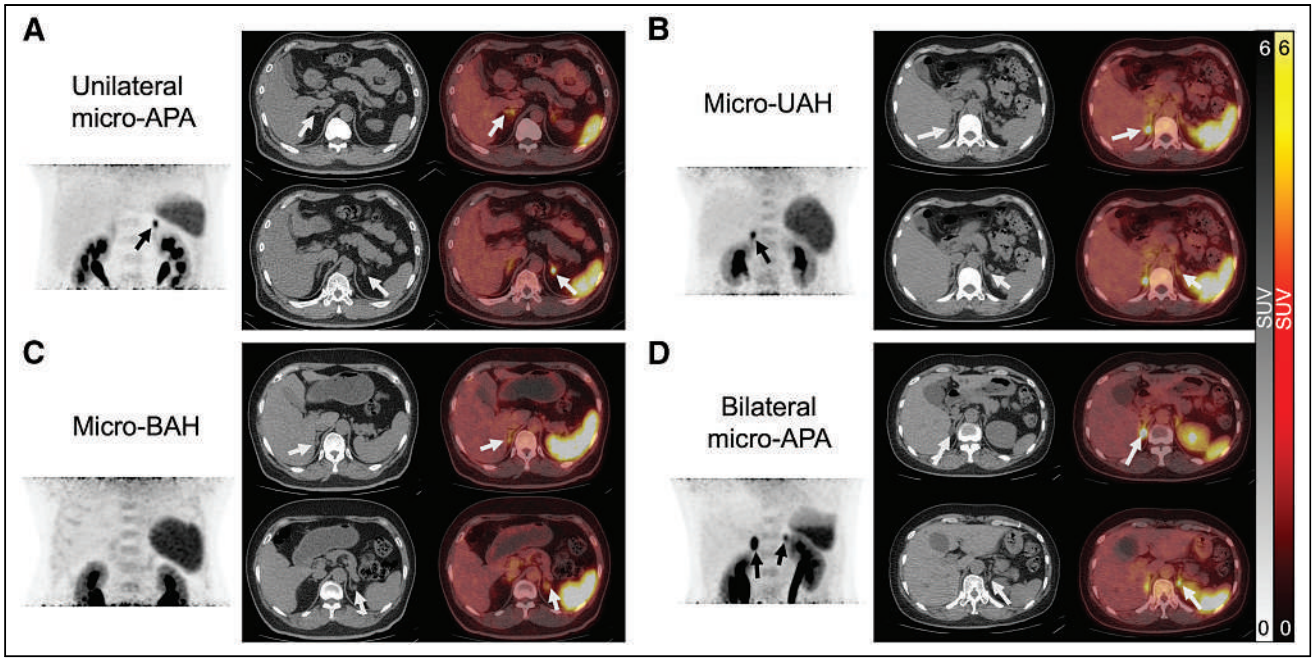

FIGURE 3. Performance of ^{68}Ga-pentixafor PET/CT in PA patients with bilateral microlesions on adrenal CT: unilateral micro-APA (A), micro-APA (B), micro-BAH (C), and bilateral micro-APA (D).

that in nodular hyperplastic lesions, and the difference was statistically significant (Supplemental Table 5).

Efficacy of ^{68}Ga-Pentixafor PET/CT for Differential Diagnosis of Micronodules

Ninety-two surgically eligible micronodules and 91 ineligible micronodules were identified. Visual analysis of ^{68}Ga-pentixafor PET/CT showed 97 positive and 86 negative micronodules. The thresholds for SUV_{max}, LLR, and LAR were 4.55, 2.17, and 1.90, respectively. The visual analysis had higher sensitivity, whereas the semiquantitative analysis had higher specificity (Table 5). Supplemental Figure 2 displays examples of surgically eligible microlesions that were positive on visual analysis but negative on semiquantitative analysis for ^{68}Ga-pentixafor PET/CT.

Relationship Between Surgical Outcome and ^{68}Ga-Pentixafor PET/CT Performance

Seventy-six surgical patients had biochemical results checked during postoperative follow-up. Among them, 63.5% achieved biochemical cure, 23.7% showed biochemical improvement, and 4.7% had absence of success (persistence). All achieved biochemical cure or improvement after the ^{68}Ga-pentixafor–positive micronodules were resected, with a cure rate of up to 80% (Supplemental Fig. 3). The adrenal micronodules had a higher ^{68}Ga-pentixafor SUV_{max}, LLR, and LAR in the patients with biochemical cure or improvement than in the persistence group (Fig. 4). Baseline clinical characteristics did not significantly differ among the 3 outcome groups (Supplemental Table 6).

In terms of clinical outcomes in the 85 surgical patients, 34 (40.0%) achieved clinical cure, 47 (55.3%) showed clinical improvement, and 4 (4.7%) had persistent clinical symptoms. All PA patients with positive adrenal micronodules on ^{68}Ga-pentixafor PET/CT achieved clinical cure or improvement after adrenalectomy, with a cure rate of 47.9%. The SUV_{max}, LLR, and LAR of the resected adrenal micronodules decreased progressively from the clinical cure group to the clinical improvement group to the clinical persistence group, with significant differences among the 3 groups (Fig. 4). Comparison of the baseline characteristics of patients with different clinical outcomes showed that female patients with a lower body mass index, shorter duration of

TABLE 3
Consistency Evaluation in Patients Undergoing Concurrent AVS and ^{68}Ga-Pentixafor PET/CT (n = 36)

	AVS					
^{68}Ga-pentixafor PET/CT	Left lateralization	Right lateralization	No lateralization	Total	κ	*P*
Left lateralization	6	0	2	8	0.45	<0.01
Right lateralization	1	4	3	8		
No lateralization	4	2	14	20		
Total	11	6	19	36		

Consistency index: (6 + 4 + 14)/36 = 66.7%. Inconsistency index: (1 + 4 + 2 + 2 + 3)/36 = 33.3%.

TABLE 4
Imaging Variables of 183 Adrenal Micronodules in All PA Patients

Variable	Micro-APA (n = 76)	Micro-UAH (n = 16)	Micro-BAH (n = 51)	Nonfunctioning micronodule (n = 40)	P
Size (cm)	0.9 ± 0.1	0.8 ± 0.1	0.8 ± 0.1	0.8 ± 0.1	0.23
SUV_{max}	8.4 ± 4.2	6.7 ± 2.3	3.9 ± 1.2	3.2 ± 0.8	<0.001
LLR	4.9 ± 3.0	4.0 ± 1.5	2.2 ± 0.7	1.8 ± 0.6	<0.001
LAR	3.5 ± 1.8	2.9 ± 1.0	1.5 ± 0.4	1.4 ± 0.5	<0.001

hypertension, nonrefractory hypertension, and lower dose of antihypertensive drugs before surgery were more likely to achieve clinical cure (Supplemental Table 7).

Correlation Between ^{68}Ga-Pentixafor PET/CT Uptake in Positive Lesions and Biochemical/Clinical Values in Surgical Patients

In further analyzing the correlation between PET/CT semiquantitative parameters and clinical indicators in 71 patients who underwent removal of PET-positive adrenal micronodules (Supplemental Table 8), we found that the greater the ^{68}Ga-pentixafor positivity in the adrenal micronodules, the greater was the decrease in postoperative systolic and diastolic blood pressure and postoperative defined daily dose and the greater was the degree of biochemical improvement and increase in blood potassium levels achieved through surgery.

DISCUSSION

The occurrence of adrenal micronodules in PA patients is common, with previous studies reporting that micro-APA lesions comprise approximately 13%–30% of all cases of APA (*12*). Because of the tendency to miss or misdiagnose these lesions using routine imaging examinations, the functional evaluation of adrenal micronodules has always been challenging in subtype classification of PA (*3*). There has been considerable interest in exploring noninvasive alternatives, particularly in the field of nuclear functional imaging. This study used ^{68}Ga-pentixafor PET/CT to subtype PA patients with adrenal micronodules and compare this modality with adrenal CT and AVS.

Adrenal CT is often recommended as the first step in the subtype classification of PA but can result in missed opportunities for adrenalectomy in some patients and unnecessary surgery in others (*13*). In the present study, ^{68}Ga-pentixafor PET/CT improved subtype diagnostic efficacy in PA patients with adrenal micronodules compared with adrenal CT and yielded consistent results in different CT morphologic subgroups. In addition, our study suggested that visual assessment of ^{68}Ga-pentixafor PET/CT images may be sufficient because of the highly specific uptake in functional adrenal micronodules. The fact that semiquantitative analysis of ^{68}Ga-pentixafor PET data had no significant impact on diagnostic

TABLE 5
Diagnostic Performance of ^{68}Ga-Pentixafor PET/CT to Distinguish Surgically Eligible and Ineligible Micronodules

Parameter	Eligible (n = 92)	Ineligible (n = 91)	Sensitivity	Specificity	Accuracy	Area under curve
Visual analysis						
Avid lesions (n = 97)	83	14	90.2% (84.1%–96.3%)	84.6% (77.2%–92.0%)	87.4% (82.6%–92.2%)	—
Nonavid lesions (n = 86)	9	77				
Semiquantitative analysis						
SUV_{max}						
≥4.55 (n = 92)	78	14	84.8% (77.4%–92.1%)	84.6% (77.2%–92.0%)	84.7% (79.4%–89.9%)	0.91 (0.87–0.95)
<4.55 (n = 91)	14	77				
LLR						
≥2.17 (n = 80)	70	10	76.1% (67.3%–84.8%)	89.0% (82.6%–95.4%)	82.5% (77.0%–88.0%)	0.88 (0.83–0.93)
<2.17 (n = 103)	22	81				
LAR						
≥1.90 (n = 87)	78	9	84.8% (77.4%–92.1%)	90.1% (84.0%–96.2%)	87.4% (82.6%–92.2%)	0.91 (0.86–0.95)
<1.90 (n = 96)	14	82				

Data in parentheses are 95% CIs.

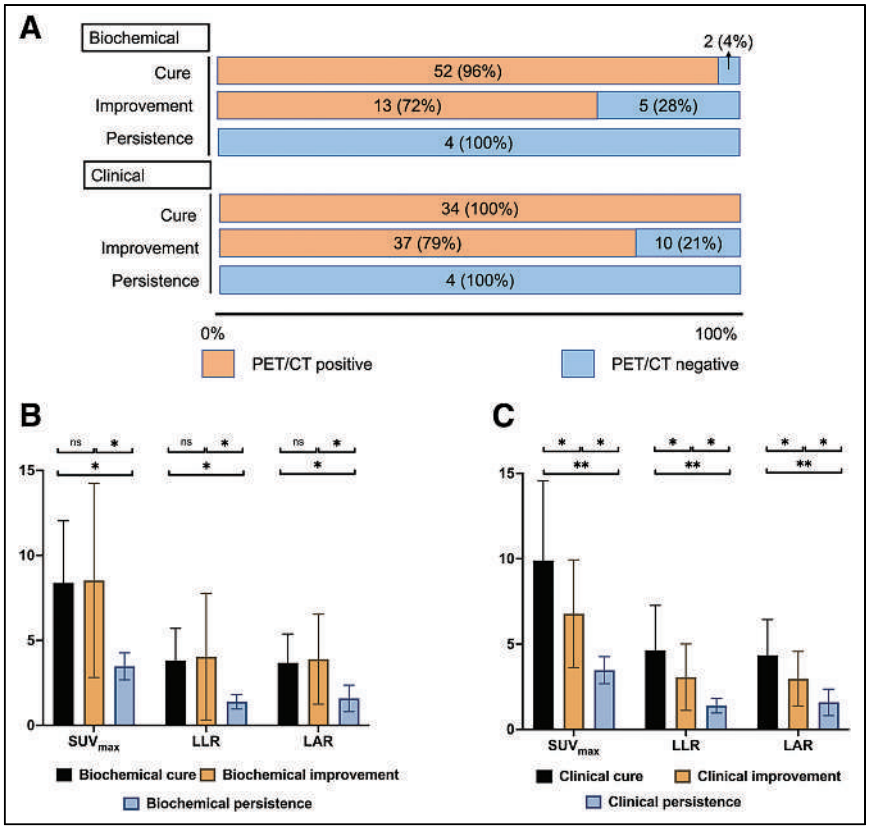

FIGURE 4. (A) Highest proportion of patients with ^{68}Ga-pentixafor PET/CT–positive adrenal microlesions was observed in biochemical/clinical cure group, followed by biochemical/clinical improvement group, whereas all patients in biochemical/clinical persistence group had negative PET/CT imaging results. (B) Patients in biochemical cure/improvement group had significantly higher ^{68}Ga-pentixafor uptake values than those in biochemical persistence group. (C) Values of SUV_{max}, LLR, and LAR of removed adrenal micronodules decreased gradually from group of patients with clinical cure to those with clinical improvement and finally to those with clinical persistence. ns = not statistically significant. $^{*}P < 0.05$. $^{**}P < 0.01$.

performance could be attributed to the variability in uptake across micro-APAs and the inherent limitations of such an analysis due to patient-specific, technical, and methodologic factors.

The incidence of nonfunctional adrenal adenoma decreases in individuals under 40 y old (*14*). Guidelines suggest that PA patients under 35 y old with unilateral adrenal nodules detected on adrenal CT may consider surgery without AVS (*15*). However, our study found that relying solely on adrenal CT results for subtyping diagnosis in such patients remains inaccurate and that surgery may be recommended directly only when ^{68}Ga-pentixafor–positive adrenal nodules are present.

A clinical study (*16*) comparing the diagnostic performance of ^{68}Ga-pentixafor PET/CT and AVS in the subtyping of 100 PA patients found a diagnostic consistency rate of 90%. However, adrenal micronodules were not analyzed further, and diagnoses were not confirmed on the basis of postsurgical follow-up. However, the consistency rate in our study was lower than in the aforementioned study, potentially because of inclusion of only patients with microlesions. Our study suggested that the results of ^{68}Ga-pentixafor PET/CT may be more consistent with postoperative efficacy than is AVS. Nevertheless, further research is necessary to substantiate these preliminary findings.

There have been studies indicating that the level of CYP11B2 is higher in micro-APA than in macro-APA (*12*). Considering the positive correlation between the expression level of CXCR4 and CYP11B2, the expression density of CXCR4 should theoretically be higher in micro-APA than in macro-APA. Nevertheless, on comparing our team's previous research (*17*), we found that the uptake of ^{68}Ga-pentixafor PET/CT is higher in macro-APA than in micro-APA (SUV_{max}, 15.3 ± 7.7 (*17*) vs. 8.4 ± 4.2). We suspect that this difference may be attributed to the limited spatial resolution of ^{68}Ga-pentixafor PET/CT. With smaller lesion volumes, partial-volume effects may be more prominent, leading to lower measured SUVs than the actual values. The smallest micro-APA lesion that could be identified in this study had a diameter of 0.6 cm. In future research, it could be beneficial to explore the potential of other technologies, such as ^{68}Ga-pentixafor PET/MRI, or more specific radiotracers in assessing uptake in small adrenal lesions.

In our study, all patients whose ^{68}Ga-pentixafor–positive microlesions were removed achieved complete or partial biochemical/clinical success postoperatively. Higher uptake of ^{68}Ga-pentixafor in the removed microlesions was associated with better surgical outcomes. We also found that female patients with a lower body mass index, shorter duration of hypertension, nonrefractory hypertension, and less antihypertensive drug use before surgery had a higher probability of achieving clinical cure after surgery, as is consistent with previous literature (*12*).

There were some limitations in this study. Because our institution did not routinely perform CYP11B2 staining on PA lesions, the latest international consensus statement on the histopathologic diagnostics of adrenal tumors and hyperplasia published by the International Endocrine Society (*18*) was not applied. Our single-center study design inherently has certain biases. Additionally, although the adrenal micronodules in our study were detectable on adrenal CT, some microadenomas might have been missed. Moreover, few patients underwent both ^{68}Ga-pentixafor PET/CT and AVS, causing potential bias. Importantly, the decision-making process in our study—to forego the established reference method, AVS, on the basis of the ^{68}Ga-pentixafor PET/CT results in certain scenarios—highlights a potential limitation. Thus, we underline the need for larger, multicenter studies to further validate the efficacy and reliability of ^{68}Ga-pentixafor PET/CT in comparison with AVS.

CONCLUSION

Our findings suggest that ^{68}Ga-pentixafor PET/CT holds promise in outperforming adrenal CT for classifying different morphologic subtypes of PA patients with adrenal micronodules. Moreover, this technique seems to offer improved consistency in predicting postoperative efficacy in PA patients compared with AVS examination. However, larger controlled clinical trials are

necessary to confirm this observation. The level of ^{68}Ga-pentixafor uptake in adrenal micronodules appears to be a valuable guide for recommending appropriate surgical treatments for PA patients, thereby facilitating the implementation of personalized management strategies.

DISCLOSURE

This work was sponsored in part by the National Natural Science Foundation of China (grant 82071967), the National Key Research and Development Program of China (grant 2020YFC2002702), the Tsinghua University–Peking Union Medical College Hospital Initiative Scientific Research Program (grant 52300300519), and the National Natural Science Foundation of China (grant 81770427). No other potential conflict of interest relevant to this article was reported.

KEY POINTS

QUESTION: How well does ^{68}Ga-pentixafor PET/CT perform in subtype diagnosis of PA patients with adrenal micronodules less than 1 cm in diameter, and how does ^{68}Ga-pentixafor PET/CT compare with standard diagnostic methods such as adrenal CT and AVS?

PERTINENT FINDINGS: ^{68}Ga-pentixafor PET/CT showed superior sensitivity, specificity, and accuracy in identifying surgically eligible PA patients compared with adrenal CT. It was also more concordant with surgical outcomes than AVS.

IMPLICATIONS FOR PATIENT CARE: This study showed that a new imaging technique, ^{68}Ga-pentixafor PET/CT, can accurately classify adrenal micronodules in PA patients, helping doctors make better treatment decisions and predict treatment outcomes.

REFERENCES

1. Rossi GP, Bernini G, Caliumi C, et al. A prospective study of the prevalence of primary aldosteronism in 1,125 hypertensive patients. *J Am Coll Cardiol.* 2006;48:2293–2300.
2. Reincke M, Bancos I, Mulatero P, Scholl UI, Stowasser M, Williams TA. Diagnosis and treatment of primary aldosteronism. *Lancet Diabetes Endocrinol.* 2021;9:876–892.
3. Rossi GP. Primary aldosteronism: JACC state-of-the-art review. *J Am Coll Cardiol.* 2019;74:2799–2811.
4. Funder JW, Carey RM, Mantero F, et al. The management of primary aldosteronism: case detection, diagnosis, and treatment: an Endocrine Society clinical practice guideline. *J Clin Endocrinol Metab.* 2016;101:1889–1916.
5. Young WF, Stanson AW, Thompson GB, Grant CS, Farley DR, van Heerden JA. Role for adrenal venous sampling in primary aldosteronism. *Surgery.* 2004;136:1227–1235.
6. Mulatero P, Bertello C, Sukor N, et al. Impact of different diagnostic criteria during adrenal vein sampling on reproducibility of subtype diagnosis in patients with primary aldosteronism. *Hypertension.* 2010;55:667–673.
7. Yen RF, Wu VC, Liu KL, et al. ^{131}I-6β-iodomethyl-19-norcholesterol SPECT/CT for primary aldosteronism patients with inconclusive adrenal venous sampling and CT results. *J Nucl Med.* 2009;50:1631–1637.
8. Heinze B, Fuss CT, Mulatero P, et al. Targeting CXCR4 (CXC chemokine receptor type 4) for molecular imaging of aldosterone-producing adenoma. *Hypertension.* 2018;71:317–325.
9. Gao Y, Ding J, Cui Y, et al. Functional nodules in primary aldosteronism: identification of CXCR4 expression with ^{68}Ga-pentixafor PET/CT. *Eur Radiol.* 2023;33:996–1003.
10. Ding J, Zhang Y, Wen J, et al. Imaging CXCR4 expression in patients with suspected primary hyperaldosteronism. *Eur J Nucl Med Mol Imaging.* 2020;47:2656–2665.
11. Williams TA, Lenders JWM, Mulatero P, et al. Outcomes after adrenalectomy for unilateral primary aldosteronism: an international consensus on outcome measures and analysis of remission rates in an international cohort. *Lancet Diabetes Endocrinol.* 2017;5:689–699.
12. Omura M, Sasano H, Saito J, Yamaguchi K, Kakuta Y, Nishikawa T. Clinical characteristics of aldosterone-producing microadenoma, macroadenoma, and idiopathic hyperaldosteronism in 93 patients with primary aldosteronism. *Hypertens Res.* 2006;29:883–889.
13. Sam D, Kline GA, So B, Leung AA. Discordance between imaging and adrenal vein sampling in primary aldosteronism irrespective of interpretation criteria. *J Clin Endocrinol Metab.* 2019;104:1900–1906.
14. Fassnacht M, Arlt W, Bancos I, et al. Management of adrenal incidentalomas: European Society of Endocrinology clinical practice guideline in collaboration with the European Network for the Study of Adrenal Tumors. *Eur J Endocrinol.* 2016;175:G1–G34.
15. Rossi GP, Auchus RJ, Brown M, et al. An expert consensus statement on use of adrenal vein sampling for the subtyping of primary aldosteronism. *Hypertension.* 2014;63:151–160.
16. Hu J, Xu T, Shen H, et al. Accuracy of gallium-68 pentixafor positron emission tomography-computed tomography for subtyping diagnosis of primary aldosteronism. *JAMA Netw Open.* 2023;6:e2255609.
17. Ding J, Tong A, Zhang Y, et al. Functional characterization of adrenocortical masses in nononcologic patients using ^{68}Ga-pentixafor. *J Nucl Med.* 2022;63:368–375.
18. Williams TA, Gomez-Sanchez CE, Rainey WE, et al. International histopathology consensus for unilateral primary aldosteronism. *J Clin Endocrinol Metab.* 2021;106:42–54.

Quality Assurance Considerations in Radiopharmaceutical Therapy Dosimetry Using PLANETDose: An International Atomic Energy Agency Study

Gunjan Kayal*[1,2], Nathaly Barbosa*[3], Carlos Calderón Marín[4], Ludovic Ferrer[5,6], José-Alejandro Fragoso-Negrín[7,8], Darko Grosev[9], Santosh Kumar Gupta[10], Nur Rahmah Hidayati[11], Tumelo C.G. Moalosi[12], Gian Luca Poli[13], Parul Thakral[14], Virginia Tsapaki[15], Sébastien Vauclin[7], Alex Vergara-Gil[1], Peter Knoll[15], Robert F. Hobbs†[16], and Manuel Bardiès†[8,17]

[1]*CRCT, UMR 1037, INSERM, Université Toulouse III Paul Sabatier, Toulouse, France;* [2]*SCK CEN, Belgian Nuclear Research Centre, Mol, Belgium;* [3]*Instituto Nacional de Cancerología, Bogotá, Colombia;* [4]*Instituto de Oncología y Radiobiología, Havana, Cuba;* [5]*Medical Physics Department, ICO René Gauducheau, Nantes, France;* [6]*CRCINA, UMR 1232, INSERM, France;* [7]*DOSIsoft SA, Cachan, France;* [8]*IRCM, UMR 1194 INSERM, Universite de Montpellier and Institut Regional du Cancer de Montpellier, Montpellier, France;* [9]*Department of Nuclear Medicine and Radiation Protection, University Hospital Centre Zagreb, Zagreb, Croatia;* [10]*Department of Nuclear Medicine and PET, Mahamana Pandit Madanmohan Malviya Cancer Centre and Homi Bhabha Cancer Centre, Varanasi, India;* [11]*Research Center and Technology for Radiation Safety and Metrology–National Research and Innovation Agency, Jakarta, Indonesia;* [12]*Department of Medical Imaging and Clinical Oncology, Medical Physics, Nuclear Medicine Division, Faculty of Medicine and Health Science, Stellenbosch University, Tygerberg Hospital, Cape Town, South Africa;* [13]*Department of Medical Physics, ASST Papa Giovanni XXIII, Bergamo, Italy;* [14]*Department of Nuclear Medicine, Fortis Memorial Research Institute, Gurugram, India;* [15]*Dosimetry and Medical Radiation Physics, International Atomic Energy Agency, Vienna, Austria;* [16]*Johns Hopkins Medical Institute, Baltimore, Maryland; and* [17]*Département de Médecine Nucléaire, Institut Régional du Cancer de Montpellier, Montpellier, France*

Implementation of radiopharmaceutical therapy dosimetry varies depending on the clinical application, dosimetry protocol, software, and ultimately the operator. Assessing clinical dosimetry accuracy and precision is therefore a challenging task. This work emphasizes some pitfalls encountered during a structured analysis, performed on a single-patient dataset consisting of SPECT/CT images by various participants using a standard protocol and clinically approved commercial software. **Methods:** The clinical dataset consisted of the dosimetric study of a patient administered with [^{177}Lu]Lu-DOTATATE at Tygerberg Hospital, South Africa, as a part of International Atomic Energy Agency–coordinated research project E23005. SPECT/CT images were acquired at 5 time points postinjection. Patient and calibration images were reconstructed on a workstation, and a calibration factor of 122.6 Bq/count was derived independently and provided to the participants. A standard dosimetric protocol was defined, and PLANETDose (version 3.1.1) software was installed at 9 centers to perform the dosimetry of 3 treatment cycles. The protocol included rigid image registration, segmentation (semimanual for organs, activity threshold for tumors), and dose voxel kernel convolution of activity followed by absorbed dose (AD) rate integration to obtain the ADs. Iterations of the protocol were performed by participants individually and within collective training, the results of which were analyzed for dosimetric variability, as well as for quality assurance and error analysis. Intermediary checkpoints were developed to understand possible sources of variation and to differentiate user error from legitimate user variability. **Results:** Initial dosimetric results for organs (liver and kidneys) and lesions showed considerable interoperator variability. Not only was the generation of intermediate checkpoints such as total counts, volumes, and activity required, but also activity-to-count ratio, activity concentration, and AD rate-to-activity concentration ratio to determine the source of variability. **Conclusion:** When the same patient dataset was analyzed using the same dosimetry procedure and software, significant disparities were observed in the results despite multiple sessions of training and feedback. Variations due to human error could be minimized or avoided by performing intensive training sessions, establishing intermediate checkpoints, conducting sanity checks, and cross-validating results across physicists or with standardized datasets. This finding promotes the development of quality assurance in clinical dosimetry.

Key Words: clinical dosimetry; SPECT/CT; quality assurance; PLANETDose; variability assessment

J Nucl Med 2024; 65:125–131
DOI: 10.2967/jnumed.122.265340

Radiopharmaceutical therapy (RPT) is based on the administration of radiolabeled vectors designed to concentrate cytotoxic levels of radiation in targets while preserving the surrounding healthy tissues. In comparison to external-beam radiation therapy, which involves personalized treatment regimens, most RPT administers a fixed activity. For example, the European Medicines Agency and the Food and Drug Administration approved [^{177}Lu]Lu-DOTATATE (Lutathera; Novartis) for treatment of neuroendocrine tumors as four 7.4-GBq injections separated by 8-wk intervals (*1,2*).

A patient-specific treatment approach would allow a major paradigm shift from the one-size-fits-all approach to personalized medicine in which the optimal activity is specifically assessed for each patient. In article 56 (Optimization) (*3*), Euratom Directive 2013/59

Received Jan. 17, 2023; revision accepted Jul. 25, 2023.
For correspondence or reprints, contact Manuel Bardiès (manuel.bardies@inserm.fr).
*Contributed equally to this work.
†Contributed equally to this work.
Published online Oct. 26, 2023.

(applicable within the European Union) requests that "For all medical exposure of patients for radiotherapeutic purposes, exposures of target volumes shall be individually planned, and their delivery appropriately verified taking into account that doses to non-target volumes and tissues shall be as low as reasonably achievable and consistent with the intended radiotherapeutic purpose of the exposure." Even though personalized planning cannot be achieved with fixed activities, the verification of irradiation delivered can always be assessed. Also, several authors (*4–7*) have advocated the feasibility of patient-specific RPT dosimetry. Evidence of the absorbed dose (AD)–effect relationship has been published in several clinical indications (*8–11*).

The clinical dosimetry workflow consists of several steps, from radiopharmaceutical pharmacokinetics determination in the volumes of interest (VOIs), most often through sequential quantitative imaging, to AD or other standardized dosimetry quantity computation, such as biologic effective dose or equieffective dose (*12*). Currently, RPT dosimetry either is not widely implemented in clinical facilities (*13–15*) or, if implemented, may differ in objectives and sophistication among centers, thereby resulting in a large variability of dosimetric approaches and results (*16*).

However, there are 2 facets of variability. Clinical choices that govern dosimetric approaches induce natural variability and should not preclude the use of personalized dosimetry. More concerning is the potential variability of results for a given clinical application, due to different methodologies or even to general lack of expertise. It is therefore desirable to be able to compare results obtained in different clinical centers for a given therapeutic approach.

The Society of Nuclear Medicine and Molecular Imaging presented the preliminary results of a study aiming to standardize and harmonize dosimetry procedures by assessing the variability introduced in various dosimetry steps. The study revealed large differences in time-integrated activity (TIA) and in ADs. The participants in this study chose their own methodologies for VOI delineation, TIA integration, TIA dosimetry, and reported volumes, TIA, AD rates (ADRs), and AD; however, neither the sources of variation nor the origins of the outliers were obvious (*17*). Subsequent detailed analysis (*18*) demonstrated that there were transcription, methodologic, and reporting errors and differences in methods and decisions that contributed substantially to the large variations. In this analysis (*18*) for pure SPECT data, removing variabilities due to errors resulted in quartile coefficients of dispersion of 10%–30% in the organs and 10%–40% in the lesions for the 2 patients used in the study. Variabilities were further reduced when participants were given VOIs or TIAs.

In 2017, the International Atomic Energy Agency initiated coordinated research project (CRP) E2.30.05, "Dosimetry in Radiopharmaceutical Therapy for Personalized Patient Treatment," to educate and train volunteer medical physicists and implement harmonized dosimetric procedures, along with assessing the global accuracy of RPT dosimetry. This was done by conducting multiple training sessions and iterations using a clinical SPECT/CT patient dataset.

Consequently, the ground truth activity and ADs of the dataset are not known and the study cannot assess for accuracy. The goal of this work is to assess variability or precision of results and to identify and eliminate methodologic errors that increase variability as part of an overall educational goal.

MATERIALS AND METHODS

Participants

The participating institutions were from Colombia, Croatia, Cuba, France, India, Indonesia, South Africa, and the United States. Each performed dosimetry with its respective expertise and the specific training acquired throughout this work. The selection of institutions was based on International Atomic Energy Agency reviews of proposals to join the CRP, except for the United States and France, whose participation was based on their substantial experience in this field.

Clinical Dataset

The clinical dataset was derived from the dosimetric study of a [^{177}Lu]Lu-DOTATATE patient from Tygerberg Hospital, South Africa. Activities of 6.24, 6.67, 6.85, and 6.03 GBq were administered in a first, second, third, and fourth therapy cycle, respectively, with an interval of 11 wk between cycles. Patient SPECT/CT images were acquired at 5 time points after injection (1–2, 4, 24, 48, and 96 h) on a GE Healthcare Infinia Hawkeye 4 (9.5-mm [$^3/_8$-in] NaI crystal thickness and medium-energy collimator) with calibration images and reconstructed on a Hermes Medical Solutions (version 4.15) workstation. A calibration phantom was imaged using the same acquisition and reconstruction settings. All parameters were specified by Kayal et al. (*19*). A calibration factor of 122.6 Bq/count (or 4.53 cps/MBq with 1,800 s of acquisition time) was obtained and provided to each center.

Definition of Standard Protocol

A standard dosimetric protocol was defined, and PLANETDose (version 3.1.1) from DOSIsoft SA was used for the first 3 therapy cycles. The fourth cycle was not examined because there was no adequate SPECT/CT imaging. Since reconstructed patient images were circulated to each center, the common dosimetry protocol was defined beginning at the registration step. All steps of the protocol were followed by all participants independently on their workstations.

Registration and Segmentation. Automatic rigid registration for all time points was performed by each site considering the first CT scan as the reference. The segmented VOIs included lesions (anterior, lateral, posterior, and inferior) along with both kidneys and whole and healthy liver. Each participating center contoured the normal organs (kidneys and liver) semimanually on the first CT scan with an interpolation process and then propagated in a rigid way through all registered CT scans while performing lesion segmentation on SPECT images at each time point using a 40% threshold of the maximal uptake. Afterward, a 4-dimensional exclusion Boolean operation between the anatomic liver (or whole liver) and the 4 lesions gave the contour of normal liver.

ADR and AD. ADRs were obtained for each VOI and cycle using the dose voxel kernel convolution algorithm with density correction within PLANETDose. ADs were obtained by integrating ADR over time. Each participant selected a fit among mono-, bi-, or triexponential fitting or trapezoidal fitting, on the basis of the participant's expertise. The fit functions and parameters used by each participant can be provided on request.

Data Exportation. For each VOI, the volume, total counts, and activity per time point were exported. The values for normal organs and lesions were taken from the anatomic and functional contouring result tables, respectively (PLANETDose uses a dual anatomic/functional mode system). The fitting parameters (fitting equation and R^2) along with the ADs in each VOI were generated and stored.

Statistics

To quantify the variations among participants, the mean and median along with the associated uncertainties were computed using previously published equations (*20*). The *t*-test was performed to examine the significance of the difference between the fitting techniques used among participants ($P \leq 0.05$) (*21,22*).

Optimization Procedure

The CRP project aimed to contribute to the standardization of RPT dosimetry and help participants develop and implement harmonized dosimetric procedures.

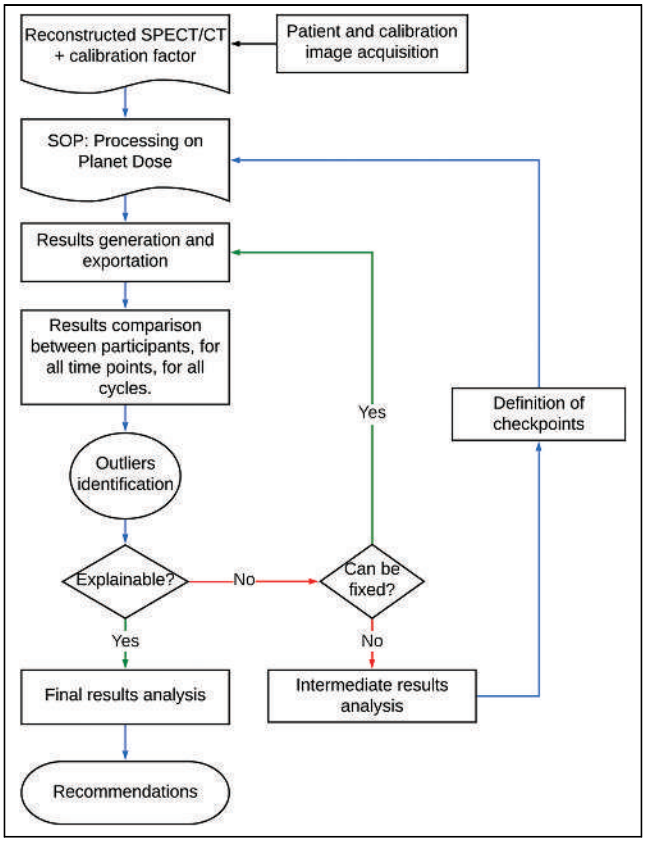

FIGURE 1. Workflow used for analyzing data and computing final results and recommendations. SOP = standard operating procedure.

During each brainstorming session, the results were discussed, and further training was provided to the participants, resulting in an iteration of the dosimetry calculations. The number of iterations for the first, second, and third therapy cycles was 1–4, 2–3, and 4 or more, respectively. Even though the results for each center were not available to all, the procedure was not a masked intercomparison but rather evolved to an elaborate training procedure, with the objective of ensuring proper dosimetric understanding and application while allowing for limited individual choices in registration, contouring, and integration.

The identification of outlier results led participants to evaluate the integrity of their results as shown in Figure 1. Other variations observed consistently throughout the data necessitated the inclusion of additional quality assurance (QA) metrics (or checkpoints) in the dosimetric procedure with subsequent iterations of results. The results presented here are therefore the best that could be obtained within the time frame of the CRP, after extensive training and iterations.

RESULTS

Results were obtained for each time point and VOI for the first 3 cycles. In this section, the salient results are highlighted as coefficients of variation of the median (CV_{med}) among participants (ratio of median uncertainty to median); however, all results are available in Supplemental Tables 1 and 2 and Supplemental Figures 1–8 (supplemental materials are available at http://jnm.snmjournals.org).

Activity Quantification

Volume Segmentation. The liver and the kidneys along with the 4 lesions defined in the patient SPECT/CT images are shown in Figure 2 for the first cycle.

The volumes obtained by the 9 centers (C1–C9) for each VOI for the first cycle are plotted in Figure 3. The CV_{med} among time points and cycles ranged from 6% to 13% for normal organs and from 3% to 20% for lesions, with the smallest lesions exhibiting the largest variability. The variations in normal-organ volumes as a function of time at each center constitute evidence of error according to the propagation process defined in the protocol, since the volume—once defined on the first time point—is propagated to the other time points. Similarly, variations of the lesion volumes between time points may be expected, and each center, in principle, should have the same volume at each time point because the lesion volumes were defined using a predefined threshold (40% of maximum activity uptake relative to each time point). The range of volumes (along with the uncertainties) obtained by various participants for each VOI and each cycle is specified in Supplemental Table 1.

Derivation of Counts and Activity. The total counts and activity in normal organs (kidneys, normal liver, and whole liver) and lesions are illustrated in Figures 4A and 4B for the third cycle. Counts and activities within each VOI tend to follow a similar trend for most time intervals and participants, although they are not identical as would be anticipated.

The whole liver demonstrated a significantly lower CV_{med} in volume and activity (~5% and 3%–5%, respectively) at each time point and cycle analyzed. The lateral lesion had the widest range in volume (8%–59%) and activity (10%–49%). The other smaller lesions had a relatively lower activity (CV_{med}, 2%–15%) comparable to that in the kidneys.

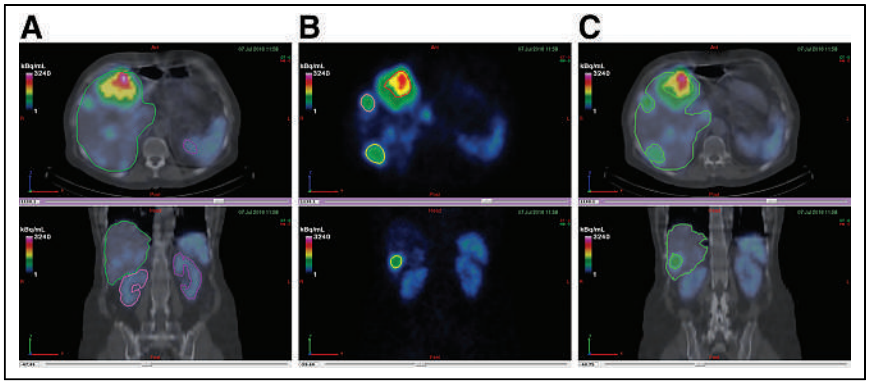

FIGURE 2. (A) Anatomic segmentation (for whole liver and kidneys). (B) Functional segmentation for lesions. (C) Normal liver from Boolean subtraction.

Outlier data are discernible. The counts and the activity for the lateral lesion were significantly higher at C6 than at the other centers (Fig. 4A) and can be attributed to this center's larger lesion segmentation. In parallel, a significant activity decrease was seen in the lesions and the normal liver for the first time point for C8. A common trend in counts and activity was not systematically observed, thereby necessitating the generation of a new checkpoint activity-to-count ratio (Fig. 4C). The activity fluctuation for C8 might be attributed to incorrect calibration factor input or a software flaw linked with a particular time point, but these possibilities require further investigation.

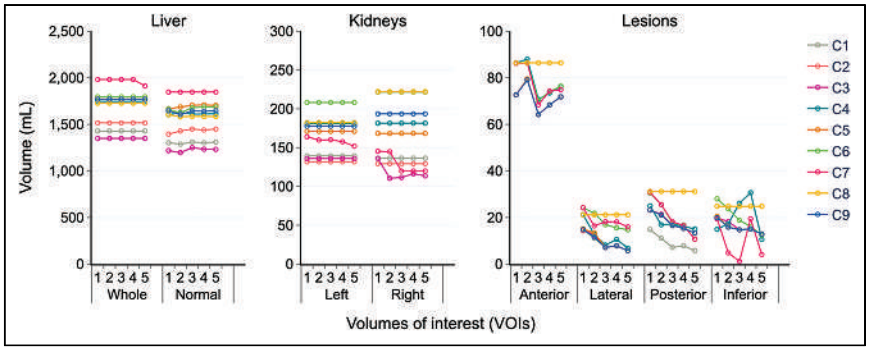

FIGURE 3. Organ and lesion volumes in first treatment cycle for 5 time points (1–5). Whole liver signifies anatomic liver, whereas normal liver represents healthy liver (whole liver − 4 lesions).

ADRs

Notable anomalies were observed for the third cycle (Fig. 5A). Except for results from C6, the ADR for time points for each organ was reasonably consistent between time points and participants. Unexpected ADR variability in lesions among participants initiated the generation of additional checkpoints: activity concentration (AC) and ADR-to-AC ratio. Since ADR is proportional to AC (for self-dose contributions to the AD dominating in regions of high uptake), it was hypothesized that the ADR-to-AC ratio would be relatively constant for each VOI.

Figure 5B shows the AC at each time point for the third cycle. All centers, including C6, had a fairly consistent AC for the liver and kidneys. Consequently, the ADR deviation of C6 in the liver and kidneys (6%–73%) cannot be directly related to volume segmentation or activity quantification but was most likely due to a transcriptional error. Additionally, the calculation of AC revealed that C8 likely overlooked some systematic error at the first time point.

The ADR-to-AC ratio (Fig. 5C) had nearly constant values (despite the presence of a few outliers) for the organs but not necessarily for the lesions. Because of the incoherent ADR and AC of C6, its ADR-to-AC ratio varied significantly. Variability in this ratio for lesions at the first time point for C8 is a consequence of error propagation from the activity quantification. Other variations were ascribed to transcriptional error.

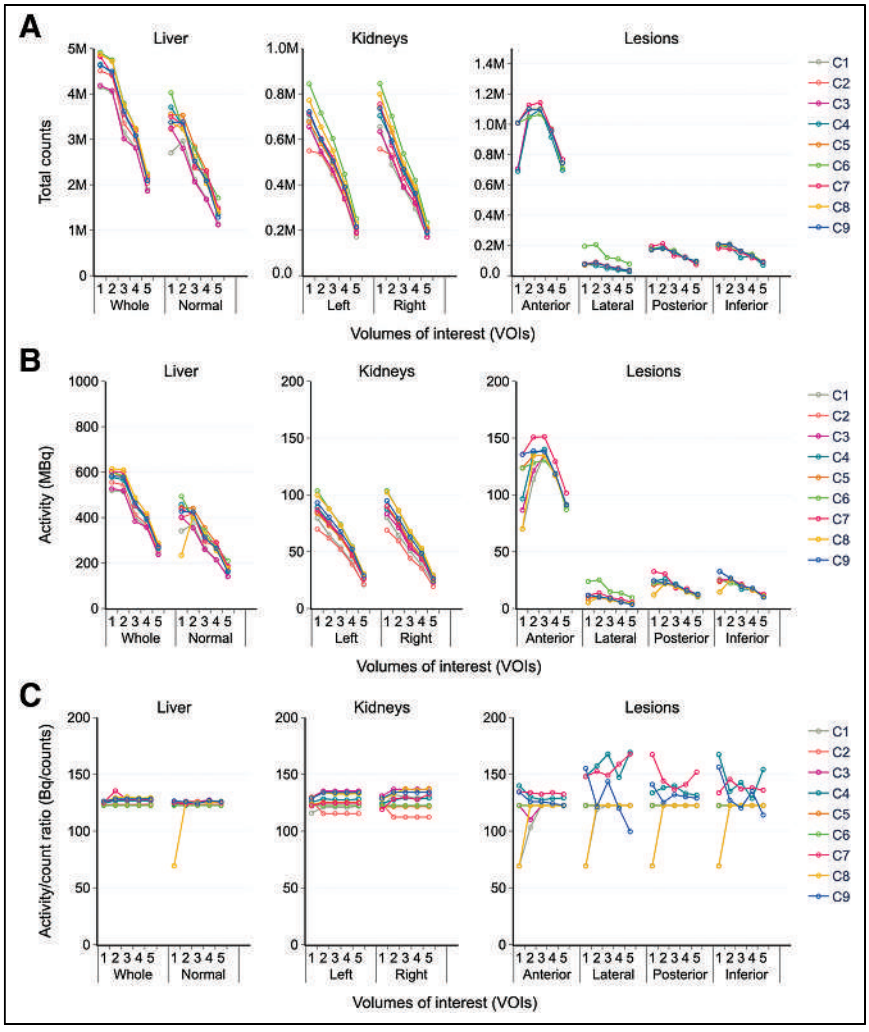

FIGURE 4. Total counts (A), activity (B), and activity-to-count ratio (C) for each VOI in third cycle for time points 1–5. Whole liver signifies anatomic liver, whereas normal liver represents healthy liver (whole liver − 4 lesions).

AD Calculations

The ADRs were integrated using either monoexponential (corresponding to washout or decay curve) or biexponential (including one uptake and one washout phase) fitting models to obtain the ADs in each VOI. The fits chosen by centers for different VOIs are presented in Table 1. ADs for the first cycle are plotted in Figure 6. Low ADs (2–4 Gy) were obtained for the liver and kidneys, whereas ADs of up to 41 Gy were obtained for lesions. The AD obtained from monoexponential ADR fitting was substantially higher than that from biexponential ADR fitting (whole liver: 3.76 ± 0.15 Gy vs. 3.21 ± 0.24 Gy with $P < 0.01$; anterior lesion: 37.85 ± 3.98 Gy vs. 29.97 ± 1.42 Gy; $P < 0.01$).

Although ADRs from one site (C6) varied by up to 73% for the third cycle, variability in organ ADs was generally acceptable across participants (Table 2). For lesions, several outliers in the AD were identified and most probably arose from the centers' respective high or low ADR (C6 and C8). The high AD in the inferior lesion from C6 was not plausible given the reduced ADR and AC and was likely a consequence of a transcriptional error or mishandling of the software.

Mean variations in the AD calculation for each cycle in each VOI can be seen in Table 2. The coefficient of variation in AD was up to 15% in the case of organs and up to 33% for the lesions.

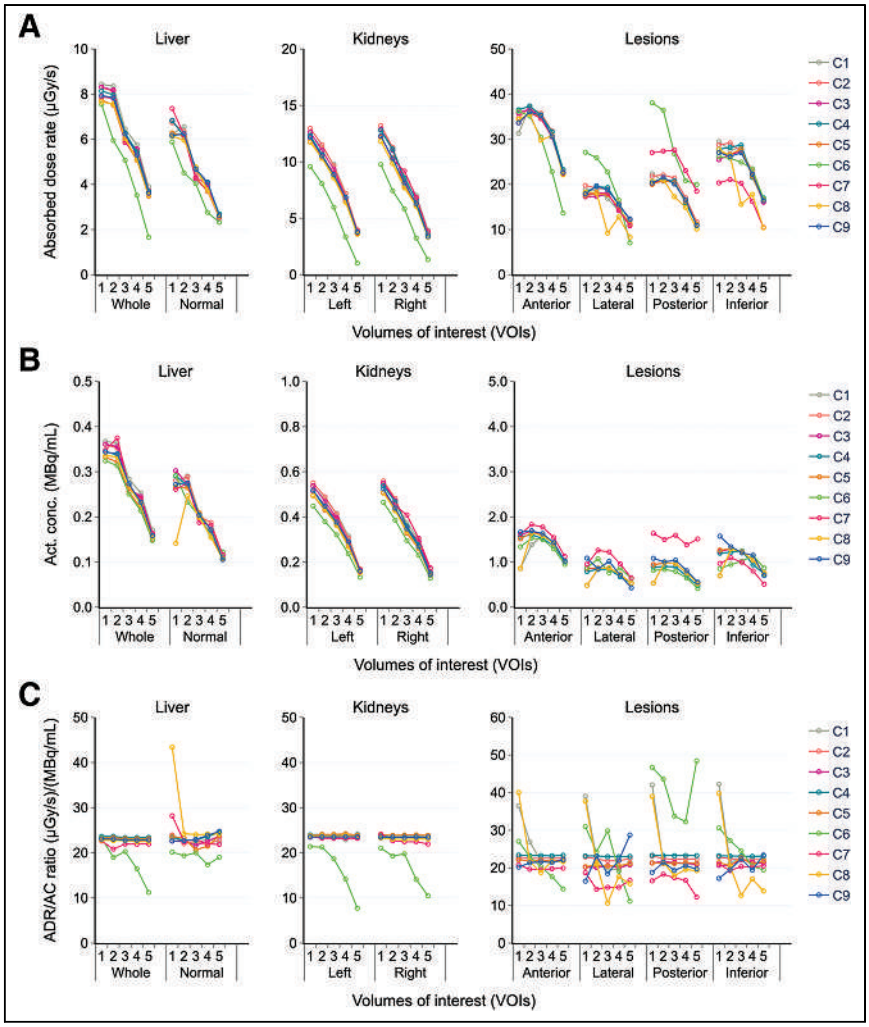

FIGURE 5. ADR (A), AC (B), and ADR-to-AC ratio (C) for each VOI in third cycle for time points 1–5. Whole liver signifies anatomic liver, whereas normal liver represents healthy liver (whole liver − 4 lesions).

TABLE 1
Fitting Chosen by Different Centers to Obtain AD for Each VOI

Treatment cycle	VOI	No. of centers	
		Monoexponential	Biexponential
	Organs	6	3
1	Anterior lesion	3	6
	Other lesions	1	8
	Organs	6	3
2	Anterior lesion*	3	5
	Other lesions	4	5
	Organs	6	3
3	Anterior lesion	3	6
	Other lesions	4	5

*Absence of fitting parameters from clinical center.

DISCUSSION

This work presents the dosimetry performed on patient image datasets acquired at different time points using PLANETDose software. Such a multicentric dosimetry comparison on a single clinical patient dataset using the same protocol and software by various centers appraises the precision of the dosimetry chain. The impact of reconstruction and calibration phases on the dosimetry chain was not considered in this work (*23*). The possibility of exporting intermediate results offered by PLANETDose facilitated the assessment of variations at each clinical dosimetry workflow step (*24*).

Although variations (CV_{med}) in organ volumes ranged from 6% to 13% for normal organs, CV_{med} increased to 38% for lesions. Even though the conversion of counts to activity was merely a reflection of the calibration factor, it was remarkable to see higher variations in counts (3%–29% for normal organs and ≤46% for lesions) but not a similar trend in discrepancies in activity, particularly for normal organs (13%). The ADR varied by a maximum of 12% and 17%, respectively, for normal organs and lesions, whereas the integration of ADR to obtain ADs reduced the variation in normal organs (<8%) and increased it in lesions (≤33%).

Every iteration evidenced significant disparities among participants, mostly derived from the heterogeneity of their initial level of expertise. To obtain more explainable results, these discrepancies were identified and addressed until the last iteration. Some of the observed issues were transcriptional error (improper unit conversions, use of a comma to represent decimals, errors in copying and pasting exported data), improper segmentation (inappropriate use of the thresholding technique, resulting in smaller segmented volumes; Fig. 7), and software mishandling (software data output formats were multiple and confusing, leading to incorrect reporting). However, since this was an educational and learning experience, most of these errors were deemed to be correctable.

Several additional checkpoints were defined during this dosimetric analysis: activity-to-count ratio, AC, and ADR-to-AC ratio. The 2 latter checkpoints could be incorporated in the software.

Even after compensation for obvious methodologic errors, the user-dependent fitting model generated significant variability. Providing users with additional leeway to choose their preferred methodologic dosimetric approach will probably lead to an even wider range of outcomes. This was seen in recently published data from Society of Nuclear Medicine and Molecular Imaging challenge users when allowed to choose the methodology (*17*) and when segmentation and TIA were provided (*18*).

The initial hypothesis that the same patient data, with the same processing workflow and using the same software, would yield relatively low interoperator variability proved to be false. Variable results were

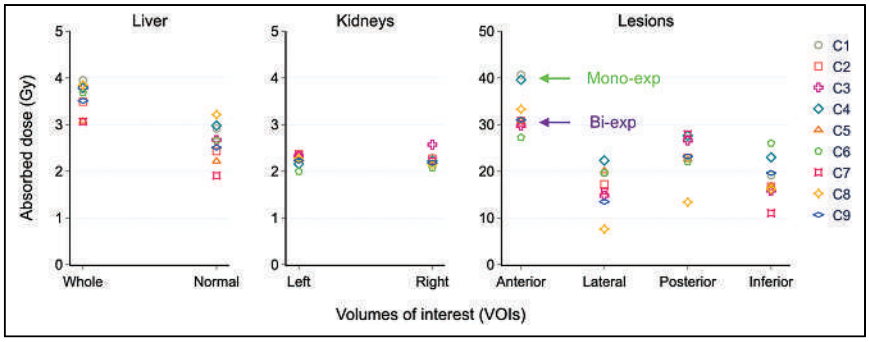

FIGURE 6. AD (in Gy) for each VOI (organs and lesions) in first cycle. Whole liver signifies anatomic liver, whereas normal liver represents healthy liver (whole liver − 4 lesions).

TABLE 2
AD in Each VOI for Each Treatment Cycle

VOI	Cycle 1	Cycle 2	Cycle 3
R kidney	2.24 ± 0.14	3.51 ± 0.29	3.33 ± 0.25
L kidney	2.25 ± 0.12	3.48 ± 0.18	3.50 ± 0.18
Whole liver	3.58 ± 0.33	3.87 ± 0.21	3.35 ± 0.17
Normal liver	2.61 ± 0.40	2.94 ± 0.28	2.28 ± 0.15
1, anterior	32.60 ± 4.56	34.68 ± 6.73	24.60 ± 2.00
2, lateral	16.73 ± 4.45	20.29 ± 6.40	12.22 ± 2.90
3, posterior	23.69 ± 4.53	28.57 ± 9.16	11.34 ± 3.75
4, inferior	18.27 ± 4.35	23.94 ± 6.36	15.77 ± 4.85

Data are mean ± SD (Gy).

examined closely in peer review training sessions, the source of the discrepancy was searched for, and it was decided whether an avoidable error had been made, warranting a teaching moment, or whether the discrepancy was a justified user variation.

The large number of iterations needed to increase the proficiency of each user with the software highlighted the importance of training. Often, insufficient training is delivered to users after the acquisition of new software packages. Several practical training sessions (along with theory) could increase proficiency in clinical dosimetry. Also, having access to a benchmark clinical dataset that comes with a set of expected results, or at least a range of acceptable results, would be an invaluable asset of the training.

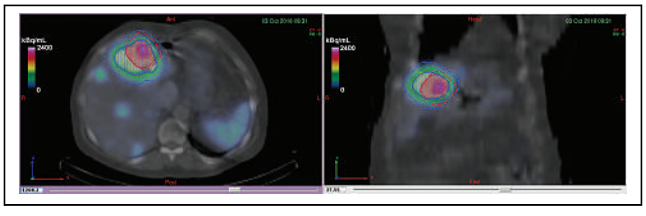

FIGURE 7. Typical error illustrating selection of small bounding box (in red) for anterior lesion while performing threshold-based segmentation. Blue VOI represents correct segmentation. *Bounding box* refers to predetermined subregion or selection in which thresholding is performed. By performing single click in area of high uptake, it is possible to generate tumor contour, thus preventing any potential correlation with uptake regions that are near tumor (e.g., organ, another tumor).

Best practices in RPT should be adopted to ensure that results are reliable, traceable, and reproducible—in other words, that they include robust QA. This comprises (but is not limited to) double processing using independent software (or free open-source tools) and cross-verification across physicists, as is current practice in external-beam radiation therapy. Because most clinical dosimetry software companies, even those with a long history in imaging, are relatively new to the field, a critical eye (and QA) on the procedure implemented by the user should also be accompanied by an equally critical use, including commissioning and regular QA of the software. In the present case, no commissioning or QA was performed initially, although several checks evolved to account for possible software inconsistencies (e.g., count-to-activity ratio).

Also, collaboration between physicists and physicians and between external-beam radiation therapy and RPT physicists would be a good starting point for implementing dosimetry QA since external-beam radiation therapy physicists are more experienced with error and failure mode analysis, therapeutic QA, and procedures. This requires a willingness to adapt to a new workplace culture of increasing cooperation (*25*).

It is vital to assess not only the precision but also the accuracy of the clinical dosimetry workflow. A possible way forward for this objective is the DosiTest project, in which simulated patient datasets (with activity being perfectly characterized at the voxel level for each time point) are used as the ground truth (*26*).

Finally, although not implemented here, using biologic effective dose or equieffective dose along with AD is an essential part of standardizing the dosimetric process and reporting (*27,28*).

CONCLUSION

This paper illustrates how dosimetric analysis performed by various operators using the same protocol and software on one patient dataset may still result in large variations, as well as how practice and experience are needed after initial training to obtain reliable results in RPT dosimetry. Making the distinction between expected variability (related to legitimate operator choices) and erroneous processing (due to a variety of causes) was deemed crucial. The analysis of the results revealed the following important points.

Software Commissioning

Use of software for calculation of AD and other dosimetric quantities requires a rigorous validation of the software itself, including checks on intermediate results and an end-to-end test.

Checkpoints

The possibility to extract results at various intermediate steps of the clinical dosimetry workflow should be integrated, such as activity-to-count ratio or ADR-to-AC ratio.

Sanity Checks

Internal checks implemented in the dosimetry package should minimize human mistakes: when obviously aberrant results are obtained, warning messages or even fatal errors should be generated.

Result Validation

Most errors could be related to the fact that dosimetry was performed by single individuals. Cross-verification of results among physicists and clinicians should be systematically implemented, when possible.

This CRP enabled defining some aspects to include in a clinical dosimetry QA procedure. As such, it represents a stepping stone toward the definition of reliable and reproducible dosimetry procedures. This project also resulted in the creation of a benchmark dosimetry dataset that is adapted for training individuals in dosimetry. This should set a model for other clinical indications and software. The expected results and associated variability are now available for this patient dataset and procedure and will be the topic of further communication.

DISCLOSURE

Sébastien Vauclin is employed by DOSIsoft. The PhD work of José-Alejandro Fragoso-Negrín is sponsored by DOSIsoft and supervised by Manuel Bardiès and Sébastien Vauclin. This work was partially funded by the ENEN+ project, which received funding from EURATOM research and training program 2016-2017-1 under grant agreement 75576. Alex Vergara-Gil was supported by the MEDIRAD project, which received funding from EURATOM research and training program 2014-2018 under grant agreement 755523. No other potential conflict of interest relevant to this article was reported.

KEY POINTS

QUESTION: How can the sources of variation associated with clinical dosimetry be evaluated?

PERTINENT FINDINGS: Dosimetry performed by several users on a single patient dataset with the same software and the same standard protocol resulted nonetheless in high variations and discrepancies among participants. The in-depth analysis required implementing checkpoints and internal sanity checks.

IMPLICATIONS FOR PATIENT CARE: Implementing QA in clinical dosimetry starts with providing sufficient training and implementing cross validation of dosimetry results.

REFERENCES

1. Hennrich U, Kopka K. Lutathera®: the first FDA- and EMA-approved radiopharmaceutical for peptide receptor radionuclide therapy. *Pharmaceuticals.* 2019;12:114.
2. Glatting G, Bardiès M, Lassmann M. Treatment planning in molecular radiotherapy. *Z Med Phys.* 2013;23:262–269.
3. Council of the European Union. European Council Directive 2013/59/Euratom on basic safety standards for protection against the dangers arising from exposure to ionising radiation and repealing Directives 89/618/Euratom, 90/641/Euratom, 96/29/Euratom, 97/43/Euratom and 2003/122/Euratom. *Official J Eur Union.* 2014;L13:1–73.
4. Flux G, Bardiès M, Monsieurs M, et al. The impact of PET and SPECT on dosimetry for targeted radionuclide therapy. *Z Med Phys.* 2006;16:47–59.
5. McGowan DR, Guy MJ. Time to demand dosimetry for molecular radiotherapy? *Br J Radiol.* 2015;88:20140720.
6. Ljungberg M, Sjögreen Gleisner K. Personalized dosimetry for radionuclide therapy using molecular imaging tools. *Biomedicines.* 2016;4:25.
7. Stokke C, Gabiña PM, Solný P, et al. Dosimetry-based treatment planning for molecular radiotherapy: a summary of the 2017 report from the Internal Dosimetry Task Force. *EJNMMI Phys.* 2017;4:27.
8. Sundlöv A, Gleisner KS, Tennvall J, et al. Phase II trial demonstrates the efficacy and safety of individualized, dosimetry-based ^{177}Lu-DOTATATE treatment of NET patients. *Eur J Nucl Med Mol Imaging.* 2022;49:3830–3840.
9. Strigari L, Konijnenberg M, Chiesa C, et al. The evidence base for the use of internal dosimetry in the clinical practice of molecular radiotherapy. *Eur J Nucl Med Mol Imaging.* 2014;41:1976–1988.
10. Wahl RL, Sgouros G, Iravani A, et al. Normal-tissue tolerance to radiopharmaceutical therapies, the knowns and the unknowns. *J Nucl Med.* 2021;62(suppl 3): 23S–35S.
11. Sgouros G, Dewaraja YK, Escorcia F, et al. Tumor response to radiopharmaceutical therapies: the knowns and the unknowns. *J Nucl Med.* 2021;62(suppl 3):12S–22S.
12. Bardiès M, Gear JI. Scientific developments in imaging and dosimetry for molecular radiotherapy. *Clin Oncol.* 2021;33:117–124.
13. Haug AR. PRRT of neuroendocrine tumors: individualized dosimetry or fixed dose scheme? *EJNMMI Res.* 2020;10:35.
14. Sgouros G, Bodei L, McDevitt MR, Nedrow JR. Radiopharmaceutical therapy in cancer: clinical advances and challenges. *Nat Rev Drug Discov.* 2020;19:589–608.
15. Gear JI, Cox MG, Gustafsson J, et al. EANM practical guidance on uncertainty analysis for molecular radiotherapy absorbed dose calculations. *Eur J Nucl Med Mol Imaging.* 2018;45:2456–2474.
16. Sjögreen Gleisner K, Spezi E, Solny P, et al. Variations in the practice of molecular radiotherapy and implementation of dosimetry: results from a European survey. *EJNMMI Phys.* 2017;4:28.
17. Uribe C, Peterson A, Van B, et al. An international study of factors affecting variability of dosimetry calculations, part 1: design and early results of the SNMMI dosimetry challenge. *J Nucl Med.* 2021;62(suppl 3):36S–47S.
18. Brosch-Lenz J, Ke S, Wang H, et al. An international study of factors affecting variability of dosimetry calculations, part 2: overall variabilities in absorbed dose. *J Nucl Med.* 2023;64:1–7.
19. Kayal G, Chauvin M, Vergara-Gil A, et al. Generation of clinical ^{177}Lu SPECT/CT images based on Monte Carlo simulation with GATE. *Phys Med.* 2021;85:24–31.
20. Müller JW. Possible advantages of a robust evaluation of comparisons. *J Res Natl Inst Stand Technol.* 2000;105:551–555.
21. Meyers N, Jadoul A, Bernard C, et al. Inter-observer variability of ^{90}Y PET/CT dosimetry in hepatocellular carcinoma after glass microspheres transarterial radioembolization. *EJNMMI Phys.* 2020;7:29.
22. Cicone F, Denoël T, Gnesin S, et al. Preclinical evaluation and dosimetry of [^{111}In]CHX-DTPA- scFv78-Fc targeting endosialin/tumor endothelial marker 1 (TEM1). *Mol Imaging Biol.* 2020;22:979–991.
23. Zimmerman BE, Grošev D, Buvat I, et al. Multi-centre evaluation of accuracy and reproducibility of planar and SPECT image quantification: an IAEA phantom study. *Z Med Phys.* 2017;27:98–112.
24. Della Gala G, Bardiès M, Tipping J, Strigari L. Overview of commercial treatment planning systems for targeted radionuclide therapy. *Phys Med.* 2021;92:52–61.
25. Lawhn-Heath C, Hope TA, Martinez J, et al. Dosimetry in radionuclide therapy: the clinical role of measuring radiation dose. *Lancet Oncol.* 2022;23: e75–e87.
26. Kayal G, Clayton N, Vergara-Gil A, Struelens L, Bardiès M. Proof-of-concept of DosiTest: a virtual multicentric clinical trial for assessing uncertainties in molecular radiotherapy dosimetry. *Phys Med.* 2022;97:25–35.
27. Barone R, Borson-Chazot F, Valkema R, et al. Patient-specific dosimetry in predicting renal toxicity with ^{90}Y-DOTATOC: relevance of kidney volume and dose rate in finding a dose-effect relationship. *J Nucl Med.* 2005;46(supp 1):99S–106S.
28. Wessels BW, Konijnenberg MW, Dale RG, et al. MIRD pamphlet no. 20: the effect of model assumptions on kidney dosimetry and response–implications for radionuclide therapy. *J Nucl Med.* 2008;49:1884–1899.

Imaging of Myocardial $\alpha_v\beta_3$ Integrin Expression for Evaluation of Myocardial Injury After Acute Myocardial Infarction

Wail Nammas*[1,2], Christian Paunonen*[1], Jarmo Teuho[1], Reetta Siekkinen[1,3], Pauliina Luoto[1], Meeri Käkelä[1], Ari Hietanen[1], Tapio Viljanen[1], Matthieu Dietz[4], John O. Prior[4], Xiang-Guo Li[1,5,6], Anne Roivainen[1,6], Juhani Knuuti[1,6], and Antti Saraste[1,2,6]

[1]*Turku PET Centre, Turku University Hospital and University of Turku, Turku, Finland;* [2]*Heart Center, Turku University Hospital, University of Turku, Turku, Finland;* [3]*Department of Medical Physics, Turku University Hospital, Turku, Finland;* [4]*Department of Nuclear Medicine and Molecular Imaging, Lausanne University Hospital, Lausanne, Switzerland;* [5]*Department of Chemistry, University of Turku, Turku, Finland; and* [6]*InFLAMES Research Flagship Center, University of Turku, Turku, Finland*

[^{68}Ga]Ga-NODAGA-Arg-Gly-Asp (RGD) is a PET tracer targeting $\alpha_v\beta_3$ integrin, which is upregulated during angiogenesis soon after acute myocardial infarction (AMI). We prospectively evaluated determinants of myocardial uptake of [^{68}Ga]Ga-NODAGA-RGD and its associations with left ventricular (LV) function in patients after AMI. **Methods:** Myocardial blood flow and [^{68}Ga]Ga-NODAGA-RGD uptake (60 min after injection) were evaluated by PET in 31 patients 7.7 ± 3.8 d after primary percutaneous coronary intervention for ST-elevation AMI. Transthoracic echocardiography of LV function was performed on the day of PET and at the 6-mo follow-up. **Results:** PET images showed increased uptake of [^{68}Ga]Ga-NODAGA-RGD in the ischemic area at risk (AAR), predominantly in injured myocardial segments. The SUV in the segment with the highest uptake (SUV_{max}) in the ischemic AAR was higher than the SUV_{mean} of the remote myocardium (0.73 ± 0.16 vs. 0.51 ± 0.11, $P < 0.001$). Multivariable predictors of [^{68}Ga]Ga-NODAGA-RGD uptake in the AAR included high peak N-terminal pro–B-type natriuretic peptide ($P < 0.001$), low LV ejection fraction, low global longitudinal strain ($P = 0.01$), and low longitudinal strain in the AAR ($P = 0.01$). [^{68}Ga]Ga-NODAGA-RGD uptake corrected for myocardial blood flow and perfusable tissue fraction in the AAR predicted improvement in global longitudinal strain at follow-up ($P = 0.002$), independent of peak troponin, N-terminal pro–B-type natriuretic peptide, and LV ejection fraction. **Conclusion:** [^{68}Ga]Ga-NODAGA-RGD uptake shows increased $\alpha_v\beta_3$ integrin expression in the ischemic AAR early after AMI that is associated with regional and global systolic dysfunction, as well as increased LV filling pressure. Increased [^{68}Ga]Ga-NODAGA-RGD uptake predicts improvement of global LV function 6 mo after AMI.

Key Words: myocardial infarction; PET; angiogenesis; myocardial strain; coronary artery disease

J Nucl Med 2024; 65:132–138
DOI: 10.2967/jnumed.123.266148

Acute myocardial infarction (AMI) initiates maladaptive changes in cardiac myocytes and the extracellular matrix, which can contribute to left ventricular (LV) dysfunction, adverse remodeling, and eventual failure (*1*). The repair process aimed at restoration of the capillary network, elimination of necrotic tissue, and deposition of new extracellular matrix is essential for healing of AMI and can counteract the development of chronic LV dysfunction (*1*). In parallel with inflammation and fibrosis, angiogenesis (sprouting of preexisting capillaries) plays an important role in myocardial repair after AMI (*2*).

Integrin $\alpha_v\beta_3$ is a glycoprotein transmembrane receptor the expression of which is upregulated in proliferating endothelial cells and can serve as a biomarker of angiogenesis (*3*). After AMI, $\alpha_v\beta_3$ integrin expression increases in vascular structures during the early repair process (*4*). Studies in experimental models and humans demonstrated the feasibility of using radiolabeled tracers containing the Arg-Gly-Asp (RGD) motif for the noninvasive detection of $\alpha_v\beta_3$ integrin expression after AMI (*5–13*). However, the clinical utility of $\alpha_v\beta_3$ integrin as a biomarker after AMI remains uncertain.

We sought to study the determinants of $\alpha_v\beta_3$ integrin expression and its association with LV function after AMI. We prospectively evaluated myocardial uptake of [^{68}Ga]Ga-NODAGA-RGD (*10,14*), a PET radiotracer targeting $\alpha_v\beta_3$ integrin, within 2 wk of reperfusion in patients with AMI. The function of the LV was evaluated by echocardiography at the time of the PET scan and 6 mo later.

MATERIALS AND METHODS

Study Cohort and Design

We prospectively recruited patients who underwent primary percutaneous coronary intervention because of ST-elevation AMI and who had an LV ejection fraction (LVEF) of less than 50% during the index hospitalization in Turku University Hospital from December 2018 to January 2021. Exclusion criteria are listed in the supplemental materials (available at http://jnm.snmjournals.org). Each patient signed an informed consent form. The study conforms to the Declaration of Helsinki, and the institutional review boards of the Hospital District of Southwest Finland, Finnish Medicines Agency, and Turku University Hospital approved the study. The study was registered in clinicaltrials.gov with identifier NCT04871217.

To evaluate myocardial $\alpha_v\beta_3$ integrin expression, patients underwent [^{15}O]O-water PET followed by [^{68}Ga]Ga-NODAGA-RGD PET within 3 to 14 d after AMI. To evaluate LV function, echocardiography was performed at baseline on the day of PET imaging and at the 6-mo follow-up. Peak cardiac troponin T and N-terminal pro–B-type natriuretic peptide (NT-proBNP) levels were recorded during hospitalization and at the time of PET imaging. Data on cardiovascular risk factors, medications, and cardiovascular events were collected from

Received Jun. 8, 2023; revision accepted Sep. 27, 2023.
For correspondence or reprints, contact Antti Saraste (antti.saraste@utu.fi).
*Contributed equally to this work.
Published online Nov. 16, 2023.

electronic medical reports. The myocardial area at risk (AAR) and the remote area were based on the culprit coronary arterial segment, determined from the invasive coronary angiography and electrocardiography.

PET Imaging

Synthesis of [^{68}Ga]Ga-NODAGA-RGD is described in the supplemental materials. For each patient, resting [^{15}O]O-water and [^{68}Ga]Ga-NODAGA-RGD PET scans were performed using a dedicated PET/CT scanner (Discovery MI; GE Healthcare) on the same day, as previously described (supplemental materials) (*15*). In brief, [^{15}O]O-water (Radiowater Generator; Hidex Oy) was injected as an intravenous bolus (target injected radioactivity, 500 MBq) over 15 s, and dynamic PET was performed over 4 min and 40 s, starting 25 s after injection, with the patient at rest. Then, an average of 179 ± 15 MBq of [^{68}Ga]Ga-NODAGA-RGD was injected as an intravenous bolus and was followed by a list-mode PET acquisition over 15 min after a 60-min uptake period.

PET Image Analysis and Interpretation

Images were analyzed using Carimas 2.9 software (Turku PET Centre) (supplemental materials) (*10,16*). In brief, polar maps of [^{68}Ga]Ga-NODAGA-RGD uptake (SUV) in the LV myocardium were based on myocardial contours and sampling points matching with coregistered [^{15}O]O-water images. The [^{68}Ga]Ga-NODAGA-RGD SUV_{max} was defined as the highest segmental uptake. An indexed SUV_{max} corrected for the mean myocardial blood flow (MBF) and perfusable tissue fraction in the AAR was also calculated to account for the reduced amount of viable tissue in the infarct zone (*16*).

Echocardiography

Transthoracic echocardiography was performed using Vivid E9 or E95 (GE Vingmed Ultrasound) devices equipped with MS5 and 4Vc-D 4-dimensional probes. All images were digitally stored for offline analysis (EchoPAC PC version 203; GE Vingmed) of LV global and segmental function (supplemental materials). The LV volumes and LVEF were measured using the biplane Simpson method. Myocardial global longitudinal strain (GLS) and segmental longitudinal strain (LS) were analyzed using the speckle-tracking method and reported as absolute values. Segments with a baseline LS of less than 13.5% were defined as injured (*17*).

Statistical Analysis

Continuous data are reported as mean and SD and compared using the Student *t* test when normally distributed or with the Mann–Whitney test otherwise. Categoric data are reported as count and percentage and compared with χ^2 or Fisher exact tests, as appropriate. Univariable and multivariable linear regression models were constructed to identify predictors of [^{68}Ga]Ga-NODAGA-RGD uptake at baseline and predictors of improvement in LV function from baseline to follow-up. Statistically significant variables in the univariable analysis were added to multivariable models as covariates. Intra- and interobserver reproducibility of [^{68}Ga]Ga-NODAGA-RGD SUV_{max} measures were assessed in 7 randomly selected patients by calculating the coefficient of variation. Statistical significance was set at a *P* value of less than 0.05. Statistical analyses were performed using SPSS version 25.0 (IBM Corp.).

RESULTS

We enrolled 31 patients with the first ST-elevation AMI. Table 1 summarizes the baseline characteristics of the patients. All patients underwent primary percutaneous coronary intervention at 4.9 ± 6.1 h from symptom onset. The AAR was in the left anterior descending, the right, and the left circumflex coronary artery territories in 48.4%, 29.0%, and 22.6% of patients, respectively.

TABLE 1
Patient Characteristics (*n* = 31)

Characteristic	Data
Age (y)	64.2 ± 9.2
Male sex	28 (90.3%)
Body mass index (kg/m^2)	25.4 ± 4.8
Current smoking	11 (35.5%)
Diabetes mellitus	3 (9.7%)
Hypertension	13 (41.9%)
Hypercholesterolemia	17 (54.8%)
Family history of CAD	9 (31%)
Time from symptoms to PCI (h)	4.9 ± 6.1
Culprit coronary artery territory	
Left anterior descending artery	15 (48.4%)
Circumflex artery	7 (22.6%)
Right coronary artery	9 (29%)
Post-PCI TIMI flow	
Grade 2	10 (32.3%)
Grade 3	21 (67.7%)
Peak troponin T (ng/L)	3884.3 ± 4391.7
Peak NT-proBNP (ng/L)	979.4 ± 871.5
Total cholesterol (mmol/L)	4.2 ± 1.1
LDL cholesterol (mmol/L)	2.9 ± 0.9
Duration of hospital stay (d)	3.7 ± 1.8
Loop diuretics	10 (32.3%)
Inotropic medication	7 (22.6%)
Medication at discharge	
Aspirin	30 (96.8%)
Statin	30 (96.8%)*
ACEI/ARB	29 (93.5%)
β-blocker	25 (80.6%)

*High-intensity statin in 27 (87.1%).

CAD = coronary artery disease; PCI = percutaneous coronary intervention; TIMI = thrombolysis in myocardial infarction; LDL = low-density lipoprotein; ACEI/ARB = angiotensin-converting enzyme inhibitor/angiotensin receptor blocker.

Qualitative data are number and percentage; continuous data are mean ± SD.

Patients underwent [^{15}O]O-water and [^{68}Ga]Ga-NODAGA-RGD PET scans at 7.7 ± 3.8 d (median, 8 d; interquartile range, 7 d) after AMI. The clinical characteristics were similar between patients who underwent PET at less than 7 d after AMI (*n* = 14) and patients who underwent PET at 7 d or more after AMI (*n* = 17).

One patient was lost to follow-up. Consequently, 30 patients underwent both baseline and follow-up echocardiography 210 ± 38 d after AMI. There were no deaths or heart failure hospitalizations during follow-up, but 1 patient had non–ST-elevation AMI caused by a coronary lesion other than the index lesion.

LV Function

Table 2 summarizes the echocardiography data. All patients initially had an LVEF of less than 50%, whereas at baseline evaluation

TABLE 2
Echocardiography Data

Parameter	Baseline (n = 31)	Follow-up (n = 30)	P
LV end-diastolic volume (mL)	94.7 ± 27.7	93.6 ± 30.1	0.7
LV end-systolic volume (mL)	42.7 ± 17.1	40.8 ± 19.1	0.4
LVEF (%)	55.8 ± 6.9	57.5 ± 7.3	0.2
GLS (%)	14.9 ± 4.6	15.4 ± 3.9	0.3
LS in AAR (%)	12.5 ± 6.0	13.8 ± 5.2	0.03
Mitral E/A ratio	0.96 ± 0.35	1.01 ± 0.36	0.4
E/e′ ratio	8.9 ± 2.7	7.7 ± 1.8	0.01

E/A = early diastolic filling velocity/atrial filling velocity; E/e′ = early diastolic filling velocity/early diastolic tissue velocity.
Data are mean ± SD.

on the day of PET scanning, LVEF was less than 50% in 5 patients and GLS was less than 16% in 17. In the AAR, myocardial injury (segmental LS < 13.5%) was present in 26 (84%) patients. The average number of injured segments per patient was 3.1 ± 2.2.

At follow-up, LS in the AAR showed significant improvement from baseline (P = 0.03). LVEF improved by at least 5% in 12 (40%) patients and worsened by at least 5% in 6 (20%). In turn, GLS improved by at least 3% in 9 (30%) patients and worsened by at least 3% in 4 (13%). Only 4 patients had an LV end-diastolic volume increase of at least 20%.

[^{68}Ga]Ga-NODAGA-RGD Uptake After AMI

Uptake of [^{68}Ga]Ga-NODAGA-RGD was visible in the AAR in PET images from all patients (Fig. 1; Supplemental Fig. 1). The segment with the highest [^{68}Ga]Ga-NODAGA-RGD uptake (SUV_{max}) was within or immediately adjacent to the AAR in all patients. Segments in the AAR (n = 168) showed higher [^{68}Ga]Ga-NODAGA-RGD SUV than segments in the remote area (0.66 ± 0.18 vs. 0.55 ± 0.14, P < 0.001, Fig. 2).

The [^{68}Ga]Ga-NODAGA-RGD SUV_{max} colocalized with the segment with the most severe contractile abnormality or the immediately adjacent segment in 22 patients. In the remaining patients, SUV_{max} was either in the border of a large injured area (n = 4) or there was no contractile abnormality in the AAR (n = 5). Within the AAR, the average [^{68}Ga]Ga-NODAGA-RGD SUV was higher in segments with myocardial injury (n = 97) than in other segments (0.71 ± 0.19 vs. 0.61 ± 0.14, P < 0.001, Fig. 2) and inversely correlated with LS (P < 0.001, Fig. 3A).

MBF was lower in the AAR than in remote myocardium (0.73 ± 0.23 vs. 0.83 ± 0.23 mL/g/min, P < 0.001). There was no correlation between segmental SUV and overall MBF in the AAR (P = 0.1), but SUV_{max} correlated with MBF in the noninjured myocardial segments within or immediately adjacent to AAR (r = 0.49, P = 0.017, Supplemental Fig. 2).

In patient-based analysis, SUV_{max} and indexed SUV_{max} were higher in the AAR than in remote myocardium (Table 3). SUV_{max} in the AAR was higher than blood pool SUV (0.73 ± 0.16 vs. 0.64 ± 0.15, P < 0.001) but lower than liver SUV (0.73 ± 0.16 vs. 1.04 ± 0.16, P < 0.001). SUV_{max} was similar between patients who underwent PET at less than 7 d after AMI and patients who underwent PET at 7 d or more after AMI (P > 0.05, Supplemental Table).

Measurement of SUV_{max} was reproducible, with an intraobserver coefficient of variation of 1.4% and an interobserver coefficient of variation of 10.9%.

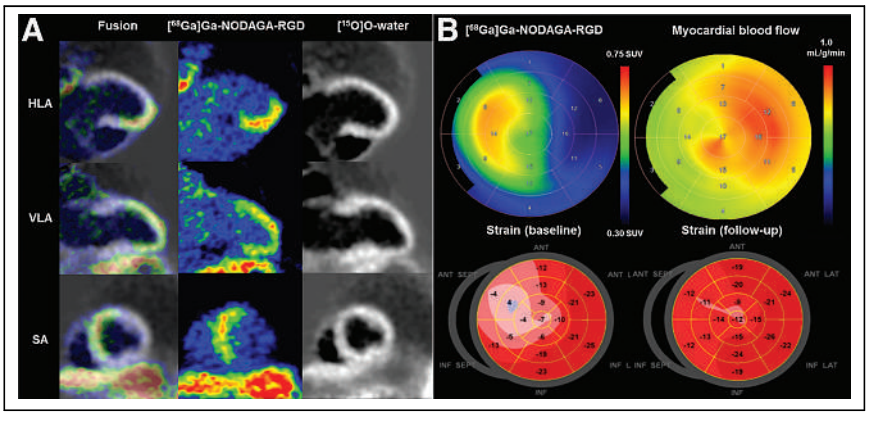

FIGURE 1. Uptake of [^{68}Ga]Ga-NODAGA-RGD 7 d after acute occlusion of proximal left anterior descending coronary artery. (A) Myocardial contours in [^{15}O]O-water images, [^{68}Ga]Ga-NODAGA-RGD uptake images, and corresponding fusion images. (B) Polar maps of [^{68}Ga]Ga-NODAGA-RGD uptake, resting MBF, and longitudinal strain at time of PET and 6 mo later. Reduced longitudinal strain is seen in anteroseptal region at baseline and partial functional recovery at 6 mo. HLA = horizontal long axis; SA = short axis; VLA = vertical long axis.

Predictors of [^{68}Ga]Ga-NODAGA-RGD Uptake After AMI

Univariable predictors of [^{68}Ga]Ga-NODAGA-RGD SUV_{max} and indexed SUV_{max} in the AAR at baseline included peak troponin T, peak NT-proBNP, GLS, and LS in the AAR (Table 4). Neither age nor peak CRP level predicted SUV_{max} or indexed SUV_{max} (P > 0.05 for both), which were similar in patients with postrevascularization thrombolysis in myocardial infarction flow grade 2 or 3 (P = 0.6).

In multivariable models, the only independent predictor of SUV_{max} in the AAR was peak NT-proBNP (Fig. 3B; Table 4), whereas peak troponin T, LVEF, and GLS predicted indexed SUV_{max} (Table 4).

[^{68}Ga]Ga-NODAGA-RGD Uptake and LV Function at Follow-up

In univariable analysis, indexed [^{68}Ga]Ga-NODAGA-RGD SUV_{max} in the AAR, peak

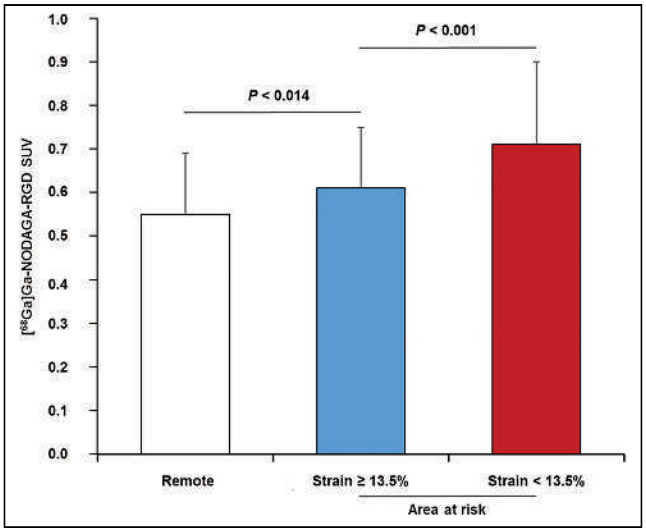

FIGURE 2. At baseline, segmental uptake of [^{68}Ga]Ga-NODAGA-RGD was higher in AAR than in remote myocardium and was highest in segments with myocardial injury (longitudinal strain < 13.5%).

troponin T, peak NT-proBNP, and baseline LVEF predicted improvement of GLS adjusted for baseline (Table 5). Neither time from symptom onset to revascularization nor the postrevascularization thrombolysis in myocardial infarction flow grade predicted improvement of GLS. In multivariable analysis, indexed SUV_{max} in the AAR was the only independent predictor of improvement of GLS at follow-up ($P = 0.002$, Fig. 4).

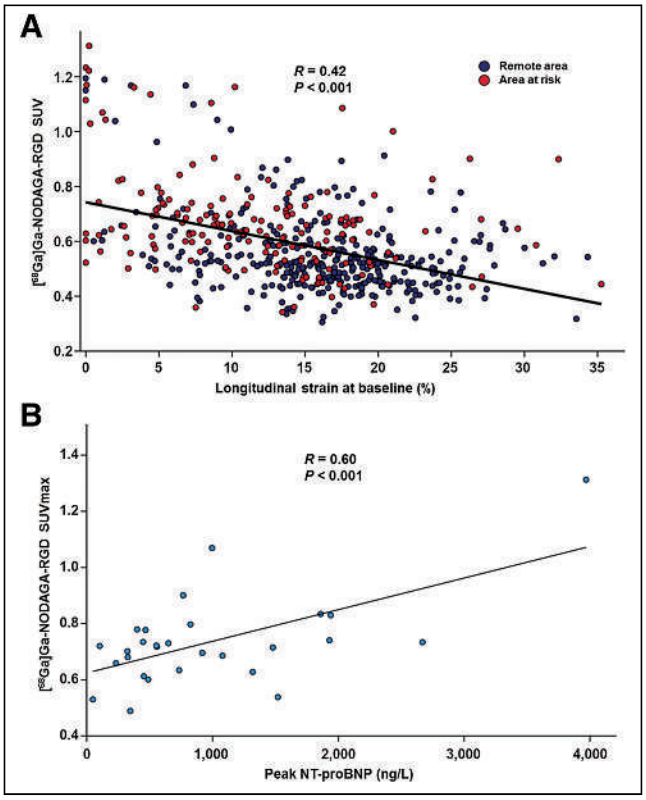

FIGURE 3. (A) Segmental uptake of [^{68}Ga]Ga-NODAGA-RGD inversely correlated with LS ($r = -0.0355$, $P < 0.001$). (B) Increased NT-pro-BNP level predicted [^{68}Ga]Ga-NODAGA-RGD SUV_{max} in AAR ($P < 0.001$).

Although associated with global LV function improvement, indexed SUV_{max} was not associated with improvement of LS in the AAR in 26 patients with myocardial injury at baseline ($P = 0.7$). Furthermore, segmental [^{68}Ga]Ga-NODAGA-RGD SUV did not correlate with change in LS in injured segments in the AAR ($P = 0.2$).

DISCUSSION

We found that uptake of [^{68}Ga]Ga-NODAGA-RGD increased in the myocardium distal to the culprit lesion of the infarct-related artery (AAR) in patients with recent ST-elevation AMI. Uptake of [^{68}Ga]Ga-NODAGA-RGD was associated with myocardial injury, regional and global LV systolic dysfunction, and increased LV filling pressure. Furthermore, the intensity of [^{68}Ga]Ga-NODAGA-RGD uptake was associated with improvement in global LV function at the 6-mo follow-up. These results indicate that [^{68}Ga]Ga-NODAGA-RGD PET provides information about the severity of acute ischemic myocardial injury and the potential for recovery of LV function.

Earlier studies demonstrated the feasibility of noninvasive nuclear imaging of $\alpha_v\beta_3$ integrin expression using radiolabeled tracers containing the RGD motif after recent AMI (*5–13*). Early after AMI, $\alpha_v\beta_3$ integrin is expressed by vascular endothelial cells (*4*), and uptake of RGD-based tracers correlates with neovascularization (*5–13*). However, $\alpha_v\beta_3$ integrin has also been implicated in mediating the macrophage response to inflammatory signals (*18*) and myofibroblast differentiation through the activation of transforming growth factor β1 (*19*), which may be also targeted by RGD-based tracers late after AMI (*20*). Thus, $\alpha_v\beta_3$ integrin expression may provide information about the activation of the repair process after ischemic myocardial injury, but its utility as an imaging biomarker after human AMI remains uncertain.

Uptake of [^{68}Ga]Ga-NODAGA-RGD After Myocardial Infarction

^{68}Ga-RGD tracers were previously demonstrated to accumulate in areas of injured myocardium in experimental models of ischemic myocardial injury and to correlate with $\alpha_v\beta_3$ integrin expression (*8,10*). In this study, we found consistently increased uptake of [^{68}Ga]Ga-NODAGA-RGD in the ischemic AAR at less than 14 d after AMI, a finding that is in line with previous studies showing accumulation of RGD-based tracers as early as 3 d after ischemic myocardial injury and then a peak at 1–3 wk (*6*). Uptake of [^{68}Ga]Ga-NODAGA-RGD was sometimes also observed adjacent to the AAR, as is consistent with previous evidence showing uptake of RGD-based tracers extending into the periinfarct zone (*12,21*). In contrast to AMI, accumulation of RGD-based tracers was not found in patients with chronic coronary total occlusion (*12*) or old myocardial infarction (*11,12,21*).

We found that the highest segmental uptake of [^{68}Ga]Ga-NODAGA-RGD (SUV_{max}) was 1.43-fold higher than the SUV_{mean} in the remote myocardium, which is similar to previous studies using different RGD-based tracers (1.34–2.33) (*11–13*). Using a rat model of AMI, we previously found that measurement of SUV using static images showed comparable results to kinetic modeling of the distribution volume of [^{68}Ga]Ga-DOTA-RGD uptake, thereby simplifying in vivo analysis (*9*). We also measured [^{68}Ga]Ga-NODAGA-RGD uptake corrected for both MBF and perfusable tissue fraction (indexed SUV_{max}) to account for reduced MBF and reduced distribution volume due to loss of viable tissue (*22*). Developments in scanner technology and motion correction algorithms may further facilitate quantification of the [^{68}Ga]Ga-NODAGA-RGD signal.

TABLE 3
[^{68}Ga]Ga-NODAGA-RGD and [^{15}O]O-Water PET Data

Parameter	AAR	Remote area	*P*
[^{68}Ga]Ga-NODAGA-RGD SUV_{max}	0.727 ± 0.16	0.529 ± 0.14	<0.001
[^{68}Ga]Ga-NODAGA-RGD SUV_{mean}	0.652 ± 0.15	0.511 ± 0.11	<0.001
Mean MBF	0.732 ± 0.23	0.827 ± 0.23	<0.001
Indexed [^{68}Ga]Ga-NODAGA-RGD SUV_{max}	1.263 ± 0.64	0.789 ± 0.24	<0.001

Data are mean ± SD.

Determinants of [^{68}Ga]Ga-NODAGA-RGD Uptake

Uptake of [^{68}Ga]Ga-NODAGA-RGD colocalized with injured myocardial areas based on reduced systolic LS on echocardiography and correlated with the degree of LS reduction after AMI. In a previous study, LS reduction was associated with the transmurality of myocardial injury according to late gadolinium enhancement on cardiac MRI (*17*). Thus, our findings are consistent with experimental (*10*) as well as clinical studies that found colocalization of RGD-based tracer uptake with resting myocardial perfusion defects (*11,13,21*), hypokinesia (*12*), and late gadolinium enhancement (*12,21*). In line with previous studies using other RGD-based tracers (*12,21*), [^{68}Ga]Ga-NODAGA-RGD uptake was also present in the periinfarct border zone and in 5 patients without wall motion abnormality at the time of the PET scan, indicating that it is a sensitive marker of recent ischemic myocardial injury.

Myocardial infarct size determined by peak troponin was not an independent predictor of the indexed [^{68}Ga]Ga-NODAGA-RGD SUV_{max}, indicating that $\alpha_v\beta_3$ integrin expression is also dependent on factors other than the extent of myocardial injury. Our finding is consistent with no association between uptake of another RGD-based tracer and infarct size quantified by cardiac MRI early after AMI (*12*). However, other studies reported correlations between uptake of other RGD-based tracers and infarct size late after AMI (31 ± 14 d and 8 wk) (*13,21*). Furthermore, an inverse relationship between ^{18}F-galacto-RGD uptake and resting MBF has been reported (*13*). In our study, uptake of [^{68}Ga]Ga-NODAGA-RGD did not correlate with overall MBF in the AAR consisting of a mixture of injured and noninjured myocardium but was associated with preserved MBF in the periinfarct border zone.

A novel finding in the present study is that in addition to LV dysfunction in the AAR, reduced LVEF, impaired GLS, and high NT-proBNP were independent predictors of [^{68}Ga]Ga-NODAGA-RGD uptake. These findings are consistent with the key roles of hemodynamic stress and pressure overload in modifying the responses of different cell types toward maintenance of cardiac function after injury (*1*). Taken together, our results are consistent with the increased expression of $\alpha_v\beta_3$ integrin after ischemic myocardial injury and with the intensity of [^{68}Ga]Ga-NODAGA-RGD

TABLE 4
Predictors of [^{68}Ga]Ga-NODAGA-RGD Uptake in AAR After AMI

	Univariable analysis			Multivariable analysis		
Predictor	B coefficient	R coefficient	*P*	B coefficient	R coefficient	*P*
SUV_{max}						
Age	0.001 (−0.005–0.008)	0.077	0.6			
Peak troponin T	0.002 (0.001–0.003)	0.603	<0.001			
Peak NT-proBNP	0.001 (0.001–0.002)	0.605	<0.001	0.001 (0.001–0.002)	0.605	<0.001
Baseline LVEF	−0.008 (−0.016–0.000)	−0.348	0.055			
Baseline GLS	0.016 (0.004–0.028)	0.447	0.01			
AAR LS	0.010 (0.001–0.020)	0.394	0.02			
Indexed SUV_{max}						
Age	−0.002 (−0.030–0.026)	−0.033	0.8			
Peak troponin T	0.011 (0.008–0.015)	0.765	<0.001	0.008 (0.005–0.012)	0.542	<0.001
Peak NT-proBNP	0.004 (0.002–0.007)	0.561	0.002			
Baseline LVEF	−0.067 (−0.093–0.041)	−0.701	<0.001	−0.045 (−0.067–0.023)	−0.476	<0.001
Baseline GLS	0.106 (0.069–0.143)	0.741	<0.001	0.061 (0.014–0.109)	0.422	0.01
AAR LS	0.071 (0.040–0.101)	0.668	<0.001	0.035 (−0.002–0.071)	0.315	0.059

Data in parentheses are 95% CI. Covariates in multivariable model were peak troponin T, peak NT-proBNP, and either LVEF, GLS, or AAR longitudinal strain. Peak troponin T is for 100-unit increment, and peak NT-proBNP is for 10-unit increment.

TABLE 5
Predictors of LV Function Improvement at Follow-up

Predictor	B coefficient	R coefficient	*P*
Improvement in LVEF*			
Age	0.004 (−0.001–0.009)	0.272	0.1
Peak troponin T	0.000 (−0.001–0.001)	−0.071	0.7
Peak NT-proBNP	0.000 (−0.001–0.000)	−0.228	0.2
SUV_{max} in AAR	0.004 (−0.309–0.316)	0.005	0.9
Indexed SUV_{max} in AAR	0.047 (−0.031–0.125)	0.233	0.2
Baseline GLS	0.007 (−0.003–0.018)	0.260	0.1
Improvement in GLS*			
Age	0.010 (−0.006–0.025)	0.232	0.2
Peak troponin T	0.004 (0.002–0.007)	0.519	0.003
Peak NT-proBNP	0.002 (0.000–0.004)	0.435	0.02
SUV_{max} in AAR	0.666 (−0.190–1.523)	0.288	0.1
Indexed SUV_{max} in AAR	0.319 (0.128–0.510)	0.550	0.002
Baseline LVEF	−0.023 (−0.042–0.004)	−0.423	0.02

*Adjusted for baseline. Peak troponin T is for 100-unit increment and peak NT-proBNP is for 10-unit increment.
Data in parentheses are 95% CI.

uptake reflecting both regional and global LV dysfunction, as well as increased LV filling pressure. Since global LV remodeling and dysfunction are robust risk factors for heart failure and mortality after AMI (*1,23*), our findings indicate that [^{68}Ga]Ga-NODAGA-RGD uptake is a potentially relevant prognostic biomarker.

Uptake of [^{68}Ga]Ga-NODAGA-RGD and Ventricular Function After AMI

Despite improvements in acute management, AMI remains one of the most important causes of chronic heart failure (*1*). Early detection of myocardial responses to injury could provide the opportunity for targeting and monitoring therapies, such as therapeutic angiogenesis, to attenuate adverse LV remodeling and systolic dysfunction (*1,3,24*). A novel finding of our study is that increased indexed [^{68}Ga]Ga-NODAGA-RGD SUV_{max} was associated with improvement in global LV function at follow-up, independently of peak troponin T, elevated NT-proBNP, and impaired LVEF. Our finding is in line with preclinical and clinical data suggesting that increased $\alpha_v\beta_3$ integrin expression after AMI predicts improvement of regional LV function (*12*) and the absence of adverse remodeling (*7,21*). However, in our study, [^{68}Ga]Ga-NODAGA-RGD was not directly associated with the functional outcome of the myocardium in the AAR. This finding may be explained by the functional outcome's being dependent mainly on the extent of irreversible myocardial injury whereas the repair processes affect viable surrounding myocardium, impacting adverse LV remodeling and global LV function (*1*).

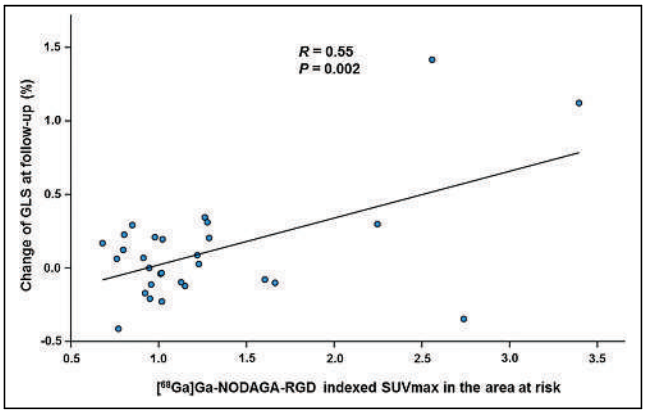

FIGURE 4. At follow-up, [^{68}Ga]Ga-NODAGA-RGD SUV_{max} in AAR predicted improvement of global longitudinal strain.

Limitations of Study

We studied patients within 3–14 d after AMI on the basis of experimental studies indicating that $\alpha_v\beta_3$ integrin expression peaks at 1–3 wk after AMI (*6*). There was no difference in the uptake of [^{68}Ga]Ga-NODAGA-RGD between patients scanned before versus after 7 d after AMI, indicating relatively stable uptake at this time. Our ability to detect associations between the uptake of [^{68}Ga]Ga-NODAGA-RGD and changes in LV structure and function may have been limited by the modest degree of changes and limited number of patients with significant LV remodeling despite a relatively long time from symptom onset to revascularization. Furthermore, cardiac MRI could have provided more precise quantification of cardiac structure and function than echocardiography despite a standardized, predefined protocol. The predictive value of endothelial progenitor cells, proposed to contribute to angiogenesis, versus [^{68}Ga]Ga-NODAGA-RGD PET for functional recovery remains to be explored in future studies. Although a formal power calculation was not feasible, the sample size of 30 patients would be sufficient—on the basis of a previous experimental study (*7*)—to detect differences in tracer uptake between those with and without significant remodeling.

CONCLUSION

In patients with AMI, [^{68}Ga]Ga-NODAGA-RGD uptake was increased in the ischemic AAR, correlating with the extent of myocardial injury, global and regional LV dysfunction, and LV filling pressure. Furthermore, [^{68}Ga]Ga-NODAGA-RGD uptake predicted global LV function improvement at the midterm follow-up. These results suggest that targeted imaging of $\alpha_v\beta_3$ integrin is a potential approach to evaluate myocardial injury responses after AMI.

DISCLOSURE

Financial support was received from grants from the Academy of Finland, the Finnish Foundation for Cardiovascular Research, and State Research Funding of Turku University Hospital. Antti Saraste discloses speaker or consultancy fees from Amgen, Abbott, Astra Zeneca, Bayer, Novartis, and Pfizer outside the submitted work. Juhani Knuuti discloses consultancy fees from GE Healthcare and speaker fees from GE Healthcare, Bayer, Lundbeck, Boehringer Ingelheim, Pfizer, Siemens, and Merck outside the submitted work. No other potential conflict of interest relevant to this article was reported.

KEY POINTS

QUESTION: We prospectively evaluated determinants of [^{68}Ga]Ga-NODAGA-RGD uptake, a PET tracer targeting $\alpha_v\beta_3$ integrin, after myocardial infarction and its associations with LV function at follow-up.

PERTINENT FINDINGS: In 31 patients with AMI, [^{68}Ga]Ga-NODAGA-RGD uptake increased in the ischemic AAR early after myocardial infarction, and this increase was associated with the severity of myocardial injury, LV systolic dysfunction, and increased LV filling pressure. Increased [^{68}Ga]Ga-NODAGA-RGD uptake predicted improvement of global LV function.

IMPLICATIONS FOR PATIENT CARE: Uptake of [^{68}Ga]Ga-NODAGA-RGD is a potentially relevant prognostic biomarker in AMI and might identify patients who could benefit from therapeutic interventions aimed at improving myocardial repair after AMI.

REFERENCES

1. Frantz S, Hundertmark MJ, Schulz-Menger J, Bengel FM, Bauersachs J. Left ventricular remodelling post-myocardial infarction: pathophysiology, imaging, and novel therapies. *Eur Heart J.* 2022;43:2549–2561.
2. Wu X, Reboll MR, Korf-Klingebiel M, Wollert KC. Angiogenesis after acute myocardial infarction. *Cardiovasc Res.* 2021;117:1257–1273.
3. Simons M, Alitalo K, Annex BH, et al. State-of-the-art methods for evaluation of angiogenesis and tissue vascularization: a scientific statement from the American Heart Association. *Circ Res.* 2015;116:e99–e132.
4. Sun M, Opavsky MA, Stewart DJ, et al. Temporal response and localization of integrins beta1 and beta3 in the heart after myocardial infarction: regulation by cytokines. *Circulation.* 2003;107:1046–1052.
5. Meoli DF, Sadeghi MM, Krassilnikova S, et al. Noninvasive imaging of myocardial angiogenesis following experimental myocardial infarction. *J Clin Invest.* 2004;113:1684–1691.
6. Higuchi T, Bengel FM, Seidl S, et al. Assessment of αvβ3 integrin expression after myocardial infarction by positron emission tomography. *Cardiovasc Res.* 2008;78:395–403.
7. Sherif HM, Saraste A, Nekolla SG, et al. Molecular imaging of early αvβ3 integrin expression predicts long-term left-ventricle remodeling after myocardial infarction in rats. *J Nucl Med.* 2012;53:318–323.
8. Laitinen I, Notni J, Pohle K, et al. Comparison of cyclic RGD peptides for αvβ3 integrin detection in a rat model of myocardial infarction. *EJNMMI Res.* 2013;3:38.
9. Kiugel M, Dijkgraaf I, Kytö V, et al. Dimeric [^{68}Ga]DOTA-RGD peptide targeting αvβ 3 integrin reveals extracellular matrix alterations after myocardial infarction. *Mol Imaging Biol.* 2014;16:793–801.
10. Grönman M, Tarkia M, Kiviniemi T, et al. Imaging of alphavbeta3 integrin expression in experimental myocardial ischemia with [^{68}Ga]NODAGA-RGD positron emission tomography. *J Transl Med.* 2017;15:144.
11. Sun Y, Zeng Y, Zhu Y, et al. Application of ^{68}Ga-PRGD2 PET/CT for αvβ3-integrin imaging of myocardial infarction and stroke. *Theranostics.* 2014;4:778–786.
12. Jenkins WS, Vesey AT, Stirrat C, et al. Cardiac αVβ3 integrin expression following acute myocardial infarction in humans. *Heart.* 2017;103:607–615.
13. Makowski MR, Rischpler C, Ebersberger U, et al. Multiparametric PET and MRI of myocardial damage after myocardial infarction: correlation of integrin αvβ3 expression and myocardial blood flow. *Eur J Nucl Med Mol Imaging.* 2021;48:1070–1080.
14. Gnesin S, Mitsakis P, Cicone F, et al. First in-human radiation dosimetry of ^{68}Ga-NODAGA-RGDyK. *EJNMMI Res.* 2017;7:43.
15. Lehtonen E, Teuho J, Koskinen J, et al. A respiratory motion estimation method based on inertial measurement units for gated positron emission tomography. *Sensors (Basel).* 2021;21:3983.
16. Grönman M, Tarkia M, Stark C, et al. Assessment of myocardial viability with [^{15}O]water PET: a validation study in experimental myocardial infarction. *J Nucl Cardiol.* 2021;28:1271–1280.
17. Rost C, Rost MC, Breithardt OA, et al. Relation of functional echocardiographic parameters to infarct scar transmurality by magnetic resonance imaging. *J Am Soc Echocardiogr.* 2014;27:767–774.
18. Antonov AS, Antonova GN, Munn DH, et al. αVβ3 integrin regulates macrophage inflammatory responses via PI3 kinase/Akt-dependent NF-κB activation. *J Cell Physiol.* 2011;226:469–476.
19. Sarrazy V, Koehler A, Chow ML, et al. Integrins αvβ5 and αvβ3 promote latent TGF-β1 activation by human cardiac fibroblast contraction. *Cardiovasc Res.* 2014;102:407–417.
20. van den Borne SW, Isobe S, Verjans JW, et al. Molecular imaging of interstitial alterations in remodeling myocardium after myocardial infarction. *J Am Coll Cardiol.* 2008;52:2017–2028.
21. Verjans J, Wolters S, Laufer W, et al. Early molecular imaging of interstitial changes in patients after myocardial infarction: comparison with delayed contrast-enhanced magnetic resonance imaging. *J Nucl Cardiol.* 2010;17:1065–1072.
22. MacAskill MG, Stadulyte A, Williams L, et al. Quantification of macrophage-driven inflammation during myocardial infarction with ^{18}F-LW223, a novel TSPO radiotracer with binding independent of the rs6971 human polymorphism. *J Nucl Med.* 2021;62:536–544.
23. Konstam MA, Kramer DG, Patel AR, Maron MS, Udelson JE. Left ventricular remodeling in heart failure: current concepts in clinical significance and assessment. *JACC Cardiovasc Imaging.* 2011;4:98–108.
24. Huang CC, Wei HJ, Lin KJ, et al. Multimodality noninvasive imaging for assessing therapeutic effects of exogenously transplanted cell aggregates capable of angiogenesis on acute myocardial infarction. *Biomaterials.* 2015;73:12–22.

Automated Motion Correction for Myocardial Blood Flow Measurements and Diagnostic Performance of ^{82}Rb PET Myocardial Perfusion Imaging

Keiichiro Kuronuma[1,2], Chih-Chun Wei[1], Ananya Singh[1], Mark Lemley[1], Sean W. Hayes[1], Yuka Otaki[1], Mark C. Hyun[1], Serge D. Van Kriekinge[1], Paul Kavanagh[1], Cathleen Huang[1], Donghee Han[1], Damini Dey[1], Daniel S. Berman[1], and Piotr J. Slomka[1]

[1]*Division of Artificial Intelligence in Medicine, Imaging, and Biomedical Sciences, Department of Medicine, Cedars-Sinai Medical Center, Los Angeles, California; and* [2]*Department of Cardiology, Nihon University, Tokyo, Japan*

Motion correction (MC) affects myocardial blood flow (MBF) measurements in ^{82}Rb PET myocardial perfusion imaging (MPI); however, frame-by-frame manual MC of dynamic frames is time-consuming. This study aims to develop an automated MC algorithm for time–activity curves used in compartmental modeling and compare the predictive value of MBF with and without automated MC for significant coronary artery disease (CAD). **Methods:** In total, 565 patients who underwent PET-MPI were considered. Patients without angiographic findings were split into training (n = 112) and validation (n = 112) groups. The automated MC algorithm used simplex iterative optimization of a count-based cost function and was developed using the training group. MBF measurements with automated MC were compared with those with manual MC in the validation group. In a separate cohort, 341 patients who underwent PET-MPI and invasive coronary angiography were enrolled in the angiographic group. The predictive performance in patients with significant CAD (≥70% stenosis) was compared between MBF measurements with and without automated MC. **Results:** In the validation group (n = 112), MBF measurements with automated and manual MC showed strong correlations (r = 0.98 for stress MBF and r = 0.99 for rest MBF). The automatic MC took less time than the manual MC (<12 s vs. 10 min per case). In the angiographic group (n = 341), MBF measurements with automated MC decreased significantly compared with those without (stress MBF, 2.16 vs. 2.26 mL/g/min; rest MBF, 1.12 vs. 1.14 mL/g/min; MFR, 2.02 vs. 2.10; all $P < 0.05$). The area under the curve (AUC) for the detection of significant CAD by stress MBF with automated MC was higher than that without (AUC, 95% CI, 0.76 [0.71–0.80] vs. 0.73 [0.68–0.78]; $P < 0.05$). The addition of stress MBF with automated MC to the model with ischemic total perfusion deficit showed higher diagnostic performance for detection of significant CAD (AUC, 95% CI, 0.82 [0.77–0.86] vs. 0.78 [0.74–0.83]; P = 0.022), but the addition of stress MBF without MC to the model with ischemic total perfusion deficit did not reach significance (AUC, 95% CI, 0.81 [0.76–0.85] vs. 0.78 [0.74–0.83]; P = 0.067). **Conclusion:** Automated MC on ^{82}Rb PET-MPI can be performed rapidly with excellent agreement with experienced operators. Stress MBF with automated MC showed significantly higher diagnostic performance than without MC.

Key Words: motion correction; myocardial perfusion imaging; myocardial blood flow; PET; rubidium

J Nucl Med 2024; 65:139–146
DOI: 10.2967/jnumed.123.266208

PET myocardial perfusion imaging (PET-MPI) with pharmacologic stress can assess absolute myocardial blood flow (MBF), which relates to disease severity in patients with coronary artery disease (CAD) (*1*). Myocardial motion is frequently observed during pharmacologic stress PET-MPI and can significantly affect MBF measurements (*2–6*). Hence, motion correction (MC) is crucial to obtain reliable MBF measurements by PET-MPI (*3*,*7*). We recently showed that the diagnostic performance of stress MBF and myocardial flow reserve (MFR) computed with the compartmental model and manual MC of time–activity curves was superior for predicting significant CAD when compared with stress MBF and MFR without correction in ^{18}F-flurpiridaz PET-MPI (*8*). However, frame-by-frame manual adjustment of image positions to correct time–activity curves is tedious and operator-dependent. This manual step adds difficulty to highly complex cardiovascular PET protocols. Recent studies showed that the automated MC yields MBF measurements similar to those of manual MC and improves repeatability and reproducibility (*9*,*10*). However, the diagnostic performance of MBF measurements with automated MC for predicting significant CAD compared with those without MC has not been studied.

We aimed to develop an automated MC algorithm for MBF quantification, compare MBF measurements with automated MC to those with manual MC, and assess the predictive performance of MBF with automated MC compared with MBF without MC for significant CAD by invasive coronary angiography (ICA).

MATERIALS AND METHODS

Study Population

To develop and validate the automated MC algorithm, 224 patients who underwent stress and rest ^{82}Rb PET-MPI at Cedars-Sinai Medical Center were retrospectively selected. The 224 patients were split into a training (n = 112) and a validation group (n = 112). Apart from this population, 341 consecutive patients without a history of prior CAD who underwent ^{82}Rb PET-MPI and ICA within 6 mo at Cedars-Sinai Medical Center from 2011 to 2018 were enrolled as an angiographic group. The study complies with the Declaration of Helsinki and was

Received Jun. 21, 2023; revision accepted Oct. 17, 2023.
For correspondence or reprints, contact Piotr Slomka (piotr.slomka@cshs.org).
Published online Nov. 30, 2023.

approved by the institutional review board at Cedars-Sinai Medical Center. All participants gave informed consent.

ICA

Significant CAD was visually evaluated using ICA by an experienced interventional cardiologist. Significant CAD was defined as having at least 50% stenosis in the left main trunk or at least 70% stenosis in the left anterior descending artery, left circumflex artery, or right coronary artery (RCA). For per-vessel analysis, significant left main trunk CAD was considered a disease in the left anterior descending and left circumflex arteries.

PET Protocol

Same-day, rest, and pharmacologic stress ^{82}Rb PET-MPI studies were performed for all patients on a Biograph 64 PET/CT scanner (Siemens Healthineers) or a Discovery 710 scanner (GE Healthcare). A 6-min rest list-mode acquisition was started immediately before the injection of weight-based doses of 10–12 MBq/kg of ^{82}Rb (925–1,850 MBq [25–50 mCi]). Pharmacologic stress with regadenoson, adenosine, or dipyridamole was performed, and a 6-min stress imaging acquisition was simultaneously initiated with the start of the ^{82}Rb infusion (10–12 MBq/kg). A low-dose helical CT scan was acquired before each rest and stress PET scan for attenuation correction as previously described (*11*).

Reconstruction

PET images were reconstructed using standard PET corrections (attenuation, randoms, scatter, dead time, decay). The 6-min list-mode data were reconstructed into 16 frames (12 frames, 10 s; 2 frames, 30 s; 1 frame, 60 s; and 1 frame, 120 s).

Automated Myocardial Contour Positioning

Left ventricular (LV) and right ventricular (RV) contours were automatically segmented from the summed image data from the last 4 min of the 6-min list-mode acquisition by QPET software (Cedars-Sinai) (*12*). PET images were automatically reoriented into short-axis and vertical and horizontal long-axis views. Quality control for all myocardial contours was performed by experienced technologists. Stress and rest total perfusion deficit was derived automatically using QPET software (*12*).

Manual MC

MC for the LV contour was performed manually in 1-mm steps at stress and rest to align the myocardial tracer uptake frame by frame by 2 experienced operators. For each frame, the operators shifted the image position to match the position of the LV contour. The third experienced operator reviewed the motion-corrected data and reconciled the MC results by a consensus with each operator. The MC in millimeters was quantified in 3 orthogonal directions (septal–lateral, superior–inferior, and apical–basal).

Automated MC

The motion of the heart in 3-dimensional space was automatically detected on each frame using the automatically segmented LV and RV contours as references. The image of each frame was translated in all 3 axes (septal–lateral, superior–inferior, and apical–basal directions) by the algorithm to align with the static contours. A previous study showed that over 5 mm of myocardial motion can lead to significant alterations in the MBF measurements (*13*), so we defined significant myocardial motion as a maximum shift greater than 5 mm in an acquisition. All cases were processed in a fully automated batch mode.

Algorithm for Automated MC

The LV and RV contours generated by segmenting the summed image of the last 4 min of the acquisition were used to define a static 3-dimensional geometric model of the ventricles, which included the endocardial and epicardial surfaces of the left and right ventricles, the cavities within the endocardial surfaces, and the myocardium between. Our automated MC algorithm was based on aligning individual image

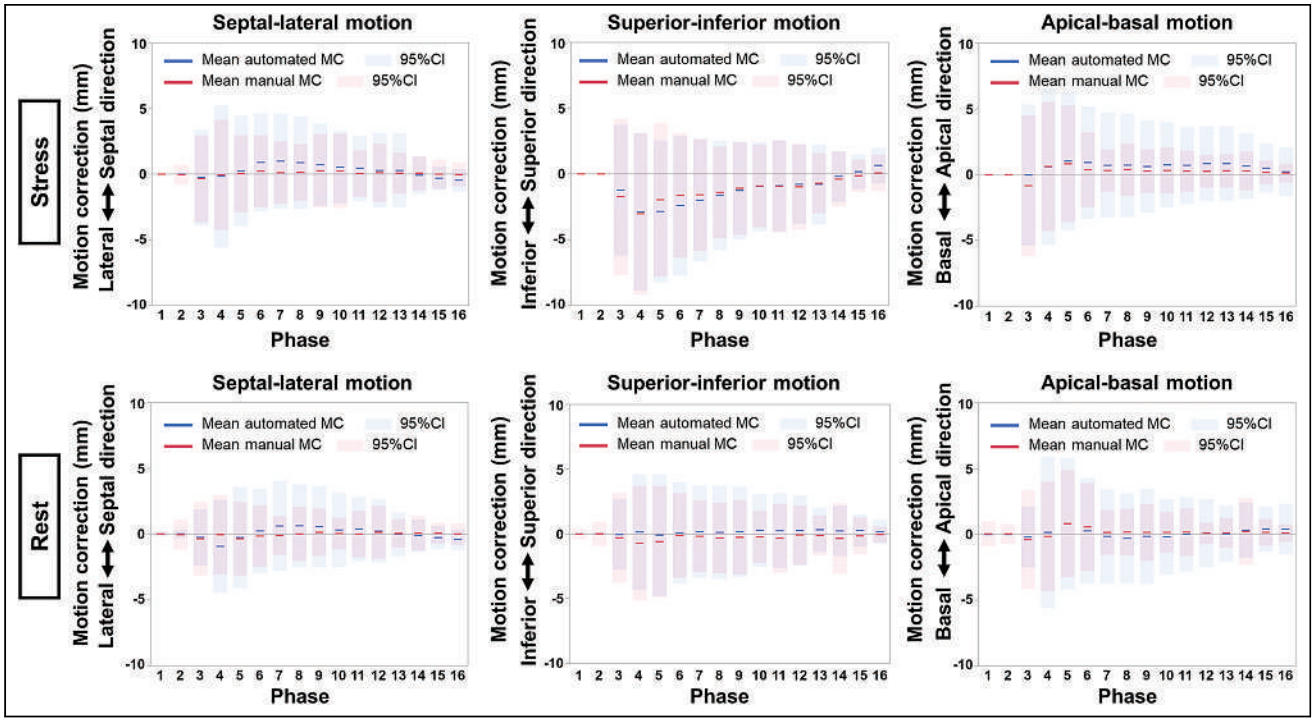

FIGURE 1. Mean automated and manual MC on stress (top) and rest (bottom) acquisition per phase in validation group. Solid lines indicate means, and shaded areas indicate 95% CIs (blue for automated and red for manual MC).

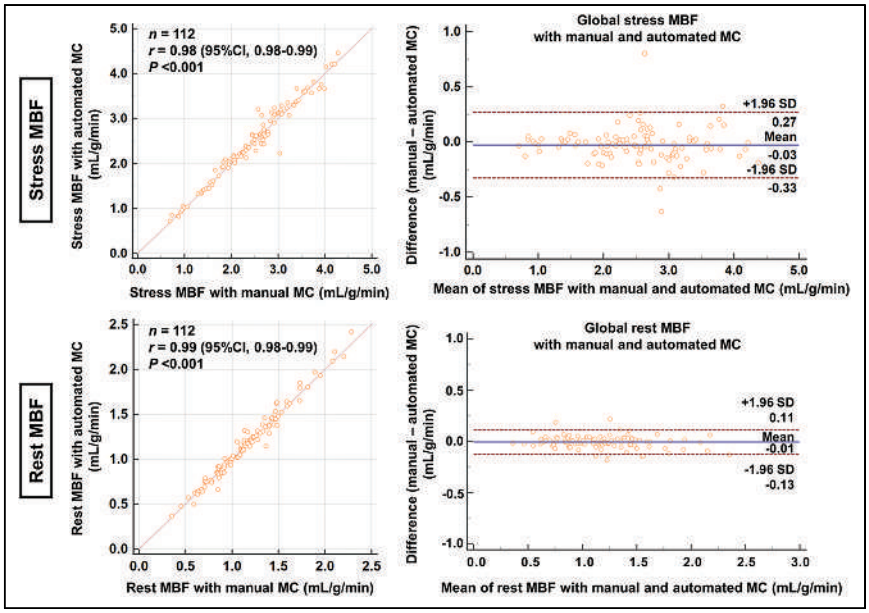

FIGURE 2. Correlation and Bland–Altman plots between MBF measurements with automated and manual MC in validation group for global stress MBF (mL/g/min) (top) and global rest MBF (mL/g/min) (bottom).

frames to this geometric model using 3-dimensional rigid-body translations. Stress and rest acquisitions were corrected independently.

For image frames in the LV blood-pool phase, the LV myocardium phase, and the transition between, 3 key frames based on the time–activity curves of the LV input region of interest (ROI) and LV myocardium were identified: an LV blood-pool peak frame where the LV input ROI activity curve had a maximal value, an LV blood-pool and myocardium crossover frame where the LV input ROI and LV myocardium curves intersected, and the very last frame with nearly all the counts in the myocardium. These key frames were selected for the well-defined correspondence of their tracer activity distribution to the regions defined in the geometric model of the heart. Each of the 3 key frames was aligned independently to the geometric model by numeric maximization of similarity metrics. Components of similarity metrics included total counts in different regions defined in the model (to be maximized or minimized), gradients of counts at the epi- and endomyocardial surfaces, uniformity of counts within the LV myocardium, and mutual information between the original image and a pseudo one generated from numerically labeling the model regions. Three different similarity metric functions based on these components were used to reflect the different characteristics of tracer activity distribution to separately align each of these 3 key frames of the kinetic study to the model as follows: LV blood-pool peak, where tracer activity was expected to concentrate in the cavity within the LV endocardial surface; LV blood-pool and myocardium crossover, where activity was expected to fill both the LV cavity and myocardium; and end of acquisition, where activity was concentrated within the LV myocardium.

For each frame between the LV peak and LV crossover key frames, the 2 key frames were linearly blended into a synthetic reference using the ratios of total counts in the LV myocardium to counts in the LV input ROI as weights. Similarly, a synthetic reference was generated for each frame between the LV crossover and the end of acquisition

TABLE 1
Patient Characteristics of Angiographic Group

Parameter	Overall	Significant CAD	No significant CAD	*P*
n	341	206 (60.4)	135 (39.6)	
Age (y)	71.3 ± 12.2	73.5 ± 11.5	68.0 ± 12.6	<0.001
Male sex	229 (67.2)	142 (68.9)	87 (64.4)	0.411
Body mass index (kg/m^2)	28.5 ± 6.7	28.0 ± 6.1	29.2 ± 7.4	0.127
Hypertension	260 (76.2)	161 (78.2)	99 (73.3)	0.362
Dyslipidemia	214 (62.8)	130 (63.1)	84 (62.2)	0.909
Diabetes	122 (35.8)	74 (35.9)	48 (35.6)	0.999
Family history of CAD	50 (14.7)	29 (14.1)	21 (15.6)	0.755
Smoking	31 (9.1)	14 (6.8)	17 (12.6)	0.083
PVD	38 (11.1)	29 (14.1)	9 (6.7)	0.035
History of CAD	0 (0)	0 (0)	0 (0)	
Stress agent				
Regadenoson	324 (95.0)	196 (95.1)	128 (94.8)	0.576
Adenosine	16 (4.7)	10 (4.9)	6 (4.4)	
Dipyridamole	1 (0.3)	1 (0.7)	0 (0)	

PVD = peripheral vascular disease.
Categoric values are expressed as *n* with percentage in parentheses; continuous values are expressed as mean ± SD.

TABLE 2
ICA Results in Angiographic Group (n = 341)

Result	Number
Significant LM disease	12 (3.5%)
Significant LAD disease	137 (40.2%)
Significant LCX disease	90 (26.4%)
Significant RCA disease	112 (32.8%)
Significant CAD	206 (60.4%)

LM = left main trunk; LAD = left anterior descending artery; LCX = left circumflex artery.

by the same linear blending process. These in-between frames were then registered to the references using simplex maximization of the mutual information criterion (*14*).

Lastly, image frames in the RV phase before the LV blood-pool phase, which were defined as any frames at or after the RV input ROI peak and before the LV input ROI peak, were individually registered to the geometric model using a fourth similarity metric designed to align the activity with the right ventricle while minimizing counts in the LV myocardium.

MBF and MFR Quantification

Rest and stress MBF was calculated by clinical software (QPET) with a 1-tissue-compartment kinetic model (*15*). MBF and the spillover fraction from the blood to the myocardium were computed by numeric optimization. Stress and rest MBF values in mL/g/min were computed for each sample on the polar map. The rate–pressure product (RPP) was calculated by heart rate (bpm) times systolic blood pressure (mm Hg) and used for rest MBF adjustment in the angiographic group by (rest MBF × RPP average)/RPP. The average RPP value in the angiographic group was 9,720 bpm × mm Hg (*16*). MFR was computed as the ratio of stress over the rest MBF adjusted by RPP. All MBF values were calculated automatically in batch mode.

Diagnostic Performance for Predicting Significant CAD

To evaluate the diagnostic performance for significant CAD, minimal vessel stress MBF or MFR (lowest stress MBF or MFR value in the left anterior descending artery, left circumflex artery, and RCA territories) was used.

Statistical Analysis

Categoric variables are presented as frequencies, and continuous variables as mean ± SD or median and interquartile ranges. Variables were compared using the Pearson χ^2 statistic for categoric variables. For continuous variables, a 2-sample t test was used to compare unpaired samples, and a paired t test was used to compare paired samples. The correlation of stress and rest MBF values between automated and manual MC was assessed using Pearson correlation analysis and Bland–Altman plots. Homogeneity of variances between automated and manual MC was checked by the Levene test for stress and rest MBF. The diagnostic performance of minimal vessel stress MBF, MFR, and ischemic total perfusion deficit (iTPD) (stress total perfusion deficit − rest total perfusion deficit) for predicting significant CAD was evaluated by pairwise comparisons of the areas under the receiver operating characteristic curve (AUC) by DeLong et al. (*17*) and paired binary comparisons using a threshold of 2.0 mL/g/min for MBF and 2.0 for MFR (*18*) by the McNemar test (*19*). Since minimal

TABLE 3
Global and Territorial MFR, Stress MBF, and Rest MBF According to Myocardial Motion in Angiographic Group

	Overall (n = 341)			Motion ≤ 5 mm at stress*			Motion > 5 mm at stress†		
Parameter	Auto MC	No MC	P	Auto MC	No MC	P	Auto MC	No MC	P
MFR									
Global	2.02 ± 0.85	2.10 ± 0.85	<0.001	1.99 ± 0.77	1.98 ± 0.76	0.788	2.04 ± 0.89	2.15 ± 0.89	<0.001
LAD	2.02 ± 0.89	2.00 ± 0.89	0.201	2.02 ± 0.82	1.98 ± 0.80	0.071	2.02 ± 0.93	2.01 ± 0.93	0.554
LCX	2.00 ± 0.82	2.04 ± 0.80	0.009	1.94 ± 0.72	1.93 ± 0.69	0.521	2.03 ± 0.86	2.12 ± 0.87	0.002
RCA	2.06 ± 0.93	2.23 ± 1.02	<0.001	2.00 ± 0.84	2.04 ± 0.88	0.141	2.08 ± 0.89	2.29 ± 1.03	<0.001
Stress MBF									
Global	2.16 ± 0.86	2.26 ± 0.86	<0.001	2.27 ± 0.87	2.29 ± 0.90	0.229	2.11 ± 0.85	2.25 ± 0.84	<0.001
LAD	2.19 ± 0.91	2.21 ± 0.93	0.232	2.33 ± 0.92	2.32 ± 0.95	0.861	2.12 ± 0.91	2.15 ± 0.91	0.175
LCX	2.19 ± 0.85	2.30 ± 0.86	<0.001	2.27 ± 0.85	2.30 ± 0.88	0.085	2.16 ± 0.86	2.30 ± 0.85	<0.001
RCA	2.11 ± 0.89	2.28 ± 0.95	<0.001	2.20 ± 0.92	2.24 ± 0.97	0.117	2.07 ± 0.87	2.30 ± 0.95	<0.001
Rest MBF									
Global	1.12 ± 0.42	1.14 ± 0.41	0.021	1.18 ± 0.44	1.18 ± 0.44	0.241	1.05 ± 0.38	1.07 ± 0.37	0.042
LAD	1.14 ± 0.44	1.17 ± 0.44	<0.001	1.19 ± 0.46	1.21 ± 0.45	0.005	1.08 ± 0.39	1.11 ± 0.41	0.008
LCX	1.15 ± 0.42	1.17 ± 0.42	0.002	1.20 ± 0.45	1.21 ± 0.45	0.110	1.07 ± 0.37	1.10 ± 0.37	0.009
RCA	1.08 ± 0.42	1.08 ± 0.42	0.474	1.14 ± 0.44	1.13 ± 0.44	0.262	1.00 ± 0.39	1.00 ± 0.38	0.963

*n = 106 for MFR and stress MBF but 202 for rest MBF.
†n = 235 for MFR and stress MBF but 139 for rest MBF.
LAD = left anterior descending artery; LCX = left circumflex artery.
MBF measurements according to significant myocardial motion, myocardial motion greater than 5 mm.

vessel stress, MBF, and MFR showed higher diagnostic performance than global stress MBF and MFR, we used minimal vessel stress MBF and MFR to assess the diagnostic performance (*8*). The vascular territorial segmentation was based on standardized myocardial segmentation (*20*). A 2-tailed P value of less than 0.05 was considered statistically significant. All statistical analyses were performed with R version 4.2.0 (R Foundation for Statistical Computing) or MedCalc version 20.210 (MedCalc Software).

RESULTS

Comparison of Stress and Rest MBF with Automated MC and Manual MC Table

Figure 1 shows the mean MC and 95% CI per frame for stress and rest imaging in each direction in the validation group. Although the direction of MC was similar between automated and manual MC, the variances (ranges of the adjustment) were greater for the automated software (all $P < 0.005$). Supplemental Figure 1 shows the scatterplots of the automated and manual MC per frame for stress and rest imaging (supplemental materials are available at http://jnm.snmjournals.org). MC at stress in the inferior direction, especially in the early phase, was greater than in the other directions (Fig. 1; Supplemental Fig. 1). The processing time of the automatic MC was less than 12 s, which was faster than the manual MC, which took approximately 10 min per case. Figure 2 shows the correlation and Bland–Altman plots between stress and rest MBF with automated and manual MC. Strong correlations between automated and manual MC were seen in the stress MBF ($r = 0.98$, $P < 0.001$) and the rest MBF ($r = 0.99$, $P < 0.001$). There was no significant difference between stress and rest MBF with automated and manual MC ($P = 0.068$ for stress MBF and $P = 0.157$ for rest MBF).

Patient Characteristics of the Angiographic Cohort

The baseline characteristics of the angiographic group are shown in Table 1. The mean age was 71 y, and 67% (229/341) were male. The mean interval between the PET-MPI and ICA was 19 d, and 60% (206/341) of patients had significant CAD. Table 2 shows the results of the ICA.

Comparison Between MBF and MFR With and Without Automated MC

Similar to the validation group, myocardial motion in the inferior direction, especially in the early phase at stress, was greater than in the other directions in the angiographic group (Supplemental Fig. 2). The MFR and stress and rest MBF measurements before and after MC for global and each vascular territory measurement are shown in Table 3. Overall, mean flow measurements and SD were lower for those with automated MC than without MC (Table 3). In the angiographic group, 52 of 341 (15.2%) and 62 of 341 (18.2%) patients had a change of more than 20% before and after MC in global stress MBF and global MFR, respectively. Among the 3 vascular territories, the stress MBF and MFR in the RCA territory showed the largest decrease after automated MC compared with those without MC (mean stress MBF in RCA, 2.11 ± 0.89 mL/min/g vs. 2.28 ± 0.95 mL/min/g; $P < 0.001$; mean MFR in RCA, 2.06 ± 0.93 vs. 2.23 ± 1.02; $P < 0.001$) (Table 3). When patients were divided into groups with and without myocardial motion greater than 5 mm, those with greater myocardial motion showed larger differences in flow measurements before and after MC than those with less myocardial motion (Table 3). Myocardial motion over 5 mm was observed in 69% (235/341) of patients at stress and 41% (139/341) at rest (Table 3). Global and territorial spillover fractions for stress and rest images were lower for images with automated MC than for those without (Supplemental Table 1). Figure 3 and Supplemental Figure 3 show a case example of a significant change in flow measurements before and after automated MC.

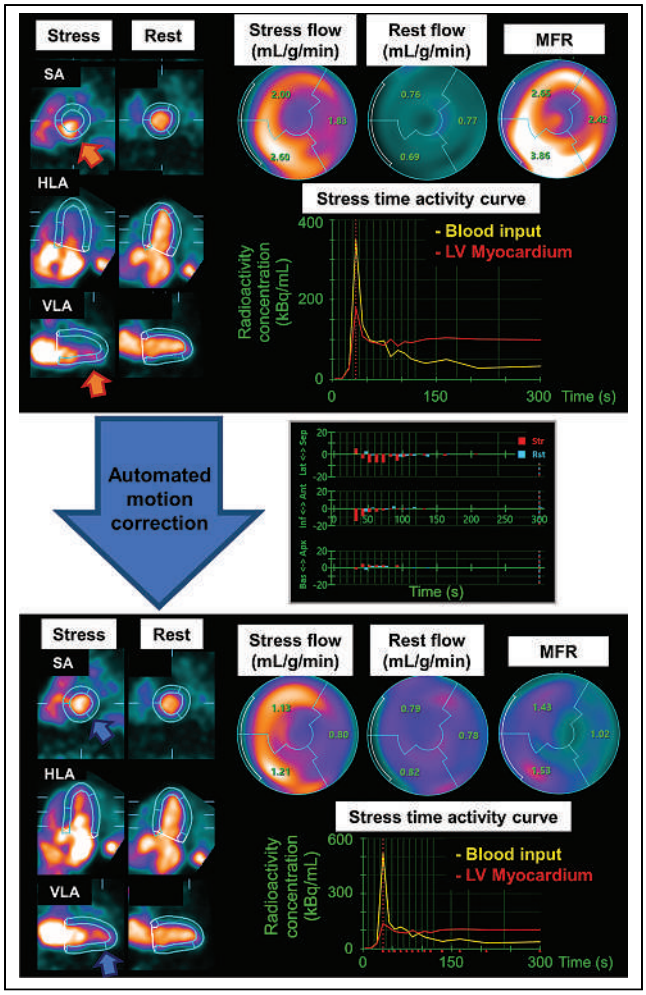

FIGURE 3. Case example of automated MC in patient with significant myocardial motion: early dynamic images before (above) and after (below) automated MC. LV contours before MC were automatically computed from summed frames after 2 min. Before correction, inferior LV contour overlapped substantially with activity of blood pool, and anterior LV contour was far from actual LV myocardium (orange arrows). Time–activity curve shows LV myocardial activities are overestimated before MC (red curve). Curves were corrected after automated MC (blue arrows); however, myocardial contours after automated MC contain some remaining activity at apex. Middle graph shows MC results for each direction and each frame (maximum magnitude of MC was 19.9 mm at stress and 6.3 mm at rest). Global MFR decreased from 2.90 to 1.33 after MC. Although patient showed normal perfusion, coronary angiography showed significant stenosis in proximal left anterior descending (LAD) artery and RCA (Supplemental Fig. 3). Ant = anterior; Apx = apical; Bas = basal; HLA = horizontal long axis; Inf = inferior; Lat = lateral; SA = short axis; Sep = septal; VLA = vertical long axis.

Diagnostic Performance of Stress MBF and MFR With and Without Automated MC

The AUC of minimal vessel stress MBF with automated MC for predicting significant CAD was significantly higher than that without MC (AUC, 0.76 vs. 0.73; $P = 0.047$) (Fig. 4). The AUC

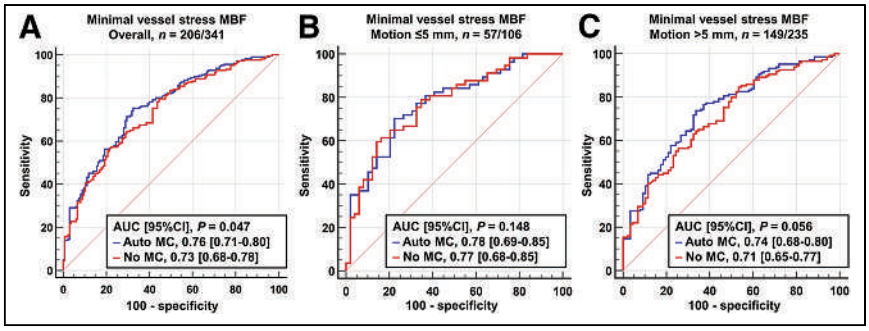

FIGURE 4. Diagnostic performance of minimal vessel stress MBF for prediction of significant CAD in angiographic group in all patients (A), patients without significant myocardial motion (B), and those with significant myocardial motion (C).

of minimal vessel MFR with automated MC was trending higher than that without MC (AUC, 0.74 vs. 0.72; $P = 0.073$) (Supplemental Fig. 4). When the patients were stratified into groups with and without motion greater than 5 mm at stress ($n = 235$), a myocardial motion greater than 5 mm trended toward higher AUC by stress MBF with automated MC than that without MC (AUC, 0.74 vs. 0.71; $P = 0.056$), but the AUCs with and without automated MC were comparable in patients with myocardial motion less than 5 mm (AUC, 0.78 vs. 0.77; $P = 0.148$) (Fig. 4).

Figure 5 shows the sensitivity and specificity for predicting significant CAD by minimal vessel stress MBF with and without automated MC using the threshold of 2.0 mL/g/min. The sensitivity using automated MC was significantly higher than that without (75.2% vs. 68.4%; $P = 0.002$). Overall, the minimal vessel stress MBF measurements with automated MC performed significantly better than without MC (difference, 5.9% [95% CI, 2.5%–9.3%]; $P = 0.001$) (Supplemental Table 2). Supplemental Figure 5 shows the results of the same analysis using minimal vessel MFR. Although there was no significant difference for sensitivity (77.7% vs. 77.2%, $P = 0.999$), the specificity using automated MC was significantly higher than that without MC (57.0% vs. 49.6%, $P = 0.021$). Overall, minimal vessel MFR measurements with automated MC tended to agree better with ICA; however, the difference was not significant (difference, 3.2% [95% CI, −0.1%–6.5%]; $P = 0.080$) (Supplemental Table 3).

The addition of minimal vessel stress MBF with automated MC to the model with iTPD alone improved discrimination for predicting significant CAD (AUC, 0.82 vs. 0.78; $P = 0.022$), but the addition of stress MBF without MC to iTPD alone did not (AUC, 0.81 vs. 0.78; $P = 0.067$) (Fig. 6). Similar findings were observed when using minimal vessel MFR (Supplemental Fig. 6).

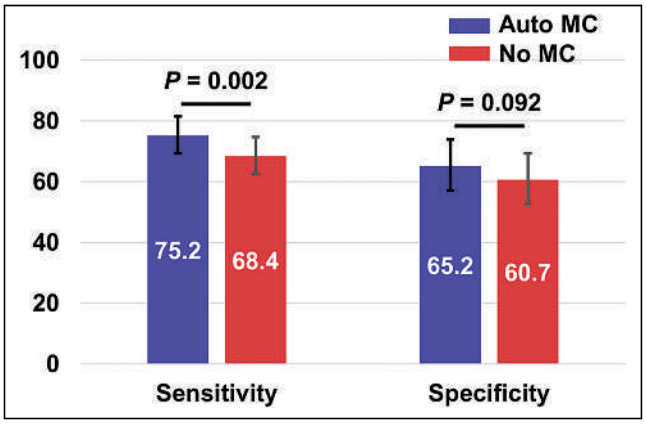

FIGURE 5. Sensitivity and specificity for predicting significant CAD by minimal vessel stress MBF of 2.0 mL/g/min in angiographic group.

DISCUSSION

We developed an algorithm of automated MC for dynamic PET-MPI to improve the reliability of MBF measurements. We compared, for the first time to our knowledge, the diagnostic performance of MBF measurements with automated MC to those without MC. The main findings of this study are as follows: in the validation group, there were strong correlations and no significant difference between MBF measurements with automated and manual MC; in the angiographic group, MBF measurements decreased significantly after automated MC compared with those before MC; minimal vessel stress MBF with automated MC showed higher diagnostic performance for predicting significant CAD; and adding stress MBF with automated MC to the model with only iTPD significantly improved the diagnostic performance, but adding stress MBF without MC did not.

In the validation group, stress and rest MBF results with automated MC were strongly correlated with manual MC by experienced operators ($r > 0.95$), and there was no significant difference between those ($P > 0.05$). These results were in line with previous studies using automated MC by different software (*9*,*10*). In addition, the processing time of the automatic MC was shorter than that of the manual MC (<12 s vs. 10 min per case). Thus, MBF quantification using automatic MC software could be incorporated into clinical practice, reducing cardiovascular PET protocol complexity. Our algorithm performs the rigid-body translation. It is possible that excluding rotational correction may lead to suboptimal MC especially for the patients with rotational heart motion. However, the degree of rotational correction is usually small. In previous studies, it was reported to be less than 2° for over 90% of patients (*21*). It is unclear how the addition of rotational MC to a simple 3-dimensional translational MC affects the MBF measurements. Adding rotational correction may provide an optimal MC, especially for the patients with rotational motion of the heart; however, the addition of rotational correction is complicated and may not be suitable for MC in daily clinical settings because of time-consuming quality checks. The algorithm was designed to automate only the steps that are currently performed manually by the clinicians, so in the case of failure, they could be easily adjusted by a human operator. In the angiographic group, we compared MBF measurements before and after automated MC. Overall, MBF measurements with automated MC decreased significantly compared with those without automated MC, which is consistent with prior studies (*3*,*4*,*9*). The most significant changes in the MBF and MFR were in the RCA territory (Table 3), consistent with previous studies (*4*,*9*). The etiology of myocardial motion during dynamic scanning is considered to be primarily myocardial creep (*22*). Previous studies showed that up to 66% of patients undergoing pharmacologic stress dynamic PET-MPI showed significant myocardial motion (>5 mm) or myocardial creep during dynamic scans, primarily in the inferior direction (*3*–*6*). This largely inferior direction of myocardial motion, myocardial creep, could cause a spillover of blood-pool activity during the early phase into the LV myocardial contour and increase MBF measurements, especially in the RCA

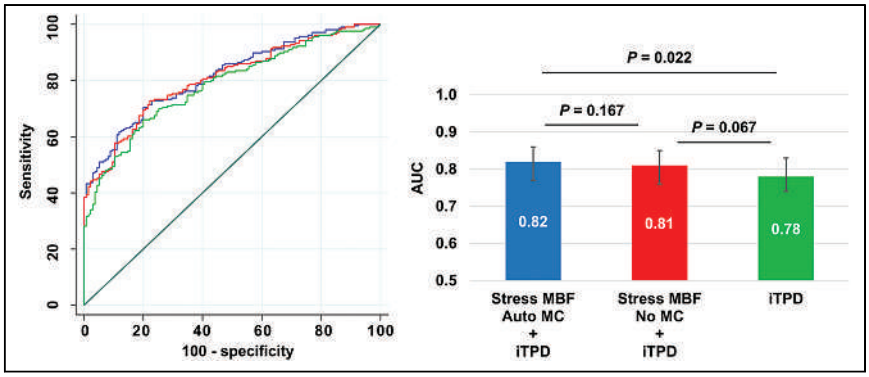

FIGURE 6. Receiver operating characteristic curves (left) and AUC bar plots (right) for predicting significant CAD in angiographic group.

territory (*23*). In the present study, a trend similar to that in previous studies was shown (*3*–*6*); myocardial motion at stress in the inferior direction was greater than in the other directions, and 69% of patients showed significant myocardial motion at stress (>5 mm). Because MC had a greater impact on MBF measurements in patients with significant myocardial motion than in those without (Table 3), MC would be important, especially for the patients with significant myocardial motion (>5 mm), to obtain dependable MBF measurements.

A previous study demonstrated the feasibility of automated MC for MBF measurements on dynamic PET-MPI (*9*). In our study, we show, for the first time to our knowledge, that the diagnostic performance of stress MBF with automated MC for predicting significant CAD was significantly higher than without MC. The AUCs of minimal vessel stress MBF with automated MC were significantly higher than those without. The addition of stress MBF with automated MC to the model with iTPD alone showed significantly higher AUC, but the addition of stress MBF without MC to iTPD did not. There was significant difference between stress MBF with and without MC alone (AUC, 0.76 vs. 0.73; $P = 0.047$; Fig. 4). This seemingly minor difference would have a substantial impact on significant CAD prediction given the large number of PET-MPI studies performed. Because MBF measurements with automated MC showed a consistently higher diagnostic performance for predicting significant CAD than those without, MC should be considered an essential processing step when performing MBF measurements.

Although there is an inherent uncertainty of MBF measurements of approximately 20% (*24*), part of this variability is likely due to myocardial motion. In our population, 52 of 341 patients (15.2%) changed stress MBF by over 20% before and after the MC. Therefore, MC can potentially reduce the variability of MBF measurements.

Our study results should be interpreted in the context of some limitations. Our MC algorithm was developed using ^{82}Rb PET-MPI studies only; however, over 90% of cardiac PET studies in the U.S. use ^{82}Rb for PET-MPI (*25*). This MC algorithm has been evaluated with a compartmental modeling approach. The effect of this approach has not been evaluated for net retention models. Because we defined significant CAD only by the visual assessment on ICA, some patients without significant stenosis (<70%) may have physiologically significant CAD and some with at least 70% stenosis may not (*26*,*27*), and the use of flow fractional reserve values may be more accurate for assessing physiologically significant CAD. In addition, patients without significant stenosis may have impaired stress MBF and MFR due to coronary microvascular disease (*28*). Finally, because our study is a single-center retrospective study, it may have an inherent selection bias, and our results may not generalize to other populations.

CONCLUSION

An automated MC algorithm for dynamic PET-MPI showed good agreement with manual MC by experienced operators. Compared with MBF measurements without MC, those with MC were significantly decreased and had a consistently higher diagnostic performance for predicting significant CAD. Automated MC can be performed rapidly to obtain reliable MBF measurements; therefore, it should be incorporated into routine PET-MPI studies to reduce the complexity of cardiovascular protocols.

DISCLOSURE

This research was supported in part by grant R01EB034586 from the National Institute of Biomedical Imaging and Bioengineering at the National Institutes of Health (to Piotr Slomka) and a grant from the Dr. Miriam and Sheldon G. Adelson Medical Research Foundation. The content is solely the responsibility of the authors and does not necessarily represent the official views of the National Institutes of Health. Daniel Berman, Piotr Slomka, Serge Van Kriekinge, and Paul Kavanagh participate in software royalties for QPET software at Cedars-Sinai Medical Center. Daniel Berman is a consultant for GE Healthcare. Piotr Slomka received grants from Siemens Medical Systems and consulting fees from Synektik, S.A. No other potential conflict of interest relevant to this article was reported.

KEY POINTS

QUESTION: What is the effect of the automatic MC algorithm for MBF measurements of PET on the diagnostic performance of MBF for predicting CAD?

PERTINENT FINDINGS: For the first time to our knowledge, we demonstrated that stress MBF with automated MC had significantly higher diagnostic performance in predicting significant CAD than without the MC.

IMPLICATIONS FOR PATIENT CARE: MC for MBF measurements can be performed fully automatically, and MBF with automated MC has better diagnostic performance than without. Therefore, this approach should be incorporated into routine PET-MPI studies.

REFERENCES

1. Uren NG, Melin JA, De Bruyne B, Wijns W, Baudhuin T, Camici PG. Relation between myocardial blood flow and the severity of coronary-artery stenosis. *N Engl J Med.* 1994;330:1782–1788.
2. Votaw JR, Packard RRS. Technical aspects of acquiring and measuring myocardial blood flow: method, technique, and QA. *J Nucl Cardiol.* 2018;25:665–670.

3. Lee BC, Moody JB, Poitrasson-Rivière A, et al. Blood pool and tissue phase patient motion effects on ^{82}rubidium PET myocardial blood flow quantification. *J Nucl Cardiol.* 2019;26:1918–1929.
4. Koenders SS, van Dijk JD, Jager PL, Ottervanger JP, Slump CH, van Dalen JA. Impact of regadenoson-induced myocardial creep on dynamic rubidium-82 PET myocardial blood flow quantification. *J Nucl Cardiol.* 2019;26:719–728.
5. von Felten E, Benetos G, Patriki D, et al. Myocardial creep-induced misalignment artifacts in PET/MR myocardial perfusion imaging. *Eur J Nucl Med Mol Imaging.* 2021;48:406–413.
6. van Dijk JD, Jager PL, Ottervanger JP, Slump CH, van Dalen JA. No need for frame-wise attenuation correction in dynamic rubidium-82 PET for myocardial blood flow quantification. *J Nucl Cardiol.* 2019;26:738–745.
7. Koenders SS, van Dijk JD, Jager PL, Ottervanger JP, Slump CH, van Dalen JA. How to detect and correct myocardial creep in myocardial perfusion imaging using rubidium-82 PET? *J Nucl Cardiol.* 2019;26:729–734.
8. Otaki Y, Van Kriekinge SD, Wei C-C, et al. Improved myocardial blood flow estimation with residual activity correction and motion correction in ^{18}F-flurpiridaz PET myocardial perfusion imaging. *Eur J Nucl Med Mol Imaging.* 2022;49:1881–1893.
9. Lee BC, Moody JB, Poitrasson-Rivière A, et al. Automated dynamic motion correction using normalized gradient fields for ^{82}rubidium PET myocardial blood flow quantification. *J Nucl Cardiol.* 2020;27:1982–1998.
10. Choueiry J, Mistry NP, Beanlands RSB, deKemp RA. Automated dynamic motion correction improves repeatability and reproducibility of myocardial blood flow quantification with rubidium-82 PET imaging. *J Nucl Cardiol.* 2023;30:1133–1146.
11. Miller RJH, Han D, Singh A, et al. Relationship between ischaemia, coronary artery calcium scores, and major adverse cardiovascular events. *Eur Heart J Cardiovasc Imaging.* 2022;23:1423–1433.
12. Nakazato R, Berman DS, Dey D, et al. Automated quantitative Rb-82 3D PET/CT myocardial perfusion imaging: normal limits and correlation with invasive coronary angiography. *J Nucl Cardiol.* 2012;19:265–276.
13. Rajaram M, Tahari AK, Lee AH, et al. Cardiac PET/CT misregistration causes significant changes in estimated myocardial blood flow. *J Nucl Med.* 2013;54:50–54.
14. Slomka PJ, Dey D, Przetak C, Aladl UE, Baum RP. Automated 3-dimensional registration of stand-alone ^{18}F-FDG whole-body PET with CT. *J Nucl Med.* 2003;44:1156–1167.
15. Dekemp RA, Declerck J, Klein R, et al. Multisoftware reproducibility study of stress and rest myocardial blood flow assessed with 3D dynamic PET/CT and a 1-tissue-compartment model of ^{82}Rb kinetics. *J Nucl Med.* 2013;54:571–577.
16. Murthy VL, Naya M, Taqueti VR, et al. Effects of sex on coronary microvascular dysfunction and cardiac outcomes. *Circulation.* 2014;129:2518–2527.
17. DeLong ER, DeLong DM, Clarke-Pearson DL. Comparing the areas under two or more correlated receiver operating characteristic curves: a nonparametric approach. *Biometrics.* 1988;44:837–845.
18. Murthy VL, Bateman TM, Beanlands RS, et al. Clinical quantification of myocardial blood flow using PET: joint position paper of the SNMMI Cardiovascular Council and the ASNC. *J Nucl Med.* 2018;59:273–293.
19. McNemar Q. Note on the sampling error of the difference between correlated proportions or percentages. *Psychometrika.* 1947;12:153–157.
20. Pereztol-Valdés O, Candell-Riera J, Santana-Boado C, et al. Correspondence between left ventricular 17 myocardial segments and coronary arteries. *Eur Heart J.* 2005;26:2637–2643.
21. Nye JA, Piccinelli M, Hwang D, et al. Dynamic cardiac PET motion correction using 3D normalized gradient fields in patients and phantom simulations. *Med Phys.* 2021;48:5072–5084.
22. Votaw JR, Packard RRS. Motion correction to enhance absolute myocardial blood flow quantitation by PET. *J Nucl Cardiol.* 2020;27:1114–1117.
23. Armstrong IS, Memmott MJ, Saint KJ, Saillant A, Hayden C, Arumugam P. Assessment of motion correction in dynamic rubidium-82 cardiac PET with and without frame-by-frame adjustment of attenuation maps for calculation of myocardial blood flow. *J Nucl Cardiol.* 2021;28:1334–1346.
24. Kitkungvan D, Johnson NP, Roby AE, Patel MB, Kirkeeide R, Gould KL. Routine clinical quantitative rest stress myocardial perfusion for managing coronary artery disease: clinical relevance of test-retest variability. *JACC Cardiovasc Imaging.* 2017;10:565–577.
25. Klein R, Celiker-Guler E, Rotstein BH, deKemp RA. PET and SPECT tracers for myocardial perfusion imaging. *Semin Nucl Med.* 2020;50:208–218.
26. Pijls NH, De Bruyne B, Peels K, et al. Measurement of fractional flow reserve to assess the functional severity of coronary-artery stenoses. *N Engl J Med.* 1996;334:1703–1708.
27. Bech GJ, De Bruyne B, Pijls NH, et al. Fractional flow reserve to determine the appropriateness of angioplasty in moderate coronary stenosis: a randomized trial. *Circulation.* 2001;103:2928–2934.
28. Mileva N, Nagumo S, Mizukami T, et al. Prevalence of coronary microvascular disease and coronary vasospasm in patients with nonobstructive coronary artery disease: systematic review and meta-analysis. *J Am Heart Assoc.* 2022;11:e023207.

MRI or ^{18}F-FDG PET for Brain Age Gap Estimation: Links to Cognition, Pathology, and Alzheimer Disease Progression

Elena Doering[1,2], Georgios Antonopoulos[3,4], Merle Hoenig[1,5], Thilo van Eimeren[1,2], Marcel Daamen[2], Henning Boecker[2], Frank Jessen[2,6], Emrah Düzel[7], Simon Eickhoff[3,4], Kaustubh Patil*[3,4], and Alexander Drzezga*[1,2,5]
for the Alzheimer's Disease Neuroimaging Initiative and the DELCODE Study Group

[1]*Department of Nuclear Medicine, Faculty of Medicine and University Hospital Cologne, University of Cologne, Cologne, Germany;* [2]*German Center for Neurodegenerative Diseases, Bonn, Germany;* [3]*Brain and Behavior, Research Center Juelich, Juelich, Germany;* [4]*Institute of Systems Neuroscience, Heinrich Heine University, Duesseldorf, Germany;* [5]*Molecular Organization of the Brain, Research Center Juelich, Juelich, Germany;* [6]*Department of Psychiatry, Faculty of Medicine and University Hospital Cologne, University of Cologne, Cologne, Germany; and* [7]*German Center for Neurodegenerative Diseases, Magdeburg, Germany*

Deviations of brain age from chronologic age, known as the brain age gap (BAG), have been linked to neurodegenerative diseases such as Alzheimer disease (AD). Here, we compare the associations of MRI-derived (atrophy) or ^{18}F-FDG PET–derived (brain metabolism) BAG with cognitive performance, neuropathologic burden, and disease progression in cognitively normal individuals (CNs) and individuals with subjective cognitive decline (SCD) or mild cognitive impairment (MCI). **Methods:** Machine learning pipelines were trained to estimate brain age from 185 matched T1-weighted MRI or ^{18}F-FDG PET scans of CN from the Alzheimer's Disease Neuroimaging Initiative and validated in external test sets from the Open Access of Imaging and German Center for Neurodegenerative Diseases–Longitudinal Cognitive Impairment and Dementia studies. BAG was correlated with measures of cognitive performance and AD neuropathology in CNs, SCD subjects, and MCI subjects. Finally, BAG was compared between cognitively stable and declining individuals and subsequently used to predict disease progression. **Results:** MRI (mean absolute error, 2.49 y) and ^{18}F-FDG PET (mean absolute error, 2.60 y) both estimated chronologic age well. At the SCD stage, MRI-based BAG correlated significantly with beta-amyloid$_{1\text{-}42}$ ($A\beta_{1\text{-}42}$) in cerebrospinal fluid, whereas ^{18}F-FDG PET BAG correlated with memory performance. At the MCI stage, both BAGs were associated with memory and executive function performance and cerebrospinal fluid $A\beta_{1\text{-}42}$, but only MRI-derived BAG correlated with phosphorylated-tau$_{181}$/$A\beta_{1\text{-}42}$. Lastly, MRI-estimated BAG predicted MCI-to-AD progression better than ^{18}F-FDG PET–estimated BAG (areas under the curve, 0.73 and 0.60, respectively). **Conclusion:** Age was reliably estimated from MRI or ^{18}F-FDG PET. MRI BAG reflected cognitive and pathologic markers of AD in SCD and MCI, whereas ^{18}F-FDG PET BAG was sensitive mainly to early cognitive impairment, possibly constituting an independent biomarker of brain age-related changes.

Key Words: machine learning; cognitive impairment; neuroimaging

J Nucl Med 2024; 65:147–155
DOI: 10.2967/jnumed.123.265931

Brain aging entails changes in cognitive performance, brain function, and structural parameters of brain integrity. Brain age can be modeled using machine learning algorithms by estimating a person's chronologic age from their neuroimaging data. Higher brain age than chronologic age, that is, a positive brain age gap (BAG), is associated with neurodegenerative diseases such as Alzheimer disease (AD). A recent study (*1*) linked BAG with PET AD biomarkers in patients with mild cognitive impairment (MCI) and with progression from cognitively normal (CN) to MCI, or MCI to dementia. This warrants further research on BAG as a marker of individual cognitive performance and neuropathologic burden in at-risk populations for AD dementia (subjective cognitive decline [SCD] and MCI).

Age-related changes are evident in the brain's anatomy, such as loss of brain volume (atrophy), as well as in metabolism (neuronal dysfunction), which can be quantified by T1-weighted MRI and ^{18}F-FDG PET, respectively. ^{18}F-FDG PET is generally acknowledged as an earlier indicator of neurodegeneration than is structural MRI, as neuronal dysfunction precedes atrophy (i.e., neuronal loss). Moreover, regional proneness to age-related decline is different when assessed with ^{18}F-FDG PET or MRI (*2*). Consequently, it is plausible to assume that an ^{18}F-FDG PET–derived BAG is more sensitive to neuronal changes preceding neurodegeneration, such as neuropathologic burden or cognitive deficits below the threshold of AD. To date, however, brain age estimation (BAE) frameworks are almost exclusively modeled from MRI data. One recent study compared the 2 modalities and showed highly accurate BAE when using either MRI or ^{18}F-FDG PET (*1*). This argues for further exploration of ^{18}F-FDG PET–derived BAG and its performance in delineating the earliest deviations from normal aging in the absence of dementia.

Here, we investigated ^{18}F-FDG PET– and MRI-derived BAE, with a particular focus on how BAG is associated with cognitive performance, neuropathologic burden, and disease progression in cognitively unimpaired individuals and MCI patients. First, we estimated brain age in cohorts of individuals who were CN, had subjective but not objective cognitive impairment (SCD), or showed MCI. Second, we calculated BAG and compared associations of

Received May 5, 2023; revision accepted Sep. 27, 2023.
For correspondence or reprints, contact Elena Doering (elena.doering@uk-koeln.de).
*Contributed equally to this work.
Published online Nov. 30, 2023.

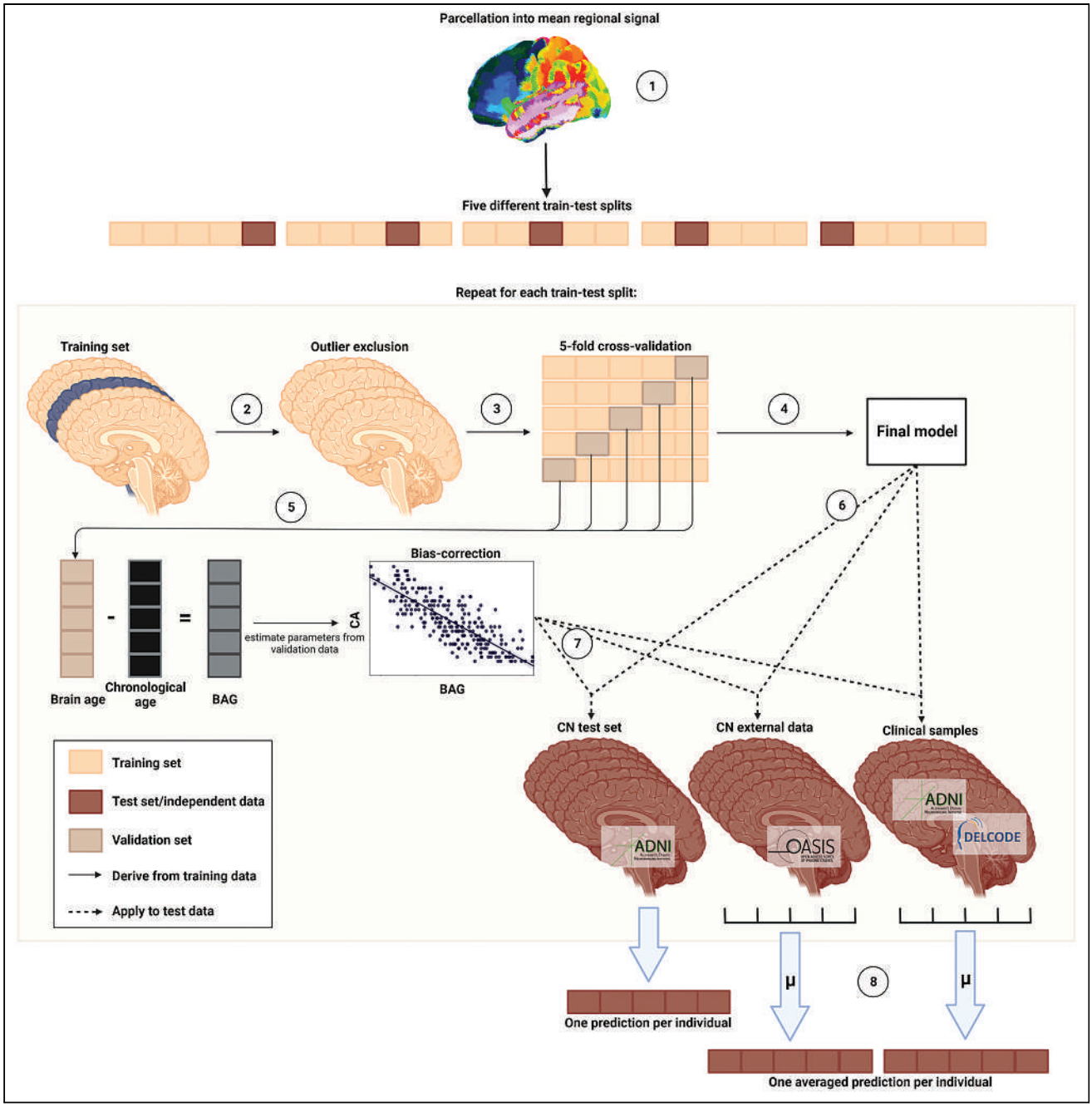

FIGURE 1. Nested cross-validation approach for brain age prediction. (*1*) Region-of-interest parcellation. (*2*) Outlier exclusion. (*3*) Five-fold cross-validation. (*4*) Final model selection. (*5*) Bias correction. (*6*) Estimation of brain age in test sets. (*7*) Bias correction in test sets. (*8*) Ensemble averaging. (Created with BioRender.com.)

^{18}F-FDG PET– or MRI-derived BAG with cognitive performance and AD neuropathology in these cohorts. Finally, we evaluated the prognostic value of BAG in predicting disease progression as compared with other established risk factors of cognitive decline.

MATERIALS AND METHODS

The code used for this project is available on GitHub.

Participants

Baseline T1-weighted MRI and ^{18}F-FDG PET scans of 185 CNs (interscan interval, 28 ± 23 d) were acquired from the Alzheimer's Disease Neuroimaging Initiative (ADNI) database (https://adni.loni.usc.edu/). For external validation, 49 MRI and ^{18}F-FDG PET scans of CNs were acquired from the Open Access of Imaging Studies database, release 3 (*3*) (OASIS, https://www.oasis-brains.org/). We also assessed brain age in clinical samples of SCD (n = 102) and MCI (n = 595) patient groups from ADNI. The significant findings from these analyses were subsequently validated in SCD (^{18}F-FDG PET, n = 88) and MCI (MRI, n = 80) samples from the German Center for Neurodegenerative Diseases–Longitudinal Cognitive Impairment and Dementia study (DELCODE) (*4*). CN, SCD, and MCI diagnoses from ADNI, OASIS, and DELCODE followed current recommendations for the respective

TABLE 1
Overview of Samples

Parameter	ADNI CN	OASIS CN	ADNI SCD	ADNI MCI	DELCODE SCD	DELCODE MCI
n total	186	49	102	595	88	80
Age at PET scan (y)	73.8 (6.46)	70.6 (5.07)*	72.3 (5.60)*	73.2 (6.93)	70.9 (5.57)*	NA
Age at MRI scan (y)	73.8 (6.44)	69.2 (4.98)*	72.3 (5.60)*	73.2 (6.92)	NA	73.4 (5.87)
Sex (female, %)	53% (0)	53% (0)	59% (0)	42% (2)*	36% (0)*	36% (0)*
MMSE score	29 (1.26)	29 (0.78)	29 (1.20)	28 (1.75)*	29 (1.03)	28 (1.67)*
Education (y)	16 (2.54)	16 (2.51)	17 (2.50)*	16 (2.67)	16 (3.00)	14 (3.06)*
CSF $A\beta_{1\text{-}42}$–positive (%)	41% (27)	NA	35% (9)	64% (126)*	22% (28)*	38% (38)
APOE-ε4 carrier (%)	29% (1)	NA	31% (0)	49% (4)*	38% (3)	49% (0)*
Progression status decliner (%)	10% (32)	NA	12% (19)	25% (135)	NA	38% (12)

*Significantly different from ADNI CD. $P < 0.05$.
NA = not applicable.
Categorical data are percentages with number of individuals with missing information in parentheses; continuous data are means with SD in parentheses. Percentage of CSF $A\beta_{1\text{-}42}$ status indicates percentage of amyloid-positive individuals according to established thresholds.

groups (details are provided in Supplemental Section 1a; supplemental materials are available at http://jnm.snmjournals.org) (*5,6*). All participants gave written consent. Data collection was approved by local institutional review boards, and ethics proposals for retrospective dataset analysis were approved by Heinrich Heine University Düsseldorf.

Estimation of Brain Age

Standardized MRI and ^{18}F-FDG PET scans were used to compute brain age (details on acquisition and preprocessing are in Supplemental Section 1b). We implemented a pipeline (Fig. 1) in Python 3.8.5 using the Julearn library (https://juaml.github.io/julearn/main/index.html), which is based on scikit-learn (*7*). The same pipeline was run independently for MRI and ^{18}F-FDG PET. First, a modality-specific signal of 90 cortical and subcortical regions of interest was extracted (MRI: gray matter volume; ^{18}F-FDG PET: SUV ratio) using the automated anatomic labeling atlas (*8*). The atlas dependence of our results was assessed by repeating our analyses with a second composite atlas (Schaeffer + Tian atlas). We applied a nested cross-validation approach, with 5 folds in both the outer and the inner cross-validation. Outlier exclusion was performed in the outer cross-validation. Subsequently, support or relevance vector regression models, recommended for small sample sizes (*9*), were trained with hyperparameter optimization to compute brain age in the inner cross-validation loop. Selection of the final model across support and relevance vector regression models was based on the mean absolute error of the validation folds. Estimation of bias correction parameters was then based on predictions from the validation folds (*10*). The final model was used to estimate brain age in the test and clinical samples, and bias correction was applied (Supplemental Sections 1c–1e).

The nested cross-validation approach yielded one brain age per nonoutlier subject in the ADNI CNs, who were evenly spread across 5 test sets. Each cross-validation fold additionally yielded one estimate per subject in the OASIS and clinical samples; thus, the average of 5 estimates was treated as the final brain age (ensemble averaging).

Statistical Analyses

BAG was calculated for each individual as the difference between brain age and chronologic age, such that higher BAG reflected more advanced brain age and vice versa.

Accuracy, Generalizability, and Variation of BAG. The accuracy of age estimation from MRI or ^{18}F-FDG PET was assessed by comparing the mean absolute error of BAE across modalities using a paired t-test in the ADNI CN sample. To assess the generalizability of our BAE frameworks, we compared the mean absolute error of MRI- or ^{18}F-FDG PET–based BAE between ADNI CNs and OASIS CNs using t-tests. Whether BAG was higher in the clinical populations was assessed by t-test comparisons of average BAG between ADNI CNs and each clinical sample.

Regional Importance. To understand the similarity of brain age models and to test whether AD-typical regions are relevant in BAE from MRI or ^{18}F-FDG PET, we assessed Pearson correlations of BAG and feature importance (δ) across modalities in ADNI CNs. Feature importance was computed using permutation importance, with higher values corresponding to greater relevance of a feature for the model. For simplicity, we computed correlations using the average feature importance over all final models per modality. We further summarized regional feature importance per modality into median signal for lobes (frontal, temporal, limbic, subcortical, occipital, parietal; details are in Supplemental Section 1f), hemispheres (left, right), and lobes by hemisphere to assess whether brain regions of a particular category were preferred for BAE in a given modality.

Cognitive and AD-Neuropathologic Associations. To assess whether BAG is associated with cognitive performance, we calculated partial correlations between BAG and composite scores of memory (ADNI memory) (*11*) and executive function (ADNI executive function) (*12*) for the ADNI CN, ADNI SCD, and ADNI MCI groups (Supplemental Section 1g). In addition, partial correlations of BAG with PET amyloid load (^{18}F-AV-45 PET) (*13*), and cerebrospinal fluid (CSF) markers (*14*) of beta-amyloid$_{1\text{-}42}$ ($A\beta_{1\text{-}42}$), and phosphorylated-tau$_{181}$ (p-tau$_{181}$)–to–$A\beta_{1\text{-}42}$ ratio (p-tau$_{181}$/$A\beta_{1\text{-}42}$) (Supplemental Section 1h) (*15*) were calculated to assess whether BAG is associated with AD neuropathology. Pearson or Spearman correlations were assessed, depending on normality (Shapiro–Wilk test), and all partial correlations were corrected for age, sex, education, and APOE-ε4 carriership. Individuals with missing data for the dependent variable were excluded for each respective correlation. A P value of less than 0.1 was considered trend-significant, and a P value of less than 0.05 was considered significant. We also assessed the significance after Bonferroni correction (cognitive performance: $\alpha = 0.05/2$, AD neuropathology: $\alpha = 0.05/3$).

TABLE 2
Accuracy of Estimating Age from ^{18}F-FDG PET and MRI Scans

Parameter	Modality	*n*	MAE	Range	BAG	R^2	Accuracy (MAE MRI vs. ^{18}F-FDG PET)	Generalizability (MAE current vs. ADNI CN)	Brain age advancement (BAG current vs. ADNI CN)
ADNI CN	MRI	175*	2.49	−9.4 to 8.7	0.06	0.74	t = 0.48 (−0.33 to 0.55)	NA	NA
	^{18}F-FDG PET	175*	2.60	−10.1 to 9.6	−0.10	0.70		NA	
OASIS CN	MRI	49*	2.92	−7.1 to 8.4	0.13	0.42	t = −0.94 (−1.20 to 0.43)	t = 1.16 (−0.31, 1.18)	t = 0.12 (−1.12, 1.26)
	^{18}F-FDG PET	49*	2.54	−5.0 to 6.8	0.89	0.63		t = −0.18 (−0.64, 0.53)	t = 2.00† (0.01, 1.97)
ADNI SCD	MRI	102	2.50	−6.6 to 7.0	0.11	0.69	t = 0.26 (−0.42 to 0.54)	NA	t = 0.11 (−0.73, 0.82)
	^{18}F-FDG PET	102	2.56	−5.6 to 9.8	0.64	0.69		NA	t = 1.86‡ (−0.05, 1.53)
ADNI MCI	MRI	595	3.30	−10.5 to 13.5	2.16	0.65	t = −5.72¶ (0.95 to 0.46)	NA	t = 7.47¶ (1.55, 2.65)
	^{18}F-FDG PET	595	2.59	−10.0 to 11.0	0.55	0.78		NA	t = 2.23† (0.08, 1.22)
DELCODE SCD	^{18}F-FDG PET	88	3.16	−2.7 to 9.3	2.77	0.52	NA	NA	t = 7.45¶ (2.11, 3.63)
DELCODE MCI	MRI	80	3.69	−5.1 to 11.6	2.89	0.38	NA	NA	t = 6.04¶ (1.90, 3.75)

*After outlier exclusion using CN train set (IQR > 6).
†$P < 0.05$.
‡$P < 0.1$.
¶$P <$ Bonferroni correction.
MAE = mean absolute error.
Data in parentheses are 95% CIs.

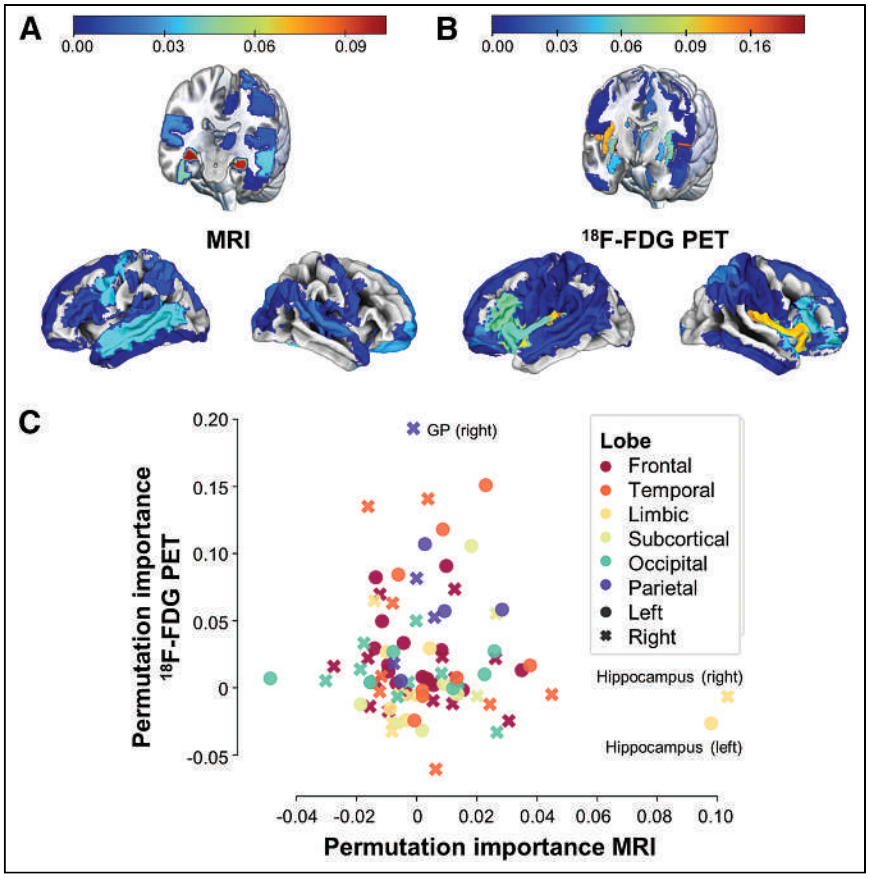

FIGURE 2. Feature importance for brain age prediction. (A and B) Average regional importance for brain age prediction using MRI (A) and ^{18}F-FDG PET (B, threshold applied at 0). (C) Average feature importance across final models from ^{18}F-FDG PET and MRI by lobe (colors) and hemisphere (shapes). GP = globus pallidus.

Disease Progression. Finally, we assessed whether BAG is associated with or even predicts disease progression. Relative to baseline BAG assessment, we differentiated between cognitively stable individuals, who maintained their baseline diagnosis until the 2-y follow-up, and decliners, who received a diagnosis of more severe cognitive impairment within follow-up (Supplemental Section 1i). Using analysis of covariance, the BAG between stable individuals and decliners was compared, while correcting for sex, education, and APOE-ε4 carriership in ADNI CNs and ADNI SCD subjects and additionally for age in ADNI MCI subjects (where bias correction did not eliminate the correlation between age and MRI BAG, Supplemental Section 2a). Subsequently, we trained multiple single-feature logistic regression classifiers using stratified 10-fold cross-validation to predict progression to AD in ADNI MCI from ^{18}F-FDG PET BAG; MRI BAG; hippocampal volume (*16*); global ^{18}F-AV-45 PET SUV ratio; ^{18}F-FDG PET SUV ratio in the precuneus (*17*); ^{18}F-FDG PET SUV ratio in a meta–region of interest, previously suggested relevant for the progression of AD (*18*); p-tau$_{181}$/A$\beta_{1\text{-}42}$ ratio; ADNI memory score; or age. Notably, the small number of decliners prevented the development of reliable predictive machine learning models in the ADNI CN and ADNI SCD groups. To correct for the effects of age, sex, education, and APOE status, standardized residuals were computed for all

TABLE 3
Associations of BAG with Cognitive Performance and AD Neuropathology

Parameter	Modality	Cognitive performance		AD neuropathology		
		ADNI executive function	ADNI memory	^{18}F-AV-45	CSF A$\beta_{1\text{-}42}$	p-tau$_{181}$/A$\beta_{1\text{-}42}$
ADNI CN	MRI	r = 0.016 (−0.14 to 0.18)	r = −0.001 (−0.16 to 0.16)	ρ = −0.003 (−0.17 to 0.16)	ρ = 0.004 (−0.17 to 0.18)	ρ = 0.029 (−0.15 to 0.20)
	^{18}F-FDG PET	r = 0.101 (−0.06 to 0.26)	r = 0.095 (−0.07 to 0.25)	ρ = 0.011 (−0.15 to 0.17)	ρ = −0.110 (−0.28 to 0.06)	ρ = 0.141 (−0.03 to 0.31)
ADNI SCD	MRI	r = 0.048 (−0.18 to 0.27)	r = −0.132 (−0.34 to 0.09)	ρ = 0.014 (−0.21 to 0.24)	r = −0.238* (−0.44 to −0.01)	ρ = 0.017 (−0.21 to 0.25)
	^{18}F-FDG PET	r = −0.190† (−0.39 to 0.03)	r = −0.259‡ (−0.45 to −0.04)	ρ = 0.191† (−0.03 to 0.40)	r = −0.161 (−0.38 to 0.07)	ρ = 0.087 (−0.15 to 0.31)
ADNI MCI	MRI	r = −0.225‡ (−0.31 to −0.14)	ρ = −0.397‡ (−0.47 to −0.32)	ρ = 0.095† (−0.01 to 0.02)	ρ = −0.230‡ (−0.32 to −0.13)	ρ = 0.200‡ (0.10 to 0.30)
	^{18}F-FDG PET	r = −0.238‡ (−0.32 to −0.15)	ρ = −0.179‡ (−0.27 to −0.09)	ρ = 0.056 (−0.05 to 0.16)	ρ = −0.126* (−0.22 to −0.02)	ρ = 0.101† (−0.00 to 0.20)

*P < 0.05.
†P < 0.1.
‡P < Bonferroni correction.
n is described in Supplemental Tables 1 and 2. Data in parentheses are 95% CIs.

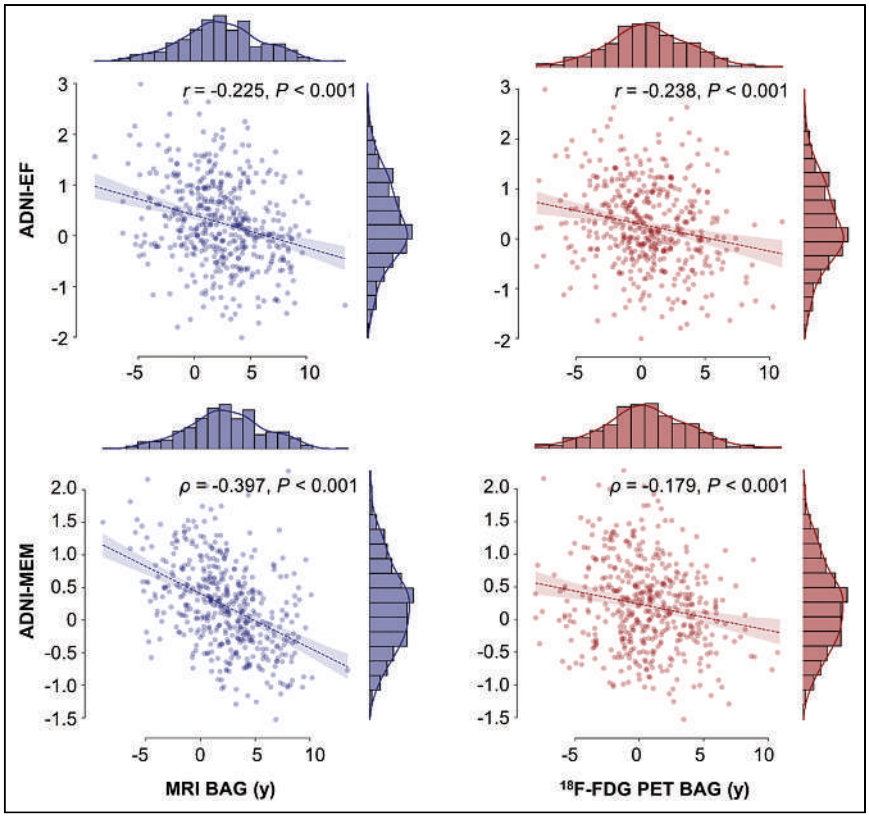

FIGURE 3. Correlation of BAG with cognitive performance in ADNI MCI. EF = executive function; MEM = memory. Correlations include correction for age, sex, and education.

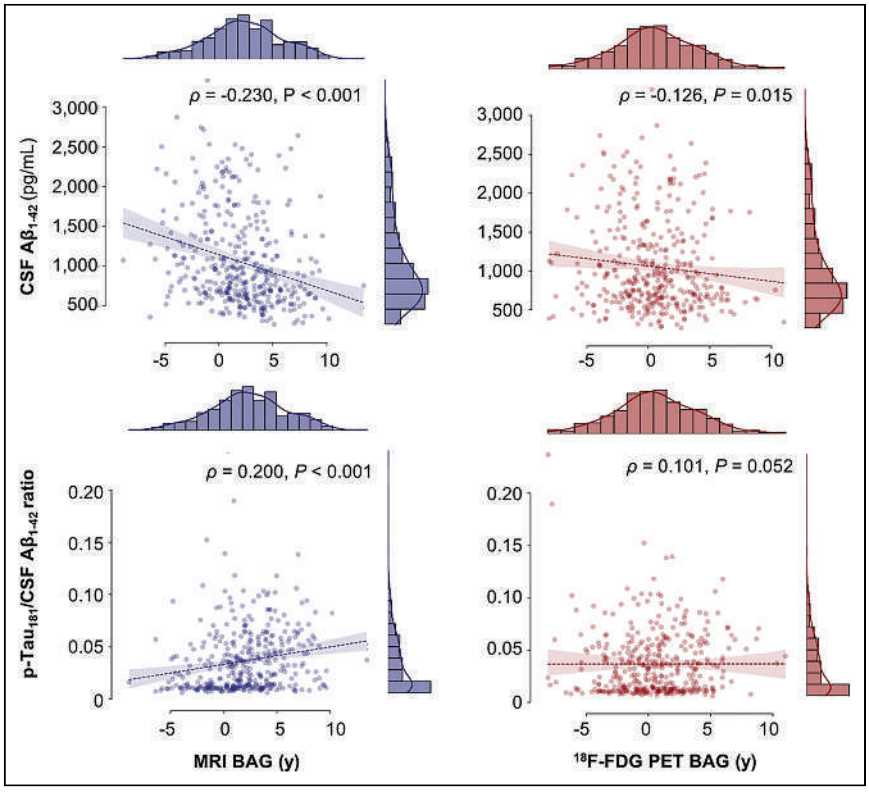

FIGURE 4. Correlation of BAG with AD neuropathology in ADNI MCI. Correlations include correction for age, sex, and education.

individuals and for each predictor variable using a linear model trained on the stable individuals in each training fold (*19*). We compared the mean area under the curve (AUC) obtained from the validation folds across all predictors. If the BAG of one modality predicted disease progression (AUC > 0.7), we derived a cutoff given the a priori probability of disease progression in each training fold and validated this cutoff in the DELCODE MCI cohort.

RESULTS

Participants

An overview of participant characteristics is shown in Table 1. OASIS CN, ADNI SCD, and DELCODE SCD subjects were significantly younger than the main ADNI CN cohort. The SCD and MCI cohorts further differed from ADNI CNs in terms of cognitive performance (ADNI MCI and DELCODE MCI), years of education (ADNI SCD and DELCODE MCI), amyloid status (DELCODE SCD and ADNI MCI), and APOE-ε4 carriership distribution (ADNI MCI and DELCODE MCI).

Accuracy, Generalizability, and Variation of BAG

MRI and ^{18}F-FDG PET estimated age with comparably high accuracy in ADNI CNs (mean absolute error, 2.49 for MRI and 2.60 for ^{18}F-FDG PET; Table 2). Within-modality comparison of mean absolute error in OASIS CNs and ADNI CNs yielded no significant differences (2.92 for MRI OASIS and 2.54 for ^{18}F-FDG PET OASIS), suggesting that our frameworks have high generalization performance to external datasets comprising CN populations. Average ^{18}F-FDG PET–derived, but not MRI-derived, BAG was trend-significantly advanced in ADNI SCD subjects. Comparably, ^{18}F-FDG PET BAG was significantly advanced in DELCODE SCD subjects. In all MCI samples, BAG was significantly higher than in ADNI CNs across modalities. Bias correction successfully eliminated the correlation of BAG and age with the exception of MRI-derived BAG in ADNI MCI individuals (Supplemental Table 3). Results using the composite atlas were largely comparable to those obtained here (Supplemental Table 4).

Regional Importance

BAG was trend-significantly correlated between MRI- and ^{18}F-FDG PET–based models (r = 0.128; P = 0.09; 95% CI, −0.02 to 0.27). Model selection returned different model types with mostly linear

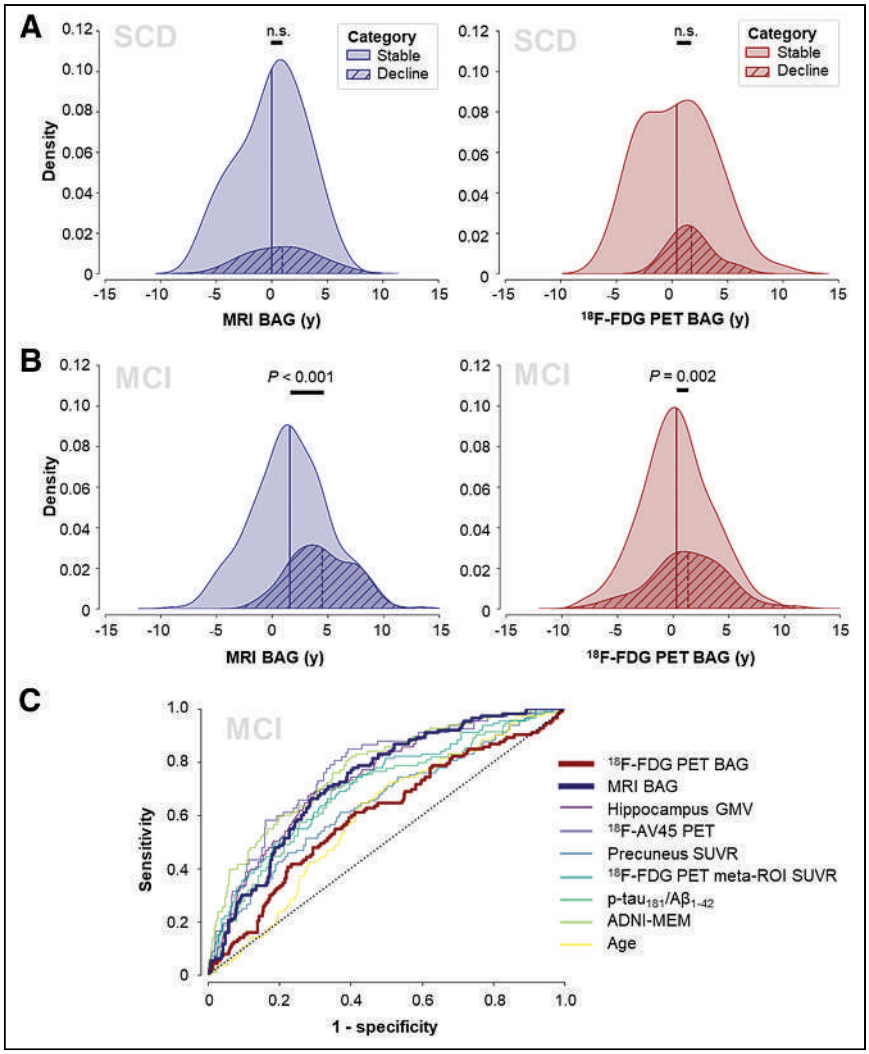

FIGURE 5. BAG for prediction of disease progression. Density plots show MRI and ^{18}F-FDG PET BAG distribution by disease progression status in ADNI SCD (A) and ADNI MCI (B) and AUCs of prediction of disease progression (C). GMV = gray matter volume; MEM = memory; n.s. = not statistically significant; SUVR = SUV ratio.

kernels (Supplemental Table 5). The left and right hippocampi were most relevant for MRI-based BAE (δ = 0.098 on left and 0.103 on right), whereas median permutation importance in the lobes, hemispheres, or lobes by hemisphere showed no obvious trends (Fig. 2). The subcortical regions (δ = 0.058: 0.058 on left and 0.067 on right) and, to a lesser extent, the left-hemispheric frontal (δ = 0.013) and temporal (δ = 0.012) regions were most relevant for ^{18}F-FDG PET–based BAE. No overall hemispheric preference was observed for ^{18}F-FDG PET models. Average regional importance did not correlate between MRI- and ^{18}F-FDG PET–based models (r = −0.069; P = 0.52; 95% CI, −0.27 to 0.14).

BAG and Cognitive Performance

In ADNI CNs, neither MRI nor ^{18}F-FDG PET BAG was associated with cognitive performance (Table 3). In the ADNI SCD group, ^{18}F-FDG PET BAG was significantly negatively associated with memory performance after Bonferroni correction and was trend-significantly associated with executive function. MRI BAG did not correlate with these measures (Table 3). In the ADNI MCI group, both MRI- and ^{18}F-FDG PET–derived BAG was significantly negatively correlated with executive and memory performance after Bonferroni correction (Table 3; Fig. 3).

BAG and AD Neuropathology

BAG and AD neuropathology did not significantly correlate in ADNI CNs. In the ADNI SCD group, lower levels of amyloid in CSF significantly correlated with increased MRI BAG, and a higher amyloid load in PET was trend-significantly associated with elevated ^{18}F-FDG PET BAG (Table 3). In the ADNI MCI group, MRI BAG was trend-significantly correlated with all 3 markers of AD neuropathology, whereas ^{18}F-FDG PET BAG was associated only with the CSF pathology markers (Table 3; Fig. 4).

BAG and Disease Progression

Baseline BAG did not differ between stable individuals and decliners in the ADNI CN group (MRI BAG: $F_{1,149}$ = 0.617, P = 0.43; ^{18}F-FDG PET BAG: $F_{1,149}$ = 0.023, P = 0.88; Supplemental Fig. 1) or the ADNI SCD group (MRI BAG: $F_{1,78}$ = 0.247, P = 0.62; ^{18}F-FDG PET BAG: $F_{1,78}$ = 1.66, P = 0.20; Fig. 5A). In the ADNI MCI group, we found a significant main effect of group for both MRI and ^{18}F-FDG PET BAG (MRI BAG: $F_{1,454}$ = 59.64, P < 0.001; ^{18}F-FDG PET BAG: $F_{1,454}$ = 10.18, P = 0.002), with decliners showing advanced baseline BAG (MRI: mean of 4.51 y and SD of 2.79 y; ^{18}F-FDG PET: mean of 1.35 y and SD of 3.38 y) compared with stable individuals (MRI: mean of 1.58 y and SD of 3.40 y; ^{18}F-FDG PET: mean of 0.31 y and SD of 3.14 y; Fig. 5B). Men had a higher BAG than women across groups. Covariate effects are reported in detail in Supplemental Section 2d.

Next, we trained a logistic regression classifier to predict MCI-to-AD progression using corrected predictors. Progression to AD was predicted by MRI BAG (AUC, 0.73), ADNI memory (AUC, 0.78), ^{18}F-AV-45 PET (AUC, 0.77), hippocampal volume (AUC, 0.75), SUV ratio in the ^{18}F-FDG meta–region of interest (AUC, 0.72), and CSF p-tau$_{181}$/Aβ_{1-42} ratio (AUC, 0.70). ^{18}F-FDG PET BAG (AUC, 0.60) did not predict progression. Receiver operating characteristics are shown in Figure 5C. In the external DELCODE MCI cohort, MRI BAG predicted progression to AD with a similar AUC of 0.75. From a priori probabilities of cognitive decline in each training fold, we derived a mean probability cutoff of 0.25 in the MRI BAG–based model (range, 0.24–0.25), yielding sensitivities and specificities of 0.69 and 0.69, respectively, in the ADNI MCI group and 0.69 and 0.62, respectively, in the DELCODE MCI group.

DISCUSSION

Previous studies mainly used MRI to estimate brain age. Here, we compared the accuracy of ^{18}F-FDG PET– and MRI-estimated age and provided a comprehensive overview of the associations of

BAG from either modality with cognitive performance, AD neuropathology, and disease progression in at-risk populations for AD dementia. Similar to Lee et al. (*1*), we found that BAE from the 2 modalities was comparably accurate. No associations were found for BAG and cognitive performance or neuropathologic burden in CNs. At the SCD stage, MRI-based BAG correlated significantly with CSF $A\beta_{1\text{-}42}$, whereas ^{18}F-FDG PET BAG, which was trend-significantly elevated in SCD, was linked to memory performance. In MCI, both BAGs were significantly elevated and associated with cognitive performance and CSF $A\beta_{1\text{-}42}$. Only MRI-derived BAG correlated with p-$tau_{181}/A\beta_{1\text{-}42}$ and predicted MCI-to-AD progression.

MRI BAG was elevated in MCI patients compared with CNs and reflected AD neuropathologic burden both in SCD subjects and in MCI subjects. Moreover, MRI BAE was based mostly on hippocampal volume, a measure known to be associated with risk for dementia, and MRI BAG showed a moderate potential to predict MCI-to-AD progression. The increased association with CSF, compared with PET amyloid information, is likely due to the comparably early abnormality of CSF amyloid versus PET amyloid (*20*), as fluid amyloid biomarker signal disrupted amyloid metabolism whereas amyloid PET reveals resultant plaque aggregation. Therefore, MRI BAG closely reflects cognitive performance and relatively early pathologic markers of AD in SCD and MCI. The moderate predictive performance of not only MRI BAG but also the established biomarkers of MCI-to-AD progression suggests that a multimodal framework is required for an accurate prognosis in AD. To test the combined potential of established biomarkers and MRI BAG for risk assessment of AD, and possibly neurodegeneration in general, presents an interesting question for future research.

^{18}F-FDG PET BAG was related to memory performance in SCD and MCI subjects but not in CNs. In SCD subjects, although memory performance is not yet objectively impaired, elevated ^{18}F-FDG PET BAG may reflect its incipient decline. The regions we reported as relevant for ^{18}F-FDG PET BAE are consistent with previous findings (*1*). Yet, we found no significant indications that ^{18}F-FDG PET BAG is a prognostic biomarker. MRI and ^{18}F-FDG PET BAG associations may differ because of regional differences in the BAE or the relative timing of MRI (atrophy) and ^{18}F-FDG PET (neuronal dysfunction) changes in the course of AD. Future research is warranted to explore whether longitudinal ^{18}F-FDG PET BAG may be valuable in tracking disease progression given its sensitivity to early cognitive impairment, its association with CSF amyloid burden in MCI, and the observed elevation of ^{18}F-FDG PET BAG in SCD and MCI individuals.

Some limitations should be acknowledged. First, ^{18}F-FDG PET BAG did not predict MCI-to-AD progression, although ^{18}F-FDG PET itself is an established marker of AD progression (*21*). However, our algorithms were trained to estimate age, and the fact that relevant regions for ^{18}F-FDG PET BAG did not include typical AD signature areas might explain this paradox. Second, although generalizability to OASIS data proved to be accurate, and despite training on multicentric data, we observed strong cohort effects for BAE in the external clinical samples. These results suggest that clinical and methodologic differences, such as variation in the extent of pathology, or in the diagnostic or scan procedure (e.g., the different acquisition times in DELCODE vs. ADNI or OASIS), can significantly influence the applicability of BAE frameworks. Finally, because of data availability and increased risk of cognitive deficits due to neurodegenerative processes, we included participants only over the age of 60 y. Thus, we did not investigate BAE before this age.

CONCLUSION

BAE from MRI or ^{18}F-FDG PET was highly accurate. MRI BAG reflected cognitive and pathologic markers of AD in SCD and MCI subjects, whereas ^{18}F-FDG PET BAG related mainly to early cognitive impairment. Our study suggests that MRI BAG may especially complement the identification of patients who are likely to develop AD, whereas ^{18}F-FDG PET BAG may represent a more independent biomarker of brain age-related changes, possibly occurring ahead of the clinical onset of neurodegeneration.

DISCLOSURE

This work was partly supported by the Helmholtz Portfolio Theme "Supercomputing and Modelling for the Human Brain." The DELCODE study was funded by the Deutsches Zentrum für Neurodegenerative Erkrankungen, German Center for Neurodegenerative Diseases (reference number BN012). Data collection and sharing for this project were funded by the ADNI (National Institutes of Health grant U01 AG024904) and the Department of Defense ADNI. Specific disclosures from ADNI and individual authors can be found in the supplemental materials. No other potential conflict of interest relevant to this article was reported.

ACKNOWLEDGEMENTS

Data used in preparation of this article were obtained from the ADNI database. As such, the investigators within the ADNI contributed to the design and implementation of ADNI or provided data but did not participate in the analysis or in writing this article. A complete listing of ADNI investigators is available (http://adni.loni.usc.edu/wp-content/uploads/how_to_apply/ADNI_Acknowledgement_List.pdf). We gratefully acknowledge data provision by the ADNI, OASIS, and DELCODE studies for the preparation of this article. We further thank the IPMM at the University of Cologne for support.

KEY POINTS

QUESTION: How are BAGs that are derived from structural MRI or ^{18}F-FDG PET linked to cognitive performance, AD neuropathology, and AD progression?

PERTINENT FINDINGS: BAG was computed from structural MRI or ^{18}F-FDG PET and subsequently associated with cognitive performance, neuropathologic markers of AD, and disease progression. ^{18}F-FDG PET and MRI BAG were sensitive mainly to cognitive performance and amyloid burden in SCD, respectively. In MCI, both MRI and ^{18}F-FDG PET BAG reflected cognitive performance and neuropathology. Finally, MRI BAG predicted MCI-to-AD conversion comparably well to established biomarkers.

IMPLICATIONS FOR PATIENT CARE: Brain age is a thoroughly discussed concept, and its applicability must be evaluated in a modality- and group-specific manner. MRI-derived BAG may be particularly useful to complement the identification of patients who are likely to develop AD. MRI BAG may therefore benefit diagnostic procedures or clinical trials.

REFERENCES

1. Lee J, Burkett BJ, Min HK, et al. Deep learning-based brain age prediction in normal aging and dementia. *Nat Aging.* 2022;2:412–424.

2. Dukart J, Kherif F, Mueller K, et al. Generative FDG-PET and MRI model of aging and disease progression in Alzheimer's disease. *PLOS Comput Biol.* 2013;9:e1002987.
3. LaMontagne PJ, Benzinger TLS, Morris JC, et al. OASIS-3: longitudinal neuroimaging, clinical, and cognitive dataset for normal aging and Alzheimer disease. medRxiv website. https://www.medrxiv.org/content/10.1101/2019.12.13.19014902v1. Published December 15, 2019. Accessed October 30, 2023.
4. Jessen F, Spottke A, Boecker H, et al. Design and first baseline data of the DZNE multicenter observational study on predementia Alzheimer's disease (DELCODE). *Alzheimers Res Ther.* 2018;10:15.
5. Jessen F, Amariglio RE, Van Boxtel M, et al. A conceptual framework for research on subjective cognitive decline in preclinical Alzheimer's disease. *Alzheimers Dement.* 2014;10:844–852.
6. Albert MS, DeKosky ST, Dickson D, et al. The diagnosis of mild cognitive impairment due to Alzheimer's disease: recommendations from the National Institute on Aging-Alzheimer's Association workgroups on diagnostic guidelines for Alzheimer's disease. *Alzheimers Dement.* 2011;7:270–279.
7. Pedregosa F, Varoquaux G, Gramfort A, et al. Scikit-learn: machine learning in Python. *J Mach Learn Res.* 2011;12:2825–2830.
8. Tzourio-Mazoyer N, Landeau B, Papathanassiou D, et al. Automated anatomical labeling of activations in SPM using a macroscopic anatomical parcellation of the MNI MRI single-subject brain. *Neuroimage.* 2002;15:273–289.
9. Beheshti I, Ganaie MA, Paliwal V, Rastogi A, Razzak I, Tanveer M. Predicting brain age using machine learning algorithms: a comprehensive evaluation. *IEEE J Biomed Health Inform.* 2022;26:1432–1440.
10. Beheshti I, Nugent S, Potvin O, Duchesne S. Bias-adjustment in neuroimaging-based brain age frameworks: a robust scheme. *Neuroimage Clin.* 2019;24:102063.
11. Crane PK, Carle A, Gibbons LE, et al. Development and assessment of a composite score for memory in the Alzheimer's Disease Neuroimaging Initiative (ADNI). *Brain Imaging Behav.* 2012;6:502–516.
12. Gibbons LE, Carle AC, Mackin RS, et al. A composite score for executive functioning, validated in Alzheimer's Disease Neuroimaging Initiative (ADNI) participants with baseline mild cognitive impairment. *Brain Imaging Behav.* 2012;6:517–527.
13. Landau S, Jagust W. *Florbetapir Processing Methods.* Alzheimer's Disease Neuroimaging Initiative; 2011.
14. Blennow K, Shaw LM, Stomrud E, et al. Predicting clinical decline and conversion to Alzheimer's disease or dementia using novel Elecsys Aβ(1-42), pTau and tTau CSF immunoassays. *Sci Rep.* 2019;9:19024.
15. Shaw LM, Vanderstichele H, Knapik-Czajka M, et al. Cerebrospinal fluid biomarker signature in Alzheimer's disease neuroimaging initiative subjects. *Ann Neurol.* 2009;65:403–413.
16. Ebenau JL, Pelkmans W, Verberk IMW, et al. Association of CSF, plasma, and imaging markers of neurodegeneration with clinical progression in people with subjective cognitive decline. *Neurology.* 2022;98:e1315–e1326.
17. Wagner M, Jessen F, Scheef L, et al. Glucose metabolism, gray matter structure and memory decline in subjective memory impairment. *Neurology.* 2012;79:1332–1339.
18. Jack CR, Wiste HJ, Weigand SD, et al. Defining imaging biomarker cut points for brain aging and Alzheimer's disease. *Alzheimers Dement.* 2017;13:205–216.
19. Dukart J, Schroeter ML, Mueller K. Age correction in dementia: matching to a healthy brain. *PLoS One.* 2011;6:e22193.
20. Reimand J, De Wilde A, Teunissen CE, et al. PET and CSF amyloid-β status are differently predicted by patient features: information from discordant cases. *Alzheimers Res Ther.* 2019;11:100.
21. Mosconi L, Berti V, Glodzik L, Pupi A, De Santi S, De Leon MJ. Pre-clinical detection of Alzheimer's disease using FDG-PET, with or without amyloid imaging. *J Alzheimers Dis.* 2010;20:843–854.

Prognostic Value of ^{18}F-FDG PET Radiomics Features at Baseline in PET-Guided Consolidation Strategy in Diffuse Large B-Cell Lymphoma: A Machine-Learning Analysis from the GAINED Study

Thomas Carlier[1,2], Gauthier Frécon[1,2], Diana Mateus[3], Mira Rizkallah[3], Françoise Kraeber-Bodéré[1,2], Salim Kanoun[4], Paul Blanc-Durand[5], Emmanuel Itti[5], Steven Le Gouill[6], René-Olivier Casasnovas[7], Caroline Bodet-Milin[1,2], and Clément Bailly[1,2]

[1]Nantes Université, INSERM, CNRS, CRCI[2]NA, Université d'Angers, Nantes, France; [2]Nuclear Medicine Department, University Hospital, Nantes, France; [3]Laboratoire des Sciences Numériques de Nantes, Ecole Centrale de Nantes, CNRS UMR 6004, Nantes, France; [4]Nuclear Medicine, Georges-François Leclerc Center, Dijon, France; [5]Nuclear Medicine, CHU Henri Mondor, Paris-Est University, Créteil, France; [6]Haematology Department, University Hospital, Nantes, France; and [7]Hematology, CHU Dijon Bourgogne, Dijon, France

The results of the GA in Newly Diagnosed Diffuse Large B-Cell Lymphoma (GAINED) study demonstrated the success of an ^{18}F-FDG PET–driven approach to allow early identification—for intensification therapy—of diffuse large B-cell lymphoma patients with a high risk of relapse. Besides, some works have reported the prognostic value of baseline PET radiomics features (RFs). This work investigated the added value of such biomarkers on survival of patients involved in the GAINED protocol. **Methods:** Conventional PET features and RFs were computed from ^{18}F-FDG PET at baseline and extracted using different volume definitions (patient level, largest lesion, and hottest lesion). Clinical features and the consolidation treatment information were also considered in the model. Two machine-learning pipelines were trained with 80% of patients and tested on the remaining 20%. The training was repeated 100 times to highlight the test set variability. For the 2-y progression-free survival (PFS) outcome, the pipeline included a data augmentation and an elastic net logistic regression model. Results for different feature groups were compared using the mean area under the curve (AUC). For the survival outcome, the pipeline included a Cox univariate model to select the features. Then, the model included a split between high- and low-risk patients using the median of a regression score based on the coefficients of a penalized Cox multivariate approach. The log-rank test *P* values over the 100 loops were compared with a Wilcoxon signed-ranked test. **Results:** In total, 545 patients were included for the 2-y PFS classification and 561 for survival analysis. Clinical features alone, consolidation features alone, conventional PET features, and RFs extracted at patient level achieved an AUC of, respectively, 0.65 ± 0.07, 0.64 ± 0.06, 0.60 ± 0.07, and 0.62 ± 0.07 (0.62 ± 0.07 for the largest lesion and 0.54 ± 0.07 for the hottest). Combining clinical features with the consolidation features led to the best AUC (0.72 ± 0.06). Adding conventional PET features or RFs did not improve the results. For survival, the log-rank *P* values of the model involving clinical and consolidation features together were significantly smaller than all combined-feature groups ($P < 0.007$). **Conclusion:** The results showed that a concatenation of multimodal features coupled with a simple machine-learning model does not seem to improve the results in terms of 2-y PFS classification and PFS prediction for patient treated according to the GAINED protocol.

Key Words: DLBCL; ^{18}F-FDG PET; GAINED study; radiomics

J Nucl Med 2024; 65:156–162
DOI: 10.2967/jnumed.123.265872

The use of PET with ^{18}F-FDG is now considered the standard imaging procedure not only for staging but also for therapeutic response assessment of patients with diffuse large B-cell lymphoma (DLBCL) (*1*). Yet, the number of patients who do not respond after standard front-line therapy—that is, a combination of anti-CD20 monoclonal antibody with cyclophosphamide, doxorubicin, vincristine, and prednisone chemotherapy—is still significant (30%–40%) (*2*) and advocates for the use of new biomarkers to determine patients with a high risk of relapse. In that respect, approaches based on interim PET to identify these patients and to adapt consolidation strategies accordingly have been explored for over 10 y (*3*). Several studies also evaluated the potential benefit of using imaging biomarkers extracted from PET volumes (*4*) in combination (or not) with other clinical or demographic features at baseline. Most of the studies focused primarily on assessment of the SUV extracted from the most intense lesion (SUV_{max}), the total metabolic tumor volume (TMTV), and dissemination. Although the role of SUV_{max} at baseline to predict 2-y progression-free survival (PFS) or overall survival was shown to be limited (*4*), TMTV (*5*) and dissemination (*6*) appeared to be promising at baseline (*7*).

Another area related to the high-throughput extraction of quantitative data from medical images has gained importance by considering the measurement of the spatial heterogeneity within a tumor (hereafter called radiomics) (*8*). Evaluation of the predictive values of these other potential image-based biomarkers in DLBCL patients has recently been considered (*9–17*). However, the usefulness of complex radiomics in this context remains controversial, as some studies reported a potential added value (*9–11*,*14–17*) whereas others concluded that there is a lack of, or only a moderate,

Received Apr. 14, 2023; revision accepted Oct. 17, 2023.
For correspondence or reprints, contact Clément Bailly (clement.bailly@chu-nantes.fr).
Published online Nov. 9, 2023.

predictive value for 2-y PFS when these biomarkers are considered alone or combined (*12*,*13*). These contradictory results may be explained partly by the prospective or retrospective nature of each study, the population size and type, the presence (or not) of a test dataset, the monocentric or multicentric characteristic of the study, the heterogeneity in immunochemotherapy regimen and patient management, and the features considered in the model.

The GA in Newly Diagnosed Diffuse Large B-Cell Lymphoma (GAINED) randomized phase III trial was the first study demonstrating the success of a PET-driven strategy. Interim PET interpretation criteria were simple and based on SUV_{max} reduction (ΔSUV_{max}) (*18*). The purpose of our work was to explore the prognostic added value on 2-y PFS and survival (using PFS as the endpoint) of a combination of clinical, PET-based, and radiomics features (RFs) extracted at baseline in DLBCL patients included in this latter prospective multicenter cohort in which patient management is driven by PET follow-up. A secondary objective was to identify whether baseline PET characteristics could predict patients' response after 4 cycles of chemotherapy and consequently the treatment arm to which they would be assigned. Finally, a third was to assess whether a specific volume of interest (VOI) was more relevant for radiomics computation when the 2-y PFS classification and treatment prediction are considered.

MATERIALS AND METHODS

Patients and PET/CT Imaging

The GAINED phase 3 trial (NCT 01659099) was conducted in 99 centers and enrolled newly diagnosed untreated DLBCL patients between 18 and 60 y old. The main exclusion and inclusion criteria have already been reported (*18*). The patients received cyclophosphamide, doxorubicin, vincristine, and prednisone or ACVBP (doxorubicin, cyclophosphamide, vindesine, bleomycin, and prednisone) on a 14-d schedule plus obinutuzumab (GA-101) or rituximab. Interim PET was performed at diagnosis and after 2 and 4 cycles of chemotherapy (respectively, PET2 and PET4) and analyzed according to ΔSUV_{max}. Patients with an early good response (defined as negative PET2 and PET4) continued the planned immunochemotherapy; slow responders (positive PET2 and negative PET4) received intensification therapy with 2 courses of high-dose methotrexate followed by autologous stem cell transplantation. Patients with positive PET after 4 induction cycles received salvage therapy. No difference in terms of 2-y PFS was reported between the 2 induction arms (GA-101 vs. rituximab). Early good responders and slow responders had similar 2-y PFS and overall survival. ^{18}F-FDG PET scans were performed according to the local procedure of each center. All images were reconstructed in SUV normalized for body weight.

Segmentation, Features Processing, and Selection

A gross VOI was manually delineated for each tumor, removing nontumor adjacent regions when needed. The final segmentation for each tumor was extracted using a fixed SUV threshold of 4.0 (*19*). Several PET-based imaging biomarkers were extracted from each reconstructed volume using PyRadiomics version 3.0 (*20*). Four conventional PET features were extracted: TMTV, whole-body total lesion glycolysis, SUV_{max}, and dissemination (maximum distance between 2 lesions normalized by body surface area). Among the RFs available for computation, a subset of 39 features was preselected (Supplemental Fig. 1; supplemental materials are available at http://jnm.snmjournals.org), choosing those that presented the best properties of repeatability (*21*–*23*). Before RF computation, PET images were resampled to the same voxel size ($2 \times 2 \times 2$ mm) using a bicubic spline interpolation. Data were subsequently normalized using 2 approaches: a linear equalization using 64 bins and a fixed bin width of SUV 0.3. A subsequent preprocessing step was used to enhance imaging characteristics: a wavelet transform using coiflet-1 filters to decompose the original image into 8 decomposition frequencies and an edge-enhancement Laplacian of gaussian filter (with 2- and 6-mm σ). This led a total of 647 RFs, which were computed from 3 different VOIs: the VOI with the most intense SUV_{max} (named hottest), the VOI that corresponded to the largest volume (named largest), and TMTV.

The RF selection step was divided into 3 parts. First, the reliability of textural RFs (excluding first-order and shape features) was derived

TABLE 1
Description of Different Models

Model no.	Model name	Associated features
1	aaIPI	aaIPI
2	Consolidation	Chemotherapy regimen, autologous cell transplantation, salvage therapy
3	Clinical	Age, Ann Arbor stage, ECOG status, number of extranodal sites, LDH
4	Conventional PET	TMTV, total lesion glycolysis, SUV_{max}, sDmax
5	Radiomics PET	Selected RFs after selection step using largest lesion
6	Consolidation + clinical (models 2 + 3)	All features from clinical and consolidation
7	Consolidation + clinical + conventional PET (models 2 + 3 + 4)	All features from clinical, conventional (PET), and consolidation
8	Consolidation + clinical + radiomics PET (models 2 + 3 + 5)	All features from clinical, radiomics (PET), and consolidation
9	Consolidation + clinical + conventional PET + radiomics PET (models 2 + 3 + 4 + 5)	All features from clinical and conventional (PET), radiomics (PET). and consolidation

aaIPI = age-adjusted international prognostic index; ECOG = Eastern Cooperative Oncology Group; LDH = lactate dehydrogenase; sDmax = maximum distance between 2 lesions normalized by body surface area.

TABLE 2
Patient Characteristics

Characteristic	2-y PFS classification (n = 545)	Survival (n = 561)
Events	86 (100%)	107 (100%)
Age (y)	48 (18–60)	48 (18–60)
Sex, male	305 (56%)	314 (56%)
aaIPI		
0–1	230 (42%)	242 (43%)
2–3	315 (58%)	319 (57%)
Ann Arbor stage		
I–II	102 (19%)	106 (19%)
III–IV	443 (81%)	455 (81%)
Extranodal involvement		
<2	259 (48%)	269 (48%)
≥2	286 (52%)	292 (52%)
Performance status		
0–1	470 (86%)	485 (86%)
>1	75 (14%)	76 (14%)
LDH		
≤Normal	147 (27%)	155 (28%)
>Normal	398 (73%)	406 (72%)
Treatment arm		
GA-101	278 (51%)	286 (51%)
Rituximab	267 (49%)	275 (49%)
Induction treatment		
GA-101-CHOP	142 (26%)	145 (26%)
Rituximab-CHOP	144 (26%)	148 (26%)
GA-101-ACVBP	136 (25%)	141 (25%)
Rituximab-ACVBP	123 (23%)	127 (23%)

aaIPI = age-adjusted international prognostic index; CHOP = cyclophosphamide, doxorubicin, vincristine, and prednisone.

Qualitative data are number and percentage; continuous data are mean and range.

following the methodology proposed by Pfaehler et al. (*24*). Briefly, for each patient and each RF, the signal within the ROI was randomly shuffled 50 times and RF subsequently computed. The RF was considered unreliable if its original value lay within the 95% CI computed using the random shuffling. Finally, the RF was kept if its original value was outside the proposed CI for 90% of the patients. Second, all RFs that correlated strongly (Spearman correlation higher than 0.9) with 1 of the 4 conventional PET features were removed. Lastly, a hierarchic agglomerative clustering was applied to manage multicollinearity between features (supplemental methods).

All features were then standardized, setting the mean to zero and the SD to 1 to make the feature space homogeneous.

Machine-Learning Models

The population was split into training and testing datasets with a ratio of 80% to 20%, stratified according to the 2-y PFS outcome for the 2-y PFS classification objective and according to the censorship and number of events per quartile for the survival analysis. Data augmentation was used on the training dataset to increase the minority class cardinal to the cardinal of the majority class. Both the synthetic minority oversampling technique (*25*) and the adaptive synthetic sampling approach for imbalanced learning (*26*) were considered one of the hyperparameters of the model.

For the 2-y PFS classification objective and the PET4 prediction, a logistic regression (LR) including elastic net regularization was considered. A 4-fold cross validation for the grid search was used on the training dataset (parameters detailed in Supplemental Table 1), with an objective of maximizing the area under the receiver operator characteristic (ROC) curve (AUC). The whole process was repeated 100 times to assess the variance of the model linked to the choice of the test dataset (Supplemental Fig. 2).

For the survival analysis, the model building was done in 2 main steps. A univariate analysis for each considered feature was conducted by fitting the Cox proportional-hazards model on the training dataset to select only those features significantly associated with the patient outcome using the training dataset. A penalized multivariate Cox analysis was then conducted using a 4-fold cross validation on the training dataset to select the best hyperparameters among the penalization strengths (Supplemental Table 2). A regression score (RS) was then derived for each patient by summing each term of the Cox proportional-hazards model (weight multiplied by the corresponding feature) (*15*). The population was then split according to the median of the RS to derive 2 survival groups. This RS cutoff was subsequently applied to the testing dataset. This process was repeated 100 times as for the previous 2-y PFS classification objective (Supplemental Fig. 3).

The 2 models (one for classification and one for survival) were implemented for 9 groups of different feature subsets, summarized in Table 1. Model 3, termed clinical, includes the same features as model 1, termed age-adjusted international prognostic index, with the difference being that the features are considered continuous in model 3 whereas a categorical score is used in model 1.

Since the consolidation arm was included in the features groups, none of the patients who died before the consolidation phase were considered in the study. Moreover, patients censored before 24 mo were not included for the 2-y PFS classification task.

Patient Follow-up and Statistical Analysis

The 2-y PFS was defined as the time from randomization to disease progression, relapse, or death of any cause. A mean ROC curve for 2-y PFS and PET4 classification was generated taking into account the 100 loops. Accuracy, balanced accuracy, sensitivity, specificity, and AUC were computed. AUC among the 100 loops was compared using a 1-sided Wilcoxon

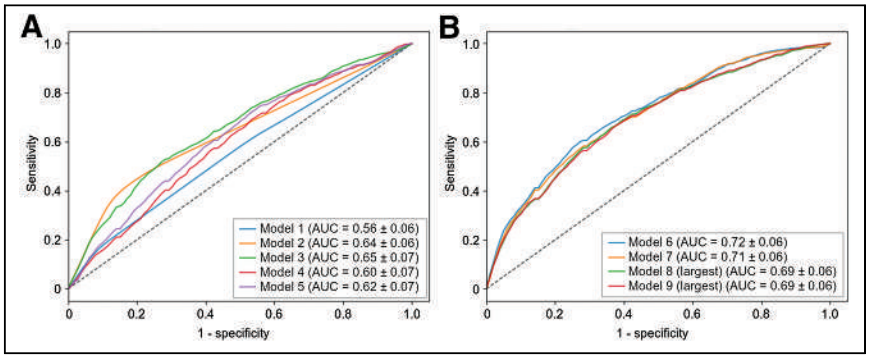

FIGURE 1. Mean ROC curves for models 1–5 (A) and 6–9 (B) for 2-y PFS classification.

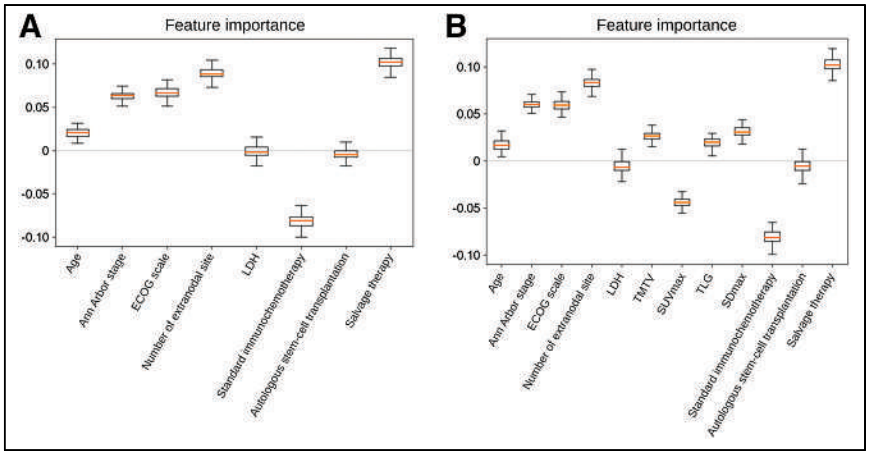

FIGURE 2. Feature importance according to relative weight attached to each feature in LR model for models 6 (A) and 7 (B) for 2-y PFS classification. ECOG = Eastern Cooperative Oncology Group; LDH = lactate dehydrogenase; SDmax = maximum distance between 2 lesions normalized by body surface area; TLG = total lesion glycolysis.

signed-rank test among the 9 models embedding different feature subsets. A similar approach was used to derive the most valuable ROI (among the 3 studied) to compute RFs. We reported the results of the 9 models using only the ROI leading to the best performance when radiomics is involved in the considered models. Feature importance was subsequently derived from the LR weights to highlight which features were the most informative. To this end, the best parameters of LR were chosen by 4-fold cross-validation on the training dataset, and then LR was retrained 100 times (Supplemental Fig. 2). Finally, box plots and sorted bar charts of absolute values were derived from LR weights.

Patient survival was estimated by Kaplan–Meier analysis, and survival curves were compared using the log-rank test. Box plots of *P* values related to each model (over the 100 loops) were plotted and then were compared using a 1-sided Wilcoxon signed-rank test. The probability of selecting a feature after the univariate Cox analysis was also computed to highlight feature importance. All statistical analyses were done using Python version 3.7.9. A *P* value of less than 0.05 was considered statistically significant.

RESULTS

Patient Characteristics

Among the 670 patients enrolled in the GAINED study, 561 were considered for this analysis. For the 2-y PFS classification approach, the study included 545 patients, of whom 86 underwent an event before 24 mo. For the survival approach, the study included 561 patients, of whom 107 underwent an event before the last follow-up. These patients have demographic and clinical characteristics similar to those of the entire GAINED population. Patient characteristics are summarized in Table 2. Among the 561 patients in our cohort, there were 386 early responders, 84 slow responders, and 91 who did not respond.

2-Year PFS Classification

Comparisons of the predictive values of radiomics extracted from different VOIs are presented in Supplemental Figure 4. The mean AUC was 0.62 ± 0.07 for radiomics extracted from both the largest lesion and the TMTV but was 0.54 ± 0.07 for radiomics extracted from the hottest lesion. Since the Wilcoxon test reported a significant difference ($P < 0.0001$) between results extracted from either the largest lesion or TMTV and the hottest lesion, only radiomics computed from the largest lesion were considered.

ROC curves for models involving 1 group of features (from models 1 to 5) are shown in Figure 1A. The model with the highest predictive value was that including clinical features (model 3), with a mean AUC of 0.65 ± 0.07. Models involving consolidation features (model 2) and conventional PET (model 4) achieved a mean AUC of 0.64 ± 0.06 and 0.60 ± 0.07, respectively, which are better than for model 1 (age-adjusted international prognostic index), which achieved a mean AUC of 0.56 ± 0.06. Only model 1 was significantly different from all others ($P < 0.001$). Models combining several groups of features (from models 6 to 9) reached a mean AUC from 0.72 ± 0.06 to 0.69 ± 0.06 without significant differences in between.

The importance of each feature was derived from the weights resulting from the LR attached to each feature. A positive weight sign tends to classify patients in the positive class (progression occurred) when the feature value increases. Inversely, a negative weight sign tends to classify patients in

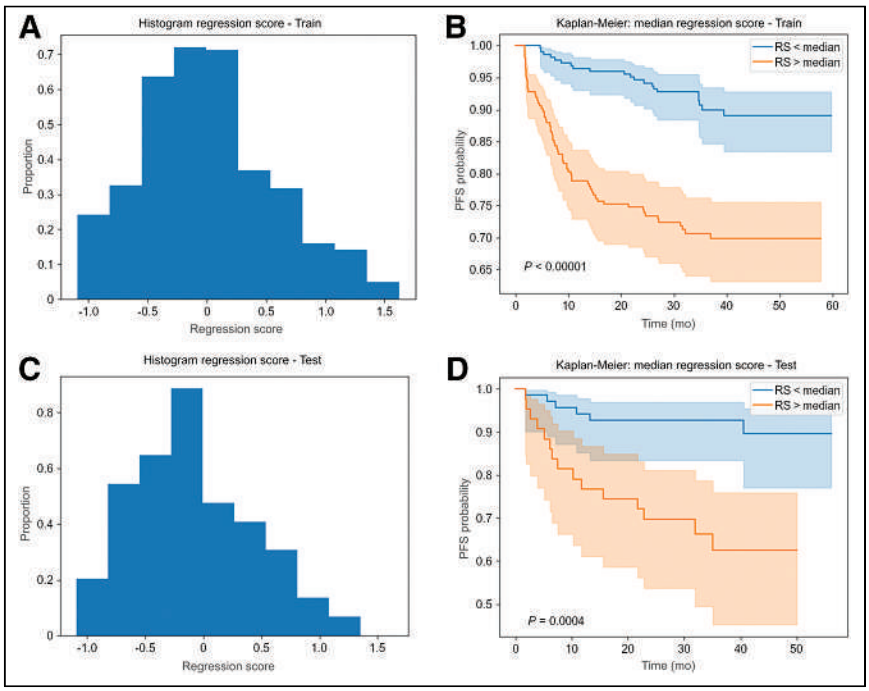

FIGURE 3. Example of RS for training set (A) and corresponding test set (C), along with associated Kaplan–Meier plots for PFS for training set (B) and test set (D). Low- and high-risk groups were dichotomized using median RS determined on training set and applied on test set.

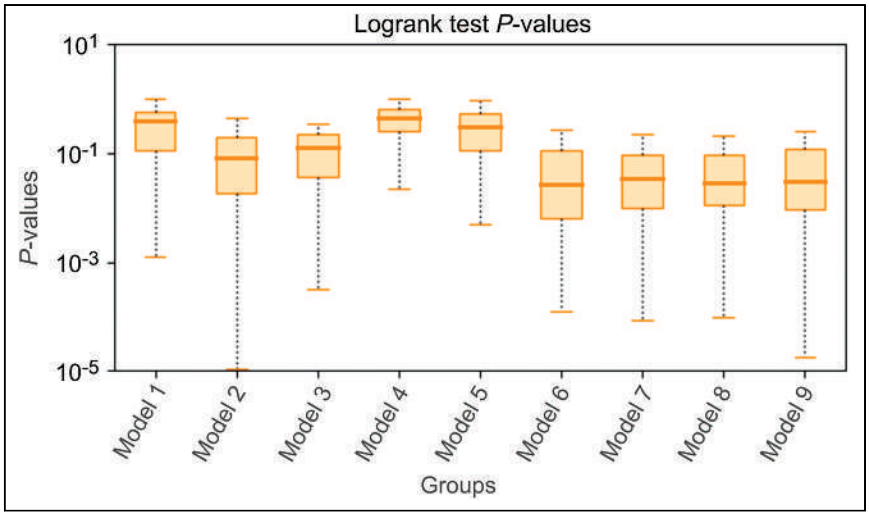

FIGURE 4. Log-rank *P* values over 100 loops for 9 models considered for survival analysis study.

the negative class when the feature value increases. The feature importance for models 6 and 7 is plotted in Figure 2. The number of extranodal sites, Eastern Cooperative Oncology Group scale, and Ann Arbor stage were among the most important features when considering clinical features. The consolidation treatment regimen received was also highly predictive of 2-y PFS. Adding conventional PET features (Fig. 2B) or radiomics did not notably change the ordering of the most important features (Supplemental Fig. 5).

Survival Analysis for PFS

The probability of selecting each feature for its superior significance compared with others (computed over the 100 loops) using the models combining several groups of features (from models 6 to 9) is presented in Supplemental Figure 6. The most important features selected in the previous classification task were also always selected for this current survival analysis study. An example relative to 1 loop of an RS histogram and associated Kaplan–Meier curves built using the median cutoff RS is shown in Figure 3 for model 6. The corresponding log-rank *P* values for the test dataset are presented in Figure 4. The median *P* value for models involving 1 group of features (from models 1 to 5) was lowest for the model involving only the consolidation treatment (model 2) and was significantly different from models involving age-adjusted international prognostic index (model 1, $P < 0.0001$), clinical parameters (model 3, $P < 0.05$) conventional PET features (model 4, $P < 0.0001$), or RFs (model 5, $P < 0.0001$). Among models that combined the consolidation treatment plus one or more feature groups (from models 6 to 9), the median *P* value was the lowest for model 6 but without being significantly lower than for all other models (from models 7 to 9).

PET4 Prediction

Comparisons of predictive values of radiomics extracted from different VOIs are presented in Supplemental Figure 7. No significant difference was highlighted between the different VOIs. Then, for consistency reasons with the 2-y PFS classification, the largest one was retained.

ROC curves for models involving 1 group of features (models 1, 3, 4, and 5) are shown in Figure 5A. The model involving radiomics (model 5) was significantly better than all others ($P < 0.0001$), with a mean AUC of 0.61 ± 0.07. When combined, only the models involving radiomics exhibited the best performance (Fig. 5B), with a mean AUC of 0.62 ± 0.07 ($P < 0.0001$).

DISCUSSION

The last 2 decades witnessed multiple trials exploring a PET-driven strategy to identify poorly responding DLBCL patients requiring more intensive salvage therapy. These works have yielded heterogeneous results, as many relied on qualitative visual evaluation (*3*). Assessing ΔSUV_{max} after 2 and 4 cycles of induction regimens showed improved reproducibility and significantly reduced false-positive rates. This semiquantitative criterion was applied in 2 large multicentric prospective PET-guided trials (PETAL and GAINED). The first one, although disappointingly reporting no efficacy in escalation of PET2-positive patients to an intensified Burkitt chemotherapy, clearly defined ΔSUV_{max} as a valid measure to differentiate patients with chemotherapy-sensitive tumors from those with chemotherapy-resistant tumors. In the GAINED study, as opposed to PETAL, positive interim PET's unfavorable prognostic value could be overcome with escalation of therapy and autologous stem cell transplantation. These data represented an important cornerstone in the management of DLBCL patients, suggesting that quantitative ΔSUV_{max} criteria can be applied in routine practice to evaluate metabolic response and drive the therapeutic strategy. The question now arises as to what additional data would refine the prediction of early response to therapy. In a multiparametric approach, some teams are exploring circulating tumor DNA analysis, whereas some are investigating the value of PET biomarkers at baseline. Although the role of SUV_{max} at baseline to predict the 2-y PFS or overall survival was shown to be limited (*4*), evaluation of predictive value in DLBCL

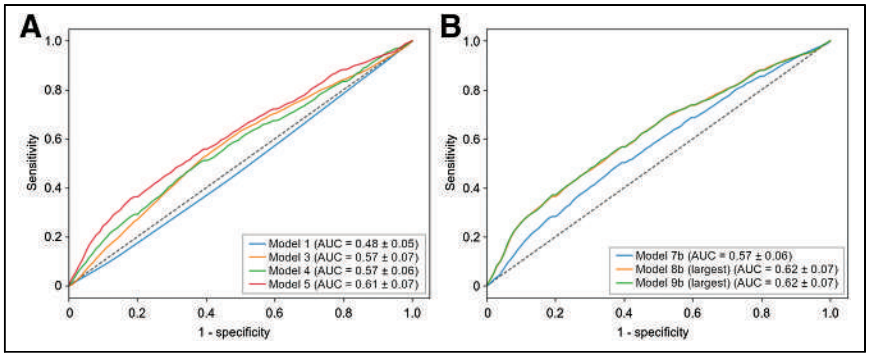

FIGURE 5. Mean ROC curves for models 1, 3, 4, and 5 (A) and for models that combined several features (B) for PET4 prediction. Model 7b = combination of clinical and conventional PET features; model 8b = combination of clinical and radiomics; model 9b = combination of clinical and conventional PET features and radiomics.

patients using TMTV (*5*), dissemination (*6*), and RFs (*9*–*17*) has recently been considered.

In this study, our findings supported the fact that conventional PET metrics, dissemination, or RFs are predictive of outcome. Nevertheless, we extend these results by showing that these features seem to have no additional predictive capabilities compared with treatment arm or clinical features in the frame of the GAINED protocol. Interim PET assessment through the use of ΔSUV_{max} allowed an accurate stratification of DLBCL patients into 3 risk groups, of which PET4-positive patients are those with the worst outcome, despite salvage therapy. The impact of the GAINED strategy in modifying conventional immunochemotherapy on the basis of these findings significantly and sufficiently improved patient outcome to override the value of the other PET parameters. The results were also suggested by the HOVON-84 trial, in which baseline TMTV did not add prognostic value to ΔSUV_{max} (*27*).

This work also allowed exploration of the influence of VOI choice on the prognostic performance of radiomics. We were able to confirm the results of Eertink et al. (*13*) on interest in computing RFs from the TMTV or the largest lesion rather than the hottest lesion. Although this observation may seem surprising, it provides a better understanding of intrapatient interlesional tumor heterogeneity. This is an important factor that is actually also explored by the ΔSUV_{max} method. It compares the lesion with the highest SUV_{max}, at baseline and at interim PET, which is not necessarily the same hottest lesion as before the start of treatment, to measure the metabolic activity of the most active or aggressive tumor contingent.

Baseline PET characteristics showed limited performance in predicting results at PET4 and subsequently each patient's risk group and treatment arm. Nevertheless, unlike the 2-y PFS classification, radiomics seems to be of importance in that context since it outperformed the models that involved only the clinical information or the PET conventional features. This paves the way to the development of more advanced machine-learning models taking into account (or not) hand-crafted radiomics. Moreover, early identification of patients at highest risk could be of relevance in a context where innovative treatments, such as cell-based therapies, require a significant preparation and set-up phase.

CONCLUSION

This study suggests that metrics extracted from ^{18}F-FDG PET at baseline for this cohort of DLBCL patients and treated according to the PET-driven design of the GAINED protocol do not improve the 2-y PFS classification and PFS prediction. The model including the consolidation strategy, which was in turn directed by ΔSUV_{max}, combined with clinical features achieved the best performances.

DISCLOSURE

This work has been supported in part by ISITE NExT (No. ANR-16-IDEX-0007), the French National Research Agency Labex IRON (No. ANR-11-LABX-0018-01), the INCa-DGOS-Inserm-12558 (SIRIC ILIAD), and the European Regional Development Fund, Pays-de-la-Loire (Connect Talent MILCOM), Nantes Métropole (Convention 2017-10470). Steven Le Gouill reports grants, personal fees, or nonfinancial support from Roche Genentech during the conduct of the study; personal fees from Celgene; and grants and personal fees from Janssen-Cilag, GILEAD/kite, and Servier outside the submitted work. René-Olivier Casasnovas reports grants, personal fees, and nonfinancial support from Roche Genentech during the conduct of the study; personal fees from MSD, BMS, Abbvie, Amgen, Celgene, Janssen, and Astra Zeneca; and grants and personal fees from Takeda and GILEAD/kite outside the submitted work. No other potential conflict of interest relevant to this article was reported.

ACKNOWLEDGMENT

We warmly thank Enzo Lepoivre for his invaluable support in finalizing the manuscript.

KEY POINTS

QUESTION: Do baseline ^{18}F-FDG PET biomarkers add prognostic value to the PET-driven strategy of the GAINED study in DLBCL patients?

PERTINENT FINDINGS: Regardless of the VOI or features selection, conventional or radiomics ^{18}F-FDG PET biomarkers extracted at baseline do not seem to improve the results in terms of 2-y PFS and survival prediction for patients treated according to the GAINED protocol.

IMPLICATIONS FOR PATIENT CARE: Interim PET assessment using ΔSUV_{max} variation allows for accurate and simple monitoring and should be considered for use in routine practice in patients with advanced DLBCL.

REFERENCES

1. Al Tabaa Y, Bailly C, Kanoun S. FDG-PET/CT in lymphoma: where do we go now? *Cancers (Basel).* 2021;13:5222.
2. Sehn LH, Salles G. Diffuse large B-cell lymphoma. *N Engl J Med.* 2021;384:842–858.
3. Le Gouill S, Casasnovas R-O. Interim PET-driven strategy in de novo diffuse large B-cell lymphoma: do we trust the driver? *Blood.* 2017;129:3059–3070.
4. Frood R, Burton C, Tsoumpas C, et al. Baseline PET/CT imaging parameters for prediction of treatment outcome in Hodgkin and diffuse large B cell lymphoma: a systematic review. *Eur J Nucl Med Mol Imaging.* 2021;48:3198–3220.
5. Ceriani L, Gritti G, Cascione L, et al. SAKK38/07 study: integration of baseline metabolic heterogeneity and metabolic tumor volume in DLBCL prognostic model. *Blood Adv.* 2020;4:1082–1092.
6. Cottereau A-S, Nioche C, Dirand A-S, et al. ^{18}F-FDG PET dissemination features in diffuse large B-cell lymphoma are predictive of outcome. *J Nucl Med.* 2020;61:40–45.
7. Eertink JJ, Zwezerijnen GJC, Heymans MW, et al. Baseline PET radiomics outperforms the IPI risk score for prediction of outcome in diffuse large B-cell lymphoma. *Blood.* 2023;141:3055–3064.
8. Hatt M, Cheze Le Rest C, Antonorsi N, et al. Radiomics in PET/CT: current status and future AI-based evolutions. *Semin Nucl Med.* 2021;51:126–133.
9. Parvez A, Tau N, Hussey D, Maganti M, Metser U. ^{18}F-FDG PET/CT metabolic tumor parameters and radiomics features in aggressive non-Hodgkin's lymphoma as predictors of treatment outcome and survival. *Ann Nucl Med.* 2018;32:410–416.
10. Aide N, Fruchart C, Nganoa C, Gac AC, Lasnon C. Baseline ^{18}F-FDG PET radiomic features as predictors of 2-year event-free survival in diffuse large B cell lymphomas treated with immunochemotherapy. *Eur Radiol.* 2020;30:4623–4632.
11. Senjo H, Hirata K, Izumiyama K, et al. High metabolic heterogeneity on baseline ^{18}FDG-PET/CT scan as a poor prognostic factor for newly diagnosed diffuse large B-cell lymphoma. *Blood Adv.* 2020;4:2286–2296.
12. Eertink JJ, van de Brug T, Wiegers SE, et al. ^{18}F-FDG PET baseline radiomics features improve the prediction of treatment outcome in diffuse large B-cell lymphoma. *Eur J Nucl Med Mol Imaging.* 2022;49:932–942.
13. Eertink JJ, Zwezerijnen GJC, Cysouw MCF, et al. Comparing lesion and feature selections to predict progression in newly diagnosed DLBCL patients with FDG PET/CT radiomics features. *Eur J Nucl Med Mol Imaging.* 2022;49:4642–4651.
14. Lue KH, Wu YF, Lin HH, et al. Prognostic value of baseline radiomic features of ^{18}F-FDG PET in patients with diffuse large B-cell lymphoma. *Diagnostics (Basel).* 2020;11:36.
15. Ceriani L, Milan L, Cascione L, et al. Generation and validation of a PET radiomics model that predicts survival in diffuse large B cell lymphoma treated with R-CHOP14: a SAKK 38/07 trial post-hoc analysis. *Hematol Oncol.* 2022;40:11–21.

16. Zhang X, Chen L, Jiang H, et al. A novel analytic approach for outcome prediction in diffuse large B-cell lymphoma by [^{18}F]FDG PET/CT. *Eur J Nucl Med Mol Imaging.* 2022;49:1298–1310.
17. Jiang C, Li A, Tend Y, et al. Optimal PET-based radiomic signature construction based on the cross-combination method for predicting the survival of patients with diffuse large B-cell lymphoma. *Eur J Nucl Med Mol Imaging.* 2022;49:2902–2916.
18. Le Gouill S, Ghesquières H, Oberic L, et al. Obinutuzumab vs rituximab for advanced DLBCL: a PET-guided and randomized phase 3 study by LYSA. *Blood.* 2021;137:2307–2320.
19. Barrington SF, Zwezerijnen BGJC, de Vet HCW, et al. Automated segmentation of baseline metabolic total tumor burden in diffuse large B-cell lymphoma: which method is most successful? A study on behalf of the PETRA consortium. *J Nucl Med.* 2021;62:332–337.
20. van Griethuysen JJM, Fedorov A, Parmar C, et al. Computational radiomics system to decode the radiographic phenotype. *Cancer Res.* 2017;77:e104–e107.
21. Bailly C, Bodet-Milin C, Couespel S, et al. Revisiting the robustness of PET-based textural features in the context of multi-centric trials. *PLoS One.* 2016;11: e0159984.
22. Desseroit MC, Tixier F, Weber WA, et al. Reliability of PET/CT shape and heterogeneity features in functional and morphologic components of non-small cell lung cancer tumors: a repeatability analysis in a prospective multicenter cohort. *J Nucl Med.* 2017;58:406–411.
23. van Velden FHP, Kramer GM, Frings V, et al. Repeatability of radiomic features in non-small-cell lung cancer [^{18}F]FDG-PET/CT studies: impact of reconstruction and delineation. *Mol Imaging Biol.* 2016;18:788–795.
24. Pfaehler E, Mesotten L, Zhovannik I, et al. Plausibility and redundancy analysis to select FDG-PET textural features in non-small cell lung cancer. *Med Phys.* 2021; 48:1226–1238.
25. Chawla NV, Bowyer KW, Hall LO, Kegelmeyer WP. SMOTE: synthetic minority over-sampling technique. *J Artif Intell Res.* 2002;16:321–357.
26. He H, Garcia EA. Learning from imbalanced data. *IEEE Trans Knowl Data Eng.* 2009;21:1263–1284.
27. Burggraaff CN, Eertink JJ, Lugtenburg PJ, et al.; HOVON imaging working group and the HOVON Lymphoma Working Group. ^{18}F-FDG PET improves baseline clinical predictors of response in diffuse large B-cell lymphoma: the HOVON-84 study. *J Nucl Med.* 2022;63:1001–1007.

C-X-C Motif Chemokine Receptor 4–Directed Scintigraphy of Multiple Myeloma Using [^{99m}Tc]Tc-PentixaTec

Johanna S. Enke[1], Nic G. Reitsam[2], Bianca Grosser[2], Malte Kircher[1], Alexander Dierks[1], Ralph A. Bundschuh[1,3], Georgine Wienand[1], Luise Uhrmacher[4], Martin Trepel[4], Margret Schottelius[5], Constantin Lapa[1,3], and Christian H. Pfob[1]

[1]Nuclear Medicine, Faculty of Medicine, University of Augsburg, Augsburg, Germany; [2]Pathology, Faculty of Medicine, University of Augsburg, Augsburg, Germany; [3]Bavarian Center for Cancer Research (BKFZ), Erlangen, Germany; [4]Hematology and Oncology, Faculty of Medicine, University of Augsburg, Augsburg, Germany; and [5]Translational Radiopharmaceutical Sciences, Departments of Nuclear Medicine and Oncology, Centre Hospitalier Universitaire Vaudois and University of Lausanne, Lausanne, Switzerland

In multiple myeloma, C-X-C motif chemokine receptor 4 (CXCR4) plays a pivotal role in cell migration, bone marrow infiltration, and resistance to therapy (*1*). Recently, CXCR4-directed theranostics has increasingly aroused clinical interest in the management of multiple myeloma, as CXCR4-directed PET/CT has proven a versatile tool both for detecting intra- and extramedullary manifestations (*2,3*) and for selecting patients who might benefit from chemokine receptor–directed therapy (*4,5*).

A 63-y-old woman with relapsed multiple myeloma was referred for further diagnostic work-up. After tandem autologous stem cell transplantation and maintenance therapy with lenalidomide, the patient experienced full-blown recurrence with disseminated intramedullary (90% infiltration of the bone marrow) and hepatic, renal, and cutaneous manifestations (as documented by [^{18}F]FDG PET/CT and CD138 immunohistochemistry of a bone marrow biopsy [Fig. 1A]). Subsequently, treatment with daratumumab, bortezomib, and dexamethasone was initiated. However, 3 wk later, rapid further disease progression with multiple new intramuscular and cutaneous lesions was noticed. Therapy was changed to carfilzomib, cyclophosphamide, and dexamethasone, but only exerted a good response of intramedullary multiple myeloma (with a reduction of malignant plasma cells to 10%) and the renal manifestation.

Consequently, the possibility of CXCR4-directed endoradiotherapy was assessed. Whole-body imaging with the novel tracer [^{99m}Tc]Tc-N4-L6-CPCR4 ([^{99m}Tc]Tc-PentixaTec) was performed, demonstrating marked receptor expression of the cutaneous and intramuscular lesions (Fig. 1B). Histopathology of a cutaneous nodule on the right upper thigh confirmed infiltration by CXCR4-positive malignant clonal plasma cells (Fig. 1C).

Given the increasing clinical interest in noninvasive, in vivo CXCR4 visualization, [^{99m}Tc]Tc-PentixaTec as a receptor ligand

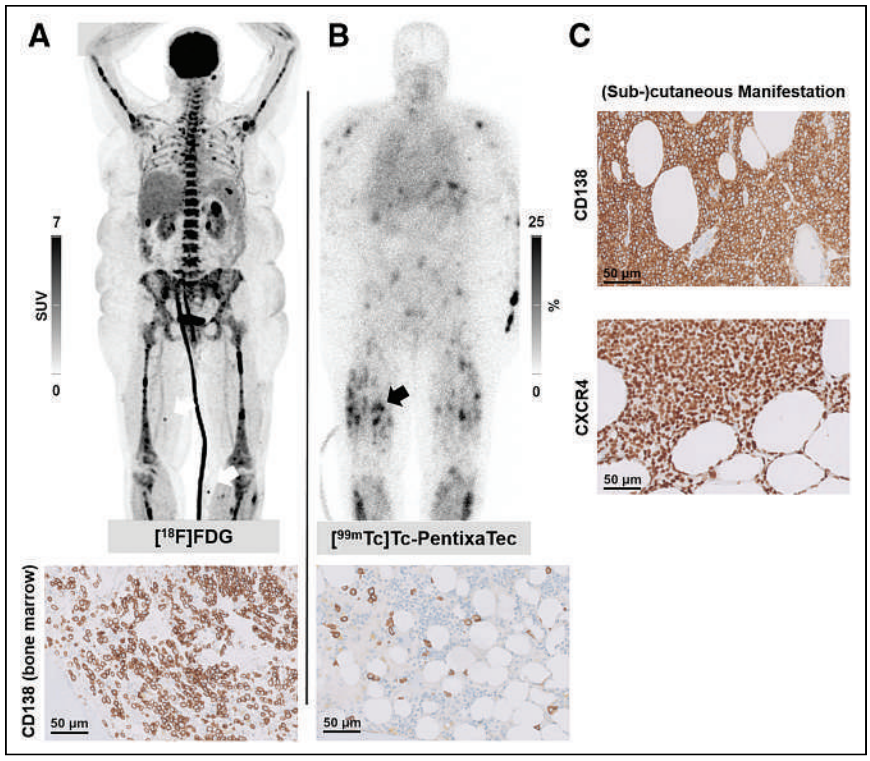

FIGURE 1. (A) Maximum-intensity projection of [^{18}F]FDG PET/CT (218 MBq, 60 min after injection), showing extensive CD138-positive intramedullary as well as hepatic, renal, and cutaneous (arrows) extramedullary lesions. Treatment with daratumumab, bortezomib, and dexamethasone was initiated. However, clinical progression with emergence of multiple new cutaneous lesions was noticed 3 wk later. (B) Subsequent planar whole-body scintigraphy with [^{99m}Tc]Tc-PentixaTec (470 MBq, 60 min after injection) depicts extensive CXCR4-positive cutaneous, subcutaneous, and intramuscular lesions (in contrast to good response of intramedullary multiple myeloma as proven by CD138 immunohistochemistry). (C) Immunohistochemistry staining of CD138 and CXCR4 of a subcutaneous lesion of thigh (black arrow, B) confirms marked chemokine receptor expression of nearly all malignant plasma cells.

Received Jul. 7, 2023; revision accepted Aug. 22, 2023.
For correspondence or reprints, contact Constantin Lapa (constantin.lapa@uk-augsburg.de)
Published online Sep. 14, 2023.

DOI: 10.2967/jnumed.123.266305

for use in conventional imaging with its lower costs and general availability might prove an interesting alternative to CXCR4-targeting PET vectors.

DISCLOSURE

No potential conflict of interest relevant to this article was reported.

REFERENCES

1. Alsayed Y, Ngo H, Runnels J, et al. Mechanisms of regulation of CXCR4/SDF-1 (CXCL12)-dependent migration and homing in multiple myeloma. *Blood.* 2007; 109:2708–2717.
2. Lapa C, Schreder M, Schirbel A, et al. [^{68}Ga]pentixafor-PET/CT for imaging of chemokine receptor CXCR4 expression in multiple myeloma: comparison to [^{18}F]FDG and laboratory values. *Theranostics.* 2017;7:205–212.
3. Pan Q, Cao X, Luo Y, Li J, Feng J, Li F. Chemokine receptor-4 targeted PET/CT with ^{68}Ga-pentixafor in assessment of newly diagnosed multiple myeloma: comparison to ^{18}F-FDG PET/CT. *Eur J Nucl Med Mol Imaging.* 2020; 47:537–546.
4. Lapa C, Herrmann K, Schirbel A, et al. CXCR4-directed endoradiotherapy induces high response rates in extramedullary relapsed multiple myeloma. *Theranostics.* 2017;7:1589–1597.
5. Herrmann K, Schottelius M, Lapa C, et al. First-in-human experience of CXCR4-directed endoradiotherapy with ^{177}Lu- and ^{90}Y-labeled pentixather in advanced-stage multiple myeloma with extensive intra- and extramedullary disease. *J Nucl Med.* 2016;57:248–251.

Debating the Future of Nuclear Medicine: The Greek Experience

TO THE EDITOR: We read with great interest the recent editorial by Graham regarding the progressive staffing shortage experienced by nuclear medicine in the United States (*1*). As the authors noted, the shortage is associated with inadequate production of well-trained nuclear medicine physicians during the last 2 decades. Interestingly, this workforce problem can be closely linked to a trend in hiring—in both academic programs and the private sector—diagnostic radiologists with minimal nuclear medicine training (1 y) instead of nuclear medicine physicians (*1*). Consequently, nuclear medicine has been considered a less attractive specialty by medical students, in parallel with a drop in the quality of applicants for nuclear medicine residency.

Notably, in some countries, such as Greece, nuclear medicine is a separate discipline, whereas in other parts of the world, such as the United States, nuclear medicine studies can also be performed by diagnostic radiologists. This heterogeneity has been reinforced by the introduction of hybrid systems (SPECT or PET combined with CT, and PET combined with MRI). Because both nuclear medicine physicians and diagnostic radiologists are involved in the performance of these techniques, a proposed solution was the establishment of joint training programs for hybrid imaging, currently available in only some countries (*2*).

From our point of view, nuclear medicine should continue as a separate discipline as we enter the era of personalized practice. Undoubtedly, the molecular imaging findings of SPECT or PET represent the most clinically valuable information obtained using hybrid systems. In particular, the functional–pathophysiologic findings of SPECT and PET are based on the principles of molecular imaging, and implementation of these techniques requires training in clinical medicine, as well as a thorough knowledge of radiochemistry (radiopharmacology, medical physics, and radiation protection). In addition, the development of radioactive agents able to diagnose and treat certain types of cancer (theranostics) may lead to crucial advancements in the management of oncology patients. Therefore, the growing field of theranostics applications for nuclear medicine should be prioritized and further supported, given the potential clinical impact on our patients.

At this point, we would like to add some information concerning the training and practice of nuclear medicine in Greece. The Hellenic Society of Nuclear Medicine and Molecular Imaging was founded in 1968, one of the oldest societies of nuclear medicine in Europe. The 5-y curriculum of residency includes training not only in nuclear medicine (33 mo) but also in radiology (9 mo, with a 6-mo internship in a CT unit and 3 mo in ultrasound or MRI studies), internal medicine (12 mo), cardiology (6 mo), or, alternatively, cardiology (4 mo) and oncology, hematology, pediatrics, or endocrinology (2 mo). There are more than 20 centers for residency across the country, including laboratories in university hospitals and departments in public and military hospitals. As far as the practice of nuclear medicine is concerned, the corresponding diagnostic and therapeutic applications can be performed only by nuclear medicine physicians. Particularly for hybrid imaging techniques, an experienced nuclear medicine physician can interpret a PET or SPECT scan combined with low-dose CT (used for localization, attenuation correction, and scatter correction), based on recent changes in state regulations. On the other hand, full diagnostic CT (or MRI) hybrid examinations are interpreted by an experienced nuclear medicine physician in cooperation with an experienced radiologist.

Under the current status of nuclear medicine practice in Greece, the departments of nuclear medicine provide services independently in public hospitals and the private sector. Recently, 4 modern PET/CT scanners were installed in nuclear medicine departments of university hospitals in the peripheral cities of Larissa (Thessaly), Heraklion (Crete), Ioannina (Epirus), and Alexandroupolis (Thrace), and 1 more PET/CT scanner was also installed in the nuclear medicine department of a military hospital, through a grant from the Stavros Niarchos Foundation. In parallel, despite a significant decrease in applications for nuclear medicine residency during the last decade, an increase in the number of residents has been observed recently, reflecting a positive message for the future of our discipline in Greece.

REFERENCES

1. Graham MM. The future of nuclear medicine in the United States. *J Nucl Med.* 2023;64:1352–1353.
2. Stokkel MPM, Owers EC. Hybrid training in nuclear medicine: where are we going to? *Eur J Nucl Med Mol Imaging.* 2023;50:2231–2235.

Panagiotis Georgoulias
George Angelidis*
Sophia Koukouraki
John Koutsikos
**University Hospital of Larissa*
Larissa, Greece
E-mail: angelidis@protonmail.ch

Published online Sep. 14, 2023.
DOI: 10.2967/jnumed.123.266646

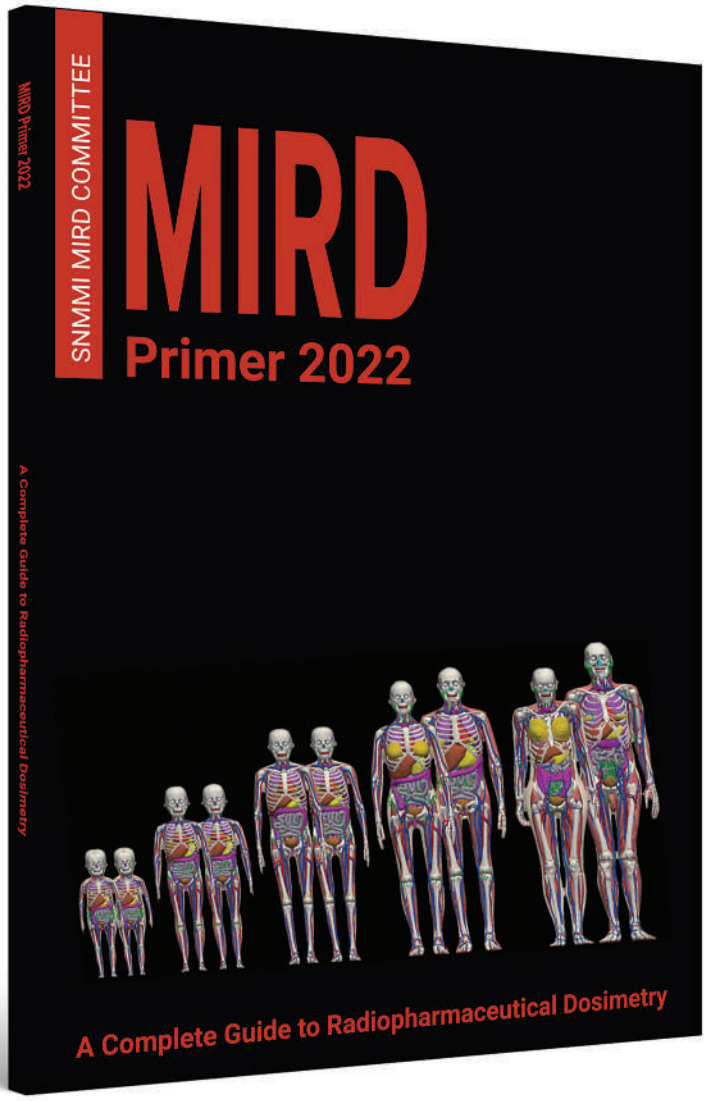

MIRD Primer 2022
A Complete Guide to Radiopharmaceutical Dosimetry

Richly illustrated and thoroughly referenced, the **MIRD Primer 2022** is a comprehensive, state-of-the-art guide to radiopharmaceutical dosimetry that reflects the dramatic evolution of the field of nuclear medicine, including molecular imaging and, increasingly, radiopharmaceutical therapy.

The MIRD Primer 2022 serves as

- a foundation for nuclear medicine and other medical professionals who require a working knowledge of internal radionuclide dosimetry and its radiobiological implications—without having to delve too deeply into the underlying mathematics.
- an authoritative reference on the latest, complete mathematical formulation of the MIRD schema for those seeking a more rigorous understanding of internal dosimetry.
- an invaluable teaching tool, with a large number and wide variety of clinically relevant calculational examples.

Order your copy today!

WWW.SNMMI.ORG/MIRD2022

SNMMI SOCIETY OF NUCLEAR MEDICINE & MOLECULAR IMAGING

The most powerful words you'll ever hear.

"Thank You."

With your contribution, our profession can continue efforts leading to critical advances in cancer treatments and care.

The **Mars Shot Research Fund** is the cornerstone for making these efforts a reality for patients of all ages.

The world needs more "thank you's."

Help improve the life of a patient. Lend your support today.

Help support the
SNMMI Mars Shot Research Fund:
WWW.SNMMI.ORG/MARSSHOT

SNMMI SOCIETY OF NUCLEAR MEDICINE & MOLECULAR IMAGING

SNMMI SOCIETY OF NUCLEAR MEDICINE & MOLECULAR IMAGING
MID-WINTER MEETING

ACNM
ANNUAL MEETING

REGISTER TODAY

WWW.SNMMI.ORG/MWM

SCAN QR CODE TO REGISTER

Feb. 1-3 2024 SNMMI Mid-Winter and ACNM Annual Meeting

Hilton Orlando Lake Buena Vista
ORLANDO, FLORIDA

The 2024 SNMMI Mid-Winter and ACNM Annual Meeting—February 1-3 in Orlando, FL—will feature three educational tracks highlighting the latest innovations and techniques in the field, including a dedicated track on therapeutics.

1/24

The Journal of Nuclear Medicine

January 2024 ▪ Vol. 65 ▪ Pages 1–165